JOURNAL OF THE
Electrochemical Society

VOL. 117 NO. 10 OCTOBER 1970

IMPROVE

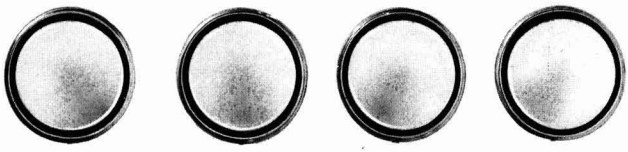

BATTERY

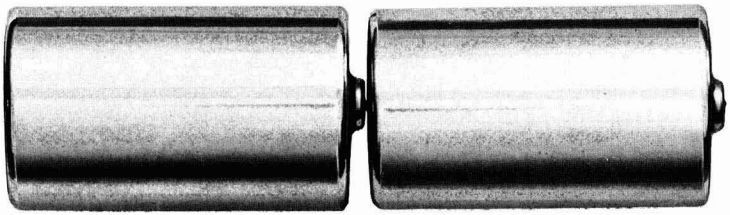

PERFORMANCE

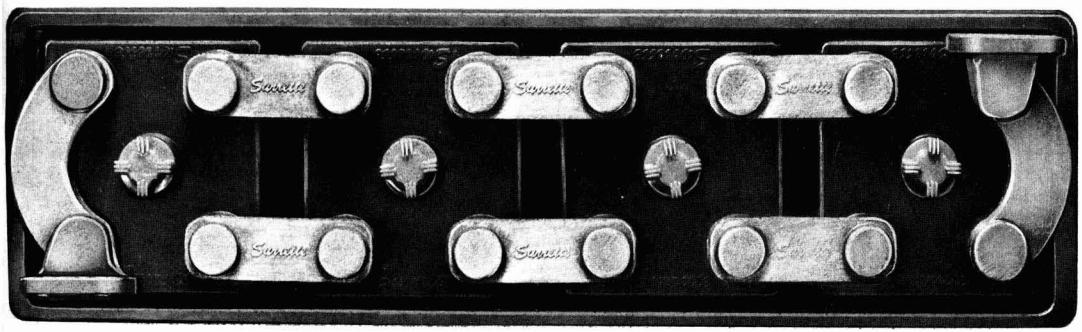

Battery performance gets a boost when you use Webril® nonwoven fabrics for separators and absorbers. For a number of very good reasons.

If primary and secondary battery systems are to perform much more reliably, they must inhibit dendrite growth and passage. Permit free ionic passage. Remain unaffected by acid or alkali. Loss of active plate material must be minimized. And electrolyte contact with plates must be assured. Webril nonwoven fabrics can do all this.

They have been performance-tested for over millions of hours in mercury-zinc, zinc-air, lead-acid, cuprous chloride, and nickel-cadmium systems. The unusually broad line of fine Webril products gives you greater design flexibility . . . even in fuel cells. You can choose from polypropylene, Dynel*, nylon, highly purified cotton, modified cellulose, and other fibers.

Find out more today. Write to Mr. P.N. Dangel, Electrical Specialties Department.

KENDALL

The Kendall Company
Fiber Products Division Walpole, Mass. 02081

*Union Carbide Corp. trademark for its modacrylic fiber.

JOURNAL OF THE

OCTOBER 1970

ELECTROCHEMICAL SCIENCE

TECHNICAL PAPERS

TECHNICAL NOTES

ELECTROCHEMICAL SOCIETY

Vol. 117 • No. 10

SOLID STATE SCIENCE

TECHNICAL PAPERS

Manuscripts submitted to the Journal should be sent, in triplicate, to the Editorial Office at 30 East 42 St., New York, N. Y., 10017. They should conform to the revised "Instructions to Authors" available from Society Headquarters. Manuscripts so submitted, as well as papers presented before a National technical meeting, become the property of the Society and may not be published elsewhere in whole or in part without written permission of the Society. Address such requests to the Editor.

The Electrochemical Society does not maintain a supply of reprints of papers appearing in its Journal. A photoprint copy of any particular paper may be obtained from University Microfilms, 300 North Zeeb Road, Ann Arbor, Michigan 48106.

Inquiries re positive microfilm copies of volumes should be addressed to University Microfilms, Inc., 300 N. Zeeb St., Ann Arbor, Mich. 48106.

Walter J. Johnson, Inc., 111 Fifth Ave., New York, N. Y., 10003, have reprint rights to out-of-print volumes of the Journal, and also have available for sale back volumes and single issues, with the exception of the current calendar year. Anyone interested in securing back copies should correspond direct with them.

Published monthly by The Electrochemical Society, Inc., at 215 Canal St., Manchester, N. H.; **Executive Offices, Editorial Office, and Circulation Dept.,** and **Advertising Office** at 30 East 42 St., New York, N. Y., 10017, combining the JOURNAL and TRANSACTIONS OF THE ELECTROCHEMICAL SOCIETY. Statements and Opinions given in articles and papers in the JOURNAL OF THE ELECTROCHEMICAL SOCIETY are those of the contributors, and The Electrochemical Society assumes no responsibility for them.

Claims for missing numbers will not be allowed if received more than 60 days from date of mailing plus time normally required for postal delivery of JOURNAL and claim. No claims allowed because of failure to notify the Circulation Dept., The Electrochemical Society, 30 East 42 St., New York, N. Y., 10017, of a change of address, or because copy is "missing from files." Subscription to members as part of membership service; subscription to nonmembers $40.00 plus $3.00 for postage outside U.S. and Canada. Single copies $2.50 to members, $4.00 to nonmembers. © 1970 by The Electrochemical Society, Inc. Second Class Postage Paid at New York, New York, and Manchester, N. H. Printed in U.S.A.

SOLID STATE SCIENCE (Cont.)

TECHNICAL NOTES

ELECTROCHEMICAL TECHNOLOGY

TECHNICAL PAPERS

TECHNICAL NOTE

REVIEWS AND NEWS

Only one company has developed compatible systems for all gases and handling equipment

In the world of computer systems, the word "compatible" has become almost synonymous with efficiency. The same can be said for the world of total gas systems, where it is now imperative that a system be customized to the gas being handled, if it is to perform efficiently and safely. Only Matheson can and does perform such compatible "marriages." A Matheson system consists of completely integrated equipment, such as regulators, valves, flowmeters, purifiers and generators — all blended together by Matheson's unique knowledge of speciality gases. The result is a system that will work! So if you are currently operating a system that is breaking down because of component incompatibility, check Matheson. Matheson marriages are not made in heaven, but here on earth they are the closest thing to it.

MATHESON GAS PRODUCTS
A Division of Will Ross, Inc.
East Rutherford, N. J.; Cucamonga, Calif.;
Gloucester, Mass.; Joliet, Ill.; LaPorte, Texas;
Morrow, Ga.; Newark, Calif.; Whitby, Ont.

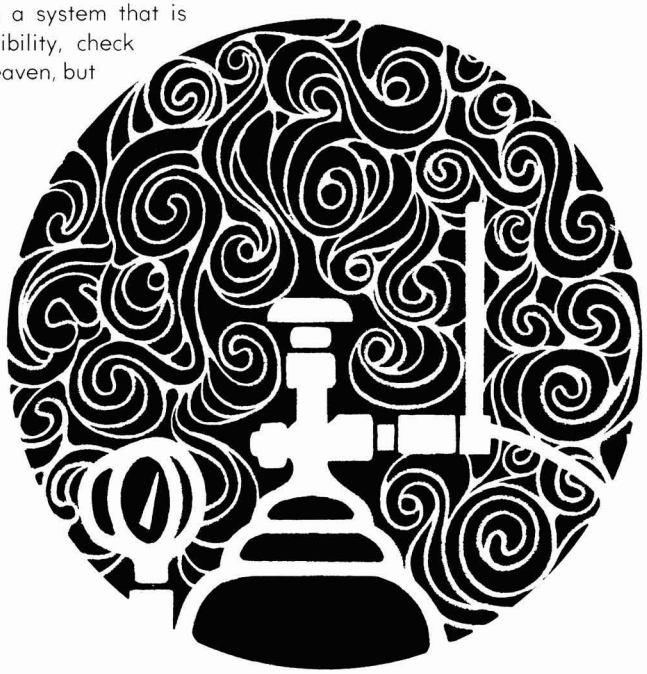

Write us for answers to your gas systems problems. Address: Matheson Gas Products, P. O. Box 85, East Rutherford, N. J. 07073

Matheson,

of course

26-70G

You're no better

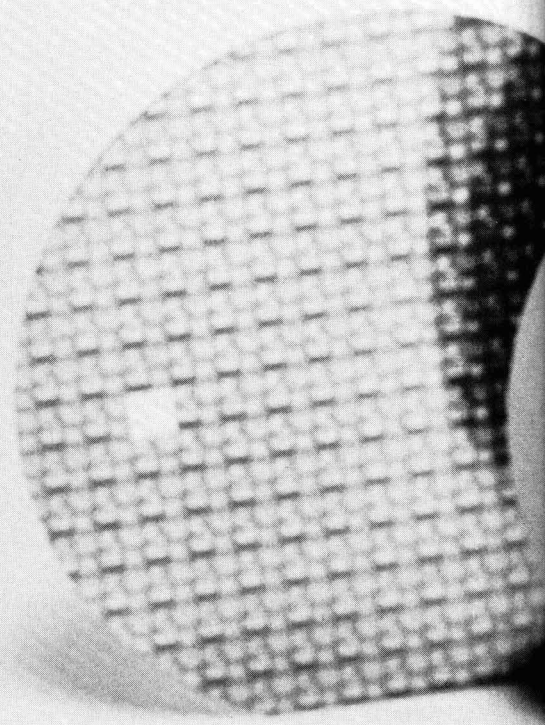

When the chips are down, no semiconductor device is better than the process equipment used to make it. If it isn't in the wafer, it isn't going to be. And that's where we can give you better control, tighter tolerances, endless repeatability and unsurpassed thin film uniformity and quality.

We manufacture the best epitaxial reactors and vapor phase deposition equipment in the industry. Bar none. Laboratory models that give you state-of-the-art processing to match your creative capabilities. Production models that transfer state-of-the-art achievements into large volume production quantities.

With Applied Materials, you get true uniformity of film characteristics not only across the wafer and from wafer-to-wafer within a run, but most important—the same degree of uniformity in run after run after run. Thickness, resistivity, dielectric characteristics and surface quality are often uniform beyond current capabilities in delta measurement techniques.

Applied Materials' specifications weren't developed

than your wafers.

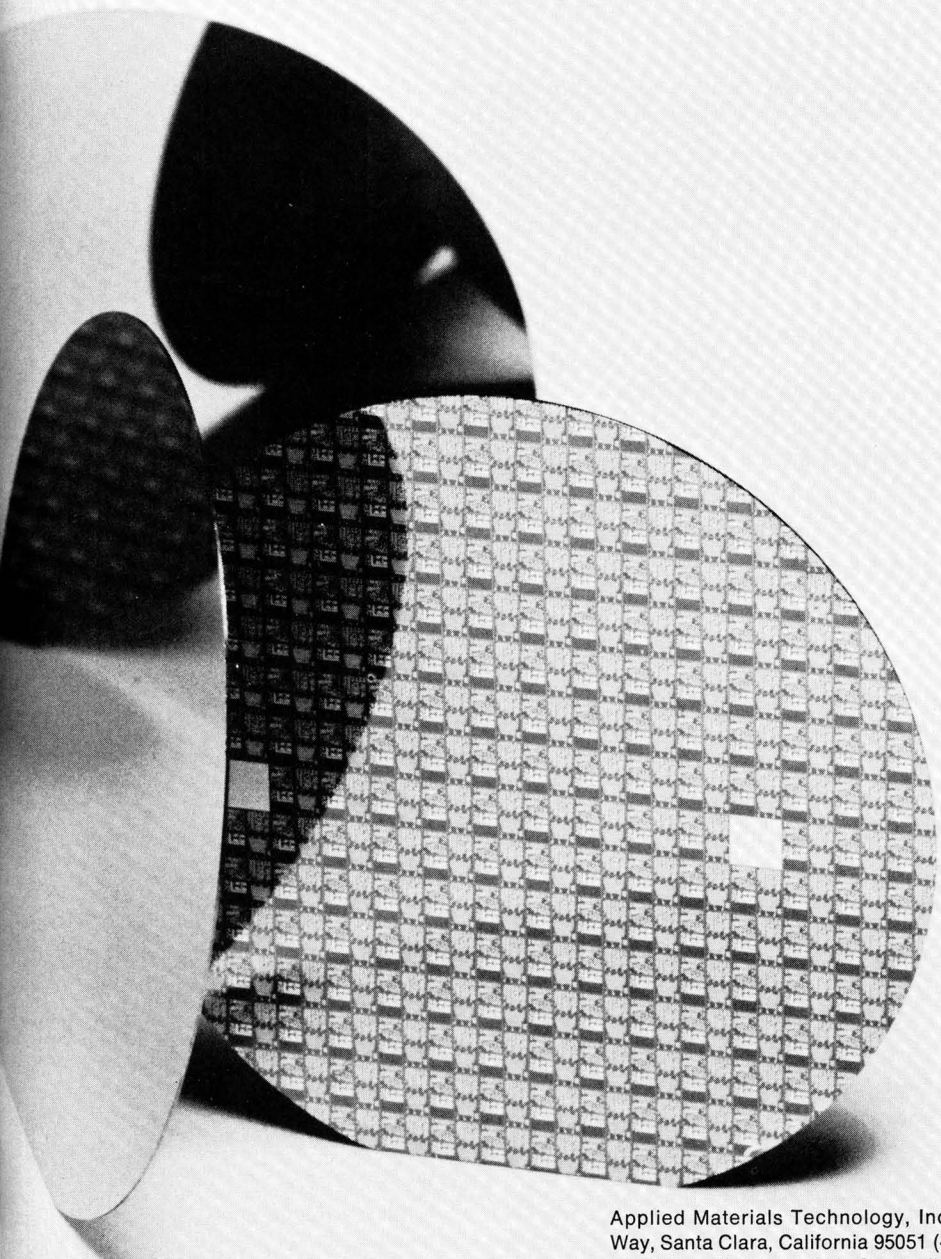

solely for exotic requirements. Backing up impressive technological accomplishments are the most rugged workhorses available for quantity production. Wafer to wafer. Run to run. You'll consistently produce better devices in thin film systems from Applied Materials Technology.

May we quote on your next purchase? Call collect for immediate requirements.

Applied Materials Technology, Inc., 2999 San Ysidro Way, Santa Clara, California 95051 (408) 738-0600 Telex: 34-6332 • 63 Route 206, Somerville, N.J. 08876, (201) 722-3300 Telex: 83-3439 • In Europe: Advanced Semiconductor Materials, Wokingham, U. K. Bilthoven, Netherlands; München, West Germany. In Japan: Kanematsu-Gosho, Tokyo.

applied materials

THE ELECTROCHEMICAL SOCIETY, INC.

The Electrochemical Society is an international organization of individuals and companies concerned with or interested in Electrochemistry and allied subjects.

OBJECTIVES

1. The advancement of the theory and practice of electrochemistry, electrometallurgy, electrothermics, electronics, solid state and allied subjects.
2. To encourage research and the reporting of such research for the dissemination of knowledge in the field of electrochemistry and solid state.
3. To insure the availability of adequate training in the field of electrochemistry for chemists, engineers, metallurgists, physicists, and solid state investigators.

BENEFITS OF MEMBERSHIP

1. Assurance of keeping abreast of the latest scientific developments in your particular fields of interest.
2. Enjoyment of personal association with fellow scientists and engineers in the professions.
3. Opportunity to contribute to the advancement of the science and application of electrochemistry and solid state in your areas of interest.
4. Stimulation of interdisciplinary exchanges.

DIVISIONS

The activities of the Society are carried on by its nine divisions as follows:

Battery
Corrosion
Dielectrics and Insulation
Electrodeposition
Electronics (Including Semiconductors and Luminescence)
Electro-Organic
Electrothermics and Metallurgy
Industrial Electrolytic
Theoretical Electrochemistry

SECTIONS

Local Sections of the Society have been organized in the following cities and regions:

Boston
Chicago
Cleveland
Columbus
Detroit
Indianapolis
Midland (Michigan)
Metropolitan New York
National Capital Area
Niagara Falls
North Texas
Ontario-Quebec
Pacific Northwest
Philadelphia
Pittsburgh
San Francisco
Southern California-Nevada
South Texas

JOURNAL OF THE ELECTROCHEMICAL SOCIETY

ELECTROCHEMICAL SCIENCE

OCTOBER 1970

The Sulfur Cathode in Liquid Ammonia

M. H. Miles*

Department of Chemistry, Middle Tennessee State University, Murfreesboro, Tennessee 37130

and W. S. Harris*,[1]

Naval Weapons Center, Corona Laboratories, Corona, California 91720

ABSTRACT

Electrochemical studies of sulfur-H_2S solutions in acid liquid ammonia electrolytes on silver and platinum surfaces over the temperature range of $+20°$ to $-50°C$ show that sulfur is a useful cathode for low-temperature fuel cells and batteries. The maximum theoretical coulombic efficiency of two electrons per sulfur atom can be obtained. The potentiostatic reduction of the sulfur species in stirred solutions shows that even at subzero temperatures the reactions achieve rates limited only by mass transport. The reaction on platinum apparently involves physical adsorption of the reacting sulfur species, while the reaction on silver involves chemical bonding of the sulfur species and formation of Ag_2S. Insoluble, electronically conducting Ag_2S should prove useful as a rechargeable cathode in batteries and fuel cells.

Solutions of elemental sulfur in liquid ammonia have been proposed for use as cathodes in low-temperature batteries (1-3). The actual species present when sulfur is dissolved in ammonia is still in question, especially since recent work has refuted the existence of S_4N_4 to any appreciable extent (4-8). The high solubility of sulfur in ammonia (5, 7) makes this inexpensive element attractive for use as the oxidant in low-temperature fuel cells and batteries using liquid ammonia electrolytes. A fuel cell consisting of liquid lithium ammoniate as the fuel and sulfur as the oxidant gives a theoretical energy density comparable to that of the H_2/O_2 fuel cell and, furthermore, shows promise of operation at subzero temperatures. Studies on the liquid lithium anode are in progress; results presented here are restricted to electrochemical investigations of sulfur solutions in liquid ammonia.

Experimental

The chemicals used include Matheson N.F. sublimed powder sulfur, Baker reagent NH_4NO_3 and $LiNO_3$, and Matheson anhydrous ammonia (99.99%), each used without further purification.

Potentiostatic measurements were made in liquid ammonia solutions stirred by a stream of ammonia gas. The current between the working and counterelectrodes was recorded *vs.* time and usually appeared to be fairly constant after several minutes. Measurements were made in the direction of both increasing and decreasing potentials, and the average value is reported.

Solution preparation, electrochemical cells, reference electrodes, temperature control, and electronic equipment is described elsewhere (9-10).

* Electrochemical Society Active Member.

[1] Present address: Mare Island Naval Shipyard, Vallejo, California.

Key words: ammonia, cathode, electrocatalysts, platinum, polysulfides, silver, silver sulfide, reduction, sulfur.

Results

Rate of solution.—Although sulfur is soluble in ammonia solutions in excess of 30% by weight (10M), the rate of solution is often slow; for example, in attempting to prepare a 0.1M sulfur solution in concentrated NH_3-$LiNO_3$ a dichroic blue-red solution formed which changed gradually to a yellow solution, but some of the sulfur remained undissolved even after ten days. During potentiostatic reduction, the color of this solution changed to a deep brownish red, and the excess sulfur dissolved. When H_2S is present even in low concentrations, however, the rate of solution of sulfur in ammonia is very rapid.

Electrocatalysts.—The electrochemical oxidation or reduction reactions of the sulfur-H_2S solution in acid liquid ammonia depend markedly on the nature of the metal electrode used. The platinum metals tested (Pt, Pd, Ir, Rh) along with Re, Au, W, Mo, and V show a large (over 0.3V) difference in the potentials at which significant electrode oxidation and reduction of the sulfur solution occur. For Ag, Hg, Cu, Pb, and Sn the oxidation reactions of the sulfur-H_2S solution are observed at potentials considerably more negative than for the Pt metals, and the reduction occurs at potentials close to those of oxidation. Results for Co and Ni are intermediate to those for Ag and Pt. For Fe, a large oxidation peak is observed, but no subsequent reduction peak could be detected.

The metals Ti, Zr, Hf, Th, Nb, Ta, Al, Ga, and In are completely inert toward any electrochemical reaction of the sulfur solution.

The results for the various metals are summarized in Table I by listing the metal at the potential (to the nearest 0.1V) where the oxidation and reduction currents due to sulfur or H_2S attain a value of 2 mA/cm^2 when the sweep rate is 125 mV/sec. Oxidation is repre-

Table I. Sulfur reactivity on various metals in NH_3-NH_4NO_3 at 20°C from cyclic voltammetric experiments

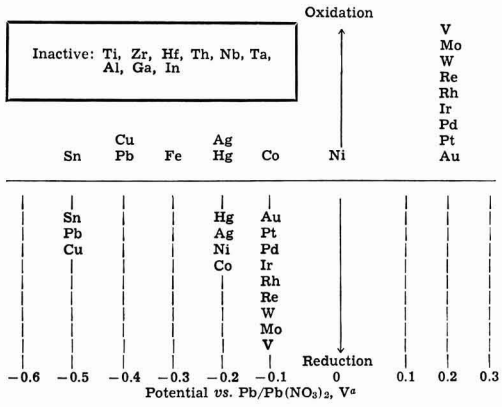

[a] The potential where the current density for the sulfur reaction is 2 mA/cm² at a sweep rate of 125 mV/sec (0.02M S + H_2S).

sented above and reduction below the center horizontal line.

Cyclic voltammetric experiments.—Figures 1-3 show cyclic voltammograms of sulfur-H_2S solutions in acid liquid ammonia. Figure 1 shows a typical cyclic voltammetric trace for sulfur on a platinum electrode with the dashed line indicating the background current of the NH_3-NH_4NO_3 solution alone.

Figure 2 shows the effect of the potential sweep rate on the oxidation and reduction peaks when a silver electrode is used. Making repeated sweeps with no wait time between successive sweeps gave very reproducible results. The anodic and cathodic peak currents are proportional to the square root of the sweep rate. The displacement of the peak potentials with increasing scan rates suggests uncompensated iR effects (11, 12) due to the large currents obtained. From Fig. 2, this effect is about 1.5 V/A, suggesting that the uncompensated resistance between the reference and working electrodes is a reasonable value of about 1.5 ohms. Figure 3 shows the sulfur reactions on the silver

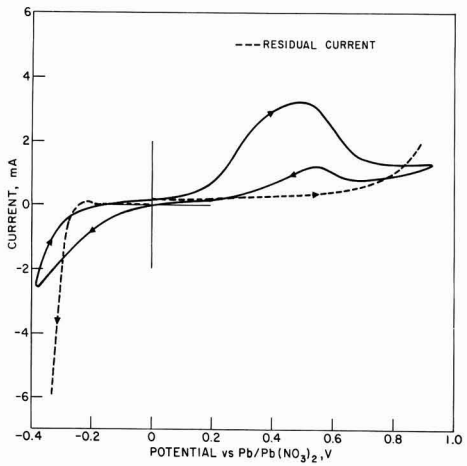

Fig. 1. Cyclic voltammogram for 0.1M sulfur, H_2S solution in NH_3-NH_4NO_3 at 15°C using platinum wire electrode with geometrical area = 0.3 cm². Potential sweep began at 0.0V and swept first in the anodic direction. Sweep rate = 100 mV/sec.

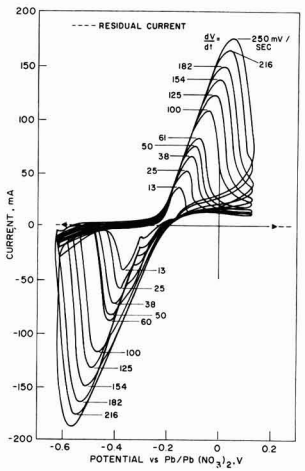

Fig. 2. Effect of potential sweep rate on cyclic voltammograms for 0.1M sulfur, H_2S solution in NH_3-NH_4NO_3 at 15°C using silver wire electrode with geometrical area = 0.3 cm².

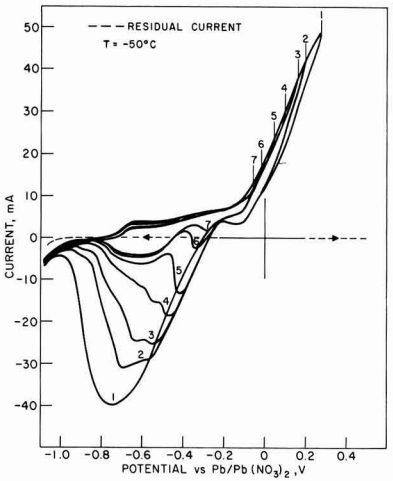

Fig. 3. Cyclic voltammograms for 0.1M sulfur, H_2S solution in NH_3-1M NH_4NO_3 at −50°C on the silver wire electrode as a function of the anodic potential sweep limit.

electrode at −50°C as a function of the anodic sweep range limit during continuous potential sweeps.

Constant current experiments.—Typical curves for the constant current reduction of sulfur in stirred acid ammonia solutions at 15°C on silver and platinum electrodes are shown in Fig. 4. A sharp inflection in potential is observed when 2 electrons are consumed in the reaction per atom of sulfur initially present. A similar study at −10°C on silver also gave nearly 2 electrons per sulfur atom. Constant current studies on nickel show evidence for sulfur reduction but gave no clear inflection, while tantalum showed complete inactivity toward any sulfur reduction.

Potentiostatic experiments.—Potentiostatic studies of the electrochemical reduction of sulfur solutions on silver and platinum surfaces in stirred acid liquid ammonia solutions at 15° and −35°C are presented in Fig. 5-6. The residual current shown is the current obtained before sulfur and H_2S were added and results mainly from the reduction of NH_4^+ to hydrogen gas. The rest potential in the 0.1M sulfur, H_2S solution was −0.15V with the silver electrode and 0.0V for the

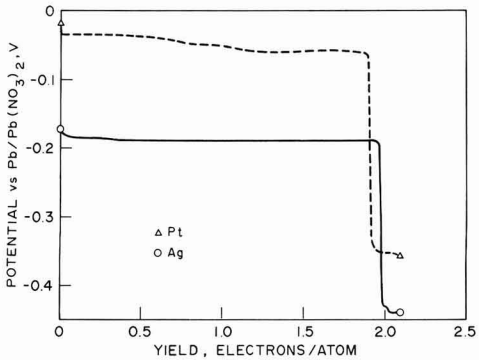

Fig. 4. Constant current reduction of sulfur, H_2S solutions in stirred NH_3-NH_4NO_3 on platinum and silver electrodes of about 50 cm^2 geometrical area. $I = 1.00$ mA; $T = 15°C$.

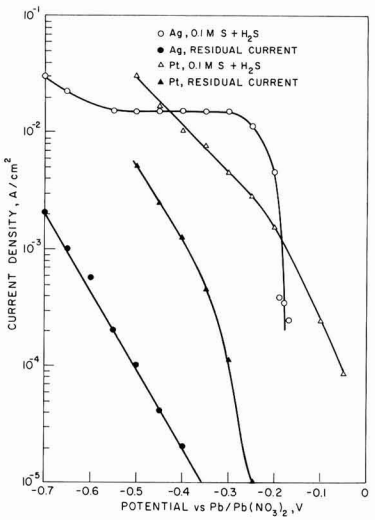

Fig. 5. Potentiostatic reduction of 0.1M sulfur, H_2S solutions in NH_3-NH_4NO_3 on silver and platinum electrodes. $T = 15°C$.

platinum electrode, both potentials measured at 15°C against a Pb/saturated $Pb(NO_3)_2$ reference electrode. The reaction rate for the reduction of sulfur appears to be faster on silver than on platinum since with the silver electrode there is a sharper increase in reduction current density with overvoltage (Fig. 5). The reduction of sulfur on silver achieves mass transport limitation since a limiting current is reached which is markedly dependent on the rate of stirring. Stopping the stirring action causes the current to fall suddenly; recovery is quick when stirring is resumed. The reduction current for the sulfur reaction on platinum at high overvoltage is also affected by the rate of stirring. Note that the limiting current attained on silver is higher at −35°C (Fig. 6) than at +15°C, probably resulting from the lower viscosity of the less concentrated 1M NH_4NO_3 solution.

Neutral solutions.—Thus far the results have all been for acid (NH_4NO_3) ammonia solutions to which H_2S was added to accelerate the rate of solution of the sulfur. The results are quite different for sulfur dissolved in neutral ($LiNO_3$) ammonia solutions where no H_2S is used. Cyclic voltammetric experiments on the sulfur dissolved in neutral liquid ammonia showed no evidence for any electrochemical oxidation or reduction of sulfur on silver or platinum electrodes. Con-

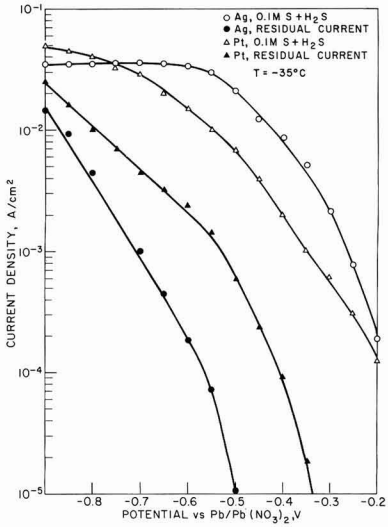

Fig. 6. Potentiostatic reduction of 0.1M sulfur, H_2S solutions in NH_3-1M NH_4NO_3 at −35°C on silver and platinum electrodes.

stant current experiments in stirred neutral ammonia solutions on silver and platinum electrodes showed similar negative results. Unlike the behavior shown in Fig. 4, when reduction begins, the potential quickly drops to about −2.3V, indicating that the sulfur remains unreacted, and lithium ions are being reduced. Addition of Li_2S produced no change in these experiments, but the addition of H_2S quickly rendered the sulfur reducible. Similarly, potentiostatic measurements showed very little reduction of sulfur until H_2S is added to the solution.

These very different effects of Li_2S and H_2S on the sulfur solution in neutral ammonia supports the findings of Nelson and Lagowski (8) that H_2S in ammonia forms a hydrogen-bonded species, $[SHNH_3]^-$, but produces no free sulfide ions, while sulfide ions added to ammonia do not undergo ammonolysis to HS^-. Apparently, the species $[SHNH_3]^-$ is necessary to render the dissolved sulfur electrochemically active. The reactive forms of sulfur probably are polysulfides since solutions of sulfur and H_2S in liquid ammonia have been shown to produce polysulfides, and the compound $(NH_4)_2S_5$ has been isolated (5, 13).

Discussion

In evaluating the sulfur cathode for fuel cell or battery use in liquid ammonia electrolytes, the constant current studies are a measure of the coulombic efficiency. The constant current studies of sulfur reduction on platinum and silver (Fig. 4) show that, within experimental error, the maximum theoretical coulombic efficiency of two electrons per sulfur atom can be obtained on these two metals. This indicates that there are no detrimental side reactions or decomposition of the reactant during the 40-hr time span of the experiments. Similar studies on silver at −10°C gave approximately the same results as obtained at +15°C, showing that this high coulombic efficiency does not decrease appreciably with decreasing temperature.

The potentiostatic investigations in the stirred solutions are a measure of the dynamic performance of the sulfur cathode in a flowing electrolyte feed fuel cell. Figures 5 and 6 indicate that the dynamic performance of the sulfur cathode is at least as good on silver as on platinum. The rest potential of the sulfur cathode is more negative on silver than on platinum, but a limiting current is reached at considerably lower overvoltages on the silver electrode. The dynamic performance of the sulfur cathode at −35°C (Fig. 6) indicates

satisfactory low-temperature operations, especially considering that the reactions achieve rates limited only by mass transport, and that much higher sulfur concentrations are feasible. Using the expression (14)

$$i_L = n\mathbf{F}D\delta^{-1}C \qquad [1]$$

for the limiting current dsnsity, i_L, where D is the diffusion coefficient, δ is the thickness of the diffusion layer, C is the bulk concentration of reactant, and n and $\mathbf{F}$ are the usual electrochemical quantities, we calculate from the results on silver (Fig. 5 and 6) that $D\delta^{-1} = 10^{-3}$ cm sec^{-1}. Since δ is usually about 10^{-3} cm in stirred systems, the diffusion coefficient of the reacting sulfur species is roughly 10^{-6} cm^2 sec^{-1}, a reasonable value (10), indicating that the reaction is indeed limited by mass transport.

A probable general reaction mechanism for the sulfur reactions in ammonia is

$$x\mathrm{M} + y\mathrm{S} \rightleftharpoons \mathrm{M}_x \ldots \mathrm{S}_y \underset{-2ye^-}{\overset{+2ye^-}{\rightleftharpoons}} x\mathrm{M} + y\mathrm{S}^= \qquad [2]$$

where M represents the electrode metal and S and $S^=$ are likely part of a polysulfide ion, $S_x^=$. The $M_x \ldots S_y$ bond may range from simple electrode absorption to an actual metallic sulfide compound. Both Ag_2S and PtS, like most sulfides of the electrode metals tested, are black compounds which are insoluble in liquid ammonia, and therefore readily detectable if formed in significant amounts. During the electrochemical studies on platinum of the sulfur-H_2S solutions in liquid ammonia, the platinum electrodes maintain a bright, metallic luster indicating very little build-up of any metallic sulfide compounds. However, when a silver electrode remains at open circuit in the sulfur-H_2S solution, or during electrochemical oxidation of the solution on silver, the silver electrode becomes black, indicating formation of Ag_2S from the chemical reaction

$$2\mathrm{Ag} + \mathrm{S} \rightleftharpoons \mathrm{Ag_2S} \qquad [3]$$

or from the electrochemical reaction

$$2\mathrm{Ag} + \mathrm{S}^= \rightleftharpoons \mathrm{Ag_2S} + 2e^- \qquad [4]$$

Constant current coulometry experiments show that the electrochemical oxidation of ammonia-H_2S solutions on silver produces insoluble products which can be quantitatively reduced. An acid ammonia solution saturated with H_2S was oxidized on silver for 1800 sec at 0.500 mA, turning the electrode black. The solution was then stirred for 30 min to allow any soluble sulfur products to dissolve, then the electrode was transferred to a separate compartment with fresh electrolyte. Reduction at the same current, 0.500 mA, produced a gradual fading of the black color with a sharp inflection in potential after 1815 sec, indicating that the silver had been oxidized to insoluble Ag_2S and then was quantitatively reduced. Figure 7 shows the results of this test and results for a silver control electrode in a similar solution showing that the reduction is not observed without first forming silver sulfide. Similar tests on platinum showed oxidation of the ammonia-H_2S solution at about 0.0V with the electrode remaining bright. Reduction in a separate compartment showed only hydrogen evolution, indicating that no insoluble platinum sulfide compounds were formed on the platinum electrode during oxidation of the ammonia-H_2S solution. These experiments suggest that in reaction [2], $M_x \ldots S_y$ represents chemical bonding with formation of a metallic sulfide compound on silver while the bonding on platinum is of a different nature.

The very different peak potentials and peak currents observed in the cyclic voltammetric experiments on platinum and silver (Fig. 1 and 2) reflect the different nature of the sulfur reactions on these two surfaces. On the silver electrode, formation of the electronically conducting Ag_2S greatly increases the

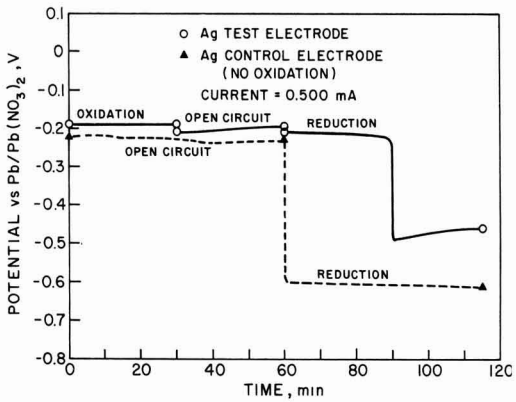

Fig. 7. Constant current coulometry experiments on silver in NH_3-NH_4NO_3 solutions containing H_2S using constant currents of 0.500 mA. Electrode area = 2 cm^2, T = 15°C.

effective electrode area, resulting in higher currents. The peak currents on the silver electrode in sulfur-H_2S solutions are quite insensitive to the bulk sulfur concentration; also the number of coulombs involved in the reaction peaks (Fig. 2) are independent of the potential sweep rate, indicating that we are essentially observing reaction [4] involving insoluble Ag_2S. The reversibility of this reaction suggests use of Ag_2S as a rechargeable cathode in liquid ammonia batteries or fuel cells. Figure 3 indicates that reaction [4] occurs readily even at −50°C, indicating good performance of the Ag_2S cathode at subzero temperatures.

Table II gives the free energy of formation, ΔG_f°, for several metallic sulfides along with the calculated standard electrode potential for the reaction $M_xS_y + 2ye^- \rightleftharpoons xM + yS^=$ in aqueous solutions. The variation in the standard potentials from that for silver, E°-$E^\circ_{Ag_2S}$, reflects solely the differences in ΔG_f° for the metallic sulfide, hence the variation should be the same in liquid ammonia solutions for the above reaction. The difference in the potentials in Table I at which electrochemical oxidation of the sulfur-H_2S solution in ammonia is observed may reflect such thermodynamic effects when the $M_x \ldots S_y$ bond involves chemical bonding. Comparing Tables I and II indicates that the sulfur reactions on Hg, Fe, Cu, Pb, and Sn probably involve chemical bonding as found for silver since, as thermodynamically expected, the reactions are observed at potentials negative to the reaction on silver. The sulfur oxidation reactions on Pt, Ir, Mo, Ni, and Co are observed at potentials considerably more positive than thermodynamically expected,

Table II. Thermodynamic data[a]

Compound	ΔG_f°, kcal/mole[b]	E°, V[c]	$E^\circ - E^\circ_{Ag_2S}$, V
Ag_2S	−9.72, α	−0.66	0.00
HgS	−11.4, black	−0.69	−0.03
PtS_2	−23.8	−0.70	−0.04
CuS	−12.8	−0.72	−0.06
IrS_2	−33.0*	−0.80	−0.14
PtS	−18.2	−0.84	−0.18
NiS	−19.0	−0.86	−0.20
CoS	−19.8*	−0.87	−0.21
FeS_2	−39.9	−0.88	−0.22
Cu_2S	−20.6, α	−0.89	−0.23
SnS	−23.5	−0.95	−0.29
PbS	−23.6	−0.96	−0.30
FeS	−24.0	−0.97	−0.31
MoS_2	−54.0	−1.03	−0.37

[a] See USNBS Tech. Notes 270-3 (Jan., 1968) and 270-4 (May, 1969).
[b] Gibbs free energy of formation for the metallic sulfide compound.
[c] Standard electrode potential at 25°C for the reaction $M_xS_y + 2ye^- \rightarrow xM + yS^=$ in aqueous solution. For $S^=$(aq), ΔG_f° = 20.5 kcal/mole from the above reference.
* ΔH_f° (ΔG_f° is not given).

indicating that metallic compounds are not involved in these reactions. Much weaker $M_x \ldots S_y$ bonds are apparently formed on these metals. From the difference in rest potentials for the Ag and Pt electrodes in sulfur-ammonia solutions (0.15V), it is estimated that $\Delta G_f^\circ = -3$ kcal/mole for the Pt . . . S bond formed in the electrochemical reaction. This small value suggests that weak, adsorption bonding of the sulfur species to the platinum surface is involved.

Other metals which form weak, adsorption bonds with the sulfur species would be expected to show electrochemical behavior similar to platinum. The metals inactive toward the sulfur-ammonia solution apparently do not form either chemisorption or physical adsorption bonds with the sulfur species. This inactivity may be due to oxide or nitride films on the metal which persist during the electrochemical experiments.

Summary

1. The reduction of sulfur in platinum and silver electrodes in acid ammonia solutions yields the maximum theoretical coulombic efficiency of two electrons per sulfur atom.

2. Potentiostatic measurements in stirred solutions show that even at subzero temperatures the reactions achieve rates limited only by mass transport.

3. The electrochemical reactions of sulfur on platinum and silver are different in nature. Apparently, physical adsorption is involved on platinum, while chemisorption and Ag_2S formation occurs on silver.

4. Electronically conducting Ag_2S may be useful as a rechargeable cathode in liquid ammonia batteries and fuel cells. The oxidation and reduction reactions involving this compound occur readily even at $-50°C$.

5. Cyclic voltammetric screening of various metals indicates their activity toward the sulfur reactions. Interpretations of these results are given in terms of the thermodynamics of the metal-sulfur bond.

Manuscript submitted Nov. 17, 1969; revised manuscript received *ca.* April 15, 1970. This is Paper 59 which was presented at the Atlantic City Meeting of the Society, Oct. 4-8, 1970.

Any discussion of this paper will appear in a Discussion Section to be published in the June 1971 JOURNAL.

REFERENCES

1. W. F. Meyers, U.S. Pat. 2,996,562 (*C.A.*, **56**, 1294, 1962).
2. A. L. Almerini and H. R. Knapp, U.S. Pat. 3,309,230 (*C.A.*, **67**, 17317, 1967).
3. K. Posey and J. K. Truitt, U.S. Pat. 3,408,299 (*C.A.*, **69**, 112904, 1968).
4. A. P. Zipp, Ph.D. Dissertation, University of Pennsylvania, 1964.
5. A. P. Zipp and S. G. Zipp, *Sulphur Inst. J.*, **2** (Spring, 1968).
6. A. P. Zipp and E. C. Evers, *Inorg. Chem.*, **8**, 1746 (1969).
7. J. T. Nelson and J. J. Lagowski, *ibid.*, **6**, 1292 (1967).
8. J. T. Nelson and J. J. Lagowski, *ibid.*, **6**, 862 (1967).
9. M. H. Miles and P. M. Kellett, *This Journal*, **115**, 1225 (1968).
10. M. H. Miles and P. M. Kellett, *ibid.*, **117**, 60 (1970).
11. R. S. Nicholson, *Anal. Chem.*, **37**, 667 (1965).
12. B. L. Funt and D. G. Gray, *Can. J. Chem.*, **46**, 1337 (1968).
13. P. J. Durrant and B. Durrant, "Introduction to Advanced Inorganic Chemistry," p. 829, John Wiley & Sons, Inc., New York (1962).
14. K. R. Williams, Editor, "An Introduction to Fuel Cells," pp. 36-40 Elsevier Publishing Co., New York (1966).

Anodic Polarization of Passive Electrodes

D. A. Vermilyea*

Surfaces and Reactions Branch, Physical Chemistry Laboratory, General Electric Company, Schenectady, New York 12301

ABSTRACT

Anodic current flow at a passive electrode lowers the surface *p*H and increases the corrosion and film dissolution rates. Analytical expressions are obtained to permit the calculation of the rates of formation of new film and soluble species. It is shown that when equilibrium is achieved between the film and the solution, as with magnesium, polarization of only a few tens of millivolts can result in current densities of the order of 1 A/cm². For metals forming films which dissolve more sluggishly it is often necessary to exceed the oxygen evolution potential before large currents can be achieved. Thick anodic films can be formed when the film blocks oxygen evolution and when the film dissolution rate constant is small. Buffers suppress the *p*H change at the surface and may prevent rapid dissolution and corrosion.

The purpose of this paper is to discuss the effects on the current and corrosion rate of the application of anodic currents to passive metals. Passivity is difficult to define adequately, and for this discussion a passive metal is one covered with an oxide or hydroxide film which substantially impedes corrosion. Such a film will often comprise a dense barrier layer of a poorly crystallized material next to the metal and a porous layer of a better crystallized product next to the solution. Application of an anodic current will usually lower the *p*H at the electrode surface, and that in turn will effect the rate of dissolution of the protective film. It is this effect of *p*H on film dissolution which is to be considered. Localized attack is outside the scope of this paper.

* Electrochemical Society Active Member.
Key words: corrosion, films, dissolution.

The Initial Condition

Consider a film covered specimen in a nearly steady state, with a barrier layer of constant thickness and a porous layer whose thickness is changing slowly. Corrosion at this specimen produces more film (which could be oxide or hydroxide) at a rate r_{f_0} according to a reaction like

$$M + zH_2O \rightarrow M(OH)_z + z/2\, H_2 \qquad [1]$$

where z is the metal valence, and soluble species at a rate r_{s_0} according to

$$M + zH_2O \rightarrow M^{+z} + zOH^- + z/2\, H_2 \qquad [2]$$

the total rate being r_0.

Application of Current

Upon application of an external current, additional hydroxide will be formed at a rate r_f according to

$$M + zH_2O \rightarrow M(OH)_z + zH^+ + ze \quad [3]$$

and additional metal ions at a rate r_s according to

$$M \rightarrow M^{+z} + ze \quad [4]$$

It may be noted that, as far as soluble species are concerned, metal ions are generated by r_s and r_{so}, hydroxyl ions are generated by r_{so}, and protons are generated by r_f.

For simplicity it will be assumed that the solution is sufficiently concentrated that electrical transport can be neglected and the Nernst approximation will be used to describe diffusion near the specimen. Equations for mass balances are then the following

$$\dot{n}_M + z = \frac{10^{-3}D_{M+z}\,\Delta C_{M+z}}{\delta} = r_{so} + r_s \quad [5]$$

$$\dot{n}_{H+} = \frac{10^{-3}D_{H+}\,\Delta C_{H+}}{\delta} = zr_f - zr_{so} \quad [6]$$

if there is a net production of protons in an acid solution

$$\dot{n}_{H+} = \frac{10^{-3}[D_{H+}(C_{H+})_i + D_{OH-}C_{OH-}]}{\delta} = zr_f - zr_{so} \quad [7]$$

if there is a net production of protons in a solution containing C_{OH-} hydroxyl ions per liter

$$\dot{n}_{OH-} = \frac{10^{-3}\,D_{OH-}\,\Delta C_{OH-}}{\delta} = zr_{so} - zr_f \quad [8]$$

if there is a net production of hydroxyl ions in a basic solution; and

$$\dot{n}_{OH-} = \frac{10^{-3}[D_{OH-}(C_{OH-})_i + D_{H+}C_{H+}]}{\delta} = zr_{so} - zr_f \quad [9]$$

if there is a net hydroxyl ion production in an acid solution with a proton concentration C_{H+}. In Eq. [5]-[9] the $\dot{n}$'s represent rates of generation or removal of the various species, the D's represent diffusion coefficients, δ (assumed the same for all ions) is the thickness of the Nernst layer, the ΔC's represent the concentration difference in moles per liter between the surface and the bulk solution, and the subscript i indicates an interface concentration.

The total external current density, i, is given by

$$i = \sum_j m_j \mathbf{F} \dot{n}_j \quad [10]$$

in which the summation is over all species, and where m_j is the charge on each particle. It can readily be verified that $i = z\mathbf{F}(r_f + r_s)$. Equations [5]-[10] can now be used to find out how an external current will influence the corrosion of the metal. There are two situations of interest, depending on whether or not equilibrium is achieved at the film-solution interface.

Case I. Equilibrium at Film-Solution Interface

For this case the equilibrium conditions are given by

$$K_s = (M^{+z})(OH^-)^z \quad [11]$$

and

$$K_w = (H^+)(OH^-) \quad [12]$$

where the quantities in brackets represent activities. From Eq. [11] and [12], approximating activities with concentrations

$$(C_{M+z})_i = \frac{K_s(C^z{}_{H+})_i}{K_w{}^z} \quad [13]$$

Equation [10] can now be used with Eq. [13] to find the current density in situations of interest.

Two examples of the use of the equations will illustrate their utility. Consider first magnesium with a film of $Mg(OH)_2$,[1] with $z = 2$, $\delta = 10^{-2}$ cm, $D_{Mg+2} = 10^{-5}$ cm^2/sec, $D_{OH-} = 3 \cdot 10^{-5}$ cm^2/sec, $D_{H+} = 10^{-4}$ cm^2/sec, $\mathbf{F} = 10^5$ coul/eq., $K_s = 10^{-11}$, $K_w = 10^{-14}$, and in the bulk solution $C_{OH-} = 10^{-4}$ moles/liter. In this example there is a net production of protons in an alkaline solution, assumed to contain an excess of supporting electrolyte. Equations [5], [7], [10], and [13] give for the current density

$$i = \frac{10^{-3}\mathbf{F}[D_{H+}(C_{H+})_i + D_{OH-}C_{OH-}]}{\delta} + \frac{10^{-3}z\mathbf{F}}{\delta} D_{M+z} \frac{K_s}{K_w{}^z} (C^z{}_{H+})_i \quad [14]$$

For a current density of 10^{-1} A/cm^2 the surface concentrations of magnesium ions and protons are found to be 0.5M and 2.24 x 10^{-9}M (pH 8.65), respectively, and nearly all the current is carried by Mg^{+2}. Previous studies of corrosion of magnesium and of dissolution of $Mg(OH)_2$ (2) have shown that a dissolution or corrosion rate of 10^{-10} moles/cm^2 sec can be expected at about pH 9. Using that rate for r_{so} in Eq. [7] we find $zr_f = 2.14 \times 10^{-10}$ moles/cm^2 sec, or $i_f = 2.14 \times 10^{-5}$ A/cm^2. Thus a very small fraction of the applied current produces more film.

Magnesium does actually behave in solutions with pH > 5 as predicted by these equations. The hydroxide layer covering the surface is porous and its growth slows the reaction only moderately (1). Presumably this porous film can readily accept the additional small amount of reaction product corresponding to r_f without blocking the reaction. As a result of this film formation, however, the pH is reduced and the magnesium ion concentration becomes large enough to carry a high current. The end result of anodic corrosion of thin magnesium specimens is a very porous, fragile, but coherent hydroxide replica of the original specimen, which shows that hydroxide is indeed formed by the passage of current.

As a second example consider beryllium, with a film of $Be(OH)_2$ having $K_s = 10^{-26}$ in a pH 5 solution containing excess supporting electrolyte. Taking $D_{Be+2} = 10^{-5}$, Eq. [5], [6], [10], and [13] show that for $i = 10^{-1}$ A/cm^2 $C_{H+} = 0.05$ moles/liter, $C_{Be+2} = 0.25$ moles/liter. If r_{so} is assumed to be 10^{-14} moles/cm^2 sec, a value calculated from the solubility product of $Be(OH)_2$ assuming that the spontaneous reaction is diffusion controlled in the pH 5 solution, then Eq. [6] gives $zr_f = 5 \times 10^{-7}$ moles/cm^2 sec so that $i_f = 0.05$ A/cm^2 and $i_s = 0.05$ A/cm^2. In this example a very large change in pH is required to produce a high current density, so that a large amount of new film must be produced, and both protons and metal ions carry a significant fraction of the current. The experimental situation is not so well known for beryllium as for magnesium, and in particular it is not known whether equilibrium is achieved at the solution-film interface.

Discussion of Case I.—Constancy of r_{so} was assumed and in the examples given the values of r_{so} were so low compared to other rates that the approximation is reasonable. Usually anodic polarization would decrease the spontaneous cathodic reaction and hence decrease r_{so}, and for some situations a good approximation may be to ignore r_{so} in Eq. [5]-[9]. On the other hand, strong anodic polarization and a large decrease in pH may decrease the barrier film thickness significantly and result in an enhanced cathodic reaction and increased r_{so}.

It is possible that the specimen may become film free as a result of anodic polarization. For example, for a metal which is relatively unreactive in a thermodynamic sense the hydrolysis of metal ions may produce a pH low enough to make the film unstable at

[1] There may be a MgO layer between this film and the metal, but at long times the $Mg(OH)_2$ layer controls the corrosion behavior.

the applied potential. The present analysis does not apply to such a situation.

Finally, the current-potential behavior is of interest. If equilibrium is achieved at the interface, and if the solution is very concentrated so that no changes in the total ion concentration take place in the Nernst layer, then only a resistive polarization occurs. In a less concentrated solution concentration polarization occurs in the Nernst layer and some additional polarization will be present. Such concentration polarization can be calculated from the equation (3)

$$E = \frac{RT}{z\mathbf{F}} \ln \left(1 + \frac{i\delta}{z\mathbf{F}D \cdot 10^{-3}C_o} \right) \qquad [15]$$

in which E is the potential difference and C_o is the bulk anion concentration. If $C_o = 1$ mole/liter, for a current density of 1 A/cm^2 $E = 0.023$V for a divalent anion. It can be seen that the electrode polarization (exclusive of iR drop) for such anodic corrosion can be very small.

Case II. Equilibrium Not Achieved at Film-Solution Interface

If equilibrium is not achieved it is convenient to use the relationship

$$i = z\mathbf{F}(r_f + r_s) \qquad [16]$$

It has been predicted theoretically (4) and observed experimentally (2, 5) that the relationship between dissolution rate and hydrogen ion concentration for oxides and hydroxides has the form

$$r_s = k\, C^n{}_{H+} \qquad [17]$$

in which k is the dissolution rate constant and n has values which differ markedly for various systems and range from 0 to 4/3. For the situation in which Eq. [6] is valid, Eq. [6], [16], and [17] give

$$i = z\mathbf{F}\left[r_f + k\left\{ \frac{\delta}{10^{-3}D_{H+}} (zr_f - zr_{so}) \right\}^n \right] \qquad [18]$$

A slight rearrangement, the substitution of values for δ, D_{H+} and $\mathbf{F}$, and of i_f for $z\mathbf{F}r_f$ and i_{so} for $z\mathbf{F}r_{so}$ gives

$$i = i_f + z\mathbf{F}k(i_f + i_{so})^n \qquad [19]$$

Three ranges of values of n are of interest:

(*a*) $n = 0$.

It has been observed (5) that the rate of dissolution of anodic Al_2O_3 films in aqueous solutions at 100°C is nearly independent of pH between pH 1 and pH 10, so that $n = 0$.[2] Then

$$i = i_f + z\mathbf{F}k \qquad [20]$$

In such a situation, if k is small, most of the current produces more oxide and the film simply thickens. The case $n = 0$ is of great practical importance in anodic oxidation, for if $n = 0$ and k is small then large currents and low pH can be tolerated without the disruption of film formation.

(*b*) $0 < n < 1$.

Magnesium hydroxide dissolves with $n \sim \frac{1}{2}$ at $p\text{H} < 5$ (2), and it is expected theoretically (4) that many oxides and hydroxides would have n between 0 and 1. Note that equilibrium is not achieved for $Mg(OH)_2$ at $p\text{H} < 5$, where a surface reaction controls the rate. Figure 1 shows the behavior of various currents as functions of i_f for a hypothetical material with $n = \frac{1}{2}$ and $k = 10^{-7}$ (the value of k for $Mg(OH)_2$ is 10^{-7}), and for which $r_{so} = 0$. The dissolution current, i_s, increases less rapidly than does i_f, and the total current may produce mostly ions at low current density and mostly film at high current density. Having most of the applied current produce ions as in this example at low currents does not necessarily mean that there is a net film dissolution and eventual cleaning of the specimen in a real situation, for the spontaneous corrosion rate may be high enough to keep the specimen covered with a film.

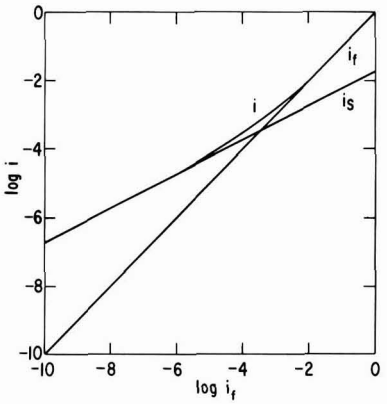

Fig. 1. Relationship between total current density i, the current density of formation of metal ions i_s, and the current density of film formation i_f, for a hypothetical metal covered with an oxide whose rate of dissolution is given by Eq. [17] with $k = 10^{-7}$ and $n = \frac{1}{2}$.

(*c*) $n > 1$.

For $n > 1$ the dissolution rate increases faster with total current than does the film formation rate. Depending on the value of k, therefore, it is possible that film formation could predominate at low currents with mostly dissolution at high currents. A practical example is not known.

Discussion of Case II.—Absence of surface equilibrium is probably the situation existing with many metals forming dense barrier films having low values of spontaneous corrosion (r_o). Such dense barrier films grow by high field ion conduction, and as the film thickness increases a considerable potential drop occurs in the film. In order to reach the large currents needed to lower the pH sufficiently to increase the film dissolution rate it is necessary to raise the potential to a point where some proton producing electrode reaction other than film formation occurs. A common situation is that large currents are not found until oxygen evolution occurs in the transpassive region. Rapid corrosion of the metal usually accompanies such oxygen evolution, possibly because of the enhanced proton concentration. When the film is a good insulator or blocks current for any reason so that no oxygen evolution occurs then application of very large potentials and growth of thick anodic films may be possible, as with Al, Ta, Zr, Nb, etc.

General Discussion

Two major problems in predicting results of anodic polarization are that it is not now possible to predict (except from experience) what will happen to any new film which is produced, and it is not possible to predict when surface equilibrium may be achieved or what values of k and n will be encountered when equilibrium is not achieved. If the new film is added to the dense barrier, then application of an additional anodic potential may simply thicken the barrier and the current may remain low. It seems generally true that metals yielding films with low values of k (the dissolution rate constant, Eq. [17]) are also the ones which give dense barrier films, but evidence is fragmentary. Future progress requires studies of the character of reaction products and of their reactivity.

The role of anions in these phenomena is important. Buffers, for instance, may prevent any large pH change until a critical film forming current is reached. If the hydroxyl ion or a buffer ion is the only anion present,

[2] The rates in ref. (5) are initial rates and decrease with time at pH 4-10 due to the formation of a porous AlOOH layer. This example is thus only valid for $p\text{H} < 4$. For other systems this restriction may not be present.

then current flow may concentrate the ion in the solution near the specimen so that little pH change can occur despite large polarization. For example, when magnesium is polarized to +1.2V on the standard hydrogen electrode scale in a 10^{-2}M solution of KOH the current is only a few microamperes per square centimeter, while in 10^{-2}M Na_2SO_4 a current of 0.1 A/cm^2 is reached at a potential of −1.26V (open-circuit potential −1.39V). The explanation for this fact is the following. Most of the large potential difference in the KOH solution is doubtless applied across the film. Should any break occur in the film so that a large local anodic current starts to flow the concentration of hydroxyl ions near the break would be increased by the current so that further precipitation of $Mg(OH)_2$ would occur and the break would be healed. In the Na_2SO_4 solution, on the other hand, any rupture of the film and accompanying current flow concentrates sulfate ions which are not effective buffers. The pH is then free to fall, and the dissolution rate can become very large.

Acknowledgment

The author is grateful to M. Indig and C. S. Tedmon, Jr., for comments regarding the manuscript. He is also indebted to two very able reviewers whose pertinent comments have resulted in a considerable clarification and simplification of the paper.

Manuscript submitted Feb. 24, 1970; revised manuscript received *ca.* May 14, 1970. This was Paper 224 presented at the Atlantic City Meeting of the Society Oct. 4-8, 1970.

Any discussion of this paper will appear in a Discussion Section to be published in the June 1971 JOURNAL.

REFERENCES

1. D. A. Vermilyea and C. F. Kirk, *This Journal*, **116**, 1487 (1969).
2. D. A. Vermilyea, *ibid.*, **116**, 1179 (1969).
3. D. A. Vermilyea and C. S. Tedmon, Jr., *ibid.*, **117**, 437 (1970).
4. D. A. Vermilyea, *ibid.*, **113**, 1067 (1966).
5. W. Vedder and D. A. Vermilyea, *Trans. Faraday Soc.*, **65**, 561 (1969).

The Anodic Behavior of Zn-Cd Binary Alloys in 1M Sulfamic Acid-Formamide Solutions

I. A. Menzies, R. A. Brodie, D. Gearey, and G. W. Marshall

Corrosion Laboratories, Department of Chemical Engineering, University of Manchester Institute of Science and Technology, Manchester 1, England

ABSTRACT

The anodic behavior of zinc, cadmium, and Cd-Zn binary alloys has been studied in 1M sulfamic acid-formamide solution. The anodic polarization curves for the single metals and alloys containing 90, 81.9, and 40% Cd are typical of electropolishing systems. In all cases a-c impedance measurements indicate the formation of solid anodic films at the onset of polishing. Under steady-state conditions of dissolution (300 coulombs) of the alloys the ratios of metal dissolved anodically are similar to those in the original alloys. All current efficiencies were 100 ± 2.5%. All of the alloys are deeply etched under appropriate conditions and considerable phase contrast is found during polishing conditions. Here there is a small amount of preferential dissolution of Cd-rich phases which give rise to phase contrast while film formation suppresses crystallographic etching. The effects of anode shape and method of polarization on polarization data in sulfamic acid-formamide solutions are also discussed.

The present work is a continuation of previous studies (1-4) of the anodic dissolution and polishing of metals in organic electrolyte solutions. Among the organic systems which have been investigated, a solution of sulfamic acid in formamide has proved to be a highly versatile polishing medium producing good results on Cu, Sn, Pb, Zn, Cd, and Ag. It has also been shown that Mo, W, and Ti can also be polished at high overpotentials. Zinc and cadmium have both been found to polish well in sulfamic acid-formamide solutions, dissolving at current efficiencies close to 100%. Most recently (4) evidence has been obtained from viscosity and a-c impedance measurements which indicate that anodic dissolution of Zn is under diffusion control and that polishing occurs by random dissolution through an anodic film with suppression of crystallographic etching. The present study is concerned with a number of aspects of the behavior of Zn-Cd alloys. In choosing an alloy system for this initial work on dissolution in organic electrolytes the Zn-Cd system was selected since both of the single metals were known to electropolish and the associated limiting current densities were similar. Furthermore the alloy system is a simple eutectic system.

Key words: anodic dissolution, zinc-cadmium alloys, organic electrolytes, electropolishing, electro-etching, formamide.

The objectives of the work were: (*a*) to obtain preliminary data concerning the polarization characteristics of a range of Zn-Cd alloys; (*b*) to confirm and extend previous investigations (4) concerning the presence of films using a-c impedance techniques; (*c*) to determine metal dissolution ratios and current efficiencies and to relate the nature of the surfaces produced to conditions of polarization. Since previous investigations (3-4) had shown that in this particular system potentiostatic and galvanostatic polarization curves were similar, the galvanostatic technique used previously (4) was used again.

Experimental

Preparation and purification of materials.—Alloys.—The alloys were prepared from 99.9999% purity zinc and cadmium by melting in Pyrex glass tubes under an argon atmosphere. After the alloys had melted, the tubes were vigorously agitated and the contents maintained in the molten state for some time to ensure homogeneity of the liquid. After cooling the alloys were placed in 'Pyrex' casting tubes with a little 'Analar' $ZnCl_2$ to act as a flux. This improved the quality of the cast rods by reducing porosity and oxide inclusions. During heating the casting tube was evacuated and flushed with purified argon twice, and after

melting of the alloys the tubes were evacuated to remove residual gas. Finally, the alloy was allowed to solidify slowly under dry argon. Samples of the castings were removed for metallographic examination. Two diameters of rod (1 and 0.75 cm) were prepared and the larger rods were rolled to sheet while the smaller ones were used as electrodes in galvanostatic polarization studies.

Solute and solvent.—Microanalytical reagent grade sulfamic acid was supplied by British Drug Houses Ltd., to the following specification: acidimetric assay >99.9% moisture <0.1%; sulfate <0.05%; nonvolatile matter <0.05%. This material was stored in a vacuum desiccator before use. Formamide was purified as described elsewhere (1, 3).

Apparatus and experimental methods.—Electrolyte preparation and metering systems.—The electrolyte preparation and metering systems used were as described previously (1, 5, 6). A weighed quantity of sulfamic acid was placed in the electrolyte vessel, and the required volume of purified formamide to give a 1N sulfamic acid solution was metered from the burette. These operations were carried out under dry nitrogen flow, and on completion the electrolyte vessel was sealed, removed, and shaken at intervals. After complete dissolution had taken place the solution was ready for transfer to the electrolysis cell.

Constant current measurements.—Cells of the pattern previously described (1) were used for these measurements. The alloy anode Fig. 1A was 1.5 x 1.0 cm and approximately 0.1 cm thick, and the surrounding cathode was a Ta cylinder of ~84 cm^2 surface area. For the measurement of anodic current efficiencies at constant current density a Wareham Measuring Systems Ltd. galvanostat type C223 capable of delivering 1A at 80V was used with a copper coulometer in series. In all experiments a total of 300 coulombs was passed. The anodes were gently abraded to 600 grade SiC paper, pickled lightly in 10 v/o (volume per cent) HNO_3 to remove surface films, washed with distilled water and acetone and finally dried in a stream of warm air, weighed and placed in the cell. All measurements were carried out at 25° ± 0.1°C in an atmosphere of purified and dried nitrogen.

A.C. impedance measurements.—These measurements were made using the same type of cell but with a central anode of the type shown in Fig. 1B, all details of the method of measurement and bridge circuit being as previously described (4). Various current densities in the range 1-100 mA/cm^2 were applied using a 120V dry battery and the corresponding readings of resistance and capacitance recorded.

Galvanostatic measurement of polarization curves.—The cell used for these measurements was similar to that described previously (3) and used for potentiostatic measurements. The technique used in the present work was similar to that in previous work (4) all potentials being measured with respect to the Cd/$CdCl_2$, KCl (satd)-formamide reference electrode. In the polishing region it was found that potential fluctuations tended to occur irregularly, and potential readings were taken at fixed time intervals. The current was raised in increments of 5 mA by means of the calibrated control, and the potential reading was noted 15 sec later and the current again increased. A fresh solution was used for each experiment.

Analytical procedures.—The metal dissolution ratios were determined by atomic absorption spectrophotometry (7) and over-all current efficiencies from weight loss measurements. There was some random scatter in the results of atomic absorption measurements, and total metal dissolution was found to be more accurately represented by weight loss measurements. However, the metal dissolution ratios were considered to be sufficiently accurate for the results to be meaningful.

Results

Anodic polarization curves measured galvanostatically with respect to the reference electrode.—Excellent reproducibility was obtained except in the very high current density regions where considerable oscillations of potential tended to occur. For each metal or alloy all of the points obtained during four separate measurements were plotted on a large scale, the best line drawn through the experimental points, and the resulting smoothed lines are shown in Fig. 2. At all current densities in the etching range zinc and cadmium had lower overpotentials for normal dissolution than any of the alloys. The transition from etching to polishing was sharp in all cases. The limiting current density for zinc was ~54 mA/cm^2 while that for cadmium and the alloys was 65-70 mA/cm^2. Although the transitions and limiting current densities were well defined the upper parts of the polishing regions were much less well defined. However, the anodic overpotential ranges

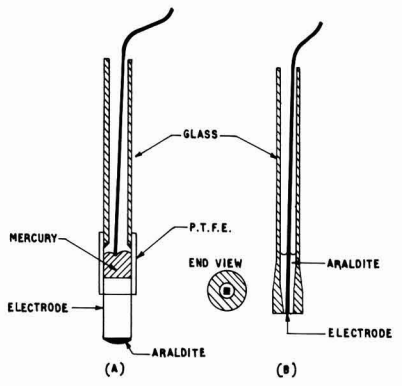

Fig. 1. Electrodes used for polarization measurements: (a) galvanostatic, (b) a-c impedance.

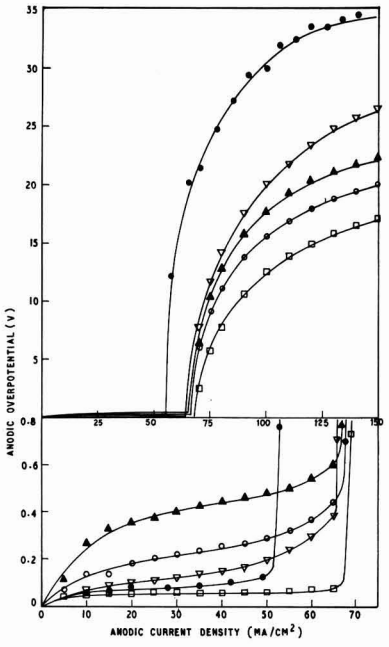

Fig. 2. Galvanostatic polarization curves for Zn, Cd, and three alloys at 25°C. (a) upper part polishing range (b) lower part etching range. ● Zn, ▽ alloy 1 (60% Zn), ▲ alloy 2 (18.1% Zn), ○ alloy 3 (10% Zn), □ Cd.

Table I. Polishing voltage ranges for Zn, Cd, and binary alloys of these elements in sulfamic acid-formamide solutions at 25°C

Material	Galvanostatic anodic overpotential, V
Zinc	11.0
Alloy 1 (60% Zn)	8.0
Alloy 2 (18.1% Zn)	6.0
Alloy 3 (10% Zn)	5.5
Cadmium	3.0

at the limiting current density decreased with increasing cadmium content of the alloy (Table I).

A-C impedance measurements.—The curves for resistance as a function of current density are shown in Fig. 3, the main feature in all cases being the sudden extremely large increase in resistance (5-150 ohm-cm^2) coinciding with the onset of polishing conditions. When no net current was flowing through the electrode the resistances, with the exception of cadmium, were ~4 ohm-cm^2. On applying a net current the initial resistances all fell to slightly lower values which rose again with increasing current density until the limiting current density was reached when the very large increase in resistance was observed. After the limiting current density, the resistances for zinc and alloy 1 (60% Zn 40% Cd) increased slowly with current density whereas materials with a cadmium content of >40% the resistance became completely unstable and violent oscillations of the null detector made it impossible to obtain more than one reading for each specimen. The limiting current densities from these measurements were 50-60 mA/cm^2 for Zn, alloy 1, and alloy 3, 65 mA/cm^2 for alloy 2 (18.1% Zn, 81.9% Cd) and 80 mA/cm^2 for cadmium.

The initial capacitance for all specimens was ~10 μF/cm^2 Fig. (4), and initially there was a rapid rise to ~100 μF/cm^2 with increasing applied current density. Following this there was a slight increase in capacitance with increasing current density until the limiting current density was attained when the capacitance fell sharply to values ~0.5 μF/cm^2. Since the bridge could not be balanced at current densities high in the polishing region for specimens containing >40% cadmium, curves for such specimens have only one point in this region.

Over-all it is clear from these measurements that the anode resistance is extremely high in the polishing region and that under these conditions the capacitance is correspondingly low.

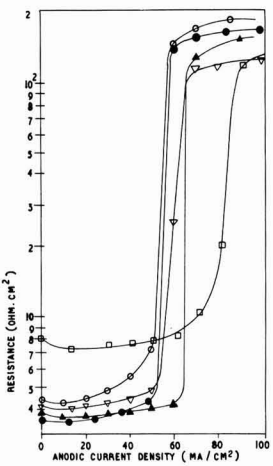

Fig. 3. Series resistances of Zn, Cd, and three alloys as a function of current density at 25°C. (10 kHz) ● Zn, ▽ alloy 1 (60% Zn), ▲ alloy 2 (18.1% Zn), ○ alloy 3 (10% Zn), □ Cd.

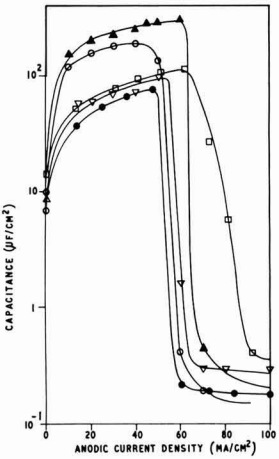

Fig. 4. Series capacitances of Zn, Cd, and three alloys as a function of current density at 25°C. (10 kHz) ● Zn, ▽ alloy 1 (60% Zn), ▲ alloy 2 (18.1% Zn), ○ alloy 3 (10% Zn), □ Cd.

Anodic dissolution ratios and dissolution efficiencies at constant current density.—After each anodic dissolution experiment the electrolyte was analyzed for zinc and cadmium and the proportions of each metal dissolved was calculated for comparison with the proportions present in the alloy (Table II). For alloy 1 (60% Zn 40% Cd) there is some evidence that at the lowest current density (8 mA/cm^2) the Zn:Cd ratio in solution was slightly greater than that in the alloy whereas at current densities >70 mA/cm^2 the ratio was lower. For alloy 2 (18.1% Zn 18.9% Cd) the dissolution ratio was 17 Zn : 83 Cd, *i.e.*, slightly lower than that in the alloy. In the case of alloy 3 the ratio in solution was 11 Zn : 89 Cd and hence a slightly higher proportion of Zn appears in solution than that nominally present in the alloy (10% Zn 90% Cd). Overall, however, it is clear that the metal dissolution ratios are similar in all cases to the ratios initially present in the alloys. The total metal dissolution efficiencies did not vary significantly with anodic current density or alloy composition since all were within the range 100 ± 2.5%. There was some indication that the current efficiencies increased slightly (~1%) with increasing cadmium content of the alloy.

Observations of surface features after treatment at constant current density.—The surface features of all three alloys were recorded as a function of current density.

Alloy 1. (*60% Zn 40% Cd*).—This alloy has a composition midway between the eutectic composition and pure zinc and in the as-cast condition (Fig. 5a) is composed of primary dendrites of Zn-rich solid solu-

Table II. Proportions of zinc and cadmium in solution after anodic dissolution of binary alloys of these metals in sulfamic acid-formamide solutions at 25°C

Anodic current density, mA/cm^2	Alloy 1 60% Zn 40% Cd		Alloy 2 18.1% Zn 81.9% Cd		Alloy 3 10% Zn 90% Cd	
	Proportion of each element in solution after dissolution, w/o					
	Zn	Cd	Zn	Cd	Zn	Cd
8	65.6	34.4	18.5	81.5	12.4	87.6
16	57.0	43.0	16.9	83.1	10.1	89.9
24	60.1	39.9	17.7	82.3	10.8	89.2
32	56.1	43.9	18.2	84.8	9.5	90.5
40	54.5	45.5	16.2	83.8	9.8	90.2
48	59.5	40.5	18.8	81.2	11.9	88.1
56	60.1	39.9	18.9	81.1	11.1	88.9
64	55.7	44.3	15.2	84.8	9.9	90.1
72	58.7	41.3	18.1	81.9	11.0	89.0
80	55.3	44.7	15.6	84.4	11.5	88.5
96	54.2	45.8	15.8	84.2	10.7	89.3

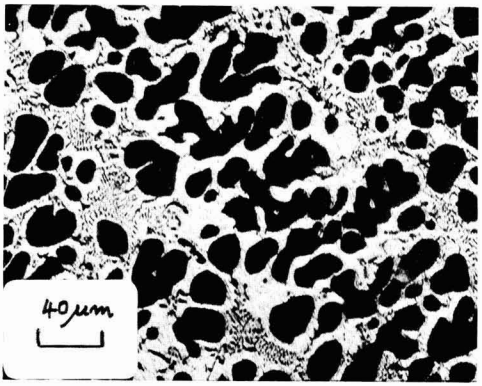

Fig. 5a

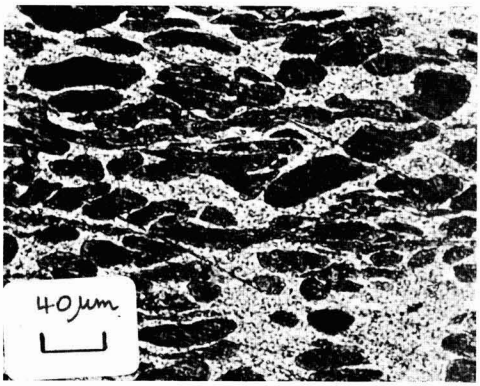

Fig. 5b

Fig. 5c

Fig. 5d

Fig. 5. Photomicrographs of specimens of alloy 1 (60% Zn) (a) as-cast structure; (b) as-rolled structure; (c) polished zinc dendrites (72 mA/cm^2); (d) polished zinc dendrites (72 mA/cm^2) dark ground illumination.

tion (dark phase) in a matrix of eutectic composed of the cadmium-rich solid solution (light phase) and the zinc-rich phase. After rolling into strips the dendritic pattern was distorted but still recognizable (Fig. 5b).

Anodic treatment of sheet specimens of the alloy at constant current density resulted in two distinct types of surface. At current densities <32 mA/cm^2 the specimen surfaces were dull matt gray and etched. However, pits were also present and these were found to correspond in shape, size, and depth (12-20 μm) to areas of zinc-rich phase present in the alloy. At intermediate current densities (32-56 mA/cm^2) polishing specimens where the local current density was highest was evident on the lower corners and edges of the specimens where the local current density was highest due to rather poor current distribution. Completely bright and reflective surfaces were obtained at current densities >56 mA/cm^2. A fine relief pattern was apparent even to the naked eye. Examination of the specimen surface under oblique illumination (Fig. 5c) indicated by the shadows produced that either the height of the eutectic phase was lower than that of the zinc-rich phase or that a groove was present at the boundary between the two phases. By changing to dark ground illumination (Fig. 5d) all light directly reflected from the specimen surface was eliminated, and at the same time scattered light was brought into focus producing an image of all surfaces which were not plane and perpendicular to the optical axis. The light areas in Fig. 5d thus represent the hollows or grooves at the edges of the zinc-rich phase. Most of the central areas of the dendrites were polished to a smooth highly reflective surface.

Alloy 2. (*18.1%* Zn *81.9%* Cd).—This alloy was close to the eutectic composition (17.4% Zn) and the as-cast structure was almost completely eutectic (Fig. 6a), the presence of a few small particles of zinc-rich phase confirming that the zinc content was slightly in excess of the true eutectic composition. Rolling of the alloy did not change the structure significantly. Overall, the general relationship between structure and current density observed with alloy 1 was also observed with this alloy. At current densities ≤32 mA/cm^2 there was poor definition of grain boundaries and in this case no etch pits were observed. The first signs of polishing were observed on the lower corners and edges of specimens exposed at 32 mA/cm^2 and increasing the current density from 32 to 56 mA/cm^2 progressively increased the area of the specimen which was polished. At current densities >56 mA/cm^2 the whole specimen surface became bright and polished although relief

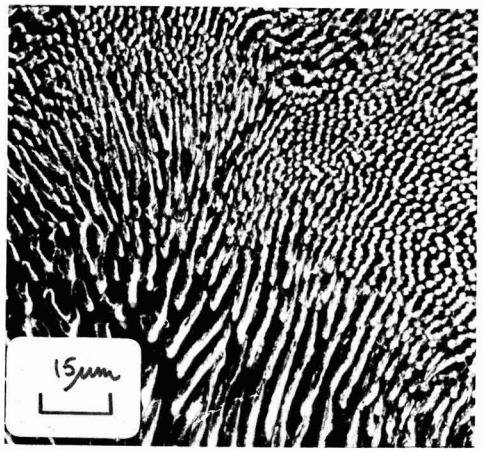

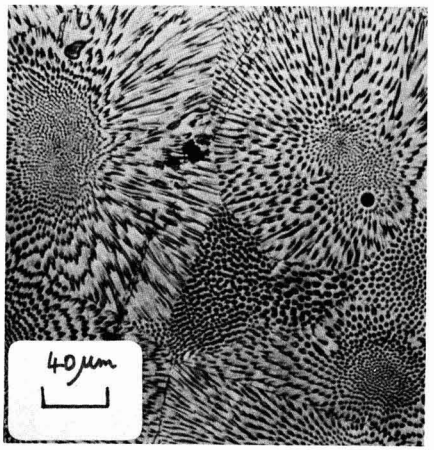

Fig. 6. Photomicrographs of specimens of alloy 2 (18.1% Zn-eutectic) (a) (top) as-cast structure (b) (bottom) polished surface (72 mA/cm^2) showing selective removal of one component during polishing.

effects were observed (Fig. 6b), the Zn-rich phase being proud of the eutectic. This was, however, best observed under dark ground illumination at relatively high magnifications, and under normal direct illumination at moderate current densities only a low degree of relief was observed due to the relatively fine structure and uniformity in the alloy.

Alloy 3. (10% Zn 90% Cd).—The composition of this alloy was intermediate between that of the eutectic and pure cadmium and in the as-cast condition (Fig. 7a) it consisted of primary dendrites of cadmium-rich phase set in a fine eutectic mixture. The lens-shaped markings on some of the dendrites are probably deformation twins induced during metallographic preparation. After rolling the cadmium-rich phase was irregularly shaped.

Again the over-all anodic behavior of this alloy was similar to that of alloys 1 and 2. Deep etching occurred at current densities up to ~32 mA/cm^2, and the individual phases could not be readily distinguished. Again the first signs of polishing appear round the bottom edges and corners of the specimen at 32 mA/cm^2, and the area of polished surface increased with increasing current density up to 56 mA/cm^2. The surfaces resulting from anodic treatments at 56-96 mA/cm^2 were completely polished although slight relief effects were observed. The cadmium-rich phase was generally

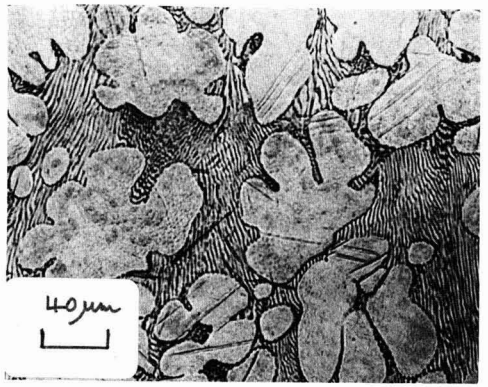

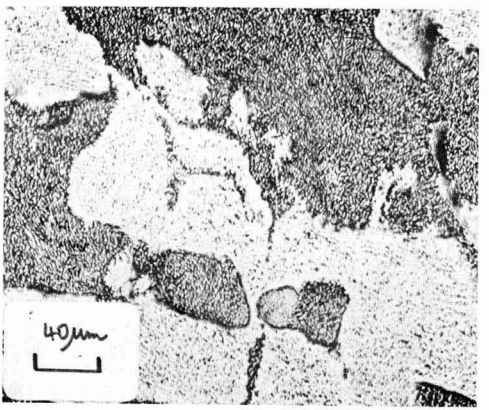

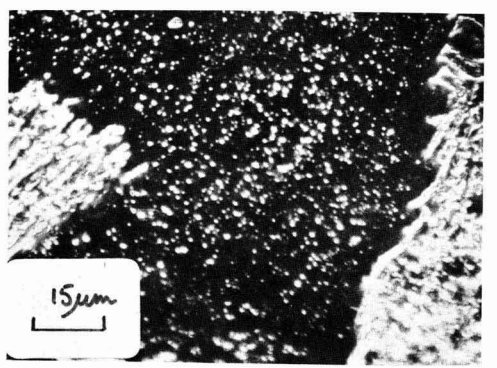

Fig. 7. Photomicrographs of specimens of alloy 3 (10% Zn): (a) (top) as-cast structure; (b) (center) polished surface (72 mA/cm^2) showing depression of Cd-rich phase; (c) (bottom) as (b) dark ground illumination, showing rounded pits in cadmium phase as light spots.

1-2 μm below the general level of the eutectic as can be seen by the shadows in this phase in Fig. 7b. The surfaces of the cadmium-rich dendrites, although highly reflective, were covered with minute pits (0.25-1.50 μm diameter), and this could best be seen at higher magnification under dark ground illumination where the pits are seen as light spots on a dark background. (Fig. 7c)

Additional general observations.—Polished specimens after removal from the solution very rapidly formed a dull gray film on the surface if they were not washed

immediately after breaking the electrical circuit. These films were studied using electron microscopy. Black particles with angular shapes (cf. Fig. 8a) were found associated with the fine two-phase material of the eutectic, the single phase zinc-rich areas being free of such particles. This close association of the particles with the intimate mixture of phases in the eutectic is seen in more detail in Fig. 8b where it is clear that they appear to propagate from the rods of the dispersed phase. An extensive study of the particles was made using transmission electron diffraction, but diffractograms of sufficient quality to permit measurement and calculation of lattice parameters could not be obtained. The material was certainly crystalline, often opaque to electrons, and probably metallic. A particularly interesting dendritic formation is shown in Fig. 8c, and despite the lack of direct evidence it seems almost certain that crystals of cadmium were deposited on the surface by an exchange reaction between zinc in the eutectic phase and cadmium ions in solution.

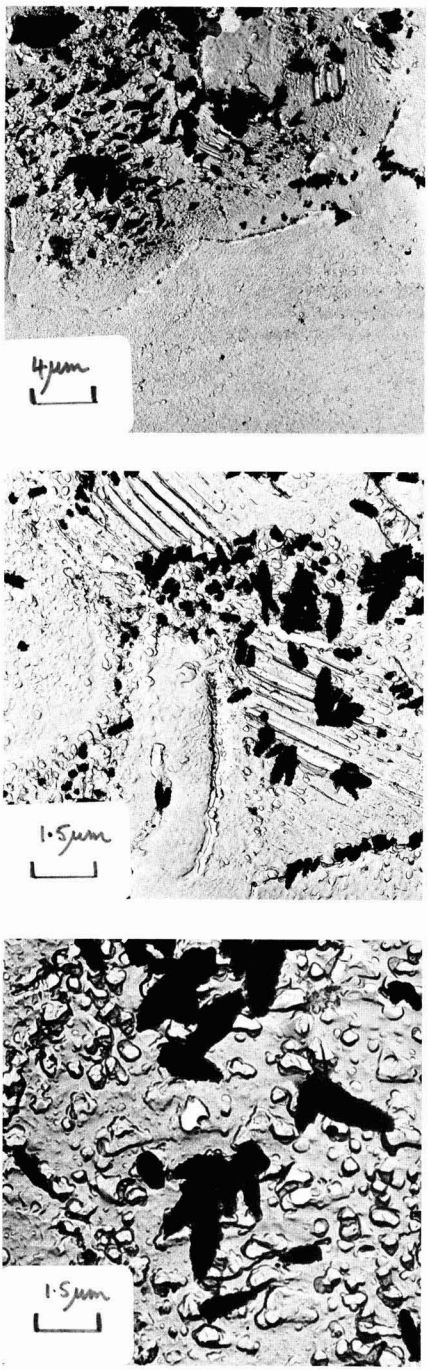

Fig. 8. Electron micrographs of precipitates on polished specimen: (a) (top) presence of particles only on eutectic areas; (b) (center) association of particles with rods of dispersed phase; (c) (bottom) metallic dendrites.

During anodic dissolution of the alloys qualitatively similar viscous layers were observed streaming from the electrode surfaces and these were observed during both etching and polishing. Since there was evidence of film formation during polishing some of the polished specimens were subjected to electron probe microanalysis for sulfur in plan, but the presence of this element could not be confirmed.

Discussion

The present work represents one of the first investigations of the anodic behavior of alloys in organic electrolyte solutions and as such must be regarded as exploratory and rather general in nature. It must however be pointed out at the outset that the anodic dissolution ratios and the metallographic features represent long-term steady-state conditions and not the early stages of dissolution. Caution is therefore necessary in discussing these features in relation to the galvanostatic polarization curves.

Dissolution of alloy 1 (60%) Zn at 16 mA/cm^2 within the etching range resulted in deep pitting and metallographic examinations suggested that this was associated with preferential dissolution of Zn-rich dendrites. Clearly although preferential dissolution of zinc may occur in the early stages cadmium dissolution also occurs, and only at the lowest current density (8 mA/cm^2) was there significant evidence of preferential dissolution of zinc under steady-state conditions. At 72 mA/cm^2 there was evidence that the Zn-rich dendrites were raised above the matrix of Cd-rich eutectic. There was also some indication (Table II) that the solution contained a slightly higher proportion of cadmium than the alloy. This is no doubt associated with the higher limiting current density for cadmium dissolution (Fig. 2 and 3).

In the case of alloy 2 it was not possible because of the fine eutectic structure to determine which phase was preferentially dissolved during etching and polishing. Again under steady-state conditions there was little preferential dissolution of either metal (Table II). With alloy 3 the metallographic evidence suggested some slight preferential dissolution of cadmium.

Under the etching conditions used in the present work good metallographic contrast apparently was not obtained. This was most probably due to excessive surface roughening during steady-state dissolution. A much higher degree of contrast was obtained during polishing, the difference in height between the phases being 4-8 x 10^{-5} in. In the polishing region the differentiation ratio for cadmium (D_{Cd}) as defined by Greene, Rudlaw, and Lee (8), is given by $(i_{\lim Cd}/i_{\lim Zn})_E$ at any potential (E) where $i_{\lim M}$ are the observed limiting current densities for dissolution of Zn and Cd. At almost all potentials in the polishing region D has values of ~1.2. Thus under steady-state conditions during polishing there appears to be a difference in height ~10^{-4} in. and phase contrast with a dissolution ratio somewhat lower than that specified as necessary by Greene, Rudlaw, and Lee. This is not surprising as their criteria were derived for short-time etching conditions. It must however be made clear that in the present work crystallographic etching was sup-

pressed in the polishing region. It is noteworthy that long-term dissolution (300c) results in a Zn/Cd dissolution ratio the same as the Zn/Cd weight ratio in the alloy over a range of current densities in both polishing and etching regions. Generally accepted theory (9-11) indicates that in the initial stages of dissolution the two constituents in the alloy dissolve independently of each other at the current density appropriate to the potential or overpotential setting (heterogeneous or homogeneous alloys) as derived from the polarization data for the single constituents. Then, taking the fraction of the alloy surface occupied by each component to be proportional to its volume fraction in the alloy and assuming two constituents 1 and 2 with molecular weights M_1, M_2, dissolution valencies Z_1, Z_2, and current densities of dissolution i_1, i_2 under set conditions we have

$$\frac{\text{Weight of 1 dissolved}}{\text{Weight of 2 dissolved}} = \frac{i_1 M_1 x_1 \rho_2 z_2}{i_2 M_2 x_2 \rho_1 x_1} \qquad [1]$$

where x_1, x_2 are weight fractions of 1 and 2 in the alloy and ρ_1, ρ_2 are respective specific gravities.

In the polishing range in the present results the rates in Eq. [1] becomes approximately

$$\frac{\text{Weight of Cd dissolved}}{\text{Weight of Zn dissolved}} \approx 3\,\frac{x_{Cd}}{x_{Zn}}$$

since $i_{Cd} \sim 7/5\ i_{Zn}$ (Fig. 2), $Z_{Cd} = Z_{Zn}$, $\rho_{Cd} \approx \rho_{Zn}$, and $M_{Cd} \approx 2M_{Zn}$. Thus the ratios of metal dissolved according to Eq. [1] are a factor of ~3 different from that actually observed.

Several modifications of the above behavior have been suggested usually in connection with the protective properties of components in strongly passivating systems. Thus it has been suggested that modification results from the accumulation of the less active component on the surface by re-orientation of the latter after dissolution of the more active atoms, or alternatively by re-precipitation of less active atoms after primary dissolution (11). In the present results the remarkable consistency of the dissolution ratios in etching and polishing regions despite a variety of alloy structures seems to indicate a more general explanation. In any case, on a geometrical basis it can easily be appreciated that there must be a tendency for less active atoms to accumulate on the surface. Thus if the dissolution rates of the two components are at all comparable long-term dissolution will not result in over-all preferential dissolution of one component, although at any time a certain amount of preferential dissolution, of the order of the grain or particle size, of the more active component would be expected. Hence in the polishing region a rather fine etch of the eutectic is noticed, Fig. 6b, although it must be stressed again that crystallographic etching is suppressed. This is indeed an attractive demonstration of the primary importance of the suppression of crystallographic etching in polishing phenomena. The larger scale component etching (which, of course, would not be suppressed by the polishing film) does not prevent the appearance of a visually polished surface.

The results of the a-c impedance measurements on the alloys and cadmium were generally similar to those previously obtained (4) for zinc. The magnitude of the increase in resistance corresponding to the onset of the limiting current and the associated decrease in capacitance are again best interpreted in terms of formation of anodic films. Over-all anodic dissolution is controlled by diffusion processes in solution at higher potentials, and this may well be true at potentials in the etching range. Most theoretical treatments of alloy dissolution processes (9-12) are based on short-term activation controlled processes, and it is not possible to discuss the present system in detail until further studies of dissolution as a function of time have been completed.

The solutions produced by the anodic dissolution of alloys 2 and 3 (Cd-rich) frequently contained a cloudy yellow precipitate which was shown to be cadmium sulfide. The cathodic reaction in 1M sulfamic acid-formamide must therefore include the reduction of sulfamic acid to sulfide ion either directly or by means of cathodic hydrogen. Redeposition, presumably of Cd, the more noble metal, was also a problem with polished specimens unless these were removed from the electrolyte while they were still connected to the power supply and washed immediately in pure formamide. Similar difficulties have been reported by Moulen (13) during the electropolishing of Pb-Sn alloys in aqueous fluoboric acid.

Acknowledgments

The authors wish to thank Professor T. K. Ross for the provision of laboratory facilities and the Science Research Council for their support. Two of us (D.G. and G.W.M.) wish to thank the Council for the award of postdoctoral research assistantships whilst one of us (R.A.B.) wishes to thank the Council for the award of an Advanced Course Studentship.

Manuscript submitted Feb. 20, 1970; revised manuscript received May 14, 1970.

Any discussion of this paper will appear in a Discussion Section to be published in the June 1971 JOURNAL.

REFERENCES

1. I. A. Menzies, D. N. Bulgin, and G. W. Marshall, *Trans. Inst. Metal Finishing*, **45**, 122 (1967).
2. I. A. Menzies and A. F. Averill, *Electrochim. Acta*, **13**, 807 (1968).
3. I. A. Menzies, G. W. Marshall, and G. B. Griffin, *Corrosion Sci.*, **9**, 287 (1968).
4. I. A. Menzies, G. W. Marshall, D. Gearey, and G. B. Griffin, In press.
5. I. A. Menzies, T. Broughton, and V. O. Nwoko, *Trans. Inst. Metal Finishing*, **43**, 9 (1965).
6. I. A. Menzies, P. J. Moreland, and S. R. Oulsnam, *ibid.*, **45**, 181 (1967).
7. "Atomic Absorption Analytical Methods," Vol. 1, Evans Electroselenium Ltd., Halstead, Essex.
8. N. D. Greene, P. S. Rudlaw, and L. Lee, *Corrosion Sci.*, **6**, 371 (1966).
9. R. F. Steigerwald and N. D. Greene, *This Journal*, **109**, 1026 (1962).
10. M. Stern, *Corrosion*, **14**, 329t (1958).
11. W. A. Mueller, *ibid.*, **18**, 73t (1962).
12. H. W. Pickering and C. Wagner, *This Journal*, **114**, 698 (1967).
13. A. W. Moulen, *ibid.*, **99**, 133c (1952).
14. R. A. Brodie, M.Sc. Dissertation, Manchester, England, 1968.

A Rapid Anodic Porosity Test for Ni-Fe Electrodeposits on Copper Wire

W. O. Freitag*

UNIVAC, Division of Sperry Rand Corporation, Blue Bell, Pennsylvania 19422

ABSTRACT

A 10-min semiquantitative polarographic test is described which measures the area of copper substrate left exposed by pinholes or defects in electrodeposited memory wire. The wire sample is made the anode in an electrolytic cell, the Ni-Fe outer film is rendered passive with a controlled potential sequence, and the anodic current due to oxidation of exposed copper is recorded as a function of potential. The height of a copper passivation peak is measured, and this height is shown to be proportional to exposed Cu area. The method is useful in quality control and in following the course of corrosion in environments when the attack at local defects is the major mechanism.

The occurrence of pinholes or other plating defects which leave some of the substrate exposed is a familiar problem with decorative or protective electrodeposits. As a part of the development of plated wires for computer memories, it became necessary to measure the porosity of thin magnetic alloy films on copper. The test developed for this purpose is described, and we believe that the same general approach might be applicable to other situations.

The plated wire memory elements consist of a substrate of beryllium-copper wire 0.005 in. in diameter coated with an electrodeposited film of permalloy. Wires of this type were prepared first by Long (1) and the process was described more recently by Sagal (2). The alloy films have an average composition near 80% Ni and are generally about 8000Å in thickness. Usually, a layer of pure copper is interposed between the substrate and the magnetic alloy. Pinholes or other defects which leave part of the copper substrate exposed affect the magnetic performance of the wires. Furthermore, pinholes could provide sites for corrosion and so affect the long-term stability and reliability of the elements.

Tests for porosity in electrodeposits usually consist in rendering the pores visible by means of some chemical reaction which is specific to the substrate material and leaves the deposit unchanged. Evaluation is then carried out by visual or microscopic examination. In electrography, the test panel is made anodic in a cell and is held in contact with filter paper which is saturated with an appropriate electrolyte so that ions from the exposed substrate areas produce a colored precipitate. These methods are not easily applied to cylinders of small diameter, such as plated memory wire.

The literature describes methods wherein anodic currents are measured which represent metal dissolution from the basis metal at pores in the deposit under conditions at which the deposit is passive. Ehrhardt (3) applied this approach to gold on copper by measuring the diffusion limited anodic current of copper dissolution in 5% H_2SO_4 at a potential at which no other electrode reaction was occurring. Khan recently reviewed this method (4) and found that the gold layers were not sufficiently passive during this treatment and gave background currents which rendered the tests inaccurate. Shome and Evans (5) reported on the use of a corrosion cell for determining porosity of nickel deposits on iron. They used a large auxiliary cathode of copper and measured either the corrosion current or the amount of iron accumulating in the electrolyte after a period of time. Clarke and Britton (6), dealing with tin, nickel, or copper on steel, related the slope of E *vs.* i curves to the resistance of electrolyte within the pores. Their approach, however, depends on certain conditions being valid which are difficult to achieve experimentally, and is not applicable to very thin deposits in any event.

In the present work, pores in nickel-iron alloy films on copper are detected by measuring the anodic passivation current peaks from exposed copper areas after a prescribed polarization sequence which leaves the Ni-Fe areas passive.

Pinhole Test Sequence

The wire sample is made the working electrode in a polarographic cell using dilute sodium pyrophosphate as electrolyte. Figure 1 summarizes the polarization sequence and diagrams the currents observed.

First, a negative potential, −1.8V *vs.* SCE, is applied to reduce surface oxides and effect a certain degree of cathodic cleaning. Then the sample is brought to +800 mV whereupon passivating films grow on both the permalloy and the copper areas. After the observed current falls to a very low level, usually 0.6 to 0.8 μA/cm of sample length (in about 4 min) the cell is placed on open circuit.

The anodic film which formed on copper is soluble and dissolves within 2 min after removing the potential (the "reactivation" time), while the anodic film on the magnetic alloy remains intact. After this reactivation step, the potential scan is begun at −200 mV and run to about +300 mV at a rate of 200 mV/min. An anodic current peak is observed as the copper

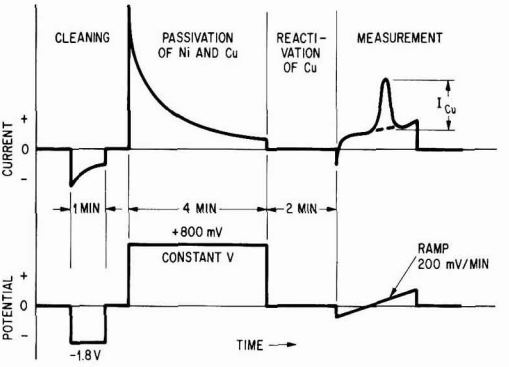

Fig. 1. Potential sequence applied to test wire (lower line) and typical current response (upper line). Ordinate units are arbitrary and not to scale.

* Electrochemical Society Active Member.

Key words: polarograph, pyrophosphates, corrosion, passivity, magnetic alloys for computer memories.

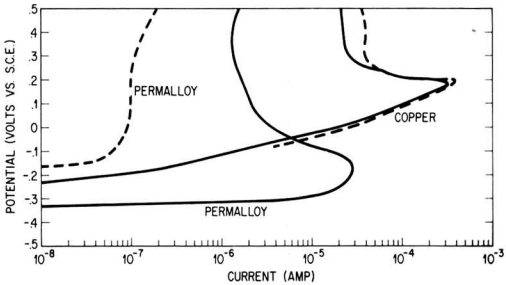

Fig. 2. Anodic traces of unplated copper and solid permalloy wires in the active condition (solid lines) and after polarization as in Fig. 1 (dashed lines). The electrolyte is 0.085M $Na_4P_2O_7$ at pH = 5.2.

areas repassivate, and the height of this peak is measured.

Apparatus and Procedure

Two kinds of electrolytic cells were used in this work. One was a simple "H-cell"[1] one leg of which was a saturated calomel electrode with a mercury surface about 1 in. in diameter. The calomel cell was used as the counterelectrode under the assumption that up to 400 μA of current (the upper limit of the polarograph) would not polarize it, and that any polarization which might occur would not alter test results. Potentials are not measured more accurately than $\pm$10 mV. The H-cell could accommodate sample lengths up to 5 cm. When longer lengths of wire were tested, a three-electrode cell was used which consisted of a platinum foil counterelectrode and a standard calomel reference electrode.[2] The relative location of the three electrodes was not controlled since, again, critical voltage control was not necessary. A Fisher Elecdropode with recorder was used with both cells, but an operational amplifier circuit was added to drive the three-electrode cell.

Wire samples were masked top and bottom with Scotch Electroplater's Tape (3M Company) making sure that the immersed end was completely insulated. There was no evidence that impurities from the tape interfered in any way with the test.

The electrolyte was 0.085M $Na_4P_2O_7$ adjusted to a pH of 5.2 with H_3PO_4. The tests were carried out at room temperature. A very few test runs were done with the electrolyte saturated with O_2 or swept with N_2, but no significant differences were immediately apparent, and virtually all of the work was done under ambient conditions.

Identification of Passivation Current Peaks

The passivation behavior of copper and permalloy in this electrolyte are shown in Fig. 2. The solid lines are taken from current voltage traces while scanning 0.005 in. diameter solid permalloy wire[3] (1 cm) and copper plated beryllium-copper wire (0.2 cm). Voltage scanning was started at -500 mV (*vs.* SCE) at $+200$ mV/min. The cathodic currents are not shown.

The dashed lines in Fig. 2 are traces of scans of the same samples run according to the procedure in Fig. 1; the permalloy is passive but the copper was virtually unchanged.

The passivation behavior for the alloy is similar to that described for Fe-Ni alloys by Economy *et al.* (7) in sulfuric acid solutions. The passivation current density for permalloy in Fig. 2 is on the order of 1 mA/cm^2, compared to a value less than 25 mA/cm^2 extrapolated from Economy's results, which covered a pH range only up to 3.7. The location of the current peak is about -0.18V (SCE) in pyrophosphate at pH = 5.2 compared to -0.15V (SCE) in H_2SO_4 at pH 2.7, *i.e.*, in fair agreement and not much affected by pH.

Figure 3 shows a trace made on a plated wire before and after the alloy deposit was deliberately nicked with a razor blade. The resulting scratch was sufficient to render that point on the wire useless for memory application. The occurrence of the copper passivation peak is clearly evident at $+100$ mV. In practice, the copper peak occurs at $+20$ to $+120$ mV (SCE), with larger copper areas usually peaking at the higher potentials. This shift is expected to be related to the voltage scanning rate. The method used to measure the peak height is also illustrated in Fig. 3.

The scan is started at a potential such that little or no cathodic current flows. Cathodic current will, of course, reduce some of the nickel passivation and a current peak due to the repassivation of nickel will appear. However, some nickel passivation current can be tolerated since the Ni peak usually does not interfere with observations of the Cu peak.

The electrode reaction mechanisms are doubtlessly complex. In broad terms, the rate of formation of the passivating copper pyrophosphate film is determined by competition between a precipitation reaction

$$Cu^{++} + P_4O_7^{----} \rightarrow \text{insoluble salt}$$

and a dissolution reaction:

$$\text{insoluble salt} + P_4O_7^{----} \rightarrow \text{soluble complex}$$

The existence of insoluble salts and complex ions in the copper pyrophosphate system at pH 5.2 is well known (8-11), but no attempt is made here to identify the species involved. Above a pH of about 6, where no copper-pyrophosphate precipitate is found, the present method fails. On the other hand, below pH 4 passivity is difficult to obtain, direct attack on the nickel is excessive, and samples are rapidly destroyed.

Area Calibration of the Copper Peak Current

In order to validate the test sequence, it is necessary to prove that a direct correlation exists between the height of the copper passivation peak and the area of exposed copper. Electrodes of known area were prepared by potting 1-mil diameter copper wires so that only polished cross sections were exposed to the electrolyte. The peak heights of assemblies containing from 1 to 25 wires were measured. The results are shown in line A, Fig. 4, which has the expected slope of 1. Similarly potted electrodes containing single wires of larger diameter yielded curve B, which has a slope of about 0.8.

Neither of these lines can properly be extrapolated to lower currents to provide a quantitative calibration curve. The peak current is at least partially controlled by diffusional processes whose rate is maximized by multiple small-sized copper electrodes which permit essentially three-dimensional supply of reactants to the electrode. Large cross-section electrodes undergo a transition from three- to one-dimensional diffusion behavior with an expected reduced over-all rate or

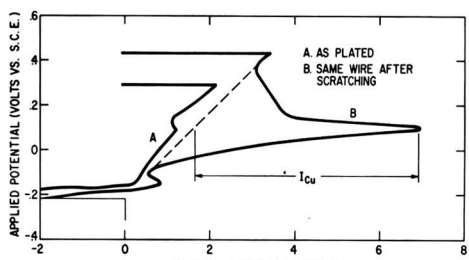

Fig. 3. Anodic traces of a plated wire before (curve A) and after (curve B) scratching the permalloy deposit with a razor blade.

[1] Sargent, H-Form Electrolysis Vessel, S-29401.
[2] A. H. Thomas, 4851-K30.
[3] 18.94% Fe, Hamilton Precision Metals, Lancaster, Pennsylvania.

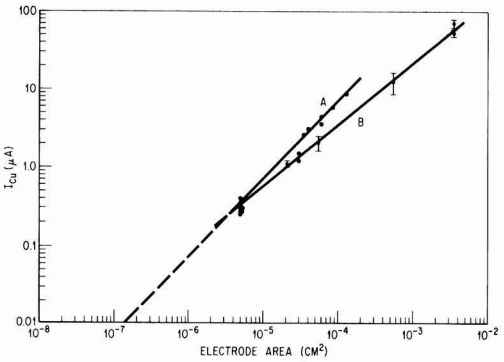

Fig. 4. Copper peak current vs. electrode area correlation curves for multiple electrodes comprised of 1 mil diameter sections (curve A) and single electrodes of larger diameters (curve B).

current. Pinhole arrays in actual plated wires will behave as isolated multiple electrodes of various diameters. The smaller pinholes will contribute disproportionately large partial currents to the total current until other effects predominate, such as high electrolyte resistance in very small pinholes, failure of the previously formed anodic film on copper to dissolve in the allowed two minutes, or failure of the electrolyte to penetrate very small pinholes. A true calibration curve would lie to the left of the extrapolation of line A, Fig. 4, and would be parallel to line A only if the pinholes have approximately the same diameter.

The repeatability of the measurement on sanded electrodes consisting of a single 1-mil diameter copper wire was slightly better than ±20%. Eleven measurements taken from four different electrodes gave an average I_{Cu} value of 0.30 μA, with a standard deviation of 0.05 μA. Standard derivations of measurements using the larger diameter single-wire electrodes are indicated by the error flags in Fig. 4. Most of this error arises from real surface area variations due to roughness of the copper cross sections. The peak heights found for a 25-mil diameter copper section were consistently lower when the surface was prepared by electropolishing than when it was sanded.

The advantage of this method over Ehrhardt's (3) is that the effects of solution convection, which must be dealt with when measuring a diffusion limited anodic current, are minimal. Copper wire calibration samples gave essentially the same distribution of peak heights when the copper electrode faced downward in the electrolyte, or was inverted to face upward. The peak of the copper current is reached in 15-30 sec, a time apparently too short for the buildup of density gradients which are sufficient to cause local convection. Furthermore, any Ni-Fe passivity that is lost between the initial passivation and the measuring sweep, is quickly re-established during the sweep before the copper dissolution potential is reached. Thus the passivation peak for copper stands out unambiguously.

The repeatability of measurements on plated wire samples could not be determined because of the cumulative destructive effects described below. It is believed that except for the occurrence of gross defects, most acceptable wire deposits are characterized by microfissures which are relatively uniformly distributed. All-in-all the method yields useful data over a range of five orders of magnitude. Acceptable plated wires display copper peaks of 0.03-0.005 μA or less per centimeter of wire length, while poorly plated wires ranged from 0.1 to 1 μA. Variation of the thickness of the permalloy deposit from 3000 to 10,000Å, plated under "acceptable" conditions, had little or no effect on the observed defect area. Badly corroded wires have been observed with currents up to 400 μA, or about 50% exposed substrate area.

Effect of Repeated Scanning

Some of the charge passed during the initial passivation step represents active dissolution of nickel and iron. Thus, there exists the possibility that high results would be obtained if the passivation stage removes some of the magnetic alloy. Existing pinholes could be enlarged or thinly plated areas could be stripped and a pinhole generated.

To estimate the magnitude of this source of error, the cumulative effect of repeated pinhole test cycles was examined. Figure 5, line A, shows that when passivation is carried out as in Fig. 1, there is indeed a slow increase in the measured copper peak height, but that this levels off after about 8–10 test cycles. The increase in copper peak height from the first to the second scan of a given sample was usually found to be about 20 to 30%. It is estimated, therefore, that the true copper height would lie about 20-30% below that measured by the first scan. The test is clearly partially destructive, but the error is no greater than other uncertainties.

Line B in Fig. 5 shows the effect of using a passivation technique which permitted much greater anodic currents to flow. Instead of polarizing at a constant +800 mV, passivation was done by scanning from −200 to +800 mV at 200 mV/min. This provided greater opportunity for active dissolution of nickel, and the more rapid sample destruction is evident in curve B. The passivation of a normal wire requires passage of about 6×10^{-4} to 30×10^{-4} coulombs/cm length. If all of this charge represents dissolution, distributed uniformly, a layer of magnetic alloy 50-250Å is lost. As a check, a portion of electrolyte that has been used to test a total of 90 cm of wires was analyzed by atomic absorption and found to contain Ni in an amount equivalent to the dissolution of 20 ± 20 Å/cm of wire. The dissolution is almost surely not uniform, and pinhole enlargement has not been preventable.

Dissolution is even more serious when impurities are present which prevent the passivation of the Ni-Fe. Such impurities are provided, for example, by tarnish layers which form under certain conditions during corrosion tests in sulfur-containing atmospheres. A dip in 1:1 HCl was found adequate for removing the tarnish layers, but this operation also removes up to 300Å of alloy.

Selection of Sample Length

Production wire batches consisting of 20 to several hundred 20-in. long wires, are characterized by apply-

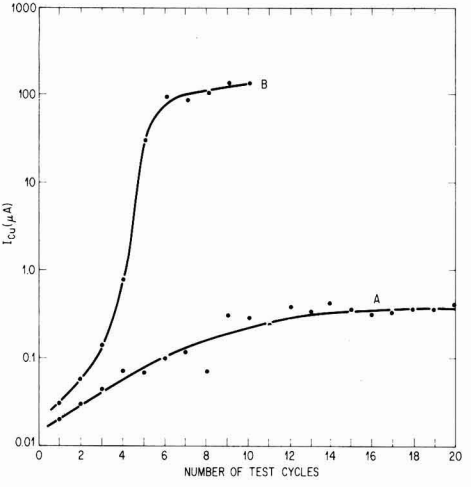

Fig. 5. Effect of repeated test cycles on the observed copper peak height, I_{Cu}. Curve A, procedure as in Fig. 1; curve B, first passivation done by slow scan to +800 mV.

ing the test to a 10-cm length from each of several wires, and copper peak currents range from <0.005 to 0.03 μA/cm. When plating defects other than microfissures occur, they are scattered at random along the length of the wire. A short sample could obviously lead to erroneous interpretations if it happens to fall between defects. Too long a sample, on the other hand, could cause an infrequent defect to be averaged over too long a length with an equally erroneous underestimation. For example, when one 38-cm length was tested 1 cm at a time, all sections fell in the range of 0.01-0.1 μA except one with the abnormally high reading of 0.7 μA. The same wire taken as a whole showed an average current of 0.04 μA/cm which would have been considered only slightly outside the "normal" range. While the statistically ideal sample length was not determined, a length of 10 cm was selected as a good working compromise and in general two such lengths were cut from each production wire tested.

Conclusions

A porosity test has been worked out which gives a measure of the substrate area left exposed by plating defects or pinholes in Ni-Fe alloy films plated on copper. Even with the errors discussed above, the test is useful in quality control of the plating process and in following the course of corrosion reactions. The accuracy has proved more than adequate for measurements of exposed substrate area ranging from less than 0.0004 to 50% and can undoubtedly be improved by optimizing the test conditions.

The method makes use of the current peak associated with a metal being anodically passivated during a potential scan. The technique might be adaptable to other metal pairs if an electrolyte can be found in which the two passivating layers have widely different rates of dissolution.

Acknowledgments

The writer wishes to express his appreciation to Dr. Leonard Nanis for much helpful discussion and to Mr. Andrew Sloss who spent many tedious hours before the polarograph.

Manuscript submitted Nov. 12, 1969; revised manuscript received June 8, 1970.

Any discussion of this paper will appear in a Discussion Section to be published in the June 1971 JOURNAL.

REFERENCES

1. T. R. Long, *J. Appl. Phys.*, **31**, 123S (1960).
2. S. W. Sagal, *This Journal*, **112**, 174 (1965).
3. R. A. Ehrhardt, *Proc. Am. Electroplaters' Soc.*, **47**, 78 (1960).
4. A. A. Khan, *Plating*, **57**, 1374 (1969).
5. S. C. Shome and V. R. Evans, *J. Electrodepositors' Tech. Soc.*, **27**, 45 (1951).
6. M. Clarke and S. C. Britton, *Trans. Inst. Met. Finishing*, **36**, 58 (1959).
7. G. Economy, R. Speisor, F. H. Beck, and M. G. Fontana, *This Journal*, **108**, 337 (1961).
8. O. E. Schupp, P. B. Sturrock, and J. I. Watters, *Inorg. Chem.*, **2**, 106 (1963).
9. C. Heitner-Wirguin and J. Kendy, *J. Inorg. Nucl. Chem.*, **22**, 253 (1961).
10. J. I. Watters and A. Aaron, *This Journal*, **75**, 611 (1953).
11. L. B. Rogers and C. A. Reynolds, *J. Am. Chem. Soc.*, **71**, 2081 (1949).

The Approach to Limiting Current in a Stagnant Diffusion Cell

Limin Hsueh and John Newman*

Inorganic Materials Research Division, Lawrence Radiation Laboratory, and Department of Chemical Engineering, University of California, Berkeley, California 94720

ABSTRACT

The transient behavior of surface concentration and current density in a stagnant diffusion cell has been worked out with consideration of surface and concentration overpotentials and the ohmic resistance of the solution. Both theoretically and experimentally, the current density is found to overshoot the limiting current density during part of the transient.

A stagnant diffusion cell is a capillary cell with an electrode at one end of a capillary filled with solution and open at the other end into a container with solution and containing the counterelectrode. Such a cell is commonly used for diffusivity measurements (1, 2) because of its simple experimental setup and the easy measurement of current and time.

Early analyses (3, 4) showed that, for a constant concentration at the electrode surface, the current decreases in inverse proportion to the square root of time in an unsteady, one-dimensional diffusion, or $i\sqrt{t}$ is a constant for a given concentration of solution. Accordingly, the current would be infinite at zero time. Actually, for a constant applied potential, the current is finite and remains more or less constant until the reactant concentration at the electrode surface approaches a value of zero. The time required for this depends on the potential difference applied across the two electrodes and the properties of the solution itself. It may range from less than 100 sec in a well-supported solution to several tens of thousands of seconds in a solution of a single electrolyte.

Davis, Horvath, and Tobias (2) have included the surface overpotential for linear electrochemical kinetics in their treatment. In the present work, the analyses is extended to include the ohmic resistance of the solution, as well as nonlinear electrochemical kinetics.

This work was motivated not so much by the ohmic and kinetic limitation at short times but more by the shape of the logarithmic current-time curves obtained in the measurement of integral diffusion coefficients (5), the study of the effect of ionic migration on limiting currents (6), and attempts to obtain limiting currents in cupric sulfate solutions in the absence of sulfuric acid (7). Under certain conditions, the current overshoots the limiting current. A similar phenomenon was predicted in the analysis of the current distribution on a rotating disk electrode (8-10) and on

* Electrochemical Society Active Member.
Key words. mass transfer, current distribution, copper sulfate-sulfuric acid system, polarization.

plane electrodes in the walls of a flow channel (11, 12). Experimental confirmation obtained in the present work may thus lend support to those analyses. The similarity to polarography in a binary salt solution (13) should also be noted. No overshoot was predicted in that work, but a recalculation for that system shows that there can be an overshoot for large applied potentials.

Analysis

With the assumption of constant physical properties, the equation for unsteady diffusion in a stagnant diffusion cell for a solution without supporting electrolyte or with an excess of supporting electrolyte reduces to

$$\frac{\partial c}{\partial t} = D\frac{\partial^2 c}{\partial y^2} \qquad [1]$$

where $c = c_+/\nu_+ = c_-/\nu_-$ and

$$D = \frac{z_+u_+D_- - z_-u_-D_+}{z_+u_+ - z_-u_-}$$

for a solution of a single electrolyte, and where c and D represent the concentration and effective diffusion coefficient of the reactant for a solution with an excess of supporting electrolyte.

Equation [1] should be solved with the initial condition that the concentration is uniform, $c = c_\infty$, throughout the capillary at $t = 0$. The concentration at the electrode surface can be taken, for the moment, to be an unknown function of time, $c = c_0(t)$ at $y = 0$. By taking the Laplace transform of Eq. [1] with respect to time and solving the resulting ordinary differential equation, one obtains for the transform of the concentration

$$\bar{c} = \frac{c_\infty}{s} + \left[\bar{c}_0(s) - \frac{c_\infty}{s}\right] e^{-y\sqrt{s/D}} \qquad [2]$$

where s is the Laplace transform variable. The length of the capillary has been taken to be much greater than the thickness of the diffusion layer. Differentiation of Eq. [2] with respect to y, setting y equal to zero, and inversion by means of the convolution integral produce an equation relating the concentration gradient at the surface to the variation of the surface concentration

$$\left.\frac{\partial c}{\partial y}\right|_{y=0} = \frac{-1}{\sqrt{\pi D}}\int_0^t \frac{dc_0(t')}{dt'}\frac{1}{\sqrt{t-t'}}\,dt' \qquad [3]$$

This equation is useful because the current density is also related to the concentration gradient at the surface

$$i = \frac{n\mathbf{F}D}{1-t_R}\left.\frac{\partial c}{\partial y}\right|_{y=0} \qquad [4]$$

where t_R is the transference number of the reactant ($t_R = 0$ with an excess of supporting electrolyte). The current density is further related to the surface overpotential η_s by

$$i = i_o\left(\frac{c_0}{c_\infty}\right)^\gamma\left[\exp\left\{\frac{\alpha Z\mathbf{F}}{RT}\eta_s\right\} - \exp\left\{-\frac{\beta Z\mathbf{F}}{RT}\eta_s\right\}\right] \qquad [5]$$

where i_o is the exchange current density, αZ and βZ are the transfer coefficients, and γ expresses the concentration dependence of the exchange current density.

The ohmic drop in a capillary of length L is

$$\Delta\Phi_{ohm} = iL/\kappa_\infty \qquad [6]$$

and the concentration overpotential is (14)

$$\eta_c = \frac{RT}{Z\mathbf{F}}\left[\ln\left(\frac{c_0}{c_\infty}\right) + t_R\left(1 - \frac{c_0}{c_\infty}\right)\right] \qquad [7]$$

where $Z = -z_+z_-/(z_+ - z_-)$ for reaction of a cation from a solution of a single electrolyte, and $Z = -n$ for a solution with an excess of supporting electrolyte. For the case of metal deposition from a solution of a single electrolyte, the concentration overpotential expressed by Eq. [7] includes an ohmic contribution due to the variation of the conductivity in the diffusion layer (14). Hence, it is appropriate to use the conductivity of the bulk solution in Eq. [6]. The total potential difference V^* applied between the electrode and the solution outside the capillary (as measured by a reference electrode of the same kind as the working electrode) is the sum of the concentration overpotential, the surface overpotential and the ohmic potential drop

$$V^* = \eta_c + \eta_s + \Delta\Phi_{ohm} \qquad [8]$$

It seems appropriate to define a dimensionless current density I and a dimensionless exchange current density J as

$$I = \frac{Z\mathbf{F}L}{RT\kappa_\infty}i, \quad J = \frac{Z\mathbf{F}L}{RT\kappa_\infty}i_o \qquad [9]$$

to define a dimensionless applied potential V and total overpotential η as

$$V = \frac{Z\mathbf{F}}{RT}V^*, \quad \psi = \frac{Z\mathbf{F}}{RT}(\eta_c + \eta_s) \qquad [10]$$

and a dimensionless surface concentration θ as

$$\theta = c_0/c_\infty \qquad [11]$$

Then Eq. [5] through [8] can be rewritten as

$$I = V - \psi = J[\theta^\gamma e^{\alpha E} - \theta^\gamma e^{-\beta E}] \qquad [12]$$

where

$$E = \psi - t_R(1-\theta) \qquad [13]$$

and Eq. [3] and [4] can be combined to read

$$I = \frac{NL}{\sqrt{\pi D}}\int_0^t \frac{d\theta(t')}{dt'}\frac{1}{\sqrt{t-t'}}\,dt' \qquad [14]$$

where

$$N = -\frac{n\mathbf{F}^2Dc_\infty}{(1-t_R)RT\kappa_\infty} \qquad [15]$$

If we now define a dimensionless time τ by

$$\tau = t/t_c \qquad [16]$$

where

$$t_c = N^2L^2/\pi D \qquad [17]$$

then Eq. [14] can be written as

$$I = \int_0^\tau \frac{d\theta(\tau')}{d\tau'}\frac{1}{\sqrt{\tau-\tau'}}\,d\tau' \qquad [18]$$

Equations [12], [13], and [18] constitute four equations for the determination of the time dependence of I, θ, and ψ, as well as E. They can be solved numerically when the six parameters, α, β, γ, J, V, and t_R are known for a given system. One more parameter, V, could be eliminated, but this might obscure the physical significance of the results.

Numerical Calculation Method

The integral in Eq. [18] was approximated by a sum by an adaptation of the method of Acrivos and Chambré (15). Since Eq. [18] involves an indefinite integral, it is only necessary to solve a nonlinear set of equations at each time step. By the nature of the problem, $\theta = 1$ at $\tau = 0$. For the details of the calculation method, one may refer to ref. (16).

Theoretical Results

The dimensionless current density I is plotted against the dimensionless time τ in Fig. 1 with V as a parameter. The values of α, β, γ, J, and t_R are all taken to be equal to 0.5. The higher the total applied potential V, the shorter the flat part of the curve. For high values of V, the current density overshoots the limiting cur-

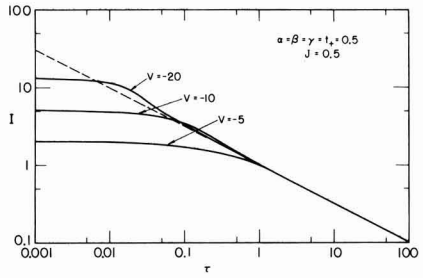

Fig. 1. Decrease of current density in a stagnant diffusion cell

rent, a phenomenon that has been observed experimentally in many of our curves of log current *vs.* log time. For a given value of V, the flat part of the curve persists longer for larger values of the characteristic time t_c. A high value of t_c results from a high transference number of the reactant and a low conductivity of the solution.

For a capillary tube of $L = 10$ cm, some estimated values of t_c for copper sulfate and sulfuric acid at 25°C are

$[CuSO_4]$	$[H_2SO_4]$	t_c
M	M	sec
0.05	0	3.0×10^6
0.5	0	6.7×10^6
0.05	1.0	5.6×10^2

In the calculations, $Z = 1$, $t_R = t_+ = 0.4$ for copper sulfate only. $Z = 2$, $t_R = 0$ for the solution with sulfuric acid as supporting electrolyte.

The decrease of surface concentration θ with time is plotted in Fig. 2 with identical parameters. The higher the applied potential, the faster the surface concentration drops to zero. The time required for the surface concentration to drop to 10 and 1% of the bulk value is plotted in Fig. 3.

Experimental Results

Figure 4 shows the transient behavior of the current density with various amounts of supporting electrolyte. These curves have qualitatively the same shape as the theoretical curves in Fig. 1, particularly with regard to the transient overshooting of the limiting current.

The surface concentration was also measured optically for an unsupported, 0.0385M cupric sulfate solution at 25°C; the results are shown in Fig. 5 for two values of the applied potential, 0.80 and 0.60V. The measured variations of the surface concentration are compared with the theoretical predictions in Fig. 5. The following data were used for the calculations:

		ref.
Conductivity κ_z	4.13×10^{-3} mho/cm	(17)
Diffusivity D	6.07×10^{-6} cm²/sec	(18)
Transference number t_R	0.383	(19)
Kinetic parameters, α, β, γ	0.5	
Z	1	

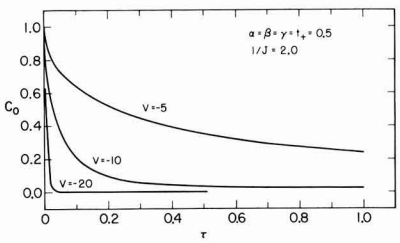

Fig. 2. Decrease of surface concentration in a stagnant diffusion cell.

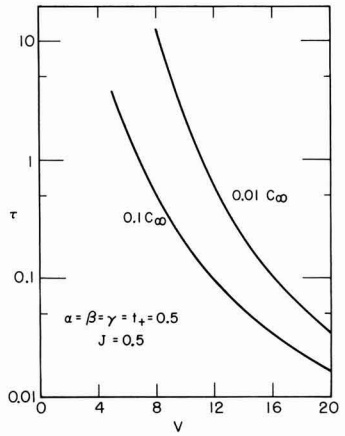

Fig. 3. Transient time in a stagnant diffusion cell, showing the dimensionless time required for the surface concentration to drop to 10 and 1% of the bulk value.

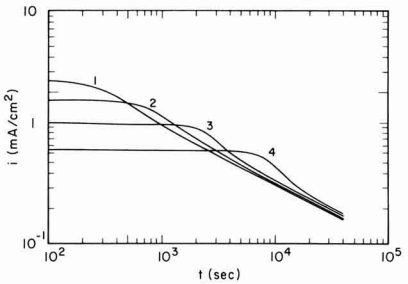

Fig. 4. Observed transient behavior in a stagnant diffusion cell (5 cm long), showing the effect of concentration of supporting electrolyte.

	$CuSO_4$ M	H_2SO_4 M	Applied potential V	t_c/V^2 sec
1	0.1003	0.175	0.355	28.5
2	0.0998	0.100	0.355	71.2
3	0.0999	0.050	0.355	198
4	0.1001	0.020	0.350	553

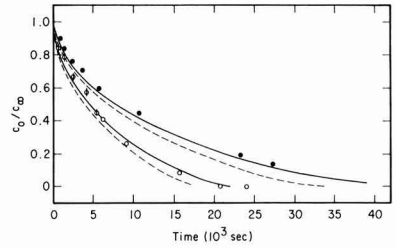

Fig. 5. Transient behavior of surface concentration of copper sulfate (0.0385M) in a stagnant diffusion cell: ● 0.60V; ○ 0.80V; dashed lines, $i_o = 1.0$ mA/cm², solid lines, $i_o = 0.1$ mA/cm²).

The length of the cell L was 15 cm, the area of the electrode was 0.178 cm², and the calculated characteristic time t_c was 5.60 x 10^6 sec. There are no exchange current density data available in the literature for an unsupported $CuSO_4$ solution, a reasonable estimate being that it lies between 0.1 and 1.0 mA/cm². The solid lines are theoretical calculations at an exchange current density of 0.1 mA/cm², and the dashed lines

are calculated at 1.0 mA/cm². The solid lines represent a satisfactory fit to the experimental results.

An unexplained observation should be recorded here. For a solution 0.1*M* in $CuSO_4$ and 1.375*M* in H_2SO_4, the current time curves in Fig. 6 were obtained. The current drops suddenly at about 0.3 sec. This phenomenon was fairly reproducible in a well-supported electrolyte. No such step change was observed for solutions with little or no supporting electrolyte.

Before the runs, the electrode was predeposited with copper at 0.1V for 1 to 3 min. Values of the parameters for the theoretical calculations are $\alpha = 0.75$, $\beta = 0.25$, $\gamma = 0.5$, $t_R = 0$, $\kappa_x = 0.4925$ mho/cm, $Z = 2$, $L = 7.0$ cm, $D = 5.09 \times 10^{-6}$ cm²/sec, $t_c = 740$ sec, $V^* = 0.225$V, and the exchange current density is estimated to lie between 1 and 10 mA/cm² for a cathode surface prepared by electrodeposition (20).

Before the step change of current density, the horizontal part of the curve was found to fall between the curves for theoretical predictions of exchange current of 1 and 10 mA/cm². The charging of the electrode double layer should be complete in a time of about 0.5 msec.

A reviewer suggests the following possible explanations for the step change of current density: (*a*) cuprous ions are initially present in the solution in equilibrium with cupric ions and will tend to react before the cupric ions due to kinetic factors (20); (*b*) crystallographic defects in the deposit may be different from those in the substrate metal and thus lead to a change of kinetic parameters with time; and (*c*) adsorption of inhibitors or impurities may lead to changes of kinetic parameters although the effect would not be expected to be reproducible. However, calculations based on the equilibrium concentration of cuprous ions suggest that the transition time for their concentration to drop to zero at the electrode surface would be much smaller than the time at which the step change in current density occurs.

Conclusion

In this work, the transient behavior has been worked out for a stagnant diffusion cell. The resulting time dependence of the surface concentration for an unsupported electrolyte agrees with the theoretical predictions within the uncertainty of the available electrochemical kinetic parameters. The current density is found, experimentally and theoretically, to overshoot the limiting current, in harmony with predictions for the current distribution on plane and disk electrodes.

Acknowledgment

This work was supported by the United States Atomic Energy Commission and by the Petroleum Research Fund, administered by the American Chemical Society.

Manuscript submitted Dec. 10, 1969; revised manuscript received *ca.* May 26, 1970.

Any discussion of this paper will appear in a Discussion Section to be published in the June 1971 JOURNAL.

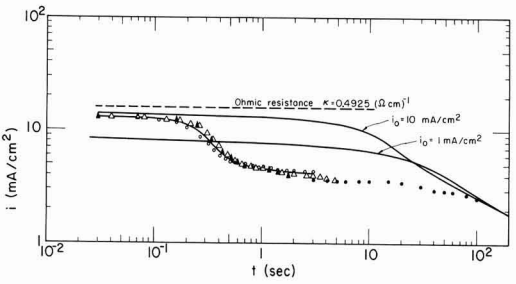

Fig. 6. Theoretical and observed transient behavior at very short time. Total applied voltage 0.225V; ● run 82; ○ run 83; ▲ run 84; △ run 85.

LIST OF SYMBOLS

c_i	concentration of species i, mole/cm³
c_o	surface concentration of reactant, mole/cm³
D	diffusion coefficient, cm²/sec
$\mathbf{F}$	Faraday's constant, 96,500 coul/equiv
i	current density, A/cm²
i_o	exchange current density, A/cm²
I	dimensionless current density
J	dimensionless exchange current density
L	length of diffusion cell, cm
n	number of electrons produced when one reactant ion or molecule reacts
N	dimensionless parameter
R	universal gas constant, joule/mole-deg
s	Laplace transform variable, sec⁻¹
t	time, sec
t_c	characteristic time, sec
t_R	transference number of reactant
T	temperature, °K
u_i	mobility of species i, cm²-mole/joule-sec
V	dimensionless applied potential
V^*	applied potential, V
y	distance from electrode, cm
z_i	charge number of species i
Z	$-z_+z_-/(z_+ - z_-)$ for unsupported electrolyte $-n$ with excess supporting electrolyte
α, β, γ	electrochemical kinetic parameters
ψ	dimensionless total overpotential
η_c	concentration overpotential, V
η_s	surface overpotential, V
θ	dimensionless surface concentration
κ_x	conductivity of the bulk solution, mho/cm
ν_+, ν_-	numbers of cations and anions produced by dissociation of one molecule of electrolyte
τ	dimensionless time
$\Delta\Phi_{ohm}$	ohmic potential drop, V

REFERENCES

1. M. v. Stackelberg, M. Pilgram, and V. Toome, *Z. Electrochem.*, **57,** 342 (1953).
2. R. E. Davis, G. L. Horvath, and C. W. Tobias, *Electrochim. Acta,* **12,** 287 (1967).
3. F. G. Cottrell, *Z. physik. Chem.,* **42,** 385 (1903).
4. N. Ibl and G. Trümpler, *Helv. Chim. Acta,* **34,** 1217 (1951).
5. Limin Hsueh and John Newman, UCRL-19101, In preparation.
6. Limin Hsueh and John Newman, UCRL-19102. July 1970.
7. Limin Hsueh and John Newman, UCRL-19099, October 1969.
8. John Newman, *This Journal,* **113,** 1235 (1966).
9. John Newman, *ibid.,* **114,** 239 (1967).
10. Vinay Marathe and John Newman, *ibid.,* **116,** 1704 (1969).
11. W. R. Parrish and John Newman, *ibid.,* **116,** 169 (1969).
12. W. R. Parrish and John Newman, *ibid.,* **117,** 43 (1970).
13. Thomas W. Chapman and John Newman, *J. Phys. Chem.,* **71,** 241 (1967).
14. John Newman, *Intern. J. Heat Mass Transfer,* **10** 983 (1967).
15. Andreas Acrivos and P. L. Chambré, *Ind. Eng. Chem.,* **49,** 1025 (1967).
16. Limin Hsueh, Dissertation, University of California, Berkeley, December, 1968. (UCRL-18597).
17. B. B. Owen and R. W. Gurry, *J. Am. Chem. Soc.,* **60,** 3074 (1938).
18. W. G. Eversole, H. M. Kindsvater, and J. D. Peterson, *J. Phys. Chem.,* **46,** 370 (1942).
19. J. J. Fritz and C. R. Fuget, *ibid.,* **62,** 303 (1958).
20. E. Mattsson and J. O'M. Bockris, *Trans. Faraday Soc.,* **55,** 1586 (1959).

Stoichiometry of Anodic Copper Dissolution at High Current Densities

K. Kinoshita,*[1] D. Landolt,*[2] R. H. Muller,* and C. W. Tobias*

Inorganic Materials Research Division, Lawrence Radiation Laboratory and Department of Chemical Engineering, University of California, Berkeley, California 94720

ABSTRACT

The influence of current density, flow rate, and electrolyte composition on the stoichiometry of anodic copper dissolution was investigated under conditions comparable to those of electrochemical machining. Weight loss measurements, x-ray diffraction, and chemical analysis were used for the characterization of the dissolution reaction. A sharp change in dissolution mechanism coincided with the transition from active to transpassive dissolution. For active dissolution, an apparent valence of the dissolution process of two was found in sulfate and nitrate electrolytes, and of one in chloride electrolytes. For transpassive dissolution, mixed valences lying between 1 and 2 were found in all electrolytes. The mixed valences are interpreted to result from the simultaneous production of monovalent and divalent reaction products, some of which are in solid form.

Anodic dissolution of metals at current densities of up to several hundred amperes per square centimeter and with electrolyte flow velocities of many meters per second is being carried out on a technical scale in the process of electrochemical machining (ECM). In an attempt to provide quantitative information on the electrochemical processes under high current densities, the anodic dissolution of copper is being investigated (1-3). Copper was chosen because its electrochemical properties are reasonably well understood (4-8). In a previous paper (1), the role of mass transfer in determining the occurrence of passivation phenomena during copper dissolution in K_2SO_4 and KNO_3 solutions has been reported. It was found that apparent anode potentials and surface textures resulting from dissolution changed drastically while going from a low voltage (active) to a high voltage (transpassive) mode of dissolution.[3]

In the present study, the valence of the electrode reaction and the composition of reaction products of copper have been investigated in nitrate, sulfate, and chloride electrolytes. Weight loss measurements of the anode, x-ray diffraction analysis of solids, and chemical analysis of the solution were used for the characterization of the dissolution reaction. Current densities employed ranged from 0.1 to 80 A/cm^2. Experiments were performed under forced convection conditions in a flow channel at flow rates from 30-700 cm/sec, as well as in unstirred solutions under free convection conditions.

Experimental

Most experiments were carried out under forced convection conditions in an experimental flow system similar to that described in a previous study (1) and schematically shown in Fig. 1. The electrolyte was pumped by a positive displacement pump,[4] and the flow rate was measured with a rotameter.[5] One half inch stainless steel pipes were used throughout the system.

A 30 cm long rectangular flow channel of 1 x 3 mm cross section, constructed of laminated polyvinyl chloride, was positioned upstream of the experimental cell to establish fully developed velocity profiles at

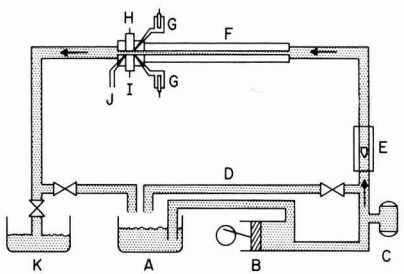

Fig. 1. Schematic of flow system: A, supply tank; B, dual piston pump; C, accumulator; D, bypass line; E, rotameter; F, entrance length of flow channel; G, reference electrodes; H, cathode; I, anode; J, capillary for precipitate collection; K, drain tank.

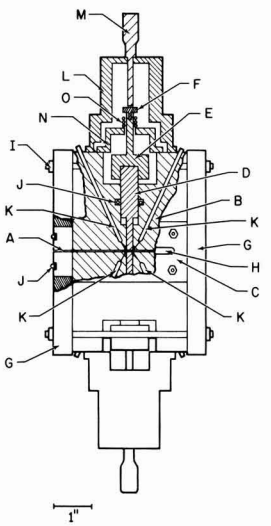

Fig. 2. Side view of experimental cell with partial cross sectioning: A, rectangular flow channel; B, epoxy cell body; C, stainless steel side plate; D, copper electrode; E, aluminum cap; F, nylon screw; G, stainless steel end flange; H, glass side window; I, bolt and nut assembly; J, O-ring seal; K, liquid junction connection to backside capillaries; L, aluminum micrometer holder; M, micrometer head; N, aluminum base plate; O, coil spring.

* Electrochemical Society Active Member.

[1] Present address: Pratt & Whitney Aircraft Corporation, Middletown, Connecticut 06457.

[2] Present address: University of California, School of Engineering & Applied Science, Los Angeles, California 90024.

Key words: anodic metal dissolution, copper anode, passivity.

[3] Different definitions for the phenomenon of passivation can be found in the literature. The term is used here to describe an abrupt increase in measured anode potential with time for certain combinations of flow rate and current density (see *e.g.*, Fig. 3).

[4] Constametric Pumps, Milton Roy Company, Philadelphia, Pennsylvania. Varidrive Motor, U. S. Electrical Motors, Inc., Los Angeles, California.

[5] Type 18410, Schutte and Koerting Company, Cornwall Heights, Pennsylvania.

the electrodes (1). The electrolysis cell is shown schematically in Fig. 2. The cell body (B) was made of epoxy resin with the two glass side walls (H) held together by plates (C). The cell was connected to the inlet and outlet channel by end flanges (G). Optical observation of the interelectrode gap could be performed through the glass walls. Back-side capillaries (K) which enter the channel walls next to the electrodes were used for electrode potential measurements and, in some experiments, for the sampling of solution on the downstream side of the electrodes. The copper electrodes (D) (purity ≥99.9%) had a geometrical surface area of 3 x 3 mm. The electrodes could be advanced manually by turning micrometer head (M). The electrode assembly was pushed back against insert (F) by sprint (O). Silicone rubber gaskets[6] cast between glass wall and epoxy cell body were used for sealing the cell.

Measurements of cell voltage, electrode potentials, and current were made simultaneously on a multi channel light beam oscillograph.[7] Electrical power connections to the cell were made by threaded connections screwed into aluminum cap (E). The current was recorded by measuring the voltage drop across a shunt. Anode and cathode potentials were measured with respect to saturated calomel reference electrodes, which were placed in small glass containers connected to the capillaries by Tygon tubing. The electrolysis current was provided by an electronically controlled constant current supply.[8]

Prior to each run, the electrodes were ground on 600 grit emery paper and washed with aqueous detergent. Following a dip in concentrated HCl, they were rinsed with distilled water and reagent grade acetone and stored in vacuum until use. The electrodes were aligned with the channel wall by using a microscope with 20X magnification. During electrolysis, the 1 mm electrode gap was approximately maintained by manual adjustment of the micrometer.

During a typical experiment, 25 mg of copper were dissolved, which corresponded to an average depth of dissolution of about 0.3 mm. After each run, the anode was removed from the cell, rinsed with water, dried with acetone, and weighed on an analytical balance. The accuracy of the weight loss determination is estimated at ±1-2%. The amount of charge passed during the experiment was determined from the oscillographically recorded current trace. The accuracy of the charge measurement is estimated at ±2-3%.

From the measurement of charge and weight loss, an apparent valence n of the dissolution process was calculated according to Eq. [1]

$$n = \frac{ItM}{\Delta W \mathbf{F}} \qquad [1]$$

where I is the current passed during time t, M is the atomic weight of copper, ΔW is the anode weight-loss, and $\mathbf{F}$ is the Faraday constant.

Solid reaction products formed during the anodic dissolution of copper were analyzed by x-ray diffraction. Initial analyses were made using a 11.46 mm Debye-Scherrer powder camera mounted on an x-ray diffraction unit.[9] Ni filtered Cu radiation (40 kV, 20 mA) was used.

A sample of the anodic reaction product from the flow cell was collected by rubbing a glass fiber through the precipitate adhering to the wet surface. Diffraction patterns obtained were, however, difficult to analyze because of the faintness of the diffraction lines. Also, because of the small samples, exposure times to the x-ray beam from 6-12 hr were necessary.

[6] Encapsulant 502 RTV, Dow Corning Corporation, Midland, Michigan.
[7] Series 2300, Brush Instrument Division, Cleveland, Ohio.
[8] Type C618, Electronic Measurements Company, Eatontown, N. J. or Model KS 120-10M, Kepco Inc., Flushing, New York.
[9] Norelco X-Ray Diffraction Unit, Type 12045 with Debye-Scherrer Camera Type 52056-O, North American Philips Company, Inc., New York, N. Y.

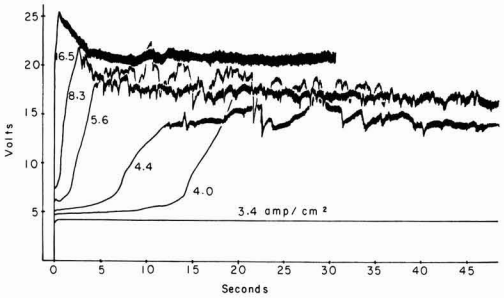

Fig. 3. Cell voltage transients measured in 2N KNO_3 at different current densities, flow rate 30 cm/sec.

To provide a larger specimen, a continuous sampling technique was developed. An x-ray diffractometer[10] using a Ni filtered Cu radiation (40 kV, 14 mA) could then be used. Solution escaping through the (0.014 in. diameter) capillary on the downstream side of the anode was collected on a Whatman No. 41 paper by continuous vacuum filtration. Without washing, the filter paper with adhering precipitate was dried under vacuum, mounted on a Lucite sample holder using double-sided adhesive tape, and placed in the diffractometer. A preliminary x-ray pattern of the blank showed strong diffraction peaks at low θ values which did, however, not interfere with the diffraction peaks of possible compounds present in the precipitate.

In order to substantiate the apparent valence determination carried out under forced convection conditions, some experiments were performed in a stagnant electrolyte which allowed quantitative determination of dissolved Cu^+ and Cu^{2+} ions. Since Cu^+ is unstable in aqueous solution unless complexing agents are present, only chloride electrolytes were analyzed this way. The electrolysis was carried out in an H cell with a glass frit separating anode and cathode compartments (2). In contrast to the highly diluted dissolution products obtained in the flow channel, concentrations which can be determined by simple analytical techniques could be obtained in this system. The analytical determination of Cu^{2+} and Cu^+ was based on that given by Vogel (9). Cuprous ion was oxidized with ferric ammonium sulfate, and the resulting ferrous ion was titrated with ceric sulfate. The cupric ion concentration was obtained as the difference between total copper concentration and cuprous ion concentration. The total copper concentration was determined iodometrically after oxidation of cuprous ion to cupric ion by sodium peroxide.

Results

Current-voltage behavior.—Figure 3 illustrates the transient cell voltage behavior during galvanostatic copper dissolution in 2N KNO_3 under a given flow rate (30 cm/sec). At low current density (3.4 A/cm²), the dissolution proceeds indefinitely in a low voltage (active) mode. Above a critical current density, which is shifted to higher values by increased flow rates, the dissolution process switches to a high voltage (transpassive) mode, after a transition time with active dissolution. The length of the transition period decreases with increasing current density and decreasing flow rate (not shown). Figures 4 and 5 are examples of transient cell voltage behavior with K_2SO_4 and KCl solutions. In all cases, dissolution in the transpassive mode occurs at a cell voltage which is 10-20V higher than in the active mode. Voltage fluctuations are observed in the transpassive region and, at the higher current densities, a voltage maximum occurs before steady state is reached.

Apparent valence.—Average steady-state values of the cell voltage and apparent valence values are

[10] Picker X-Ray Corporation, Waite Manufacturing Division, Inc., Cleveland, Ohio.

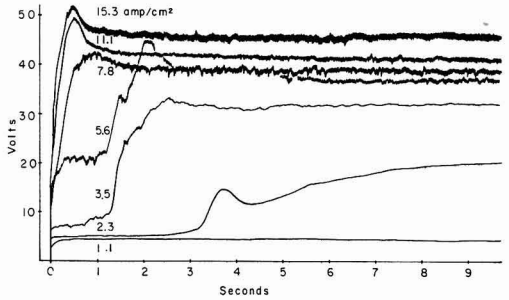

Fig. 4. Cell voltage transients measured in 1*N* K_2SO_4 at different current densities, flow rate 50 cm/sec.

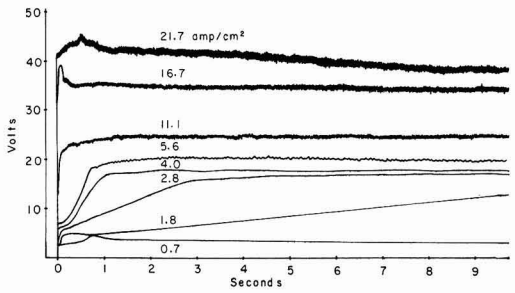

Fig. 5. Cell voltage transients measured in 2*N* KCl at different current densities, flow rate 50 cm/sec.

plotted *vs.* current density in Fig. 6 to 8. The behavior in 2*N* KNO_3 and 1*N* K_2SO_4 solutions is very similar. With the transition from active to transpassive dissolution, a sharp drop in apparent valence occurs. The apparent valence value of $n = 2$ observed in the active region indicates that copper is dissolved almost exclusively to divalent cupric ions. This is consistent with expectations based on thermodynamic considerations of the reversible potential of a copper electrode in contact with dissolved mono and divalent copper ions (8). In the transpassive region, on the other hand, the apparent valence depends on the value of the applied current density with respect to the current density at which passivation occurs. A limiting value of $n \simeq 1.5$-1.6 is reached at high current densities. In order to account for this value of n, it has to be assumed either that part of the copper is dissolved to a monovalent form, or that part of the metal disintegrates during the dissolution process. Since *p*H might have an influence in determining the reaction path (8), additional experiments were performed in a 2*N* KNO_3 solution adjusted to *p*H 1 by the addition of concentrated nitric acid, and also in a 1*N* H_2SO_4 solution. Voltage readings and apparent valences obtained in both of these electrolytes corresponded within experimental accuracy to those of the nitrate and sulfate solutions, respectively. This indicates that, within the range studied, *p*H has a negligible influence on apparent valence of the dissolution process. As illustrated by Fig. 8, the behavior in KCl solutions was quite different from that in KNO_3 and K_2SO_4 solutions. A sharp transition between active and transpassive dissolution was absent. Instead, periodic fluctuations occurred (indicated by dotted lines in Fig. 8) in the transition region. Such oscillations in the copper/chloride system have also been reported in the literature for low current density conditions (6, 10). Periodic oscillations have also been observed during high rate copper dissolution in sulfate and chlorate electrolytes under certain conditions (1-3). The apparent valence, in the case of chloride solution, is $n = 1$ at low current densities. A maximum of $n = 1.4$ is observed at intermediate current densities, and the apparent valence drops to $n \simeq 1.2$ in the range of high current densities. While it appears that the observed changes in apparent valence are related to the occurrence of passivation, the relationships are not as clear cut as in

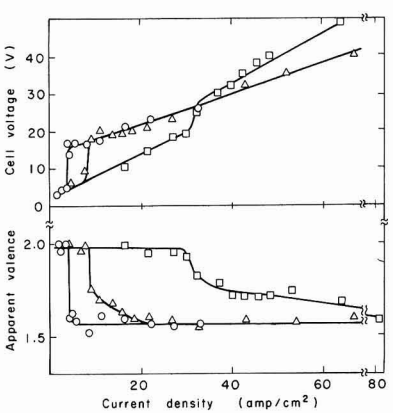

Fig. 6. Variation of apparent valence and cell voltage with current density in 2*N* KNO_3 for different flow rates: ○, 30 cm/sec; △, 200 cm/sec; □, 627 cm/sec.

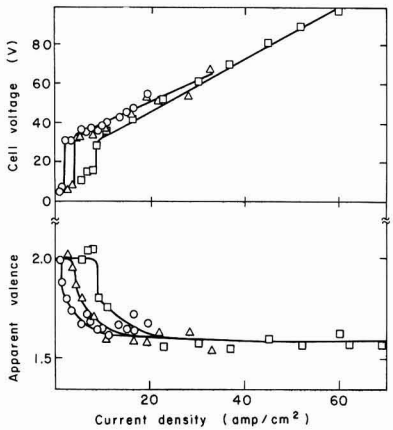

Fig. 7. Variation of apparent valence and cell voltage with current density in 1*N* K_2SO_4 for different flow rates: ○, 50 cm/sec; △, 200 cm/sec; □, 686 cm/sec.

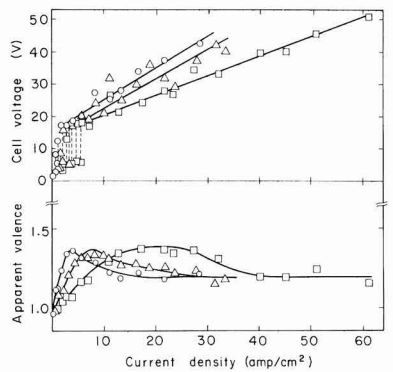

Fig. 8. Variation of apparent valence and cell voltage with current density in 2*N* KCl for different flow rates: ○, 50 cm/sec; △, 200 cm/sec; □, 606 cm/sec.

Table I. X-ray analysis of anode solid reaction products

Electrolyte	Compounds identified
2*N* KNO_3	Cu_2O, Cu
2*N* KNO_3 + HNO_3 (pH 1)	Cu
1*N* K_2SO_4	Cu_2O, Cu
1*N* H_2SO_4	Cu

nitrate and sulfate solutions. For example, at the highest flow rate (606 cm/sec), the maximum value of n was attained at much higher current density than that corresponding to the active-passive transition derived from cell voltage measurements.

Analysis of solid reaction products.—Anode precipitates were found during transpassive dissolution only. X-ray analysis of precipitates collected from experiments performed in KNO_3 and K_2SO_4 solutions showed Cu_2O to be the principal copper compound. Diffraction peaks for metallic copper were also present in some experiments. The metallic copper contents of precipitates from acidified solutions was increased at the expense of the cuprous oxide contents (Table I). No analysis of anodic precipitates in chloride solution was possible because precipitates could not be collected in sufficient amounts. A typical diffraction pattern of anode precipitate is given in Fig. 9 together with patterns of known samples of Cu_2O and Cu. Precipitates collected in the drain tank showed a different composition from those collected close to the anode. They contained basic oxides of complex composition, owing to contact with the alkaline solution produced at the cathode.

Analysis of dissolved reaction products.— Apparent valence determinations in chloride solution were also carried out in a separate cell under absence of forced convection. In these experiments, values of apparent valence obtained from weight loss measurements could be compared with those obtained by chemical analysis of dissolved reaction products. Calculation of the chemically determined apparent valence n^* was based on Eq. [2]

$$Cu \rightarrow xCu^+ + yCu^{2+} + n^*e \qquad [2]$$

where x and y are the fractional amounts of Cu^+ or Cu^{2+}, respectively. Since, from the mass balance $x + y = 1$ and from the charge balance $x + 2y = n^*$, one gets Eq. [3]

$$n^* = 2 - x = 1 + y \qquad [3]$$

The results given in Table II illustrate the good agreement between the valence determined by chemical analysis with that derived from weight loss measurements for a wide range of current densities. In all cases a mass balance could be established within 1-2%. Changes in apparent valence with current density in chloride solutions are therefore indeed due to different ratios of Cu^+ and Cu^{2+} produced. No oxygen evolution was observed during the experiments. The experiments also confirmed that the anodic behavior, *i.e.*, the occurrence of active and transpassive dissolution, was essentially the same in stagnant as in flowing solutions,

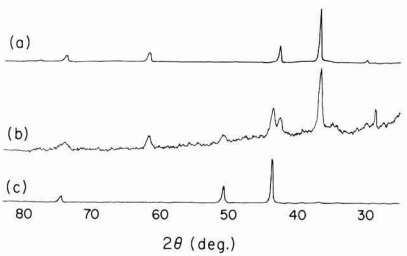

Fig. 9. X-ray diffractometer trace of anode precipitate (b) compared to known samples of Cu_2O (a) and Cu (c). Anode precipitate obtained at 11.1 A/cm² and 50 cm/sec in 1*N* K_2SO_4.

Table II. Chemical analysis of dissolved reaction products in 3*N* KCl solution after passage of 60 coul, anode area 1 cm²

Current density, A/cm²	Valence from dissolved Cu^+ and Cu^{++}	Valence from weight loss
0.05	1.00	1.00
0.10	1.19	1.15
0.13	1.21	1.28
0.16	1.27	1.31
0.21	1.28	1.30
0.26	1.26	1.28
0.51	1.22	1.20
0.82	1.19	1.20
1.00	1.13	1.10
1.31	1.14	1.16
1.58	1.10	1.08
1.87	1.08	1.06
1.98	1.07	1.07

with the exception that passivation sets in at much lower current densities in the absence of external convection.

Discussion

Nitrate and sulfate solutions.—Two dissolution modes, active and transpassive, were found differing in overvoltage and apparent valence of dissolution. The transition between active and transpassive dissolution depends on mass transfer conditions. Using the mass transfer correlations for channel flow discussed earlier (1), the interfacial concentration of ionic dissolution product at the onset of transpassive dissolution was estimated from the passivation current density for different flow rates and electrolytes. (A diffusion coefficient of 5×10^{-6} cm²/sec was assumed for this calculation.) A comparison of the results shown in Table III with solubility data given in Table IV indicates that the onset of transpassive dissolution coincides, at least qualitatively, with the limiting transport of dissolved reaction products by convective diffusion. This substantiates the validity of previous results (1) which were obtained in a different flow system, mostly at higher current densities and flow rates. In addition, it was found here that passivation current densities in 1*N* H_2SO_4 were essentially the same as in 1*N* K_2SO_4. This suggests that limitations in the transport of cupric salt, rather than the formation of oxide or hydroxide, initiates the change to transpassive dissolution.

The present study also demonstrates that the transition between active and transpassive dissolution is associated with a drastic change in current efficiency for the metal removal process, with more copper being

Table III. Calculated interfacial concentration of copper salts at onset of transpassive dissolution

Electrolyte	Flow velocity, cm/sec	Reynolds number	Passivation current density, A/cm²	Interfac. conc., moles/l
2*N* KNO_3	30	510	3.8	4.5
	200	3390	8.5	4.6
	627	10600	31.0	8.5
1*N* K_2SO_4	50	730	1.5	1.4
	200	2920	4.1	2.2
	686	10000	8.5	2.2
1*N* H_2SO_4	50	770	3.6	3.4
	200	3090	4.7	2.5
	686	10600	11.8	3.0
2*N* KCl	50	820	0.4	0.8
	200	3270	1.2	1.2
	606	10000	2.5	1.2

Table IV. Solubilities of copper salts at room temperature

Salt	Solvent	Solubility, moles/l	Reference
Cupric nitrate	H_2O	7.0	(24)
Cupric sulfate	H_2O	1.4	(24)
	1*N* H_2SO_4	1.1	(25)
Cuprous chloride	2*N* KCl	1.0	(17), (18)
	3*N* KCl	1.9	(17), (18)

dissolved for a given amount of charge in the transpassive region. A mechanism involving the formation of monovalent copper species at the anode, especially cuprous oxide, rather than anodic disintegration by grain boundary attack (11, 12), seems to be the cause for the apparent increase in current efficiency. The above conclusion, although it cannot be rigidly proven on the grounds of our results, is supported by the following experimental observations: (*A*) Cuprous oxide has been found to be the main constituent of anodic films. (*B*) Substantial amounts of metallic copper were observed in the x-ray patterns in acidic solutions only, consistent with the fact that Cu_2O disproportionates in these solutions into Cu^{2+} and Cu. (*C*) No grain boundary attack was observed microscopically in the transpassive region. Instead, the surfaces after transpassive dissolution had a shiny appearance and were almost randomly pitted (1, 2). (*D*) At least in the case of chloride solutions, the presence of cuprous ion could be verified quantitatively. All these factors indicate that a distintegration mechanism, which has been proposed primarily for more reactive metals (beryllium, magnesium, cadmium, zinc) at low current densities (13-16), is not likely to be of importance in the present anodic dissolution process.

Measured apparent valences tended to reach a constant limiting value at high current densities. No satisfactory explanation for this phenomenon can be given at the present time. From a purely kinetic point of view we would expect a continuous variation of n with current density. A possible explanation of the observed constancy of n may, perhaps, be sought in a model viewing the surface as an ensemble of small surface area elements randomly fluctuating between active and passive states. Such active-passive fluctuations, which are most pronounced in chlorate electrolytes (2, 3), are now being studied in this laboratory.

Chloride solutions.—The dissolution behavior in chloride electrolytes is different because the monovalent ionic state becomes thermodynamically more favorable than the divalent state due to the formation of cuprous ion complexes (17, 18). Thus, disproportionation of Cu^+, which usually occurs in aqueous solutions is avoided. Since a variety of different complexes may be formed, depending on the local chloride concentration, the dissolution process in chloride solutions is expected to be much more complicated than in nitrate and sulfate solutions. For example, due to the effect of chloride concentration on the solubility of cuprous ion, the formation of precipitate layers depends not only on the rate of departure of cations from the interface, but also on the rate of arrival of anions. In addition to the mass transport of the dissolution product, the mass transport of chloride ion may therefore become a limiting factor, since chloride ions are consumed at the anode by complex formation. Such a mechanism has, for example, been reported by Landsberg *et al.* (19) for the dissolution of gold in HCl. During the course of stoichiometric determinations in stagnant solution, a number of transient measurements were performed in 3*N* KCl solutions at constant current density. Table V summarizes the transition times determined for the onset of transpassive behavior. In spite of that the geometrical arrangement was not ideal to exclude free convection completely, the application of Sand's equation is justified because of the short times involved. From the average measured quantity $i\sqrt{\tau}$, a value for ΔC, the rate-limiting concentration difference, was calculated according to Eq. [4]

$$\Delta C = \frac{2i\sqrt{\tau}}{n\mathbf{F}\sqrt{\pi D}} \qquad [4]$$

assuming $D = 5 \times 10^{-6}$ cm²/sec and $n = 1$. The resulting value of $\Delta C = 3.6$ mole/liter is similar in magnitude to the solubility of CuCl in 3*N* KCl [1.9 mole/liter (17)]. This indicates that, under the conditions of these experiments, passivation may have been caused by a similar precipitation mechanism as in nitrate and sulfate solutions.

Table V. Transition times τ for copper dissolution at different current densities i in 3*N* KCl without external convection

i, A/cm²	τ, sec	$i\sqrt{\tau}$
0.10	38.90	0.62
0.16	11.60	0.56
0.21	9.20	0.69
0.26	5.63	0.62
0.51	1.85	0.70
0.82	0.65	0.68
1.00	0.48	0.69
1.31	0.28	0.69
1.58	0.20	0.70
1.87	0.16	0.75
1.98	0.15	0.77

The increase in apparent valence n on passivation (Fig. 8) is consistent with the fact that at higher anode potentials, the reaction $Cu \rightarrow Cu^{2+}$ becomes thermodynamically possible. No true anode potential measurements were possible under the conditions of this study; therefore, a discussion has to remain qualitative. The subsequent decrease in n at still higher current densities may then be explained by assuming formation of Cu_2O, as observed in the case of nitrate and sulfate solutions. The oozing of a reddish brown, finely dispersed dissolution product from localized anode areas which changed their positions during electrolysis was observed visually in stagnant KCl solutions in the transpassive region (2). This solid might have been Cu_2O, but it was not possible to collect the precipitate due to its chemical instability in the chloride electrolyte. The formation of cuprous oxide during copper dissolution in chloride media has also been reported in the literature (20-23). The formation of a thin cuprous chloride film during transpassive dissolution in chloride solution was indicated by the white appearance of the surface.

Summary and Conclusions

1. The present study has confirmed earlier findings (1) obtained under different experimental conditions that in nitrate and sulfate electrolytes the transition from active to transpassive dissolution of copper is controlled by the mass transfer of dissolved dissolution products.

2. Although the details of copper dissolution in chloride solution are probably different from those in nitrate and sulfate, the gross current-voltage behavior is similar. Ionic mass transfer limitations seem, therefore, to be the dominating factor determining the onset of passivation in chloride solutions, too.

3. The apparent valence of the dissolution process undergoes a noticeable change with the transition from active to transpassive dissolution. In nitrate and sulfate solutions, active dissolution proceeds with an apparent valence of 2. Transpassive dissolution leads to a lower apparent valence, which reaches a limiting value of 1.6 at high current densities. This drop in apparent valence is interpreted to be caused by the anodic production of monovalent copper species, rather than by anodic disintegration.

4. Active dissolution in chloride solution occurs with an apparent valence of one. This is due to the stabilization of cuprous ion by complex formation. Upon passivation the apparent valence increases, going through a maximum of 1.4 with increasing current density before reaching a limiting value of 1.2. This increase in apparent valence on passivation is due to part of the copper being dissolved in divalent form.

5. No significant oxygen evolution occurred during copper dissolution under all the experimental conditions employed.

6. The formation of solid anodic dissolution products during transpassive dissolution has been demonstrated in agreement with earlier optical observations. Anal-

ysis of the precipitates by x-ray diffraction has shown Cu_2O to be the main constituent produced in potassium nitrate and sulfate solutions. Metallic copper, resulting from disproportionation of Cu_2O, is found in acidified solutions. In chloride solutions optical observation indicated the formation of cuprous chloride films.

Acknowledgment

This work was done under the auspices of the U. S. Atomic Energy Commission.

Manuscript received May 13, 1970.

Any discussion of this paper will appear in a Discussion Section to be published in the June 1971 JOURNAL.

REFERENCES

1. D. Landolt, R. H. Muller, and C. W. Tobias, *This Journal*, **116,** 1384 (1969).
2. K. Kinoshita, Ph.D. Thesis, University of California, Berkeley, UCRL-19051, Sept. 1969.
3. D. Landolt, R. Acosta, R. H. Muller, and C. W. Tobias, *This Journal*, **117,** 839 (1970).
4. E. Mattson and J. O'M. Bockris, *Trans. Faraday Soc.*, **55,** 1586 (1959).
5. A. Hickling and D. Taylor, *ibid.*, **44,** 262 (1948).
6. R. S. Cooper and J. H. Bartlett, *This Journal*, **105,** 109 (1958).
7. F. H. Giles and J. H. Bartlett, *ibid.*, **108,** 266 (1961).
8. M. Pourbaix, "Atlas of Electrochemical Equilibria in Aqueous Solutions," p. 384, Pergamon Press, New York (1966).
9. A. I. Vogel, "A Textbook of Quantitative Inorganic Analysis Including Elementary Instrumental Analysis," 3rd ed., John Wiley & Sons, Inc., New York (1961).
10. H. Lal and H. R. Thirsk, *J. Chem. Soc.*, **1953,** 2638.
11. U. R. Evans, "Corrosion and Oxidation of Metals," Arnold, London (1960).
12. I. A. Menzies and A. F. Averill, *Electrochim. Acta*, **13,** 807 (1968).
13. M. E. Straumanis and Y. Wang, *Corrosion*, **22,** 132 (1966).
14. M. E. Straumanis, J. L. Reed, and W. J. James, *This Journal*, **114,** 885 (1967).
15. M. E. Straumanis and B. K. Bhatia, *ibid.*, **110,** 357 (1963).
16. W. J. James, M. E. Straumanis, and J. W. Johnson, *Corrosion*, **23,** 15 (1967).
17. W. U. Malik, S. M. F. Rahman, and S. A. Ali, *Z. anorg. u. allgem. Chem.*, **299,** 322 (1959).
18. W. U. Malik, S. M. F. Rahman, and S. A. Ali, *ibid.*, **301,** 220 (1959).
19. G. Just and R. Landsberg, *Electrochim. Acta*, **9,** 817 (1964).
20. R. S. Cooper, *This Journal*, **103,** 307 (1956).
21. D. Miller, *J. Phys. Chem.*, **13,** 256 (1909).
22. H. W. Gillett, *ibid.*, **13,** 332 (1909).
23. A. G. Arend, *Paint Tech.*, **13,** 265 (1948).
24. Int. Crit. Tables 4, 222, McGraw-Hill (1928).
25. W. J. Muller and L. Holleck, *Monatsh. Chem.*, **52,** 409 (1929).

Comparative Activity of (111), (100), (110), and Polycrystalline Platinum Electrodes in H_2-Saturated 1M H_2SO_4 under Potentiostatic Control

Sigmund Schuldiner,* Murray Rosen,*[1] and David R. Flinn*[1]

Electrochemistry Branch, Naval Research Laboratory, Washington, D. C. 20390

ABSTRACT

Potentiostatic measurements of the three principle faces of oriented single Pt crystals and polycrystalline Pt showed some interesting comparisons. True areas are based on Pt atom densities, and under the electrochemical treatment used, no changes in these areas were found once the initial surface cleaning was completed. The hydrogen overvoltage was independent of crystal orientation or other metallurgical factors; however, the passivation of the hydrogen oxidation reaction and the oxygen generation reactions were different for each single crystal orientation with a large difference between these faces and a polycrystalline bead electrode. Steady-state relations between potential and amounts of associated H atoms and number of sites available for coverage with O atoms were determined also. These steady-state values are generally less than the comparative amounts found under transient conditions. Oxygen evolution on the Pt faces was not observed below a potential of 1.8V. It appears that grain boundaries, stress, and impurity inclusions may have more effect in determining the catalytic activity for some reactions than does the actual atomic density or geometry of Pt atoms.

Although there have been numerous investigations of the hydrogen reaction on polycrystalline Pt electrodes and of the potentiostatic behavior of Pt in H_2-saturated solutions, our knowledge of the effects of the geometry of Pt atoms on such behavior is very limited. Using the voltage sweep method, Will (1) studied the relationship between hydrogen adsorption and potential on single Pt crystals of (111), (100), and (110) orientations.

Our approach was to conduct a comparative investigation of polycrystalline Pt with Pt single crystal orientations with respect to reactivity for steady-state hydrogen generation, hydrogen oxidation, and oxygen generation reactions. In addition, steady-state relations between surface coverage with potential were determined, both in the presence and absence of dermasorbed oxygen.

Experimental

The high-purity, gas-tight electrochemical system, the experimental conditions, and the method of measurement were the same as used in ref. (2). Three single crystal Pt electrodes with orientations (111), (100), and (110) were in the cell. A fourth Pt electrode, polycrystalline bead, similar to previous ones (2), was substituted for one of the single crystal electrodes to confirm that the experimental conditions

* Electrochemical Society Active Member.

[1] National Academy of Sciences-National Research Council Postdoctoral Research Associates at NRL.

Key words: overvoltage, adsorption, catalysis, atom geometry, dermasorption.

used for the single crystal electrodes duplicated the previous work.

The single crystal Pt electrodes were prepared and mounted in the following way. Three high-purity (99.999%, 3 pass electron beam zone refined) single crystals were welded to Pt wires and then were spark cut to the three principle faces (111), (100), and (110).[2] The faces were then electropolished in a melt consisting of equal weights of KCl and NaCl at 700°C in accordance with the procedure reported by Brouillet and Epelboin (3). After rechecking the orientation by x-ray diffraction, each crystal was mounted by placing a thin cylinder of virgin polyethylene (this polyethylene gave a water-clear melt) snugly against the sides of each crystal. A tightly fitting heat-shrinkable TFE Teflon tube was then placed over the polyethylene sleeve. Upon heating with an electric heat gun the polyethylene melted and the Teflon tube shrunk. Upon cooling the single crystal is tightly enclosed in a Teflon-polyethylene envelope. During heating some molten polyethylene covered part of the oriented Pt face. This polyethylene was largely removed by carefully cutting with a razor around the edge of the squeezed out polyethylene and carefully stripping the excess polyethylene from the Pt surface. Photomicrographs[3] showed that tiny particles of polyethylene remained on the surface; however, these were removed during the initial electrolysis as was shown by photomicrographs taken after such treatment. (A polyethylene particle is shown in the encircled area on Fig. 1a as a dark gray fragment. Similar fragments are apparent).

The Pt wire connected to the single crystal, which is covered by the Teflon tube, is sealed through a glass cap. Upon insertion of the electrode into the cell, the glass cap, which has a ¼ in. standard glass pipe connector, is connected to the cell via a Viton-A ring and screw clamp which gives a gas-tight seal.

The initial set of three oriented faces was carefully wiped with a fine soft paper and then cleaned with concentrated nitric acid and rinsed with triply distilled water. Upon close examination scratches were noted on these electrodes, and after the electrochemical measurements were made, photomicrographs showed many fine scratches on each crystal face. These crystal faces were re-electropolished, and after mounting great care was taken not to contact the exposed faces with anything but nitric acid, triply distilled water, and electrolyte. This careful treatment avoided scratches on the soft exposed Pt face. Potentiostatic measurements on each face were repeated after another polishing, and for the scratch-free surfaces, the results were essentially the same. However, the scratched surfaces showed some important variations which will be discussed.

The first measurements on the Pt bead (mounted in glass) were taken after the forming of the bead by melting the end of a Pt wire in a H_2/O_2 flame, cleaning in nitric acid, rinsing, and pre-electrolysis. To assure that the electropolishing procedure itself did not cause changes or leave a residue on the single crystal surfaces which could affect their electrochemical properties, a second set of potentiostatic measurements was made on the bead after electropolishing it under the same conditions used for the single crystals. The electropolished Pt bead, after the usual cleaning treatment, gave essentially the same results as were initially obtained before electropolishing.

All of the Pt electrodes had mirror bright surfaces, but as Fig. 1 shows they were by no means flat surfaces. Mechanical means of flattening the surface were avoided since it was felt that scratching or the inclusion of polishing agents could have strong effects. It seems obvious that atomically smooth surfaces are not feasible at the present time, and it is felt that the predominant orientation of surface atoms is influenced by the underlying Pt atoms of the given orientation.

True area (4) was calculated on the basis of a one-to-one correspondence between each Pt atom and O_{ad}. Since different crystal orientations were used, it was necessary to determine the number of Pt at./cm^2 for each face and bead. Atom densities for perfectly smooth electrodes of the (111), (100), and (110) orientations were calculated to be 1.5×10^{15}, 1.31×10^{15}, and 0.92×10^{15}, respectively, using 3.9231Å (5) as the lattice parameter. The atom density for the bead was assumed to be 1.31×10^{15} (2). On this basis and correcting for double layer charging (36 μC/cm^2), the number of μC/cm^2 for a 1 cm^2 true area electrode for each face and bead was calculated. The experimental true area of each electrode was then determined, and Table I shows areas of unscratched electrodes. All areas given in this paper are so-defined true areas.

Two types of electrochemical measurements were performed. The first was the type of potentiostatic measurement previously reported (2) for a bead electrode and gave the steady-state current density *vs.* potential relation for each electrode in H_2-saturated 1M H_2SO_4 under conditions of very rapid stirring with H_2 gas (> 1000 ml H_2/min).

The second type of measurement gave anodic charging curves taken by applying galvanostatic pulses (1.2-2 A/cm^2) after potentiostating the electrodes until steady state was reached. In this case steady state refers to no change in the number of coulombs of charge

[2] The orientation, spark cutting, and x-ray diffraction confirmation of the orientation was done by C. L. Vold, Metallurgy Division, Naval Research Laboratory.

[3] Photomicrographs of the Pt electrodes were made by A. C. Simon, Electrochemistry Branch, Naval Research Laboratory.

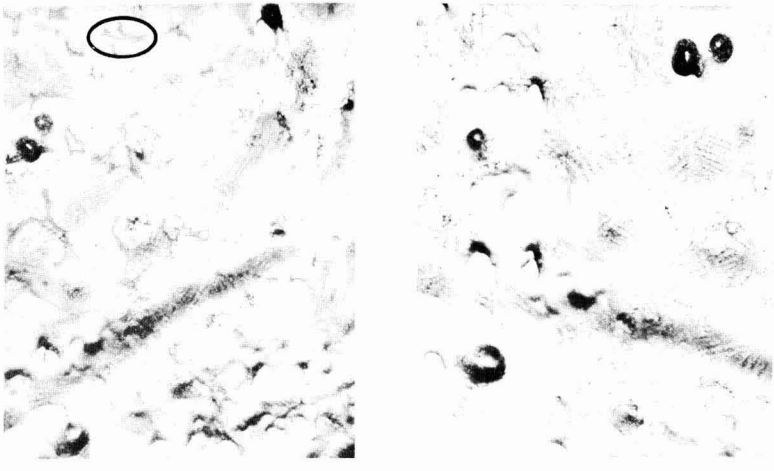

Fig. 1. Comparative photomicrographs of Pt (111) before (a, left, 100X) and after (b, right, 135X) electrolysis.

Table I. Pt electrode true areas

Electrode	$\mu C/cm^2$	Area,* cm^2
Bead	420	0.54 ± 0.01
Bead, electropolished	420	0.60 ± 0.01
(111), first electropolish	484	0.15 ± 0.01
(111), second electropolish	484	0.125 ± 0.01
(100), first electropolish	420	0.20 ± 0.01
(100), second electropolish	420	0.15 ± 0.01
(110), first electropolish	294	0.048 ± 0.001
(110), second electropolish	294	0.043 ± 0.006

$$* \text{Area} = \frac{\text{current } (A) \times \mu\text{sec to form one monolayer of } O_{ad}}{(\mu C + 36)/cm^2}$$

required to oxidize sorbed H atoms and/or to saturate the surface with O_{ad}. The steady state obtained in the first type of measurements meant no change in current density with time. The times required in most cases to reach coulombic steady state was shorter than the time required to reach steady-state current densities. However, under conditions of initially high dermasorbed O content followed by a lowering of potential to a value that resulted in a large loss of dermasorbed O, overnight potentiostating was necessary. After steady state was reached, the high-speed switching arrangement previously reported (6) was used to switch from potentiostatic control to a galvanostatic anodic charging pulse. These measurements were carried out under initial electrode conditions of either no dermasorbed O (by first taking the potential to 0V for at least 5 min) or fully charged with dermasorbed O (by first taking the potential to 1.8V for at least 30 min). After the initial treatment, the electrode was potentiostated to a set value.

The determination of the amounts of sorbed H atoms oxidized and O atoms formed during galvanostatic anodic charging was done in the following way. Anodic charging curves applied at the H^+/H_2 equilibrium potential for each electrode were determined at the beginning and end of each set of measurements. The end of the hydrogen region and the length of the linear atomic oxygen adsorption, O_{ad}, region were determined in the standard way (4) by drawing a straight line through the linear O_{ad} region and finding the intercepts with straight lines drawn from the slope of the so-called double layer region (from about 0.5 to 0.9V) and from the linear extrapolation of the O_2 generation region starting at about 1.75V. Dropping a perpendicular line from the intercepts at the beginning and end of the O_{ad} linear region to the anodic charging curve gave potentials that were considered to be the end of the H oxidation region and the end of the O_{ad} formation region, respectively. The voltages determined in this way varied from 0.8 to 0.95V for the end of the H oxidation region and varied from 1.65 to 1.85V for the end of the O_{ad} formation region. The specific voltages for a given run were very reproducible, and the actual values were directly dependent on the actual current densities used in the anodic charging pulse. The voltages determined in this way were used to calculate the number of coulombs, q_H and q_O [after correcting for double layer charging (4)], of sorbed H and O_{ad} formation for each anodic charging curve for each electrode at the various potential settings. This method of determining the H and O regions differs from the procedure used in earlier work (7) where these regions were always determined by intercepts from the linearly extended O_{ad} region. Although the linear extrapolation method is basic in determining the area of the Pt electrodes (4) and is a reliable technique, under anodic potentiostatic control the H associated with the Pt is low at potentials above 0.3V and the linearity of the O_{ad} region decreases. Therefore, the difficulty of determining the length of the O_{ad} regions increases. Although a determination of coverage of O_{ad} is possible by the method used in ref. (7), we feel that the present technique is less subjective and better defines the method of determining surface coverage. Later in the paper data will be given which can be compared with the data given in Fig. 2 of ref. (7). Such a comparison will show fairly good correspondence for the two methods. Although our measurements do not assure an absolute relation of amounts of H and O_{ad} and potential, the values obtained do give a valid comparison of the four different Pt electrodes. The temperature was 25° ± 1°C, and all measurements were made in H_2-saturated (1 atm) 1M H_2SO_4.

Results and Discussion

Area determinations.—Will (1) concluded from his experimental results that the areas (roughness factors) of his Pt single crystal faces increased with increased number of potential sweeps. Recently, Biegler (8) reviewed the problem of area increases on polycrystalline Pt and also concluded from his own work that there are significant increases in electrode area under repetitive, cyclic treatment that involved fast reduction of surface oxide and that smoothening can occur under slow reduction of oxide. Our own experience with Pt electrodes over a period of many years showed that under our experimental conditions no significant changes in electrode areas were found either in the pre-electrolysis treatment or in use of polycrystalline electrodes over long periods of time. Taking into consideration the findings of Will and Biegler, we decided to investigate carefully the problem of surface roughening and to determine if recrystallization or significant changes in surface atom arrangement occurred.

We point out that our electrodes were not subjected to rapid repetitive, cyclic treatment and that the only rapid potential changes experienced by the electrodes were during anodic charging and switching. Figure 1a is a photomicrograph (100X) of the (111) Pt face electrode. This picture was taken immediately after electropolishing and placing the electrode in the Teflon-polyethylene mount. The encircled area shows a typical remnant of the polyethylene film stripped from the surface during electrode mounting. Many other similarly shaded and appearing particles of polyethylene can be observed on the surface. After cleaning the electrodes and placing them in the cell, the equilibrium hydrogen potential was obtained on each electrode before any electrolysis was applied. Upon applying an anodic charging pulse to each electrode, it was observed that the hydrogen regions were very short and indistinct and that the oxygen regions were somewhat rounded. After applying about 10 pulses, the hydrogen region lengthened and the oxygen region became less rounded. Each electrode was then potentiostated to 1.5V for a period of at least 16 hr. After this time the anodic charging curves for each face showed a normally clean linear oxygen region. Significant increases in area were observed over a period of several days. The largest change was experienced in one run with the (110) electrode which underwent a change from 0.0264 to 0.047 cm^2 over a period of one week. After these inital area changes frequent area determinations showed that each electrode experienced no further significant change.

Figure 1b is a photomicrograph (135X) of the same electrode shown in Fig. 1a after that electrode (111) was in the cell for a period of two months. During that time the electrode underwent potentiostatic polarization ranging from −0.04 to 2.1V for eight days and was subjected to potentiostatic control and anodic charging during a period of four more days. Figure 1b shows the complete removal of the bits of polyethylene and further shows no significant change in the Pt surface. The same dendritic areas, pits, terraces, and structure are apparent in both photos.

Our interpretation of the initial area changes and shape of the anodic charging curves is that the polyethylene residue in contact with the electrodes is being

removed primarily by being scrubbed off by the formation of oxygen. Some oxidation of the polyethylene in close contact with the surface may occur. It may take quite a bit of time (possibly as long as a week) to remove the last trace of polyethylene. Once this initial cleaning of the surface occurs, photomicrographic evidence and electrochemical area determinations show that actual roughening or structure changes on the electrode surface do not occur under the conditions of our experiments. Our findings do not mean that roughening could not occur under Biegler's (8) or Will's (1) experimental conditions. However, there is a possibility that Will's polishing of the single crystal faces with alumina powder did result in an incorporation of some alumina in the surface layer. The two hundred or more sweeps required to get a reproducible surface may be related to the removal of some, if not all, of the alumina by a scrubbing action by hydrogen and oxygen.

Hydrogen overvoltage.—Hydrogen overvoltage data are shown in Fig. 2 and 3. The interesting feature of these curves is that there is no significant difference between the bead and (111), (100), and (110) faces. The Tafel b slope is -0.025, and the i_o for the equilibrium hydrogen/hydrogen ion exchange is 1.9 mA/cm^2. The assumed atomic densities of the four electrodes in terms of atoms per square centimeter are: 1.5 x 10^{15} for (111), 1.31 x 10^{15} for (100), 0.92 x 10^{15} for (110), and 1.31 x 10^{15} for the polycrystalline bead. Hence, since the calculated true areas are based on these numbers of Pt atoms per square centimeter, one can conclude that Pt atom density and spacing do not determine the kinetics. It may be argued that diffusion is the rate-controlling process; however the true areas include a roughness factor, and since the geometric area is the important consideration in diffusion, it would be necessary to show that the roughness factor for all the electrodes are essentially the same. The method we used to mount the single crystals left an uneven rim of polyethylene around the edge of the electrode so that accurate determination of the geometric area was difficult. However, several determinations of geometric area by use of a Bausch and Lomb Measuring Magnifier showed differences in roughness factor. For example, for the (110) face the roughness factor after the first electropolishing was 2.1, whereas after the second electropolishing it was 1.4. However, the hydrogen overvoltage results, based on true area, were essentially the same.

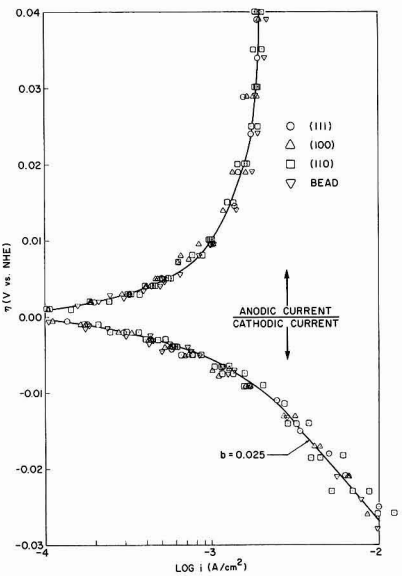

Fig. 2. Dependence of current density on hydrogen overvoltage

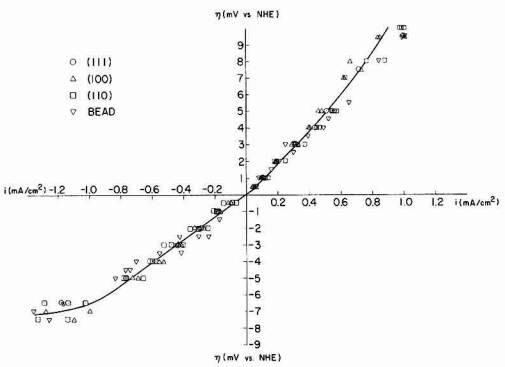

Fig. 3. Dependence of current density on hydrogen overvoltage at low values of η.

The data in Fig. 3 satisfactorily compares with data previously obtained [(9) Fig. 4], however, the Fig. 3 data are on a more expanded potential scale. This expansion clearly illustrates that for $\eta > 0.5$ mV the experimental data points do not fit on an extrapolated linear curve from -6 mV through zero. This deviation shows that the amount of adsorbed H which is in rapid equilibrium with H^+ and H_2 dissolved in solution is very small.

Potentiostatic anodic current density vs. voltage relations.—Figures 4-6 show the potentiostatic anodic current density *vs.* voltage relations for the (111), (100), and (110) faces. Figures 7 and 8 compare the three crystal faces with previous results (2) for a polycrystalline bead electrode for the increasing and decreasing potential sequences, respectively. The former bead electrode results were checked with a new bead electrode, both before and after the same electropolishing used on the single crystal faces. The present results confirmed the previously reported values and further demonstrated that effects due to electropolishing and differences in solution composition were negligible. In addition, Fig. 9 and 10 compare three lightly scratched (by rubbing with soft tissue paper) principle faces and a Pt bead electrode.

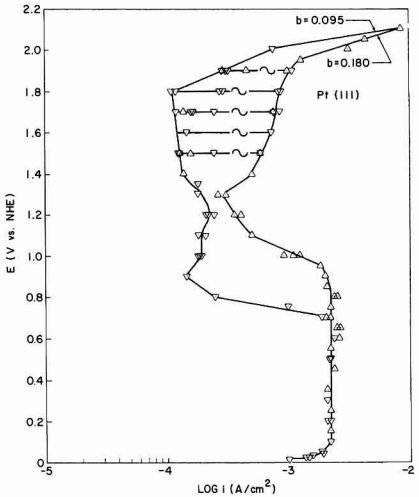

Fig. 4. Potentiostatic dependence of current density on potential for Pt (111): △ increasing potential sequence; ▽ decreasing potential sequence; ~ cyclic behavior, frequency about 20 min.

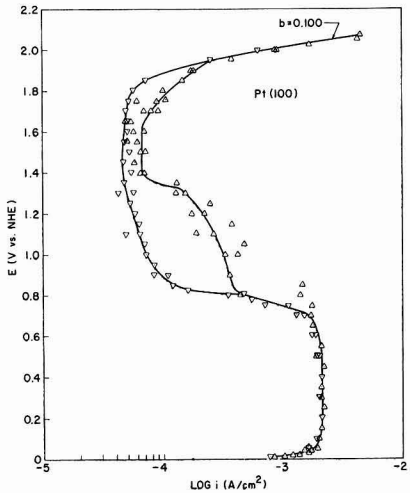

Fig. 5. Potentiostatic dependence of current density on potential for Pt (100): △ increasing potential sequence; ▽ decreasing potential sequence.

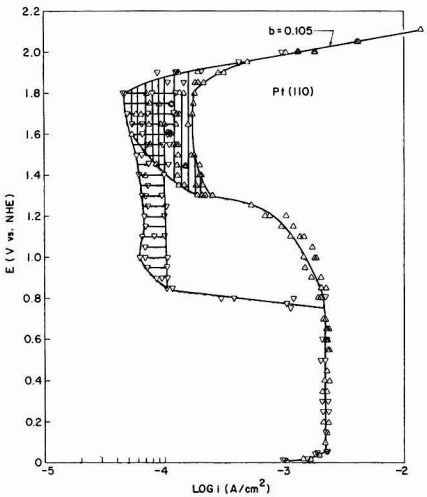

Fig. 6. Potentiostatic dependence of current density on potential for Pt (110): △ increasing potential sequence; ▽ decreasing potential sequence.

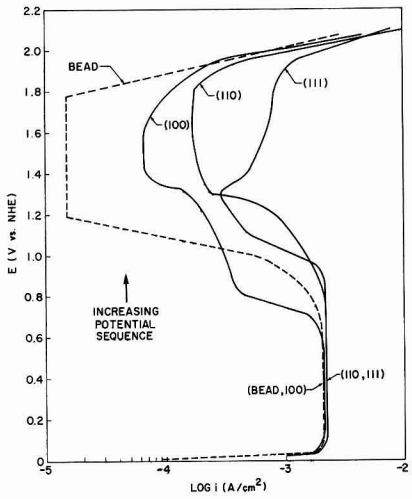

Fig. 7. Comparative potentiostatic relations for increasing potential sequence. Curves are lines shown in Fig. 4-6.

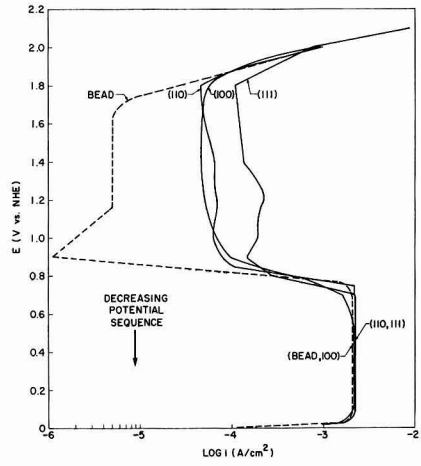

Fig. 8. Comparative potentiostatic relations for decreasing potential sequence. Curves are lines shown in Fig. 4-6.

The data in Fig. 4-10 show that the limiting H_2 oxidation reaction is esssentially independent of crystal orientation. Small differences are noticeable for the bead and the (100) face which had about 10% lower limiting current densities than the (111) and (110) faces (see Fig. 7 and 8). Small differences can also be seen for the lightly scratched faces (Fig. 9 and 10). These differences are just about within the limits of the experimental error (about 10%), and even though these differences were consistent after two electropolishings, they are too uncertain to be considered significant. The fact that the scratched electrodes which would, of course, have higher roughness factors than the smooth electrodes gave virtually the same limiting current densities further demonstrates that the limiting current density is not primarily diffusion-controlled. This conclusion holds because the data in Fig. 4-10 are plotted on the basis of true area (4) which means that if the data were plotted on the basis of geometric area, there would be significant differences between the scratched and unscratched Pt faces.

The really significant differences in the three principle faces and the bead are in the passive (decreased rate of H_2 oxidation) region and the transpassive (oxygen evolution) region. Figure 7 shows that the onset of passivity and the shape of the passive region is very much dependent on the orientation. For example, the potential at which passivity commences increases in the order (100), bead, (110) and (111), whereas for the decreasing potential sequence, Fig. 8, the activation (increased rate of H_2 oxidation) of each electrode has little dependence on orientation. The differences for the scratched electrodes (Fig. 9 and 10) are significantly less.

The differences in behavior shown in the shapes of the passive regions and the Tafel slopes of the oxygen generation region are at the same time remarkable and unexplicable on the basis of Pt atom geometry. Figure 4 shows that for the (111) face at potentials between 1.4 and 1.9V the current density, for both the increasing and decreasing potential sequences, is cyclic (at about 20-min intervals) over one order of magnitude. At and below 1.4V, dermasorbed oxygen

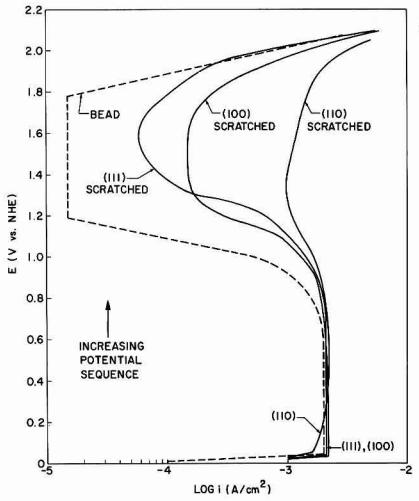

Fig. 9. Comparative potentiostatic relations for scratched single crystals. Increasing potential sequence. Curves represent maximum current densities. Bead electrode is unscratched.

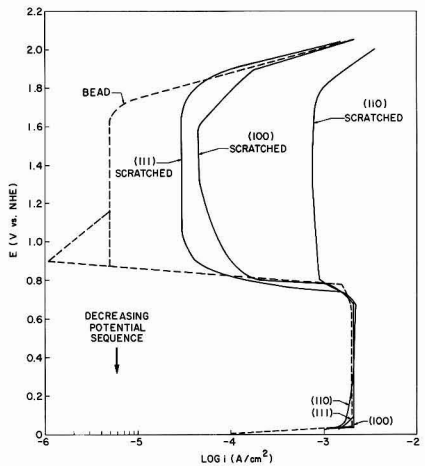

Fig. 10. Comparative potentiostatic relations for scratched single crystals. Decreasing potential sequence. Curves represent minimum current densities. Bead electrode is unscratched.

(decreasing potential sequence data) reduces the rate of hydrogen oxidation until 0.7V where the dermasorbed oxygen is removed. The Tafel slope of the oxygen evolution reaction is 0.180 for the increasing potential sequence and 0.095V for decreasing potentials. The Tafel slope for both the increasing and decreasing potential sequence for the bead was 0.13 (2).

The (100) face, Fig. 5, shows no cyclic behavior at potentials above 1.4V, but the differences in the rates of oxidation between 1.4 to about 1.7V is small. Dermasorbed oxygen appears to only have a significant effect from 1.4 to 0.8V. For this electrode, the O_2 evolution Tafel b value is 0.100 for both the increasing and decreasing potential sequence.

For the (110) face, Fig. 6, there is a great deal of overlap and scatter of points from 1.4 to 1.9V for the increasing and decreasing potential sequence. Below 1.4V the separation due to dermasorbed oxygen is apparent down to 0.75V. The O_2 evolution Tafel b value for both the increasing and decreasing potential sequence is 0.105.

Figures 7 and 8 show that the passivation of the oriented single crystals are all significantly less than that of the bead, but there is no order as far as Pt atom densities are concerned. All that one can say is that the presence of grain boundaries or stress in the beads or differences in impurities in the bead and the single crystals greatly enhance passivation. Figures 9 and 10 for the scratched oriented crystals also show enhanced activity over the bead. In this case the (110) scratched face is the least passivated of all the electrodes investigated. For this electrode the change in activity above 0.7V was small for both the increasing and decreasing potential sequences. In fact, the presence of dermasorbed oxygen (Fig. 10) has only a minor effect on the activity of this electrode.

Another interesting observation that was made during the course of the potentiostatic measurements on the unscratched faces was the potential at which visible oxygen evolution occurred. Each of the faces was mirror bright so that under bright illumination, if gas evolution occurred, the formation of extremely small bubbles would be obvious. On the three oriented faces it was noticed that bubbles of oxygen were not observed unless the electrodes were potentiostated at 1.8V or above. Figures 4 to 8 showed that at potentials from 1.4 to 1.8V, the current densities for each crystal face did not vary greatly, and at potentials down to 0.7V the current densities generally increased. In addition, Fig. 7 shows that at the three faces the current densities varied considerably at, and immediately below, 1.8V. If the net reaction were an electrochemical generation of O_2, the potential at which this reaction occurs should be detected easily, especially since measurements at potentials above 0.7V took anywhere from an hour to hours to reach steady state. The fact that no oxygen bubbles were evident below 1.8V shows that the net reaction below this value was not the formation of O_2.

This conclusion means that there must have been some interaction of molecular hydrogen with whatever current-consuming reaction occurred. The following possibilities are apparent:

$$H_2 \rightarrow 2H^+ + 2e \quad [I]$$

$$2H_2O + Pt \rightarrow 4H^+ + Pt - O_2 + 4e \quad [IIa]$$

$$Pt - O_2 + 2H_2 \rightarrow Pt + 2H_2O \quad [IIb]$$

$$H_2O + Pt \rightarrow 2H^+ + Pt - O + 2e \quad [IIIa]$$

$$Pt - O + H_2 \rightarrow Pt + H_2O \quad [IIIb]$$

$$H_2O + Pt \rightarrow H^+ + Pt - OH + e \quad [IVa]$$

$$2Pt - OH + H_2 \rightarrow 2H_2O + 2Pt \quad [IVb]$$

Other oxygenated species can be visualized also.

The important conclusion that one can derive from the observation that O_2 bubbles are not formed until a potential of 1.8V is reached is that for the oriented single crystals, and as was previously concluded for a heterogenous Pt electrode (2, 7, 10), H_2 in solution reacts with oxygen or oxygenated products of water in the passive region. Only when the rate of oxygen generation (1.8V) exceeds the rate of the interaction of H_2 with the oxygenated species is the net reaction the formation of O_2. This conclusion does not, of course, mean that oxygenated products of water may not exist on the surface of Pt (or O be dermasorbed in Pt) in the passive region below 1.8V, but it does imply that below 1.8V saturation of the surface with oxygenated species of water is infeasible. In addition, support is given to the previously reported conclusion from this laboratory (2, 7, 10) that the cause of the initiation of passivation at 0.7V on a Pt bead is not due to surface coverage with oxygen or an oxygenated product of water, but rather by anion adsorption. As the potential is increased above the value where passivation is initiated, the amount of oxygen or oxygenated products of water is increased, but sulfate ions also play an important role. In summary, the fact that a high voltage of 1.8 is required before visible O_2 evolution occurs is strong evidence that under steady-state conditions, the net accumulation of water oxida-

tion products on the Pt surface is strongly restricted both by the interaction with H_2 and by the presence of sulfate ions.

Relation between potential and amount of associated H atoms.—Figure 11 shows the relationships obtained for the dependence between the amount of hydrogen, q_H, oxidized by a high current density anodic pulse and the potentiostated steady-state potential for all electrodes. Figure 12 compares the four electrodes on a normalized scale, $q_H/q_{H,E=0}$. Since on the normalized scale, the q_H of each electrode is compared to its q_H at the H^+/H_2 equilibrium, the amount of coulombs is related to the number of Pt atoms per square centimeter for each electrode since the ratio q_H/q_O was about the same for all three faces. Thus the atom densities for the three faces and for the bead are normalized, and the curves in Fig. 12 show the fraction of the number of the equilibrium associated H atoms at each potential. On the normalized scale, the differences between the four electrodes are small. Only at potentials of 0.1V and below does there appear to be a significant difference between the (111) and (100) compared to the (110) and bead. However, Fig. 11 shows that on the defined (4) true area scale, there are considerable differences in the amounts of H associated with each electrode. It is interesting that Fig. 11 shows that under steady-state conditions small amounts of hydrogen are associated wtih Pt at potentials above 0.35V.

The dashed line for the bead data in Fig. 11 is the q_H *vs.* E relation for a single anodic charging curve from the H^+/H_2 equilibrium. This dashed curve shows that transient and potentiostatic H content do not have the same dependence on potential. The steady-state amount of H associated with Pt at any potential above 0V is always less than the high current density transient values.

Will (1), using a cyclic voltametric technique, obtained a normalized $q_H/q_{H,E=0}$ separation between the three faces in the order (100) > (111) > (110). Our comparative data (Fig. 12) gives (100) = (111) > (110) = bead.

Relation between potential and amount of O atoms formed by anodic charging.—A series of anodic charging curves typical for any of the electrodes is represented in Fig. 13 by a (100) electrode. Figure 14 gives the q_O *vs.* potential data for all electrodes and Fig. 15 gives the normalized $q_O/q_{O,E=0}$ data for all electrodes. As brought out in the experimental section of this paper, q_O is the number of coulombs per square centimeter of oxygen atoms formed on the electrode surface with a high current density galvanostatic pulse under the given potentiostatic conditions.

All of the open symbols signify that the electrode was taken to open circuit (zero volt) for at least 5 min before the given potential was applied. The closed symbols signify that the electrode was taken to 1.8V for at least 30 min. Thus, for the open symbols, the initial electrode condition was the equilibrium hydrogen electrode free of dermasorbed oxygen, whereas

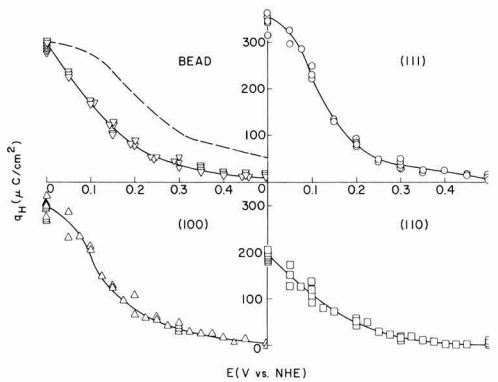

Fig. 11. Steady-state amounts of H atoms, q_H, associated with each Pt electrode at given potentials. See text for meaning of dashed line.

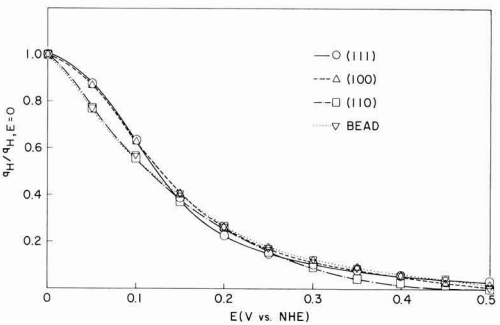

Fig. 12. Normalized ($q_H/q_{H,E=0}$) steady-state amounts of H atoms associated with each Pt electrode at given potentials.

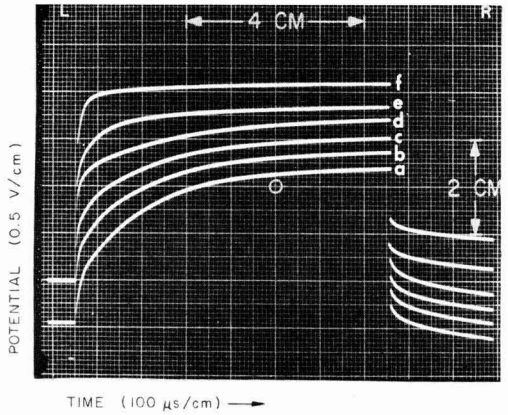

Fig. 13. Anodic charging curves for Pt (100) from set potentiostated values. i = 1.824 A/cm^2

a, 0.3V
b, 0.5V
c, 0.7V
} potentiostated for 5 min at each potential

d, 0.9V
e, 1.1V
f, 1.3V
} Starting at H^+/H_2 equilibrium followed by potentiostating for 15 min at each potential

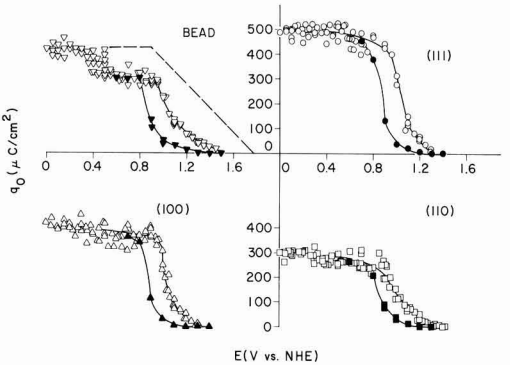

Fig. 14. Amounts of O atoms, q_O, formed on each Pt electrode when an anodic galvanostatic pulse is applied at given steady-state potentials. Open symbols are values for initial potentiostating at 0V. Closed symbols are values for initial potentiostating at 1.8V. See text for meaning of dashed line.

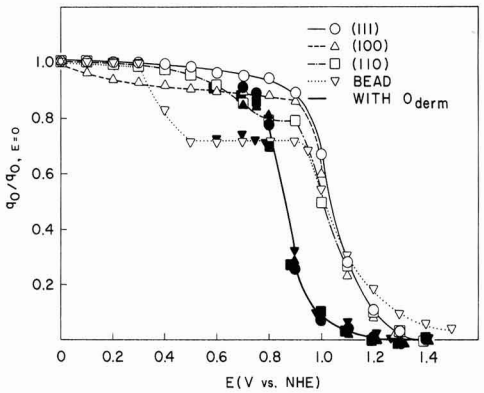

Fig. 15. Normalized ($q_O/q_{O,E=0}$) amounts of O atoms formed on each Pt electrode when an anodic galvanostatic pulse is applied at given steady-state potentials. Open symbols are values for initial potentiostating at 0V. Closed symbols are values for initial potentiostating at 1.8V.

for the closed symbols the initial electrode condition was saturation with dermasorbed oxygen.

The data in Fig. 14 and 15 show that for all of the oriented faces, there is a relatively small decrease in the amount of O atoms required to form a monolayer with the anodic charging pulse from zero to 0.9V. On the other hand, the data for the bead is similar to previously reported data (7) and shows a significant decrease in the required amount of O to form a monolayer at 0.4V, followed by a plateau to 0.9V and then a sharp drop similar to the oriented faces. The hysteresis (closed symbols) is believed to be caused by dermasorbed oxygen. The data in Fig. 14 and 15 show that dermasorbed oxygen is virtually completely removed at a potential of 0.8V. About 16 hr of potentiostating at 0.8V (after saturating the electrode at 1.8V with O) was required before the steady-state q_O was found for all electrodes. This q_O at 0.8V, as were closed symbol values at lower potentials, corresponded to the open symbol, initially dermasorbed O-free cases.

The dashed line for the bead in Fig. 14 shows the linear q_O *vs.* E relation for a single anodic charging curve beginning at the H^+/H_2 equilibrium. The amount of O_{ad} which can be formed by an anodic pulse starting at a given E above 0.5V is always less than the O_{ad} formed under high current density transient conditions starting at zero. The rapid decrease in the deposited quantity of O_{ad} at E above 0.9V supports the conclusion that sulfate ion adsorption does decrease the number of sites available for O_{ad}.

Because under steady-state potentiostatic conditions H_2 will react with oxygen and/or oxygenated water species, the large decreases in the amounts of O required to form a monolayer under galvanostatic charging are believed to be due to anion (sulfate ion) adsorption (2, 7). Further, from kinetic considerations (2), it is felt that anion adsorption not only initiates passivation, but is the major cause of the rapid decrease in the rate of H_2 oxidation up to at least 1.2V. The data in Fig. 7 and 8 correspond sufficiently well with the sharp drop at 0.9V to show a real relation between increased surface coverage and decreased rate of H_2 oxidation. The most pronounced difference in the four electrodes is the comparison of the bead to the three oriented faces. Both the drop in q_O at 0.4V and the much lower minimum current densities shown in Fig. 7 and 8 indicate that such differences as grain boundaries, stress, or differences in impurities in the Pt play an important role both in anion adsorption and passivation. The differences in the three faces are too small to be highly significant, but several trends are apparent. There is a sharper decrease in q_O at potentials in excess of 0.4V for the (110) face (Fig. 15), and at potentials from 0.7 to 0.9V, its behavior is intermediate to the (111), (100), and the bead. The q_O for the (100) face drops significantly at 0.1V but then changes very little until 0.9V.

In summary, differences in behavior of the various orientations are apparent, but they are small and follow no logical sequence, such as atom density or spacing. The really significant differences are those between the oriented single crystal faces and the polycrystalline bead. This difference indicates that factors such as grain boundaries, stress, and possible variations in impurities in the Pt can play an important role in some adsorption phenomena and may influence the catalytic activity of some reactions. Another possible variation may be differences in the potential of zero charge between the bead and single crystal faces.

The open-circuit rate of reaction of a rapidly generated monolayer of Pt-O formed by an anodic galvanostatic charging pulse with H_2 in solution (11) was determined in the hope that single crystals, which would be in an essentially ideally annealed state, would differ significantly from a bead electrode which would contain strains. The rates of the $Pt - O_{ad} + H_2$ reaction for all four electrodes varied from about 1 to 5 mA/cm^2. These differences were random and were independent of orientation or polycrystallinity. Actually, previous work (11) with bead electrodes gave rates which ranged both lower or higher than these values, so that no particular relation between the metallurgical state or single crystal orientation of Pt and the rate of the reaction of $Pt - O + H_2$ was obtained.

Conclusions

Figure 16 shows photomicrographs at magnification of 325X of (111), (100), and (110) faces after prolonged electrochemical measurements. These photomicrographs show no particular metallurgical changes on the electrode surface as compared to those taken before electrochemical treatment (see Fig. 1 also). The present study has shown that there are areas of marked differences in electrochemical behavior of single crystal orientation as compared with a polycrystalline electrode, and that for some reactions (*i.e.*, hydrogen overvoltages below 0.7V) the effects of metallurgical fac-

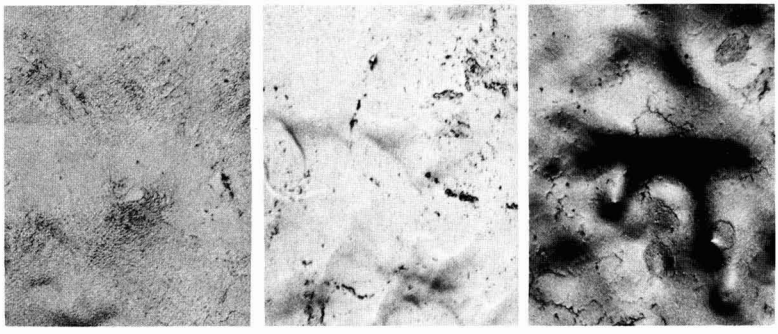

Fig. 16. Photomicrographs of (a) (left) Pt (111), (b) (center) Pt (100), and (c) (right) Pt (110) after electrolysis (325X).

tors are minor. Changes in electrode area or in character of the electrode surfaces were not found. Undoubtedly an improved technique for polishing the electrode to give orientations that approach atomic smoothness would be desirable as would observations of surface atomic arrangement by such techniques as LEED. It is apparent that grain boundaries, stress, and impurity inclusions in the electrode may be of much more importance in determining catalytic activity for some reactions than is the actual atomic density or geometry of platinum.

Surface defects on oriented single crystals caused by scratching had marked effects on the passivation of Pt electrodes for hydrogen oxidation starting at about 0.7V. Comparisons with a polycrystalline bead showed large differences which were most likely caused by grain boundaries, stress, and possibly metallic impurities. It is believed that the passivity behavior is due to anion (sulfate ion) adsorption and that the various defects somehow influence this factor.

The primary conclusion that this investigation has led to is that there is no simple correlation between atomic geometry and electrode behavior. Investigations of other more complex electrochemical reactions and better definition and control of metallurgical factors are required before generalizations concerning atomic geometry should be made.

Manuscript submitted Nov. 25, 1969; revised manuscript received May 20, 1970.

Any discussion of this paper will appear in a Discussion Section to be published in the June 1971 JOURNAL.

REFERENCES

1. F. G. Will, *This Journal*, **112**, 451 (1965).
2. S. Schuldiner, *ibid.*, **115**, 362 (1968).
3. P. Brouillet and I. Epelboin, *Rev. Met.*, **51**, 693 (1954).
4. S. Schuldiner and R. M. Roe, *This Journal*, **110**, 332 (1963); M. Rosen and S. Schuldiner, *ibid.*, **117**, 35 (1970).
5. R. W. G. Wyckoff, "Crystal Structures," 2nd ed., Vol. I, p. 10, Interscience Publishers, New York (1963).
6. T. B. Warner and S. Schuldiner, *This Journal*, **114**, 359 (1967).
7. S. Schuldiner, *ibid.*, **115**, 897 (1968).
8. T. Biegler, *ibid.*, **116**, 1131 (1969).
9. S. Schuldiner, *ibid.*, **106**, 891 (1959).
10. S. Schuldiner, *ibid.*, **116**, 767 (1969).
11. S. Schuldiner and T. B. Warner, *ibid.*, **112**, 212 (1965); T. B. Warner, S. Schuldiner, and B. J. Piersma, *ibid.*, **114**, 1120 (1967).

Electrochemical Oxidation of Guanine at the Pyrolytic Graphite Electrode

Glenn Dryhurst and Gerald F. Pace[1]

Department of Chemistry, The University of Oklahoma, Norman, Oklahoma 73069

ABSTRACT

The electrochemical oxidation of guanine at the pyrolytic graphite electrode was investigated by linear and cyclic scan voltammetry between pH 0-12.5 and by controlled electrode potential electrolysis in aqueous 1M acetic acid solution. Guanine is oxidized by an initial $2e/2H^+$ potential determining attack at the —N(7) = C(8)— double bond followed by a further $2e/2H^+$ oxidation of the —C(4) = C(5)— double bond to give 2-amino-6,8-dioxypurine-4,5-diol which, being unstable, undergoes further reaction by two routes: (*a*) further electrochemical oxidation to parabanic acid, guanidine, and carbon dioxide; and (*b*) hydrolysis to oxalyl guanidine and carbon dioxide. The exact nature of intermediate species in the electro-oxidation of guanine and uric acid were more thoroughly established by extensive use of fast sweep cyclic voltammetry. In particular it appears that in ammonia buffers at moderately high pH, the intermediate is a 4,5-diamine rather than a 4,5-diol.

Guanine (2-amino-6-oxypurine) is one of the two principal purines found in nucleic acids and as such is involved in many biological processes. Previous work has indicated a similarity between the heterogeneous electrochemical and enzymatic oxidation of naturally occurring purines such as adenine or uric acid (1, 2), although this parallelism does not appear to extend to purines with exocyclic sulfur atoms (3, 4). Nevertheless, the observed electrochemistry of these latter compounds might aid in interpreting the very incompletely understood biological oxidation. Fast scan cyclic voltammetry of several nonsulfur-containing purines has indicated that a general mechanism might be operative involving formation of a common ultimate primary electrochemical product which has been postulated to be a dicarbonium ion or a 4,5-diol (5). However, recent results on some methylated xanthines (6) which will be published shortly indicates that if the N-7 position is methylated, then no intermediate comparable to those observed for other purines can be detected or is much smaller than for other compounds. Faradaic n values also support this idea. In view of these latter findings and the importance of guanine in biological systems, it was felt that the electrochemical oxidation mechanism for this compound should be elucidated in detail rather than arbitrarily assuming that its oxidation proceeded by a route essentially identical to uric acid. A further reason for studying guanine was that if parabanic acid was an electrochemical product, then as a result of the effective labeling of the pyrimidine ring by the 2-amino group, it should be possible to assign correctly the ring origin of this acid which was not possible with adenine and uric acid.

Many of the biological and chemical reactions of purines are presented in the reviews of Lister (7) and Robins (8). Little, however, appears to be known of the mechanism of biological oxidation of guanine. Generally, biological oxidation processes are characterized only in terms of the major or most easily detected products. In many animals guanine is converted

[1] Present address: Continental Oil Company, Ponca City, Oklahoma.

Key words: guanine, electro-oxidation, 2-amino-6-oxypurine, bioelectrochemistry, pyrolytic graphite.

to uric acid and allantoin (9) although in xanthinuric man, guanine ingested as yeast RNA or as 3′-guanylic acid appears to be converted primarily to xanthine (10). Guanine is oxidized only slowly in the presence of very large excesses of xanthine oxidase to uric acid. Wyngaarden (11) has suggested that this process might be brought about by traces of guanase present in the xanthine oxidase. In rat liver, guanine is converted to hypoxanthine (12). Photodynamic inactivation of DNA on irradiation with visible light in the presence of the dye lumichrome is due to breakdown of guanine (13). Using tracer techniques, the photodynamic degradation of guanine involved formation primarily of guanidine and parabanic acid. Urea has also been detected as a photo-oxidation product (14). Chemical oxidation of guanine by MnO_2 in aqueous suspension at 100° gave guanidine and urea (15).

The study reported here of the electrochemical oxidation of guanine at controlled electrode potential at the pyrolytic graphite electrode (PGE) indicates a mechanism whereby guanine is oxidized in a primary 4e process to give an unstable compound which has been characterized as 2-amino-6, 8-dioxypurine-4, 5-diol or -4, 5-diamine in ammonia containing backgrounds [equivalent to the dicarbonium ion intermediate postulated for uric acid and adenine (1)]. The subsequent chemical or electrochemical reactions of this primary product decides the final nature of the over-all reaction. Again, it appears as if the initial sites of electrochemical and biological oxidation are similar, but the normal biological deamination reaction at C-2 does not occur under electrochemical conditions.

Experimental

Chemicals.—Chemicals were obtained from the sources listed; guanine (Nutritional Biochemicals); parabanic acid, guanidine sulfate, 4-chloro-meta cresol (Eastman); guanidine hydrochloride (Matheson); 2, 3-butanedione monoxime (Fisher). Buffer solutions were prepared from reagent grade chemicals.

Argon (Linde) used for deoxygenating purposes was equilibrated with water; no other purification was necessary.

Apparatus.—Polarograms and voltammograms were recorded on a Sargent Model XVI Polarograph using a water-jacketed three-compartment cell maintained at 25° ± 0.1°C and containing a saturated calomel reference electrode (SCE) and a platinum gauze counterelectrode in saturated potassium chloride solution. All potentials are referred to the SCE at 25°C. The dropping mercury electrode had normal m and t values. The preparation of the various pyrolytic graphite electrodes was described earlier (1). Apparatus for cyclic voltammetry, controlled potential electrolysis, coulometry, and lyophylization are described elsewhere (3, 5). Ultraviolet absorption spectra were recorded on a Perkin Elmer-Hitachi Model 124 Spectrophotometer; infrared spectra were recorded on a Beckman IR8 spectrophotometer.

Voltammetric procedure.—Because of the low solubility of guanine, saturated solutions in appropriate buffers were prepared, the excess of guanine removed by filtration, and the concentration computed by measurement of the u.v. absorbance. A portion of these solutions was then placed in the polarographic cell and deaerated with argon for about 10 min. Once in position, the 4 mm diameter PGE was allowed to stand for about 30 sec without applied potential; the starting potential was then applied for 5 sec (usually 0.00V) and the voltammetric scan commenced.

The PGE was resurfaced before every run by polishing on a 600 grade silicon carbide paper disk mounted on a motor driven rotating disk. The electrode was washed thoroughly with a jet of distilled water; the surface was then very gently touched onto a clean paper tissue to remove excess of water.

Coulometry.—A measured volume of background solution was electrolyzed at the appropriate potential in the working electrode compartment until the titration coulometer (16) gave a small constant titration rate. Then, between 0.1 to 0.2 mmole of guanine was introduced. The electrolysis was then continued until all of the suspended guanine had disappeared and the current had decayed to the background level. Completion of the electrolysis was always confirmed by the disappearance of the characteristic guanine u.v. absorption peak.

Macroscale electrolysis.—The same apparatus was used for macroscale electrolysis as for coulometry except that between 1 and 2 mmoles of guanine was suspended in 200 ml of 1*M* HOAc. Electrolysis was continued until no suspended guanine remained and the characteristic u.v. absorption of guanine had disappeared. At completion of the electrolysis, the solution in the working electrode compartment was shell frozen onto the walls of a 1 liter flask and lyophilized which resulted in a white fluffy powder.

Thin layer chromatography.—With the exception of urea, which was spotted as a solution (1 mg/ml), all reference compounds and the lyophilized electrolysis product were applied to thin layer sheets as very small crystals and were dissolved by repeated addition of water. Two different solvent systems were employed, n-butanol, acetic acid, water (120-30-50) and n-propanol, water (70-30). Two thin layer supports were employed, silica gel with fluorescent indicator (Eastman Chromogram 6060) and alumina (Eastman Chromogram 6062).

Parabanic acid was identified as a major product as a spot on the fluorescing silica gel plate having an r_f value in butanol, acetic acid, water solvent of 0.83, and 0.70 in propanol, water both being identical with authentic parabanic acid.

Urea was detected as a very minor product using butanol, acetic acid, water as solvent, and the silica gel adsorbent with Ehrlich's reagent ($r_f = 0.68$). Allantoin was not detected under the same conditions.

Ammonia was tested for on silica gel in the same solvent with Nessler's reagent but was not detected.

Guanidine was identified in the product on an alumina plate using propanol, water as solvent with sodium nitroprusside reagent (17) (r_f of 0.43), and on silica gel in butanol, acetic acid, water with the same reagent ($r_f = 0.63$).

Ion exchange isolation and identification of guanidine.—Thin layer chromatography indicated that guanidine was a product of electro-oxidation. Since all other products or potential products except urea, which was only a very minor product, were acidic or could be hydrolyzed to salts in strong base, isolation of guanidine was attempted.

One hundred milligrams of lyophylized electrolysis product was dissolved in 30 ml water and passed through a Dowex X-8 ion exchange column (hydroxide form) and washed with 150 ml water. The effluent was neutralized with hydrochloric acid and lyophylized. The infrared spectrum of the product was essentially identical to authentic guanidine hydrochloride.

Ion exchange isolation and identification of parabanic acid.—One hundred milligrams of lyophylized electrolysis product was dissolved in 30 ml water and passed through a column of Dowex 50W-X8 ion exchange resin (strongly acid form) and washed with 150 ml of water. The product was lyophylized. The infrared spectrum of the product was essentially identical to that of authentic parabanic acid.

Parabanic acid was further confirmed by the polarographic behavior of the product in 1M acetic acid ($E_{1/2} = -0.68$V) and ammonia buffer pH 9 ($E_{1/2} = -1.06$V) and from the fact that in the latter solution it rapidly decomposed to oxaluric acid ($E_{1/2} = -1.60$V) (18).

Determination of parabanic acid.—At completion of the electrolysis, parabanic acid was determined by transferring about 20 ml of the electrolysis solution to

a polarographic cell, and after deaeration a polarogram was run between 0 and −1.4V. The height of the wave at *ca.* −0.7V was compared with a calibration curve prepared from authentic parabanic acid.

Determination of guanidine and guanidyl residues.—Guinidine or guanidyl residue was determined by modification of the procedure described by Staron *et al.* (19). In our hands the sensitivity of this procedure was about five to ten times lower than claimed. In order to overcome this low sensitivity, the solution produced on electrolysis of 0.1-0.2 mmole guanine was lyophylized and the resulting solid product dissolved in 10.0 ml water. To 2.0 ml of this latter solution was added 2.0 ml of a 10% solution of 4-chloro-meta cresol in 95% ethanol. After agitating, 2.0 ml of *N* sodium hydroxide was added followed by 1.0 ml of freshly prepared sodium hypobromite solution (1 ml Br_2 in 99 ml *N* NaOH). The absorbance of the yellow color which developed was measured at 440 mμ in a 1.0 cm stoppered quartz cell. Calibration curves were prepared with guanidine sulfate solutions which contained between 0.2 and 2 mg guanidine in the initial 2.0 ml aliquot of solution.

Determination of oxalyl guanidine.—Oxalyl guanidine, allantoin, or any other similar species capable of being quantitatively hydrolyzed to glyoxylic acid by sequential base then acid hydrolysis responds quantitatively to the method of Young and Conway (20). The experimental procedure is described elsewhere (1) except that under the present conditions, a 3.0 ml aliquot of the electrolysis solution diluted to 5.0 ml with 1*M* HOAc was employed.

Results and Discussion

Voltammetry.—Guanine shows a single well-formed anodic voltammetric peak at the stationary PGE between *p*H 0 and 12.5. Above *p*H 11 there was some indication of a small second wave close to background discharge. Because these latter waves appeared only occasionally at very high *p*H, they were not examined further. The peak potential, E_p, for the main guanine wave shifts linearly more negative with increasing *p*H

$$E_p = 1.115 - 0.065\ pH$$

at 3.33 mV sec^{-1} scan rate. The shift of peak potential of 65 mV per *p*H unit is in fairly close agreement with that expected for a process where the rate-controlling step involves an identical number of protons and electrons. Considering the guanine peak observed over the whole *p*H range study, an average current density of 3.72 μA · $mmole^{-1}$ mm^{-1} was obtained. However, between *p*H 2.3-10 guanine is rather insoluble so that the data in these regions corresponds to that observed for essentially saturated solutions, and in these regions the current density was much more variable, no doubt reflecting contributions of adsorbed guanine to the total current. Below *p*H 2 where guanine is somewhat more soluble and solutions well below the saturation limit were employed, the mean current density was 2.72 μA · $mmole^{-1}$ mm^{-2}. This latter figure is in good agreement with that expected for involvement of 4e per guanine molecule. In 2*M* H_2SO_4 guanine shows linear ip-C curves between 0.005-1.0 m*M* which indicates that the electrochemical reactions are probably diffusion controlled.

Coulometry.—At *p*H 2.3, coulometry at a potential corresponding to the crest of the guanine oxidation peak gave faradaic *n* values ranging from 4.2 to 4.7e. At completion of the electrolysis, the characteristic u.v. absorption spectra of guanine (λ max = 275 mμ) had disappeared.

Preparative electrolysis.—Exhaustive electrolysis of guanine at fixed anodic potential allowed the preparation of sufficiently large amounts of products to permit their isolation, identification, characterization, and quantitative determination. Several isolation and detection approaches were employed including lyophylization (freeze drying), ion exchange, thin layer chromatography, polarography, u.v. and *IR* spectrophotometry, and other physical measurements. These revealed the presence of guanidine and parabanic acid as major products along with a slight trace of urea. Neither allantoin nor ammonia was detected. A species was detected, however, which when subjected to a sequential base then acid hydrolysis gave rise to glyoxylic acid; the latter compound is readily detected and quantitatively determined by formation of its condensation product with phenylhydrazine which is oxidized by ferricyanide to the characteristic red chromophore (20).

Quantitative analysis (typical) of a solution after complete electrolysis of 0.22 mmole of guanine in 200 ml of 1M HoAc revealed that 1 mole of guanine yielded 0.35 mole parabanic acid (polarography), 0.90 mole of guanidyl residue [procedure of Staron *et al.* (19)] and 0.55 mole of a species which could be hydrolyzed to glyoxylic acid [Young and Conway procedure (20)]. It was noted that the value of the measured *n* value in excess of 4.0 was numerically twice the moles of parabanic acid produced per mole of guanine.

Cyclic voltammetry.—The involvement of about 4e per molecule of guanine in the oxidation suggested a mechanism similar to that observed for adenine (1), *i.e.*, initial oxidation at C-8 followed by further oxidation of the C(4)-C(5) double bond. In order to gain more detail into these processes, cyclic voltammetry, at fast scan rates, was employed.

Scanning from 0.0V at a clean electrode toward positive potential only a single anodic peak (peak I_a) is observed for guanine. Once having scanned this peak and then sweeping toward negative potential, however, at least two cathodic peaks are observed. The first (peak I_c) always occurs at potentials more positive than zero, the second (peak II_c) occurs at much more negative potential. On the second sweep toward positive potential a new anodic peak (peak II_a) appears before the peak I_a and forms an almost reversible couple with peak I_c.

Figure 1A shows a voltammogram for these first and second cycles. In order to detect peaks I_c and II_a, it is necessary to employ high sweep rates, *i.e.*, > 300 mV sec^{-1} (5), indicating that the product of the main oxidation peak I_a is very unstable. Earlier reports of the electro-oxidation of uric acid (2) and adenine (1) postulated that the primary electrochemi-

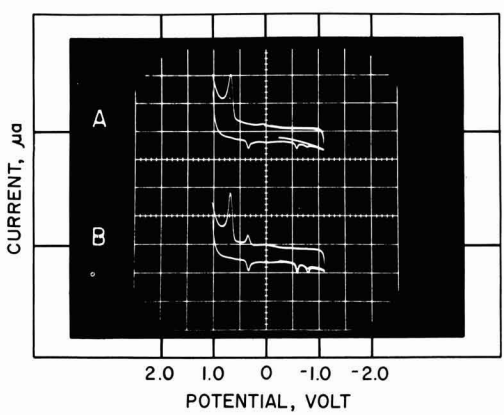

Fig. 1. Cyclic voltammogram of saturated solution of guanine in MacIlvaine buffer *p*H 6 at PGE. Scan rate 8.8 $Vsec^{-1}$. A, First scan at a clean electrode, sweep started at 0.0V and run toward negative potential; scan pattern, 0.0V → −1.1V → +1.05 → −1.1V. B, Second scan. Scan pattern: 0.0V → −1.1V → +1.05V → 0.0V. Calibration marks on current axis indicate zero current for the appropriate voltammogram. Current above the calibration mark is anodic (—). Current sensitivity 200 μA per div.

cal product was a dicarbonium ion formed by removal of two π electrons from the —C(4) = C(5)—double bond. However, since the peak potential for uric acid oxidation was shown to be pH dependent, although only two pH values were examined (2), and involved direct attack at the 4,5 position unlike adenine and guanine which must involve attack elsewhere in the molecule before the 4,5 bond is oxidized (*vide infra*), then protons must be involved in the energy (*i.e.*, potential) controlling process. This led to the suggestion that the intermediate in uric acid oxidation was in fact 2,6,8-trioxypurine-4,5-diol (5). We have confirmed that uric acid is oxidized in a pH dependent process and that the cathodic peak due to reduction of the unstable 4,5-diol is also pH dependent. At a scan rate of 8.8 $Vsec^{-1}$ the primary uric acid oxidation peak followed the relation

$$(E_p) = 0.83 - 0.071\ pH$$

between pH 1 and 12.5. The reversible cathodic peak followed the relation

$$(E_p)_{red} = 0.68 - 0.061\ pH$$

although it was only observed distinctly between pH 1 and 8.

All of the peaks observed for guanine are pH dependent at 8.8 $Vsec^{-1}$ being described by the relations: $E_p = 1.20\text{-}0.077$ pH for peak I_a; $E_p = 0.72\text{-}0.059$ pH for peak I_c; $E_p = -0.54\text{-}0.026$ pH for peak II_c, and $E_p = 0.9\text{-}0.077$ pH for peak II_a. A peak of similar appearance and pH dependence to peak II_a was also observed for uric acid. Actually one or occasionally two additional cathodic peaks were also observed at many pH values. These usually occurred at more positive potential than peak II_c except occasionally at high pH. An example is shown in Fig. 1B where a clear peak at −0.6V is observed before peak II_c at −0.75V. These additional peaks were most clearly observed at pH 2.3 (acetate), 3.0 (MacIlvaine), 4.0 (MacIlvaine), 4.9 (MacIlvaine), and 6.0 (MacIlvaine).

In ammonia background pH 9.1 the cyclic voltammetry of guanine was considerably different to that observed at all lower and higher pH values (Fig. 2). Thus, after scanning peak I_a the primary oxidation peak, a peak corresponding to peak I_c at positive potential did not appear (from the pH dependence of peak I_c it should have occurred at +0.19V). Instead, a new peak at −0.55V appeared followed by three more negative peaks one of which corresponded to peak II_c. Then on the second anodic sweep a new anodic peak at −0.52V appeared forming a reversible couple with the cathodic peak at −0.55V. In addition, however, a peak corresponding to peak II_a also appeared ($E_p = 0.13$V)

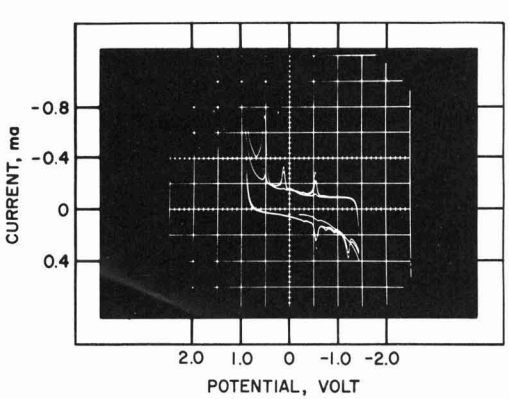

Fig. 2. Cyclic voltammogram of a saturated solution of guanine in ammonia-ammonium chloride buffer pH 9.1 at PGE. Scan rate 10 $Vsec^{-1}$. First scan started at 0.0V and swept toward negative potential.

although under no conditions did the reversible $II_a - I_c$ couple appear. Uric acid showed similar behavior, namely after scanning the primary oxidation peak; no reversible cathodic peak was observed but a new reversible couple at $(E_p)_{cathodic} = -0.55$V and $(E_p)_{anodic} = -0.52$V appeared.

Mechanism

The characteristic uv absorption spectrum of guanine ($\lambda_{max} = 275$ mμ in 1M HOAc) is due to the —C(4) = C(5) — C(6) = 0 chromophore (21, 22). In view of the disappearance of this spectrum and consideration of the adenine and uric acid mechanisms it is likely that the —C(4) = C(5)—double bond is oxidized.

Removal of 4e from guanine along with the observed pH dependence of the anodic peak suggests that the process proceeds by two sequential two-electron, two-proton oxidations. Enzymes such as xanthine oxidase, always preferentially attack an —N=CH— double bond. In guanine only the —N(7)=C(8)H— bond of this type is available. Theoretical calculation of the nucleophilic localization energy of this same bond predicts that it will be preferentially oxidized (23). Accordingly it appears that the —N(7)=C(8)— bond is that which would be initially attacked electrochemically. It is observed experimentally (1-5, 24) and predicted theoretically, from the energies of the highest occupied molecular orbitals (23), that the ease of electron removal from purines increases with the number of ring substituted oxygen groups in the molecule. Accordingly, once the initial potential controlling oxidation at —N(7)=C(8)— has occurred, further oxidation should take place; since the u.v. spectrum of guanine is lost, it must take place at the —C(4)=C(5)— double bond.

Fast sweep cyclic voltammetry clearly allows observation of the reduction of the unstable product (peak I_c) of the primary electrochemical reaction (peak I_a) and re-oxidation in turn of the product (peak II_a) of this secondary reduction at a less positive potential than required for the initial oxidation of guanine. These latter redox processes are essentially reversible and are pH dependent to an extent indicative of the involvement of an identical number of protons and electrons. The reversible couple occurs at potentials very similar to those observed for the uric acid oxidation-reduction couple. Accordingly, the electrochemistry of the cyclic voltammetry of guanine (I, Fig. 3) can be interpreted as an initial two-electron, two-proton rate-determining oxidation to 2-amino-6,8-dioxypurine (II, Fig. 3) followed by a further rapid two-electron, two-proton oxidation to 2-amino-6,8-dioxypurine-4,5-diol (some of which is even further electrochemically oxidized to parabanic acid and guanidine III) (Fig. 3) which corresponds to peak I_a. Provided a fast enough sweep rate is employed, reduction of III to II can be observed and corresponds to peak I_c, and on the next anodic sweep, peak II_a is observed which corresponds to oxidation of II back to III.

The cathodic peak (peak II_c) observed for both guanine and uric acid is probably due to reduction of a product of partial further oxidation of III, namely, parabanic acid (V, Fig. 3) (25). Authentic parabanic acid shows a similar pH dependence to peak II_c although the peak potential for its reduction generally occurred at somewhat more negative potential. A possible explanation of this effect is that the parabanic acid produced by breakdown of intermediate III (Fig. 3) is situated very close to the electrode surface and is reduced under pH conditions which are quite appreciably lower than those extant in the bulk solution owing to the liberation of protons as a result of reaction I → II, the result being therefore a shift in the peak to more positive potential. The peak observed at more negative potential than II_c at high pH is no doubt due to oxaluric acid which is known to the hydrolysis product of parabanic acid at high pH and

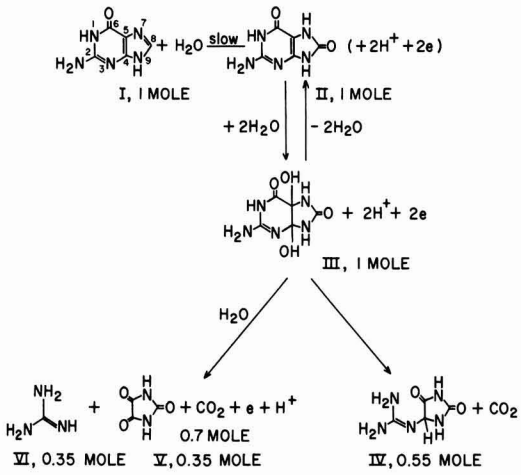

Fig. 3. Proposed pathways for electrochemical oxidation of guanine in moderately acidic solution. The molar quantities refer to the amount involved per mole of guanine. Compounds listed are as follows: I, guanine; II, 2-amino-6,8-dioxypurine; III, 2-amino-6,8-dioxypurine-4,5-diol; IV, oxalyl guanidine; V, parabanic acid; VI, guanidine.

which is electrochemically reducible at more negative potential (26).

The nature of the processes giving rise to other cathodic peaks at various *p*H values is difficult to assign. It is possible that intermediates such as the so called "Behrend Compound" postulated for uric acid oxidation (2) might exist at certain *p*H values and be electroactive. However, saturated solutions of guanine were employed at most *p*H values for cyclic voltammetry; the presence of adsorption or capacitive peaks is also likely. The reversible redox couple observed for guanine and uric acid in ammonia buffer at *p*H 9 is not observed at any other *p*H in the absence of ammonia and hence must be specifically associated with this latter species. The likely explanation of the effect is shown in Fig. 4, namely, that the primary potential controlling step is identical to that at other *p*H values, *i.e.*, two-electron, two-proton oxidation of the —N(7)=C(8)—bond to give 2-amino-6,8-dioxypurine (II, Fig. 4). However, in the presence of ammonia two-electron, two-proton oxidation results in formation of 2-amino-6,8-dioxypurine-4,5-diamine (III, Fig. 4). It would then seem that it is this latter species

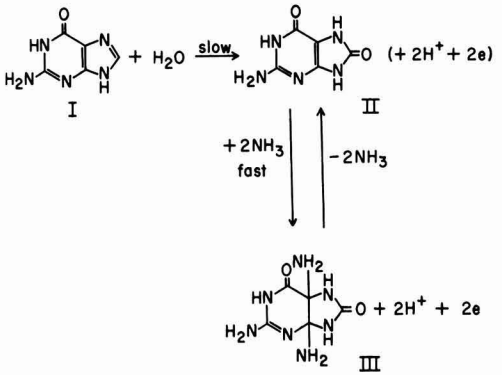

Fig. 4. Proposed primary electrochemical pathways for electrochemical oxidation of guanine in ammonia buffer *p*H 9.1. Compounds listed are as follows: I, guanine; II, 2-amino-6,8-dioxypurine; III, 2-amino-6,8-dioxypurine-4,5-diamine.

which forms the reversible redox couple at *ca.* −0.5V. The explanation of the anodic peak at 0.15V, which is the potential expected for the normal peak II_a is difficult to decide. A possible cause is decomposition of the 4,5-diamine (III, Fig. 4) to an electroactive species capable of being oxidized in this potential region. The most negative cathodic peak ($E_p = -1.4$V) most probably is due to oxaluric acid. In moderately acid solution, it is clear that the primary 4,5-diol product (the most usual product) is unstable and under conditions of constant potential oxidation decomposes by two routes, the first by further electro-oxidation to parabanic acid, guanidine, and carbon dioxide. Solution analysis supports this view since the faradaic n value and parabanic acid produced are in agreement with theory, *i.e.*, 0.35 mole parabanic acid per mole of guanine with an n value of 4.7e. In addition, the total guanidyl residue found per mole of initial guanine accounts for 0.9 mole, while oxalyl guanidine (IV, Fig. 3) determined by hydrolysis to glyoxylic acid accounts for only 0.55 mole, which therefore by difference indicates that 0.35 mole of free guanidine (VI, Fig. 3) is produced. This latter figure is in accord with the 0.35 mole of parabanic acid detected. These data further support the view that the parabanic acid is derived exclusively from the imidazole ring of guanine.

The material balance achieved accounts for only 90% of the initial guanine. No doubt additional hydrolysis of the above products accounts for the remaining 10%.

Conclusions

Guanine is electrochemically oxidized by a mechanism very similar to that observed for other naturally occurring purines such as uric acid and adenine. The evidence put forward supports the view that the locus of initial electron removal is the same for enzymic and electrochemical processes and is in accord with theoretical molecular orbital predictions. Unlike most enzyme reactions where the 2-amino group of guanine is removed, this group remains intact under electrochemical conditions, and further electrochemical reaction is centered at the —C(4)=C(5)—bond.

It is particularly striking that the photodynamic degradation of guanine and indeed DNA appears to be identical to the electrochemical degradation.

Acknowledgment

The authors would like to thank the National Science Foundation which supported the work described through Grant No. GP 8151.

Manuscript submitted Dec. 4, 1969; revised manuscript received May 25, 1970.

Any discussion of this paper will appear in a Discussion Section to be published in the June 1971 JOURNAL.

REFERENCES

1. G. Dryhurst and P. J. Elving, *This Journal,* **115,** 1014 (1968).
2. W. A. Struck and P. J. Elving, *Biochem.,* **4,** 1343 (1965).
3. G. Dryhurst, *This Journal,* **116,** 1097 (1969).
4. G. Dryhurst, Work in progress (1969).
5. G. Dryhurst, *This Journal,* **116,** 1411 (1969).
6. G. Dryhurst and B. J. Hansen, Work in progress (1969).
7. J. H. Lister, "Advances in Heterocyclic Chemistry," Vol. 6, p. 1, A. R. Katritsky and A. J. Boulton Editors, Academic Press, New York (1966).
8. R. K. Robins, "Heterocyclic Compounds," Vol. 8, p. 162, R. C. Elderfield, Editor, John Wiley & Sons, Inc., New York (1967).
9. G. P. Wheeler and J. A. Alexander, *Cancer Research,* **21,** 390 (1961).
10. J. H. Ayvazian and S. Skupp, *J. Clin. Invest.,* **45,** 1859 (1966).
11. J. B. Wyngaarden, *J. Biol. Chem.,* **224,** 453 (1957).
12. A. J. Guarino and G. Yuregir, *Biochem. Biophys. Acta,* **36,** 157 (1959).
13. J. S. Sussenbach and W. Berends, *ibid.,* **95,** 185 (1965).

14. L. A. Waskell, K. S. Sastry, and M. P. Gordon, *Biochem. Biophys. Acta Previews*, **6**, [3] xx (1966).
15. A. S. Jones, R. T. Walker, and A. R. Williamson, *J. Chem. Soc.*, **1963**, 6033.
16. J. J. Lingane, "Electroanalytical Chemistry," Chap. XIX, pp. 457-458, Interscience Publishers, New York (1966).
17. J. J. Pfiffner and V. C. Myers, *J. Biol. Chem.*, **87**, 345 (1930).
18. G. Dryhurst and P. J. Elving, *Anal. Chem.*, **40**, 492 (1968).
19. T. Staron, C. Allard, M. M. Chambre, and D. W. Xuong, *Compt. rend.*, **257**, 2552 (1963).
20. E. G. Young and C. F. Conway, *J. Biol. Chem.*, **142**, 839 (1942).
21. F. Bergmann and S. Dikstein, *Biochem. J.*, **77**, 691 (1955).
22. L. F. Cavalieri, A. Bendich, J. F. Tinker, and G. B. Brown, *J. Am. Chem. Soc.*, **70**, 3875 (1948).
23. B. Pullman and A. Pullman, "Quantum Biochemistry," Chap. V, Interscience Publishers, New York (1963).
24. P. J. Elving, W. A. Struck, and D. L. Smith, *Mises au Point Chim. Anal. Org. Pharm. Bromatol.*, **14**, 141 (1965).
25. W. A. Struck and P. J. Elving, *Anal. Chem.*, **36**, 1374 (1964).
26. G. Dryhurst and P. J. Elving, *ibid.*, **40**, 492 (1968).

Technical Notes

Effect of Sb_2O_3 on the Microstructure of the PbO_2 Electrode

A. C. Simon* and S. M. Caulder*[1]

Naval Research Laboratory, Washington, D. C. 20390

and E. J. Ritchie*

Eagle-Picher Industries, Incorporated, Joplin, Missouri 64801

Unusual properties have been attributed to battery plates which contain lead-antimony grids. The supposition is that antimony dissolves from the grid and then reacts in some manner with the active material.

In a comparison of lead-calcium *vs.* lead-antimony grids (1), it was reported that the presence of antimony increased the amount of α-PbO_2 during formation, helped to retain the active material and capacity during cycle tests, and modified the crystal structure of the PbO_2. Electron micrographs indicated that, in plates containing antimony in the grid metal, the PbO_2 material was in the form of complex clusters of prismatic crystals. In plates containing lead-calcium grids, however, the PbO_2 particles were nondescript globules. It was suggested that the prismatic morphology was required to maintain a firm texture in the active material of the $PbO_2/PbSO_4$ electrode. It has also been suggested (2) that antimony may act as an inhibitor of PbO_2 crystal growth, the assumption here being that increasing growth size decreased surface area and structural strength of the active material.

In the present investigation another phenomenon has been noted which is directly attributable to the antimony oxide and which offers a clue for attaining greater strength in the active material without the necessity of using lead-antimony grid alloys. A number of cells were prepared in which various oxides or oxide blends had been used in the preparation of the plates. Duplicate cells were prepared from each of these paste compositions, one with plates containing grids of lead and the other containing grids of lead-antimony. Optical microscopy was used to determine the microstructure of the cured plates, formed plates, and plates that had received a number of cycles.

In the preparation of the plates for microscopic examination, use was made of a polyester resin for impregnation. After this hardened, the plates were cut and the cross section was polished.

Usually, such polished sections, particularly of cured plates, are quite stable. It was noticed, however, that in samples taken from two of the cured plates, the polished surface had been etched by the atmosphere, after a considerable time on the shelf. The remainder of the cured plate sections were then re-examined and none was found with a similar etch pattern.

The etch pattern was quite distinct and suggested that long, needlelike crystals had been present in the polished surface that were completely invisible until the etching took place (Fig. 1). When polarized light was used to examine the specimen at the same location, it was found that crystals were present at the areas where an etch pattern was seen. These crystals were colorless, transparent, and indistinct and blended into the surrounding material, so that their outline was blurred (Fig. 2). Nevertheless, they could be seen sufficiently well to determine that they usually coincided with the etched portions of the surface and that they were actually acicular rather than cross sections through tabular crystals.

Because they had given no indication of their presence in the polished surface when examined by vertical illumination (unpolarized light) before the etching had occurred, these crystals had been completely overlooked in the original examination. This invisibility in the polished section also indicated that the crystals consisted of material different from the usual constituents found in the uncured plate which indicate their presence by differences either in reflectivity or in the amount of relief polishing.

The acicular crystals, showing atmospheric etching, were found only in cured plates to which 0.10% of

* Electrochemical Society Active Member.
[1] International Lead-Zinc Research Organization Research Associate at the Naval Research Laboratory.
Key words: antimony trioxide, Sb_2O_3, microscopy, lead dioxide electrode.

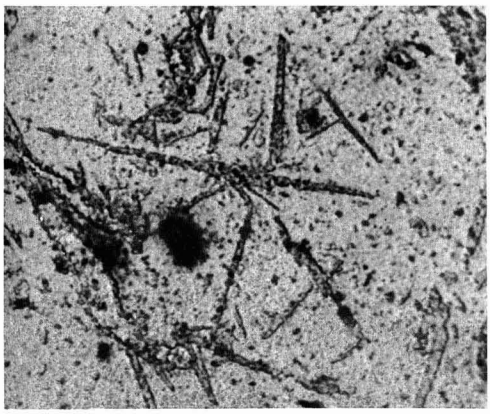

Fig. 1. Distinct etch pattern suggesting the presence of long, needlelike crystals.

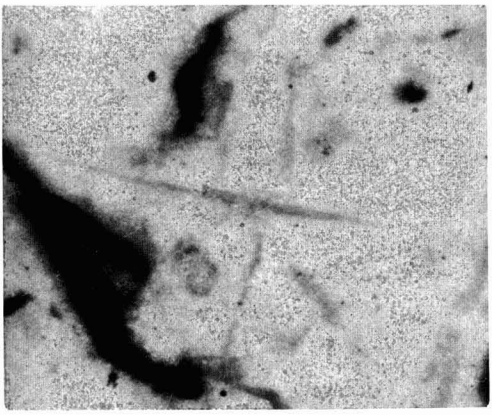

Fig. 2. Colorless, transparent, indistinct crystals found at areas where an etch pattern was seen.

Sb_2O_3 had been intentionally added to the paste during mixing. Two batches had contained this added Sb_2O_3 and both were otherwise identical except for a difference in the paste density. In the one case this was 64 g/in.^{3} and in the other, 69 g/in.^{3}. Both of these formulations had been pasted on lead grids, and both showed similar crystals and surface etching.

The same paste formulation, without the added Sb_2O_3, did not show any indication of such crystals as have been described, even when pasted on lead-antimony alloy grids. All indications were that this crystal type appeared only when Sb_2O_3 was a constituent of the paste mix.

The most interesting point, however, was that needles with very similar acicular shapes were also found in the formed plate (Fig. 3). These were composed of PbO_2 and were easily seen in the polished

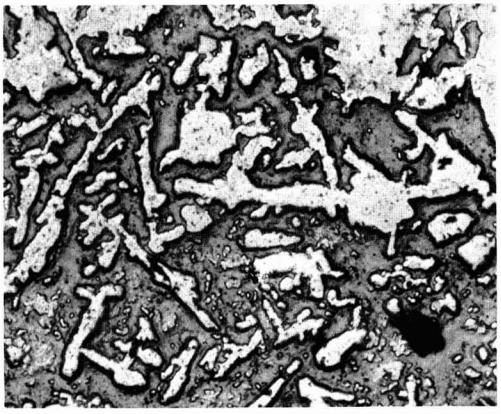

Fig. 3. Acicularly shaped needles found in the formed plate

sections and in size and shape suggested a relationship with those in the cured but unformed plate. These areas of PbO_2 with acicular external form were found only in the formed plates to which Sb_2O_3 had been added in the original mixing.

The lack of these needlelike crystals of PbO_2 in the formed plates with lead-antimony grids indicates that the amount of antimony that can be obtained from the grid is insufficient for the formation of such crystals. This is particularly true because the type of crystal responsible for the acicular PbO_2 crystals in the formed plate was first formed in the cured plate. Under curing conditions the electrolytic action necessary for solution and transport of the antimony is missing.

In the samples examined which contained 0.10% Sb_2O_3, the number of needlelike PbO_2 groups formed seemed insufficient to bind the plate active material together, either by intergrowth at contacts (such as seems to have occurred at several points in Fig. 3) or by the formation of an interlocking structure.

It would seem advisable to investigate this phenomenon further by using various amounts of Sb_2O_3 in the paste and combining this with capacity and life-cycle tests to see if this type of structure can be improved and whether it proves to be beneficial.

Acknowledgment

The International Lead Zinc Research Organization is gratefully acknowledged for maintaining the position of Postdoctoral Research Associate at NRL and for supporting that portion of the work done at Eagle-Picher through an ILZRO research contract.

Manuscript submitted April 18, 1970; revised manuscript received *ca.* June 22, 1970.

Any discussion of this paper will appear in a Discussion Section to be published in the June 1971 JOURNAL.

REFERENCES

1. J. Burbank, *This Journal*, **111**, 1112 (1964).
2. E. J. Ritchie and J. Burbank, *ibid.*, **117**, 229 (1970).

Mass Transport Limitations in Lithium-Cupric Fluoride Cells

R. Keller*

Research Division, Rocketdyne,
A Division of North American Rockwell Corporation, Canoga Park, California 91304

The lithium-cupric fluoride battery system which has an excellent theoretical energy density has been studied by various investigators (1). Severe performance limitations were encountered in regard to discharge rates. Such limitations appeared to depend on the electrolyte, *e.g.*, they were significantly greater in propylene carbonate electrolytes than in those based on methyl formate.

It appears that the performance of the cathode generally is the factor limiting the performance of lithium-cupric fluoride batteries under study. Factors possibly limiting cathode performance include (*a*) internal conductance of the cathode material, if reduction occurs *in situ;* (*b*) dissolution rate of the electroactive material, if reduction of dissolved copper species occurs; (*c*) formation of complexed copper species causing changes in discharge potentials and/or loss by diffusion and migration; (*d*) blocking of discharge sites by reaction products, particularly insoluble lithium fluoride; and (*e*) mass transport in the electrolyte. Mass transport limitations are being scrutinized in this note. It is shown below that, in certain cases, mass transport in the electrolyte alone may account for the observed performance limitations. It should not be implied, however, that the factors limiting the performance of prototype cells in actual discharge tests have been identified.

The lithium-cupric fluoride cell, *e.g.*, with a $LiClO_4$ electrolyte, is somewhat unique inasmuch as the cation of the electrolyte is being precipitated at the cathode during cell discharge, according to

$$CuF_2 + 2Li^+ + 2e = \underline{Cu} + \underline{2LiF} \qquad [1][1]$$

Lithium fluoride has generally a very low solubility in aprotic solvents and solutions; some solubility values obtained in our laboratory are given in Table I. Because of this very low solubility of LiF, and since lithium is the only cation present (disregarding copper), practically all fluoride ions potentially formed at the cathode are readily precipitated. This causes a depletion of the electrolyte at the cathode. Under limiting conditions, this depletion will be complete, and mass transport cannot be increased by higher electric fields (higher *IR*-drops). A similar effect, incidentally, can occur also in aqueous systems, *e.g.*, when insoluble hydroxide forms at the anode; in such "conventional" cases, this effect is, however, much less critical because of higher diffusion coefficients and because a higher amount of electrolyte solute (as reservoir) can be tolerated without severely jeopardizing the energy density of the cell.

In the following, a lithium-cupric fluoride cell with a 1M $LiClO_4$ in propylene carbonate (PC) electrolyte shall be considered as an example. At a discharge under mass transport limitations, an electrolyte concentration profile, shown schematically in Fig. 1, will eventually result. The electrolyte concentration at the anode will correspond to a saturated $LiClO_4$ solution and will be practically zero at the cathode.

* Electrochemical Society Active Member.
Key words: lithium cells, copper fluoride cathode, mass transport, nonaqueous battery.

[1] According to solubility studies, the reaction $2LiClO_4 + CuF_2 = 2LiF + Cu(ClO_4)_2$ may occur on open circuit, although such studies have indicated that it may progress very slowly. It is not certain how far such a reaction would extend, *i.e.*, if $Cu(ClO_4)_2$ would form in significant amounts beyond the solubility of this compound in an actual electrode. Such a process would cause a depletion of the electrolyte, but, overall, an excess of CuF_2 would have to remain because in a practical system a stoichiometric amount of ClO_4^- could not be permitted without jeopardizing the high-energy density feature of the cell. After an initial discharge of $Cu(ClO_4)_2$, the limiting conditions would therefore occur as discussed.

Table I. Solubility of LIF

Solvent/solution	Temp, °C	Solubility of LiF, moles/liter
Propylene carbonate	25; 60	$<5 \times 10^{-6}$
1M $LiClO_4$/PC	25	1×10^{-4}
Dimethyl formamide	25	3×10^{-5}
Dimethyl formamide	60	5×10^{-5}
Acetonitrile	25	2×10^{-5}
Methyl formate	25	3×10^{-5}

Table II. Calculation of limiting current

Li precipitated as LiF at cathode:	$j_{Li,c} = -\frac{i}{F}$
Li^+ transported by migration:	$j_{Li,m} = \frac{i \cdot t_+}{F}$
Li^+ transported by (linear) diffusion:	$j_{Li,d} = -D\frac{dC_{Li}}{dy}$
Li^+ transported by convection:	Zero

$$j_{Li,c} + j_{Li,m} + j_{Li,d} = 0 = -\frac{i_l}{F} + \frac{i_l \cdot t_+}{F} - D\frac{\Delta C_{Li}}{\Delta y}$$

$$i_l = -D\frac{F\,\Delta C_{Li}}{t_- \cdot d}$$

The diffusion limiting current for such a case is calculated for a simplified, linear model where: (*a*) no separator is present; (*b*) the distance between anode and cathode is $d = 1$ mm; (*c*) convection is negligible; (*e*) the diffusion coefficient, D, is constant throughout the cell; and (*f*) the solubility of $LiClO_4$ at the anode is 2.1 moles/liter, the solubility of LiF at the cathode is negligible, and a linear concentration profile for $LiClO_4$ forms between anode and cathode. The concentration gradient for the lithium ion can then be represented by

$$\frac{dC_{Li}}{dy} = \frac{\Delta C}{d} = \frac{-2.1 \times 10^{-3}}{0.1} \text{ moles cm}^{-4} \qquad [2]$$

Lithium ions are transported by migration and diffusion (convection neglected). At steady-state limiting conditions, the amount of lithium ions reaching the cathode equals the amount of lithium ions precipitated at the cathode. The limiting current, i_l, can be calculated as shown in Table II.

$$i_l = -D\frac{F \cdot \Delta C_{Li}}{t_- \cdot d} \qquad [3]$$

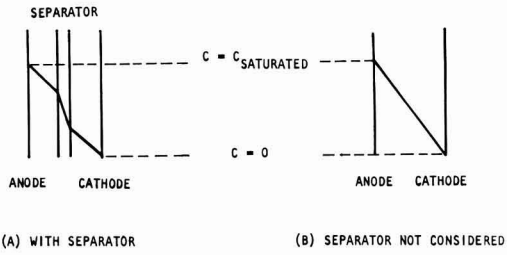

Fig. 1. Schematic electrolyte concentration profile

Selecting the value of $D = 2.6 \times 10^{-6}$ cm^2 sec^{-1} determined as the integral diffusion coefficient for a 1M $LiClO_4$/PC solution at 25°C in this laboratory (2), and a value of $t_- = 0.75$ based on transference and conductance measurements (3), a value of

$$i_l = 7 \times 10^{-3}\ \text{Acm}^{-2}$$

results for $d = 0.1$ cm and $\Delta C = -2.1$ moles/liter.

By assuming a simple cell model, some factors have not been considered:

1. Convection has been neglected. It was found experimentally by Boehm and Ibl (4) for an aqueous system that convection was negligible at electrode distances smaller than about 0.4 to 0.6 mm. Because the distances between walls in the presence of a separator should be assumed to be smaller than 0.5 mm, and, in addition, the viscosity of the propylene carbonate electrolyte is higher than the viscosity of aqueous solutions, disregard of convection effects is indeed appropriate.
2. The diffusion coefficient in the separator material is lower than in the electrolyte, and somewhat lower values for limiting currents should result if the presence of separators is considered.
3. Increases in cell temperatures during discharge cause higher diffusion rates and hence higher limiting currents; a temperature increase from 25° to 70°C might be expected to approximately quadruple the limiting current in analogy to aqueous solutions (5).
4. A reservoir of electrolyte may be contained in the cathode. However, such excessive amounts of electrolyte solution or solute depress the total cell energy density.
5. A layer of saturated $LiClO_4$ solution may build up at the anode if sufficient $LiClO_4$ is available and hence increase the concentration gradient by reducing the distance between saturated solution and cathode.
6. Higher currents will be obtained in the transition period before diffusion limitation will be reached.

Conclusions

Limitations to low or moderate discharge rates can be predicted for certain lithium cells because of transport limitations in the electrolytes. It appears essential to consider such factors.

Limitations by mass transport as discussed may be reduced by:

1. Use of electrolytes with higher diffusion coefficients;
2. Use of an electrolyte or a cathode material which does not form insoluble cathode discharge products;
3. Use of excess electrolyte solute as ion reservoir at the cathode;
4. Proper choice of separator to minimize separator action as diffusion barrier;
5. Reduction of the electrode spacing.

Acknowledgment

This paper was stimulated by the work performed under Contract NAS3-8521 which was supported by the NASA Lewis Research Center. The author wishes to thank Professor N. Ibl and Mr. R. B. King for their valuable comments.

Manuscript submitted June 16, 1969; revised manuscript received June 22, 1970. This was Paper 52 presented at the Detroit Meeting of the Society, Oct. 5-9, 1969.

Any discussion of this paper will appear in a Discussion Section to be published in the June 1971 JOURNAL.

REFERENCES

1. R. Jasinski, *Electrochem. Technol.*, **6**, 28 (1968).
2. J. M. Sullivan, D. C. Hanson, and R. Keller, *This Journal*, **117**, 779 (1970).
3. R. Keller, J. N. Foster, D. C. Hanson, J. F. Hon, and J. S. Muirhead, Contract NAS3-8521, Report No. NASA CR-1425 (August 1969).
4. U. Boehm and N. Ibl, *Electrochim. Acta*, **13**, 891 (1968).
5. S. Glasstone, "Introduction to Electrochemistry," 5th ed., p. 452 (1951).

Rapid Determination of Electronic Conductivity Limits of Solid Electrolytes

D. A. J. Swinkels*

Central Research Laboratories, The Broken Hill Proprietary Company Limited, Shortland, N. S. W. 2307, Australia

Solid oxide-ion conductive electrolytes have found many applications for the determination of oxygen activities at elevated temperatures. However, at low oxygen activities and high temperatures, such as for example in the determination of dissolved oxygen in liquid steel (1), the onset of electronic conductivity causes a reduction in cell emf from that calculated from the simple Nernst equation.

Schmalzried (2, 3) has treated the emf relationships for solid electrolyte cells in which the electrolyte shows mixed ionic and electronic conductivity. Free electrons may be generated by the reaction

$$O_o = O_2(g) + 2V_o^{\cdot\cdot} + 4e^- \qquad [1]$$

where O_o is an oxygen atom in a regular oxygen site, $V_o^{\cdot\cdot}$ is a doubly ionized oxygen vacancy, and e^- is an excess electron. For heavily doped materials such as $(ZrO_2)_{0.9}(Y_2O_3)_{0.1}$ or $(ZrO_2)_{0.88}(CaO)_{0.12}$, O_o and $V_o^{\cdot\cdot}$ are approximately constant, and hence the electronic conductivity at a given temperature will vary with oxygen pressure according to

$$\sigma_e = \sigma_e{}^o P_{O_2}{}^{-1/4} \qquad [2]$$

The resulting cell emf for a cell with oxygen pressures P_1 and P_2 is then given by

$$E = \frac{RT}{\mathbf{F}} \ln \frac{P_\circ{}^{1/4} + P_2{}^{1/4}}{P_\circ{}^{1/4} + P_1{}^{1/4}} \qquad [3]$$

where P_θ is the oxygen pressure at which the electronic conductivity becomes equal to the ionic conductivity, *i.e.*, the ionic transport number $t_i = 0.5$. Equations similar to [2] and [3] are available for materials showing hole conductivity and for materials showing both electron and hole conductivity. The current analysis is limited to materials showing only ionic and electron conductivity. Values of $P_\circ$ have been determined from resistance measurements as a function of P_{O_2} (4), from emf measurements on cells with known oxygen activities (5, 6), from polarization measurements between a reversible and a nonreversible electrode (4), and by

* Electrochemical Society Active Member.

Key words: oxide ion conductor, oxygen pump, coulometric titration.

coulometric titration procedures (7). Resistance measurements result in limited precision values of $P_{\ominus}$ since extreme experimental difficulty exists in fixing the very low P_{O_2} values which are required. At high temperatures, errors due to changes in surface and gas conduction and to contact resistances can readily occur. Methods involving emf measurements all require quite impervious electrolyte specimens and mountings since otherwise the resulting lower emf values are due to gas permeability, but may be interpreted as being due to electronic conductivity.

A new technique similar to the coulometric titration method (7) or the oxygen pumping approach of Yuan and Kröger (8) is proposed. Such a method can be used with both porous and dense samples, and $P_{\ominus}$ values, over a wide range of temperatures are determined in a single run. An emf cell is made up, from the sample of the electrolyte to be tested, with a Pt-air electrode on one side and a liquid metal electrode on the other side (see Fig. 1 for typical geometries). Fine silver (99.95%+ Ag) was used in our measurements since the temperature range of interest was 1000°-1650°C, but other metals can be used at lower temperatures. Contact to the liquid silver was made *via* an iridium wire.

Oxygen is pumped from the metal side of the cell by passing a d-c current in the appropriate direction, and the cell becomes polarized to an extent determined by the rate of oxygen removal with the current and by the leak rate of oxygen back into the system through the sample or its mounting or from the argon cover gas. The current is increased until it exceeds the total leak rate. The oxygen level in the metal is then reduced to an extremely low level. Further increases in current rapidly increase the proportion of the electronic current through the sample. Under these conditions $P_2 >> P_{\ominus} >> P_1$ and hence Eq. [3] may be simplified to

$$E_m = \frac{RT}{4F} \ln \frac{P_2}{P_{\theta}} \qquad [4]$$

where $P_2 = 0.21$ atm. E_m is obtained by momentarily interrupting the current and measuring the cell emf without *IR* drop and correcting for the Ir-Pt thermal emf. The open-circuit emf decays at a rate determined by the total leak rate of oxygen back into the silver.

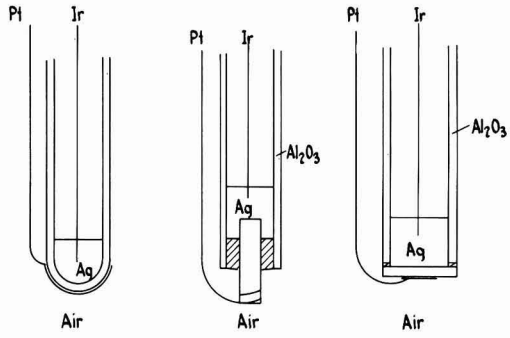

Fig. 1. Cell geometries for tube, rod, and disk shaped samples

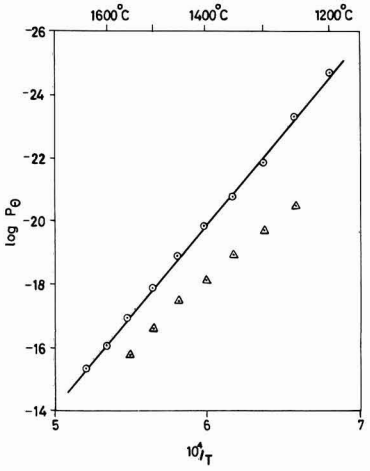

Fig. 2. Values of log $P_{\ominus}$ determined from resistance measurements (△) and by the present polarization technique (○).

i.e., the sum of molecular oxygen flow (through pores) and O^{--} flow (balanced by electronic flow).

Results obtained for a high-purity 7 m/o Y_2O_3 stabilized zirconia material prepared by coprecipitation, calcining, pressing, and sintering (9) are shown in Fig. 2. The sample consisted of a ⅛ in. diameter 1 in. long cylinder mounted in an alumina tube using Ceramabond 503 alumina cement. The polarizing current was interrupted for 0.5 msec at 50 msec intervals and the emf was measured by a track-store circuit synchronized with the interruptions and displayed on a DVM. $P_{\ominus}$ values calculated from 2 terminal resistance measurements in air and in H_2/H_2O atmospheres at 1592 Hz are shown for comparison. The resistance measurements were reproducible to ±1 in the value of log $P_{\ominus}$ calculated while the polarization measurements were generally reproducible to ±0.2 in log P_{θ}.

Manuscript submitted April 13, 1970; revised manuscript received June 25, 1970.

Any discussion of this paper will appear in a Discussion Section to be published in the June 1971 JOURNAL.

REFERENCES

1. C. Gatellier, K. Torssell, M. Olette, N. Meysson, M. Chastant, A. Rist, and P. Vicens, *Rev. Met.*, **14**, 673 (1969).
2. H. Schmalzried, *Z. Phys. Chem. N.F.*, **38**, 87 (1963).
3. B. C. H. Steele and C. B. Alcock, *Trans. Met. Soc. AIME*, **233**, 1359 (1965).
4. J. W. Patterson, E. C. Bogren, and R. A. Rapp, *This Journal*, **114**, 752 (1967).
5. R. Baker and J. M. West, *J. Iron & Steel Inst.*, **204**, 212 (1966).
6. W. A. Fischer and D. Janke, *Arch. Eisenhuettenw.*, **39**, 89 (1968).
7. Yu. D. Tretyakov and A. Muan, *This Journal*, **116**, 331 (1969).
8. D. Yuan and F. A. Kröger, *ibid.*, **116**, 594 (1969).
9. W. G. Garrett and N. A. McKinnon, Private communication.

Evidence for a Complex Chloromolybdate Ion in a Molten Salt Medium from Transference Experiments

Vernon A. Lamb

National Bureau of Standards, Washington, D. C. 20234

Considerable indirect evidence exists for the presence of anionic chloro complexes of molybdenum in molten alkali chloride media, based mainly on emf measurements (1-4). It was thought that experiments that would provide direct evidence for the existence or absence of such complexes would be worthwhile. A transference technique was chosen for this purpose. The molten system was a solution of K_3MoCl_6 in KCl-LiCl eutectic.

If, at a particular temperature, the equilibria between Mo(III) ions and chloride ions lie predominantly in the direction of negative Mo-containing species, Mo should be electrically transported from the cathode compartment to the anode compartment of a transference cell. A blank experiment (no current) run under similar conditions should give the amount of transport by diffusion. A positive difference between Mo in the anode compartment resulting from electrolysis and from diffusion would indicate the presence in the molten system of a preponderance of negatively charged complex ions. On the other hand, if no electrical transport to the anode compartment were found, it would indicate that either the transference number of the complex is zero, or that it is dissociated to such a degree that neutral $MoCl_3$ or positive chlorocomplexes of Mo(III) predominate. In the latter case, electrical transport of molybdenum into the cathode compartment could be detected by electrolysis of a cell in which the molybdenum salt was initially present only in the anode compartment.

Experimental

Preliminary experiments showed that it was necessary to pass a large number of coulombs through a cell to produce transport of sufficient molybdenum to permit its measurement with reasonable accuracy. The cell shown in Fig. 1 was, therefore, designed to permit a large coulomb flow. Silver chloride is used in cathode compartment D. This arrangement prevents deposition of molybdenum from cathode compartment E that would occur if compartment D were absent and the cathode were placed directly in compartment E. The diaphram, C, between the two sections of the anode compartment prevented large amounts of nickel from entering compartment B-C. The number of coulombs that could be passed was limited by the amount of silver ion in the cathode compartment and the mass of nickel anode in contact with the eutectic melt in the anode compartment. These had capacities of about 7000 coulombs, whereas 2600 was the largest amount passed (Table I).

Key words: hexachloromolybdate complex ion, molten salt, transference numbers.

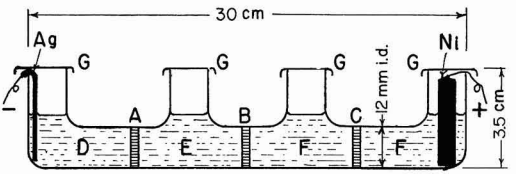

Fig. 1. Design of Vycor transference cell. A, B, C, porous quartz diaphrams; D, LiCl-KCl eutectic + AgCl, 25% by wt; E, K_3MoCl_6 + LiCl-KCl eutectic; F, LiCl-KCl eutectic; G, caps to reduce evaporation of salt.

The quartz disks shown in Fig. 1 were 1.5 mm thick and had a nominal pore diameter of <15 μm. As obtained from the manufacturer they had pore volumes ranging from 33 to 45%. Under a pressure differential of approximately 1 atm, the flow of water through these disks was 10-15 ml/min. To reduce the porosity of the disks and, hence, the interdiffusion rate between the contents of the cell compartments, the disks were partially plugged with silica by treating successively with ethyl silicate and hydrochloric acid, followed by baking at 800°C (5). Disks so treated to give a water flow under suction of about 0.5 ml/hr were used by Lunden (6), who estimated their effective total pore cross section to be about 0.3 to 0.4%. In our experience, disks this tightly plugged were extremely difficult to impregnate with molten salt, passed only a very small current at several hundred volts, and showed evidence of conductance by arcing. Most of the runs were therefore made with cells containing disks plugged to a flow under 1 atm pressure of 3-10 ml/hr. Such disks were estimated to have a pore cross section of about 3%. They permitted passage of currents of the order of 100 mA at cell potentials in the range of 5-10V, and interdiffusion was adequately reduced, as shown by the data in Table I.

Preparation of salts.—Potassium and lithium chlorides were purified by the method of Maricle and Hume (7). Potassium chloromolybdate was prepared by the method of Senderoff and Brenner (8) and purified by heating in vacuum at 150°C for ¾ hr, followed by successive washes in water, HCl-methyl alcohol, methyl alcohol, and ethyl ether, followed by vacuum removal of the ether. Analysis gave Mo, 19.95%; Cl, 49.6%. Theoretical: Mo, 23.1%; Cl, 51.2%.

Table I. Summary of experiments on transport of molybdenum

Exp. No.	Temp, °C	Current, mA	Time, hr	Coulombs	Disk flow at 1 atm, ml/hr	Initial location of K_3MoCl_6	Mo found in opposite compartment, mg	$t_{MoCl_6^{3-}}$
				Part A. Control experiment				
16B	720	None	53	None	12	—	0.55	
				Part B. Transport experiments				
5	800	80	1.8	520	42	Cathode	2.1	0.012
14	800	23	5	410	2.2	Cathode	1.5	0.011
8	800	140	4	2,000	3.5	Cathode	4.9	0.0074
15	800	180	4	2,600	10	Cathode	5.3	0.0062
12	800	100	2.8	1,000	4.0	Anode	0.9	—
							Arithmetic mean	0.009
							Standard deviation	0.0028

The found analysis is approximately accounted for if the preparation contained 12% of excess KCl. A eutectic mixture of LiCl and KCl plus potassium chloromolybdate was prepared that contained LiCl, 40%; KCl, 47%; K_3MoCl_6, 13% by weight (57, 41, and 2 m/o, respectively) of the constituent salts. On melting the molybdenum salt-eutectic mixture, a small amount of black precipitate formed, which was probably a molybdenum oxide or a higher valent chloride. It was separated by settling, freezing, and mechanical removal. Transfer and mixing operations were done in a dry-box.

Procedure.—The cells described above were filled in a dry-box and stoppered during transfer to the furnace tube. They were exposed to air only briefly while inserting the electrodes, capping the openings, and placing in the furnace tube. The Vycor furnace tube, 6 cm OD, was then sealed, evacuated, filled with argon, and heated in a horizontal tube furnace. When the salt had melted, several successive evacuations and pressurizations were usually required to cause filling of the disk pores, indicated by good electrical conductivity. Coulombs passed were measured by integrating the current-time curve recorded on a strip-chart.

After electrolysis was completed, the cell was allowed to cool in the furnace and was then removed. To recover the salt from the segment B-C (Fig. 1), the cell was broken at the respective disks and the salt dissolved in water in a beaker. Molybdenum in the portion of salt from segment B-C was determined spectrophotometrically by the thiocyanate method. Separate experiments with known mixtures showed that nickel from the anode compartment did not interfere. The accuracy of the molybdenum determinations is judged to be within ± 3%.

Results.—The results are summarized in Table I. The control experiment, 16B, shows that the amount of molybdenum transferred by diffusion to the adjacent section of the cell that initially contained no molybdenum salt is negligible (0.01 mg/hr). The amounts of molybdenum found in the anode compartments, B-C, in experiments 5, 8, 14, and 15 definitely indicate transport of molybdenum by a negative molybdenum-containing complex ion.

The data in the last line of Table I, experiment 12, show that there was no significant transport of a molybdenum-containing ion from the anode to the cathode compartment. This result reinforces the evidence of experiment No. 5, 8, 14, and 15 and indicates that any positive chloro complexes of Mo(III), if present, are in rapid equilibrium with the predominant negative complexes. (The small amount of molybdenum found in the cathode compartment in this experiment is ascribed to diffusion and to trace contamination from the adjacent Mo-containing compartment, which is difficult to avoid completely when the frozen salt is salvaged for analysis.)

The values for the transference number in the last column of Table I were calculated from

$$t_- = \frac{(96500)\ (\text{mass of Mo transferred})}{(\text{coulombs})\ (\text{Equivalent wt. of Mo})} \quad [1]$$

The undissociated hexachloro complex ion is assumed for calculating the tabulated transference numbers; hence, the equivalent weight of molybdenum is 1/3 of its molecular weight.

Conclusions

With the apparatus and procedure described, direct evidence for the existence of an anionic chloromolybdenum complex at 800°C has been obtained. Its transference number of approximately 1% in the KCl-LiCl solvent has been determined with an accuracy of about ±30%. This value of the transference number of the complex shows that alkali and free chloride ions carry most of the current, and its magnitude is reasonable in view of the mol fraction of molybdenum in the melt (2%).

Acknowledgments

Acknowledgment is made to the U.S. Atomic Energy Commission, Division of Research, Chemistry Branch, for support of this work, to Dr. Abner Brenner for helpful discussions, and to V. D. Pennington and J. F. Berkeley for determinations of molybdenum.

Manuscript submitted Dec. 4, 1969; revised manuscript received June 29, 1970.

Any discussion of this paper will appear in a Discussion Section to be published in the June 1971 JOURNAL.

REFERENCES

1. S. Senderoff and A. Brenner, *This Journal*, **101**, 16, 31 (1954).
2. M. V. Smirnov and O. A. Ryzhik, Transactions (Trudy) No. 6 of the Institute of Electrochemistry, Urals Academy of Sciences, Electrochemistry of Molten and Solid Electrolytes, Vol. 3, A. N. Baraboshkin, Editor, Sverdlovsk, USSR, pp. 9, 25 (1965). Translation by Consultants Bureau, New York, 1966.
3. S. M. Selis, *This Journal*, **113**, 37 (1966).
4. S. Senderoff and G. W. Mellors, *ibid.*, **114**, 556 (1967).
5. F. R. Duke and A. L. Bowman, *ibid.*, **106**, 626 (1959).
6. A. Lundén, *ibid.*, **109**, 260 (1962).
7. D. L. Maricle and D. N. Hume, *ibid.*, **107**, 354 (1960).
8. S. Senderoff and A. Brenner, *ibid.*, **101**, 28 (1954).

The Electrodeposition of Nickel from Heavy Water

F. E. Ammermann, S. Ghosh, J. A. Larson, and C. R. Lewis

Research Office, Product Planning and Development, Chrysler Corporation, Detroit, Michigan 48231

Since no information was available concerning the effect of substituting deuterium for hydrogen in electroplating solutions, a short experiment was undertaken to determine the effects of this substitution. Nickel was deposited from baths identical except for the presence of hydrogen in one and deuterium in the other, and the resulting deposits were subjected to metallographic and x-ray diffraction examination.

Procedure

For the electrodeposition experiment, two solutions were made, each containing 2.4g of nickel chloride ($NiCl_2$) and 13.9g of nickel sulfate ($NiSO_4$) as dessicated salts. One was dissolved in 100 ml normal water and the other in a like amount of heavy water. One drop of hydrochloric acid was added to each solution to suppress hydrolysis and each was allowed to stand for 24 hr. Anodes were prepared from rolled electrolytic nickel. Cathodes, 1 in.^{2} were cut from polished brass sheet. The anodes were bagged in filter paper.

Electrolysis was performed in glass jars at room temperature. The electrodes were spaced 1 in. apart. The systems were connected in series and current supplied from a rectifier at the equivalent density of 30 A/ft^2 at the cathode. Each jar contained one cathode

Key words: deuterium, electroplating, stresses, nickel.

and anode arranged so that the opposed surfaces carried the principal amount of current and the backs were shielded. It was recognized that the conditions of high pH, low temperature, and lack of buffer (usually boric acid) would yield a burned and brittle plate, but it was felt that the unfavorable circumstances were more likely to emphasize any significant differences in deposition.

At the onset of deposition it was noted that hydrogen evolution was much reduced in the deuterium oxide solution. The cathodes were periodically examined in order to note significant alterations in appearance. As expected, the deposits were cracked and burned but that from the deuterium oxide much less so. Deposition was stopped when a sufficient thickness of nickel had been deposited to permit further examination. The total plating time was 2.5 hr during which the current was kept constant by periodic adjustment. Visual inspection showed the deuterium plate to be relatively smooth and metallic, whereas the normal system had produced the expected scaled and discolored surface. Somewhat unexpected was the appearance of the anodes. The anode from normal water appeared uniformly pitted but the heavy water anode was distinguished by large widely spaced holes in the surface.

Metallurgical Results

Both anodes and cathodes were given a detailed metallurgical examination. Because the deposits, especially from the normal water, were curled and fragmented, superficial hardness measurements were not taken. Figures 1 and 2 show the microscopic aspects of the anode dissolution. Since both the anodes and plating conditions were the same, any differences must be attributed to the presence of the heavy water in the electrolyte. The internal cavity structure and the nature of localized, uniform, tri-axial dissolution, irrespective of grain orientation, appears to be the same in both cases. Therefore, the difference lies in the behavior of the anode surface layer in the presence of the two electrolytes. In the heavy water solution, the surface characteristics of the anode appear to present no problem for dissolution (Fig. 4), whereas in the normal water solution, the surface layer appears to be passivated (Fig. 3) to a high degree. The improved anode utilization in the heavy water cell is apparent.

Figures 5 and 6 show cross sections of the deposits from heavy and normal water, respectively. The following observations can be made:

1. Both systems produced a deposit almost similar in appearance except for depth, uniformity, and tenacity with the substrate.
2. Both deposits are difficult to etch, basically columnar in nature and similar in microstructure except for the grain size difference.
3. The deposit from the heavy water system shows more ductility and better metallurgical bond with the substrate than the deposit from normal water.
4. In both systems, the structural continuity is broken by intermittent plating, indicating perhaps the effect of oxidation. Electron microscopic investiga-

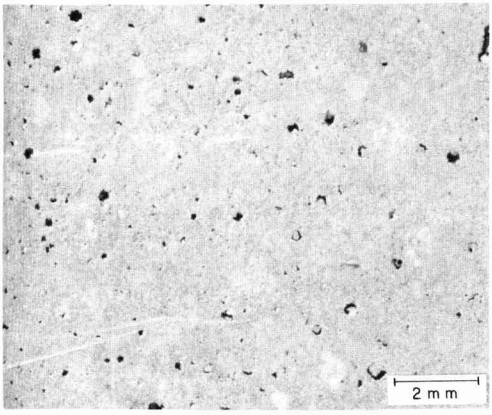

Fig. 1. Anode appearance after plating sequence in normal water

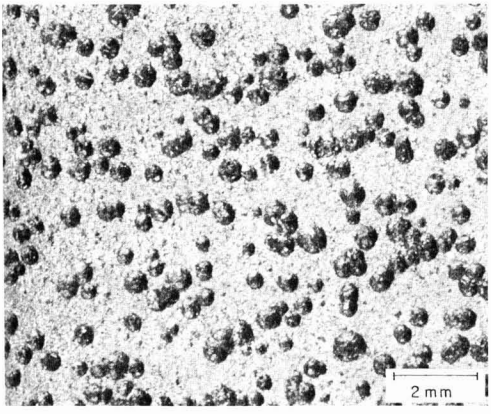

Fig. 2. Anode appearance after plating sequence in heavy water

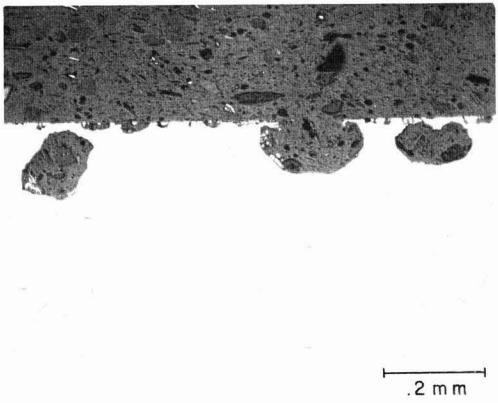

Fig. 3. Microstructure of anode surface dissolution pattern (normal H_2O) (100X).

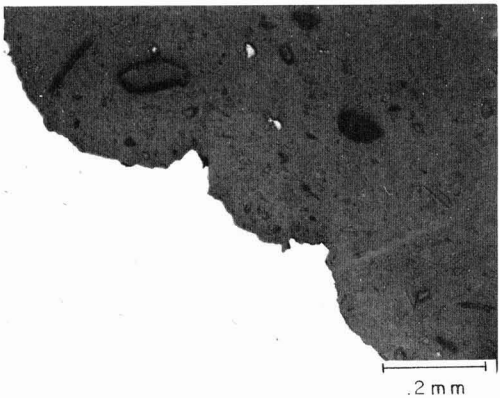

Fig. 4. Microstructure of anode surface in pit area (heavy water). (100X).

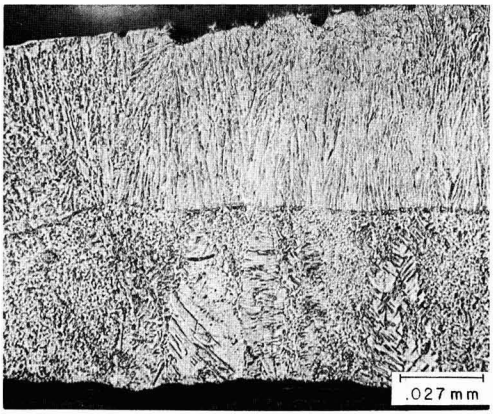

Fig. 5. Microstructure of plate from heavy water

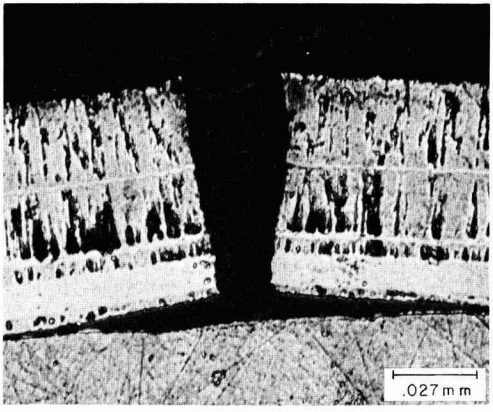

Fig. 6. Microstructure of plate from normal water

tion of the structure of both the anode and the plating is being pursued and may reveal further information.

X-Ray Results

Since distinct differences in grain size and stress levels were apparent in the two deposits, Fourier analysis of the x-ray diffraction peak shapes was undertaken to make these differences more quantitative. The analysis was performed on the (200) and (400) lines using copper radiation. Since the Rachinger (1) technique for doublet separation depends heavily on the tails of the diffraction lines, an interfering line from the brass substrate (which was evident in the tail of one diffraction line), made doublet separation difficult. Therefore, a computer program based on the unresolved doublet was used (2). The correction for instrumental broadening was made with the method devised by Stokes (3), using annealed nickel powder as the instrumental standard. The separation of the broadening into microstrain and particle size terms was accomplished utilizing the Warren and Averbach technique (4). The results of this analysis are shown in Table I.

The values of De and microstrain shown in Table I are in order-of-magnitude agreement with those given

Table I. X-ray results

Plating solution	Effective particle size De_{200}, Å	Microstrain $\langle E^2_{50Å} \rangle^{1/2}_{200}$	Microstrain $\langle E^2_{100Å} \rangle^{1/2}_{200}$
H_2O	190	14.3×10^{-4}	3.5×10^{-4}
D_2O	140	Very small	Very small

by Hinton (5) for electrodeposited silver. The general conclusion from the results shown is that the observed physical difference between the two plates can be attributed primarily to microstrains. In interpreting these microstrain differences, one must keep in mind that, since the Fourier analysis was carried out centered on the mid-point of the annealed peak, the microstrain values obtained must be corrected for any macrostrain which may be present. *i.e.*, the observed values are actually equal to $[\langle E_L^2 \rangle - \langle E_L \rangle^2]^{1/2}$. However, due to the poor adherence of the plates, it can probably be assumed, in this case, that any macrostrains have been relieved. It should also be noted that it is apparently possible for hardness (or ductility) differences to be accounted for by twin faults (5), and these were not evaluated in this case. However, it is felt that the large differences in microstrains are the primary cause of the ductility variation between the two plates, and twin fault variations are probably small.

It is apparent that visual, structural, and physical differences do exist in nickel deposited from normal and heavy water under the conditions described. The major effects are a lower stress level and smaller grain size in the nickel deposits and a more uniform removal of the anode surface from the heavy water solution. It is likely that these differences would diminish under conditions conducive to a more normal deposit such as higher temperatures, although the effects on anode dissolution should not depend strongly on this particular plating condition. The anode effect may represent a combination of D_2O as a solvent and the changes relative to H_2O during a plating cycle.

There are certain difficulties inherent in plating experiments using deuterium oxide that arise from the necessity of excluding normal hydrogen and the fairly high cost of deuterium oxide. However, the interesting results achieved in a simple experiment suggest that further investigation of deuterium oxide in both the deposition and etching of metals would be fruitful.

Acknowledgment

The authors would like to thank Mr. D. H. Mott for the photographs and Mr. T. C. Scott for help with the x-ray computer program.

Manuscript submitted May 7, 1970; revised manuscript received *ca.* June 20, 1970.

Any discussion of this paper will appear in a Discussion Section to be published in the June 1971 JOURNAL.

REFERENCES

1. W. H. Rachinger, *J. Sci. Instr.*, **25**, 254 (1948).
2. R. J. DeAngelis, "Local Atomic Arrangements Studied by X-ray Diffraction," Met. Soc. Conf., Vol. 36, p. 271, Gordon-Breach, N. Y. (1966).
3. A. R. Stokes, *Proc. Phys. Soc., London,* **61,** 302 (1948).
4. B. E. Warren and B. L. Averbach, *J. Appl. Phys.*, **21**, 595 (1950).
5. R. W. Hinton, L. H. Schwartz, and J. B. Cohen, *This Journal,* **110,** 103 (1963).

JOURNAL OF THE ELECTROCHEMICAL SOCIETY

SOLID STATE SCIENCE

OCTOBER 1970

A Kinetic Study of the Fluorination of Silver

Patricia M. O'Donnell*

Lewis Research Center, National Aeronautics and Space Administration, Cleveland, Ohio 44135

ABSTRACT

The effect of the variables, temperature, and pressure, on the kinetics of the reaction of fluorine with silver were studied. The temperature range of the investigation was from 25° to 300°C, and the reaction was measured at fluorine pressures of 50-600 Torr. The reaction was found to be pressure dependent. Three reaction products are identified: silver subfluoride, silver monofluoride, and silver difluoride. No simple rate law could describe the data over the entire time interval of the reaction.

The majority of the kinetic studies on heterogenous systems that have appeared in the literature in general discuss metal-oxygen systems. There have been some kinetic studies reported on metal-fluorine systems (1-15); however, the majority of the research on metal-fluorine systems has been compatability studies. In the present investigation the fluorination of silver was studied by exposing silver coupons to fluorine gas and following the reaction by the pressure drop method. The effect of both temperature and pressure on the rate of reaction are presented.

Experimental

The system used to study the fluorination of silver is shown in Fig. 1. Fluorine is brought from the tank through copper tubing into the system which is Pyrex throughout except for the reaction furnace which is made of quartz. A cold trap using a methylcyclohexane slush (−116°C) was used to remove any hydrogen fluoride impurity from the fluorine. The fluorine is analyzed by reaction with mercury in the still (1). Analysis of the fluorine indicated 99.83% fluorine plus 0.17% HF before purification and 100% fluorine after purification. Enough purified fluorine for one run is stored in the storage bulb. The mercury manometers in the system indicate the pressures in the storage and reaction sections of the apparatus. A layer of fluorocarbon oil is floated on top of the mercury to prevent it from reacting with the fluorine. All readings are corrected for density differences between the oil and the mercury. The metal samples are silver plates 1.27 x 15.24 x 0.012 cm. Spectrographic analysis gave a purity of 99.999%.

A plate is inserted into the cold reaction furnace under flowing argon and is positioned upright in the center of the furnace. The end plug is put in place and the argon pumped out. The furnace is turned on and the reaction section brought up to the appropriate temperature. Temperature profiles have been run with an instrumented metal sample, and the results show that the temperature variation across the sample is not more than 1°C. Meanwhile the storage section is filled with fluorine. The general experimental method used to determine the rate of fluorine consumption by silver was to measure the pressure decrease in a vessel of known volume containing the silver sample. In order to maintain approximately constant fluorine pressure, the pressure was allowed to drop only about 2 Torr and then more fluorine is introduced to return the pressure to its initial value. Pressures are recorded automatically by the pressure transducer and recording system. The perfect gas law was used to calculate the amount of fluorine consumed from the incremental pressure drop, the vessel volume, and the temperature. From the calibrated volume of the system, pressure changes on the time trace can be converted to milliliters of fluorine consumed at STP. After approximately a 4-hr exposure time the heaters were turned off, the system was allowed to cool to 25°C, and then the fluorine was pumped out of the system through the two soda lime scrubbers. The system is then brought up to atmospheric pressure with argon. A dry box is connected to the end of the furnace and the sample is pulled into it under flowing argon to prepare it for chemical and instrumental analysis.

Results and Discussion

The fluorine consumption by the silver samples was measured at several temperatures and pressures. The reaction was followed as a function of time and is reported as milliliters of fluorine consumed at STP per square centimeter of silver surface based on the geometrical area of the silver surface.

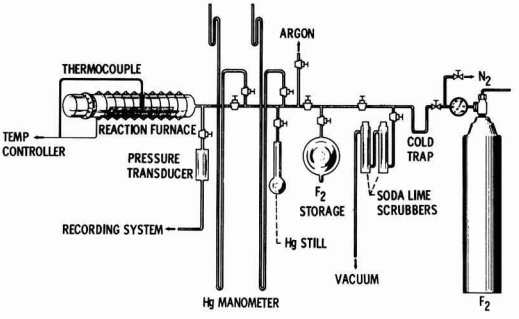

Fig. 1. Fluorination apparatus

* Electrochemical Society Active Member.

Key words: kinetics of fluorination of silver, fluorination of silver.

The effect of temperature on the reaction at a constant fluorine pressure of 50 and 200 Torr is shown in Fig. 2 and 3, respectively. The effect of pressure on the reaction at a constant temperature of 100° and 200°C is shown on Fig. 4 and 5. Note that at both temperatures there is a pressure reversal. This observed reversal in pressure dependency is not unique to this system but has been observed in other fluorination studies where multiple products are formed (16).

Data were not obtained at $t = 0$, the initial contact time of fluorine with the silver, because it takes a finite period of time to pressurize the apparatus with fluorine.

No simple rate law will describe the silver-fluorine reaction over the entire time interval studied. A linear rate law is applicable at short times, but as the time interval increases the data points deviate from a straight line as illustrated in Fig. 6. The data at the longer time intervals can best be described by a parabolic rate law as shown in Fig. 7.

Several products are formed when silver is reacted with fluorine at the temperatures and pressures studied. The products were identified by x-ray diffraction and by chemical and physical analysis as the subfluoride Ag_2F, the monofluoride AgF, and the difluoride AgF_2. Where more than one fluoride appeared the films were layered with the fluoride richest in silver adjacent to the metal and the one richest in fluorine at the gas-fluoride surface. The monofluoride was found as the middle layer. The relative amounts of

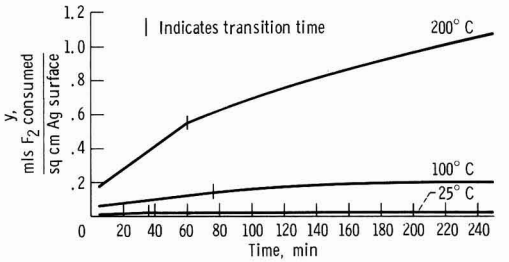

Fig. 2. Temperature effect at 50 Torr F_2 pressure

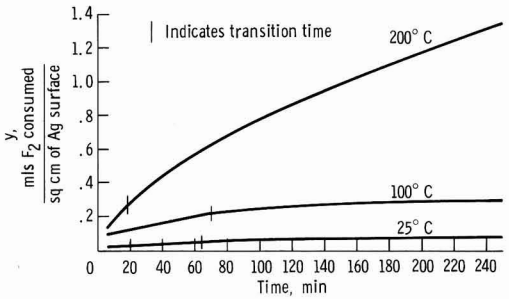

Fig. 3. Temperature effect at 200 Torr F_2 pressure

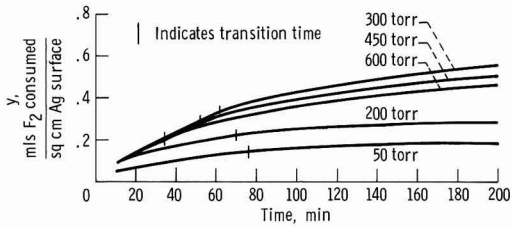

Fig. 4. Pressure effect at 100°C

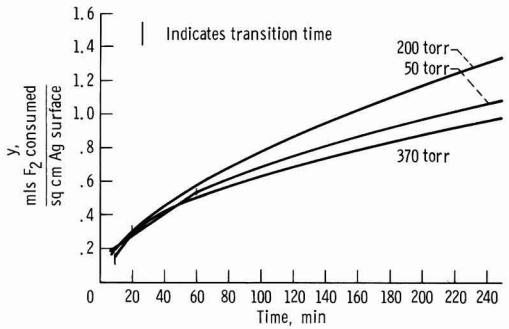

Fig. 5. Pressure effect at 200°C

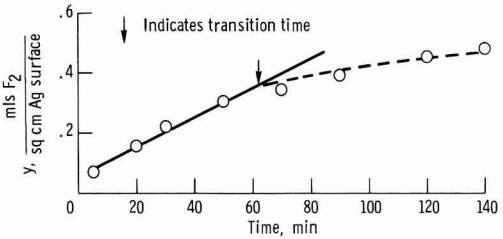

Fig. 6. Linear plot of fluorine consumption (100°C, 300 Torr)

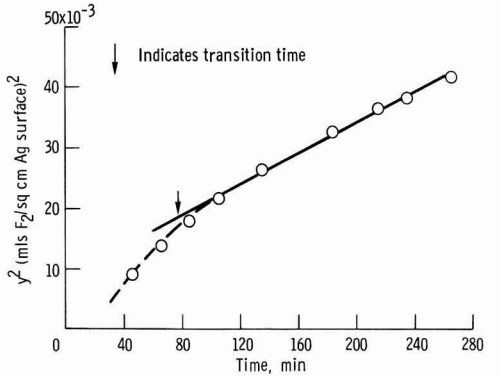

Fig. 7. Parabolic plot of fluorine consumption (50 Torr, 100°C)

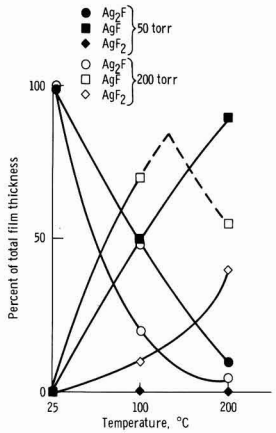

Fig. 8. Relative amounts of each product in the film

each product in the film, obtained from cross-section microscopy are shown in Fig. 8 for two pressures as a function of temperature. The amount of Ag_2F is shown by the circular symbols. As the temperature increases the amount of Ag_2F decreases. At 25°C only Ag_2F is formed at both pressures. The amount of AgF, shown by the square symbols, seems to increase to a maximum amount and then decrease as the temperature increases. The amount of AgF_2 is shown by the diamond symbols. No AgF_2 is formed at 50 Torr regardless of the temperature while at 200 Torr the amount increases as the temperature is increased. Not only temperature but pressure also affects the products formed. At 25°C and all pressures studied the only product formed was the subfluoride Ag_2F. As the temperature is increased, one or more reactions are possible including the decomposition of the subfluoride.

At 300°C the product melted even though the temperature was well below the reported melting points of the monofluoride (435°C) and the difluoride (690°C) This could be due to the formation of a known low melting eutectic $AgF \cdot AgF_2$ (17).

Reaction rate constants are plotted against $1/T$ on Fig. 9 and 10. The data on Fig. 9 show a pressure effect. Brown and Crabtree (1) observed a pressure effect on the activation energy, but could offer no explanation.

The reaction of silver and fluorine is a complex reaction and the applicability of different rate laws is difficult to explain in the absence of definitive solid-state data.

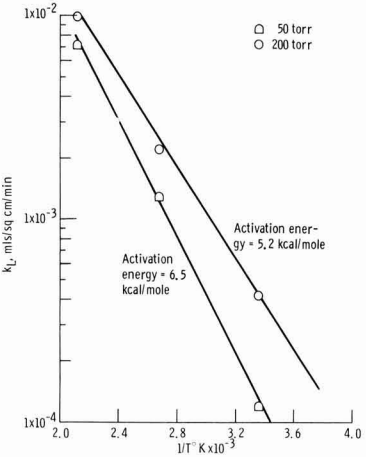

Fig. 9. Effect of temperature on rate constant in the boundary controlled region.

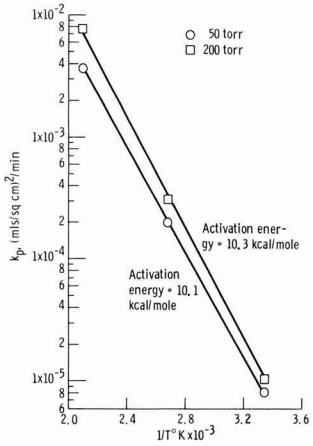

Fig. 10. Effect of temperature on rate constant in the diffusion controlled region.

Summary

The experimental results presented in this paper point to the fact that the reaction between fluorine and silver is a complex reaction, and the kinetics are not simple. In a study of this type it is the over-all rate that is determined, and no attempt was made to determine individual specific rates.

Manuscript submitted Feb. 9, 1970; revised manuscript received *ca.* June 15, 1970. This was Paper 408 presented at the Montreal Meeting of the Society, Oct. 6-11, 1968.

Any discussion of this paper will appear in a Discussion Section to be published in the June 1971 JOURNAL.

REFERENCES

1. P. E. Brown, J. M. Crabtree, and J. F. Duncan, *J. Inorg. Nucl. Chem.*, **1**, 202 (1955).
2. P. M. O'Donnell and A. Spakowski, *This Journal*, **111**, 633 (1964).
3. P. M. O'Donnell and A. Spakowski, NASA TN D-768, 1961.
4. R. K. Steunenberg, L. Seiden, and H. E. Griffin, Chemical Engineering Div. Summary Report for July, August, September 1958, Rep. ANL 5924 Argonne National Lab., pp. 42-43.
5. M. J. Steindler and D. V. Steidl, Chemical Engineering Div. Summary Report, January, February, March 1959, Rep. ANL 5996, Argonne National Lab., June 1959, pp. 135-139.
6. P. M. O'Donnell, *This Journal*, **114**, 218 (1967).
7. Iwasaki *et al.*, *Kogyo Kagakw Zassi.*, **65**, 1165 (1962).
8. A. K. Kuriakose and J. L. Margrave, *J. Phys. Chem.*, **68**, 2671 (1964).
9. A. K. Kuriakose and J. L. Margrave, *ibid.*, **68**, 2671 (1964).
10. P. M. O'Donnell, *This Journal*, **114**, 1206 (1967).
11. M. J. Steindler, D. V. Steidl, and R. K. Steunenberg, Chemical Engineering Div. Report, June 1958, Rep. ANL 5875 Argonne National Lab., June 1958.
12. R. K. Steunenberg and J. Fisher, Chemical Engineering Div. Summary Report, January, February, and March 1959, Rep. ANL 5996 Argonne National Lab., June 1959, pp. 134-135.
13. A. K. Kuriakose and J. L. Margrave, *J. Phys. Chem.*, **68**, 290 (1964).
14. A. K. Kuriakose and J. L. Margrave, *J. Phys.* Chem., **68**, 2343 (1964).
15. R. L. Ritter and H. A. Smith, *ibid.*, **71**, 2036 (1967).
16. Gerard Vandenbussche, Rep. CEA-R-2859 Centre d'Etudes Nucleaires, Dec. 17, 1964.
17. Von Otto Ruff and Manfred Giese, *Z. fur anorg. u. allgem. chem.*, **219**, 143 (1934).

Effect of Sealing Variables on the Degree-of-Seal

G. A. Dorsey, Jr.

Kaiser Aluminum & Chemical Corporation, Center for Technology, Pleasanton, California 94566

ABSTRACT

At least three separate effects occur during sealing (*a*) gross water adsorption by the bulk and surface of the porous layer, probably also accompanied by anion loss (as in the case of H_2SO_4-anodized films), (*b*) an oxide transition near the barrier-porous layer interface, which results in a net decrease in the amount of barrier layer and a net increase in the amount of porous layer cross-linking, and (*c*) a seemingly thin-layer effect that takes place with aging and may be localized in the pore base region of the porous layer. A two-step current density program was used to prepare 7.4-7.6 μm (0.3 mil) anodic films on alloy 1100, using a 1.7M H_2SO_4 electrolyte at 25°C. These coatings were then sealed for from 10 to 65 min, at temperatures from 65° to 95°C, in weakly buffered sealing baths whose *p*H was adjusted within the region of 5.0 to 6.5. Corresponding films were also left in the unsealed condition. Data for these films were obtained using 1 kHz impedance measurement of coating permeability, effluent gas detection (EGD technique) of partial water contents, and infrared determinations of coating structures. For these 7.4-7.6 μm (0.3 mil) coatings, the greatest benefit was derived with the following sealing conditions: sealing *p*H range, 6.15 ± 0.15; seal time, 30 min, but not more than 40; sealing temperature, 95°C-to-boiling, or higher, as might be achieved by pressurized steam sealing.

References (1) and (2) describe the "inner seal" effect and point out its potential importance in the over-all mechanism of sealing. This involves a structural transition that appears to take place, as a result of sealing, near the interfacial region between the secondary phase barrier layer and the anodic oxide porous layer. It seemingly is an hydration effect that has the nature of a structural hydrate rearrangement, the net result being a forming together (or agglomeration) of oxide at the base of the individual alumina fibrils that comprise the porous layer. This is apart from surface hydration changes and anion loss that occur elsewhere in the porous layer oxide.

Earlier work dealt with the "effect" itself, and not with factors introduced by changes in sealing variables. Only one set of sealing conditions was employed for this: *p*H 6.0 boiling water, with a seal time of 10 min. Now we seek to determine the varying results that are brought about by employing different sealing temperatures, seal times, and *p*H values.

This sealing effect was limited to only thin films (~2 μm) when conventional anodizing conditions were employed (2): 1.3 A/dm², 1.7M H_2SO_4 and 25°C. However, the same effect could be achieved with three-fold thicker films (7.4 μm) when the proper oxide transition structure was obtained with a two-step anodizing current density program (2) in this same electrolyte. An initial current density of 1.3 A/dm² was used to develop a near-optimum oxide structure. This structure was then "frozen" by a higher current density (3.5 A/dm²) that allowed the film to thicken normally while nevertheless maintaining the oxide structure characteristic of the thinner ~2 μm film. In this manner, at least for ~7 μm (0.3 mil) films, the inner seal effect could be realized independent of actual film thickness.

However, this sealing transition, or inner seal effect, is undoubtedly sensitive to changes in sealing variables, although in this regard it should be no different from films prepared by more common practice. High-temperature sealing conditions may rapidly create surface blockage that could close off otherwise reactive sites, or the effect that we describe could be a slow reaction and relatively independent of surface effects: dependent only on temperature, in a nondehydrating environment. Additional boiling water seal times might be required, beyond the 15-min time period normally employed with ~7 μm films, in order to realize the completion of a slow reaction. There is, too, the potential effect of sealing *p*H, which may also be a factor if the mechanism of this transition involves hydrogen or hydroxyl ion from the sealing medium.

Key words: anodic aluminas, sealing.

Experimental

Sample preparation.—Alloy AS32 (alloy 1100 clad with 1100: 99.2% Al) sheet coupons were cleaned and chemically brightened, then anodized in 1.7M H_2SO_4 at 25°C. The initial current density of 1.3 A/dm² was maintained for the first 4.84 x 10^2 coulombs/dm² of current quantity (6.25 min at 1.3 A/dm²), then the current density was immediately raised to 3.46 A/dm² and maintained at that level for the balance of the anodizing period. The total current quantity expended was 13.9 x 10^2 coulombs/dm², equivalent to a 7.4 μm film thickness.

The various seals were prepared from distilled water containing 5 x 10^{-6}M acetic acid as a buffering additive and were adjusted to the desired *p*H with sodium hydroxide. The *p*H value was measured at the temperature selected for operation of the seal. Four *p*H values were employed: 5.0, 5.5, 6.0, and 6.5. Sealing temperatures were 65°, 75°, 85°, and 95°C. Sealing times ranged from (*a*) unsealed, to (*b*) 10, 20, 30, 50, and 65 min. Impedance and EGD values were determined immediately, and the same coupons were then re-examined periodically over storage periods of up to 100 days, stored in a clean environment, at ambient room humidity. Infrared data were obtained after an approximate 30-day storage period following sample preparation.

Test methods.—Effluent gas detection (EGD) data were obtained as before (3). The anodized sample was placed in a leak-tight chamber within the oven of a gas chromatograph, then continuously purged with helium which passed on to a thermal conductivity detector. The chamber was heated from ambient temperature to 350°C, at a rate slightly less than 10°C/min (3). As volatile materials, in this case, water, are evolved from the sample, the water-bearing helium effluent is carried on to the detector which then provides a continuous plot of evolved water *vs.* temperature. The result is exactly the same as a thermobalance operated in differential mode, but provides far more sensitivity.

Impedance values were measured with a 1 kHz impedance bridge (Twin City Testing Corporation's Z-Scope), using a 3.5 w/o NaCl media. The data re-

ported are average values taken from multiple readings with each anodized coupon. Infrared spectra were obtained within the 4000-35 cm^{-1} ranges of the Beckman IR-7 and IR-11 spectrophotometers, according to procedures already described (4).

Results and Discussion

Effluent gas detection (EGD).—A limitation of this technique is its failure to allow for baking temperatures above 350°C, which is usually insufficient to allow complete dehydration of most types of anodic coatings. Nevertheless, it has been shown (1-3) that the partial water content, measured by the lower-temperature EGD method, has value. This fraction of the films' total water content apparently corresponds directly with that portion of the oxide that is altered by the barrier layer sealing transition; EGD data are seemingly a reliable indicator for the degree of completion of the inner seal effect. The partial water measured by the EGD technique is independent of total porous layer oxide thickness and is independent of total water content, with neither of these two factors directly influencing the inner seal effect. The EGD data provide isolated data pertaining only to the inner seal effect itself and, when coupled with data sensitive to other changes within the coating structure, should provide a clearer picture of over-all sealing mechanisms.

The EGD technique proved not to be sensitive to effects related to the aging of sealed coatings (Fig. 1), and these sealed films were therefore stored, for convenience, prior to EGD measurement. Unsealed films are, however, affected by aging (Fig. 1), and subsequent coatings were tested immediately after air drying. Figures 2 through 5 show these EGD data plotted *vs.* sealing time, and including the effects of different sealing *p*H and temperatures. These curves

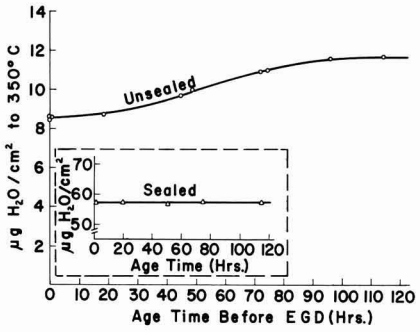

Fig. 1. Effect of aging on partial water content (EGD) of sealed and unsealed coatings.

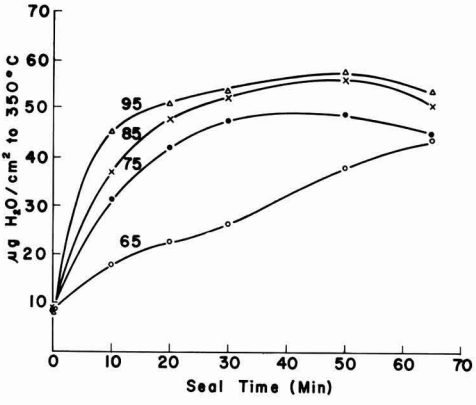

Fig. 2. Partial water content (EGD) of coatings sealed at *p*H 5.0; tie line notation gives seal temperature: °C.

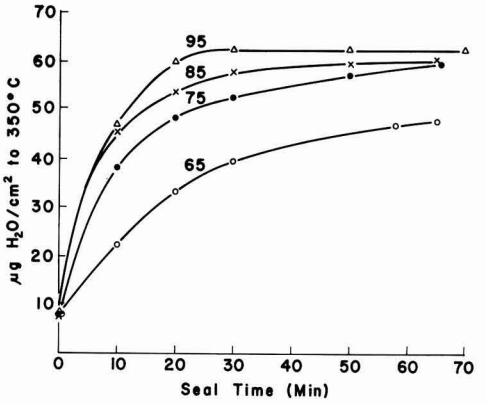

Fig. 3. Partial water content (EGD) of coatings sealed at *p*H 5.5; tie line notation gives seal temperature: °C.

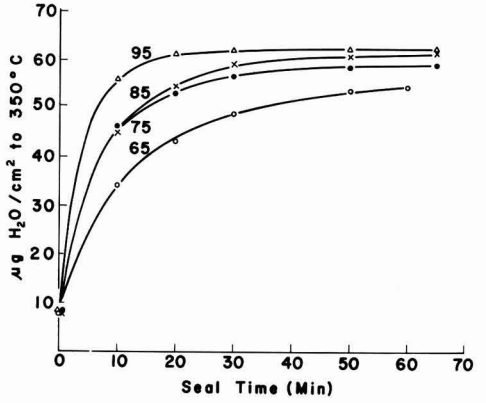

Fig. 4. Partial water content (EGD) of coatings sealed at *p*H 6.0; tie line notation gives seal temperature: °C.

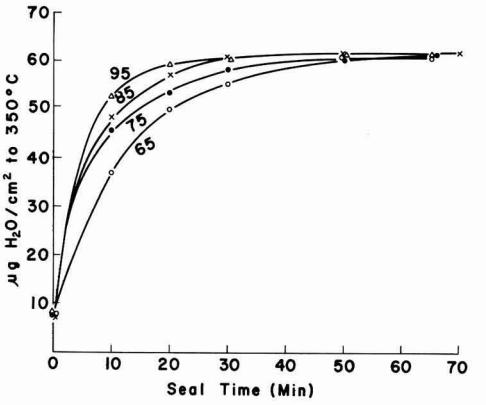

Fig. 5. Partial water content (EGD) of coatings sealed at *p*H 6.5; tie line notation gives sealed temperature: °C.

are symmetrical except for the low-*p*H seal data (Fig. 2, *p*H 5.0) which show what might be regarded as a solubility effect, with prolonged seal times, that becomes more pronounced as sealing temperature is increased toward boiling. This would indicate that, except for *p*H 5.0 seals, the apparent solubility effects did not penetrate down to that portion of the oxide that is responsible for the EGD data, the barrier-porous layer interface.

Figures 3-5 show (with seals at pH 5.5 or higher) a plateau or maximum endpoint in the sealing reaction. Beyond this point, further sealing times had no effect. This maximum value (63 μg H_2O/cm^2) represents the apparent completion of the sealing reaction, at least so far as the inner seal is concerned.

Earlier (4) the inner seal effect was proposed to be a structural conversion of pre-existing aluminum hydroxide. It was proposed that the secondary phase barrier layer hydroxide converted into a lower polymer form of hydroxide that was incorporated into the porous layer at the base of its individual alumina fibrils. If such was the case here, there should be a plateau or maximum endpoint in the sealing reaction, since all oxide (secondary phase barrier layer) available for this transition would have been converted. If the EGD technique is sensitive only to the quantity of this transformed oxide and not to other sealing reactions such as gross water content, then these data should show (as is seen in the data, Fig. 3-5) a maximum value that remains unchanged by further sealing.

With freshly anodized unsealed films, the 1 kHz a-c impedance correlates with the primary phase barrier layer thickness, giving the following relationship: 14.2 Å/kohm/cm^2 impedance. This places the average primary phase barrier layer thickness for these coatings at 180Å. Similarly, using earlier *IR* data (2, 5), and the current *IR* data to be discussed later, the average unsealed (initial) secondary phase barrier layer thickness may be calculated as 1.12 x 10^4Å. Using densities of 2.7 and 2.4 g/cm^3 for these oxides, respectively, complete dehydration to the monohydrate should release, at most, a quantity of water corresponding to 23% of the initial oxide weight. This would be 63 μg H_2O/cm^2, exactly the value of the plateau (endpoint) region shown in Fig. 3-5. Assuming, still speculatively, an initial trihydrate composition for the unsealed secondary phase barrier layer, and assuming that the plateau maximum value corresponds to an endpoint in the depolymerization reaction for this oxide, as one result of sealing, then the following interpretation can be made:

(*A*) Initially and before sealing, the EGD technique detects only a small fraction of the trihydrate water that is actually present in this oxide sublayer: about 10%.

(*B*) After a short but inadequate seal time, some of this trihydrate has undergone the depolymerization transformation. While its composition remains unchanged, the partial transformation increases the percentage of water driven off from this oxide by the temperature-limited EGD technique.

(*C*) Correspondingly more water is detectable *via* EGD as more of the oxide is converted by further sealing. Eventually, sealing consumes all of the oxide that is available for transformation. Beyond this point, the EGD data show no further increase in apparent water content as a result of further sealing. A maximum-value plateau has been reached.

(*D*) While the initial EGD data show only about 10% of theoretical water content for unsealed samples, this percentage increases as the degree of sealing becomes complete. Samples that have reached the maximum value plateau region should release (via EGD) an amount of water corresponding to 2 moles of water for each mole of sublayer oxide.

This does not mean that this particular water has been gained as a result of sealing. It may already have been present but needed the impetus of sealing to transform the oxide structure into one that dehydrates more readily: into an oxide that dehydrates under the low-temperature conditions (to 350°C) of the EGD technique.

Similar plots (unpublished) of water released *vs.* sealing pH for varying seal times at 95°C show a maximum value that appears to lie near pH 6.0. The 10-min seal data show this more clearly, since data in the plateau region mask out the effect of pH. The transformation, once complete, is unaltered by changes in seal pH (except for what might be solubility effects near pH 5.0). While sealing is ordinarily carried out in the pH range of 5.5 to 6.5 (6), there may be more advantage to sealing near pH 6.0. This is consistent with Bogoyavlenskii and Belov (7) and may also be seen with impedance data to be discussed shortly.

An attempt at kinetic data, using Van't Hoff's differential method, provides another tool for the interpretation of these data. Ordinarily, such data are obtained by measuring the decrease in reactant concentration as a function of time, with varying initial reactant concentrations. Where c_1 and c_2 denote two different initial concentrations and where n denotes the apparent order of the reaction with k being the rate constant, or specific reaction rate, then

$$-dc_1/dt = kc_1^n$$

and

$$-dc_2/dt = kc_2^n$$

and

$$n = \frac{\log(-dc_1/dt) - \log(-dc_2/dt)}{\log c_1 - \log c_2}$$

A plot of log $(-dc_1/dt)$ *vs.* log c, will be linear and the slope will be the apparent order of reaction, n, if the reaction proceeds without complication. Extraneous features in the reaction will, on the other hand, yield a curved plot to indicate that the reaction proceeds without a simple order.

Sealing eventually produced the same maximum-value plateau (end point) in the EGD data: 63.4 μg H_2O/cm^2, a value which remained unchanged with further seal times. Unsealed samples, prepared in an identical fashion, also gave a constant EGD value of 8.54 μg H_2O/cm^2. Therefore we assumed that the amount of alumina being transformed, on sealing, was equivalent to the difference between these two values, or 54.9 μg H_2O/cm^2. This value serves as "initial reactant" for the Van't Hoff concentration term "c". After, for example, a 10-min seal at pH 5.5, the EGD technique detected 22.8 μg H_2O/cm^2 indicating a "reactant" concentration equivalent to 40.6 μg H_2O/cm^2 remaining. Then one point on the plot would be represented by log $(-dc_1/dt)$ = log (54.9-40.6/10), with log c_1 = log (54.9). Similar calculations led to the values that are plotted in Fig. 6 through 8; calculations were prevented for the pH 5.0 data, because of what appear as solubility effects (Fig. 2) in this low pH seal.

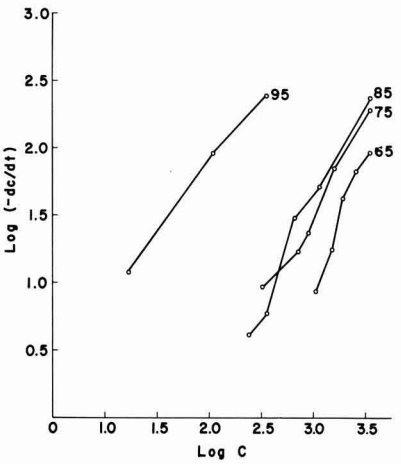

Fig. 6. Kinetic data for coatings sealed at pH 5.5, with tie line notation giving seal temperature: °C. The apparent reaction order was, at 65°C, 1.7; at 75°C, 1.4; at 85°C, 1.5 and, at 95°C, 1.0.

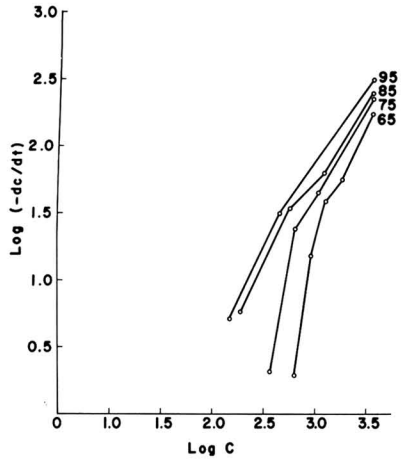

Fig. 7. Kinetic data for coatings sealed at pH 6.0, with tie line notation giving seal temperature: °C. The apparent reaction order was, at 65°C, 2.0; at 75°C, 1.8; at 85°C, 1.2 and, at 95°C, 1.2.

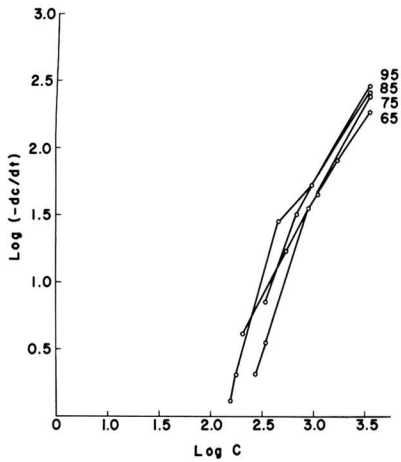

Fig. 8. Kinetic data for coatings sealed at pH 6.5, with tie line notation giving seal temperature: °C. The apparent reaction order was, at 65°C, 1.3; at 75°C, 1.7; at 85°C, 1.5 and, at 95°C, 1.5.

The apparent order of the sealing reaction was generally greatest (as high as $n = 2$) for the low temperature (65°C) seals. The reaction order approached unity as the seal temperature increased. This could be interpreted in at least two different manners

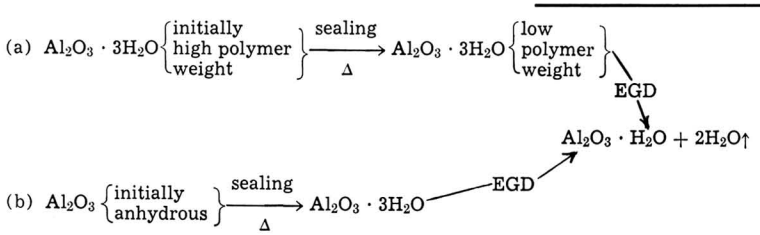

However, as seen in Fig. 6-8, the plots of log ($-dc/dt$) *vs.* log c are more nearly linear only for the 95°C sealing conditions. This implies the possibility that, at least at lower sealing temperatures, the EGD dehydration reaction proceeds with complexity: that the dehydration reaction (*via* EGD technique) has some complicating feature. This would tend to favor sealing reaction (a), which employs a depolymerization reaction on sealing rather than simple water sorption. That portion of the hydrated alumina which is detected by the low-temperature EGD technique then appears to be hydrated before sealing, and releases progressively more water (on baking via EGD) as its structural cross-linking is progressively lowered by sealing. Eventually, sealing lowers this cross-linking to a minimum value that (with the EGD technique) releases a stoichiometric amount of water, as did the mineralogical trihydrates gibbsite and bayerite (8). Further, the data show that after this point sealing produces no further change in the amount of water released (with EGD baking) by the coating. Such behavior is consistent with earlier *IR* data (1, 2, 4) which served as the basis for describing this same sealing effect. When this, the inner seal effect, is complete, the apparent order of the reaction is near unity.

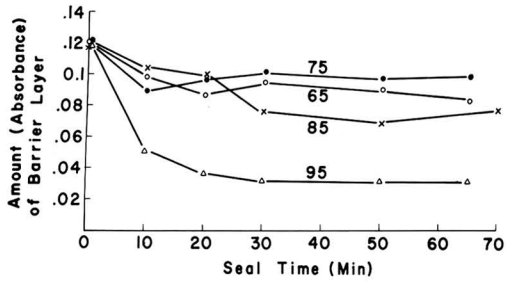

Fig. 9. Infrared absorbance (amount) of barrier layer for coatings sealed at pH 6.5; tie line notation gives seal temperature: °C.

Intermediate and far infrared analyses.—Ordinarily, *IR* data show much better precision than was obtained here. Since this poor interrelationship shows only for sealed coatings, and not for unsealed samples, it seems likely that these samples should have been analyzed immediately after preparation. As it was, they were stored at random for approximately 30 days prior to analysis. In any event, the observable trends are still valid, but what might be poor structural reproducibility (for sealed samples) makes quantitative interpretation difficult.

Figure 9 shows the amount of barrier layer plotted *vs.* sealing time. These data include each of the various sealing temperatures at pH 6.5 and are representative of the entire group. Initially, each coating (unsealed) had the same amount of barrier layer: total amount of barrier layer being comprised of both primary and secondary barrier layer phases. After sealing, the amount of barrier layer decreased due to the secondary barrier-to-porous layer conversion. At pH 5.0 the extent of this conversion was less at 65°C than at 75°C; the 85°C and 95°C data show approximately equal conversion and at about the same rates. Similar data obtained at pH 6.5 (Fig. 9) show a better differentiation between 85°C and 95°C data: the 95°C seal

causing the greater degree of transformation. At a given temperature, the pH 6.5 seal gave a greater degree of barrier-to-porous transformation than did the pH 5.0 seal.

Figure 10 shows the amount of porous layer cross-linking plotted *vs.* sealing time for each sealing temperature and at pH 6.5. Before being sealed, each coating had about the same amount of porous layer cross-linking. After sealing, this amount varied greatly depending on seal time, pH, and temperature. However, just as the amount of barrier layer always decreased on sealing, due to the secondary barrier-to-porous layer transformation, the amount of porous layer cross-linking always increased on sealing.

Figure 10 also shows the generally adverse effects of too prolonged a sealing time, although this decrease in cross-linking was usually more pronounced for the 95°C seals. These data show that maximum sealing benefit is obtained near a sealing time of 30 min. Sealing at a lower temperature tended to retard the apparently detrimental effect due to oversealing, but lower temperatures also gave lesser amounts of porous layer cross-linking. These porous layer data are, of course, not specific for changes that occur near the barrier-porous interface, but would include cross-linking changes in the bulk of the porous layer as well. While these data show the advantages of 95°C and 30-min sealing conditions (as did the EGD data) there is still reason to suggest that still higher seal temperatures would further accelerate the sealing process, perhaps a pressurized steam seal at 150°C, with condensate pH controlled.

Impedance.—Figure 11 shows the initial impedance values plotted *vs.* sealing time and temperature at a sealing pH of 5.5. These values were obtained immediately after air-drying the coatings and before any storage period. At 95°C (and regardless of seal pH) the impedance increased almost linearly with seal times of up to 30 min. After 35 min, the rate of impedance change lessened to form a plateau beyond which the impedance change (with further seal time) was comparatively slight. This point (~38 kohms/cm^2 impedance) would correspond to the total impermeability of this oxide and would reflect changes taking place both in the barrier layer region of the film and elsewhere in the porous layer, and also at the oxide surface (9, 10).

At progressively lower sealing temperatures, there appeared to be an initial period during which minimal impedance change took place. Afterward, the impedance increased quickly. The time span of this initial period was greatest at low temperatures but showed no obvious dependence on pH. This is seemingly indicative of a temperature-dependent reaction rate, consistent with the "inner seal effect" mechanism described earlier. A plot of log impedance *vs.* sealing temperature is essentially linear for most of these data.

Figure 12 shows the effect of sealing pH on impedance levels. For each sealing time period, the impedance increased as the seal pH increased toward pH 6.0, then decreased beyond that. Extrapolation would seem to indicate that optimum results (highest impedance) were obtained at pH 6.15 ± 0.15.

Aging also alters (increases) the 1 kHz a-c impedance of sealed films but, as seen in Fig. 13, aging produces little change in unsealed films. The same figure also shows data for marginally sealed films: films sealed at pH 5.0 and 65°C, also showing only a minor increase in impedance with aging. In contrast, films sealed at the same pH (pH 5.0) but at 95°C and for 30 min, showed a pronounced change in impedance value on aging. Figure 14 shows other such data for these sealing temperatures at pH 6.0 with 30-min sealing time.

Generally and exclusive of unsealed and marginally sealed films, impedance values increased most rapidly during the first 5 days of aging. The impedance increase, with aging, then lessened but continued until the film had aged ~30 days. Afterward, comparatively little or no further change in impedance took place. There are also the following additional observations that may be made for the generalized effect of aging on sealed films.

1. Aging prior to exposure has no recognized, or at least reproducible, effect on the results of outdoor service testing of sealed films.

2. Similarly, aging does not alter the results of aggressive laboratory-accelerated corrosion tests: pitting corrosion tests such as CASS, or acid solubility tests such as Kape (sulfurous acid solubility).

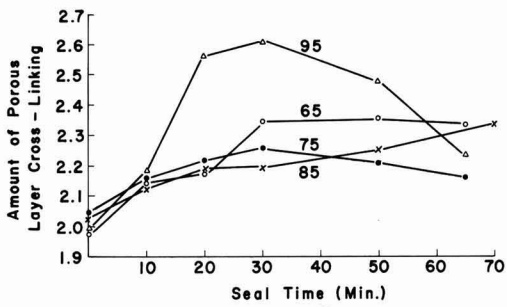

Fig. 10. Amount of porous layer cross-linking *(IR)* for coatings sealed at pH 6.5; tie line notation gives seal temperature: °C.

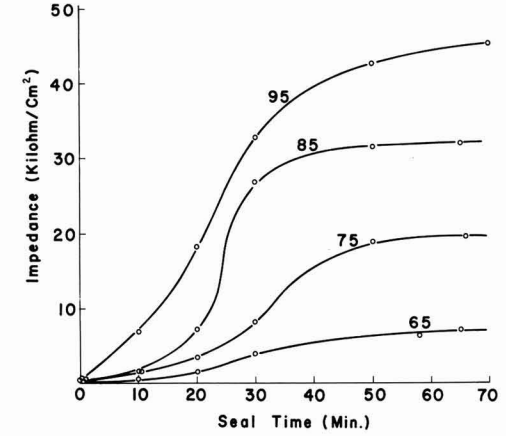

Fig. 11. Initial impedance values for coatings sealed at pH 5.5, with the tie line notation giving seal temperature: °C.

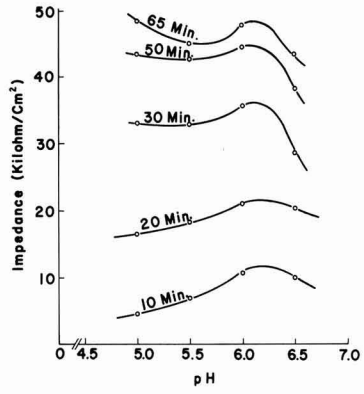

Fig. 12. Initial impedance values for coatings sealed at 95°C, with the tie line notation giving sealing times: minutes.

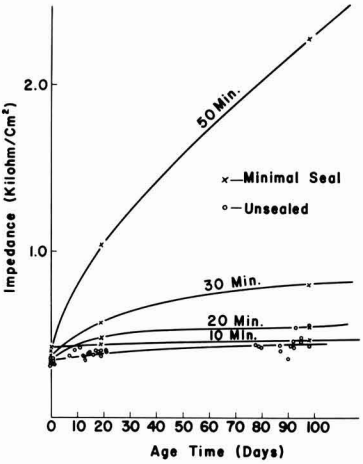

Fig. 13. Effect of aging on impedance values for (a) unsealed coatings and for coatings marginally sealed, at *p*H 5.0 and 65°C, by immersion for: (b) 10 min, (c) 20 min, (d) 30 min, and (e) 50 min.

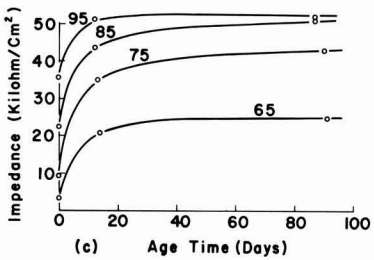

Fig. 14. Effect of aging on impedance values for coatings sealed at *p*H 6.0 for 30 min.

3. Aging (with sealed films only, not the case with unsealed films) does not alter the EGD test results, which would detect changes related to the barrier layer sealing transition, or inner seal effect.

4. Aging does alter (increase) the results of tests that are surface sensitive. The FACT test (dielectric breakdown in an acidic copper-containing electrolyte) is one such example (9).

5. While aging doubles the impedance value of sealed films, this effect may be virtually eliminated (and the impedance restored to approximately the initial value) by a brief exposure to a mildly aggressive environment (10). A few seconds in boiling distilled water, or immersion in room temperature dilute acid, will suffice.

It seems reasonable, therefore, to suggest that aging is a short-ordered effect that is of little consequence, when the anodic film is placed in a mildly aggressive environment where it is rapidly degraded. The effect of aging might be speculated to be equivalent to the formation of a thin film, from agglomerate particles. If such a filmlike thin layer were at the outer surface

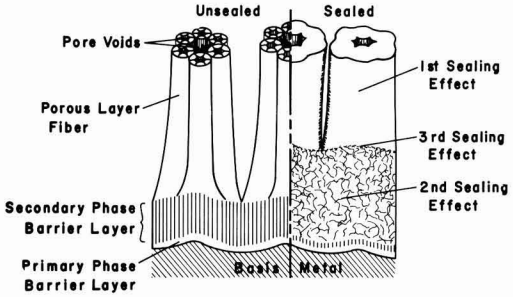

Fig. 15. Illustration of proposed sealing effects: 1st sealing effect [according to Wood *et al.* (11, 12)]: A pore closure mechanism that probably does not alter gross pore (large central pore) diameter to point of closure. Pores that are affected are micropore channels or permeable sites that lie within the fiber itself. 2nd sealing effect: An oxide transition, from barrier into porous layer oxide that results in a relatively impermeable gel formation at the base of the porous layer. 3rd sealing effect: A short-ordered thin film effect of glazing at the surface of the porous coating gel layer.

of the anodic coating, however, impedance values would likely have been increased far more than was observed; no more than a twofold increase was found on aging. By contrast, a thin oil layer at the outer coating suface raises impedance beyond the range of our instrument. Thus, instead of a surface condition, it seems reasonable to suggest that the aging effect might represent a coalescence of fibrils at the base of the porous layer, equivalent to a film at the surface of any agglomerate particles created by the inner seal effect.

A summary illustration of these sealing effects is shown in Fig. 15.

Acknowledgment

The author wishes to thank the Kaiser Aluminum & Chemical Corporation for its support of this work and for its permission to publish these results.

Manuscript submitted March 11, 1970; revised manuscript received June 2, 1970.

Any discussion of this paper will appear in a Discussion Section to be published in the June 1971 JOURNAL.

REFERENCES

1. G. A. Dorsey, Jr., *This Journal*, **117**, 1276 (1970).
2. G. A. Dorsey, Jr., *ibid.*, **117**, 1181 (1970).
3. G. A. Dorsey, Jr., *ibid.*, **115**, 1057 (1968).
4. G. A. Dorsey, Jr., *ibid.*, **115**, 1053 (1968).
5. G. A. Dorsey, Jr., *ibid.*, **116**, 466 (1969).
6. C. J. Amore and J. F. Murphy, *Metal Finishing*, **63**, 50 (1965).
7. A. F. Boguyavlenskii and V. T. Belov, *J. Appl. Chem. USSR*, **39**, 2221 (1966); UDC 620.197: 541. 183.24: 539.163.
8. G. A. Dorsey, Jr., *Anal. Chem.*, **41**, 350 (1969).
9. R. C. Spooner, *Metal Finishing*, **67**, 80 (1969).
10. E. G. Englehart and D. J. George, *Materials Protection*, **3**, 24 (1964).
11. J. P. O'Sullivan, J. A. Hockey, and G. C. Wood, *Trans. Faraday Soc.*, **65**, 535 (1969).
12. G. C. Wood and J. P. O'Sullivan, *This Journal*, **116**, 1351 (1969).

Side Reactions during the Anodization of Aluminum in a Glycol Borate Electrolyte

Robert W. Santway and Robert S. Alwitt*

Sprague Electric Company, Research and Development Laboratories, North Adams, Massachusetts 01247

ABSTRACT

A study of the anodization of aluminum in a glycol borate electrolyte at voltages sufficiently high for side reactions to occur, but below the sparking voltage, showed that the formation of barrier oxide was accompanied by solvent oxidation, aluminum dissolution, and production of a thick oxide that grew in cracks of the barrier film. Surprisingly, the presence of the crack network has little effect on electrical properties. It is believed that side reactions initiate at flaws in the barrier oxide.

In suitable electrolytes, anodic oxide films can be grown on metals such as aluminum or tantalum at 100% current efficiency. For an anodization at constant current a film thickness is finally reached, characteristic of each system, above which current is consumed in other anodic reactions and the rate of film growth decreases. Continued passage of current may ultimately result in sparking (scintillation) over the anode surface.

Some observations on the sparking process have been presented recently (1), but it is still not a well understood phenomenon. Little information appears to have been published on the processes preceding sparking (2). This region is of practical importance to the operation of electrolytic capacitors since the onset of side reactions limits the maximum voltage of these devices. In this paper we report our observations of the secondary reactions that occur at an aluminum anode in a glycol borate electrolyte. The nature of the reactions and their effect on surface morphology and electrical characteristics are considered.

This type of electrolyte was chosen for several reasons. It is typical of systems used in electrolytic capacitors. Oxide can be formed at 100% current efficiency and contains little incorporated matter from the electrolyte (3). For some electrolyte compositions there is a wide voltage range in which side reactions can be studied prior to the onset of sparking. A disadvantage of using this electrolyte is that the chemical species in solution are not well defined. Borates react with glycol to produce coordination compounds, esters, and water (4).

Experimental

Anodizations were performed in an electrolyte of 17.2 w/o (weight per cent) ammonium pentaborate ($NH_4B_5O_8 \cdot 4H_2O$) in ethylene glycol (17% APB-EG). High-purity (99.97%) aluminum foil and wire were used as anodes. These were prepared by chemical polishing in a HNO_3-H_3PO_4 mixture (15 ml of 70% HNO_3, 85 ml of 85% H_3PO_4) for 2 min at 85°C, followed by a 10-min etch in 1M NaOH at room temperature. Anodization was at room temperature at constant current densities in the range 0.1-1.2 mA/cm^2.

Series capacitance and RC of anodized foils were measured at several frequencies using a conventional resistance ratio arm bridge with an a-c signal less than 100 mV. Measurements were against platinized electrodes in either aqueous 0.8M H_3BO_3 with sufficient NH_4OH added to give a resistivity of about 225 ohm-cm, or aqueous ammonium formate with a resistivity of 10 ohm-cm (*ca.* 2*N*).

In some experiments gas generated at the anode was collected and analyzed in a dual column, programmed temperature gas chromatograph, using a molecular sieve column. Aluminum in solution was measured using a previously established photometric procedure (5).

Results and Discussion

Description of side reactions.—A typical voltage-time recorder trace is shown in Fig. 1. The voltage at which dV/dt started to decrease was little affected by current density. For example, in one experiment it was about 247V at 1.0 mA/cm^2 and increased to 260V when the current density was dropped to 0.10 mA/cm^2. Weight measurements showed that during the initial voltage rise all the charge can be accounted for by production of an anodic Al_2O_3 film. In the region of reduced dV/dt the following events were observed:

1. Sharp decreases in voltage accompanied by equally rapid return. The frequency and intensity of these excursions increased as the voltage increased.
2. Gas bubbles were evolved at points on the anode surface.
3. Weight measurements showed that anodic oxide was produced at less than 100% efficiency.
4. The anode surface appeared blemished. At low magnification it was seen that the oxide had cracked,

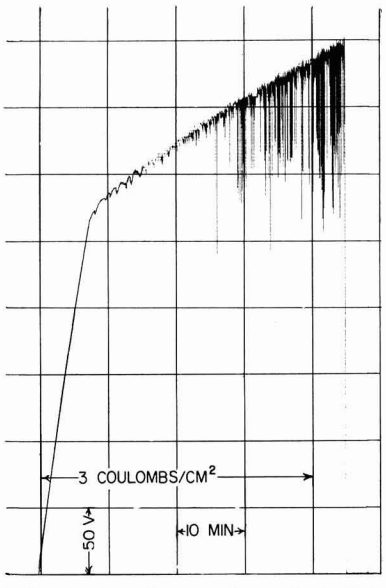

Fig. 1. Typical voltage-time trace for anodization in 17% APB-EG at 1.24 mA/cm^2.

* Electrochemical Society Active Member.

Key words: anodic oxides, aluminum, breakdown, electrolytic capacitors.

and in the cracks had grown a new solid many times thicker than the barrier film.

5. Analysis of the electrolyte showed the presence of dissolved aluminum.

6. The solution turned yellow and eventually sparking took place at about 450V.

These observations will now be described in more detail.

Gas evolution.—In a typical experiment, a current density of 0.33 mA/cm^2 applied overnight resulted in the production of a volume of gas equivalent to 0.013 ml/coulomb. Gas collection was halted prior to the onset of sparking. Analysis of the gaseous products from two experiments gave an average composition of 40% CO, 10% CO_2, and 50% H_2. The carbon monoxide and carbon dioxide must have been the products of glycol oxidation. The hydrogen did not come from the cathode compartment but was a true anode product. Since it could not be produced electrochemically at the anode, the hydrogen most likely was the result of some subsequent chemical reactions at the anode.

Cracks and new oxide growth.—Cracks in the oxide started at apparently random points on the surface and then spread in a network pattern. In Fig. 2a and 2b an early and a later state of crack development are illustrated. Examination of a number of specimens showed that in general crack initiation is not associated with grain boundaries of the substrate metal (6). Even after prolonged anodization the cracks never covered more than a few per cent of the surface.

The cracks were filled with a white solid many times thicker than the surrounding barrier oxide film. In the metal substrate was found a pattern of deep grooves identical to that of the cracks, suggesting that the new phase extended below, as well as above, the level of the original barrier film. The cracks were bounded by what appeared to be small tight cylinders of curled barrier film. The light outline of the empty cracks in Fig. 2c is believed to be an optical effect of this curled film.

No positive identification of the new solid material could be made. It was white, translucent, and gave no x-ray diffraction pattern. It was not soluble in some common organic solvents and heating for 2 hr at 900°C produced no change in appearance. We believe it to be an aluminum oxide. Perhaps it is similar to the material observed on aluminum after prolonged exposure to this 17% APB-EG electrolyte at high temperature (5).

An important observation was that during anodization gas bubbles were produced only at the tips of cracks. This indicates that the new oxide material was not a good electronic conductor, and that it maintained intimate contact with barrier film along the length of the cracks. It suggests that the secondary reactions took place only at the growing tip of a crack, a potentially complex region in which four phases could be in contact, viz., metal, barrier film, new oxide, and electrolyte.

Some of these observations are similar to those made by Vermilyea on the field crystallization of amorphous anodic Ta_2O_5 films (7). In that case, under the influence of a strong electric field, crystalline Ta_2O_5 nucleated at the metal/film interface, broke through the barrier film, and spread over the surface as irregular polygons until the amorphous film was completely replaced.

Dissolved aluminum.—During anodization up to about 250V no significant amount of aluminum was detected in solution. Coincident with a decreased dV/dt and the onset of gas evolution, the aluminum concentration began to increase uniformly with time. For a specimen that was anodized at 1.24 mA/cm^2, dissolved aluminum accounted for 10% of the charge passed following the onset of secondary reactions.

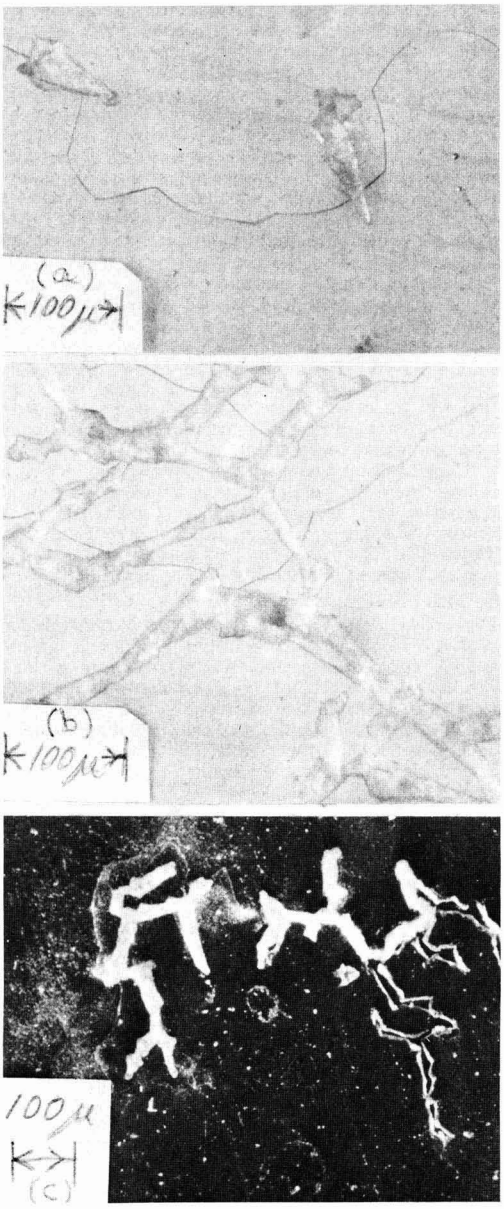

Fig. 2. Micrographs of Al foil anodized in 17% APB-EG at 0.27 mA/cm^2 to 320V. (a) Early state of crack development; (b) later state; (c) transmitted light through isolated oxide. Dark background is barrier film, white network is new oxide. Outlined pattern on right resulted from loss of new oxide during handling.

Distribution of aluminum oxidation reactions.—The amount of charge consumed in each of the aluminum oxidation processes (barrier film formation, new oxide growth, and metal dissolution) was estimated from measurements made on specimens anodized at 1.24 mA/cm^2. A typical voltage-time curve is shown in Fig. 1. The charge passed during the initial period of 100% barrier film production and the sample weight at the end of this period were measured. After further anodization the specimens were again weighed

and finally the weight was obtained after stripping oxide in H_3PO_4-CrO_3 solution. Oxide stripping was done in two stages, an initial room temperature immersion followed by one at 85°C. The new oxide was removed much more rapidly than the barrier film and the two materials could be easily distinguished at room temperature during a series of successive stripping measurements. The remaining barrier film was removed at 85°C. The weight of aluminum consumed in all oxidation reactions was determined as the difference between the specimen weight after stripping and the weight of base metal at the onset of side reactions. This latter figure was obtained by subtracting from the specimen weight at that point the calculated weight of anodic oxide produced at 100% efficiency.

The results are listed in Table I. The charge consumed in aluminum dissolution was taken as the difference between that calculated for metal consumption and that used in oxide formation. For the purpose of calculating charge consumption the thick oxide was assumed to be Al_2O_3.

It appears that these measurements were made in a region where the barrier film continued to thicken at a steady though reduced rate. This is indicated by the constant fraction of charge used for film formation. The weight of the new oxide was only about 4% of the total barrier film weight. The fraction of the surface covered by this material would be even smaller.

Other reactions.—The details of the glycol oxidation reactions resulting in CO and CO_2 production are not known, but the maximum charge consumed in these reactions was estimated by assuming that no more than three electrons were transferred per mole of CO and five electrons per mole of CO_2. From the volume and composition of gas collected it was calculated that these reactions could account for up to 9% of the charge passed in the region of low dV/dt. Since total metal oxidation accounted for less than 30% of the charge, clearly other anodic reactions took place.

In a recent study in our laboratory (8), Vijh found that in acidic aqueous solution the major products of glycol oxidation at a smooth Pt electrode were glyoxal and oxalic acid. The gaseous product accounted for only 1-2% of the total charge passed and was composed of roughly equal volumes of CO and H_2 with a slight amount of CO_2. The similarity in the compositions of the gas phases produced at the smooth Pt and the oxidized aluminum electrodes and the fact that in both cases the gaseous products accounted for only a small part of the total charge, suggested that at the aluminum electrode the remainder of the charge might be accounted for by production of glyoxal and oxalic acid. However, any glyoxal produced in the glycol borate electrolyte would be complexed by borate (9) and hence escape detection, and no test for carboxylates was found that was sufficiently sensitive in this solution. Thus, we were unable to verify the reactions that consumed more than half the charge passed during side reactions.

Effect of side reactions on electrical properties.—It was expected that the heterogeneous nature of the cracked oxide film would have a significant effect on dielectric properties. Young has suggested that the presence of fissures can be demonstrated by a dependence of impedance on measuring electrolyte resistivity (10). To investigate this, foil specimens were anodized in the 17% APB-EG electrolyte at 1.0 mA/cm² to several voltages up to 400V. At the higher voltages cracks had developed to a considerable extent. The series capacitance and resistance were measured at several frequencies in electrolytes with resistivities of 230 and 10 ohm-cm.

The frequency dependence of reciprocal capacitance and series resistance for a 400V specimen are shown in Fig. 3 and 4. The frequency dependence of $1/C$ was unaffected by electrolyte resistivity. Although a higher resistance was obtained in the low resistivity solution at low frequencies, the increase was small and no greater than was encountered with normal barrier films. Thus, at these ambient conditions there appeared to be no significant electrolyte penetration through the cracked areas.

Table I. Aluminum oxidation reactions during period of side reactions

Charge,* coul/cm²	Weights,* μg/cm² Barrier oxide	New oxide	Total Al consumed	Per cent of charge Barrier oxide	New oxide	Al diss.†	Total
1.59	45.7	4.2	37.3	16.3	1.5	7.4	25.2
2.02	56.1	5.8	51.8	15.7	1.6	10.1	27.4
2.51	73.2	6.2	69.6	16.6	1.4	11.7	29.7

* Measured from onset of side reactions.
† By difference.

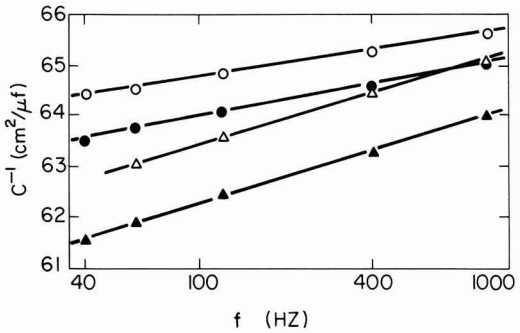

Fig. 3. Frequency dependence of series capacitance of 400V films formed in two electrolytes and measured in two solutions. Triangles = 17% APB-EG anodization; circles = 39% APB-EG anodization. Open symbols = 230 ohm-cm measuring solution; filled symbols = 10 ohm-cm measuring solution.

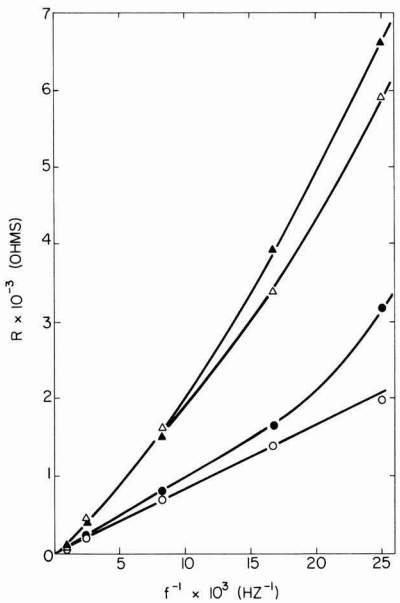

Fig. 4. Frequency dependence of series resistance of 400V films formed in two electrolytes and measured in two solutions. Same symbols as Fig. 3.

The presence of the new thick oxide within the cracks could make the film behave like a two-phase dielectric which might have different properties than a normal barrier film. To examine this, use was made of another glycol borate electrolyte. A solution of 39% APB in ethylene glycol will support anodization at 100% current efficiency up to 450V. Specimens were anodized in this electrolyte at 1.0 mA/cm² to 400V, forming barrier films free of cracks. The frequency dependence of these samples is also shown in Fig. 3 and 4.

A comparison of the results obtained with the cracked and crack-free oxides shows that the capacitance level of the films is about the same but the cracked film exhibits a slightly greater frequency dependence of capacitance and a much greater frequency dependence of series resistance. At the lowest measuring frequency the resistance of the film formed in 17% solution was more than twice that of the film formed in 39% electrolyte.

The effect of the crack network on leakage current was examined by comparing results obtained with films formed in the two electrolytes. Foils were anodized to 400V at 0.28 mA/cm² in both of the APB-EG electrolytes. The samples anodized in the 17% solution have well-developed cracks whereas those processed in the 39% solution were free of cracks. Leakage currents were measured in the 39% electrolyte at several voltages up to 350V. At all voltages, the leakage current decreased slightly with time for both sets of samples, and the current was somewhat lower for the cracked oxide. For example, after 3 hr at 350V the leakage current was 1.8 μA/cm² for the uniform film and 0.7 μA/cm² for the cracked oxide.

From the a-c and d-c properties it can be inferred that the oxide in the cracks is in sufficiently intimate contact with the barrier film to prevent electrolyte paths through the film. Also, the new oxide is an inferior dielectric, though a relatively good insulator.

Some details of anodization with side reactions.—An important observation was that when foils with uniform, thick (*e.g.*, 400V) films formed in the 39% APB-EG electrolyte were anodically polarized in the 17% solution, side reactions took place at voltages as low as 250V. After such treatment the appearance of thick films was the same as that of films grown in the 17% electrolyte (compare Fig. 5 with Fig. 2). Thus, side reactions in a particular electrolyte started at a voltage that was independent of film thickness. This is not an unusual observation, since many workers in this field have observed that anodization electrolytes appear to have a limiting voltage, as measured by leakage current, gassing, etc., that is not very dependent on barrier oxide thickness.

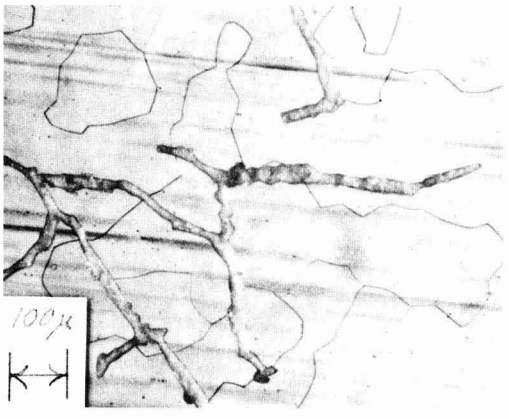

Fig. 5. Micrographs of Al foil anodized to 400V at 0.27 mA/cm² in 39% APG-EG and then held at 0.27 mA/cm² in 17% APB-EG for 140 min. Final voltage was about 300V.

The rate of the side reactions seemed to depend on film thickness and current density of formation. Foils were anodized in the 39% APB-EG electrolyte to three film thicknesses at each of three current densities. Reciprocal capacitance was the measure of film thickness. These specimens then were polarized anodically in the 17% electrolyte for 3 min at 350V. This was sufficient for new oxide growth to start at a number of points on the surface. The density of growth spots seen at 150X was taken as a measure of the extent of side reactions. The results are listed in Table II. Samples with the smallest initial film thickness had the greatest spot density. Moreover, the current density of film formation affected the extent of side reactions, with films formed at the lowest current density exhibiting the smallest amount of growth of new oxide. It should be noted that the initial films were all formed at 100% current efficiency, and bridge measurements showed no differences in dielectric properties among these samples other than those expected on the basis of film thickness.

The films formed in 39% APB-EG could be uniformly thinned in H_3PO_4-CrO_3 stripping solution at 85°C, as determined from the correlation between capacitance increase and weight loss. The films on some 400V specimens were thinned to approximate the thickness (weight basis) of 350 and 300V films. When these were immersed in 17% APB-EG electrolyte for 3 min at 350V the spot density was an order of magnitude greater than for comparable unthinned samples. The results are shown in Table III. It appears that chemical thinning exposed many points for subsequent side reactions.

Behavior of cracked oxides.—Some experiments were done using foil that was first anodized to produce a uniform film and then the oxide was cracked by bending the specimen. On re-anodizing such samples, three observations were made. First, any thick oxide growth was seen only within these cracks or in cracks that had obviously initiated at these induced cracks. Second, when re-anodization was done at constant current, thick oxide was observed only when the current density was relatively high. At low current densities the cracks appeared to be healed with normal barrier film, although voltage fluctuations accompanying this process indicated the possibility of other side reactions. For example, a 200V cracked film re-anodized to 200V in 17% APB-EG had thick oxide growth in the cracks when the C.D. was 280 μA/cm² (based on total area) but exhibited no signs of the new oxide when the C.D. was 28 μA/cm². This example also illustrates the third important observation. There was evidence of side reactions on these flexed specimens at voltages much lower than encountered during normal anodizations. In the above case, voltage fluctuations were observed at 75V when

Table II. Growth spot density as related to anodization current density and film thickness

Current density, μA/cm²	Thickness		Spots/cm²
	Volts	μFd⁻¹	
2.8	400	3.769	35
2.8	350	3.296	91 (1000)*
2.8	300	2.793	245 (5000)*
28	420	3.790	45
28	365	3.269	281
28	310	2.785	332
280	440	3.869	96
280	385	3.300	327
280	325	2.838	838

* Thinned in H_3PO_4-CrO_3 solution.

the C.D. was 280 μA/cm^2 and at 120V when the C.D. was 28 μA/cm^2.

From these observations we infer that the growth of the thick oxide occurs preferentially in cracks and is promoted by high current density. Furthermore, under normal anodizing conditions cracks must not develop until high voltages are reached, for example, 250V in 17% APB-EG and 450V in 39% APB-EG.[1]

Conclusions

It is likely that the sites for the initiation of side reactions are flaws in the barrier oxide film similar to those found in anodic Ta_2O_5 films (11). Although direct evidence for this is lacking, it does seem significant that slight chemical thinning of the oxide resulted in an order of magnitude increase in subsequent growth centers (Table II). This corresponds to Vermilyea's observation that flaws in Ta_2O_5 films were preferential sites for chemical dissolution (11).

It would be expected that reactions at a cracked flaw would be like those at a crack produced by flexing in that the resulting high local current density would result in production of thick oxide rather than barrier film. This more voluminous oxide would cause a strain in the surrounding barrier film sufficient to crack the film and side reactions would then occur in this region. The cycle would continue until the crack reached a point where the growth of new oxide sealed off the tip of the crack before the strain in the surrounding barrier film produced further extension. It is believed that the immediate cause of the formation of thick oxide rather than barrier film is the occurrence of the glycol oxidation reaction. This parallel reaction might change the local electrolyte composition so that normal barrier film could not be produced.

The high degree of reproducibility of the voltage at which side reactions start is apparently a characteristic of the initial film fracture process. From the experiments with flexed specimens it is evident that side reactions can occur over a wide range of lower voltages if cracks are present. It is surprising that the critical voltage for side reactions was independent of average film thickness in these experiments. It is reported that flaw thickness increases less rapidly with formation voltage than does the average thickness (11). Perhaps some flaws reach a limiting thickness which is maintained as the formation voltage increases.

[1] Further support for this came from an anodization in the 39% solution which was followed with an oscilloscope set at a sweep rate of 50 μsec/cm and a sensitivity of 20 V/cm. No discontinuities in the voltage trace were observed up to 350V, at which point the anodization was stopped.

Reactions at flaws may play a role in all aluminum anodizations when the eventual decrease in current efficiency occurs. Other features of the present case, such as the development of a crack network, are probably specific to the particular system. For example, one can picture a side reaction in which no product is formed that affects the composition of the growing oxide. In that case barrier film formation and side reaction would proceed in parallel at the cracked flaw until film growth stifled the side reaction. The net effect would be growth of barrier oxide at reduced current efficiency.

Apparently the presence of the thick oxide network might not be objectionable in an electrolytic capacitor since it only affects the series resistance. It is the growth process which is undesirable in a device since it would give rise to high leakage currents and inability to support a steady voltage. Moreover, the gas generated at both anode and cathode during side reactions would contribute to other failure modes (12).

Acknowledgments

The authors are grateful to Mr. J. Barry for performing the gas analyses and to Mrs. E. Vigna for obtaining many of the laboratory results reported here.

Manuscript submitted Dec. 22, 1969; revised manuscript received June 8, 1970. This was Paper 32 presented at the New York Meeting of the Society, May 4-9, 1969.

Any discussion of this paper will appear in a Discussion Section to be published in the June 1971 JOURNAL.

REFERENCES

1. R. S. Alwitt and A. K. Vijh, *This Journal*, **116,** 388 (1969); G. C. Wood and C. Pearson, *Corrosion Sci.*, **7,** 119 (1967).
2. S. Tajima, S. Itoh, T. Fukushima, *J. Electrochem. Soc. Japan*, **23,** 296, 342, 395 (1955).
3. W. J. Bernard and J. W. Cook, *This Journal*, **106,** 643 (1959).
4. H. Steinberg, "Organoboron Chemistry," Vol. 1, Interscience Publishers, New York (1964).
5. R. S. Alwitt and R. G. Hills, *This Journal*, **112,** 974 (1965).
6. R. M. Goldstein and J. E. O'Neal, *Thin Solid Films*, **4,** R21 (1969).
7. D. A. Vermilyea, *This Journal*, **102,** 207 (1955).
8. A. K. Vijh, Submitted for publication.
9. B. Pesetsky and N. R. Eldred, *Tetrahedron*, **25,** 4137 (1969).
10. L. Young, *Trans. Faraday Soc.*, **55,** 842 (1959).
11. D. A. Vermilyea, *This Journal*, **110,** 250 (1963).
12. R. S. Alwitt and R. G. Hills, *IEEE Trans.*, **PMP-1,** 28 (1965).

Effects of Material and Processing Parameters on the Dielectric Strength of Thermally Grown SiO_2 Films

N. J. Chou and J. M. Eldridge

IBM Thomas J. Watson Research Center, Yorktown Heights, New York 10598

ABSTRACT

The influence of several material and processing parameters on the dielectric strength of thermally grown SiO_2 films on silicon has been assessed. This was accomplished by statistically analyzing the breakdown characteristics of a large number of MOS capacitor structures, which had been fabricated in various ways. Although the results of this investigation are only qualitative, they clearly demonstrate that the effective breakdown strength of these films is strongly dependent on: SiO_2 purity, structural perfection and thickness; the presence of a passivating phosphosilicate glass layer; the presence and reactivity of the metal electrode; and, the duration of the post-metallization heat treatment. The morphology of certain micron-size defects which develop in the MOS structure during annealing is described in some detail, since these faults are apparently responsible for oxide shorting in some instances.

Since the oxide layer under the gate electrode in MOSFET's is subjected to very large electric fields (up to 2 MV-cm^{-1}), its dielectric strength has an important bearing on the reliability of these devices. Although interest in electrical breakdown phenomena in such films has increased in recent years, along with the rapid development of MOSFET technology, the effect of various process and material variables on the effective dielectric strength of thermally grown SiO_2 films has not yet been well characterized. This is due to the extreme sensitivity of this property to changes in oxide composition and structure, which are, in turn, quite dependent on device fabrication procedures. An additional uncertainty is introduced by the dependence of the breakdown characteristics on the particular testing technique employed.

The dielectric strength of thermally grown SiO_2 has been reported by Deal (1) to increase with the density of the insulating film, going from 4.8 to 5.5 MV-cm^{-1} as the density was raised from 2.04 to 2.22 g-cm^{-3}. Breakdown strength values of 4 to 6 MV-cm^{-1} for 2000Å thick SiO_2 films on silicon were found by Ainger (2), who also observed that lower values were encountered on oxide films grown on more heavily doped, p-type silicon. A more thorough investigation of breakdown phenomena in Al-SiO_2-Si structures has been made by Klein (3,4), who found that a succession of breakdown events could be initiated at low fields (< 2 MV-cm^{-1}) when the applied voltage was slowly increased. These events produced visible spark discharges which created individual macroscopic holes in the capacitor, due to localized evaporation of oxide and metal. Such events were labeled "single-hole" or "self-healing" because the test capacitor was still operational after they occurred. When the applied field reached the 5 to 9 MV-cm^{-1} range, the dielectric failure was accompanied by arcing or by propagation of single-hole events to adjacent sites. This resulted in permanent destruction of the capacitor. Consequently, Klein's data indicate that the effective breakdown strength of SiO_2 films does not have a well-defined value but increases as the weak spots in the oxide are eliminated by continued testing, until the ultimate value (in the range, 5 to 10 MV-cm^{-1}) is reached. It should be noted that this range of ultimate strength values is appreciably higher than those observed in earlier studies where unspecified measurement and testing techniques were employed (1, 2).

Key words: dielectrics, dielectric strength, MOSFET devices, morphology of SiO_2.

In a different approach, Fritzsche (5) examined the statistical distribution of breakdown strength values of a large number of Al-SiO_2-Si capacitors. Here, the breakdown field was taken as the value at which the first breakdown event occurred in a capacitor, self-healing or otherwise. His results are typically shown in Fig. 1, where the fraction ($\Delta N/N$) of capacitors tested, which break down in a small interval of field, is shown as a function of the corresponding field. Maxima were observed which consistently fell into three ranges: 0-0.6, 1-3, and 7-9 MV-cm^{-1}. According to Fritzsche: the peak labeled "primary" represents the intrinsic (or electronic) breakdown strength of the oxide; the "secondary" one is attributable to the presence of small, randomly distributed, crystallized regions (structurally similar to quartz, too minute to be detected by conventional techniques but large enough to cause breakdown by serving as flaws in the otherwise amorphous dielectric); and the "tertiary" to the effect of gross structural defects such as pinholes. Note that the primary strength corresponds to the ultimate dielectric strength values reported by Klein and his co-workers (3, 4). Fritzsche's interpretation was supported by the following observations: (*i*) the temperature dependences of the primary and secondary peak positions are similar to those of amorphous silica and crystalline quartz, respectively; (*ii*) as-grown anodic SiO_2 is amorphous and fails to exhibit a secondary-type peak until it has been subjected to heat treatment probably capable of inducing recrystallization; (*iii*) the tertiary failure mode is promoted by mechanically damaging the oxide; and (*iv*) the expected random nature of oxide defects can be inferred by the increase in secondary and tertiary breakdown with the electrode area (5).

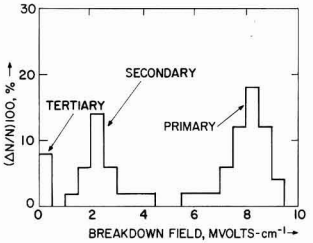

Fig. 1. Typical breakdown strength distribution curve for Al-SiO_2-Si (after Fritzsche).

Fritzsche found that the primary mode of breakdown in SiO_2 was electronic in nature, thus exhibiting no dependence on the duration of the applied field. In contrast, Worthing (6) found that when a constant, positive voltage was applied to the metal for the time required to cause breakdown, the breakdown field of SiO_2 films on n-type, degenerate Si was proportional to $(\text{time})^{-1/4}$. This particular time dependence has been frequently observed for bulk insulators where it is known as Peek's law (7). This has the effect of lowering the dielectric strength of the SiO_2 film from 6.7 MV-cm^{-1} for fast stressing rates to approximately 3 MV-cm^{-1} for a testing voltage applied at an infinitely slow rate. However, no time dependence was observed by Worthing when the metal was negatively biased.

The present investigation was undertaken to ascertain the influences of various processing and material parameters on the dielectric strength of oxide films and to resolve the apparent differences in the findings of some of the above investigations. An attempt was made to separate the effects of these variables, in view of the fact that they were found to interact frequently to alter the breakdown characteristics. Since the breakdown behavior is also affected by measurement technique, this separation was facilitated by employing a standardized testing procedure. The statistical approach (5) was then utilized to evaluate the dependence of the dielectric strength of the thermally grown oxide on SiO_2 purity and thickness, phosphosilicate glassing, electrode metal reactivity, and post-metallization heat treatment. Although most of the results of this investigation are of a semiquantitative nature, many of these will be seen to be quite relevant both to the development of MOSFET technology and to the understanding of the mechanism of oxide breakdown.

Experimental Procedure and Results

Specimen preparation.—Various types of oxide films were prepared in the following ways on Monsanto chemically-mechanically polished, <100>- and <111>-oriented silicon substrates of 2 to 10 ohm-cm resistivity.

"Regular" SiO_2 preparation.—The as-received substrates were cleaned in transistor grade reagents according to the following sequence: boiling trichloroethylene, boiling isopropyl alcohol, de-ionized (DI) water, boiling nitric acid, DI water, dilute hydrofluoric acid, DI water, and blown dry in N_2. Thermally grown SiO_2 films of so-called "regular" quality were formed with the desired thicknesses (in the 200-2000Å range) at 1100°C in a single-walled, high-purity silica tube in a resistance-heated furnace. As will be seen later, SiO_2 films prepared in this manner under normally clean laboratory conditions have quite reproducible dielectric breakdown characteristics and, as such, provided a convenient reference material for this investigation; hence, they have been designated to be of "regular" quality. The mobile cation (presumably Na^+ ions) concentration of such films, as established by measuring the flat-band voltage shift upon bias-temperature stressing (8), was typically $\sim 2 \times 10^{11}$ Na^+ ions-cm^{-2}. It should be emphasized that this concentration (assuming the mobile species is Na^+ ions) represents only a fraction of the total sodium content of the oxide (9).

"Ultraclean" SiO_2 preparation.—Ultra-pure SiO_2 films were prepared also by using extremely clean conditions. The silicon substrates were vapor-etched first in a very pure and dry HCl-H_2 ambient, followed by an *in situ* oxidation at 1100°C in dry O_2. Heating was accomplished using a silicon carbide-coated graphite susceptor placed inside a water-cooled, fused silica jacket. The mobile cation concentrations of these films was established to be $\lesssim 2 \times 10^{10}$ cm^{-2}; *i.e.*, about an order of magnitude less than that of "regular" SiO_2.

Phosphosilicate glass preparation.—Other specimens were prepared by alloying the surface of "regular" SiO_2 with P_2O_5 to form phosphosilicate glass (PSG)-SiO_2 layered structures. These glass films were typically thin and relatively low in phosphorus content [*e.g.*, 125Å thick with 4 m/o (mole per cent) P_2O_5] (10). Since these thin PSG-SiO_2 composite layers are particularly effective for preventing threshold drifts in MOSFET devices (11-13), such structures are termed "stabilized" in this paper.

Metallization and annealing.—Sixty-four metal electrodes of a given area (in the range 0.05-1.3 mm^2) were deposited through metal masks onto each wafer. The high purity metals (99.999+% aluminum, for example) were evaporated, using an electron gun heat source. Finally, the completed structures were heated for 5 min at 500°C in a nitrogen ambient in order to anneal out the E-gun induced radiation damage at the oxide-semiconductor interface. Any departures from the above preparation procedures will be detailed when necessary.

General testing procedure.—In order to select appropriate breakdown testing conditions, the following series of measurements were carried out on Al-SiO_2 (1000Å, regular)-Si structures. Large numbers of capacitors (typically 100 to 200 samples) were tested by applying a voltage, which was made to increase linearly with time, to each electrode until breakdown (self-healing or otherwise) occurred. In this technique, the development of breakdown causes the appearance of an abrupt departure from linearity in an otherwise smooth voltage *vs.* time trace. The breakdown field is evaluated at this point which corresponds to a current density on the order of approximately 10^{-6} A-cm^{-2}. The resultant breakdown distributions were then displayed as bar graphs, wherein those fractions ($\Delta N/N$) of capacitors failing in a small interval (0.5 MV-cm^{-1}) of field are plotted against the corresponding breakdown fields.

Electrode area.—Typical breakdown distributions for regular SiO_2 films are shown in Fig. 2, where it may be seen that the secondary failure mode increases with electrode area (F). As shown in the Appendix, the oxide defect concentration can be estimated from this areal dependence. When this is done, a value of ~10 defects-cm^{-2} is obtained, which is significantly lower than the estimated value (~80 cm^{-2}) (5) for the SiO_2 film shown in Fig. 1. In view of their better perfection, it is not surprising that the films in Fig. 2 do not show a tertiary peak. In general, the 0.5 mm^2 electrode seems to provide a useful reference distribution for further work because the secondary failure mode is significant with this area although most of the breakdown is still intrinsic.

Field application rate.—Both the intrinsic strength and the mode of breakdown of 1000Å, regular SiO_2 films are unaffected by decreasing the rate of field application over the range from 1 to 0.01 MV-cm^{-1}-sec^{-1}. Only for films with much higher defect con-

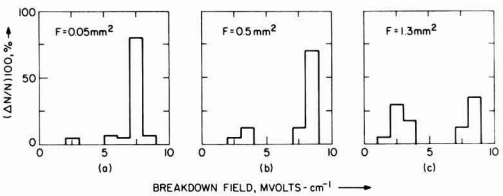

Fig. 2. Area dependence of the breakdown strength distribution for regular oxide in Al-1000Å SiO_2-Si structures.

centrations (>90 defects-cm^2) was a significant shift of the primary peak toward lower field values observed to occur with decreasing ramp speed. We believe that this effect of defect concentration on the rate dependence of breakdown strength may account for the discrepancy between the findings of Fritzsche (5) and Worthing (6). However, the relationship between the extent of this shift and the ramp speed (or biasing time) was not established in the present investigation because this would have required the preparation of oxide films with reproducibly high defect densities. Since the specimens to be tested were of a lower defect density, it was feasible to use the highest ramp speed tested (*i.e.*, 1 MV-cm^{-1}-sec^{-1}) in order to minimize the measuring time.

Temperature.—A limited amount of testing indicated that the statistical distributions of breakdown strengths were relatively insensitive to changes in the testing temperature, in the 25°-150°C range, for regular oxide and for phosphosilicate glass-SiO_2 composite layers. Hence, all subsequent measurements were done at room temperature.

Polarity.—In order to avoid loss of field across a depletion region in the semiconductor, breakdown measurements in this investigation were carried out with a field polarity such that an accumulated silicon surface was always maintained.[1] This was accomplished by biasing the metal positively for n-type and negatively for p-type substrates. When breakdown data were taken under this polarity restriction, the distribution curves for the Al-SiO_2 (1000Å, regular)-Si structures showed no significant dependence on the duration of the applied field.

Effects of material and processing parameters on oxide breakdown.—Type of oxide film.—In contrast with that observed for regular oxide films, the breakdown distribution curves for ultraclean SiO_2 exhibited no measurable areal dependence (*cf.* Fig. 2 and 3a). Although the intrinsic strengths of both grades of SiO_2 are the same (*i.e.*, 6 to 9 MV-cm^{-1}), the higher purity films exhibited no noticeable defect-related breakdowns. It is important to note that when HCl vapor-etched Si substrates are thermally oxidized in a resistance-heated, fused silica tube, the resultant breakdown properties are generally quite similar to those of regular oxide. These results suggest that the lower impurity (most likely sodium) concentrations that are typically attained in the oxidation step of the ultraclean processing procedure lead to superior SiO_2 breakdown characteristics. To understand this impurity effect, it may be instructive to note that the structure of thermally grown SiO_2 is apparently quite similar to that of fused silica. That is, it is comprised of SiO_4 tetrahedra (with Si^{+4} ions in their centers) which are linked together at the corners or oxygen sites to form a three-dimensional network essentially devoid of long-range order. Although phase transformations are very sluggish in this oxide, they are greatly accelerated by the addition of small quantities of network modifiers, such as sodium (14). For example, sodium contamination has been reported (15) to result in the formation of locally crystallized regions in thermally grown SiO_2 films, thereby causing defect-related breakdown. Depending on the magnitude of this phase transformation, it should first appear as an increase in secondary breakdown [in accord with Fritzsche's model (5)] and eventually as a rise in the incidence of tertiary oxide failures. It will also be seen that shorting can develop as a result of a solid state reaction between the metal electrode and the oxide during post-metallization annealing.

In the case of PSG-stabilized specimens, the glass addition was found to virtually eliminate defect-type breakdown in regular SiO_2, and to raise its primary strength to 9-12 MV-cm^{-1} (*cf.* Fig. 2 and 3b). The first improvement may be accounted for by the fact that the phosphosilicate layer is liquid at its temperature of formation (10, 16), and therefore would form a continuous film over the underlying SiO_2. The second beneficial effect can be largely attributed to the higher dielectric strength of the PSG itself (17).

Oxide thickness.—For regular and stabilized films prepared with various total oxide thicknesses (in the 200-880Å range), the likelihood of defect-related breakdown was found to increase appreciably with decreasing insulator thickness (see Fig. 4). The addition of a PSG layer is again seen to substantially reduce the frequency of defect-related breakdowns.

A quantitative determination of the oxide defect density (ρ, cm^{-2}) was carried out for the data in Fig. 4. The predicted proportionality between ln P (P being the fraction of primary breakdowns) and F was obtained for several thicknesses (Fig. 5). The apparent departure from linearity for the 200Å, regular SiO_2 at the largest electrode area may be due to the use of too small a sampling. Defect densities of the films were estimated from the slopes and are listed in Table I. It may be seen that the density of defects of regular SiO_2 increases by a factor of approximately sixty as the thickness is reduced from 630 to 200Å.

The enhancement of the intrinsic strength by PSG is again evident in Fig. 6. The rise in dielectric strength, on going from 880 to 410Å, can be attributed to the relative increase in the PSG-to-SiO_2 thickness ratio. However, the primary breakdown strength for both oxides decreases significantly for thinner (< 400Å) films and shows a marked dependence on area, in contrast to the thicker oxides. Thus, the

[1] Numerous comparative tests have shown that inflated values of dielectric strength are obtained when Si surfaces are depleted during breakdown measurement since part of the potential drop occurs in the semiconductor.

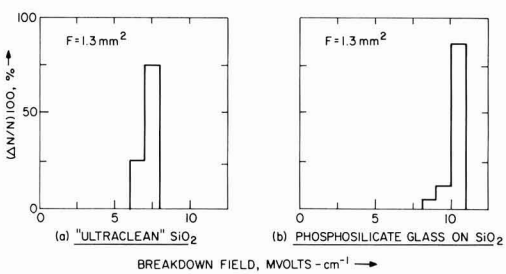

Fig. 3. Dielectric strength distributions for: *(a)* Al-SiO_2 (1000Å, ultra-clean)-Si; and *(b)* Al-PSG (125Å, 4% P_2O_5)-SiO_2 (900Å, regular)-Si structures. Note absence of defect-related breakdown in both oxides.

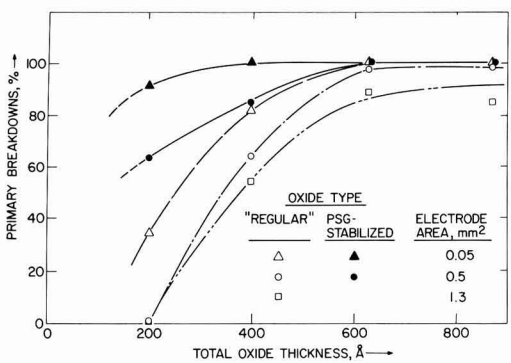

Fig. 4. Dependence of breakdown mode for regular and phosphosilicate glassed oxides on thickness. Note that the PSG addition is relatively most beneficial for the thinnest films.

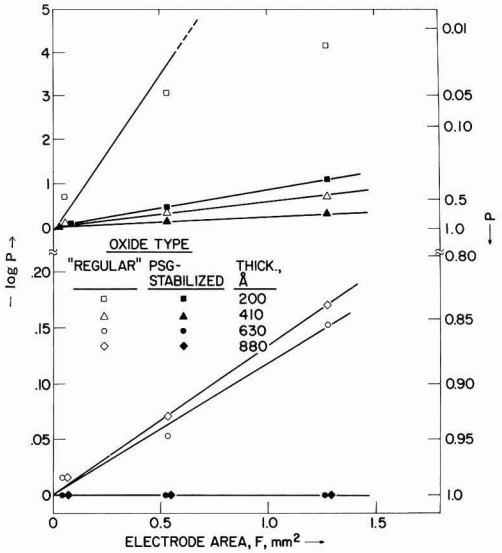

Fig. 5. Dependence of the fraction (*P*) of the total film area exhibiting primary breakdown on insulator thickness and electrode area for regular and phosphosilicate glassed oxide.

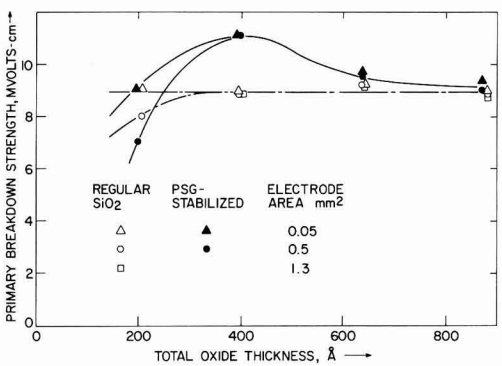

Fig. 6. Dependence of primary breakdown strength on total thickness of regular and phosphosilicate glassed SiO_2 films, where the thickness of the PSG layer is held constant at 125Å. Note that this strength is independent of electrode area, except for films thinner than 400Å.

mechanism responsible for primary-type breakdown is apparently no longer electronic in nature for these highly defected, very thin films. This change is consistent with the development of field-induced thermal instabilities at weak spots (3,4) and may well give rise to a time-dependence of the strength (6).

Impurities introduced after formation of SiO_2.—Protracted, post-metallization annealing treatments (viz., on the order of 30 min at 500°C) can promote extensive, tertiary-type breakdown (18) (see Fig. 7). The catalytic effect of certain cationic impurities in accelerating the devitrification of SiO_2 (14, 15), probably accounts for most of this behavior since it is most severe for films grown with a high sodium content and when highly reactive metal electrodes are used. In fact, electrical shorts (*i.e.*, tertiary breakdown) were rarely observed in oxide areas that were not covered by metals, or when noble metal electrodes such as gold were used, even after many hours of heating at 500°C. Mechanical stresses, arising from steps in the oxide thickness or from differences in the thermal expansion coefficients of the components on the MOS structure, may also contribute to oxide deterioration. Protracted annealing at 500°C also results in the growth of gross structural defects, under the edge of the metal electrode (18), which are probably responsible for the shorting. This particular type of tertiary failure mode will be described later.

Table I. Dependence of defect density on oxide thickness

Oxide \ *d*, Å; ρ, cm⁻²	200	410	630	880
"Regular" SiO_2	750	65	12	12
PSG-stabilized	120	30	<1	<1

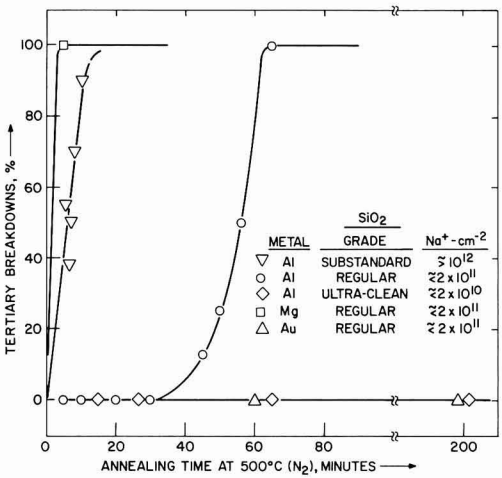

Fig. 7. Combined effects of electrode metal reactivity and post-metallization annealing on the development of electrode shorts in metal-1000Å SiO_2-Si structures, where the purity of the oxide is varied.

The role of the metal electrode on the development of tertiary breakdown in stabilized film was evaluated by depositing 0.5 mm² dots of several metals on PSG (125Å, 4 m/o P_2O_5)-SiO_2(900Å, regular)-Si substrates, followed by determinations of the statistical breakdown distributions in both the unannealed and annealed (100 min at 500°C in N_2) conditions. From the results in Fig. 8, it is apparent that Mg, Ti, and Ni markedly promote oxide failure, while Al and Au have essentially no effect for PSG-stabilized struc-

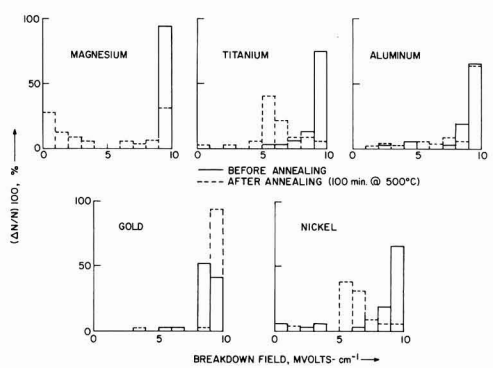

Fig. 8. Combined effects of electrode metal reactivity and post-metallization annealing on the breakdown strength distributions in PSG-stabilized, 1000Å oxide films.

tures. A comparison of the results for aluminum electrodes on regular and PSG-stabilized SiO_2 indicates that the PSG layer has the effect of retarding the development of electrical shorts due to extended annealing treatments. This retardation effect of the glass is more pronounced for structures with magnesium electrodes (*cf.* Fig. 7 and 8).

It is well-known that impurity ions can be introduced into the oxide in ways other than by electrode-oxide interactions. Thus, it is important to evaluate the possible effects of this type of contamination on breakdown. It was found in this investigation, for example, that when sodium (in concentrations of approximately 5×10^{12} cm^{-2}) was added after oxide formation (by boiling the oxidized wafers in $NaCl$-H_2O solutions prior to aluminization), relatively little additional deterioration was observed relative to the untreated, regular SiO_2 control material, for heating times up to approximately 50 min at 500°C. Therefore, it would appear that Na^+ ions which are introduced after SiO_2 formation, do not have much of an effect on crystallizing the oxide during subsequent post-metallization annealing at these temperatures.

In order to investigate the effect of localized damage in the insulator and at the insulator-semiconductor interface on tertiary breakdown, ultraclean SiO_2 films were irradiated with various O^+ dosages (using a constant beam energy of 75 keV). After deposition of 0.5 mm^2 Al dots, the capacitors were annealed for various times at 300°C in N_2 and tested in the usual way. Although the unannealed specimens exhibited the usual primary strength and essentially no indication of oxide deterioration, extensive shorting appeared after a very modest anneal of 20 min at temperatures as low as 300°C (see Fig. 9). Oxide failure was markedly increased by a small rise in the O^+ dosage and by a reduction in the oxide thickness. As in the earlier cases, oxide deterioration is intimately related to the presence and reactivity of the metal electrode. That is, electrical shorts were not observed in areas not covered by metal during heating [as subsequently established by using a removable mercury probe (19)] or when deposited gold electrodes are used. The network damage, due to implantation, apparently accelerates the metal-oxide reaction, thereby promoting shorting (18).

Glassing of Na^+*-contaminated* SiO_2.—Since sodium can be introduced inadvertently into SiO_2 during MOSFET processing before the PSG protective layer is added, it is very important to know what such contamination can do to the dielectric strength of the resulting layered oxide. This is of particular concern

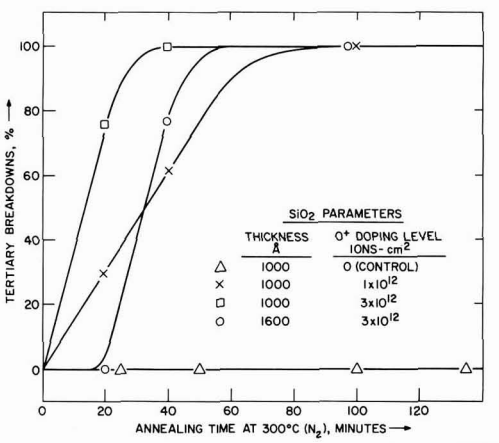

Fig. 9. Development of electrical shorts on annealing at 300°C in ultra-clean SiO_2 films, implanted with various O^+ ion dosages.

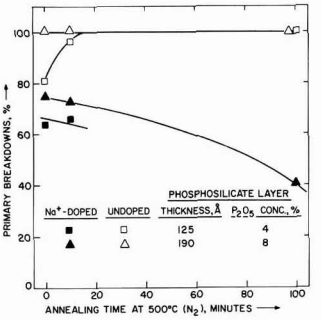

Fig. 10. Effect of post-metallization annealing on the breakdown characteristics of 1000Å SiO_2 films, deliberately contaminated with sodium, prior to phosphosilicate glassing. Characteristics of uncontaminated films are included for comparison.

because the glassing is carried out at temperatures, (800°-1100°C) where the promotion of crystallization by sodium is at a maximum (14). Therefore, the breakdown distributions were determined for oxide films prepared by: (*i*) growing 1000Å SiO_2 films of regular quality, (*ii*) immersing these oxidized substrates for 15 min in boiling $NaCl$-H_2O solutions to incorporate Na^+ ions in the oxide (8), (*iii*) diffusing P_2O_5 into the outer SiO_2 surfaces (at 800°-1000°C) to form phosphosilicate films, (*iv*) depositing 0.5 mm^2 aluminum dots, (*v*) annealing at 500°C (N_2) for various times, and (*vi*) breakdown testing. The severe deterioration of oxide quality due to Na^+ contamination is quite apparent in the results shown in Fig. 10. Experiments on regular SiO_2 films, subjected to the salt-water and subsequent high-temperature treatment (30 min at 1000°C in O_2) before aluminization, indicated that this oxide exhibited much more deterioration than the glassed ones. It may be concluded that even the addition of a PSG layer cannot prevent the formation of oxide faults at high temperatures when appreciable sodium concentrations are present in the SiO_2.

Morphology of annealing-induced defects.—The gross structural features of large defects, produced by extended annealing of Al-SiO_2-Si structures (see section on Impurities introduced after formation of SiO_2), are described below. It may be seen that these defects are quite massive, relative to the thickness of the insulating film. As such, they are probably mainly responsible for most of the tertiary breakdowns, even for the case where the capacitors have been subjected to a normal post-metallization heat treatment (*e.g.*, 5 min at 500°C).

Metallographic examination of shorted capacitors reveals the presence of well-defined, oriented defects on the periphery of the aluminum. Although partially covered by metal, their shapes are clearly rectangular and triangular for <100>- and <111>-oriented silicon, respectively, while their sides coincide with the (110) family of directions in the substrate. Evidently, the heating required to produce such defects decreases with a lowering of oxide perfection. Thus, they are readily visible at 500X magnification after an hour of annealing 1000Å, regular SiO_2 capacitors at 500°C, and ion-implanted oxide at 300°C. While becoming larger and more numerous with annealing time, they only develop under or in close proximity to reactive metal electrodes. The defects do not appear in regions away from the aluminum, for example, or in gold-deposited capacitors.

Conventional collodion replicas were made of the oxide surface for examination by electron microscopy, after removing the aluminum in a dilute HCl etchant. For specimens previously subjected to severe annealing treatments for aluminized structures (*e.g.*, ~ 2

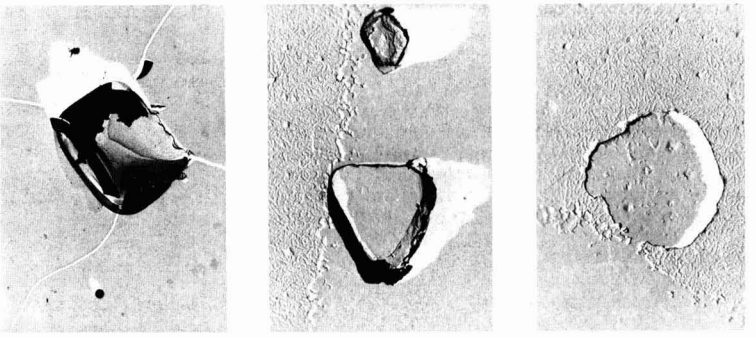

a b c

Fig. 11. Electron microscope replicas (at 9000X) of gross defects, developed in Al-SiO_2-Si structures during protracted annealing, as they appear after the aluminum is etched off. (a) and (b) show the faceted pits developed in <100>- and <111>-oriented Si, respectively, where pit sizes can be compared with that of ½μ latexsphere visible in (a). A typical, irregularly shaped raised area in the substrate is shown in (c).

hr at 500°C), the metallized oxide region was readily discernible, since considerable surface roughening had occurred as a result of a solid state reaction between the SiO_2 and Al. Electron micrographs of the replicas show that these defects are faceted pits, 1-10μ on a side and extending 1-2μ into the silicon (see Fig. 11a and b). With the aluminum removed, it was apparent that the pits are preferentially located along the perimeter of the metallized region, rather than in the center. Based on crystallographic considerations, it is evident that the facet faces are (111) planes.

Black films line the (111) faces of the pits. Since this material adheres to the collodion, it was possible to identify it as γ-Al_2O_3, using electron diffraction and microprobe analyses. Electron microprobe measurements, on specimens still covered with aluminum (*i.e.*, unetched), indicated that the faceted pits are filled with metallic aluminum, while the adjacent electrode region is depleted of metal. Finally, large irregularly shaped plateaus (approximately half a micron high) were frequently observed to occur in the substrate, adjacent to the pits (see Fig. 11c). Thus, the growth of pits and plateaus in close proximity and the presence of γ-Al_2O_3 in the pits suggests that a rapid transfer of mass occurs during annealing. It appears that silicon atoms can diffuse away from the receding faceted planes to form raised areas in the substrate covered by aluminum, while aluminum can penetrate the relatively thin oxide barrier to fill the γ-Al_2O_3 lined pits in the silicon. It is expected that large flaws in the oxide layer would also result from the development of the plateau regions. One effect of this mass rearrangement is the appearance of extensive shorting in MOS structures subjected to severe post-metallization heat treatments. As such, it constitutes another mode of tertiary failure, in addition to the presence of pinholes which develop during oxide growth.

Summary

Electrical breakdown characteristics of SiO_2 films thermally grown on silicon have been found to depend strongly on oxide preparation and various subsequent treatments:

1. While a lowering of the concentration of mobile impurities reduces the occurrence of defect-related breakdowns, it does not change the magnitude of the intrinsic breakdown strength of SiO_2. Appropriate phosphosilicate glassing, on the other hand, not only effectively obliterates oxide defects but also raises the intrinsic strength of the composite films.

2. Under identical SiO_2 growth conditions, reduction of film thickness is accompanied by an increase in the density of oxide faults. Excessively high defect density in the oxide gives rise to a time dependence of the breakdown characteristics and can therefore lower the magnitude of the primary breakdown strength under certain testing conditions. The addition of a PSG layer removes this dependence by eliminating the effect of oxide weak spots on breakdown. The amount of glassing required for this purpose is greater for SiO_2 films which have initially a higher defect density.

3. Sodium contamination can result in severe oxide deterioration, especially during film growth at temperatures in the 1000°-1200°C range. In contrast to this, sodium contamination after SiO_2 growth has much less of an adverse effect on the dielectric properties.

4. Protracted annealing of MOS structures (*e.g.*, 30 min at 500°C) can cause oxide deterioration by promoting a solid state reaction between certain electrode metals and SiO_2. This effect is more pronounced for oxides having a higher defect concentration. When aluminum is used, micron-size structural defects develop, concurrently with increased defect-related breakdown. These results suggest that another mechanism for oxide shorting can be operative, in addition to the breakdown which can be attributed to pinholes produced during oxide growth. This newer mode involves a rapid redistribution of massive quantities (relative to the dielectric thickness) of aluminum and silicon during the annealing process.

5. Lattice defects created by ion implantation have virtually no effect on the breakdown strength prior to annealing. Deterioration of implanted oxide during annealing at 300°C may be attributed to either an accelerated injection of electrode metal ions into the film, or by local crystallization facilitated by the presence of lattice defects.

The above observations are consistent with Fritzsche's breakdown model (5) which implies that processing steps promoting local crystallization of the oxide will result in an increase in defect-related breakdown, while glassing has an opposite and beneficial effect. Furthermore, the structural mismatch between the crystallites and the oxide matrix, which provides rapid diffusion paths, may also account for the observed annealing failure mode in Al-SiO_2-Si structures.

APPENDIX

The defects are assumed to be randomly distributed and have a size roughly comparable to the film thickness (therefore, much smaller than the electrode area, F). The total area (A) of the film may be subdivided into N cells of an area a, which is just large enough to accommodate a defect if it happens to be there. It follows that the probability (p) of randomly selecting an occupied cell is equal to $n/N = \rho \cdot a$, where n is the total number of occupied cells. Conversely, the probability (q) of picking an unoccupied cell is equal to ($1-p$).

When an electrode is deposited, the number of cells covered by metal is $n' = F/a$. Consequently, the probability (P) for the electrode to not cover a defect is

$$P = q^{n'} = (1 - p)^{F/a} \quad [1]$$

Since $n << N$, it can be shown that

$$\ln P = -F \cdot \rho \quad [2]$$

A fraction P, of the total film area, will consequently exhibit primary-type breakdown. Equation [2], which was also used by Fritzsche, was derived here to give the reader a better appreciation of the significance of the results that can be determined by its application.

Acknowledgments

The authors are indebted to Dr. F. X. Montillo for providing the ultraclean SiO_2 specimens, to Dr. B. L. Crowder for ion implantation of SiO_2 films, to Dr. P. Balk and Dr. T. O. Sedgwick for their comments on this manuscript, and to Messrs. R. J. Dendall, W. Gordon, Jr., R. Hammer, and D. Johnson for their invaluable assistance with the breakdown measurements, and C. F. Aliotta for the electron microscope work.

Manuscript submitted March 2, 1970; revised manuscript received May 19, 1970.

Any discussion of this paper will appear in a Discussion Section to be published in the June 1971 JOURNAL.

REFERENCES

1. B. E. Deal, *This Journal*, **110**, 527 (1963).
2. F. W. Ainger, *J. Materials Sci.*, **1**, 1 (1966).
3. N. Klein, *IEEE Trans. on Electron Devices*, **ED–13**, 788 (1966).
4. N. Klein and H. Gafni, *ibid.*, **ED–13**, 281 (1966).
5. C. Fritzsche, *Z. angew-Phys.*, **24**, 48 (1967).
6. F. L. Worthing, *This Journal*, **115**, 88 (1968).
7. D. F. Miner, "Insulation of Electrical Apparatus," p. 40, McGraw-Hill Book Co., New York (1941).
8. E. H. Snow, A. S. Grove, B. E. Deal, and C. T. Sah, *J. Appl. Phys.*, **36**, 1664 (1965).
9. E. Yon, W. H. Ko, and A. B. Kuper, *IEEE Trans. on Electron Devices*, **ED-13**, 276 (1966).
10. J. M. Eldridge and P. Balk, *Trans. Met. Soc. AIME*, **242**, 539 (1968).
11. J. M. Eldridge, R. B. Laibowitz, and P. Balk, *J. Appl. Phys.*, **40**, 1922 (1968).
12. J. M. Eldridge and D. R. Kerr, *Abs. Electronics Div., Electrochem. Soc.*, **13**, 530 (1968).
13. P. Balk and J. M. Eldridge, *Proc. IEEE*, **57**, 1558 (1969).
14. H. Rawson, "Inorganic Glass Forming Systems," pp. 51-61, Academic Press, New York (1967).
15. R. Schmidt, Silicon Interface Specialists Conference, Las Vegas, Nevada, March 1968.
16. P. Balk, C. F. Aliotta, and L. V. Gregor, *Trans. Met. Soc. AIME*, **233**, 563 (1965).
17. E. H. Snow and B. E. Deal, *This Journal*, **113**, 263 (1966).
18. N. J. Chou, J. M. Eldridge, and W. Gordon, Jr., *Abs. Electronics Div., Electrochem. Soc.*, **13**, 534 (1968).
19. R. Hammer, *Rev. Sci. Instr.*, **41**, 292 (1970).

Preparation, Forming, and Aging of Electroluminescent ZnS:Mn,Cu,Cl Films

W. Riemer*[1] and R. E. W. Lake

Department of Electrical Engineering, University of Toronto, Toronto, Ontario, Canada, and Canadian Westinghouse Company, Hamilton, Ontario, Canada, respectively

ABSTRACT

The d-c characteristics (luminance-voltage-current) of electroluminescent films of ZnS:Mn,Cu,Cl prepared by two different methods were investigated during the operating life of the films. For the devices investigated a shift in the characteristics and an increase in the efficiency with operation time was observed. It is suggested that the terms forming and aging do not describe the time-dependent changes in the characteristics, but rather reflect practical aspects of the properties of the films.

Electroluminescence (radiative emission on application of an electric field) in activated ZnS has been recently reviewed in general (1, 2) and for the case of thin film devices (3). The usual configuration for investigating the electroluminescence of thin films of ZnS resembles a capacitor in that it consists of a film of ZnS sandwiched between two parallel electrodes, of which one is transparent to permit the observation of the emitted light.

Under operation ZnS:Mn,Cu,Cl films undergo time-dependent changes in the observed characteristics which are commonly referred to as forming and aging. Forming (4, 5) describes the observation that, on first applying a voltage to a film of this composition, a large current flows but no emission occurs. With the subsequent gradual decrease in current electroluminescence commences and increases in luminance. The duration of this process depends on the fabricating method and is typically a few seconds to as much as an hour (6, 7). One of the reasons that electroluminescent devices have not been more successfully applied is the aging effect or deterioration of emission on operation (8). The longest half-life (time to half initial luminance) for a ZnS thin film was reported to be just over a thousand hours (9) under a-c excitation. The d-c half-life of thin films is considerably shorter than that obtained under a-c conditions, and in some instances the devices are unstable (10).

In common terminology forming and aging are used to designate apparently distinct periods in the operating life of ZnS:Mn,Cu,Cl films. This paper describes the results of an investigation to determine whether a significant change in the d-c device characteristics can be associated with forming and aging, and whether these two phenomena are affected by the method of preparing the devices.

Experimental

The devices investigated consisted of a layer of phosphor sandwiched between two electrodes in a capacitor arrangement, and supported by a glass substrate. The phosphor used as source material for these experiments was ZnS:Mn,Cu,Cl with the following impurity concentrations determined by activation

* Electrochemical Society Active Member.
[1] Present address: Institut für Angewandte Physik, Universität Basel, Basel, Switzerland.
Key words: aging, electroluminescence, forming, thin films, vacuum deposition, zinc sulfide.

analysis: Cu 1.6%, Mn 0.2%, and Cl less than 0.1%. It was not possible to establish the corresponding concentrations in the films. A tin oxide layer on the substrate constituted the transparent electrode, and a matrix of 1 mm square aluminum electrodes on the phosphor film completed the array of devices. All evaporations of materials other than metals were performed in an Edwards High Vacuum Ltd. Model 12EX coating unit. The equipment had been modified to accommodate the special requirements for the production of uniform thin films. In pre-evaporation pumpdown the pressure observed on the dry air calibrated ionization gauge was approximately 1×10^{-5} Torr. A range of phosphor film thicknesses between 0.2 and 2.0μ was investigated. Interferometric measurements were used to determine the thickness of the films and also to calibrate the crystal monitor used for rate control.

Two methods were employed for the preparation of phosphor films. A procedure that gives good control over the impurity incorporation and satisfactory recrystallization is based on diffusing the impurities from a relatively large bulk of powder of desired impurity content into the film, previously deposited, contiguous to the powder under equilibrium conditions (11). The substrate with the evaporated ZnS film is embedded in the activated powder and the combination is heated in a double crucible (12) to approximately 750°C for a brief period. Using diffusion-activation relatively good films can be made, although only certain types of glass substrate and tin oxide layer survive this treatment.

The alternate method, deposition-activation, is based on the crystallization and activator incorporation during the deposition of the film (13). The source material, sintered pressed pellets of phosphor, was deposited onto a heated substrate. A very efficient method of substrate heating consisted of using the tin oxide layer on the substrate (subsequently used as transparent electrode) as a resistive heater (14). In preliminary experiments it was found that the characteristics of devices prepared by deposition-activation were primarily sensitive to the substrate temperature and the deposition rate. With increasing substrate temperature, the condensation rate decreased as in Fig. 1. A series of films were deposited under similar conditions, but the deposition rate was varied over a range from 5 to 45 Å/sec by varying the source temperature. For deposition rates in excess of 10 Å/sec the breakdown field of the film decreased and reduced the attainable luminance of the device (Fig. 2). For deposition rates less than 5 Å/sec, presumably as a consequence of the residual gas at the vacuum prevailing during evaporation, the maximum attainable luminance also decreased. The properties of the deposited film depend on the constitution of the vapor from which it condenses. For the given vacuum environment and boat design an optimum substrate temperature of approximately 240°C and deposition rate of 5 Å/sec were used in the preparation of films on which change in characteristics measurements were made.

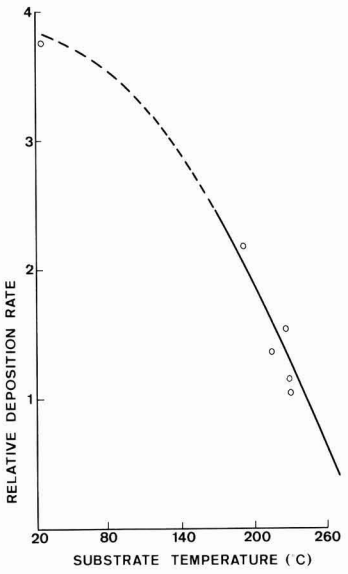

Fig. 1. Relative deposition rate as a function of substrate temperature.

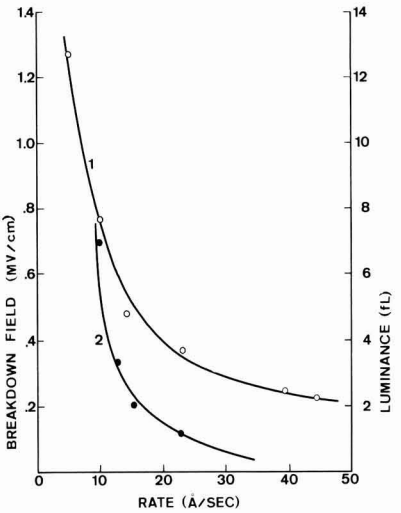

Fig. 2. Effect of film deposition rate on: 1, break-down field; 2, luminance.

The three variables that describe the operation of an electroluminescent film are the voltage (V) applied to the tin oxide and aluminum terminals, the current (I) through the device, and the luminance (L). The electrodes were connected in series with a large resistor to a stabilized voltage supply. The voltage across the film was monitored with a Keithley 601 electrometer. A small series resistor was used to record the current. Reproducible luminance results were obtained with a Spectra Pritchard photometer. The characteristic curves, L-V-I, were recorded with a Honeywell 550 recorder.

Observations

Both deposition-activated (80 films) and diffusion-activated (44 films) films were investigated. Although, under d-c operating conditions, diffusion-activated films generally showed a higher luminance (maximum observed 240 fL) than deposition-activated films (maximum observed 50 fL) the change in characteristics on operating was qualitatively similar, and consequently only representative results for deposition-activated films are presented.

In preliminary experiments it was observed that, for the devices investigated, emission was most effective when the aluminum electrode was made positive. In order to investigate the change on operation in d-c characteristics this polarity (aluminum positive) was therefore used. From first turn-on to the final breakdown of the device the current was maintained constant at 1 mA.

The voltage across the device and the luminance were continually monitored as a function of time. The voltage and luminance history for film 5-31 is described in Fig. 3. For constant current the voltage increases continuously. The actual trace, from which this graph is constructed, shows that as the break-

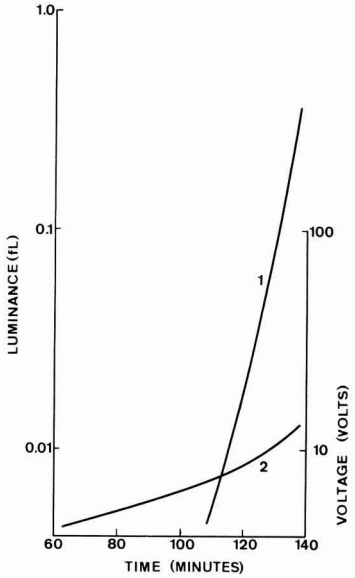

Fig. 3. Time-dependence of voltage and luminance for constant current for film 5-31. 1, Luminance; 2, voltage.

down voltage is approached the device becomes very noisy and final destructive break-down is preceded by numerous voltage spikes to low resistance values. Near break-down the luminance reaches a maximum value and decreases again. This decrease can be explained by the observation that near break-down individual portions of the device extinguished. Consequently the photometer, integrating over a large portion of the device, records a decreasing luminance.

In order to determine the change of the device characteristics as a result of operation, the V-L-I characteristics were plotted periodically. In earlier experiments it had been established that interrupting the current through a device did not result in a relaxation to a lower voltage on turning the current back on. It could be assumed, therefore, that the characteristics at any point in time described the degree of change in the device. To ensure that the measurements of the V-L-I curves did not affect the device significantly the current was limited to a range less than 1 mA.

The variation of voltage with current is shown in Fig. 4. It appears that the device was initially linear, but with operation became increasingly nonlinear and asymmetrical. Measurable emission started as the device became nonlinear and was macroscopically uniform over the entire electrode area.

Electroluminescent devices are often described by their L-V curve. The interpretation of the electroluminescence mechanism is also often based on this relationship. For the film already described the L-V graph at various points during its operating life is given in Fig. 5. It is noticed that the curves are parallel and progressively displaced to higher voltage values.

The L-I characteristics are shown in Fig. 6. It is observed that emission efficiency (in fL/mA) increases both with time of operation and, for small values of current, with current. For large currents near break-down, as for example curve 4, the efficiency decreases presumably as active areas of the device are eliminated.

In order to determine to what extent the change that had occurred during operation was irreversible, several films were operated under conditions where the voltage polarity was regularly reversed. At no point could the previous characteristics be regained. Although a minor degree of recovery occurred, a permanent change had been established that modified the device characteristics.

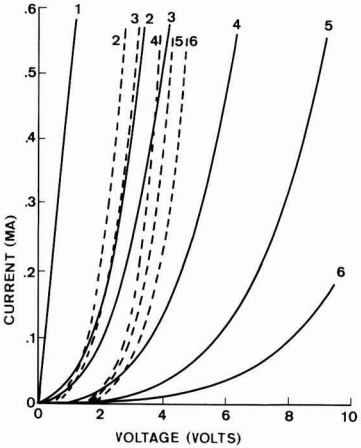

Fig. 4. For film 5-31, voltage variation with current after operating device for the following period: 1, start; 2, 72 min; 3, 117 min; 4, 133 min; 5, 141 min; 6, 157 min. Solid line: aluminum electrode positive; dashed line: aluminum electrode negative.

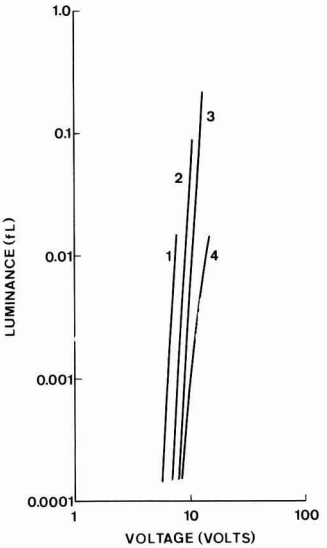

Fig. 5. For film 5-31, luminance variation with voltage after operating device for following period: 1, 117 min; 2, 133 min; 3, 141 min; 4, 157 min.

To establish whether the time-dependent effects observed could be associated with the formation of an oxide between the film and the aluminum electrode (15) the measurements were repeated on a matrix of devices which included a SiO layer between the film and the opaque electrodes, for which a number of different metals were used. For this case it was observed that emission commenced on first applying a voltage to the device, but that the same shift in characteristics occurred as with devices that did not have an oxide layer, and that in the presence of the oxide layer metals other than aluminum also led to electroluminescence.

Discussion

The terms forming and aging, as applied to thin films of ZnS:Mn,Cu,Cl, are commonly used to refer to apparently identifiable distinct processes. Thus, the virgin device on first application of a voltage under-

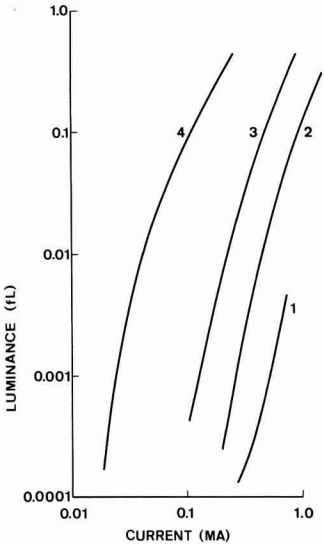

Fig. 6. For film 5-31, luminance variation with current after operating device for following period: 1, 117 min; 2, 133 min; 3, 141 min; 4, 157 min.

goes forming, whereupon electroluminescence is possible. Once emission has been achieved, the film is subject to aging, or decrease in luminance on constant voltage operation. The observations reported in this paper suggest that forming and aging are two labels that are convenient but arbitrary in the description of the time-dependent behavior of the devices under operation, since they reflect practical aspects of the devices rather than any distinct phase of device change.

For every device investigated electroluminescence was associated with nonlinear I-V characteristics. The initial linear I-V curve, not observed in the experiments with an additional oxide layer, is probably caused by parasitic conductive paths which must be eliminated for electroluminescence to occur.

Two possible explanations for the shift in device characteristics suggest themselves: the growth of an oxide layer at the aluminum electrode, and a change in the bulk of the film. The observation that, in the presence of a SiO layer, the shift in device characteristics occurred with metals other than aluminum would indicate that the formation of an aluminum oxide layer probably serves to eliminate parasitic conductive paths, but that changes in the film bulk cause the observed shift.

The nature of the change in the ZnS:Mn,Cu,Cl films has not been conclusively demonstrated. In the fabrication of certain types of rectifiers and transistors an electronically active region is created by a "forming" process that involves substantial ionic current (16). It is proposed that, in view of the concentration of copper in the films greatly in excess of the solubility (17), copper ions diffuse to capturing boundaries creating electronically active phases of Cu_xS (18, 19) and leading to an electroluminescence mechanism described by Vlasenko and Gergell (20). The constancy of slope of the shifted I-V curves and the increasing efficiency with operation of the devices support this interpretation.

Acknowledgments

This investigation was made possible by the support received from the Canadian Westinghouse Company, and by the encouragement and advice given by Professor G. Dick of the University of Toronto.

Manuscript submitted May 26, 1969; revised manuscript received June 15, 1970.

Any discussion of this paper will appear in a Discussion Section to be published in the June 1971 JOURNAL.

REFERENCES

1. A. G. Fischer, in "Luminescence of Inorganic Solids," p. 541, P. Goldberg, Editor, Academic Press, New York (1966).
2. F. F. Morehead, in "Physics and Chemistry of II-VI Compounds," p. 613, M. Aven and J. S. Prener, Editors, North-Holland Publishing Co., Amsterdam (1967).
3. P. Goldberg, in "Luminescence of Inorganic Solids," p. 385, P. Goldberg, Editor, Academic Press, New York (1966).
4. D. A. Cusano, Ph.D. thesis, Troy, 1959.
5. P. Goldberg and J. W. Nickerson, *J. Appl. Phys.*, **34**, 1601 (1963).
6. G. A. Antcliffe, Ph.D. thesis, Adelaide, 1964.
7. W. A. Thornton, N. T. D. C. Research Report BL-R-6-2329-JE3-11 (1962).
8. S. Roberts, *J. Appl. Phys.*, **28**, 2 (1957).
9. E. J. Soxman, JANAIR Report EL-1 (1965).
10. W. Riemer, Ph.D. thesis, Toronto, 1968.
11. W. A. Thornton, U.S. Pat. 3,044,902 (1962).
12. R. E. W. Lake, DIR Semi-annual Report No. 1 (1963).
13. L. R. Koller and H. D. Coghill, *This Journal*, **107**, 973 (1960).
14. J. F. O'Hanlon and R. R. Haering, *Rev. Sci. Instr.*, **38**, 1542 (1967).
15. J. L. Plumb and R. F. Cotellessa, Paper 46 presented at the Boston Meeting of the Society, May 5-9, 1968.
16. M. J. O. Strutt, in "Semiconductor Devices," Vol. 1, Academic Press, New York (1966).
17. A. A. Bundel *et al.*, *Bull. Acad. Sci. USSR, Phys. Series*, **30**, 656 (1966).
18. S. G. Ellis, *J. Appl. Phys.*, **38**, 2906 (1967).
19. S. Ruben, *Trans. Electrochem. Soc.*, **87**, 275 (1945).
20. N. A. Vlasenko and A. N. Gergell, *Phys. Stat. Sol.*, **26**, K77 (1968).

Luminescence of Pr^{+3} Activated Y_2O_2S

Lyuji Ozawa* and Philip M. Jaffe*

Zenith Radio Corporation, Chicago, Illinois 60639

ABSTRACT

The luminescent properties of the green emitting $Y_2O_2S:Pr^{+3}$ have been studied. The emission lines in the visible region are assigned to the transitions from $^3P_0$ to ^3H_J and to $^3F_2$ of Pr^{+3}; the main green emission lines around 514 nm are attributed to the transition $^3P_0 \rightarrow {}^3H_4$. There was a small shift, about 160 cm^{-1}, of the emission lines to higher energy with an increase in host cation radius (Y to Gd to La). The two broad excitation bands in $Y_2O_2S:Pr^{+3}$, centered at 255 and 290 nm, are due, respectively, to host excitation and to excitation associated with an interaction of activator and host. The optimum activator concentration of $Y_2O_2S:Pr^{+3}$ phosphor is at about 1×10^{-2} mole Pr_2O_2S per mole of phosphor. Quadrupole-quadrupole interaction is involved in the concentration quenching of the green emission.

Y(Gd and La)$_2O_2S:Pr^{+3}$ phosphors[1] emit a green emission under cathode-ray or ultraviolet excitation (1, 2). The energy levels of Pr^{+3} in $PrCl_3$ (3, 4), in $LaBr_3$ (5, 6), in YCl_3 (7), in other crystals (8, 9), and in the vapor state (10) have been studied in detail from their absorption and fluorescent spectra. However, it is somewhat difficult to assign the electronic transitions within the Pr^{+3} ($4f^2$) configuration which are responsible for the emission and excitation lines in Y(Gd and La)$_2O_2S$ because there is some discrepancy, about 400 to 1800 cm^{-1}, between the positions of the observed emission and excitation lines of Y(Gd and La)$_2O_2S$:Pr phosphors and the positions of the lines reported in ref. (3)-(10).

In this paper, the assignment of the emission and excitation lines of Y_2O_2S:Pr phosphor is made by comparison with the energy levels of Pr^{+3} in YCl_3. The small shift of the Pr^{+3} emission lines with a change in host cation radius, the origin of the two broad excitation bands, the optimum activator concentration, and the concentration quenching mechanism of the Pr^{+3} emission in Y_2O_2S are also reported.

Experimental

The rare earths used[2] were yttrium oxide 6*N*, gadolinium oxide and lanthanum oxide 5*N*, and praseodymium oxide 3*N*. The rare earth oxide as host component and praseodymium oxide were dissolved in hot nitric acid and precipitated with oxalic acid. The precipitate was dried, then heated in air at 900°C for 2 hr to convert to the oxide, using alumina crucibles. This mixed oxide (1 mole) plus sulfur (3 moles) and sodium carbonate as flux (1 mole) were mixed in a mortar and then fired at 1100°C for 2 hr in air. After firing, the samples were washed with hot deionized water several times. By this treatment, residual sulfur and sodium compounds were removed from the phosphors. The samples obtained were confirmed as the oxysulfide by x-ray diffraction analysis.

The emission, excitation, diffuse reflectance spectra, and cathodoluminescence data were obtained with the equipment described elsewhere (11). No correction of the emission spectra was made for the spectral response of the monochromator and photomultiplier. The concentration dependence of the intensity of selected lines was determined from the recorded emission spectra by measuring their amplitudes.

* Electrochemical Society Active Member.

Key words: multipolar interaction, concentration dependence, excitation spectra, transition, emission line shift.

[1] The Pr^{+3} was substituted for a portion of the rare earth host cation in all preparations as for example $(Y_{1-x}Pr_x)_2O_2S$. However, the conventional phosphor notation will generally be used, *i.e.*, Y_2O_2S:Pr. Unless indicated otherwise, Pr is always trivalent.

[2] Obtained from Lindsey Division, American Potash and Chemical Corporation.

Results and Discussion

Assignment of lines of Pr^{+3}.—The emission and excitation spectra of Y_2O_2S:Pr phosphor were similar to the spectra of Gd_2O_2S:Pr and of La_2O_2S:Pr phosphors. For this reason, the spectrum of the Y_2O_2S:Pr phosphor is primarily discussed in this paper. The small differences between the emission spectra of the Y(Gd and La)$_2O_2S$:Pr phosphors will be discussed in the section on Effect of host cation radius on the emission line wavelength.

The emission spectrum of Y_2O_2S:Pr phosphor under 254 nm radiation from a low-pressure mercury lamp is shown in Fig. 1. No change of the emission spectrum was observed under excitation by other wavelengths or by cathode rays. In Fig. 1, the weak emission lines at wavelengths longer than 540 nm are also shown with higher magnification (about 10 times). The emission spectrum consists of lines ranging from about 470 to 700 nm. The main group, which consisted of many lines, peaks at about 514 nm, so that the emission color of the phosphor appears green. The Y_2O_2S:Pr emission spectrum is due to the transitions between the energy levels of the $4f^2$ configuration of Pr^{+3}.

The position of the lines and bands in the excitation spectrum of the 514 nm emission was coincident with the position of the lines and bands in the excitation spectrum of the 670 nm emission. Since the direct excitation spectrum of the 670 nm emission clarified to a greater extent the distinctions between the excitation lines, a study of the excitation spectrum of the 670 nm emission was made.

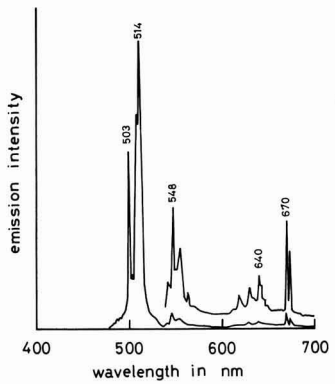

Fig. 1. Emission spectrum of $Y_2O_2S:Pr^{+3}$ phosphor. Above 540 nm the highly magnified spectrum is also shown.

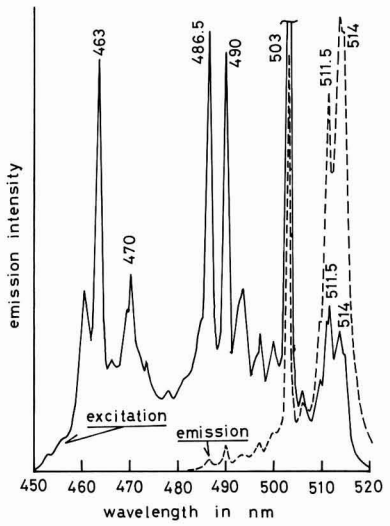

Fig. 2. Detail excitation and emission spectra of $Y_2O_2S:Pr^{+3}$ phosphor. The lines are assigned as the transition between ground level $^3H_4$ and excited levels.

The excitation spectrum of the 670 nm emission consisted of two broad and strong bands centered at about 255 and 290 nm, respectively, and of several weak lines at wavelength longer than 450 nm. The broad excitation bands are described in more detail below. The direct (line) excitation spectrum is shown in Fig. 2. Figure 2 also gives the green emission spectrum of $Y_2O_2S:Pr$ obtained with 290 nm excitation. The emission lines coincided in position with the excitation lines for the 670 nm emission. The direct excitation spectrum of $Y_2O_2S:Pr$ was classified into three groups: 463, 486.5, and 503 nm. These excitation lines may be attributable to direct transitions from the $^3H_4$ ground level to the excited levels of the Pr^{+3} ion. However, as shown in Table I the positions of the lines were about 1800 cm^{-1} lower in energy from those for the free ion (12). The large differences of the energy level positions between free Pr^{+3} and Pr^{+3} in Y_2O_2S is due to the fact that the position of the J levels of Pr^{+3} in crystals depends on bonding character of Pr^{+3} with the nearest neighbor anions and that the separation decreases in energy with an increase in covalent bonding (5, 9). Ionic character of bonding increases with an increase in electronegativity of the elements.

The Pr^{+3} energy levels which participate in the direct excitation and emission lines of $Y_2O_2S:Pr$ phosphor are comparable to the energy levels of Pr^{+3} in YCl_3 which may have a little more ionic bonding than Y_2O_2S. By assuming that the position of the energy levels of ^3P_J Pr^{+3} in Y_2O_2S is about 400 cm^{-1} lower than the corresponding position of the energy levels of Pr^{+3} in YCl_3 (7) because of more covalent bonding than in the chloride, the groups of the direct excitation lines of $Y_2O_2S:Pr$, 463, 486.5, and 503 nm, can be attributable to the transitions from the Pr^{+3} ground level $^3H_4$ to the excited levels $^3P_2$, $^3P_1$, and $^3P_0$, respectively. The strong excitation lines at 486.5 and 490 nm in Fig. 2 may be due to transitions to the sublevels of $^3P_1$ which is split by the crystal field. There may be a line around 480 nm which corresponds to the transition $^3H_4 \rightarrow {}^1I_6$ but it is too weak to verify. The weak excitation lines at wavelengths longer than 503 nm in Fig. 2 are attributable to the transitions from the $^3H_4$ ground level, which is split into many levels by the Stark effect, to the $^3P_0$ which is not split.

Table I. ^3P_J and $^1I_6$ excited energy levels of free Pr^{+3} and Pr^{+3} in yttrium compounds

Energy levels	Free ion* cm⁻¹	nm	YCl_3* cm⁻¹	nm	Y_2O_2S cm⁻¹	nm
$^3P_0$	21,390	466	20,214	495	19,460†	514
					19,880	503
$^3P_1$	22,007	455	20,831	480	20,400	490
					20,580	486
$^1I_6$	22,211	450	21,076	474		
$^3P_2$	23,161	431	21,867	457	21,320	469

* From ref. (7).
† Fluorescent main line.

In the emission spectrum of $Y_2O_2S:Pr$ shown in Fig. 1, there are no emission lines originating from the levels above $^3P_0$ because there is no change of the emission spectrum of $Y_2O_2S:Pr$ under direct excitation of the $^3P_0$, $^3P_1$, or $^3P_2$ levels, *i.e.*, with 503, 486.5, and 463 nm radiation, respectively. The emission lines of the $Y_2O_2S:Pr$ spectrum consisted of four main lines, 514, 548, 640, and 670 nm. These were attributable to the transitions from $^3P_0$ to $^3H_4$, $^3H_5$, $^3H_6$, and $^3F_2$, respectively.

The transition between $^3P_0$ and $^3H_4$ is an electric dipole transition (3, 13) and this transition is allowed when a Pr^{+3} ion occupies a lattice site lacking a center of symmetry. The crystal structure of Y(Gd and La)$_2O_2S$ crystals belongs to the D_{3d} space group and the rare earth cation site symmetry is C_{3v}(3m) (14). The rare earth ion is coordinated with seven anions; four oxygens and three sulfurs, having different bonding lengths; 2.23 and 2.90Å. The Pr^{+3} ions are expected to occupy the cation sites in Y(Gd and La)$_2O_2S$ crystals, so that electric dipole transition which give rise strong emission is allowed.

Effect of host cation radius on the emission line wavelength.—It was observed that the positions of the emission lines of Pr^{+3} in Y, Gd, and La oxysulfide phosphors did change with wavelength with a change in host cation. Since these oxysulfides all have the La_2O_3 structure, the change in line position must be due to a change in the crystal field caused by the change in host cation. Figure 3 gives the relationship between the wavelength (in cm^{-1}) of several emis-

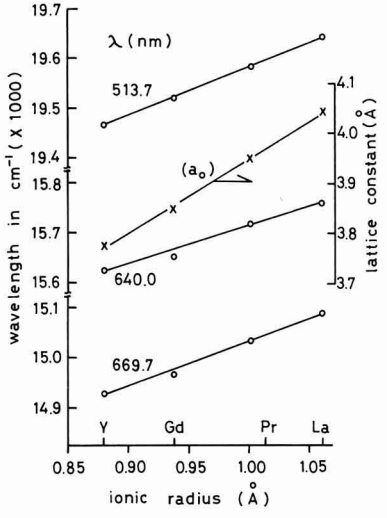

Fig. 3. Relationship between the position of the emission lines and ionic radius of rare earth cation in Y(Gd and La)$_2O_2S$. Lattice constant a_0 also indicated in the figure.

sion lines and the lattice constants as determined by x-ray analysis *vs.* the cation radius (15) of the host crystal. The wavelengths of the emission lines of Pr^{+3} in $(La_{0.5}Gd_{0.5})_2O_2S$ and its lattice constant are also plotted in Fig. 3.

All of the emission lines in the visible region shifted linearly to higher energies when the ionic radius of the rare earth cation increased, Fig. 3. The slope of the curves for 513.7 and 669.7 nm emission lines coincided with each other because the emitting level of all of these lines was the Pr^{+3} $^3P_0$ level. Because of their weak intensity, it was difficult to study the emission lines due to other emitting levels. From the slope of Fig. 3, the emission line shifted about 90 cm^{-1} when the cation radius changed by 0.1Å. The linear shift in spectral lines of Pr^{+3} in rare earth (Gd to La) trichlorides with cation radius have been reported by McLaughlin and Conway (16) and by Dieke (7). However, the shift in the rare earth trichlorides, about 50 cm^{-1} per 0.1Å change in radius is smaller than the shift observed in the rare earth oxysulfides.

The shift of emission with a change in host cation can be explained in the following way: Since the ionic radius of Pr^{+3} is 1.01Å and of La^{+3} is 1.06Å, Pr^{+3} ions substitute for La^{+3} in La_2O_2S crystal with little lattice distortion. On the other hand, in Gd_2O_2S and Y_2O_2S crystals, the Pr^{+3} ions would be incorporated with a perturbation because of the smaller radius of Gd^{+3} (0.99Å) and of Y^{+3} (0.88Å). The distortion of the Pr^{+3} center increases with a decrease in lattice constant. This distortion results in the lowering of the excited level $^3P_0$ of the Pr^{+3} ions.

The shift of the wavelength position of the emission lines of Eu^{+3} in Y(Gd and La)$_2O_2S$ with cation radius was also observed. However, the shift was half of that of Pr^{+3}. The small shift may be caused by the small difference in ionic radius between Eu^{+3} (0.95Å) and Y^{+3} and Gd^{+3}.

Excitation spectrum.—As already described in the section Assignment of lines of Pr^{+3}, the excitation spectrum of Pr^{+3} in Y_2O_2S crystals consisted of two strong broad bands centered at about 255 and 290 nm, respectively, and of many weak lines which were due to the direct excitation of the Pr^{+3} excited levels. These direct excitation lines were already described in the above mentioned section. This section discusses the origin of the broad excitation bands.

For this study, samples of $(Y_{1-x}Pr_x)_2O_2S$ were prepared in which x varied from 10^{-5} to 10^{-1}.

The broad excitation spectra obtained with representative samples are shown in Fig. 4. The relative number of quanta of each curve are comparable to each other. The 290 nm band increased with increasing praseodymium concentration, whereas the 255 nm band stayed relatively constant. The above results are more easily seen in the concentration

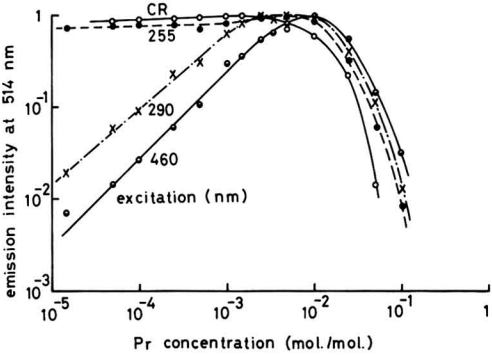

Fig. 5. Concentration dependence curves of $Y_2O_2S:Pr^{+3}$ phosphor under cathode-ray (CR), 255, 290, and 460 nm excitation.

dependence curves of the emission intensity of Y_2O_2S:Pr phosphors under various excitation modes, as shown in Fig. 5.

Since the emission intensity under 255 nm excitation was maintained at about constant level, the indication is that the amount of the energy absorbed by this excitation was independent of the activator concentration and that a constant portion of the absorbed energy was transferred to the Pr^{+3} activator ions. Therefore, it could be inferred that the 255 nm excitation band was due to the host excitation.

The emission intensity under 290 and 460 nm excitation increased linearly and with the same slope with an increase in praseodymium concentration when the praseodymium concentration was below about 1 x 10^{-3} mole Pr_2O_2S per mole of phosphor, Fig. 5. The 460 nm excitation is the direct Pr^{+3} ($4f^2$) excitation. Reflectance spectra of Y_2O_2S:Pr with various praseodymium concentration are shown in Fig. 6. When the praseodymium concentration increased, the reflectance at 290 nm decreased. From the above results, it was inferred that the 290 nm broad excitation band was due to the excitation associated with the Pr^{+3}.

Several lines superimposed on the broad excitation bands of Gd_2O_2S:Pr phosphors were observed at room temperature. The recorded uncorrected excitation spectrum of Gd_2O_2S:Pr (1 x 10^{-3} mole Pr_2O_2S) phosphor to give the 514 nm emission is given in Fig. 7. There are lines at 314, 307, 303, 282, 278, and 275 nm. These lines could be identified as the direct transitions from the ground level $^8S_{7/2}$ to the excited levels ^6P_J and ^6I_J of Gd^{+3} (17). The quantitative data on the energy transfer efficiency in mixed $(Y,Gd)_2O_2S$:Pr phosphors as a function of gadolinium concentrations were not obtained because of strong broad excitation

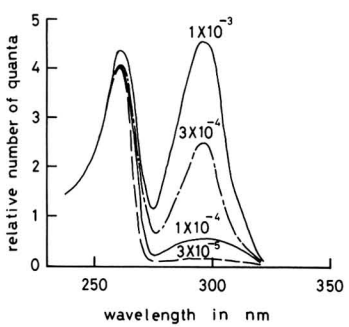

Fig. 4. Broad excitation spectra of $Y_2O_2S:Pr^{+3}$ phosphors having various activator concentrations.

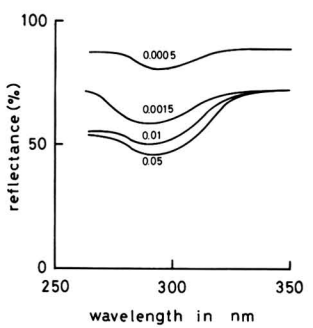

Fig. 6. Reflectance spectra in u.v. region of $Y_2O_2S:Pr^{+3}$ phosphor having various activator concentrations.

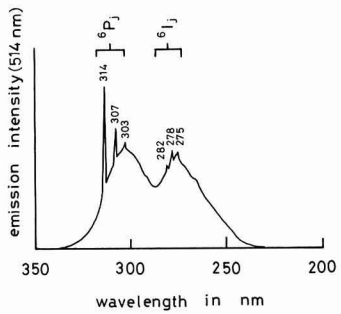

Fig. 7. Recorded excitation spectrum (uncorrected) of the green emission of $Gd_2O_2S:Pr^{+3}$ phosphor. Lines superimposed on the broad bands are believed due to absorption by paired gadolinium ions.

bands. However, there was evidence of the energy transfer from trivalent gadolinium to Pr^{+3} resulting in Pr^{+3} emission for the samples containing above 0.01 mole gadolinium, but there was no evidence of energy transfer below 0.005 mole gadolinium. This result is similar to that obtained with mixed $(Y,Gd)_2O_3$ phosphors activated with the rare earths where the energy transfer involved pairs of trivalent gadolinium ions (17). Therefore, it is deduced that the energy transfer from gadolinium to Pr^{+3} emission in $Gd_2O_2S:Pr$ may occur in a similar way.

Concentration dependence.—As already shown in Fig. 5, the optimum praseodymium concentration markedly changed with a change in the exciting modes: 0.25 m/o (mole per cent) under cathode rays, 0.3 m/o under 255 nm, 0.5 m/o under 290 nm, and 1.0 m/o under 460 nm.

Since the weighted number of nearest neighbor cation sites of Y_2O_2S crystal is twelve, the optimum activator concentration should be at 0.08 mole, if the concentration quenching is due to a decrease in the concentration of the isolated single activator ions (18). If so, an electrostatic multipolar interaction is involved in the concentration quenching (19).

When electrostatic multipolar interactions are involved in concentration quenching, the observed emission intensity I_{ob} as a function of the activator concentration is given by the following expression (20)

$$I_{ob} = KI_o\,[1 - \exp(-\alpha C)]\,[1 + \beta\,(C)^{\theta/3}]^{-1} \quad [1]$$

where I_o is intensity of the exciting light, α effective absorption coefficient for the exciting light, C activator concentration, β a constant for each interaction in a given structure, θ is 6, 8, or 10 for dipole-dipole, dipole-quadrupole, quadrupole-quadrupole interaction, respectively, and K is a constant. This expression indicates that the optimum activator concentration is not only a function of the luminescent centers but also of the absorption coefficient for exciting radiation. The experimental results agree qualitatively with the results predicted by expression [1]. Since it is difficult to determine the α value of powder phosphors, no quantitative analysis could be done. For the exciting radiation used here, Fig. 5, the absorption coefficient decreased with exciting wavelengths. For a weak absorbing exciting radiation, Eq. [1] becomes

$$I_{ob}/C = A\,[1 + \beta\,(C)^{\theta/3}]^{-1} \quad [2]$$

The value of θ for the green emission of Pr^{+3} (514 nm) in Y_2O_2S was 10.5 as indicated in Fig. 8. Therefore, quadrupole-quadrupole interaction ($\theta = 10$) was involved in the concentration quenching of the green emission of $Y_2O_2S:Pr$ phosphor. This result agrees closely with the result which quadrupole-quadrupole interaction predominantly involved in the concentration quenching of Pr^{+3} emission in LaF_3 (21). When the interaction of Pr^{+3} ions with each other increases as the praseodymium concentration increases, the excited electrons in the $^3P_0$ level of one Pr^{+3} ion relax to $^1D_2$. This relaxation energy $^3P_0 \rightarrow {}^1D_2$, 3800 cm^{-1}, is simultaneously transferred to other Pr^{+3} ions by the transition $^3H_4 \rightarrow {}^3H_6$, 4100 cm^{-1}. Because the ground level $^3H_4$ of Pr^{+3} in Y_2O_2S crystal is split into many levels (maximum of $2J + 1$) with energy difference of 450 cm^{-1}, the energy difference of 300 cm^{-1} is inconsequential and the energy transfer from $^3P_0 \rightarrow {}^1D_2$ to $^3H_4 \rightarrow {}^3H_6$ occurs readily.

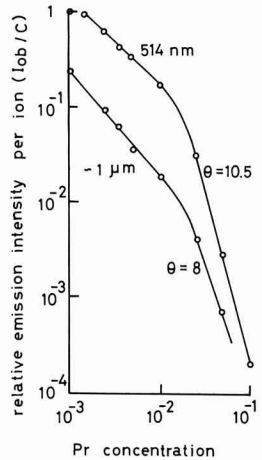

Fig. 8. Relative emission intensity from $^3P_0$ (514 nm) and from $^1D_2$ (~1 μm) per one Pr^{+3} ion (I_{ob}/C) of $Y_2O_2S:Pr^{+3}$ phosphor. θ values for 514 nm emission is 10.5 and for the 1 μm emission is 8. Concentration is mole Pr_2O_2S per mole phosphor.

When a multipolar interaction is involved in emission quenching, the decay time of the emission should vary according to the intensity of the multipolar interaction. Since the decay time of the green emission of $Y_2O_2S:Pr$ was very fast, several microseconds, the change of the lifetime due to multipolar interaction could not be detected in this study.

The optimum activator concentration of the emission from the lowest emitting levels of Eu^{+3} and of Tb^{+3} in Y_2O_2S is 0.08 mole fraction (20). However, the optimum activator concentration for the emission line from the lowest emitting level of Pr^{+3}, $^1D_2$, λ about 1 μm, was about 1×10^{-2} mole fraction. The slope of the (I_{ob}/C) curve was 8/3 as shown in Fig. 8. Thus dipole-quadrupole interaction was involved in the concentration quenching of the Pr^{+3} $^1D_2$ emission line. The transition responsible for this interaction is

$$^1D_2 \rightarrow {}^1G_4\ (6700\ cm^{-1});\ {}^3H_4 \rightarrow {}^3F_4\ (6600\ cm^{-1})$$

Under cathode-ray excitation, all of the excitation modes are involved in the excitation process. However, the host excitation may be dominant among these excitation modes. If so, then the concentration dependence curve for cathode-ray excitation of the phosphors which have a host excitation band should be similar to the concentration dependence curve under host excitation. As shown in Fig. 5, the concentration dependence curves obtained by cathode-ray excitation are indeed very similar to the concentration dependence curve obtained by 255 nm host excitation.

The green emission of $Y_2O_2S:Pr$ phosphor under cathode-ray excitation had good response to high current, *i.e.*, did not saturate at relatively low current densities like sulfide phosphors. Since the lifetime of the electrons remaining in the excited level $^3P_0$ is

very short, the saturation of the excited electrons in $^3P_0$ does not occur until very high beam current excitation. Therefore, the green emission of Y_2O_2S:Pr may be used as the green component in projection-type color TV picture tubes.

Conclusion

Y_2O_2S:Pr phosphors emit a green fluorescence under excitation by short u.v. and by cathode rays. The energy level assignment of the Pr^{+3} lines was made by the reference to the transitions within Pr^{+3} in YCl_3. In Y_2O_2S:Pr, all of the emission lines in the visible region are attributed to the transitions from $^3P_0$. The green emission lines around 514 nm are due to the transitions from $^3P_0$ to the ground level $^3H_4$ which is split into many levels with energy difference of about 450 cm^{-1}.

All of the emission lines of Pr^{+3} in Y(Gd and La)$_2O_2S$ shifted linearly to higher energy when the ionic radius of the rare earth host cation increased. This change was related to the distortion of the lattice caused by the change in size of the host cation.

The excitation spectrum consisted of two broad bands centered at 255 and 290 nm and of weak lines located around 480 nm. The latter is due to the direct excitation of Pr^{+3}. It is inferred that the 255 nm excitation band is due to host excitation and that the 290 nm excitation band is due to the excitation associated with an interaction of activator and host. The energy transfer from a pair of gadolinium ions to Pr^{+3} was observed. The optimum Pr^{+3} concentration in Y_2O_2S:Pr is around 1 x 10^{-2} mole Pr_2O_2S per mole of phosphor. Quadrupole-quadrupole interaction is involved in the concentration quenching of the green emission. The concentration dependence curve under cathode-ray excitation is almost identical to that obtained by host excitation indicating that the two process are similar.

Acknowledgment

The authors wish to thank Mrs. H. Stanczyk for her assistance in preparation of samples, Mr. L. Flemming for cathodoluminescent data, and Dr. G. Arai for x-ray data.

Manuscript submitted Feb. 20, 1970; revised manuscript received June 10, 1970. This was Late News Paper 329 presented at the New York Meeting of the Society, May 4-9, 1969.

Any discussion of this paper will appear in a Discussion Section to be published in the June 1971 JOURNAL.

REFERENCES

1. L. Ozawa, *Oyo Butsuri* (Applied Physics), **37,** 80 (1968) in Japanese.
2. M. R. Royce and A. L. Smith, Extended Abstract 34, Boston Meeting, Electrochemical Society, May 5-9, 1968.
3. G. H. Dieke and R. Sarup, *J. Chem. Phys.*, **29,** 741 (1958).
4. J. S. Morgolis, *ibid.*, **35,** 1367 (1961).
5. E. Y. Wong and I. Richman, *ibid.*, **36,** 1889 (1962).
6. N. H. Kiess and G. H. Dieke, *ibid.*, **45,** 2729 (1966).
7. G. H. Dieke, "Spectra and Energy Levels of Rare Earth Ions in Crystals," p. 200, Interscience Publishers, New York (1968).
8. J. B. Gruber, *J. Chem. Phys.*, **38,** 946 (1963).
9. E. Y. Wong, O. M. Stafsudd, and D. R. Johnston, *ibid.*, **39,** 1037 (1963).
10. J. Sugar, *Phys. Rev. Letters*, **14,** 731 (1965).
11. P. M. Jaffe and J. D. Konitzer, *This Journal*, **116,** 633 (1969).
12. H. M. Crosswhite, G. H. Dieke, and Wm. J. Carter, *J. Chem. Phys.*, **43,** 2047 (1965).
13. E. V. Sayre, K. M. Sancier, and S. Freed, *ibid.*, **23,** 2060 (1955).
14. O. J. Sovers and T. Yoshioka, *ibid.*, **49,** 4945 (1968).
15. J. A. Gibson and G. S. Harvey, Air Force Materials Laboratory, Wright-Patterson AFB, Technical Report AFML-TR-65-430, (1966).
16. R. D. McLanghlin and J. G. Conway, *J. Chem. Phys.*, **38,** 1037 (1963).
17. L. Ozawa and S. Nishikawa, *Japan. J. Appl. Phys.*, **7,** 1354 (1968).
18. L. G. Van Uitert and L. F. Johnson, *J. Chem. Phys.*, **44,** 3514 (1966).
19. D. L. Dexter and J. H. Schulman, *ibid.*, **22,** 1063 (1954).
20. L. Ozawa, H. Forest, P. M. Jaffe, and G. Ban, Extended Abstract 45, Los Angeles Meeting, Electrochemical Society, May 10-15, 1970.
21. M. R. Brown and J. S. S. Whiting, *J. Chem. Phys.*, **43,** 1 (1965).

Calculation of the Ga-In-P Ternary Phase Diagram Using the Quasi-Chemical Equilibrium Model

G. B. Stringfellow

Hewlett-Packard Company, Palo Alto, California 94304

ABSTRACT

The Ga-In-P solid-liquid-vapor equilibrium phase diagram has been calculated based on the quasi-chemical equilibrium solution model. The calculated phase diagram, both isothermal liquidus and iso-(solid concentration) lines, and P_2 and P_4 vapor pressure curves, is found to be in agreement with recently published experimental data.

The thermodynamic properties of the III-V binary system In-As, Ga-As, and In-Sb have been calculated using the quasi-chemical equilibrium (QCE) treatment of the lattice solution model (1-2). A method of calculating a general III-V ternary phase diagram was also presented in ref. (2) and applied to the calculation of the In-As-Sb and Ga-In-As systems. Because of the lack of experimental data, the accuracy of the calculated ternary phase diagrams could not be adequately tested. The Ge-Si-Sn and Ge-Si-Pb phase diagrams, calculated using the QCE treatment, were found to be in excellent agreement with experimental phase diagram data (3).

Recently, experimental phase diagram data has been obtained for the system Ga-In-P (4-5). It is the purpose of this paper to compare the calculated phase diagram with the experimental data for the system Ga-In-P and thus test the accuracy of the QCE cal-

Key words: gallium-indium-phosphorus system, calculated phase diagram.

culation and present the entire Ga-In-P solid-liquid-vapor equilibrium phase diagram.

Calculation of Ga-In-P Phase Diagram

The calculation is based on the quasi-chemical equilibrium (QCE) model. The major assumptions on which this model is based are:

1. Each atom has Z nearest neighbors.
2. Nearest neighbors interact pairwise with the temperature and composition independent interaction parameter, Ω, defined as

$$\Omega_{AB} = Z[H_{AB} - \tfrac{1}{2}(H_{AA} + H_{BB})]$$

where H_{ij} is the energy of an i-j nearest neighbor pair.

3. Only the configurational free energy of mixing is considered, *i.e.*, the vibrational free energy of mixing is neglected.
4. The distribution of constituent atoms is calculated using a mass action-like expression

$$N_{ij}N_{jj}/(N_{ij})^2 = \tfrac{1}{4}\exp(2\Omega_{ij}/ZRT)$$

where i and j each represent either A, B, or C.

The equilibrium equations for the (ternary liquid)-(binary solid) equilibrium may be written

$$\ln(\gamma_{AC}X) = \ln\left(\frac{4\gamma_A\gamma_C N_A N_C}{\gamma^{s.l.}{}_A\gamma^{s.l.}{}_C}\right) + \Delta S^F{}_{AC}(T^F{}_{AC} - T)/RT \quad [1a]$$

$$\ln\gamma_{BC}(1-X) = \ln\left(\frac{4\gamma_B\gamma_C N_B N_C}{\gamma^{s.l.}{}_B\gamma^{s.l.}{}_C}\right) + \Delta S^F{}_{BC}(T^F{}_{BC} - T)/RT \quad [1b]$$

$$N_A + N_B + N_C = 1 \quad [1c]$$

The activity coefficients, γ_{ij}, in the ternary liquid phase cannot be expressed analytically but are computed numerically in terms of temperature and composition using the QCE model. The activity coefficients in the solid phase may be written

$$\gamma_{AC} = \left(\frac{\beta - 1 + 2X}{X(\beta+1)}\right)^{Z/2}$$

$$\gamma_{BC} = \left(\frac{\beta + 1 - 2X}{(1-X)(\beta+1)}\right)^{Z/2}$$

where

$$\beta = [1 + 4X(1-X)(\eta^2 - 1)]^{1/2}$$

$$X = N_{AC}/(N_{AC} + N_{BC}) \text{ and } \eta = \exp(\Omega_{AC-BC}/ZRT)$$

For the zinc blende lattice, where AC-BC interactions are considered, the appropriate value of Z is 12.

Using the activity coefficients calculated from the QCE model, Eq. [1a-c] can be solved numerically with N_A and N_C given to yield N_B, X, and T. A detailed description of the calculation is given in ref. (2).

The equilibrium P_2 and P_4 pressures over the liquidus surface were calculated from the following equilibrium equations

$$P_{P_4} = P^\circ{}_{P_4}(N_A\gamma_A)^4$$
$$P_{P_4}{}^2/P_{P_4} = K_P(T)$$

where $P^\circ{}_{P_4}$, the P_4 pressure over pure liquid phosphorus, and $K_P(T)$ may be calculated from data available in the JANAF Tables (6).

The parameters used in the calculation are listed in Table I. The In-Ga interaction parameter was determined by Macur, Edwards, and Wahlbeck (7). The In-P and Ga-P interaction parameters were obtained by making a least squares fit of the calculated binary phase diagrams to the experimental data (8-10) (see Fig. 1). The entropy (11) and temperature (11-14) of fusion for InP and GaP were extracted from the literature. The only parameter not available from binary data is the $InP_{(s)}$-$GaP_{(s)}$ interaction parameter. It was obtained by constraining the solid in equilibrium with a liquid composed of 35% Ga, 50% In, 15% P, to be 97.2% GaP, as per Panish's data (4). It was found that the liquid composition in equilibrium with a given solid near pure GaP is the variable most sensitive to the InP-GaP interaction parameter.

Table I. Parameters used in the QCE calculation of the Ga-In-P phase diagram

Parameter	Value used in the calculation
$T^F{}_{GaP}$	1740°K (11-13)
$T^F{}_{InP}$	1333°K (10)
$\Delta S^F{}_{GaP}$	16.25 eu* (10)
$\Delta S^F{}_{InP}$	14.7 eu* (10)
Ω_{Ga-P}	−3500 cal/mole
Ω_{In-P}	0 cal/mole
Ω_{In-Ga}	1066 cal/mole (6)
$\Omega_{InP-GaP}$	4000 cal/mole

* ΔS^F was calculated from the value of ΔH^F given by Sirota (10) and the values of T^F used in the calculation; $\Delta S^F = \Delta H^F/T^F$.

The calculated results are presented in Fig. 2-5. In Fig. 2, the calculated isothermal liquidus lines are presented for comparison with points obtained from interpolating between Panish's data points. No points from the extrapolation of his data are included since they are subject to large errors. The agreement between calculated and experimental liquidus compositions is within 2 a/o (atomic per cent). Low temperature liquidus isotherms in the In-rich corner of the phase diagram are the most useful for crystal growth information. This area of the phase diagram is expanded in Fig. 3. In Fig. 4, calculated iso-(solid composition) lines are plotted along with the experimental data. Each line represents the locus of liquid compositions in equilibrium with a given solid composition. Each data point is labeled with the mole fraction GaP in the solid in equilibrium with that particular liquid composition.

The agreement between calculated and experimental liquid composition in equilibrium with a particular

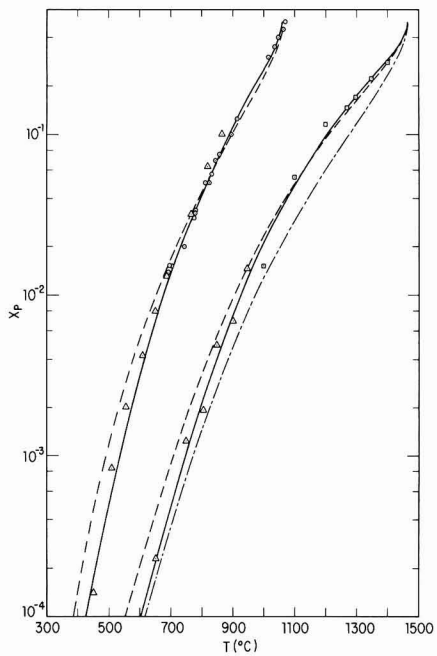

Fig. 1. Ga-P and In-P temperature-composition phase diagrams. — — — — Ideal solution calculation —GaP; — — — — QCE calculation, $\Omega_{Ga-P} = -3500$, $\Omega_{In-P} = 0$; ——— QCE calculation with temperature dependent interaction parameters $\Omega_{Ga-P} = 4650 - 5.85T$, $\Omega_{In-P} = 8220 - 7.57T$; ○ Panish (8) InP; △ Hall (9) InP, GaP; □ Rubenstein (10) GaP.

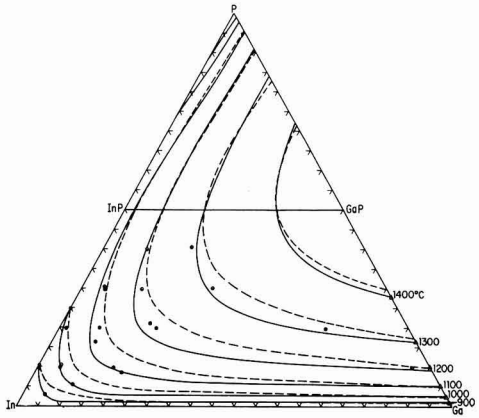

Fig. 2. Ga-In-P liquidus isotherms. ———— QCE calculation with $\Omega_{In\text{-}P} = 0$, $\Omega_{Ga\text{-}P} = -3500$; - - - - - - - - QCE calculation with temperature dependent interaction parameters $\Omega_{In\text{-}P} = 8220 - 7.57T$ and $\Omega_{Ga\text{-}P} = 4650 - 5.85T$; ○ Panish (4); △ Rubenstein (10).

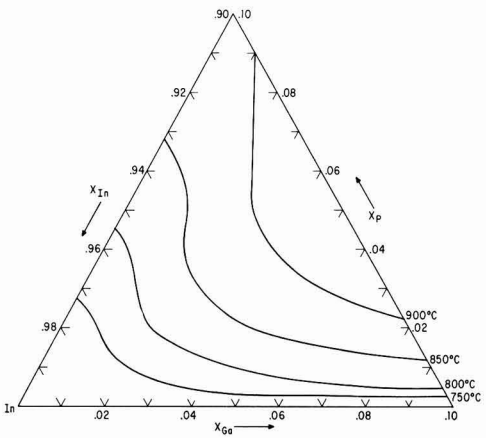

Fig. 3. Liquidus isotherms in the expanded In-rich corner of the ternary Ga-In-P phase diagram.

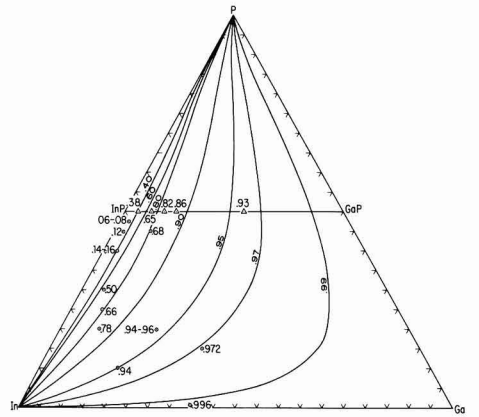

Fig. 4. Ga-In-P iso-(solid concentration) curves calculated using QCE model, $\Omega_{In\text{-}P} = 0$, $\Omega_{Ga\text{-}P} = -3500$. Each curve and point is labeled with X_{GaP}. ○ Panish (4); △ Foster (5).

solid composition is generally good. There is a systematic deviation from Panish's data at the low GaP concentrations, even though the agreement with Foster's data is excellent. It should be pointed out that Panish's method of determining the solid composition in equilibrium with a given liquid by slowly cooling to 20° below the liquidus temperature leads to errors, especially when the mole fraction of GaP in the solid is low; because the equilibrium solid composition changes on cooling. For example, cooling from 1100°C by 20°C changes the equilibrium solid composition on the pseudobinary from 30 to 14% GaP. If error bars were extended from each of Panish's data points to the liquidus 20° below the original liquidus, Panish's data would be in agreement with the calculated results.

Calculated P_2 and P_4 pressures in equilibrium with the liquid composition on the liquidus surface are plotted in Fig. 5. The calculated curves are compared with data from the interpolation of Panish's data (4), and the data of Johnson (15) for pure GaP. The agreement is excellent for pure InP and GaP; and even though the agreement is good within the Ga-In-P ternary system, the calculated curves are systematically higher than the experimental data. The curves for 750°, 800°, and 850°C where there is no experimental pressure data are included because this information is useful for crystal growth experiments in this temperature range.

Discussion

To determine the usefulness of the QCE calculation, it is necessary to compare the calculated results with experimental results and with the results calculated using other model solutions. Panish compared his experimental results with liquidus curves calculated for an ideal solution and for a solution with $\gamma_{Ga} = \gamma_{In} = 1$ and γ_P determined from experimental results. Neither method gives satisfactory results. To further compare the QCE and ideal solution calculations, the ideal Ga-P liquidus curve is included in Fig. 1. The iso-(solid concentration) curves calculated for ideal solid and liquid solutions are compared with experimental data

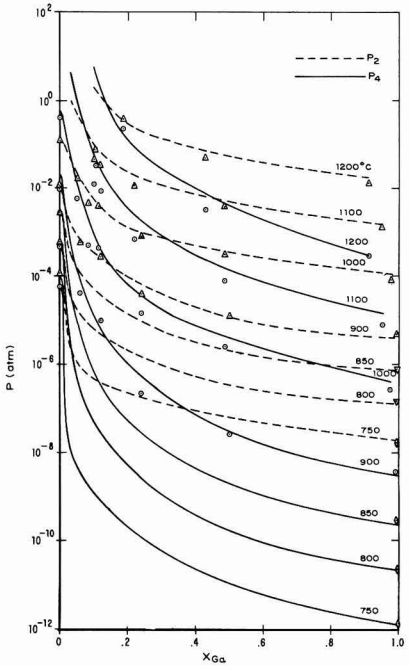

Fig. 5. P_2 and P_4 vapor pressures in equilibrium with the Ga-In-P liquidus surface. - - - - - - - - P_2; ———— P_4; △ Panish (4) P_2; ○ Panish (4) P_4; ◇ Johnson (15) P_4; ▽ Johnson (15) P_2.

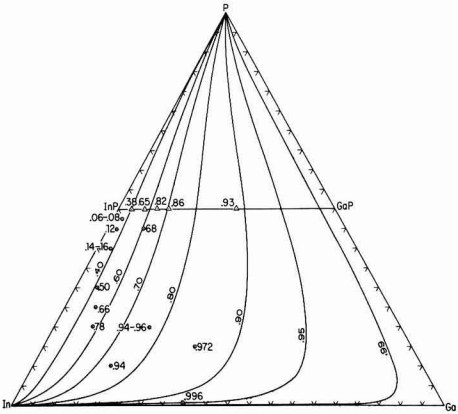

Fig. 6. Ga-In-P iso-(solid concentration) curves calculated using ideal solution model. Each curve and point is labeled with X_{GaP}. ○ Panish (4); △ Foster (5).

in Fig. 6. These comparisons clearly show the QCE calculation to be a dramatic improvement over the ideal calculation, but there is a systematic deviation from the experimental results for liquidus, iso-(solid concentration) and vapor pressure curves. This deviation can be seen in the In-P, Ga-P, In-As, Ga-As, and In-Sb binary liquidus curves (2), so it is not entirely due to the inadequacy of the QCE model in describing the solid solution, where one would expect the largest deviations from any simple model.

There are two approaches which might be taken in attempting to improve the phase diagram calculation: (*i*) use the same model and allow the interaction parameters to be an arbitrary function of T and/or X; (*ii*) use a more sophisticated model which contains the elements necessary to better describe the real solution. The first approach is simply bending the model to fit the binary data, since Ω is constant for the simple QCE model. The second approach involves trying to determine the physical processes which might make the interatomic interactions change with temperature or composition and building them into the model solution.

Guggenheim (1) suggested that Ω could be taken as a linear function of T, $L(T)$, to improve the agreement between calculated properties of the QCE solution and experimental data. An attempt was made to improve the calculation of the Ga-In-P phase diagram using this procedure. By calculating Ω for each experimental point on the liquidus and determining the $L(T)$ which best fit the data, the In-P and Ga-P interaction parameters were determined to be

$$\Omega_{\text{In-P}} = 8220 - 7.57T \text{ and } \Omega_{\text{Ga-P}} = 4650 - 5.85T$$

The respective binary phas diagrams calculated using these interaction parameters are plotted in Fig. 1. As expected, allowing $\Omega = L(T)$ improves the fit to the experimental data.

The Ga-In-P phase diagram was calculated using these new temperature dependent interaction parameters, all other parameters remaining the same as for the regular QCE calculation. The isothermal liquidus curves are compared with the regular QCE results and the experimental results in Fig. 2. The iso-(solid concentration) curves are the same as those presented in Fig. 4. The phase diagram calculated using temperature dependent, interaction parameters is in substantially worse agreement with the experimental data. This result illustrates the danger of bending the model to fit the binary results. The ternary calculation is more than an extrapolation of binary data. It is based on finding a self-consistent solution model which contains the elements necessary to describe the binary systems and then calculating the ternary using the same conceptual basis. The appropriate method of improving the calculation is to use a more sophisticated model which includes the physical processes which make the interatomic interactions temperature and composition dependent.

Kleppa (16) classfied many binary metal systems according to whether they had symmetric ΔH_M *vs.* X curves, characteristics of ideal, regular, and QCE solutions. He found that only systems from the same group of the periodic table had symmetrical ΔH_M *vs.* X curves. This is consistent with the results of Stringfellow and Greene (3) where the Ge-Si, Ge-Sn, Ge-Pb, Si-Sn, and Si-Pb systems were found to behave as QCE solutions. It would be expected that III-V systems could be better described using a more sophisticated model giving the more general asymmetrical ΔH_M *vs.* X curves.

One approach to improving the model would be to retain the lattice model but improve the QCE assumptions: (*i*) nearest neighbors interact pairwise, (*ii*) only configurational free energy of mixing is important, *i.e.*, vibrational free energy of mixing is neglected. The surrounded atom model (17) is similar to the QCE model except the basic entity is an atom with all its nearest neighbors, rather than atom pairs. This is an example of building into the model the physical processes which make the interatomic interactions change with composition. It improves the QCE approximations above and gives the more general asymmetric ΔH_M *vs.* X, but involves 12 interaction parameters for the binary system and 84 for the ternary system. Approximations can be made to reduce the number of parameters, but a calculation of the ternary phase diagram based on the surrounded atom approach is still not practical.

Other, more sophisticated models such as cell models, hard sphere models, and conformal solution theory have been developed for nonpolar spherical molecules and sophisticated models have been developed for ionic solutions. Work is needed in the construction of more sophisticated models applicable to metallic solutions. One problem is that the basic interactions in metallic systems are not well understood. Only recently has progress been made in understanding the intermolecular potentials in liquid metals (18-20). Cell models using intermolecular potentials may be useful in better describing the thermodynamic properties of liquid metals, in particular in III-V systems.

Thus, the QCE model appears to be the best, presently available, practical basis for the calculation of III-V ternary phase diagrams.

Acknowledgments

The author gratefully acknowledges the kindness of M. Panish and M. Foster for allowing him to use their results prior to publication. The author also wishes to thank R. A. Burmeister for many helpful discussions.

Manuscript submitted Feb. 13, 1970; revised manuscript received May 20, 1970.

Any discussion of this paper will appear in a Discussion Section to be published in the June 1971 JOURNAL.

REFERENCES

1. E. A. Guggenheim, "Mixtures," Oxford University Press, Oxford (1952).
2. G. B. Stringfellow and P. E. Greene, *J. Phys. Chem. Solids*, **30**, 1779 (1969).
3. G. B. Stringfellow and P. E. Greene, *This Journal*, **117**, 1075 (1970).
4. M. B. Panish, *J. Chem. Thermo.*, **2**, 319 (1970).
5. L. M. Foster and J. E. Scardefield, *This Journal*, **117**, 534 (1970).
6. JANAF, Interim Thermochemical Tables, Thermal Laboratories, Dow Chemical Co.
7. G. J. Macur, R. K. Edwards, and P. G. Wahlbeck, *J. Phys. Chem.*, **72**, 1047 (1968).
8. M. B. Panish and J. R. Arthur, *J. Chem. Thermo.*, **2**, 299 (1970).
9. R. N. Hall, *This Journal*, **110**, 385 (1963).

10. M. Rubenstein, *Electrochem Soc., Electronics Division Abstracts*, **11**, 129 (1962).
11. N. N. Sirota, in "Semiconductors and Semimetals," Vol. 4, p. 35, R. K. Willardson and A. C. Beer, Editors, Academic Press, New York (1968).
12. D. Richman, *J. Phys. Chem. Solids*, **24**, 1131 (1963).
13. K. Weiser, in "Compound Semiconductors," Vol. 1, p. 471, R. K. Willardson and H. L. Goering, Editors, Reinhold, New York (1962).
14. M. Rubenstein, *This Journal*, **109**, 69C (1962).
15. W. D. Johnson, *ibid.*, **110**, 117 (1963).
16. O. J. Kleppa, *Acta. Met.*, **6**, 225 (1958).
17. P. Hicter, J. C. Mathieu, F. Durand, and E. Bonnier, *Adv. in Physics*, **16** (62), 523 (1967).
18. M. D. Johnson and N. H. March, *Phys. Letters*, **3**, 313 (1963).
19. J. E. Enderby and N. H. March, *Adv. Phys.*, **16**, 691 (1967).
20. M. Shimoji, *ibid.*, **16**, 705 (1967).

Phase Diagram of the Zn-Cd-Te Ternary System

Jacques Steininger, Alan J. Strauss,* and Robert F. Brebrick*

Lincoln Laboratory, Massachusetts Institute of Technology, Lexington, Massachusetts 02173

ABSTRACT

The ternary Zn-Cd-Te liquidus surface and the pseudobinary CdTe-ZnTe solidus curve have been determined by thermal analysis of cooling and heating curves, respectively, of homogenized liquid and solid alloy samples. The binary Cd-Te and Zn-Te liquidus arrest temperatures are in good agreement with most of the previously published data and confirm the presence of well-defined inflections on the metal-rich and Te-rich sides of both liquidus curves. The binary interchange energy parameters calculated along each liquidus curve for the regular and quasi-chemical approximation solution models give essentially similar values for dilute solutions. Near equiatomic composition however, they show values respectively in excess of 200 kcal/mole and less than 40 kcal/mole. The pseudobinary CdTe-ZnTe liquidus and solidus curves exhibit monotonic and sublinear increases in temperature with increasing ZnTe content. The gap between the two curves remains less than 0.16 mole fraction and shows excellent agreement with the values calculated from the ideal liquidus-solidus thermodynamic relationship. The ternary liquidus temperatures form a smooth surface with a narrow ridge near the pseudobinary CdTe-ZnTe composition line and practically degenerate ternary eutectic and boundary lines.

The II-VI compounds CdTe and ZnTe form a complete series of solid solutions with cubic zincblende structure and with band gaps varying from 1.5 to 2.3 eV at room temperature. The alloys containing up to 85 m/o (mole per cent) ZnTe can be made both n- and p-type, and efficient visible electroluminescence at 77°K has been obtained with $Zn_xCd_{1-x}Te$ diodes prepared by diffusion of Zn and P into Al-doped CdTe single crystals (1). The samples prepared by this method however showed evidence of strain which became more severe with increasing x. Recently, alloy crystals have been grown directly from the liquid phase by the Bridgman and slow cooling techniques (2), but details on their crystallographic and optical quality were not reported.

Because of interest in the growth of alloy crystals from the melt and from Te-rich solutions (3), we have investigated the phase diagram of the ternary Zn-Cd-Te system by thermal analysis of homogenized liquid and solid alloy samples. Particular attention was paid to the CdTe-ZnTe subsystem, which was assumed to be pseudobinary, and to the Te-rich region of the ternary liquidus surface. The binary Cd-Te and Zn-Te liquidus curves were also re-investigated because of discrepancies in the published data. Finally, the metal-rich region of the ternary liquidus surface was selectively surveyed in order to present the first comprehensive set of data for thermodynamic analysis of ternary mixed II-VI systems.

Experimental

Thermal analyses were conducted in a vertical platinum-wound resistance furnace by slow cooling of homogenized liquid samples and slow heating of homogenized solid samples at temperatures up to 1265°C. A 10-15g charge of an accurately weighed mixture of 6-9's purity elements was placed in a 1 by 10 cm silica ampoule with a 2.5 cm re-entrant thermocouple well. The free space inside the ampoule was less than 5 cm^3, and the loss by evaporation of the most volatile component was estimated to be less than 0.1% by weight over the experimental range of temperatures. A similar ampoule containing about 8g of silicon was used as a reference. The ampoules were sealed under forepump vacuum (10^{-3} Torr) and placed in two symmetrical cavities drilled in a 5 by 12.5 cm nickel cylinder fitted with a nickel lid. A Pt-Pt 13% Rh thermocouple was inserted in each ampoule, and the two were connected for simultaneous recording of the sample temperature and of the temperature difference between sample and reference as a function of time. To increase the sensitivity of the temperature readings, the emf from the sample thermocouple was partially balanced out with a millivolt potentiometer. The outputs from the two channels were then amplified by d-c microvolt amplifiers and recorded on a two-pen recorder with 1 and 0.1 mV full scale deflection, respectively. Calibration with a gold sample (melting point 1063.0°C) gave melting and freezing arrests of 1063.0° ± 0.1°C and showed that no correction of the sample temperature readings was necessary.

The samples were slowly heated to reaction temperature, melted, and then equilibrated for at least 16 hr at 50°C above the estimated liquidus temperature. Because of apparently slow kinetics of dissolution of CdTe and ZnTe in liquid Te, shorter equilibration times produced erratic results which may explain some of the discrepancies observed in previously published data. Particular care was taken to approximate equilibrium conditions at the onset of freezing.

* Electrochemical Society Active Member.

Key words: ternary phase diagram, thermal analysis, zinc, cadmium, tellurium, alloy crystal growth, quasi-chemical interchange energy, liquidus-solidus thermodynamics.

This was achieved by cooling melts that were only slightly superheated (20°-25°C above the liquidus temperature) at sufficiently low rates (1°-2° C/min) to avoid appreciable supercooling. Under these conditions, there was usually no evidence of supercooling and the cooling curve showed a break that could be reproduced to within ± 1°C (Table I). When supercooling could not be prevented, the liquidus arrest temperature was taken to be the maximum in the recalescence curve. No attempts were made to obtain liquidus data from heating curves because the end of melting for noncongruently melting compositions is poorly defined and can be erroneously interpreted.

Solidus arrests for the pseudobinary CdTe-ZnTe system were obtained from slow heating curves (1°-2° C/min) of samples that had been melted as indicated above, resolidified and homogenized by annealing for at least 16 hr at about 20°C below the solidus temperature. X-ray powder analysis of samples annealed in this way showed no evidence of inhomogeneity and gave lattice parameters in agreement with published values. The temperature of each thermal arrest was obtained from the intersection of the nearly straight lines below and above the solidus break on the sample temperature recording. More prolonged annealing (up to 10 days) resulted in sharper breaks but did not cause any substantial displacement of the intersections. The reproducibility of the solidus arrests was about ± 3°C (Table I).

Because of the large thermal effects in this system, differential thermal recording was used only to confirm the arrests observed on the sample temperature recording. The over-all accuracy of both liquidus and solidus temperatures is estimated to vary from within ± 1°C near the compounds to within a few degrees at higher dilution in excess elements or in the middle of the pseudobinary composition range.

Table I. Experimental thermal analysis data

System	Composition Zn	Cd	Te	Supercooling, °C	Arrest temperature, °C	Reproducibility, °C
Liquidus (cooling curves)						
CdTe-ZnTe	0.10	0.40	0.50	0	1121.6	±0.6
	0.175	0.325	0.50	0	1144.5	—
	0.20	0.30	0.50	2.4	1156.6	—
	0.25	0.25	0.50	0	1176.1	±0.1
	0.30	0.20	0.50	0	1198.1	—
	0.40	0.10	0.50	0	1244.9	±0.2
Zn-Te	0.70	0	0.30	4.5	1215.5	—
	0.60	0	0.40	0	1226.2	—
	0.40	0	0.60	0	1164.7	±0.3
	0.30	0	0.70	0	1060.5	—
	0.20	0	0.80	0	967.7	±0.3
	0.10	0	0.90	0	869.5	—
Cut A: $(Zn_{0.80}Cd_{0.20})_{1-x}Te_x$	0.32	0.08	0.60	0	1124.8	±0.3
	0.24	0.06	0.70	0	1027.7	—
	0.16	0.04	0.80	0.5	927.4	—
Cut B: $(Zn_{0.50}Cd_{0.50})_{1-x}Te_x$	0.45	0.45	0.10	0	1043.5	±0.3
	0.35	0.35	0.30	0	1111.7	±0.1
	0.20	0.20	0.60	0	1052.5	±0.7
	0.15	0.15	0.70	0	959.2	±0.1
	0.10	0.10	0.80	0	870.5	—
	0.05	0.05	0.90	2.7	770.7	—
Cut C: $(Zn_{0.20}Cd_{0.80})_{1-x}Te_x$	0.18	0.72	0.10	0	969.8	±0.1
	0.14	0.56	0.30	0	1045.5	±0.7
	0.08	0.32	0.60	0	992.8	±0.8
	0.06	0.24	0.70	2.7	902.0	—
	0.04	0.16	0.80	0	819.4	—
Cd-Te	0	0.90	0.10	0	888.7	±0.8
	0	0.70	0.30	0	983.0	±0.5
	0	0.50	0.50	0	1092.0	±0.2
	0	0.45	0.55	0	1027.3	±0.6
	0	0.40	0.60	0	967.4	—
	0	0.30	0.70	0	879.2	—
	0	0.20	0.80	0.7	798.4	±0.2
	0	0.10	0.90	0.1	683.6	±2.0
Solidus (heating curves)						
CdTe-ZnTe	0.10	0.40	0.50	—	1112.0	—
	0.20	0.30	0.50	—	1130.0	—
	0.25	0.25	0.50	—	1153.5	±3.5
	0.30	0.20	0.50	—	1164.7	±2.3
	0.40	0.10	0.50	—	1218.0	—

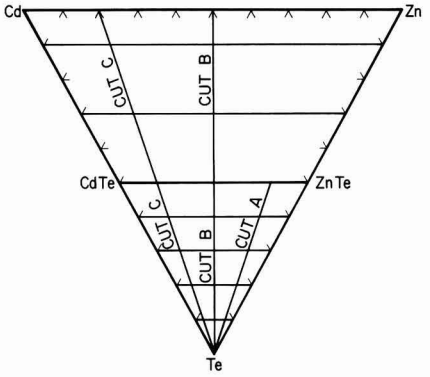

Fig. 1. Zn-Cd-Te ternary system

Results

The liquidus and solidus arrest temperatures, the amount of supercooling observed on the cooling curves, and the reproducibility of repeat runs are listed in Table I for the following subsystems (Fig. 1): Cd-Te binary liquidus; Zn-Te binary liquidus; CdTe-ZnTe pseudobinary liquidus and solidus; liquidus isopleths at constant Zn/Cd ratios of 4.0, 1.0, and 0.25 (Cuts A, B, C); and liquidus isopleths at constant Te concentrations of 0.10, 0.30, 0.60, 0.70, 0.80, and 0.90.

Binary Cd-Te *system (Fig. 2).*—The Cd-Te binary liquidus curve has been previously investigated by de Nobel (4) by visual observation of initial freezing, and by Lorenz (5) and Kulwicki (6) by DTA in sealed quartz ampoules. Their data show generally good agreement on the Cd-rich side, with the exception of the high-temperature data of de Nobel which is significantly lower, probably because of supercooling. On the Te-rich side, they also show good agreement except for the values of Kulwicki which are significantly higher in the 50 to 80 a/o (atomic per cent) Te region. Our arrest temperatures are listed in Table I and shown in Fig. 2 together with the values of Lorenz and Kulwicki. Melting and freezing arrests of 1092.0° ± 0.2°C were observed for CdTe in good agreement with the previously reported values of 1090° ± 2°C (de Nobel), 1092° ± 3°C (Lorenz), and 1091° ± 2°C (Kulwicki). Our liquidus arrests are in best agreement with the data of Lorenz, on both sides of the liquidus curve. Substantial supercooling, which might have explained the differences between the results of Lorenz and of Kulwicki on the Te-rich side, was not in evidence on our cooling curves (Table I). It is therefore suspected that the high temperatures observed by Kulwicki in both binary systems (see below) may have been caused by in-

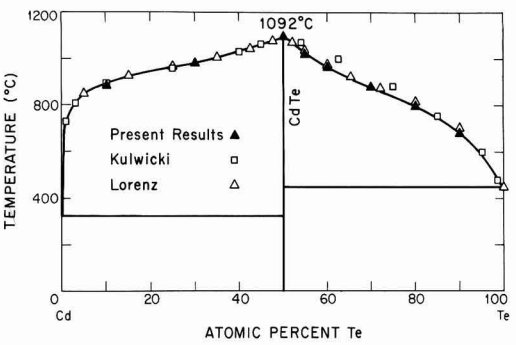

Fig. 2. Cd-Te binary liquidus curve

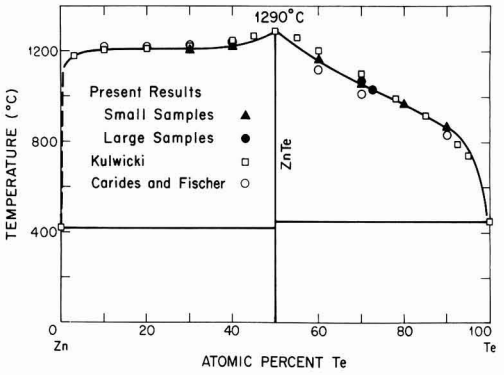

Fig. 3. Zn-Te binary liquidus curve

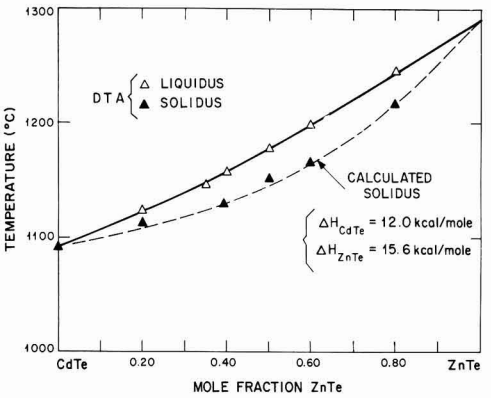

Fig. 4. CdTe-ZnTe pseudobinary liquidus and solidus curves

complete homogenization of the Te-rich liquid samples.

Binary Zn-Te *system (Fig. 3).*—The Zn-Te liquidus curve was investigated almost 60 years ago by Kobayashi (7) in an open system and more recently by Carides and Fischer (8) by thermal analysis in a high pressure autoclave and by Kulwicki (6) by DTA in sealed quartz ampoules. The data of the two more recent investigations are in generally good agreement except in the region between 50 and 80 a/o Te where the values of Kulwicki are almost 100°C above those of Carides and Fischer. Our arrest temperatures are listed in Table I and shown in Fig. 3 together with the data of Carides and Fischer and of Kulwicki. No attempt was made to redetermine the melting point of ZnTe because of its relatively high temperature, and we adopted the value of Kulwicki (1290° ± 2°C), which is in agreement with that of Carides and Fischer (1295° ± 20°C). On the Zn-rich side, our liquidus temperatures are in good agreement with the previously reported experimental curves, showing an almost horizontal inflection near 1210°C. From theoretical calculations of the activities in a regular associated solution model (see Discussion), Jordan (9) has recently suggested a miscibility gap in the liquid phase between 9 and 35 a/o Te. However, careful analysis of several of our cooling curves at 30 and 40 a/o Te did not reveal the monotectic arrest which he predicted near 1213°C. On the Te-rich side, our liquidus temperatures are intermediate between the low values of Carides and Fischer (probably due to supercooling) and the higher values of Kulwicki. Contrary to Kulwicki's diagram, our liquidus curve shows a well-defined inflection (near 1025°C and 70 a/o Te) which is comparable to that observed in the Cd-Te system in the same composition range.

Because of the discrepancies observed on the Te-rich side in both binary systems, two additional points were determined on the ZnTe-Te liquidus curve by slow cooling of large liquid samples (about 150g) in another, previously described (10), DTA apparatus. The arrest temperatures of 1070° and 1030°C of compositions of 70 and 72.5 a/o Te are in good agreement with the rest of our data (Fig. 3) and confirm the inflection on the liquidus curve.

Pseudobinary CdTe-ZnTe *system (Fig. 4).*—No previous investigation of the pseudobinary liquidus and solidus curves has been reported. X-ray diffraction data (11) show that the $Zn_x Cd_{1-x}Te$ alloys form a complete series of solid solutions and that the lattice parameter varies linearly with composition in agreement with Vegard's law.

Our liquidus and solidus arrest temperatures are listed in Table I and shown in Fig. 4. Both temperatures show a monotonic and sublinear variation with composition from the melting point of CdTe (1092°C) to that of ZnTe (1290°C). This type of variation suggests small and nearly comparable positive deviations from ideality in the liquid and solid phases (see Discussion) and is similarly observed in several other II-VI pseudobinary systems, such as HgTe-HgSe (12), ZnTe-ZnSe (13), and CdTe-CdSe (14). Of particular interest are the slow increase in liquidus temperatures and the relatively narrow gap between liquidus and solidus curves (less than 0.16 mole fraction). These are both favorable for the growth of alloy crystals from the melt in standard quartz ampoules up to relatively high values of Zn content.

Ternary liquidus surface (Fig. 5-8).—No previous study of the ternary liquidus surface has been reported.

The Te-rich ternary liquidus isopleths for constant Zn/Cd ratios (Fig. 5) show the same type of variation as the limiting CdTe-Te and ZnTe-Te binary liquidus curves, with an inflection near 70 a/o Te and a marked increase in temperature near the equiatomic composition. On the metal-rich side, there is a gradual transition from the smooth Cd-CdTe liquidus curve to the initially steep and then almost flat Zn-ZnTe curve. The inflections on both sides of the isopleths suggest a tendency for separation into different liquid phases. Such separations actually occur on the Se-rich side of other II-VI systems such as Hg-Se (10), Cd-Se (15), and probably Zn-Se (16). However, no monotectic arrests have been observed in the Zn-Cd-Te system.

Like the pseudobinary CdTe-ZnTe liquidus curve, the constant-Te isopleths exhibit slow, monotonic increases in temperature from the Cd-Te liquidus to

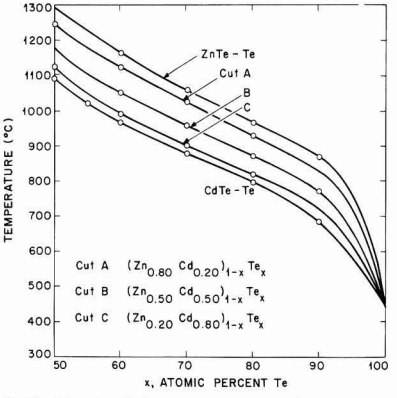

Fig. 5. Liquidus isopleths at constant Zn/Cd ratios on Te-rich side.

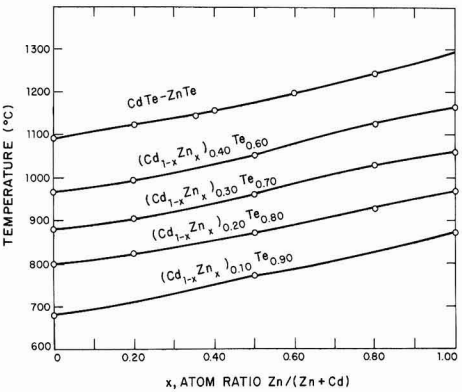

Fig. 6. Liquidus isopleths at constant Te concentrations on Te-rich side.

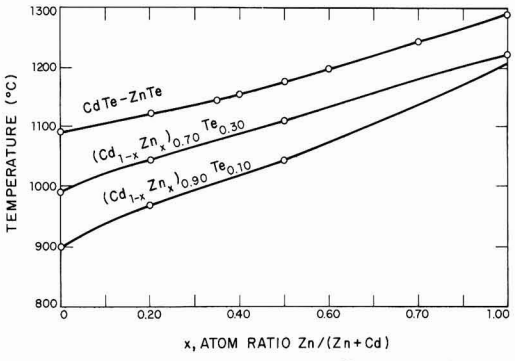

Fig. 7. Liquidus isopleths at constant Te concentrations on metal-rich side.

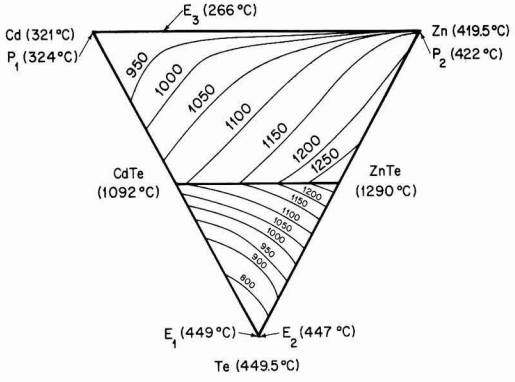

Fig. 8. Projections of Zn-Cd-Te ternary liquidus isotherms on composition plane.

the Zn-Te liquidus, both on the Te-rich side (Fig. 6) and on the metal-rich side (Fig. 7).

The projections of the ternary liquidus isotherms on the composition plane (Fig. 8) have been constructed by interpolation along the various liquidus curves. They vary smoothly between the binary Cd-Te and Zn-Te liquidus curves but show sharp peaks along the pseudobinary CdTe-ZnTe composition line which correspond to the marked increase in temperature as the composition approaches 50 a/o Te. The binary Cd-Zn system (17) shows a eutectic at 26.5 a/o Zn and 266°C. The binary Cd-Te and Zn-Te systems however show almost completely degenerate eutectics or peritectics, the thermal arrests being very close to the melting points of the pure elements (6). As a consequence, the ternary eutectic and boundary lines are also expected to be degenerate (Fig. 8).

Discussion

Liquidus surface.—Solution models of increasing complexity have been called upon to interpret the thermodynamic properties of III-V and II-VI binary and ternary systems. The relatively moderate deviations from ideality in the III-V systems led early investigators (18-20) to use expressions derived by Wagner (21) and Vieland (22) for a regular solution model with an interchange energy parameter varying linearly with temperature. Recently however, Stringfellow and Greene (23) have shown that the first-order quasi-chemical approximation of Guggenheim (24) with a temperature independent interchange energy parameter leads to satisfactory representation of the liquidus temperatures and of the activities in the III-V systems In-Sb, Ga-As, In-As, and the corresponding mixed ternary systems.

In the II-VI systems, the larger differences in electronegativity between metal and chalcogen atoms produce more ionic and stronger interactions between unlike atoms, as evidenced by the marked increase in temperature in the Zn-Cd-Te liquidus surface near the pseudobinary CdTe-ZnTe composition line (Fig. 8). As a result, the interchange energy parameter calculated along the liquidus curve from Vieland's regular solution expression exhibits a steep minimum (in excess of 200 kcal/mole) near the equiatomic composition (Fig. 9) instead of the approximately linear temperature dependence found in the III-V systems. This led Jordan (9) to propose the Regular Associated Solution model which postulates the existence of stable CdTe or ZnTe complexes in the liquid phase and effectively shows an interchange energy parameter that becomes very large at equiatomic composition.

This effect apparently stems from the failure of the regular solution model to account for the nonrandom distribution of atoms in the liquid phase. The quasi-chemical approximation, on the contrary, postulates a nonrandom distribution of pairs of atoms weighted exponentially in terms of the energy of interchange between pairs of unlike atoms and the corresponding pairs of like atoms (24).

Values of the quasi-chemical interchange energy parameter have been calculated in this study for experimental points along the Cd-Te and Zn-Te liquidus curves. A computer half-interval search method (25) was used to solve the liquidus equation derived by

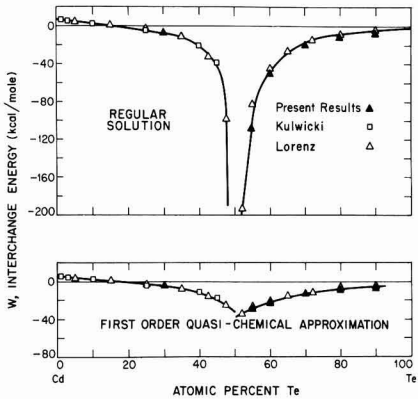

Fig. 9. Interchange energy parameter for regular and quasi-chemical approximations (Cd-Te binary system).

Stringfellow and Greene (23) from the general liquidus equation of Vieland (22) and the quasi-chemical activity coefficients of Guggenheim (24). (The values of Kulwicki (6) were used for the entropies of fusion of CdTe and ZnTe.) The variation of the interchange energy parameter for the Cd-Te system is shown in Fig. 9 for a coordination number of 4. Unlike the III-V systems investigated by Stringfellow and Greene, the II-VI systems show significant variations of the quasi-chemical parameter along the liquidus curve. The minimum near equiatomic composition however is much shallower than in the regular solution model and remains less than 30 and 35 kcal/mole on the Cd-rich and the Te-rich sides, respectively.

Both the regular and the quasi-chemical models are based on the assumption that the energy of the solution is a function solely of the number of pairs of unlike atoms and they fail to differentiate between metal-rich and chalcogen-rich solutions. The phase diagrams of the II-VI systems are highly unsymmetrical, because of the difference in energy of metal-metal and chalcogen-chalcogen bonds, and they cannot be adequately represented by either of these two models, unless they are arbitrarily separated into metal-rich and chalcogen-rich subsystems (6, 9). The more recent Non-Random Two-Liquid solution model of Renon (26) takes account of the differences in bond energy of the solvent atoms and offers the possibility of representing unsymmetrical phase diagrams with a single consistent set of parameters. Preliminary results indicate that it gives a better representation of the Ga-As liquidus curve and thermodynamic functions than the quasi-chemical model. Good fits to the Cd-Te and Zn-Te liquidus curves are also obtained, but some questions remain concerning the values of the temperature dependent bond energy parameters in these two systems.

Pseudobinary liquidus-solidus gap.— A general expression for the thermodynamic relationship between liquidus and solidus equilibrium compositions has recently been derived (27) for non-ideal but homogeneous and monotonic alloy systems (*i.e.*, systems showing complete liquid and solid mutual miscibility and monotonic variations of the liquidus and solidus curves). For a system of two components A and B with melting temperatures $T_A < T_B$, the molar fractions of A and B in the liquid and solid phases, X^l_A, X^l_B and X^s_A, X^s_B, in equilibrium at the intermediate temperature T such that $T_A < T < T_B$, are related by

$$RT\left(\ln\frac{X^s_A}{X^s_B} - \ln\frac{X^l_A}{X^l_B}\right) = \Delta H_A\left(1 - \frac{T}{T_A}\right) - \Delta H_B\left(1 - \frac{T}{T_B}\right) - D \quad [1]$$

where R is the ideal gas constant, ΔH_A and ΔH_B are the enthalpies of fusion of A and B, and D represents the difference between the partial excess free energies of mixing in the solid and liquid phases

$$D = \frac{\partial \Delta G^s_{e,m}}{\partial X^s_A} - \frac{\partial \Delta G^l_{e,m}}{\partial X^l_A} \quad [2]$$

If the liquid and solid solutions are ideal, the excess free energies of mixing are zero and $D = 0$. The ideal form cf Eq. [1] with $D = 0$ has also been found to fit the experimental data for a large number of binary and pseudobinary alloy systems (metallic, semiconducting, and ionic) in which the liquidus and solidus curves vary monotonically with composition (27). Although the liquid and solid phases in these systems are generally not ideal solutions, the ideal liquidus-solidus expression is applicable because the difference between the partial excess free energies of mixing is small enough to be neglected. The ideal expression can therefore be used to calculate one of the boundaries of the two-phase field when the other one and the enthalpies of fusion of the pure components are known. The solidus curve for the pseudobinary CdTe-ZnTe system in Fig. 4 has been calculated from our experimental liquidus data and from the enthalpies of fusion determined by Kulwicki (6). It shows excellent agreement with the solidus data (the root mean square of the difference between calculated and experimental temperatures for five points is 3.8°C), therefore confirming that the deviations from ideality in the two pseudobinary phases are small and nearly equal.

Acknowledgment

The authors wish to acknowledge the capable assistance of R. E. England and D. Apelian in the thermal analyses, of Mary C. Finn and Mrs. M. J. Button in the x-ray analyses, and of Mrs. B. Palm in computer programming. This work was sponsored by the Department of the Air Force.

Manuscript submitted Nov. 24, 1969; revised manuscript received June 15, 1970. This was Paper 118 presented at the New York Meeting of the Society, May 4-9, 1969.

Any discussion of this paper will appear in a Discussion Section to be published in the June 1971 JOURNAL.

REFERENCES

1. F. F. Morehead and G. Mandel, *Appl. Phys. Letters*, **5**, 53 (1964).
2. M. S. Brodin, M. V. Kurik, V. M. Marlak, and B. S. Oktyabr'skii, *Sov. Phys.-Semicond.*, **2**, 603 (1968).
3. J. Steininger and R. E. England, *Trans. Met. Soc. AIME*, **242**, 444 (1968).
4. D. de Nobel, *Philips Res. Rept.*, **14**, 361 (1959).
5. M. R. Lorenz, *J. Phys. Chem. Solids*, **23**, 939 (1962).
6. B. M. Kulwicki, Ph.D. Dissertation, Univ. of Michigan (1963).
7. M. Kobayashi, *Z. Anorg. Chem.*, **69**, 1 (1911).
8. J. Carides and A. G. Fischer, *Solid State Comm.*, **2**, 217 (1964).
9. A. S. Jordan, *Met. Trans.*, **1**, 239 (1970).
10. A. J. Strauss and L. B. Farrell, *J. Inorg. Nucl. Chem.*, **24**, 1211 (1962).
11. B. T. Kolomiets and A. A. Mal'kova, *Zh. Tekh. Fiz.*, **28**, 1662 (1958) [*Sov. Phys.-Tech. Phys.*, **3**, 1532 (1958)].
12. T. C. Harman, "Physics and Chemistry of II-VI Compounds," p. 786, M. Aven and J. S. Prener, Editors, John Wiley and Sons, Inc., New York (1967).
13. A. G. Fischer and W. H. Fonger, Report No. 3 (1965), Contract No. AF 19(628)-3866, U.S. Air Force, Cambridge Research Laboratories, Bedford, Mass.
14. A. J. Strauss and J. Steininger, *This Journal*, To be published.
15. A. Reisman, M. Berkenblit, and M. Witzen, *J. Phys. Chem.*, **66**, 2210 (1962).
16. M. R. Lorenz, "Physics and Chemistry of II-VI Compounds," p. 85, M. Aven and J. S. Prener, Editors, John Wiley and Sons, Inc., New York (1967).
17. M. Hansen, "Constitution of Binary Alloys," p. 446, McGraw-Hill Co., New York (1958).
18. W. F. Schottky and M. B. Bever, *Acta Met.*, **6**, 320 (1958).
19. C. D. Thurmond, *J. Phys. Chem. Solids*, **27**, 785 (1965).
20. J. R. Arthur, *ibid.*, **28**, 2257 (1967).
21. C. Wagner, *Acta. Met.*, **6**, 309 (1958).
22. L. J. Vieland, *ibid.*, **11**, 137 (1963).
23. G. B. Stringfellow and P. E. Greene, *J. Phys. Chem. Solids*, **30**, 1779 (1969).
24. E. A. Guggenheim, "Mixtures," p. 39, Clarendon Press, Oxford (1952).
25. S. S. Kuo, "Numerical Methods and Computers," p. 83, Addison-Wesley, Reading, Mass. (1965).
26. H. Renon and J. M. Prausnitz, *Chem. Eng. Sci.*, **18**, 244 (1968).
27. J. Steininger, *J. Appl. Phys.*, **41**, 2713 (1970).

Growth Characteristics of Rutile Film by Chemical Vapor Deposition

R. N. Ghoshtagore and A. J. Noreika

Westinghouse Research Laboratories, Pittsburgh, Pennsylvania 15235

ABSTRACT

Thin film rutile has been grown by the chemical vapor deposition reaction of $TiCl_4$ and O_2 on silicon and a variety of oxide substrates over a range of temperatures (673°-1320°K) and reactant partial pressures ($p_{TiCl_4} = 2.9 \times 10^{-2}$ to 9.28×10^{-1} Torr, $p_{O_2} = 2.5 \times 10^{-1}$ to 760 Torr). At high oxygen partial pressures between 990° to 1100°K, the films have been found to contain the rutile modification of TiO_2 almost exclusively. Polycrystalline deposits on silicon, fused quartz, and amorphous silica (thermally grown or chemically vapor deposited) substrates displayed some preferred growth orientation (fiber texture). Epitaxial films were obtained on (001)-, (110)- and (111)-rutile, (100)-MgO, and (0001)-sapphire substrates at elevated temperatures.

The process of chemical vapor deposition (CVD) has recently attracted considerable attention as a method of depositing thin films of refractory materials on a variety of substrates (1). However, very few data are available on the nucleation and growth behavior in CVD systems. One such CVD process of potential importance is the growth of thin film ceramic oxides on semiconductors for use as insulators or dielectrics.

Among the simple oxides, titanium dioxide in rutile modification is known to have one of the highest dielectric constants (90 $\perp$ and 180 $\parallel$ c-axis) (2). Both physical and chemical deposition techniques have been reported for the preparation of titanium dioxide films. The former include the evaporation of titanium followed by oxidation, reactive sputtering of titanium in oxygen, and rf sputtering of titanium dioxide (3). The pyrolysis of titanium alcoholates (*e.g.,* tetraisopropyl titanate) (4), hydrolysis of titanium tetrachloride (5), and anodization of titanium films (6) are examples of chemical deposition of titanium dioxide. In this study, a new chemical vapor deposition process to form TiO_2 has been explored on a variety of substrates. Where practical, the growth characteristics, *i.e.,* crystal size and orientation, have been observed. Some relevant kinetic data regarding the formation of TiO_2 films on silicon have been reported elsewhere (7).

Experimental Technique

The experiments utilize the chemical reaction between titanium tetrachloride and oxygen on a heated substrate in a conventional horizontal quartz tube "silicon epitaxial" reactor at atmospheric pressure (8). Purified titanium tetrachloride (prepared by multiple distillation of 99.995% pure material) in thermostat-held quartz bottles is used as a titanium source bubbler through which a carrier gas of ultrapure argon or ultrapure oxygen (Matheson) is passed at a controlled rate. This gas (saturated with $TiCl_4$ vapor) is then mixed with additional ultrapure oxygen and/or argon through a set of calibrated flowmeters, liquid traps, and filters and the mixture reacted on a quartz encapsulated high purity graphite susceptor heated by rf induction. The over-all reaction can be described by

$$TiCl_4(g) + O_2(g) \rightleftarrows TiO_2(\text{rutile}) \ (s) + 2Cl_2(g) \quad [1]$$

Free energy changes (ΔF) for this reaction, calculated from known thermochemical data (9), are −33.0, −30.3, −27.7, and −25.2 kcal/mole at 700°, 900°, 1100°, and 1300°K, respectively.

Single crystal silicon wafers (15-20 mils thick) of (111), (100), and (110) orientations, obtained from Texas Instruments, were lapped, polished in Linde B, and then chemically etched in 15:5:3 HNO_3:HAc:HF to a mirror finish by the supplier. Substrates for TiO_2 deposition were prepared by scribing 5 mm squares out of these wafers. The substrates were then degreased by boiling in trichloroethylene and acetone and chemically polished in 15:5:3 HNO_3:HAc:HF to remove about 5-10μ of surface layer. The substrates were then blown dry in dry nitrogen, mounted on the susceptor and baked for 20-30 min in ultrapure hydrogen at 1175°-1275°K to remove any residual oxide film (10).

The reactor atmosphere is then flushed with ultrapure argon and the substrate temperature is adjusted, the temperature being monitored with an optical pyrometer [corrected for absorption by the quartz tube wall, reactor atmosphere, and substrate emissivity (11)] and/or an infrared radiation pyrometer. Titanium tetrachloride vapor in the carrier gas is then passed into the reactor (after prolonged purging to vent), argon flow is discontinued, and mainline ultrapure oxygen is introduced at a predetermined flow rate. The deposits and substrates are then pushed off the susceptor at regular time intervals with a quartz push rod, and the deposition rate is determined from an average of 16 to 18 samples run for 8 to 9 different time periods. Film thicknesses were determined by reference to an ellipsometrically calibrated color chart (12). The temperature of titanium tetrachloride was maintained at 298° ± 0.5°K and that of the substrates to ± 5°K.

Similar experiments were performed using fused quartz and single crystal MgO, Al_2O_3, and TiO_2 (rutile) substrates, an exception to the previously described experimental procedure when using these substrates being the omission of the hydrogen anneal. The reported data on the fused quartz, MgO, and Al_2O_3 substrates were determined from the change in weight (to microgram accuracy) of several substrates of known surface area before and after depositing a 4000-6000Å thick rutile film. The theoretical density of 4.26 g/cm^3 (for bulk rutile) was used for thickness computation of the rutile film. Determinations of crystallite size and film orientation were made from transmission electron microscopy (TEM) and reflective electron diffraction (RED) studies, respectively. The Si substrates were particularly well suited for the TEM study since they lend themselves to a well-established chemical jet-etching technique (13). In this technique, selected areas of the substrates are dissolved in a chemical jet-etch solution, the remainder being retained as support for the TiO_2 membranes which span the etched areas.

Key words: rutile, film, epitaxy, nucleation, deposition, orientation, growth, dielectric.

Results and Discussion

Nucleation density and deposition rate.—Figure 1 shows Arrhenius plots relating the deposition rate of TiO_2 to substrate temperature at three constant partial pressures of titanium tetrachloride. Within the range of experimental error the rates are seen to be independent of both substrate composition and substrate orientation. Consequently, it can be inferred that the mechanism of TiO_2 film formation is identical on all the substrates studied and is that which has been elucidated by kinetic studies in the case of single crystal silicon substrates (7). Nucleation in the vapor phase by gas phase reaction becomes predominant around 1125°K in all cases, above which temperature the rates decline. The effects of vapor phase reaction and consequent reduction of the effective vapor pressure of the rate-limiting reactant $TiCl_4$ are also evident in Fig. 2, a plot of the number of embryo crystallites, *i.e.*, those formed during the first minute of deposition, as a function of temperature. At temperatures less than 1125°K, the count increases with temperature; above 1125°K, the crystallite density decreases.

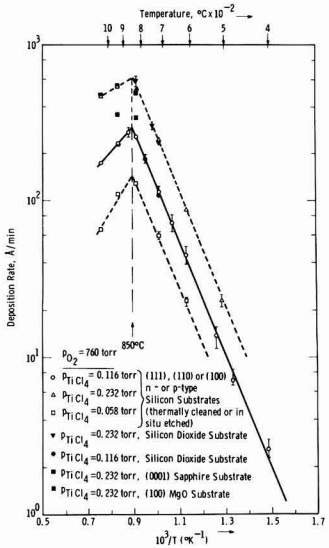

Fig. 1. Arrhenius plot of rutile thin film deposition rate

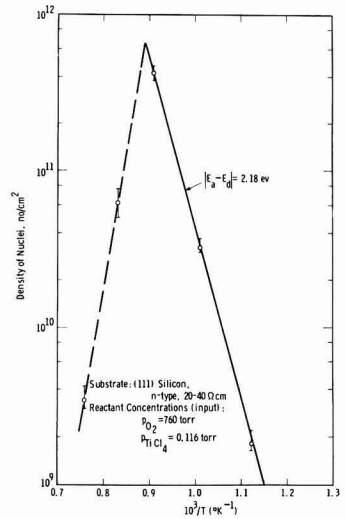

Fig. 2. Arrhenius plot of the density of TiO_2 nuclei on (111) silicon.

The trend of the data, *i.e.*, the exponential rise as a function of increasing substrate temperature, in both sets of curves (Fig. 1 and 2) below 1125°K is presumably due to two complementary effects, (*i*) an increase of the rate of reaction of component gases as the thermal energy supplied to the substrate is increased, *i.e.*, the exponential dependence of the surface reaction rate constant with temperature (7), and (*ii*) an almost negligible vapor pressure of the solid reaction product (TiO_2) in the temperature range of interest (9). The latter effect is equivalent to an "ideal" complete condensation of impinging product atoms or molecules as envisioned in physical vapor deposition systems. Coupling of the above two effects produces an effective supersaturation which also increases with temperature exponentially. Deposition rate and nucleation density, both strongly related to supersaturation, assume a similar temperature dependence. However, the activation energies of deposition and nucleation are quite different in magnitude because of the difference in the physicochemical processes involved in each phenomenon.

It is well known that when a solid surface catalyzes a hetereogeneous gas reaction, the energy of the reaction is decreased by the adsorption of one or more of the reactants. If E_H and E_s are the energies for uncatalyzed and catalyzed reactions, respectively, and E_i^A is that for the adsorption and/or desorption of the ith reaction species on the catalyst, then

$$E_H - \sum_{1}^{n} E_i^A = E_s \qquad [2]$$

where n is the number of species involved in the reaction.

E_H can be calculated from the available thermodynamic data (9) and is $\sim$ 1.25 eV whereas E_s can be obtained from Fig. 1 and is $\sim$ 0.8 eV. Since only the adsorption of atomic oxygen is involved in our CVD mechanism (7), $\sum_{i}^{n} E^A{}_{\text{atomic oxygen}} = E_o{}^A \cong 1.25 - 0.80$ eV $= 0.45$ eV.

Now, if ΔE_o is the enthalpy of activation for the reaction

$$\frac{1}{2} O_2 \rightleftarrows O \qquad [3]$$

and K is the equilibrium constant, then

$$K = \frac{p_O}{p_{O_2}{}^{1/2}} = \text{Exp} \frac{-\Delta E_o}{kT} \qquad [4]$$

or

$$p_O = p_{O_2}{}^{1/2} \text{Exp} \frac{-\Delta E_o}{kT} \qquad [5]$$

where p_O and p_{O_2} are the partial pressures of atomic and molecular oxygen, respectively.

Since TiO_2 is formed by the adsorption of atomic oxygen (charged or uncharged) (7) on the substrate, the saturation nucleation density of TiO_2 (N_s) is proportional to the density of adsorbed oxygen which, in turn is, proportional to the gas phase concentration of atomic oxygen produced by the reaction represented by Eq. [3]. Using Eq. [5], we obtain

$$N_s = C_1 p_O{}^{\text{adsorbed}} = C_1 C_2 p_O \text{Exp} \frac{E_o{}^A}{kT}$$
$$= C_1 C_2 p_{O_2}{}^{1/2} \text{Exp} \frac{-\Delta E_o + E_o{}^A}{kT} = C \exp \frac{-\Delta E_o + E_o{}^\Lambda}{kT}$$
$$= C \text{ Exp} - 2.14 \text{ eV}/kT \qquad [6]$$

where C_1, C_2, and C are constants, and $E_o^A \cong 0.45$ eV and $\Delta E_o = 2.58$ eV (14). The excellent agreement of the calculated activation energy of saturation nucleation density (Eq. [6]) with the experimental data (Fig. 2) also seems to validate earlier conclusions on the mechanism of the surface nucleation. Furthermore, the other possible mechanism of surface nucleation by the collection of the nuclei formed in the vapor phase seems to be ruled out by the experimental facts that (*i*) the nuclei do not have spherical morphology (see later), and (*ii*) the saturation nucleation density does not remain constant above 1125°K, when the gas phase reaction has overtaken the surface reaction.

When vapor phase reaction becomes predominant (above 1125°K, Fig. 1 and 2), the model described still applies although the curve appears to assume a positive slope. As the gas phase temperature is raised along with that of the substrates, nucleation in the vapor phase is enhanced, and the effective pressure of the rate-limiting reactant gas ($TiCl_4$) seen by the substrate diminishes. Since the rate of surface reaction and the supersaturation are also functions of this pressure, both deposition rate and nucleation density decrease. The data above 1125°K, in both Fig. 1 and 2, represent a sum of two competing physicochemical processes. Thus, above 1125°K, the nucleation density (N_s) can be described by Eq. [6] modified by an additional factor for the amount of unreacted $TiCl_4$ present. A similar adjustment can be made to describe the deposition rate above 1125°K.

Orientation behavior.—Some variations were observed in the crystallographic orientations adopted by TiO_2 films, on the several types of substrates used. On oriented Si wafers, for example, crystal orientation within the films was found to be independent of substrate orientation. These data obtained from RED observations are presented as functions of the substrate temperature (630°-1320°K) and orientation in Fig. 3. All Si substrates were of the low-index type, *i.e.*, (100), (110), and (111). Figure 3 indicates that with a change of substrate temperature, different crystal orientations are produced in the films. At temperatures below 630°K, the crystallites are oriented at random. A strong {110}-orientation occurs between 630° and 730°K. This is succeeded by a {101}-orientation between 730° and 990K, then by a {301}-orientation between 990° and 1125°K; and finally, by a strong {100} orientation at higher temperatures, at least to 1320°K. Deposition of TiO_2 on fused quartz substrates over a temperature range of 990°-1100°K produced films having orientations similar to those for TiO_2 on Si.

This similarity prompted additional experiments in which oxides of Si were deliberately formed on oriented Si surfaces. The oxide layers were either thermally grown or chemically vapor deposited (by the reaction of SiH_4 and O_2). When TiO_2 films were subsequently deposited, orientations were the same as those deposited on both the hydrogen annealed Si and the silica surfaces. In another experiment, *in situ* gaseous etching of Si substrates with HCl was performed prior to TiO_2 deposition. After 1-2 μm of the substrate surface had been removed, the reaction components were introduced, and films were deposited. Orientations altered slightly in this case, the onset of {100}-orientation occurred at a temperature of 1000°K, and the {301}-orientation was eliminated.

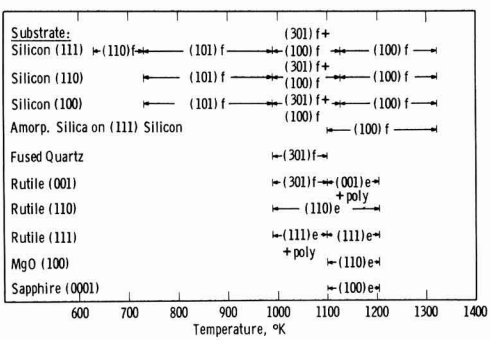

Fig. 3. Schematic representation of preferred rutile crystallite orientation in thin films (as a function of substrate material, temperature, and orientation) grown at $p_{O_2} \simeq 760$ Torr and $p_{TiCl_4} = 0.058$ to 0.232. Symbols f and e stand for fiber and epitaxial habits, respectively.

The evidence suggests that the observed TiO_2 orientations represent equilibrium orientations on both neutral and neutralized surfaces; the single crystal Si substrates being neutralized by exposure to oxygen. Moreover, the presence of neutralized surfaces is virtually inevitable since the adsorption of oxygen at the surface is a prime requirement in the reaction sequence. The cause of slight modification in the results for films etched *in situ* by HCl is, as yet, not well established. Since the etch was intended to remove the natural surface oxide, as was the hydrogen anneal, one assumes that the predeposition treatments of the substrate did not produce equivalent results and that the {301}-orientation, where it occurs, may be artificially stabilized.

Efforts to detect the presence of SiO_2 between substrate and film included infrared absorption measurements. Known thicknesses of SiO_2 in especially prepared Si-SiO_2-TiO_2 structures served as standards. Since infrared absorption was not observed for either the experimental films or for the standards in which SiO_2 thickness was less than 200Å, oxide films, if present, had not exceeded the absorption thickness limit.

Since oxygen neutralized surfaces may well be the rule on metallic and semiconductor single crystal substrates, single crystal oxide substrates appear to offer the most likely surfaces for the epitaxial growth of rutile. Deposits on cleaved and polished surfaces of rutile, MgO, and sapphire, in fact, showed varying degrees of epitaxy, Fig. 3, at temperatures between 990° and 1205°K.

Figure 3 also indicates that the best orientation match between the film and substrate occurs for (110)-oriented rutile substrates. Good epitaxial alignment is also evident on the (111)-oriented substrates at temperatures greater than 1100°K. Films deposited on (001)-oriented substrates showed a moderate degree of epitaxy at temperatures near 1200°K; orientations of deposits prepared at lower temperatures ranged from a {301}-fiber texture at 990°K to a badly twinned (001)-epitaxial layer near 1100°K. The degree of twinning was greatly reduced and often completely eliminated in all homoepitaxial growth experiments, *i.e.*, on (110), (100), and (111)-oriented rutile substrates, by *in situ* etching of the substrates in gaseous chlorine at 1320°K; 1000-1500Å of a substrate was so removed.

Films prepared on (100)-oriented MgO and (0001)-oriented sapphire substrates in a temperature range of 1100°-1205°K also exhibited strong epitaxial behavior. Some of their representative RED patterns are shown in Fig. 4. The orientation relationships between rutile films and substrates (where TiO_2 represents the rutile film and Al_2O_3 represents the sapphire substrate) were $(110)_{TiO_2} \parallel (100)_{MgO}$, $[001]_{TiO_2} \parallel [011]_{MgO}$ and $(100)_{TiO_2} \parallel (0001)_{Al_2O_3}$, $[010]_{TiO_2} \parallel [110]_{Al_2O_3}$, $[011]^*_{TiO_2} \parallel [110]_{Al_2O_3}$. ([ ]* = R.L. vector). Inspection of the orientation relationship observed for rutile films on (100)-oriented MgO substrates indicates that a continuous oxygen sublattice exists across the substrate-film interface with titanium atoms occupying unoccupied octahedral sites of MgO lattice. Since the respective oxygen ion densities for observed crystallographic planes are MgO(100) $= 1.13 \times 10^{15}/cm^2$ and rutile (110) $= 1.04 \times 10^{15}/cm^2$, some interfacial dis-

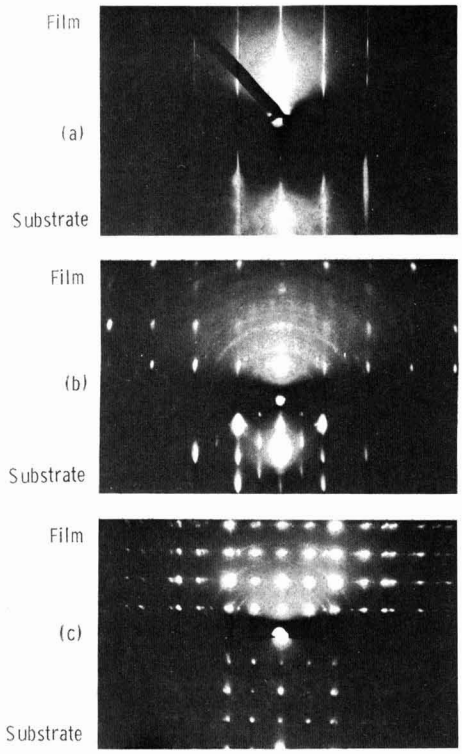

Fig. 4. Reflection electron diffraction (RED) patterns of epitaxial rutile films on (a) (110) rutile, (b) (100) MgO, and (c) (0001) sapphire. Corresponding RED patterns of substrates are shown on the bottom half of each photograph. Substrate temperature = 1100°K, $p_{O_2} \simeq 760$ Torr, $p_{TiCl_4} = 0.232$ Torr.

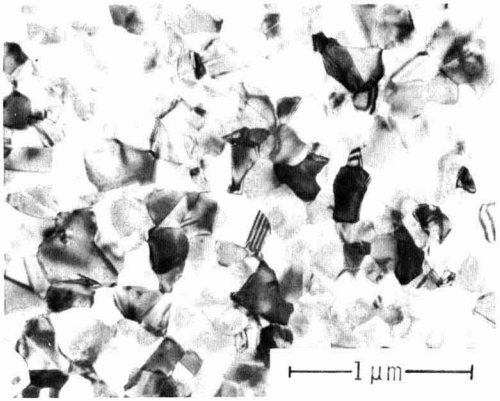

Fig. 5. Typical transmission electron micrograph of rutile film grown on silicon. $p_{O_2} \simeq 760$ Torr, $p_{TiCl_4} = 0.116$ Torr, $T = 1100°K$, $t \simeq 1500Å$.

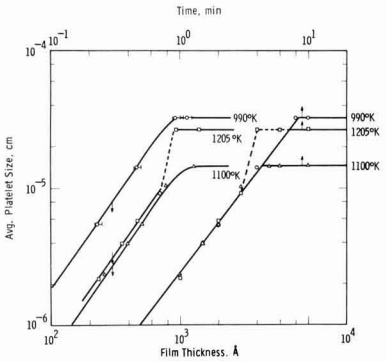

Fig. 6. Average lateral size of rutile crystallites in the thin films grown on (111) silicon single crystal substrates as functions of film thicknesses and growth times at 990°, 1100°, and 1205°K. $p_{TiCl_4} = 0.116$ Torr, $p_{O_2} \simeq 760$ Torr.

tortion is expected. A somewhat similar alignment occurs on (0001)-oriented sapphire crystals where the oxygen-filled substrate surface becomes common to both substrate and film. In this case, the respective oxygen ion densities are sapphire (0001) = 5.12 x 10^{14}/cm^2 and rutile (100) = 7.37 x 10^{14}/cm^2. In deposits on to single crystal rutile surfaces (homoepitaxy), the oxygen-titanium stacking becomes that of the substrate.

Growth behavior.—The growth behavior of TiO_2 films was most conveniently observed by transmission electron microscopy (TEM) of films deposited on Si substrates. The majority of films so investigated had mean thicknesses between 230 and 1500Å, were deposited in a fixed set of reactant partial pressures ($p_{TiCl_4} = 0.116$ Torr, $p_{O_2} \simeq 760$ Torr), and at one of three predetermined temperatures, 990°, 1100°, or 1205°K. All films on silicon showed a platelet morphology as shown in Fig. 5. The data obtained from such micrographs are given in Fig. 6 where the average platelet dimension is plotted both as functions of film thickness and equivalent growth time. The average platelet size was observed from the electron micrographs by linear analysis (error $\cong \pm 10\%$). Since average values did not change with annealing at the growth temperatures in oxygen ($p_{O_2} = 760$ Torr) (the annealing period was at least ten times the period of the deposition), they were considered to represent equilibrium dimensions. From the data in Fig. 6, deposits prepared between 990° and 1205°K show lateral extension of individual grains at almost a constant rate until a film thickness between 700 and 1000Å are reached. At these thicknesses, further lateral growth ceases. The ultimate lateral dimensions reflect the differences in nucleation densities observed earlier, *i.e.*, deposits where nucleation density was greatest show crystallites of smallest lateral dimension and vice versa. Approximate dimensions (maximum) are 1470Å (1100°K), 2700Å (1205°K), and 3300Å (990°K). The data from films deposited at 1205°K indicate that at this temperature the rate of lateral extension is irregular in the thickness range 700-900Å. These growth results are regarded as uncertain at present and are indicated by a dashed line in Fig. 6. The size irregularities are likely related to the appearance of another TiO_2 phase during deposition [electron diffraction reveals the presence of TiO_2 (anatase) in deposits prepared above 1125°K]. The observed two-component multilayered film is likely to produce crystallites of various dimensions, the averaging of which could cause the observed discrepancy. The mechanism for formation of the second phase may well occur via a homogeneous reaction between $TiCl_4$ and O_2; such a reaction has been reported in a similar CVD reaction (4) although no structural data of the reaction product is available.

Effects of partial pressure ratio.—The effects of the variation of partial pressure ratio p_{O_2}/p_{TiCl_4} on the deposition rate of TiO_2 film is shown in Fig. 7 at two substrate temperatures. The slope of 1/2 is due to the fact that atomic oxygen is a reactant species at both these temperatures; this has been discussed in detail elsewhere (7). The pressure ratio at which TiO_2

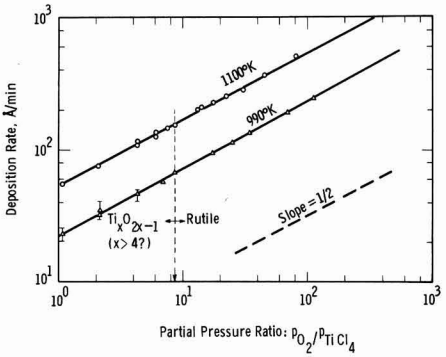

Fig. 7. TiO_2 thin film deposition rate as a function of the reactant partial pressure ratio (p_{TiCl_4} = 0.058 to 0.232 Torr, p_{O_2} = 0.25 to 25 Torr) at two substrate temperatures.

(rutile) formation is prominent is 8.62; below this ratio an unidentified reaction product is formed which is stable to the extent of complete resistance to further oxidation in pure oxygen (760 Torr) at temperatures up to 1320°K and at annealing durations of up to 8 hr. Thermodynamic calculations, using free energy change values from the JANAF thermochemical tables (9) and assuming equilibrium, *i.e.*

$$2p_{Cl_2} = p_{TiCl_4} \text{ and } p_{O_2}/p_{TiCl_4} = \tfrac{1}{4}\,Kp \qquad [7]$$

predict that the minimum p_{O_2}/p_{TiCl_4} ratio for rutile formation is 7.7 x 10^{-7} at 1100°K. This is orders of magnitude lower than the experimental value of 8.62 and is in the right direction for a reaction sequence controlled by the surface adsorption kinetics of atomic oxygen produced in the gas phase.

Refractive index data.—The refractive indices (n_D) and thicknesses of TiO_2 films on silicon were determined by ellipsometric methods (12). For films in the thickness range of 200-1500Å the average value of n_D was 2.83 ± 0.03. A few films thinner than ~ 500Å had a refractive index 5-8% lower than this average value. Such data are not uncommon in thin films, viz., indices of refraction of the oxides (Al_2O_3, Ta_2O_5, Nb_2O_5) are less in thin film form than in the bulk (15). The average refractve index of TiO_2 films (2.83 ± 0.03) produced for the present studies is greater than that obtained by a similar CVD process (n_D = 2.0) using tetrabutyl titanate and tetraisopropyl titanate (16) and compares favorably with the single crystal n_D values (17) (2.909 for the extraordinary ray and 2.613 for the ordinary ray). No reproducible behavior of change in n_D as a function of film thickness and/or deposition temperature could be detected.

Summary and Conclusions

The present study on the structure of chemically vapor deposited TiO_2 thin films on a variety of substrates has shown that (*a*) the crystallographic modification of TiO_2 produced by the reaction of $TiCl_4$ (g) and O_2(g) on all substrates studied is predominately rutile at and above a p_{O_2}:p_{TiCl_4} ratio of 8.62; (*b*) the film is always polycrystalline on single crystal silicon between 0.001 to 30 ohm-cm, p- or n-type and low-index orientations and silica (amorphous or fused quartz) substrates and exhibits a particular fiber texture which is a function of only the temperature of deposition; (*c*) at temperatures below 1100°K, growth on (001) and (111) rutile substrates generates polycrystalline films and at relatively high deposition temperatures (> 1100°K) epitaxial films were produced on single crystal rutile, MgO and sapphire substrates; (*d*) *in situ* HCl etching of single crystal substrates produces preferred crystalline orientation at lower temperatures (in the case of silicon) and better quality epitaxial films (little or no twinning) on rutile substrates; (*e*) under a fixed set of experimental conditions comparable growth rates were obtained on all substrates; (*f*) between 990° and 1205°K the rutile crystallites grew laterally (on silicon) at about the same rate up to a film thickness of about 700Å; and (*g*) the density of TiO_2 nuclei (on silicon) increased exponentially with increasing temperature up to about 1125°K with an activation energy of 2.18 eV.

The energetics of the rutile crystallite formation process (on silicon) has been analyzed to support an earlier conclusion that the kinetics of the reaction $TiCl_4(g) + O_2(g) \rightarrow TiO_2$ (rutile) + $Cl_2(g)$ (on the silicon surface) involve adsorbed atomic oxygen and $TiCl_4$ molecular species (in the gas phase). Also, the epitaxial rutile thin film grown on low-index MgO, rutile, and sapphire substrates have easily understandable film-substrate structural relationships.

Acknowledgment

The authors wish to thank R. F. Yut and J. H. Rieger for experimental assistance and Dr. J. R. Szedon for arranging to have ellipsometric measurements done by his laboratory.

Manuscript submitted Feb. 2, 1970; revised manuscript received May 1, 1970.

Any discussion of this paper will appear in a Discussion Section to be published in the June 1971 JOURNAL.

REFERENCES

1. Proc. Conf. Chem. Vap. Deposition of Refractory Metals, Alloys and Compounds, Gatlinburg, Tenn., Sept. 12-14, 1967, Am. Nucl. Soc. (1967).
2. S. Zerfoss, R. G. Stokes, and C. H. Moore, *J. Chem. Phys.*, **16,** 1166 (1948).
3. L. Holland, "Vacuum Deposition of Thin Films," p. 466, J. Wiley & Sons, Inc., New York (1956).
4. M. Yokozawa, H. Iwasa, and I. Teramoto, *Japan. J. Appl. Phys.*, **7,** 96 (1968).
5. A. E. Fuersanger, *Proc. IEEE*, **52,** 1463 (1964).
6. F. Huber, *This Journal*, **115,** 203 (1968).
7. R. N. Ghoshtagore, *ibid.*, **117,** 529 (1970).
8. E. F. Cave and B. R. Czorny, *RCA Rev.*, **24,** 523 (1963); T. L. Chu, J. R. Szedon, and G. A. Gruber, *Trans. Met. Soc. AIME*, **242,** 532 (1968).
9. JANAF Interim Thermochemical Tables, Dow Chemical Co., Midland, Mich., Dec. 13, 1960.
10. H. D. Hagstrum, *J. Appl. Phys.*, **32,** 1020 (1961); J. J. Lander and J. Morrison, *ibid.*, **33,** 2089 (1962); F. Jona, *Appl. Phys. Letters*, **6,** 205 (1965).
11. F. G. Allen, *J. Appl. Phys.*, **28,** 1510 (1957).
12. B. Schwartz and N. Schwartz, Editors, "Measurement Techniques for Thin Films," The Electrochemical Society, New York (1967).
13. G. R. Booker, and R. Stickler, *Brit. J. Appl. Phys.*, **13,** 446 (1962).
14. F. D. Rossini, D. D. Wagman, W. H. Evans, S. Levine, and I. Jaffee, Nat. Bur. Standards, 1952, Selected values of chemical thermodynamic properties.
15. J. A. Aboaf, *This Journal*, **114,** 948 (1967); M. Duffy, K. H. Zaininger, and C. C. Wang, *ibid.*, **115,** 61C (1968).
16. D. R. Harbison and H. L. Taylor in "Thin Film Dielectrics," pp. 254-278, F. Vratny, Editor, The Electrochemical Society, New York, (1969).
17. J. R. DeVore, *J. Opt. Soc. Am.*, **41,** 416 (1951).

Deposition of Silicon and Silicon Carbide by Film-Boiling

Raymond W. Conrad*

Physical Sciences Laboratory, U. S. Army Missile Command, Redstone Arsenal, Alabama 35809

When a substrate is immersed in a liquid and heated to a temperature much higher than the boiling point of the liquid, a sheath of vapor forms, separating the liquid from the substrate. This process is generally called "film boiling." If the liquid thermally decomposes or otherwise reacts to produce a substance which is nonvolatile at the temperature of the substrate, plating of this substance onto the substrate may occur. Basically, such a process is simply vapor deposition, at the high vapor concentration limit.

Recently Nieberlein (1) has used the film-boiling method to deposit polycrystalline silicon carbide onto tungsten filaments from mixtures of trimethylchlorosilane and cyclohexane at temperatures of ~900°C. Deposition rates of up to 100 μm/min were obtained. X-ray investigations (2) have not yet unraveled the crystal structure of the deposits. However, an extensive transition layer of tungsten carbide was identified.

This report presents the initial results of our attempts to adapt the film-boiling technique to the production of materials for electronics applications, particularly silicon carbide. Graphite and single-crystal silicon substrates were used in an attempt to eliminate transition layers. Several liquid systems were investigated.

Experiments and Results

The deposition system (Fig. 1) consisted of a pair of copper electrodes, with adjustable spacing, immersed in the liquid under study. The deposition cell was cooled with chilled acetone (~0°C) to minimize evaporation. The substrates were clamped between the electrodes by tightening the Teflon spacers and heated with a variable autotransformer. A current-limiting resistor was required when using silicon substrates. This consisted of a coil of resistance wire wound on a spiral-grooved ceramic core (total resistance, 15 ohm). Several intermediate taps were provided for lower resistances.

Temperature was monitored with an optical pyrometer. Sight-path effects introduced an uncertainty of ±50°C. The boiling, liquid sheath did not interfere with the temperature measurements during the early stages of deposition. However, the solutions eventually became turbid, making temperature measurements unreliable toward the end of deposition.

Graphite substrates, nominally 2 × 0.3 × 0.1 cm, were cut from disks of spectroscopic grade graphite (National Carbon, Grade CCH), lightly sanded with fine emery paper, rinsed with acetone and wiped dry. Silicon substrates, nominally 2 × 0.3 × 0.05 cm, were obtained by scribing and fracturing from 0.2 to 0.5 ohm-cm, (111), p-type silicon wafers. These were degreased in trichloroethylene and etched in $HF-HNO_3$ before use. Solutions for deposition were prepared from reagent grade materials without further purification. They were used only once because of the turbidity produced during deposition.

Graphite substrates.—Deposition from pure trimethylchlorosilane at ~1100°C produced thick, adherent layers of polycrystalline material which were identified by x-ray diffraction as the 6H polytype of α-silicon carbide. Deposition rates were ~350 μm/min for runs of up to 1½ min duration. Knoop microhardness values averaged 2200. No electrical evaluations have yet been made on these deposits, other than to note that they appeared to be n-type by thermal probe and to have relatively high resistivity.

Dilution of the trimethylchlorosilane with cyclohexane decreased the rate of deposition, but otherwise had no apparent effects on the gross characteristics of the deposits. Dilution with methanol, however, produced a rather dramatic effect. For mixtures with less than ~65 v/o (volume per cent) methanol, the deposits resembled those from pure trimethylchlorosilane. For mixtures with higher methanol concentrations, a black, lustrous deposit was obtained. Fracture surfaces of this material appeared glassy (see Fig. 2). Pro-

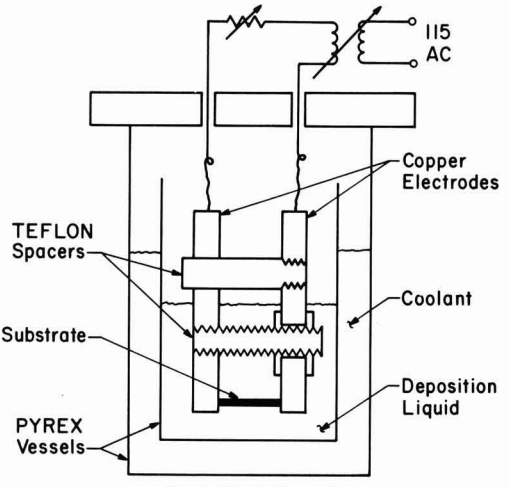

Fig. 1. Film-boiling cell

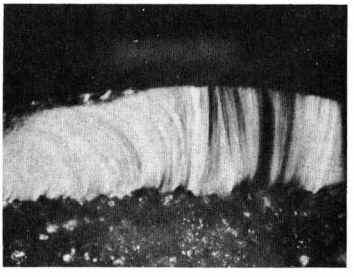

Fig. 2. Fracture surface showing a 230 μm-thick layer of glassy material deposited from a solution of 10 v/o trimethylchlorosilane in methanol, onto a graphite substrate.

* Electrochemical Society Active Member.
Key words: silicon, silicon carbide, vapor deposition, film-boiling.

longed etching in $HF-HNO_3$ (4 days in a 50-50 mixture) revealed that some areas of the deposits were not single-phase. X-ray diffraction indicated the material was indeed noncrystalline. Knoop microhardness values averaged 1800. The chemical composition has not yet been determined. However, the material was observed to form a liquid phase when heated in an inert atmosphere to 1700°C. Microscopic examination of the surface after this treatment revealed that portions of the layer had been transformed into a colorless glassy material which we suspect is silica.

The preparation of a similar, black, glassy substance by the decomposition of methyltrimethoxysilane vapor on a hot tungsten filament was reported by Hough and Early (3). They reported the composition to be $\sim Si_{33}C_6O_{40}$.

Silicon substrates.—Deposition from pure trimethylchlorosilane at ~950°C produced thick, polycrystalline layers shown by x-ray diffraction to be silicon. Deposition rates were 200 μm/min for runs of up to 1½ min duration. The deposits appeared to have relatively high resistivity. Thermal probing indicated n-type conduction.

Dilution with cyclohexane not only decreased the deposition rate but materially improved the physical quality of the deposit. Figure 3 shows a 94 μm thick layer deposited in 4½ min from a mixture containing 20 v/o trimethylchlorosilane. Back reflection x-ray diffraction indicates that some areas of the deposit are (111) single crystal. Thermal probing showed the deposit to be n-type. The electrical characteristics of the p-n junction have not yet been investigated. No deposits could be obtained using trimethylchlorosilane and methanol mixtures because the conductivity of such solutions was higher than that of the substrate.

Discussion

The deposition of silicon onto silicon substrates from trimethylchlorosilane, both with and without cyclohexane, was an unexpected result in view of the results obtained using tungsten and graphite substrates. The influence of deposition temperature on the composition of the deposit, however, has yet to be determined. The results reported here were for a relatively low deposition temperature, and the formation of silicon carbide at higher temperatures cannot be ruled out. Different results might also be obtained by using a different silane or an organic diluent or both. Nevertheless, the effect of the substrate on the course of the reactions occurring is vividly illustrated.

The suitability of material prepared by film-boiling for device fabrication has yet to be demonstrated. The rather unsophisticated technique used here can certainly be improved upon. By using highly purified liquids and inert electrodes (*e.g.*, graphite), the purity of the deposits should be substantially improved. Actually, this technique should be inherently cleaner than solution epitaxy, since the container for the liquids is not heated. Should it prove to be detrimental, the turbidity of the liquids, produced during deposition, might be eliminated by using a liquid flow system in which the liquids are continuously pumped from the deposition chamber through a filter, thence back to the chamber. Dopants might also be thus introduced.

There are several characteristics of the film-boiling technique that may limit its usefulness for epitaxial deposition. For example, there is a very large temperature gradient along the substrate major axis. This might be reduced, however, by using very long, thin substrates. High resistivity substrates obviously could not be used. The inability to vapor etch might also be a disadvantage. However, some degree of etching might be obtained by heating the substrate to a relatively low temperature if the liquid easily decomposes to produce vapors of an etchant, *e.g.*, HCl. The tendency to deposit thick polycrystalline layers from concentrated solutions, although undesirable for epitaxy, may have applications to the technology of integrated circuit fabrication using dielectric isolation.

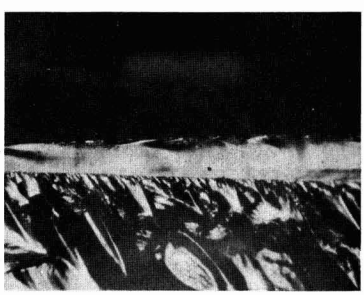

Fig. 3. Fracture surface showing a 94 μm-thick layer of silicon deposited from a solution of 20 v/o trimethylchlorosilane in cyclohexane, onto a single crystal silicon substrate.

Acknowledgments

The author thanks J. F. Bebbs, Jr. for his assistance in the laboratory, V. A. Nieberlein for his valuable discussions, and C. W. Austin for the x-ray diffraction work.

Manuscript submitted March 17, 1970; revised manuscript received *ca.* June 9, 1970.

Any discussion of this paper will appear in a Discussion Section to be published in the June 1971 JOURNAL.

REFERENCES

1. V. A. Nieberlein, *SAMPE Journal*, **4**, 72 (1968).
2. V. A. Nieberlein, PhD Thesis, University of Alabama, University, Ala. (1970).
3. R. L. Hough and D. E. Early, Technical Report AFML-TR-66-174, July 1966.

Gallium Diethyl Chloride: A New Substance in the Preparation of Epitaxial Gallium Arsenide

K. Lindeke, W. Sack, and J. J. Nickl

Forschungslaboratorium für Festkörperchemie am Institut für Anorganische Chemie der Universität München, München, Germany

Manasevit *et al.* (1, 2) and Rai-Choudhury (3) have reported on the use of alkyl-gallium compounds and arsine in the preparation of gallium arsenide epitaxial layers. However, these compounds are distinguished by a high reactivity (4) [$Ga(CH_3)_3$ ignites with O_2 even at −76°C, and a mixture of its vapor with air explodes at room temperature; $Ga(C_2H_5)_3$ ignites in air and explodes in O_2.] The use of trialkyl-gallium together with highly toxic arsine (threshold limit value 0.05 ppm) is extremely hazardous in case of any leakage.

Key words: materials, preparation, gas epitaxy, organic Ga source, arsine.

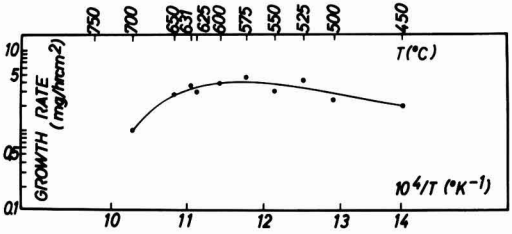

Fig. 1. Growth rate of (100) GaAs layers vs. $10^4/T$

The reaction between $Ga(CH_3)_3$ and Pyrex has also been reported (2). This causes difficulties during distillation for purification purposes. In a technical application it would be important to have a Ga-compound which is safer to handle even in large quantities.

Therefore, the comparable low reactive gallium diethyl chloride (GDC) has been used as the Ga source. This substance hydrolyzes slowly even in 0.1*N* NaOH. Although 1 mole of HCl is generated per mole GaAs, this should not have a negative influence on the layer quality because, in the Cl-transport system, layers of highest purity can also be produced (5, 6). In addition, gas-phase etching occurs in the reaction mixture just before growing the crystal by increasing the temperature to 750°C, which may be very helpful in preparing an absolutely clean surface.

GDC was obtained commercially and is used without further purification. The arsine (purity 99.5%) concentration was 5.5% in high-purity H_2. Semi-insulating Cr doped GaAs wafers of $(\bar{1}\bar{1}\bar{1})$ ("B" face), (110) and (100) orientation were etched in 10% Br_2/CH_3OH and washed in methyl alcohol just before use.

The experiments were performed in a vertical rf heated flow-type reactor designed to permit evacuation. Quartz, Pyrex, Teflon, and stainless steel have been used in constructing the system. This kind of CVD apparatus has also been used successfully in the preparation of elemental semiconductors such as Si and Ge (7, 9) and has many advantages. A thermocouple NiCr/Ni, calibrated at the freezing point of Al, was embedded in the graphite susceptor in close proximity to the GaAs wafer.[1] The susceptor was coated with pyrolytic carbon. A bubble-type vaporizer inserted into an oil bath at about 60°C contained the liquid gallium source. Three special bubblers containing H_2O, Br/H_2O, and 30% NaOH, are used downstream to destroy the waste products, especially AsH_3.

Before deposition takes place the wafers are heated to 900°C for 1 min to remove surface contaminations. In the early stage of the investigation the grown layers often showed holes; this could be prevented by this annealing step. Then the temperature is lowered to the growth temperature and the AsH_3-stream (0.7 l/hr) is started. After As deposits at the reactor walls the H_2 (3.5 l/hr) is bubbled through the GDC, and GaAs is formed on the substrate. The GaAs wafers were heated to growth temperature (450°-700°C) and after deposition cooled to room temperature in Pd-diffused H_2. It is recommended that the wafers not be cooled in the reaction mixture, since GaAs is formed down to 450°C (Fig. 1). Below growth temperature of 500°C the layers are of high resistivity and have rough surfaces. Single crystallinity as determined by reflection x-ray Laue pattern was obtained as low as 450°C. At 750°C gas-phase etching takes place, as observed by weight changes of the wafers before and after the process. The nature of this reaction is not known so far. We believe that 1 Cl from the GDC transports 1 Ga as GaCl from the surface and the other part of the GDC is evaporated as a alkyl subcompound Ga $(alkyl)_{1 \text{ or } 2}$ from the surface. However, no visible amount of metallic Ga could

[1] The influence of the rf was prevented by a capacitor shunted to the thermocouple.

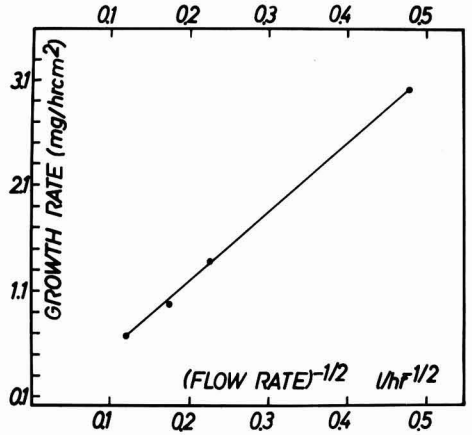

Fig. 2. Growth rate of (100) GaAs layers vs. (total flow rate)$^{-1/2}$ at constant GDC and AsH_3 flux.

be detected at the substrate or anywhere in the reaction chamber (by reaction 3 $GaR_1 \rightarrow GaR_3 + 2$ Ga).

Mirror smooth layers of epitaxial GaAs on (100), (110), $(\bar{1}\bar{1}\bar{1})$-surfaces were obtained, but the reported data are measured on layers with (100)-orientation. Layer thickness was determined by two methods: first by etching (10); second by the weight gain of the wafers. Growth rate was evaluated as function of substrate temperature (Fig. 1) and gas stream velocity at constant GDC and AsH_3 input values. Since the reaction is nearly independent of the temperature, we assume a mass transport phenomenon to be the rate-controlling step. This is supported by Fig. 2 which shows the growth rate increasing with the reciprocal square root of the gas stream velocity.

The electrical properties of the layers were assessed using the van der Pauw method (11). For this purpose contacts of Sn/In (48/52) were alloyed at about 250°C in a H_2, Ar, HCl (80/15/5) atmosphere. The ratio of the two van der Pauw resistivities $R_1:R_2$ was constant within 3% from 70° to 300°K. The Hall coefficient R_H and the resistivity ρ were measured in this temperature range. The mobility was calculated from the ratio R_H/ρ. The magnetic field was 4 kG. Plots of carrier concentrations as a function of reciprocal temperature are shown in Fig. 3. The mobility plots *vs.* temperature are shown in Fig. 4. The correlation between deposition temperature, layer thickness, the measured carrier concentration, and mobility are shown in Table I. The

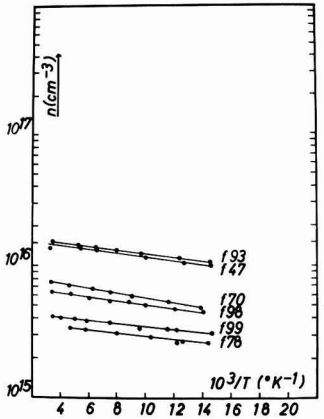

Fig. 3. Carrier concentration vs. $10^3/T$

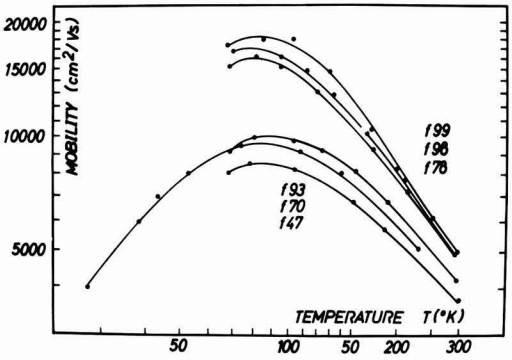

Fig. 4. Mobility vs. temperature

samples seem to have an impurity with an ionization energy of about 8 meV, calculated under the assumption of one single donor term, partly compensated by acceptor terms. The impurity has not yet been identified. No carbon could be detected in the reaction chamber or on the layers either by microanalytical methods or by x-ray investigations.

The results, listed in Table I, show that GDC is a suitable substance for the preparation of epitaxial GaAs layers. However, better results should be obtained when purer starting materials are used.

Acknowledgment

The authors are greatly indebted to Dr. Doetzer, Siemens AG. Erlangen, Germany, for supplying GDC. Thanks are given to Mrs. M. Betz for technical assistance.

Table I. Characteristics of typical GaAs layers grown by the GDC/AsH_3 CVD process

Sample No.	Thickness, μm	Depos. temp, °C	Mobility, $cm^2/vs.$ $\mu_{300°K}$	$\mu_{70°K}$	Carrier conc. $n_{300°K}$, cm^{-3}	Resistivity $\sigma_{300°K}$, ohm-cm
f 47	5-6	635	3750	8500	$1.5 \cdot 10^{16}$	0.12
f 70	5-8	631	3850	9500	$7.5 \cdot 10^{15}$	0.18
f 78	5.5	550	4800	16000	$3.5 \cdot 10^{15}$	0.33
f 93	2-3	631	4200	9800	$1.5 \cdot 10^{16}$	0.10
f 98	7.5	575	4850	16500	$6.4 \cdot 10^{15}$	0.20
f 99	11.6	575	5050	18000	$4.2 \cdot 10^{15}$	0.30

Manuscript submitted March 31, 1970; revised manuscript received *ca.* June 25, 1970.

Any discussion of this paper will appear in a Discussion Section to be published in the June 1971 JOURNAL.

REFERENCES

1. H. M. Manasevit and W. I. Simpson, Paper 63 presented at the Boston Meeting of the Society, May 5-9, 1968; Extended Abstract, Vol. 5, p. 154.
2. H. M. Manasevit and W. I. Simpson, *This Journal*, **116,** 1725 (1969).
3. P. Rai-Choudhury, *ibid.*, **116,** 1745 (1969).
4. J. A. Sheka, J. S. Chaus, and T. T. Mityureva, "The Chemistry of Gallium," Elsevier Publishing Co., Amsterdam (1966).
5. D. Effer, *This Journal*, **112,** 1020 (1965).
6. M. Maruyama, S. Kikuchi, and O. Mizuno, *ibid.*, **116,** 413 (1969).
7. H. C. Theuerer, *ibid.*, **108,** 649 (1961).
8. V. J. Silvestri, *ibid.*, **116,** 81 (1969).
9. S. A. Papazian and A. Reisman, *ibid.*, **115,** 961 (1968).
10. M. S. Abrahams and J. Buiocchi, *J. Appl. Phys.*, **36,** 2855 (1965).
11. van der Pauw, *Philips Res. Repts.*, **13,** 1 (1958).

JOURNAL OF THE ELECTROCHEMICAL SOCIETY

ELECTROCHEMICAL TECHNOLOGY

OCTOBER 1970

Development of a Controlled Porosity Silver Electrode

G. W. Mao, D. S. Polcyn,* and R. E. Tieder

Gould Incorporated, Gould Laboratories, Energy Technology, Minneapolis, Minnesota 55414

ABSTRACT

Silver electrodes which require no supporting grid and have a porosity graded structure were fabricated by combining silver powder of uniform mesh size with a plasticizer and pore forming additives. The proportions of these materials are selected to give a uniform doughlike mixture which is rolled and then sintered. Porosity control is achieved by controlled decomposition of the plasticizer and pore forming additives. Multilayered graded porosity electrodes are assembled by a combination of sintering and compaction. Performance data based on cycling tests and coulombic efficiencies demonstrated that these electrodes are comparable to conventional silver electrodes and the absence of the grid is not a limiting factor.

Silver electrodes for electrochemical cells can be produced by various methods either from silver or silver oxide powders. Junger (1), Morrison (2), and Jirsa (3) have produced silver electrodes by various methods of pasting a silver grid. Moulton and Enters (4) describe producing a sintered porous silver mass by thermally decomposing a dried silver(I) oxide pasted grid. More recently, electrodes have been prepared by application of silver(II) oxide paste to a silver grid using methylcellulose or sodium carboxymethylcellulose as binders (5). Wilburn (6) and Wilburn *et al.* (7, 8) have described methods for producing electrodes by dry compaction of silver(II) oxide to silver grids. Additional methods for producing porous silver electrodes primarily for use in fuel cells have been described by Schroeder *et al.* (9) and Niedrach and Alford (10).

Even though several methods are available for producing silver electrodes, they are normally prepared from silver powder which has been compacted on a silver grid, sintered, and electroformed (6). In these processes little regard is given to available electrode porosity, a known control factor of battery electrode performance, other than pressing sintered silver powder to various densities. Experience has shown that this practice is used to increase the A-hr/g capacity rather than controlling porosity.

Since these electrodes may be rather dense, they must be kept relatively thin; otherwise the interior active material becomes electrolyte-starved during cycling because of restricted electrolyte flow. Production of an electrode with controlled porosity would make all portions of the electrode equally accessible to electrolyte and enables the use of relatively thick electrodes for high efficiency, primarily at low discharge rates. At high discharge rates, the zinc electrode is the limiting electrode rather than the silver electrode, so the silver electrode can be made thin. However, porosity control provides an additional advantage in controlling the over-all performance of the cell. Since a controlled porosity sintered silver electrode would oxidize uniformly during charge, a silver grid would not be required since a continuous network of silver during discharge should remain throughout the electrode, and act as a more efficient conductor than the conventional silver grid. Presumably the process of hot rolling a mixture of polyethylene and silver powder followed by heating to burn out the polyethylene (11) may well be used to control porosity. No data to this effect have been published.

This paper describes the fabrication and electrochemical behavior of sintered silver electrodes of uniform pore size, produced by sintering a rolled sheet of uniformly mixed wet silver and binder powders. High efficiency thick electrodes were produced by sintering electrode material of 60% and 78% accessible porosities into a porosity-graded layered structure. It is expected that the electrochemical behavior of these porosity layered electrodes may possess good performance in comparison to conventional pressed and sintered grid-containing silver electrodes.

The work of Bogenschutz *et al.* (12) interrelating porosity and sintering temperature showed that, over the porosity range 57-65%, the capacity varied 20%. These results were used in determining our optimum sintering temperature for gridless silver electrodes.

Electrode Processing Procedure

The first processing step for producing porosity controlled silver electrodes consists of rolling a doughy silver powder-methyl cellulose mixture into a continuous sheet. The mixture is composed of 93 parts −325 mesh silver powder (44μ diam) blended with 7 parts methyl cellulose. The components are mechanically shear mixed with 10 ml of 10% aerosol and approximately 35 ml of alcohol per 100g until "dough" consistency is achieved. After suitable mixing, the material is rolled to the desired thickness and allowed to air dry. Any scrap, prior to sintering, can be reprocessed with the appropriate liquid addition. The dry material is sintered in air by placing it into a 788°C furnace for 15 min. Sintering produces a porous structure by burning out the plasticizer and creates sufficient strength by joining adjacent silver particles.

The sintered sheet (0.05 cm thick) was cut into 3.8 cm squares, and a 0.32 cm wide silver strip current collector was attached to one edge. Several methods

* Electrochemical Society Active Member.

Key words. silver electrodes, porous electrodes, sintered electrodes, gridless, porosity graded.

for attaching the current collector were tried, but the most successful method was to first position the silver strip with a single spot weld along the edge of the square electrode. Then the electrode assembly was placed in a furnace at 780°C for 3 min. While in the furnace, the current collector section of the electrode was rolled at a pressure of about 0.07 g/m². This rolling process assured contact of the strip to the silver electrode over the entire collector-electrode contact area.

In comparing the structure of gridless electrodes with conventional pressed and sintered electrodes, it was apparent that the experimental process produces an evenly distributed, uniform pore size. Many of the silver particles of conventional electrodes are massively sintered together in the press and sinter technique resulting in poor contact between portions of the supporting grid and adjoining silver. This lack of contact indicates that the sintered silver structure may be the primary current conductor instead of the grid. In the case of the gridless electrode, the interconnected silver network which remains after oxidation of the silver should provide efficient current conduction because of its uniform distribution.

Porosity Control

Available porosity can be increased by blending pore-forming agents with the silver powder and methocel. Ground charcoal and wood flour were chosen as porosity controllers, since burn-out during sintering forms gases which produce interconnecting pores upon leaving the silver mass and minimizes residual contaminants. These additives were used to increase the accessible porosity from nominal 68-80% as seen in Fig. 1. Porosity was determined by comparison of the bulk density with the true density where:

$$\text{Total porosity} = 1 - \frac{\rho\text{Bulk}}{\rho\text{True}}$$

The relationship between the amount of pore agent and per cent void volume is not linear since, as porosity increases, the silver structure partially collapses during sintering. Therefore, 80% was determined to be the practical upper porosity limit. Chemical analysis shows that −100 +140 mesh ground charcoal was completely removed during sintering. With the other porosity controllers, a trace of carbonaceous material remained. Photomicrographs showed that the wood particles contain a greater volume per mesh size, because they are fibrous, while the charcoal is particulate. Therefore, it seems reasonable to assume that wood flour would result in less surface area per unit volume in comparison to an equal volume of charcoal because of the difference in particle shape and over-all size.

Available porosity can be decreased from the nominal 68% by adding additional silver to the basic batch mix. For example, an extra 50 parts silver decrease porosity to 60%. Larger additions were not evaluated, since producing a dense electrode with little interconnection between pores was not desirable.

Porosity Layered Electrode Fabrication

In preparing porosity gradient electrodes, the sintered material of 0.05 cm thickness and of 60% and 78% accessible porosity was cut into 3.8 cm squares and three-layered assemblies of 60-60-60%, 60-78-60%, 78-60-78%, and 78-78-78% porosity were made. These layered structures are designated as *DDD, DPD, PDP,* and *PPP,* respectively, where D=60% porosity and P=78% porosity.

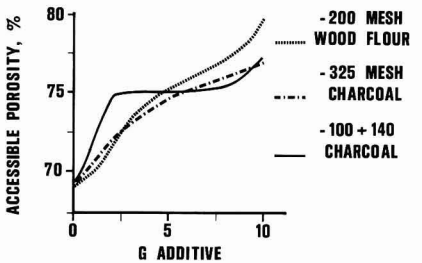

Fig. 1. Porosity effect of additives per 100g Ag-methocel

Material using −100 +140 mesh charcoal pore agent was used to produce these porosities, since it was completely removed during sintering. Furthermore, preliminary testing indicated higher capacity than with −100 +140 mesh wood flour or −325 mesh charcoal as pore-forming agents.

A 0.33 x 0.02 cm silver lead was positioned along the edge of an outside layer. Spot welding at a single point maintained alignment of the silver layers and lead. Each assembly was placed in a 788°C furnace for 3 min and hand rolled with a ceramic roller at a pressure not exceeding 0.07 g/m². The electrodes were immediately removed from the furnace to prevent densification. It was found that the rolling operation is necessary and sufficient to create sintered bonding between the layers.

Testing Procedure

Charge-discharge testing was done in open-top 5 x 6.2 x 1.8 cm cells so cycling characteristics of the electrodes could be observed. The silver electrode under test was placed between two nickel counterelectrodes (3.8 x 3.8 cm) in approximately 40 cc of 40% KOH. An Hg/HgO reference electrode which had a Luggin capillary probe was placed between the nickel and silver electrodes. During discharge, Ag/AgO, AgO_2//Hg/HgO potential was monitored to determine electrode discharge stability and capacity. This potential varied with distance between reference and silver electrode due to *IR* drop and nonuniform current distribution, but an attempt was made to minimize the variation by maintaining this distance constant. The use of nickel counterelectrodes prevented problems of zinc dendrites and corrosion that are associated with silver-zinc cells. Furthermore, the silver electrode performance here is much more favorable than would be expected in cells with separators and zinc anodes.

Experimental single-layer electrodes with 70% porous structure and a conventional silver electrode which was also 70% porous were charged and discharged at currents based on the silver weight. Porosity layered electrodes were cycled in two groups, one at charge and discharge currents determined by 70% conversion of silver weight to silver oxides, and another at a charge of 0.021 A/cm² for 8 hr, followed by alternate discharges at 2.21 A/cm² and 0.038 A/cm² to the hydrogen evolution potential. An example of the calculations based on the 70% conversion are included in the section titled Calculations.

Experimental Results

Charge/discharge of grid and gridless electrode.— Discharge curves for 0.05 cm sheet silver electrodes (3.50g, 70% accessible porosity) were measured in 40% KOH at the 5 hr, 1 hr, and ½ hr rate for a conventional grid structure and for a gridless structure. The discharge curves are shown in Fig. 2. Comparing the discharge curves at the 5 hr rate for the grid and gridless silver electrodes, the discharge times agree within 2.5%. At the 1 hr rate a difference of 1.3 min was observed, while at the ½ hr rate the conventional grid electrode discharged about 10% longer than the gridless electrode, but at a lower voltage level. Voltage decay of the conventional grid electrode is more rapid at each of the rates.

Considering voltage levels of the discharge curves, the voltage (*vs.* Hg/HgO) is lower for the grid electrode at the ½ hr and 1 hr rate, but is nearly identical at the 5 hr rate. This voltage difference may be due to lower resistivity of the gridless electrode, but there are not sufficient data to determine the variation exactly. Analysis of the two electrodes showed that

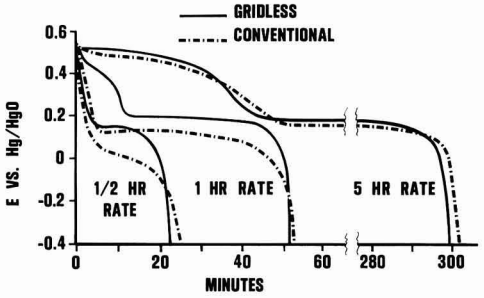

Fig. 2. Silver electrode discharge

the grid electrode contained 17.4% free silver, whereas the gridless electrode contained 14.1% silver. This slight difference in silver content is not sufficient to produce the observed voltage variations.

A characteristic of silver electrode discharge curves is the two-step voltage pattern. This two-step pattern results from the discharge of the divalent oxide to the monovalent oxide and then the monovalent oxide to the metal. Generally this two-step phenomenon is undesirable, either in battery charging or in its application as a power source. The presence or absence of this two-step discharge has been found to be dependent on the physical and electrochemical properties of silver electrodes.

Comparing discharge curves for the conventional and gridless electrodes, it is noted that at all discharge rates a two-step discharge occurred. At the ½ hr and 1 hr rate, the discharge time at the divalent oxide potential was less for the conventional electrode structure and nearly identical at the 5 hr rate.

Further evidence of the improved electrochemical behavior of these electrodes is that, after extended cycling, the cells maintained their performance at a high level. The cells were cycled over 100 times in an open-cell configuration without any significant decrease in performance. It is expected that cell life could be increased considerably by using a closed cell in which the electrodes maintain their physical shape due to tight packing.

During the test period no evidence of unusual charge acceptance, discharge behavior, or physical deterioration was noticed on visual examination of the electrodes. After cycling, both electrode structures, conventional and gridless, are quite brittle. With severe deformation, the gridless electrode fractures quite easily, breaking up into several small parts. The grid electrode is also brittle after cycling, but on deformation the electrode is held together by the grid. This should not be a problem in application since, in the cell assembly, the electrodes are tightly packed and breakage will be minimal.

On the basis of the experimental observations, the gridless electrode performs as well or better than the conventional electrode, indicating that the silver electrode is not limited by the absence of a supporting internal grid. Furthermore, comparing the voltage levels, discharge times, and capacities for the two structures, the gridless electrode is superior to the conventional electrode.

Electrochemical behavior of layered silver electrodes with constant current charge/discharge.—Four electrodes of graded porosity construction were tested. The 60% porous material is designated by *D* and the 78% by *P*. Four combinations of these abbreviations are used to refer to the different electrode structures. The data on physical properties are summarized in Table I.

These electrodes were charged for 8 hr at 0.21 A/cm² and then discharged at two different currents, alternately at 0.021 A/cm² and 0.038 A/cm². At this low rate of charge, the four different structures showed essentially the same charge rate on the basis of the amount of silver present. It is expected that at high-rate charging the more porous electrodes would have improved charge acceptance when compared with the dense structures.

Table I. Physical dimensions of graded porosity electrodes

Porosity layer, %	Electrode	Weight, g	Thickness, cm
60-60-60	*DDD*	7.87	0.152
60-78-60	*DPD*	6.48	0.147
78-60-78	*PDP*	5.27	0.142
78-78-78	*PPP*	4.14	0.142

The average A-hr/g capacity of four discharges was used as the basis for determining the average discharge curves of Fig. 3 and 4. Since the discharge time is proportional to the electrode weight and the weights of the various assemblies were different, a nondimensional time scale was chosen to allow direct comparison of the discharges. The time scale is $t/t_{\text{theoretical}}$, where $t_{\text{theoretical}}$ is the time for discharge assuming 100% utilization of the silver. In addition, the coulombic efficiency was found to be independent of the discharge rate.

From Fig. 3, at a discharge current of 100 mA/cm², the voltage levels and discharge times are similar for the mixed porous structures with *PDP* having the longest discharge time and *DPD* discharging at a higher voltage. The monoporous structures, *DDD* and *PPP*, have nearly identical discharge curves, indicating that the porosity or layered structure is not a controlling factor at this discharge current.

Figure 4 shows the discharges of these graded electrode structures at a current density of 20 mA/cm². The discharge times and voltage levels are similar for

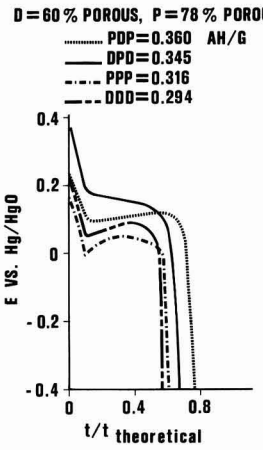

Fig. 3. 100 mA/cm² discharge

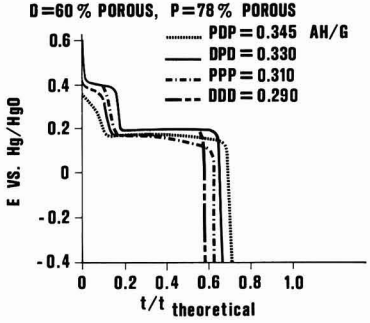

Fig. 4. 20 mA/cm² discharge

Table II. Charge-discharge rate based on electrode weight

Porosity layer, %	Electrode	Weight, g	Thickness, cm	Charge, A 5 hr	Charge, A 25 hr	Discharge, A ½ hr	Discharge, A 5 hr
60-60-60	*DDD*	8.32	0.154	0.582	0.116	5.82	0.582
60-78-60	*DPD*	6.92	0.149	0.484	0.097	4.84	0.484
78-60-78	*PDP*	5.39	0.142	0.377	0.075	3.77	0.377
78-78-78	*PPP*	4.15	0.142	0.290	0.058	2.90	0.290

the multiporous layered electrodes, *PDP* and *DPD*, and, as at the high rate, the DDD and PPP show nearly identical behavior. Discharge time at the divalent oxide potential is longest for the *DPD* structure and decreases in the order *PPP*, *DDD*, and *PDP*. However, no significant differences in the discharge curves are noted at this low rate which could be attributed to variations in the layered structure.

Electrochemical behavior of layered silver electrodes with charge discharge rate determined by electrode weight.—These electrodes were discharged alternately at the ½ hr and 5 hr rates for eight cycles, with the charging done in two steps: charge at a 5 hr rate until oxygen evolution occurs, followed by charging at a 25 hr rate until oxygen evolution again occurs. The experimental data for these electrodes are given in Table II.

The average ampere-hour/gram capacity of four discharges was used for determining the average ½ hr and 5 hr rate discharge curves of Fig. 5 and 6. The coulombic efficiency was found to depend directly on the electrode weight.

From Fig. 5, at the ½ hr discharge rate, the porous outside layers appear to control the discharge, since *PPP* and *PDP* both show higher discharge efficiency than electrodes with dense outer layers. Furthermore, the *PPP* electrode appears most efficient. This was expected, since a more porous electrode outperforms a dense electrode structure at relatively high rates because of the lower effective current density on the porous structure and accessibility of the active material for reaction. It appears that highly porous gridless electrodes have an optimal pore size for the ½ hr rate discharge, as evidenced by the similarity of the discharge voltage-time relationship and the efficiency data. However, the *DDD* structure shows a significant voltage drop at this discharge rate, indicating that only the surface layer is discharged and the discharge process is probably mass transport limited.

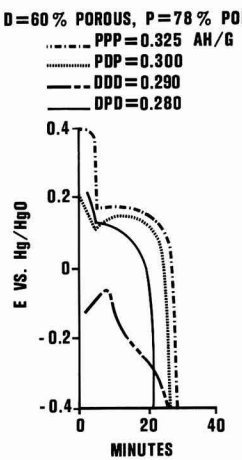

Fig. 5. One half hour rate discharge

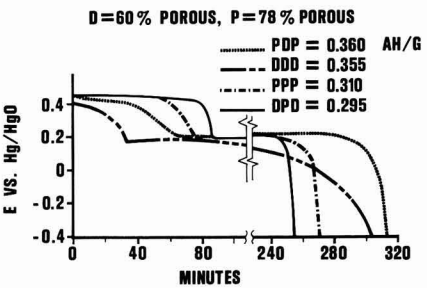

Fig. 6. Five hour rate discharge

Discharge curves at the 5 hr rate are shown in Fig. 6. Here the discharge is at a low enough current density so that the dense inside layer is also discharging and becomes the control layer. This is evidenced by *PDP* and *DDD* electrodes outperforming the electrodes with porous centers. However, the electrodes with porous outside layers outperform the electrodes with dense outside layers, regardless of center layer porosity. Even at low rates the porous layers control the discharge, especially at the divalent oxide potential.

The divalent oxide potential is markedly evident at the 5 hr rate, especially for the *DPD* structure where about one third the discharge time is at the higher potential. The other structures also discharge at this higher potential, but for much shorter times. Probably, explanations for the presence of the divalent oxide potential are weak metal contact between the layered structures, decreased conductivity, nonuniform current distribution due to the porous structure, and poor contact between the silver-to-silver bonds due to the semiconductor AgO in the electrode.

Since discharge time at the divalent oxide potential is greatest for the *DPD* structure and decreases in the order *PPP*, *PDP*, and *DDD*, it appears that the center porous layer may be a controlling factor. However, the manner in which the porous layers control the divalent potential for these electrodes has not been thoroughly investigated in this work, and will be considered in future studies.

Conclusions

The gridless electrode has been shown to have physical and electrochemical properties exceeding, or as good as, those of the conventional grid structured silver electrode. The manufacturing process is simple and economical. Considerable savings will be realized on the total amount of silver used by elimination of the grid. Furthermore, the process permits controlling the porosity of the silver electrode which is not realizable with the conventional silver electrode.

Comparing the electrochemical performance of the (0.05 cm thick) gridless and grid electrodes, the gridless electrode's performance was not limited by the absence of a conducting grid, as evidenced by the discharge data.

On extending the controlled porosity layer concept, to a multiporosity structure, the mixed porosity combinations performed significantly better than the monoporosity combinations. In fact the *PDP* structure was superior in three of the four tests, with the *DPD* closely approximating it. It also appears that, in the conventional Ag-Zn battery, several thin electrodes could be replaced by a single thick graded structure, if the separator and anode space requirements, as well as the discharge rate, are considered.

Although it has been demonstrated that the layered structure is feasible, no attempt has been made to determine the optimum pore size of the layered structure. This will be considered in further investigations of gridless electrodes. Further testing of these electrodes at higher rates is also under investigation, since the high discharge rate performance was not thoroughly studied.

CALCULATIONS

70% Conversion

As an example of charge/discharge cycling with currents determined by silver weight, consider the following example for a silver electrode weighing 2.8g.

From Faraday's law it can be shown that 1.0g of silver will theoretically require 0.5 A-hr to be produced from AgO. Therefore:

$$2.8g\ Ag = 1.4\ A\text{-}hr\ theoretical$$

Actual conversion based on AgO is 70% since some Ag^+ and Ag^0 remain during charging to Ag^{++}. Therefore

$$1.4 \times 70\% = 0.98\ A\text{-}hr$$

is actually expected to force discharge 1.0g of fully charged silver. Testing commences by charging at a 5 hr rate until oxygen evolution. The charging current is decreased to 25 hr rate until oxygen evolution once again occurs.

Currents would be

$$\frac{0.98\ A\text{-}hr}{5\ hr} = 0.196A\text{—}5\ hr\ rate\ charge$$

$$\frac{0.98\ A\text{-}hr}{25\ hr} = 0.039A\text{—}25\ hr\ rate\ charge$$

Testing continues by discharging at a 1 hr rate until hydrogen evolution

$$\frac{0.98\ A\text{-}hr}{1\ hr} = 0.98A\ discharge$$

Note that the discharge time is such that, in 1 hr, 70% efficiency based on Ag^{++} would be achieved. Theoretically, the longest discharge would be

$$\frac{1.4\ A\text{-}hr}{0.98A} \times 60 = 85.8\ min\ at\ the\ 1\ hr\ rate$$

Manuscript submitted Nov. 3, 1969; revised manuscript received *ca.* May 1, 1970. This was Paper 26 presented at the Detroit Meeting of the Society, Oct. 5-9, 1969.

Any discussion of this paper will appear in a Discussion Section to be published in the June 1971 JOURNAL.

REFERENCES

1. E. W. Junger, U.S. Pat. 692,298 (1902).
2. W. Morrison, U.S. Pat. 975,980 (1910).
3. F. Jirsa, *Z. Elektrochem.*, **88**, 129 (1927).
4. J. D. Moulton and R. F. Enters, U.S. Pat. 2,615,930 (1952).
5. J. R. Coleman and T. E. King, "Power Sources 1966," p. 193, D. H. Collins, Editor, Symposium Publications Division, Pergamon Press, New York (1967).
6. N. T. Wilburn, Abstract No. 303, *Electrochem. Soc. Extended Abstracts*, p. 57, Montreal, Oct. 6-11, 1968.
7. N. T. Wilburn, K. E. Meade, and C. J. Bradley, "Dry Process Divalent Silver Oxide Electrodes," Tech. Report ECOM-2628 USAECOM, Fort Monmouth, N. J. (1965).
8. N. T. Wilburn, K. E. Meade, and C. J. Bradley, "Dry Process Divalent Silver Oxide Electrodes," Tech. Report ECOM-2749 USAECOM, Fort Monmouth, N. J. (1966).
9. J. E. Schroeder, D. Pouli, and H. J. Seim, Abstracts, 154th National Meeting of the American Chemical Society, September 1967, Chicago, Ill.
10. L. W. Niedrach and H. B. Alford, *This Journal*, **112**, 117 (1965).
11. ESB Incorporated, Union of South Africa Pat. 59/2001 (1959).
12. A. F. Bogenschütz, P. Krahl, and V. Schulz, *Electrochem. Technol.*, **5**, 405 (1967).

Study of Lithium-Lead Alloys as Grid Material for Lead-Acid Batteries

G. W. Mao, T. L. Wilson,* and J. G. Larson

Gould Incorporated, Research Division, Minneapolis, Minnesota 55414

ABSTRACT

Lithium-lead alloys with low contents of lithium were investigated for lead-acid battery grids. The metallographical alloy structures, mechanical properties, anodic corrosion resistance, cell performance, and castability were determined. Experimental data are interpreted and compared with the well-known antimony-lead and calcium-lead battery grid alloys. A useful lithium-lead alloy range is presented. The potential electrochemical superiority and economical feasibility are discussed.

Although the positive grid does not participate directly in primary discharge/charge processes, it is this member that often limits battery life and utility. A suitable positive grid must: (*a*) have sufficient mechanical strength to support its own weight and that of the active material, (*b*) conduct electrical current evenly and efficiently, (*c*) provide a low impedance electrical contact between grid and active material, (*d*) be relatively resistant to anodic corrosion, and (*e*) be easily formed.

Antimony-lead alloys in the range of 4.5-12 w/o (weight per cent) Sb are generally used as battery grids in lead-acid batteries; the presence of antimony, however, enhances self-discharge (1). In addition, stibine gas evolution excludes use of these alloys in confined areas.

Over 30 years ago, the advantages of using alloying elements electronegative to lead were outlined, and the properties of a 0.1 w/o Ca alloy were discussed (2, 3). Although similar compositions still serve as alloys for storage battery grids, poor cycling characteristics have limited their use in many applications. In addition, corrosive attack under anodic conditions can be selective, causing problems in dimensional stability (4).

Chemically, lithium resembles calcium in the free state, whereas it resembles antimony metallurgically (5). Lithium-lead binaries were thus selected for study as possible grid alloys with the expectation that they would possess some of the better properties of both the calcium- and antimony-lead alloys. The possibility of using alloys containing lithium as grid alloy has not gone without previous investigation (6). Earlier investigators, however, were probably concerned with alloys too rich in lithium.

This paper presents experimental results that are believed to have a bearing on the applicability of lithium-lead as a positive grid alloy. The mechanical strength, resistance to anodic corrosion, cell performance, and castability are compared with similar data for calcium- and antimony-lead alloys. A usable alloy

* Electrochemical Society Active Member.

Key words: battery grid, lithium-lead, lead-acid battery.

range is outlined and the characteristics of the lithium alloys are compared with grid alloys used at present.

Procedure

The alloys referred to in this paper were prepared from Tadanac lead of 99.998% purity (principal impurities were copper, silver, antimony, and bismuth) and 99.9+% lithium (Na 0.007-0.01%, Ca 0.02-0.05%, Fe 0.001-0.01%, Si 0.006-0.01%). Alloys were prepared either by adding lithium directly to a melt held at 650°F, or by adding a concentrated master alloy to lead in iron crucibles. The combination of reactivity of lithium in the melt, stirring, and a nominal holding time after the melt had stabilized appeared adequate to insure homogeneity of the alloy. Flame spectroscopy of nitric acid solutions of samples systematically selected during casting gave no indication that segregation had occurred.

All melting and casting was done under an inert atmosphere of argon. Except where noted, the melt temperature prior to pouring was maintained at 700°F and the mold temperature 350°F. The molds were coated with a layer of a silicate-cork dust slurry as standard practice. The alloy compositions referred to later represent the chemical analyses of gates taken from the castings and are generally the average of several such samples. Cast ¼ in. by 5 in. rods were used as the anodes for corrosion studies. Tensile specimens were cast to the shape prescribed for sheet lead samples, *i.e.* providing a gauge area of 2 x ½ x ⅛ in. The castability data were obtained using the method described in the literature (7).

Briefly, castability was determined by pouring the lead alloy into an inverted tree-type mold cavity at controlled melt and mold temperatures, and cast samples were compared. Casting was scored by assigning points to each portion of the inverted tree mold. The more difficult areas to fill were given higher values than the easier to fill areas. The highest possible index score was arbitrarily set at 100.

The metallographic techniques of sample preparation have been presented in detail in an earlier paper (8). Briefly, these comprised mounting the sample in a low-temperature setting plastic, polishing through successively finer lubricated abrasives to a final 0.1μ alumina slurry, and etching in a dilute citric acid-ammonium molybdate solution.

Alloy rods were corroded separately at constant potential (the potential being higher than the solvent decomposition voltage) or at constant current in 1.115 sp gr sulfuric acid at room temperature. Pure lead sheet cathodes with a surface area of 170 cm^2 were concentrically arranged at a distance of 3 cm from the anode (surface area of 17 cm^2). Current and voltage were recorded throughout the experiments, and weight losses due to corrosion were determined by stripping the corrosion product from the surface of the corroded rods in a hot alkaline mannitol solution. Duplicate alloy rods were corroded so one experiment could be interrupted to metallographically observe the progress and the morphology of the anodic corrosion.

Battery grids were cast under inert atmosphere using optimum mold and melt temperatures. Grids were hand pasted in a manner simulating commercial practice and formed accordingly. Cells constructed from these grids were discharged in deep cycle tests. Historically, cycle life tests have been proven indicative of a grid alloy's capability. Although pure, calcium-, and dispersion-strengthened-lead satisfy many of the requirements of grid alloys, they are characterized by an inability to maintain cyclic capacity (9-12). Lithium-lead alloys were therefore submitted to a comparison with commercial alloys in cycle life tests.

Five-plate, miniature cells were constructed with paste:grid weights resembling industrial conditions. Theoretical capacities were approximately 3 A-hr so that at 35% efficiency a reasonable charge:discharge cycle could be maintained daily with a 16 hr overcharge. Cells were discharged at a theoretical 4 hr rate (thus taking 1 hr at 25% efficiency) and charged back at a theoretical 20 hr rate (normally taking 6 hr). A particularly deep cycle (1.1V cutoff) was used to accelerate failure—as much paste as possible was used in each cycle without deliberate sulfation. It was commonly observed that nonantimony cells fell to one third their capacity under this test regime.

A 16 hr, 2.2V float cycle (64 hr on weekends) was incorporated into the test procedure. Earlier results had indicated that grain boundary corrosion was severe in two-phase, lithium-lead alloys. Despite the fact that cells normally spent 520 hr on overcharge compared to 20 on discharge, tests were invariably terminated because of paste, not grid, failures.

Experimental Results

Anodic corrosion.—Under conditions of exceeding the $PbO_2/PbSO_4$ potential, the net effect of making dilute additions of lithium to lead is to reduce the anodic corrosion rate, as shown in Fig. 1. Corrosion was carried out at 82 mA/cm^2 constant current density for a period of 4 weeks in 1.115 sp gr sulfuric acid.

Two composition-dependent types of corrosion morphology were found, and these areas are noted in Fig. 1. For dilute alloys (lithium content less than 0.02 w/o) attack was generally uniform, maintaining much the same characteristics as pure lead. For lithium contents between 0.02-0.03 w/o lithium, penetration was concentrated at grain boundaries. Examples of these morphologies are illustrated in Fig. 2.

The critical composition distinguishing these classes of alloys, based on anodic corrosion, essentially defines and restricts the maximum alloying addition that may be made to obtain a usable binary. Grids containing greater amounts of lithium would be expected to "grow" during service, and this penetration type of attack may lead to premature grid fracture.

In the accelerated corrosion tests of this study, the kinetics of corrosion appeared to be chemically controlled since the depth of grain boundary penetration exceeded the grain size in alloys containing more than

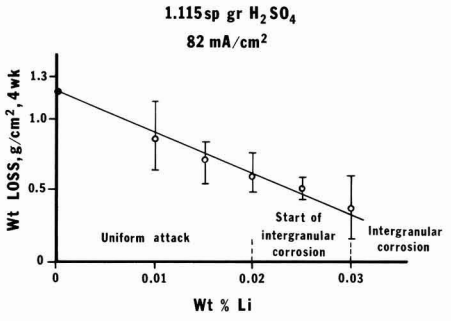

Fig. 1. Anodic corrosion of Li-Pb

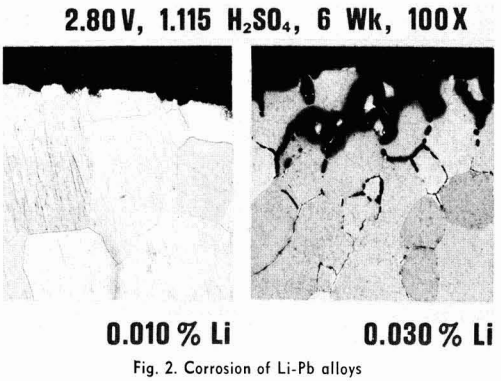

Fig. 2. Corrosion of Li-Pb alloys

0.03 w/o Li. This undoubtedly is a consequence of the dissolution of the LiPb intermetallic compound. Such chemical attack leads both to increasing the area exposed to corrosion and to locally increasing the alloy temperature. The latter factor could lead to catastrophic failure because it accelerates the rate of anodic attack and favors the kinetics of precipitation resulting in increased rate of precipitation.

On anodic corrosion, the deceptiveness of weight loss data cannot be overemphasized in interpreting corroded microstructures. The corrosion of lithium-lead alloys is a classic example of the necessity of microscopically studying the morphology of corrosion attack. The tendency for grain boundary attack increases with increasing lithium content, but catastrophic dissolution does not occur until alloy compositions in excess of 0.03 w/o Li are reached. Apparently, once started, the process of grain boundary consumption is one that propagates itself on a localized basis.

X-ray diffraction analyses of the oxide films stripped or brushed from the surface of the anodically corroded rods indicated that the corrosion products resulting from the conditions referred to above were largely αPbO_2. Both free lead and βPbO_2 patterns were observed but only in minor quantities. In a 0.03 w/o Li-Pb alloy, these phases were observed to constitute 5% free lead and 3% βPbO_2 of the total oxide film. The elemental lead is thought to result from complete grain boundary dissolution, thus mechanically freeing individual grains. The beta lead dioxide is also tentatively associated with the corrosion of the alloy-rich boundary layer. This latter conclusion was reached largely on the basis of a 3% shift in lattice parameter of the beta phase. The lattice parameter, a_o, for beta lead dioxide formed on lithium-lead differs from the value for beta lead dioxide formed from pure lead. It would appear from this latter observation that selective partitioning of lithium occurs between the oxides.

Chemical analysis of corroded rods proved that there was a slight decrease in lithium content. However, no lithium was found either in the cell electrolyte or the cell sludge. The other possible place where lithium could concentrate is in the adherent oxide layer. As the lithium contents were extremely low, x-ray diffraction did not detect its definite presence.

Comparisons of type of anodic attack were made with pure lead and representative calcium and antimony alloys. Corrosion was carried out at constant potential (2.8V) to get an indication of the alloy performance during overcharge conditions. Lithium-lead appeared to be very similar to pure lead both in degree of attack and corrosion morphology. Typical results of observed weight losses are reproduced in Table I and the general features of corrosion morphology are shown in Fig. 3.

Alloys corroded anodically above the decomposition potential of the electrolyte illustrate decisively the tendency for preferential grain boundary attack of the alloys. Even the cast 99.998% pure lead demonstrated a tendency toward preferential grain boundary penetration, presumably due to the segregation of elements to the boundary area. Westbrook and Aust have documented the propensity of solutes to segregate to grain boundaries in dilute lead alloys (13).

Mechanical strength and metallography.—Photomicrographs of cast structures of compositions ranging

Table I. Anodic corrosion of lead alloys at constant voltage

2.8 V 1.115 H_2SO_4 4 weeks total time	
Alloy composition (w/o)	Corrosion weight loss (mg/cm²)
4.5 Sb-Pb	135.4
0.07 Ca-Pb	49.5
0.01 Li-Pb	46.8
0.02 Li-Pb	48.0
0.03 Li-Pb	63.1
Pure Pb	61.1

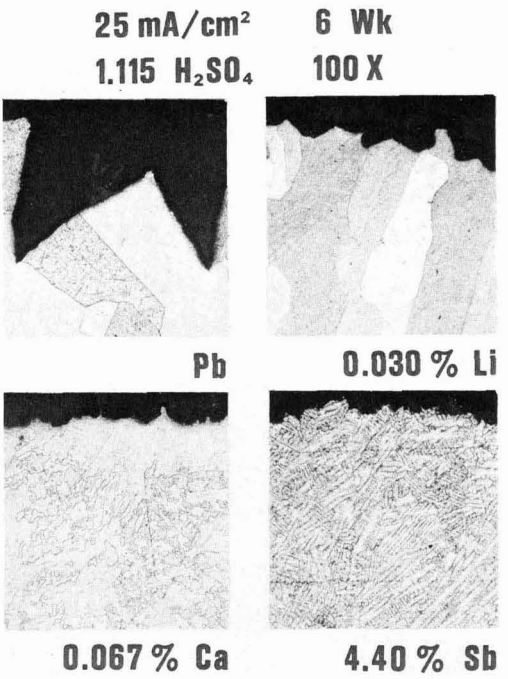

Fig. 3. Anodic corrosion of grid alloys

from 0.01 to 0.10 w/o Li are reproduced in Fig. 4. These figures reflect directly on the corrosion performance noted previously and the mechanical strength results presented in this section. As might be expected from the broad two-phase liquid plus solid field, the effects of coring in the lithium-lead system are quite evident. The first interdendritic type intermetallic compound is observed in alloys containing less than 0.04 w/o Li. In the 0.10 w/o alloy, the intermetallic is continuous and defines the grain size.

The kinetics of precipitation are reasonably rapid. At room temperature, the alpha solid solution grain boundaries of alloys containing 0.02 w/o Li are decorated with the intermetallic precipitates. Complete coverage ostensibly occurs in 0.04 w/o Li alloys. This heterogeneous precipitate morphology strongly affects the chemical reactivity of alloys in this system, as mentioned previously in corrosion studies.

The other effect that lithium has on the as-cast structure is a marked reduction in primary grain size. The 0.01 w/o Li alloy has a grain size approximately one fourth that of pure lead cast under identical conditions, and increasing the lithium content from 0.01 to 0.05 w/o reduces the grain size further by a factor of two. This observation of a decrease in grain size within the solid solution is in agreement with that reported by Greenwood (14). Although this grain size reduction has only a secondary effect on the chemical behavior of the alloys, it does contribute to its strength characteristics.

Tensile results are in general accord with an age-hardening system in which precipitation occurs from a supersaturated solution. Figure 5 shows a rapid increase in strength for alloys of less than 0.02 w/o Li and then a more gradual, linear increase for richer alloys. The rapid increase is primarily associated with solid solution strengthening, with the remaining 25% contribution from grain refinement. The linear portion of the strength increase is a consequence of the dispersion hardening influence of the intermetallic.

Tensile strength, yield strength, and per cent elongation varied only slightly with aging time for compositions up to 0.015 w/o Li. For compositions up to 0.025

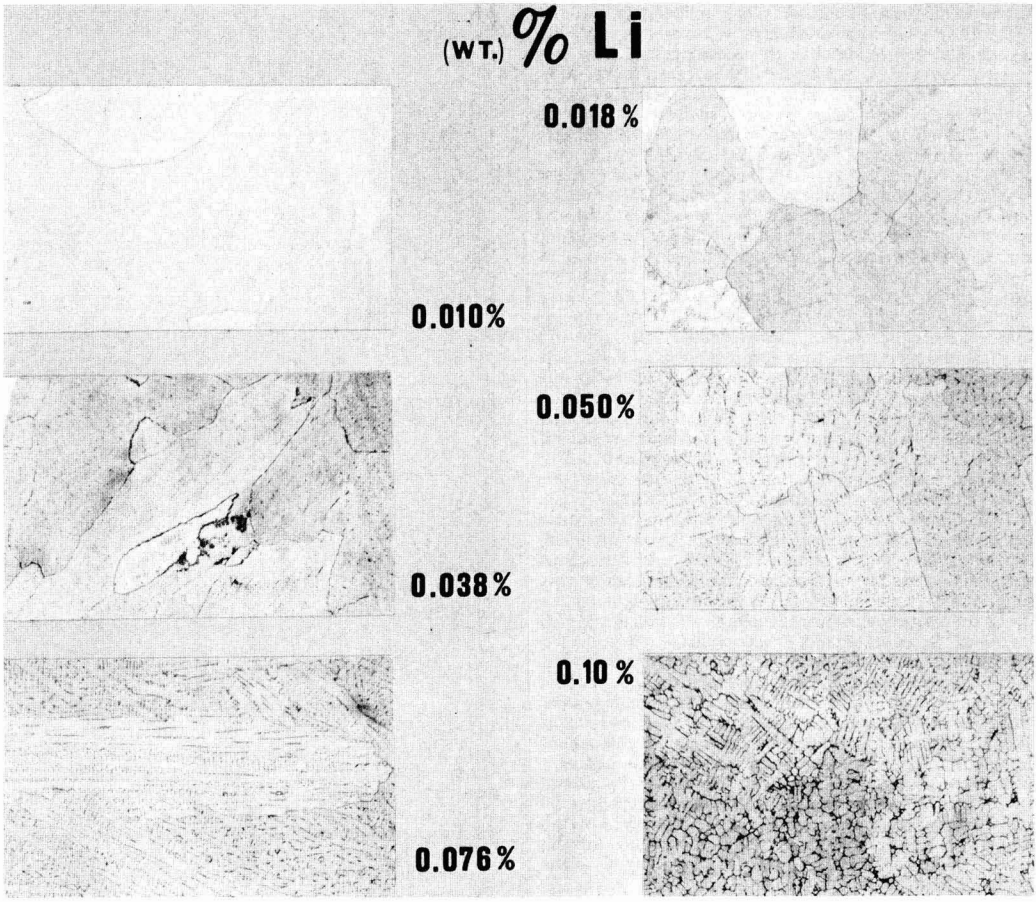

Fig. 4. Li-Pb microstructures

w/o, changes were noted largely in yield strength, whereas ultimate strength and elongation were relatively stable. An embrittlement associated with precipitation from the supersaturated solid solution existed above 0.025 w/o Li, however. The instability was the type where both the ultimate strength and elongation decreased, while the yield strength increased. In other age-hardening systems where this occurs, embrittlement is associated with overaging at grain boundaries, frequently with solute depleted regions (15).

Aging at room temperature apparently imparts a ripening process to the precipitate. Samples tested after a period of 4 weeks lost the dispersion hardening contribution to their tensile strength, whereas the ultimate tensile strength levels out to a value of about 5000 psi. The instability that exists in the richer alloys correlates qualitatively with the corrosion results. The corrosion as well as strength results indicate that

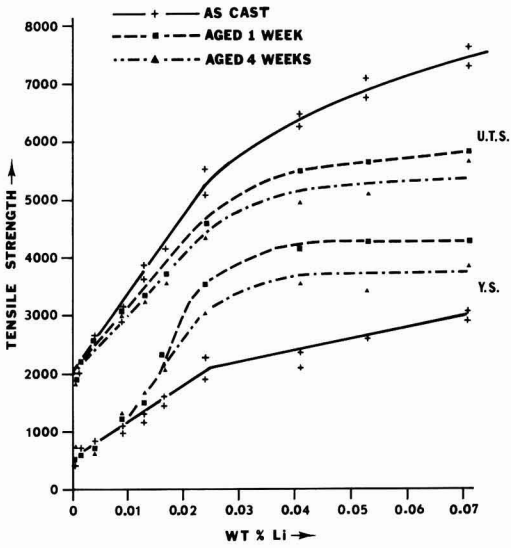

Fig. 5(a). Tensile properties of cast Li-Pb alloys

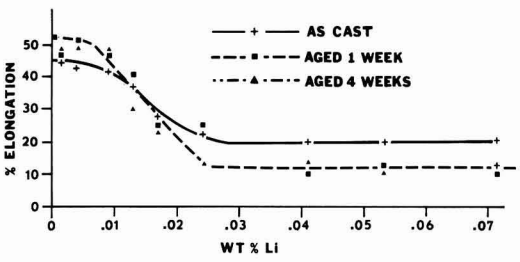

Fig. 5(b). Elongation of cast Li-Pb alloys

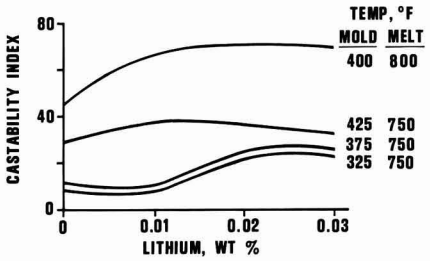

Fig. 6. Castability of dilute Li-Pb

ripening must proceed to a greater extent at grain boundaries. The aging data are included in Fig. 5.

For comparison, tensile strengths of calcium and antimony alloys are reproduced in Table II for two aging conditions that simulate conditions met during stripping, pasting, and use. Relatively dilute lithium alloys are comparable with the other two alloys.

Casting behavior of lithium-lead.—Inasmuch as the general grid fabrication process is one of casting, the casting behavior of any grid alloy is of primary concern. Both castability and the shrink associated with solidification were determined for standard casting practice for the alloys of concern. Castability data are illustrated in Fig. 6 and Table III. The internal shrink of alloy rods was determined by rolling samples into sheets and determining the change in density before and after rolling. The porosities (*i.e.*, per cent change in density values) for pure lead, 0.03 w/o Li-Pb, 0.07 w/o Ca-Pb, and 4.5 w/o Sb-Pb rods were 0.20, 0.08, 1.16, and 0.00%, respectively.

These casting parameters show antimony-lead is superior to the other alloys with which it was compared, since it solidifies with an eutectic phase present in the lead-rich matrix. Lithium-lead is a reasonably castable alloy in the useful grid composition range. Since the castability test essentially describes the ability to fill 1/16 in. diameter capillaries under various conditions (7), it is apparent that this may be done with little internal porosity with lithium alloys in the solid solution range. Grids of various shapes, and as thin as 0.06 in., are cast freely with lithium-lead.

Cell Performance.—Under the test regime used in this study, it was observed that nonantimony cells lost capacity from cycle to cycle. Antimony cells, on the other hand, regained and maintained their capacity after an initial loss. Both observations are in substantial agreement with earlier studies. The data gathered for the standards (7.0 antimony-, 0.07 calcium-, and unalloyed-lead) are reproduced in Fig. 7.

For comparison, the data for the lithium alloys are shown in Fig. 8. It appears that the performance of lithium-lead is composition-independent in the range studied and most similar to pure lead.

Table II. Ultimate tensile strength of lead alloys

Alloy composition (w/o)	As-cast, psi	Aged 1 week (room temp) psi
4.5 Sb-Pb	5100	5400
0.07 Ca-Pb	4200	5300
0.01 Li-Pb	3300	3100
0.02 Li-Pb	4700	4250
0.03 Li-Pb	5700	5000

Table III. Castability index of lead alloys

Melt temp, °F	Mold temp, °F	4.5% Sb-Pb	0.07% Ca-Pb	0.01% Li-Pb	0.02% Li-Pb	0.03% Li-Pb
700	325	56	8	7	28	23
700	425	80	27	39	31	33
800	400	84	48	74	67	71

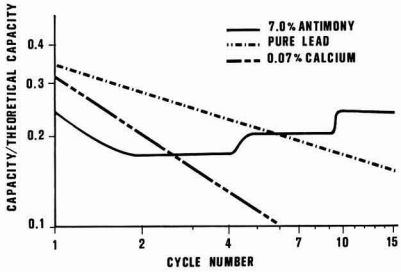

Fig. 7. Cyclic characteristics of grid alloys

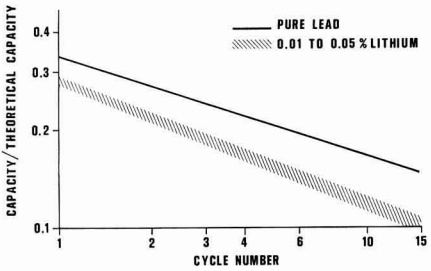

Fig. 8. Cyclic characteristics of Li-Pb alloys

Discussion

The useful composition range for lithium-lead binary alloys as battery grids is limited by anodic corrosion to lithium contents of less than 0.03 w/o. Lithium-lead binary alloys with lithium content higher than 0.03 w/o do not withstand high rate anodic corrosion. Below 0.03 w/o, the grid strength will be 4000-4500 psi and castability is midway between commercial antimony-lead and calcium-lead alloys. Total casting porosity should, however, be less than that generally obtained in the latter type grids. Under deep cycling, performance is similar to that obtained in pure lead grids.

If a general comparison is made with present alloys, it becomes immediately evident that lithium-lead alloys present the possibility for construction of low self-discharge grids at low material cost, due to the low alloy content. Balancing these merits are problems like the difficulty in maintaining lithium within the melt at high temperatures.

Positive grid elements of the three main classes of lead-acid batteries are constructed of particular alloys because of performance requirements. A review of these three classes is useful to place lithium-lead in perspective and to assess the merits of lithium-lead grids.

Automotive grids require frequent high-rate discharges, in which only a portion of the capacity is used, and reasonable life on overcharge. Strength and ease of casting are important because it is desirable to have the grids made as thin as possible (usually of 0.060 in. thickness). Lithium-lead, even with its pure lead type cycle behavior, might satisfy these requirements, but the castability of a hypoeutectic definitely surpasses that of a single-phase alloy. Competition with 4.5% antimony alloys would be enhanced if a different method of casting lithium-lead grids other than gravity casting is developed. On the other hand, if the industry is considering a maintenance-free, quasi-sealed, storage battery, then an alloy of the lithium-lead type would be a necessity.

Grids of industrial batteries where a long cycle (8 hr discharge rate) is desired are made of even richer antimony alloys (7.5-12 w/o). The chief requirement in the class is the cycle life and this parameter for Li-Pb appears to be an area open for improvement. In this respect, additives to the grid, paste, or electrolyte might be considered to obtain a flatter capacity:cycle

number curve. This general problem is something the whole lead-acid industry is considering due to the mounting price of antimony.

Finally, industrial standby cells utilize calcium-lead or pure lead grids because of low self-discharge requirements. Li-Pb alloys should perform adequately in this respect because they possess many of the properties necessary for this use. In addition, good welding and casting properties of lithium-lead should be a definite advantage.

Manuscript submitted Nov. 3, 1969; revised manuscript received *ca.* June 19, 1970. This was Paper 38 presented at the Detroit Meeting of the Society, Oct. 5-9, 1969.

Any discussion of this paper will appear in a Discussion Section to be published in the June 1971 JOURNAL.

REFERENCES

1. J. J. Lander, *This Journal*, **99**, 339 (1952).
2. H. E. Haring and U. B. Thomas, *Trans. Electrochem. Soc.*, **68**, 293 (1935).
3. E. E. Schumacher and G. S. Phipps, *ibid.*, **68**, 309 (1935).
4. J. B. Burbank, *This Journal*, **104**, 693 (1957).
5. M. Hansen and K. Anderko, "Constitution of Binary Alloy," p. 200, McGraw-Hill, New York (1958).
6. (*a*) German Pat. 476,259; (*b*) Brit. Pat. 494,069; (*c*) U.S. Pat. 1,360,269; (*d*) U.S. Pat. 1,791,148; (*e*) U.S. Pat. 1,926,545; (*f*) U.S. Pat. 2,140,544.
7. J. O. Johnstone, Metals Refining Publication (1935).
8. G. W. Mao, J. G. Larson, and P. Rao, *Metallography*, **1**, 399 (1969).
9. E. J. Ritchie and J. Burbank, *This Journal*, **117**, 299 (1970).
10. J. Burbank, *ibid.*, **111**, 1112 (1964).
11. S. Tudor, A. Weisstrech, and S. V. Davary, *Electrochem. Technol.*, **4**, 406 (1966).
12. N. E. Bagshaw and T. A. Hughes, "Batteries 2," p. 1, D. H. Collins, Editor, Pergamon Press (1964).
13. J. H. Westbrook and K. T. Aust, *Acta Met.*, **11**, 1151 (1963).
14. J. N. Greenwood, *Met. Rev.*, **6**, 279 (1961).
15. A. Kelly and R. B. Nicholson, *Prog. Mater. Sci.*, **10**, 151 (1963).

The Effect of Several Electrode and Electrolyte Additives on the Corrosion and Polarization Behavior of the Alkaline Zinc Electrode

F. Mansfeld*,[1] and S. Gilman*

NASA/Electronics Research Center, Cambridge, Massachusetts 02139

ABSTRACT

The corrosion behavior of zinc in 6*N* KOH at 25°C was investigated through measurement of the rate of hydrogen evolution (r_{H_2}) at the corrosion potential. Anodic and cathodic potentiostatic polarization curves as a function of alloying and additions to the electrolyte were obtained. It was found that the corrosion and polarization behavior of 99.999% zinc can be explained by mixed-potential theory assuming that the reactions were $Zn + 4\,OH^- \rightleftharpoons Zn(OH)_4^{2-} + 2e^-$ and $H_2O + e^- \rightleftharpoons \frac{1}{2}H_2 + OH^-$. Good agreement between theoretical curves obtained by computer solution of the kinetic equations corresponding to the above reactions and actual polarization measurements was obtained in the absence and presence of zincate. Theoretical and experimental corrosion rates also agreed well. Binary Zn-Pb alloys [0.2-1.0 w/o (weight per cent)] and Zn-Al alloys (0.2-0.8 w/o) made up from high-purity metals had r_{H_2}-values which were lower than those for zinc, while r_{H_2}-values of commercial zinc alloys were much higher than those of zinc, most likely due to the presence of low overvoltage impurities such as Cu, Ni, or Fe. Addition of 10^{-3}M copper, tin, or lead ions to the electrolyte also influenced r_{H_2}, which in the presence of metal ions noble to zinc is no longer equivalent to the corrosion rate. The strong increase of r_{H_2} in the presence of Cu ions is explained by the low hydrogen overvoltage of Cu, while the decrease of r_{H_2} in the presence of Pb ions is explained by the high hydrogen overvoltage of Pb. Anions such as Cl^- or Br^- do not affect r_{H_2}. In the presence of thiourea, r_{H_2} increases steadily, while S^{2-} leads to severe corrosion.

The rate of hydrogen evolution on zinc in slightly acid and in concentrated alkaline solutions has been measured on zinc sheets, rods, powders, and on battery electrodes. Correlation of the few data obtained until now is very difficult. Dirkse and Timmer (1) found a decrease of the rate of hydrogen evolution (r_{H_2}) on zinc wire (99.999%) in 20-45% KOH with increasing concentration of KOH, saturation of the electrolyte with ZnO, or amalgamation of the wire. Oxley and Humphrey (2) observed that As, Co, and Cu ions increased r_{H_2} on zinc ribbon (99.99%) in 30% KOH at 60°C in measurements which extended over several days, while Sn, Cd, and Pb ions decreased r_{H_2}, Pb having the most pronounced effect. The effect of Pb was also observed at a practical zinc electrode, although to a somewhat smaller extent. Additions of zincate also lowered r_{H_2} as observed in (1). The effect of additions of metal ions to the electrolyte has been also studied by Era *et al.* (3) on zinc sheets (99.99%) in a solution of 25% NH_4Cl + 10% $ZnCl_2$ + HCl at $pH = 5$, 50°C. Additions of Pb decreased r_{H_2}, while Fe, Cu, Ni, As, and Sb increased r_{H_2} in tests which were conducted for 14 days. Krug and Borchers (4) found that alloying with Fe (up to 310 ppm) increased r_{H_2} in a solution of 1% NH_4Cl + 0.12% HCl ($pH = 2$) at 45°C; alloying with Pb up to 1% reduced this increase. Zinc alloys with small additions were studied earlier by Vondracek and Izak-Krizko (5) who found that, in 0.5*N* H_2SO_4, additions of Cd, As, Sn, Sb, Fe, and Cu increase r_{H_2}, while additions of Al, Pb, and Hg decrease r_{H_2}.

* Electrochemical Society Active Member.
[1] Present address: Science Center, North American Rockwell Corporation, Thousand Oaks, California 91360.
Key words: hydrogen evolution, electrode kinetics, zinc and zinc alloys, alkaline batteries.

It is difficult to arrive at mechanistic interpretations or even to derive general trends, based on the experiments cited above, since the data are scanty for the considerable number of experimental parameters being varied. The present study of the effect of Pb and other metal ions on corrosion and hydrogen evolution on zinc was made as a logical sequel to the authors' (6) previous studies of the effect of Pb ions on Zn dissolution and deposition. The topic is of additional interest from a theoretical standpoint since it was reported in (2) that current-voltage curves in 30% KOH at room temperature exhibited a higher hydrogen overvoltage on zinc than on all other metals studied in (2). The authors point out that the overvoltage characteristics of the metal added to the electrolyte alone cannot explain the observed behavior.

The corrosion potential of zinc in a solution of KOH is a mixed potential, the partial oxidation reaction being

$$Zn + 4\,OH^- = Zn(OH)_4^{2-} + 2e^- \qquad [1]$$

while the partial reduction mechanism is

$$H_2O + e^- = \tfrac{1}{2}H_2 + OH^- \qquad [2]$$

The relationship between current and potential for reaction [1] can be expressed as (7)

$$i_{Zn} = i_{Zn}^{o}\,\frac{\exp\left\{\frac{n\alpha_{Zn}\mathbf{F}}{RT}\Delta\phi_{Zn}\right\} - \exp\left\{-\frac{n(1-\alpha_{Zn})\mathbf{F}}{RT}\Delta\phi_{Zn}\right\}}{1 + \frac{i_{Zn}^{o}}{i_{Zn}^{L}}\exp\left\{\frac{-n(1-\alpha_{Zn})\mathbf{F}}{RT}\Delta\phi_{Zn}\right\}} \qquad [3]$$

where i_{Zn}^{o} is the exchange C.D. for reaction [1], $\Delta\phi_{Zn}$ the deviation from the reversible potential ϕ_{rev} of reaction [1] and i_{Zn}^{L} is the limiting C.D. for zinc deposition. The other symbols have their usual meaning. The form of Eq. [3] results from the fact that there is a limiting diffusion C.D. for metal deposition, but not for metal dissolution under ordinary corrosion conditions (7). If it is assumed that the concentration of zincate in the electrolyte is small (corroding zinc specimen in pure KOH) with a value of $C_{Zn(OH)_4^{2-}} = 10^{-5}$M, one obtains

$$i_{Zn}^{L} = 2\mathbf{F}DC/\delta = 1.4 \times 10^{-6}\ \text{A/cm}^2 \qquad [4]$$

by assuming a value for the diffusion coefficient D of 7×10^{-6} cm^2/sec (7) and a value of $\delta = 10^{-2}$ cm (unstirred solutions).

Theoretical polarization curves according to Eq. [3] have been calculated using an IBM 7094 computer for values of i_{Zn}^{o} from 10^{-1} to 10^{-6} A/cm^2 using $n = 2$, $\alpha = 0.5$, and $T = 298$°K (Fig. 1). ϕ_{Zn}^{rev} was calculated (8) as -532 mV with respect to a hydrogen electrode in the same solution,[2] pH = 14 and $C_{Zn(OH)_4^{2-}} = 10^{-5}$M.

The hydrogen-evolution reaction [2] can be expressed by the simple relationship

$$i_H = i_H^{o}\left[\exp\left\{\frac{(1-\beta_H)\mathbf{F}}{RT}\phi\right\} - \exp\left\{\frac{-\beta_H\mathbf{F}}{RT}\phi\right\}\right] \qquad [5]$$

Plots of ϕ *vs.* log i_H, assuming values of i_H^{o} from 10^{-10} to 10^{-8} A/cm^2 and $\beta_H = 0.5$ are also given in Fig. 1. Their intersection with the anodic part of the zinc curves gives the corrosion potentials and currents. It is evident that for the range of i_H^{o} values under consideration here, the value of i_{Zn}^{o} would have to be decreased drastically by additives to the electrode or electrolyte (to $<\sim 10^{-5}$ A/cm^2) from the literature value of 0.1 A/cm^2 (9) before there is an effect on the corrosion potential and corrosion current density. Significant effects on both these quantities will, however, always be produced by variations in i_H^{o}.

[2] All potentials cited in this paper are based on this electrode.

If the ion of a metal which is more noble than zinc (*e.g.*, Cu, Pb, Sn) is added to the electrolyte, an additional reduction process will occur and the corrosion current will increase, if the hydrogen overvoltage stays constant

$$i_{corr} = i_{Zn}^{ox} = i_H(\phi_{corr}) + i_{Me}^{red}(\phi_{corr}) \qquad [6]$$

where $i_H(\phi_{corr})$ and $i_{Me}^{red}(\phi_{corr})$ are the respective hydrogen and metal reduction currents at ϕ_{corr}. In this case a measurement of the rate of hydrogen evolution cannot give the exact value of the corrosion C.D., a fact which has been overlooked in previous work (2-5). Figure 2 shows this relationship for the same conditions as in Fig. 1 with the current-voltage curve for metal ions other than zinc added. It is assumed that ϕ_{rev}^{Me} of these metal ions is sufficiently noble to ϕ_{rev} of zinc; the reduction process is therefore completely under diffusion control. For the values of i_H assumed, $i_{Me}^{red}(\phi_{corr})$ is larger than $i_H(\phi_{corr})$ and

$$i_{corr} \approx i_{Me}^{red}(\phi_{corr}) \qquad [7]$$

For this case, corrosion potential and current are almost independent of the parameters of hydrogen evolution. Polarization curves in the anodic region are independent of i_H^{o} and i_{Zn}^{o} as long as $i_{Zn}^{o} > 10^{-3}$ A/cm^2.

In the present work the effect of addition of ions, neutral molecules, or metal cations to the electrolyte and alloying of small amounts of metals to zinc has been investigated and an attempt has been made to explain the results obtained by the mechanism outlined below.

Experimental

Zinc rod used for studies of hydrogen evolution was of 99.999% purity.[3] Alloys of Zn-Pb and Zn-Al were made by Ventron Electronics Corporation from Zn(99.999%), Pb(99.99%), and Al(99.98%). The content of Pb or Al was increased step-wise from 0.2 to 1.0 w/o. The commercial alloys Zamak 3, 5, and 7, and zinc alloy "955" were donated by Belmont Smelting and Refining Works, Incorporated, Brooklyn, New York. A typical analysis is given in Table I.

Solutions of 6*N* KOH were prepared using AR grade KOH pellets and triple-distilled water (quartz still).

[3] The effect of purity and temperature is reported in (18).

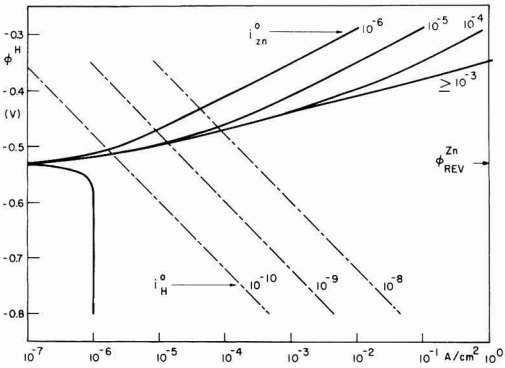

Fig. 1. Theoretical Tafel plots for the zinc dissolution-deposition and hydrogen evolution processes as a function of the exchange current density: ——— Eq. [3], — — — Eq. [6] (assuming $\alpha_{Zn} = \beta_H = 0.5$, $n = 2$, $\phi^{Zn}_{rev} = -0.532$V, $i_{Zn}^{L} = 10^{-6}$ A/cm^2, $T = 298$°K).

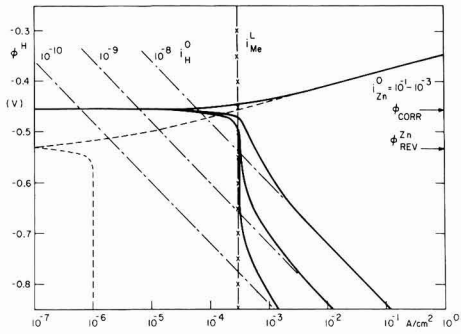

Fig. 2. Theoretical Tafel plots for reactions at a zinc electrode in the presence of added reducible metal ions: ——— Zn dissolution-deposition (Eq. [3], assuming $i_{Zn}^0 \geq 10^{-3}$ A/cm²); — — — hydrogen evolution (Eq. [6]); x – x – deposition current, i_{Me}^L, for added metal ions; ——— Over-all reaction.

The rate of hydrogen evolution (r_{H_2}) was measured in cells as proposed in (3) or (10) in a water-thermostat at 25°C. Lead was added to the electrolyte as the acetate, tin and copper as chlorides. These, and all other additives, were of AR grade purity.

Zinc electrodes (zone refined) were degreased in benzene for 5 min at 80°C and then etched for 2 min in 10% $HClO_4$. Samples of Pb and Sn were etched in 5% HNO_3. The electrodes were then washed with distilled H_2O and immediately immersed in the electrolyte. Polishing with emery paper was avoided, since this led to irregular behavior in some cases.

Polarization curves were carried out in deaerated 6*N* KOH at room temperature (24° ± 1°C) using zinc rod counterelectrodes and a hydrogen electrode in the same solution as reference electrode. When polarization curves on Pb or Sn were measured, Pt counterelectrodes were used, since it was observed that small amounts of zincate produced while the working electrode was cathode diffused from the counterelectrodes to the Pb or Sn electrode and were reduced or oxidized during potential sweeps from the rest potential of Pb or Sn to H_2 evolution and back.

Potentiostatic polarization curves were obtained using a Tacussel potentiostat and function generator. Values of current were recorded on a Moseley strip chart or X-Y recorder and the potential was monitored on a Keithley electrometer. Runs were usually started at a potential of −900 mV. The potential was then increased step-wise in the noble direction and the current recorded after 1 min at each potential. To obtain a quick survey of the polarization behavior of zinc or the zinc alloys, cyclic voltammetry was carried out between −1.5 and +3.0V at sweep speeds of 4.5-45 mV/sec. When the effect of such additives to the electrolyte as Sn, Pb, Sn, and Cu ions was studied, runs were started at the corrosion potential and the potential was increased step-wise to more cathodic values.

Results

Corrosion tests.—The effect of metal ions in the electrolyte on r_{H_2} is shown in Fig. 3. While additions of

Table I. Typical analyses of Asarco die casting alloys

	Zamak 3	Zamak 5	Zamak 7	"955"*
Mg	0.03-0.04%	0.03-0.04%	0.010-0.020%	
Pb	0.002	0.002	0.002	
Cd	<0.001	<0.001	<0.001	
Sn	n.d.	n.d.	n.d.	
Fe	0.001	0.001	0.001	
Al	4.0	4.0	4.0	5.5
Cu	<0.01	1.0	<0.01	
Ni	—	—	0.007	
Zn	Balance	Balance	Balance	

* No exact analysis for the alloy "955" was obtained.

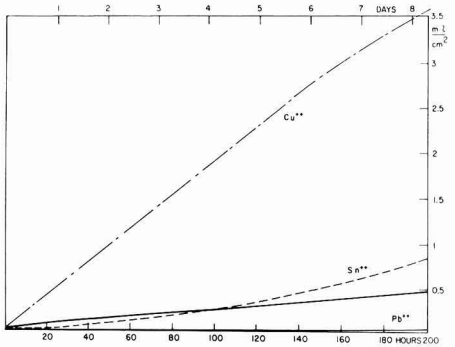

Fig. 3. Effect of 10^{-3}M of $CuCl_2$, $SnCl_2$, or PbAC on hydrogen evolution from zinc; 6*N* KOH, 25°C.

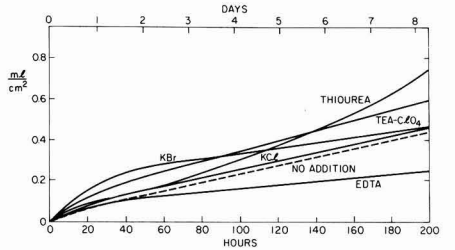

Fig. 4. Effect of 10^{-3}M of KCl, KBr, tetraethylammonium-ClO_4, thiourea and EDTA on hydrogen evolution from zinc; 6*N* KOH, 25°C.

10^{-3}M Cu markedly increase r_{H_2}, additions of 10^{-3}M Pb decrease r_{H_2}. The effect of 10^{-3}M Sn is the same as observed in 0.5*N* H_2SO_4 (5) for a Zn-1% Sn alloy. The curves of hydrogen evolution *vs.* time for pure Zn-Pb and Zn-Al alloys were similar in appearance to those of zinc. The r_{H_2} values are summarized in Table II, which also contains the values for the commercial die casting alloys. The rate of hydrogen evolution was lower for the Zn-Pb alloys than for zinc; it was also lower for the Zn-Al alloys except for the alloy with the highest Al content. The commercial zinc alloys have much higher r_{H_2} values, especially the alloy containing 1% Cu. Additions[4] of KCl apparently do not change r_{H_2} (Fig. 4), while the Br^- ions increase r_{H_2} in the initial stage of the experiments. Tetraethylammonium-perchlorate increases and EDTA lowers r_{H_2},

[4] The concentration of additions was 10^{-3}M.

Table II. Corrosion rates r_{H_2} $\left[\frac{\text{ml } H_2}{\text{cm}^2 \text{ day}}\right]$ of zinc and zinc alloys

Specimen	r_{H_2} (5 hr)	r_{H_2} (29 hr)	r_{H_2} (53 hr)	r_{H_2} (200 hr)
Zinc 99.999%	f(t)	0.065	0.050	0.050
Zn-Pb-alloys				
0.2 w/o	f(t)	0.011	0.011	0.011
0.4 w/o	f(t)	0.009	0.009	0.009
0.6 w/o	f(t)	0.067	0.023	0.023
0.8 w/o	f(t)	0.026	0.013	0.013
1.0 w/o	f(t)	0.010	0.010	0.010
Zn-Al-alloys				
0.2 w/o	f(t)	0.026	0.026	0.026
0.4 w/o	f(t)	0.009	0.009	0.012
0.6 w/o	f(t)	0.009	0.009	0.012
0.8 w/o	f(t)	0.042	0.042	0.042
1.0 w/o	f(t)	0.29	0.29	0.29
"955"	6.5	3.4	3.4	—
Zamak 3	8.9	5.0	7.0	—
Zamak 5	17.6	11.0	11.0	—
Zamak 7	7.2	3.4	2.3	—

while r_{H_2} increases steadily in the presence of thiourea. The S^{--} ion had a catastrophic effect on the zinc: after several hours r_{H_2} increased greatly, the specimen was full of holes and deep pits, while a white deposit (probably ZnS) covered the bottom of the test cell.

Polarization curves.—In order to obtain a better understanding of the effect of additives on the rate of hydrogen evolution and corrosion of zinc, polarization curves have been recorded for pure zinc (with or without additions to the electrolyte) and for zinc alloys. Figure 5 shows a polarization curve for zinc in 6*N* KOH, 25°C in the region of hydrogen evolution and active dissolution. Included for comparison is a theoretical curve using Eq. [3] and [5] for $i_H{}^o = 10^{-9}$ A/cm² and $i_{Zn}{}^o = 10^{-1}$ A/cm², $i_{Zn}{}^L = 10^{-6}$ A/cm², $\phi^{Zn}{}_{rev} = -532$ mV, $\alpha = \beta = 0.5$. The agreement is very good considering that only approximate values were chosen for these parameters. The corrosion potential obtained in this measurement was −505 mV, which agrees well with corrosion potentials extrapolated from measurements of Bartelt and Landsberg (11). The corrosion C.D. obtained by extrapolation from the anodic Tafel line to the corrosion potential was found to be 7 μA/cm² corresponding to a corrosion rate of 20 mdd, compared to a theoretical value of 13 μA/cm² obtained by the same extrapolation, *i.e.* 38 mdd. The initial rate of H_2 evolution in corrosion tests at 25°C was 0.065 ml/cm² day which corresponds to 10 mdd. The satisfactory agreement of two independent measurements (10 and 20 mdd) with theoretical value (38 mdd) shows that the corrosion behavior of zinc in 6*N* KOH in the absence of additives can be very well explained by the mechanisms in Eq. [3] and [5].

Polarization curves in the active and passive region for zinc and the commercial die-casting alloys were rather similar except for a lowering of oxygen overvoltage produced by the alloyed impurities. Curves for the pure Zn-Pb and Zn-Al alloys were very similar to those of pure zinc.

Figure 6 shows the effect of addition of ZnO to the electrolyte on the shape of the polarization curves. A plot of the limiting C.D. for zinc deposition in the concentration range of 10^{-3}M to 0.25M ZnO *vs.* concentration gave a value of $D/\delta = 2.9 \times 10^{-4}$ cm/sec. This value justifies the value for $i_{Zn}{}^L$ of 10^{-6} A/cm² used for the theoretical curves in Fig. 1, where it was assumed that a "pure" solution of KOH contains about 10^{-5}M of zincate (based on polarization curves measured in KOH equilibrated with Zn) due to the corrosion of zinc. Higher amounts of ZnO decrease the critical C.D. for passivation of zinc and lead to passivation at a more active potential. Theoretical corrosion rates as a function of ZnO concentration, have been calculated using values of $i_{Zn}{}^L$ based on the experimental value of $D/\delta = 2.9 \times 10^{-4}$ cm/sec, values of $\phi^{Zn}{}_{rev}$ from Ref. (8) and assuming no effect of zincate additions on $i_H{}^o$ which was again taken as 10^{-9} A/cm². Table III shows theoretical and experimental values for the corrosion potential and corrosion rates. Agreement is fair except at high ZnO concentration.

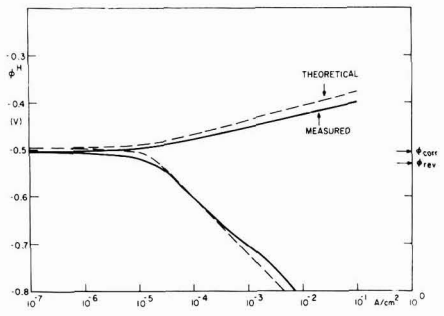

Fig. 5. Theoretical and measured polarization curves on zinc in 6*N* KOH, 25°C.

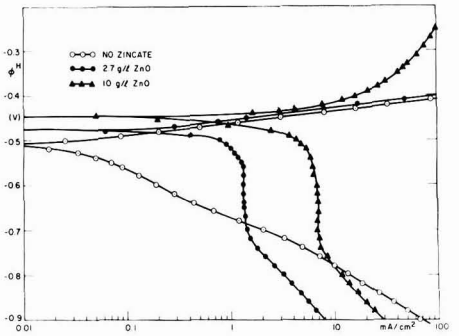

Fig. 6. Polarization curves for zinc with and without additions of ZnO, 6*N* KOH, 25°C.

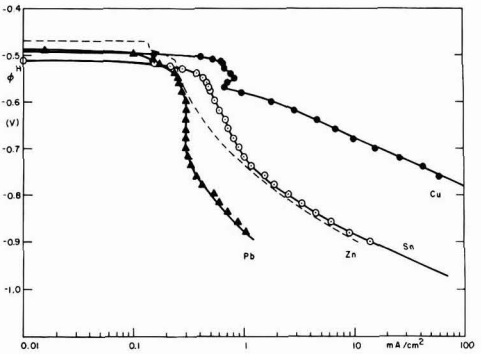

Fig. 7. Polarization curves for zinc in the presence of 10^{-3}M of ZnO, $CuCl_2$, $SnCl_2$, or PbAC; 6*N* KOH, 25°C.

The effect of additions of 10^{-3}M Cu, Sn, Pb, or Zn to the electrolyte on the polarization behavior of zinc in 6*N* KOH is shown in Fig. 7. Copper decreases hydrogen overvoltage markedly, Sn seems to have no effect compared to a solution containing equal amounts of zincate, while Pb increases overvoltage for hydrogen evolution markedly. The limiting C.D. for deposition of all these metals on zinc is near the value for Pb of 3×10^{-4} A/cm² which was used in Fig. 2. A comparison of Fig. 7 and Fig. 2 shows good agreement of theoretical and measured polarization curves in the regions of the limiting C.D. and hydrogen evolution. According to these curves, the exchange C.D. for the hydrogen evolution reaction on zinc in the presence of 10^{-3}M Cu would be between 10^{-8} and 10^{-7} A/cm², and between 10^{-11} and 10^{-10} A/cm² in the presence of 10^{-3}M Pb. Measurements of polarization curves on pure Sn or Pb in deaerated 6*N* KOH (Fig. 8) are not easy to interpret since Tafel behavior was not found, which is partly due to hydride formation observed at more negative potentials for both metals. In general it seems that the overvoltage for hydrogen evolution is somewhat higher for Pb than for Sn and that both metals have a higher hydrogen overvoltage than zinc, contrary to what was observed by Oxley and Humphrey (2).

Table III. Corrosion potentials and rates of hydrogen evolution as a function of ZnO additions to 6*N* KOH, 25°C

[ZnO] (mole/liter)	$\phi^{exptl}{}_{corr}$ (mV)	$\phi^{th.}{}_{corr}$ (mV)	$r_{H_2}{}^{exptl}$ (mdd)	$r_{H_2}{}^{th.}$ (mdd)
0	−497	−497	8	38
0.0625	−445	−419	—	9
0.125	−446	−410	1.8	7
0.25	−436	−401	0.8	6

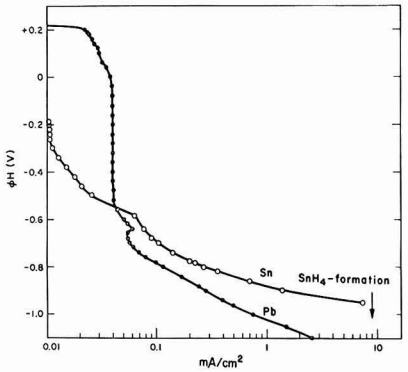

Fig. 8. Polarization curves for tin (AR) and lead (99.999%) in 6*N* KOH, 25°C.

Discussion

The good agreement between experimental and theoretical corrosion rates (Table III) and polarization curves (Fig. 5) confirms our assumption that the corrosion behavior of zinc in KOH can be readily explained by mixed potential theory; zinc metal is oxidized to the zincate ion, while water is reduced to hydrogen gas. It is not necessary to consider the rate of dissolution of interfacial ZnO or $Zn(OH)_2$ as rate controlling as done by Rüetschi (10) and partly by Dirkse and Timmer (1). The formation of ZnO or $Zn(OH)_2$ in 6*N* KOH at the rest potential seems unlikely, since the reversible potential for these reactions is more noble than the observed corrosion potential of zinc. An over-all reaction similar to the one assumed by Dirkse and Timmer (1)

$$Zn + 2H_2O \rightleftharpoons H_2 + Zn(OH)_2 \qquad [8]$$

with a reversible potential of $\phi_{rev} = -439$ mV (12) is not consistent with a corrosion potential of $\phi_{corr} = -497$ mV in 6*N* KOH, 25°C.

The effect of addition of the metal cations Cu, Sn, or Pb on hydrogen evolution rates and polarization behavior can be explained only on a qualitative basis since a third process (reduction of the metal ions) is added to the process of zincate formation and water reduction. In this case a measurement of r_{H_2} no longer gives the exact value of corrosion rates (Eq. [6]). It seems, however, still possible to explain the changes of r_{H_2} (Fig. 3) by assuming that the large increase of r_{H_2} upon additions of Cu results from a lowering of hydrogen overvoltage on the surface of the test specimen, while the decrease of r_{H_2} upon additions of Pb results mainly from an increase of hydrogen overvoltage. The high rate of hydrogen evolution of the commercial alloys (Table II) must result from low overvoltage impurities[5] and, characteristically, the alloy containing 1% Cu (Zamak 5) has the highest corrosion rate.

The effect of zincate (Table III) can be explained by mixed potential theory by considering the decrease in r_{H_2} and the shift of the polarization curve of zinc in the noble direction as zincate is added to the electrolyte (ϕ^{Zn}_{rev} becomes more noble). The fact that experimental corrosion rates are lower and experimental corrosion potentials more active than the theoretical values based on constant hydrogen overvoltage could be explained using the suggestion by Dirkse and Timmer (1) that dissolved zincate lowers the activity of water according to

$$ZnO + H_2O + 2\,OH^- \rightleftharpoons Zn(OH)_4^{2-} \qquad [9]$$

which thereby increases the hydrogen overvoltage slightly. Evidence for this can be found in Fig. 6 where increasing amounts of zincate increase hydrogen overvoltage at the most negative potentials.

From Eq. [3] it follows that for $i^o_{Zn} \geqq 10^{-3}$ A/cm^2, variations in the value of i^o_{Zn} caused by additions to the electrolyte or the electrode would not influence the polarization curve for zinc oxidation. It is for these reasons not expected that anions which, through adsorption, affect the dissolution of other metals, as for example of Fe in H_2SO_4 (14), would have a similar effect for zinc in KOH. An effect of anions is unlikely also in view of the fact that the point of zero charge for zinc is approximately at +0.16V *vs.* hydrogen electrode at pH = 14 (15) and therefore noble to the corrosion potential of zinc by about 0.7V. In fact, as can be seen from Fig. 4, addition of KCl had no effect of r_{H_2}, while the effect of KBr is small. The small increase in r_{H_2} in the presence of tetraethylammonium ions is presumably due to the effect of specific adsorption on the kinetics of hydrogen evolution (16). The tremendous effect of the S^{2-} ion also observed by Merkulov and Flerov (17) might result from formation of ZnS, while the effect of thiourea (Fig. 4) which produced a constantly increasing corrosion rate might result from complex formation between the sulfur group and the zinc.

Conclusions

1. The polarization and corrosion behavior of zinc with and without additions of zincate is accounted for by mixed potential theory. In the presence of metal cations which are more noble than zinc and which therefore plate out on zinc at the rest potential, the rate of hydrogen evolution can increase or decrease, depending on the relative values of hydrogen overvoltage of zinc and the metal deposit on zinc.

2. The low corrosion rates of Zn-Pb alloys suggest that the rate of hydrogen evolution of zinc can be lowered if the impurity level of the electrode is carefully controlled. This and the beneficial effect of lead additions to the electrolyte on growth morphology reported by the authors (6) explain the beneficial action of lead in zinc batteries.

3. The expected absence of an effect of inorganic anions on gassing rates has been confirmed experimentally.

4. Compounds containing sulfur and especially the $S^=$ ion must be avoided since they increase hydrogen evolution rates to very high values.

Acknowledgments

One of the authors (F.M.) acknowledges support under a National Academy of Sciences Postdoctoral Research Associationship. The authors are indebted to Dr. M. Salomon for the writing of the computer program and many helpful discussions, and to Dr. A. Glatz and Mr. A. Pinella for help and advice in metallurgical questions.

Manuscript submitted Jan. 30, 1970; revised manuscript received *ca.* June 1, 1970.

Any discussion of this paper will appear in a Discussion Section to be published in the June 1971 JOURNAL.

REFERENCES

1. T. P. Dirkse and R. Timmer, *This Journal*, **116**, 162 (1969).
2. J. E. Oxley and J. R. Humphrey, Final Report for NASA, Contract NAS 7-671, July 22-Oct. 22, 1968.
3. A. Era, Z. Takehara, and S. Yoshizawa, *Electrochim. Acta*, **13**, 383 (1968).
4. H. Krug and H. Borchers, *ibid.*, **13**, 2203 (1968).
5. R. Vondracek and I. I. Izak-Kriszko, *Rec. Trav. Chim.*, **44**, 376 (1925).
6. F. Mansfeld and S. Gilman, *This Journal*, **117**, 588 (1970).
7. H. Kaesche, "Die Korrosion der Metalle," Springer-Verlag, Berlin, Heidelberg, New York (1966).
8. F. Jolas, *Electrochim. Acta*, **13**, 2207 (1968).
9. J. P. G. Farr and N. A. Hampson, *J. Electroanal. Chem.* **13**, 433 (1967).

[5] Although the typical analysis (Table I) shows a Fe content of only 0.001%, it is possible that the alloys contain more Fe if prepared in Fe containers, a possibility discussed by Drotschmann (13).

10. P. Rüetschi, *This Journal*, **114**, 301 (1967).
11. H. Bartelt and R. Landsberg, *J. Phys. Chem.* **222**, 217 (1963).
12. M. Pourbaix, "Atlas of Electrochemical Equilibria in Aqueous Solutions," Pergamon Press (1966).
13. C. Drotschmann, *Korrosion*, **19**, 156 (1965).
14. G. M. Florianovitch, L. A. Sokolova, and Ya. M. Kolotyrkin, *Electrochim. Acta*, **12**, 879 (1967).
15. L. I. Antropov, "Kinetics of Electrode Processes and Null Points of Metals," Council of Scientific and Industrial Research, New Dehli (1960).
16. K. J. Vetter, "Electrochemical Kinetics," p. 567 Academic Press, New York London (1967).
17. A. V. Merkulov and V. N. Flerov, *Elektrokhimiya*, **4**, 587 (1968); *Soviet Electrochemistry*, **4**, 527 (1968).
18. F. Mansfeld, Submitted for publication in *Electrochim. Acta*.

Anodic Discharge of Chloride Ions on Pt-Ir Alloy Electrodes

G. Faita and G. Fiori

Laboratory of Electrochemistry and Metallurgy, University of Milan, Milan, Italy

and A. Nidola

Oronzio De Nora-Impianti Elettrochimici, Milan, Italy

ABSTRACT

The behavior of Ti-supported Pt-Ir alloys in the electrolysis of NaCl has been examined as a function of Ir content, NaCl concentration, and electrolysis time. Short-time experiments show that an iridium content as low as 0.5% is sufficient to eliminate almost completely the passivation effects (in 1M and saturated NaCl solution). Long-run experiments make clear that the minimum percentage of 5/10% Ir is necessary in order to have low potentials after thousands of hours; in such a case, however, complicating factors such as mechanical stability and chemical corrosion should be taken into account.

It is known that Pt electrodes undergo strong passivation (1) when used as anodes in brine electrolysis. A previous work (1) showed that Pt-Ir electrodes (30% Ir) do not passivate under similar experimental conditions. The aim of the present paper is to deal with the behavior of Pt-Ir electrodes as function of Ir content, NaCl concentration, and electrolysis time.

Experimental Methods

The measurements were carried out by means of a rotating disk electrode (2); this equipment allows the Cl_2 bubbles to be quickly removed from the surface. Consequently, currents and potentials are highly stable and their value can be read with sufficient precision and accuracy.

Pt, Pt-Ir alloys, and Ir coatings were obtained by a new thermal method (3): the titanium matrices were turned into a cylindrical shape (10 mm diameter) and were degreased, ground, and painted with a mixture containing $(NH_4)_2PtCl_6$ and $(NH_4)_2IrCl_6$ in the suitable ratio (see below). The painting was followed by decomposition at 500°C in air; the sequence, painting and decomposition, was repeated five times. Annealing at 550°C (2 hr) and air quenching completed the thermal treatment.

In the case of 30% Ir alloy, the following amount of mixture was applied to each square centimeter:

$(NH_4)_2PtCl_6$	6.4 mg
$(NH_4)_2IrCl_6$	2.8 mg
NH_4Cl	1-4 mg
$HCONH_2$	0.2-0.5 ml
Polyrad 1110/A (Hercules)	0.1-0.3 ml

The same amount of mixture was used in the preparation of the other alloys, the only difference being in the ratio of Pt and Ir salts.

Key words: chlorine electrochemistry, chlorine Pt/Ir electrodes, anode chlorine evolution.

Electrochemical measurements were carried out both in potentiostatic and galvanostatic conditions; electrode potentials were read by means of a 610B Keithley electrometer and were freed from ohmic drop contributions. These were determined by the usual current interruption technique, using a Tektronix mod. 531A oscilloscope and a transistor-driven mercury relay. Typical rise times were in the 1.5-2μs range. Before each experiment, the electrodes were brought to a reproducible state of activity by polarizing for 10 sec alternatively at 1.7V (NHE) and at −0.4V (NHE) for ten times. In addition, before each measurement the electrodes were held at −0.4V (NHE) for 3 sec: this treatment appeared to remove all oxides from the electrode surface. During each experiment, nitrogen containing 1% chlorine was bubbled through the NaCl solutions whose *pH* was held to a value of 3.

Results

Potentiostatic measurements.—In 0.1M NaCl (Fig. 1), all electrodes follow the Tafel law (slope: 0.03V/decade of current) up to 40 mA/cm^2; at higher current densities, Pt and Pt-Ir 0.5% show a kind of limiting current which can be attributed to a passivation process (see discussion below).

Ir, Pt-Ir 4%, Pt-Ir 2% show quite smaller deviations from the Tafel straight line at current densities above 90 mA/cm^2.

In 1M and saturated NaCl solution, the electrode behavior is qualitatively similar to that in 0.1M NaCl: again, the electrodes follow Tafel law with a slope of 0.03V/decade of current. Pt shows clearly a beginning of passivation (see discussion below) at 140 mA/cm^2 in 1M NaCl and 300 mA/cm^2 in saturated NaCl solution.

It must be mentioned that the potentiostatic measurement current values were always read after 15 sec.

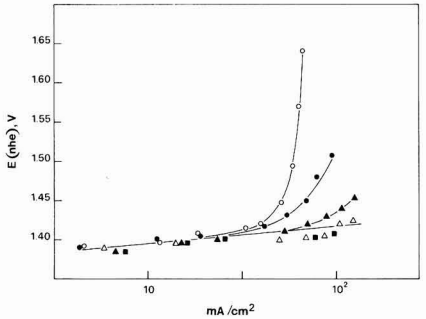

Fig. 1. Polarization curves in 0.1M NaCl, pH = 3, Cl_2 1%, T = 30°C, rotation speed = 2800 rpm. ○, Ti/Pt; ●, Ti/Pt-Ir (0.5%); △, Ti/Pt-Ir (2%); ▲, Ti/Pt-Ir (4%); ■, Ti/Ir.

Galvanostatic measurements.—Figure 4 shows the behavior in galvanostatic conditions (current density: 8 mA/cm²) in 0.1M NaCl: the increase in potential difference with respect to the value after 15 sec ($\Delta\eta$) has been plotted against time. This difference is time dependent and increases as Ir content decreases.

The Pt-Ir alloys (5, 10, 20, and 30%) were also tested under more drastic conditions: 1 A/cm² (constant current density), 70°C, 310 g/l NaCl. In this case, the coatings were deposited on the Ti network by the previously described procedure and the electrodes were used as anodes in pilot brine cells.

From Fig. 5 it can be seen that Pt-Ir 20% and 30% display a potential as low as 1.6V (NHE) after 8000 hr of electrolysis, whereas the potential of the Pt-Ir 5% and 10% is higher than 2V (NHE) after 1000 and 7000 hr, respectively.

Pt electrodes show a sufficiently low potential, about 1.5V (NHE), during the first few hours of electrolysis. After this time, quick passivation takes place; *i.e.*, the electrode potential jumps to values of about 2.5-3.0V (NHE) in the space of a few minutes.

Discussion

The different behavior between Pt and Ir electrodes can be explained by the different properties of chemisorbed oxygen.

The chemisorbed oxygen on Pt is characterized by some degree of irreversibility: capacitance measurements (4), for instance, show that the "oxide" amount is nearly constant when the electrode potential is decreased from 1.4V (NHE) to 0.9V (NHE). A similar conclusion can be drawn from the analysis of the current/potential curves obtained when a periodic triangular voltage is applied potentiostatically to the electrode (4).

In addition, it has been found (5) that the building up of the "oxide" layer on Pt starts at more anodic potentials in solutions containing halide ions; moreover, the amount of chemisorbed oxygen decreases when halide ion concentration increases. In the short-time experiments (5), the oxygen chemisorption disappears almost completely when chloride ion concentration is higher than 0.01M.

More likely, under these conditions oxygen adsorption has been considerably slowed down rather than completely prevented. Now from Fig. 1 to 3 it can be concluded that Cl^- ions are discharged at a Pt electrode at low potentials only when the surface is free from chemisorbed oxygen, whose formation rate is inversely proportional to Cl^- concentration and electrode potential. Clearly, the amount of chemisorbed oxygen is proportional to the electrolysis time; this means that under potentiostatic conditions the current values decrease with time, whereas under galvanostatic conditions the electrode potentials increase with electrolysis time (see Fig. 4).

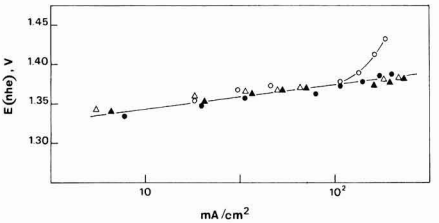

Fig. 2. Polarization curves in 1M NaCl, pH = 3, Cl_2 1%, T = 30°C, rotation speed = 2800 rpm. ○, Ti/Pt; ●, Ti/Pt-Ir (0.5%); △, Ti/Pt-Ir (2%); ▲, Ti/Pt-Ir (4%).

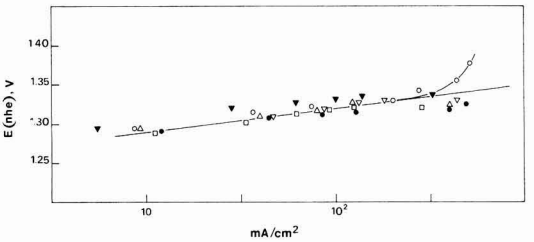

Fig. 3. Polarization curves in saturated NaCl, pH = 3, Cl_2 1%, T = 30°C, rotation speed = 2800 rpm. ○, Ti/Pt; ●; Ti/Pt-Ir (0.5%); △, Ti/Pt-Ir (2%); □, Ti/Pt-Ir (10%); ▽, Ti/Pt-Ir (20%); ▼, Ti/Pt-Ir (30%).

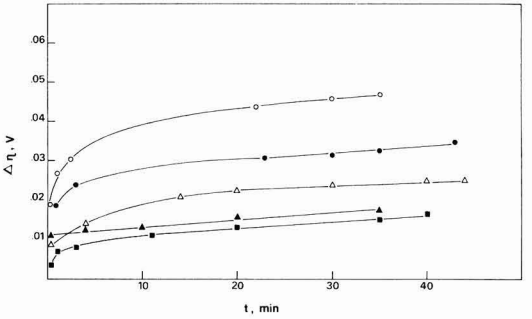

Fig. 4. Potential difference (with respect to the value after 15 sec) against time. Constant current density = 8 mA/cm². 0.1M NaCl, pH = 3, Cl_2 = 1%; T = 30°C, rotation speed = 2800 rpm. ○, Ti/Pt; ●, Ti/Pt-Ir (0.5%); △, Ti/Pt-Ir (2%); ▲, Ti/Pt-Ir (4%); ■, Ti/Ir.

Ir, on the contrary, shows a nearly reversible behavior with respect to the formation and removal of the chemisorbed oxygen (4). The breaking of the Ir-O bond is characterized by an absence of significant energy barrier; an irreversible passivation of the surface due to an "oxide" layer cannot take place (see Fig. 4).

As regards Pt-Ir alloys, the potentiostatic measurements (short-time experiments) in 1M and saturated NaCl solutions show that very low percentages (0.5%) of Ir are quite effective in decreasing the passivation effect (see Fig. 2 and 3). Long-run experiments (Fig. 5) show clearly that a minimum content of 5-10% in Ir is necessary in order to assure a lifetime of thousands of hours. In such a case, however, a number of phenomena must be taken into account, especially:

(*i*) mechanical stability related to gas evolution in the pores of the coating
(*ii*) chemical corrosion which can be brought about in the pores by the acidity due to some oxygen evolution.

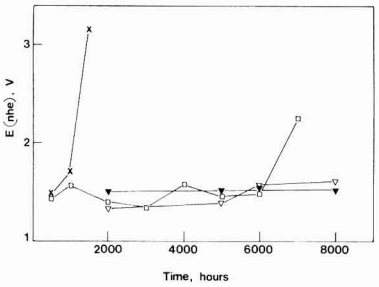

Fig. 5. Electrode potential as a function of electrolysis time. Constant current density = 1 A/cm². NaCl = 310 g/l, pH = 3, T = 70°C. ×, Ti/Pt-Ir (5%); □, Ti/Pt-Ir (10%); ▽, Ti/Pt-Ir (20%). ▼, Ti/Pt-Ir (30%).

It should be remembered that the lowest pH value where Pt is stable in the presence of the chlorine and chlorides is about 2. However, it is apparent that mechanical stability and chemical corrosion are negligible in short-time experiments where the catalytic properties of the electrode surface are predominant.

As regards the kinetics, it must be pointed out that all the electrodes show a Tafel b-coefficient equal to 0.03 V/decade of current; according to this low value, the electrode mechanism could be the following one

$$Cl^- \rightleftarrows Cl_{ads} + e$$
$$2Cl_{ads} \rightarrow Cl_2$$

The second step being rate determining.

Manuscript submitted March 9, 1970; revised manuscript received June 3, 1970.

Any discussion of this paper will appear in a Discussion Section to be published in the June 1971 JOURNAL.

REFERENCES

1. G. Faita, G. Fiori, and J. W. Augustynski, *This Journal*, **116**, 928 (1969).
2. G. Faita, G. Fiori, and J. W. Augustynski, *Electrochim. Metall.*, **2**, 437 (1967).
3. G. Bianchi and A. Nidola, I, 795, 565 (1.12.67).
4. M. W. Breiter, *Electrochim. Acta*, **8**, 973 (1963).
5. M. W. Breiter, *ibid.*, **8**, 925 (1963).

Technical Note

Polarization Cell for Potentiostatic Crevice Corrosion Testing

E. A. Lizlovs*

Climax Molybdenum Company of Michigan, Research Laboratory, Ann Arbor, Michigan 48106

Several electrochemical methods, including potentiostatic techniques, have been proposed in recent years for the investigation of crevice corrosion (1-6). In general, two major problems are involved in designing a suitable electrode for crevice corrosion studies: elimination of unwanted crevices while maintaining a well-defined exposed electrode area, and introduction of a reproducible crevice. Considering that fissures involved in crevice corrosion of stainless steels are of the order of 10^{-3} in. or less, both of these problems are quite formidable. The present investigation was prompted by the observations of crevice attack during potentiodynamic polarization experiments with stainless steels in hydrochloric acid (7). It was envisioned at that time that, if an appropriate working electrode could be designed, the potentiostatic polarization current in the passive state could be utilized to measure the progress of crevice corrosion. In addition, if reproducible crevices could be introduced in electrode design, the relative resistance to crevice corrosion of a series of alloys could be determined by comparing the polarization current at some selected potential.

Experimental

Crevice corrosion cell.—The polarization cell for the crevice corrosion studies consisted of a 5 in. long, 3½ in. diameter glass tubing mounted between two rectangular polycarbonate blocks. The essential parts of the cell are shown in Fig. 1. The cell was equipped with two 10/30 and two 24/40 standard taper ground glass necks to accommodate the electrolytic bridge from the reference electrode, inlet and outlet tubes for purging gas, and auxiliary platinum electrode, which was separated from the bulk of the solution by a fritted glass disk. The glass tube was mounted to polycarbonate blocks by placing the tube on the blocks in a proper position and applying silicone rubber (G.E. RTV-12 adhesive) around it and allowing the adhesive

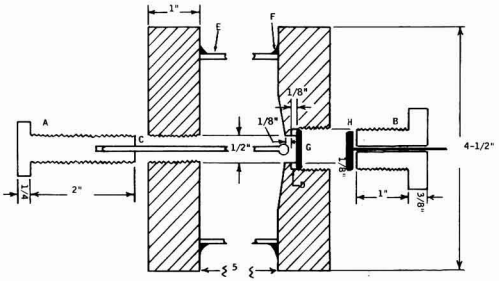

Fig. 1. Cross section through polycarbonate end-blocks and plastic bolts of crevice corrosion cell: A—Teflon bolt ½-20 thd; B—PVC bolt with hexagonal head, ⅞-14 thd; C—⅛ in. diameter glass rod with 4 mm diameter glass bead at the end; D—Teflon gasket, ⅛ in. thick by 0.810 in. OD; E—3 ½ in. OD glass tubing; F—silicone rubber mount; G—stainless steel working electrode; H—copper disk with copper lead wire.

* Electrochemical Society Active Member.

Key words: crevice corrosion, potentiostatic, testing, stainless steel, molybdenum, chloride.

Table I. Compositions of alloys studied

Alloy	Composition, %								
	C	Cr	Ni	Mo	Mn	Si	P	S	N
Type 304	0.063	18.55	10.48	—	1.72	0.43	0.026	0.013	—
Type 316	0.059	17.20	13.27	2.83	1.20	0.32	0.019	0.011	—
17% Cr	0.003	17.08	—	0.03	—	0.05	0.009	—	0.0065
17% Cr-3% Mo	0.003	16.68	—	2.99	—	0.06	0.007	—	0.0048
25% Cr	0.002	25.66	0.13	0.002	—	~0.02[a]	~0.01[a]	~0.002	~0.01[a]
25% Cr-3.5% Mo	0.002	25.58	0.13	3.49	—	~0.02[a]	~0.01[a]	~0.001	~0.01[a]

[a] Not analyzed but assumed to be approximately at indicated levels. See Ref. (9).

to solidify for a day. One of the end-blocks served as a working electrode holder. The design of the electrode holder was a modified version of the electrode holder described by France (8). The working electrode, which was a disk approximately ¾ in. in diameter, was pressed against a Teflon washer by a PVC[1] bolt. Electrical contact to the sample was established by a copper back-up disk and copper wire extending through the PVC bolt. The opposite end-block contained a threaded ½ in. diameter hole, concentric with the working electrode opening. This opening was fitted with a Teflon bolt with inserted glass rod with a smooth, approximately 4 mm diameter, glass bead at the end. A variable crevice was produced by advancing the bolt through the threaded hole until the bead was pressed against the surface of the working electrode. If the same glass bead is employed for all experiments, it can be assumed that crevices of equal geometries are produced. The crevice can be applied or removed as desired at any stage of the experiment by simply manipulating the Teflon bolt.

Materials.—Commercial stainless steels, Types 304 and 316, and high-purity laboratory alloys, 17% Cr, 17% Cr-3% Mo, 25% Cr and 25% Cr-3.5% Mo, were selected for the evaluation of the performance of the crevice corrosion cell and feasibility of the potentiostatic method for crevice corrosion tests. Chemical compositions of the steels are given in Table I.

Procedures.—All experiments were performed in N_2-saturated 1*N* NaCl at room temperature (24° ± 1°C). The working electrode was first polarized for 10 min at −1.00V (SCE), then the potentiostat was switched off for 10 min, and then switched on again. The potential of the working electrode was then carefully changed from −1.00 to −0.20V, and the electrode was passivated at this potential for 2 hr. Timing was started from the moment the polarization current fell down to 5 μA. After a 2 hr passivation, the potential was scanned from −0.20 to 0.00V at the rate of 0.15 mV/sec, and then the glass bead was pressed to the surface. The electrode with the "crevice applied" was kept at 0.00V for 1-3 hr, and then the crevice was removed. Polarization current and potential were recorded continuously throughout the above operations by a two-pen strip chart recorder.

After the experiment, the electrode was removed from the assembly and inspected for corrosion damage. Only those experiments were considered acceptable in which corrosion occurred under the glass bead and no place else.

Results and Discussion

A noticeable polarization current rise, indicating the onset of crevice corrosion, usually started almost immediately after the glass bead was pressed against the electrode surface. No critical potential for crevice corrosion was found and the attack could be initiated at potentials as low as −0.20V. Polarization current as a function of time for various stainless steel electrodes is shown in Fig. 2. Since the electrode area for samples was the same (1.26 cm^2) and the same glass bead was applied to the surface, the polarization current itself rather than current density may be used to compare the relative rates of crevice corrosion. Polarization current-time curves at 0.00V in the presence of a crevice were for the most part quite irregular and indicated a complex corrosion process. Comparison of the behavior of various grades of stainless steels and evaluation of the relative resistance to crevice corrosion, however, were possible. Type 304 and high-purity 25% Cr stainless steels showed about the same relative resistance to crevice corrosion and both materials repassivated immediately upon removal of the crevice. The high-purity 17% Cr alloy showed the highest polarization current of all materials over a 1 hr period and it did not repassivate immediately after removal of the crevice. Instead, the 17% Cr alloy continued to corrode at almost the same rate for at least 1 min after removal of the crevice, after which time the experiment was interrupted. Examination of the electrode showed that corrosion was localized under the glass bead. Apparently, for the 17% Cr alloy, a stable pit could be formed at 0 volt at the site of the crevice damage. Both Type 316 stainless steel and 17% Cr-3% Mo steel repassivated while the bead was still applied to the surface. The 17% Cr-3% Mo alloy repassivated within 30 min of the initiation of crevice corrosion, while Type 316 repassivated 90 min after crevice was applied. Apparently the potential of 0.00V was not sufficiently oxidizing to sustain corrosion under the bead for these alloys. Type 316 steel also showed higher polarization current than the 17% Cr-3% Mo alloy. No crevice corrosion could be initiated for the 25% Cr-3.5% Mo alloy either at 0 volt or at +0.80V. This alloy was also tested for crevice corrosion in 1*N* hydrochloric acid at room temperature. In this experiment, the electrode was first activated, then allowed to corrode for about 7 min, then the potentiostat with potential set at +0.80V was switched on. Immediately after the potential was applied to the electrode, the glass bead was brought against the electrode surface. The polarization behavior under these drastic conditions is shown in Fig. 3. The electrode completely passivated and no effect of the presence of a crevice on the electrode surface was discernible on the polarization current-time curve.

The results of the two successive applications of the crevice to two different points of the same 17% Cr-3% Mo alloy are shown in Fig. 4, which illustrates the kind of reproducibility expected in the operation of the crevice corrosion cell. Both curves were quite

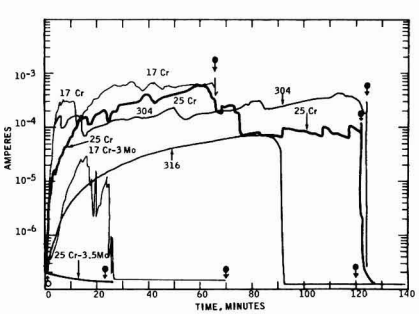

Fig. 2. Variations in polarization currents with time at 0.00V (SCE) in 1*N* NaCl at 24° ± 1°C: ⛢, crevice applied to the electrode surface; ⇕, crevice removed from electrode surface.

[1] Polyvinyl chloride.

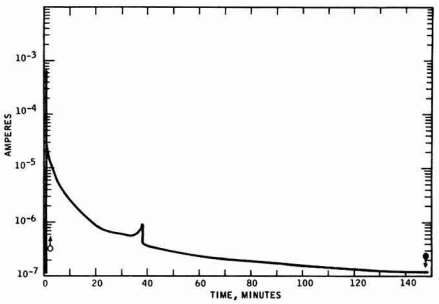

Fig. 3. Variation in polarization current with time at 0.80V for 25% Cr-3.5% Mo in 1*N* HCl (24° ± 1°C): ♁, crevice applied to the electrode surface; ↕, crevice removed from electrode surface.

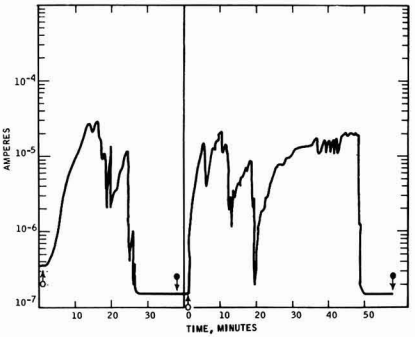

Fig. 4. Two successive polarization current-time curves at 0.00V (SCE) for 17% Cr-3% Mo alloy in 1*N* NaCl (24° ± 1°C): ♁, crevice applied to the electrode surface; ↕, crevice removed from electrode surface.

irregular and, in both, repassivation occurred before the removal of the crevice. In the first curve, repassivation occurred in about 25 min and in the second in about 50 min. Maximum current reached for both was about the same.

On the basis of the above observations, it can be concluded that the relative order of the resistance to crevice corrosion is 17% Cr (least resistant) <T304 = 25% Cr <T316 <17% Cr-3% Mo<<25% Cr-3.5% Mo (immune to crevice corrosion at room temperature in 1*N* Cl^-). In previous qualitative work, with 25% Cr alloys in acidified 10% Fe Cl_3 solution with crevice applied by means of a rubber band and Teflon disk, it was found that 25% Cr alloy did suffer crevice attack, while the 25% Cr-3.5% Mo alloy was immune to crevice as well as pitting corrosion. Earlier potentiostatic experiments in 1*N* HCl also indicated that 25% Cr-3.5% Mo alloy should be immune to crevice corrosion, while 25% Cr alloy would suffer crevice corrosion under the same conditions (9). Thus, these previous results with 25% Cr alloys are in agreement with the results from this investigation. Furthermore, all other stainless steels investigated here are known to suffer crevice corrosion in chloride media.

Conclusion

The crevice corrosion cell described in this paper makes it possible to obtain potentiostatic measurements with simple and easily prepared electrodes. Since the same crevice geometry is employed in every experiment, a relative resistance to crevice corrosion for a series of alloys can be deduced from comparison of polarization current-time curves at a given potential. Furthermore, the initiation and progress of the crevice attack can also be conveniently observed. Since the crevice can be applied or removed at will, many experiments which would not be possible with a fixed crevice can be performed.

Manuscript submitted April 1, 1970; revised manuscript received *ca.* June 15, 1970.

Any discussion of this paper will appear in a Discussion Section to be published in the June 1971 JOURNAL.

REFERENCES

1. I. L. Rozenfel'd and I. K. Marshakov, *Zavodskaya Lab.*, **21**, 1346 (1955).
2. R. R. Salem, *Zavodskaya Lab.*, **26**, 291 (1960); Transl. *Industrial Lab.*, **26**, 306 (1960).
3. I. B. Ulanovskii, *Zhur. Prikl. Khim.*, **39**, 814 (1966); Transl. *J. Appl. Chem. U.S.S.R.*, **39**, 768 (1966).
4. G. Bombara, D. Sinigaglia, and G. Taccani, *Electrochim. Metal.*, **3**, 81 (1968).
5. W. D. France and N. D. Greene, *Corrosion*, **24**, 247 (1968).
6. D. A. Jones and N. D. Greene, *ibid.*, **25**, 367 (1968).
7. E. A. Lizlovs and A. P. Bond, *This Journal*, **116**, 574 (1969).
8. W. D. France, *ibid.*, **114**, 818 (1967).
9. E. A. Lizlovs and A. P. Bond, "Anodic Polarization Behavior of 25% Chromium Ferritic Stainless Steels," *This Journal*, submitted for publication.

ELECTROCHEMICAL BOOKS IN PRINT

John Wiley Publications In-Print

The following are books developed and sponsored by The Electrochemical Society and published by John Wiley & Sons Inc., 605 Third Ave., New York, N. Y., 10016. Members of the Society can receive a 33% discount by ordering from Society Headquarters. Book and invoice mailed by the publisher. Nonmembers (including subscribers) must order direct from the publisher.

Corrosion Handbook. Edited by Herbert H. Uhlig. Published 1948, 1188 pages, **$21.00.**

Modern Electroplating, Second Edition. Edited by Frederick A. Lowenheim. Published 1963, 769 pages, **$16.00.**

Electrochemistry in Biology and Medicine. Edited by Theodore Shedlovsky. Published 1955, 369 pages, **$12.50.**

Arcs in Inert Atmospheres and Vacuum. Edited by W. E. Kuhn. Published 1956, 188 pages, **$7.50.** A 1956 Spring Symposium.

Ultrafine Particles, Editor-in-Chief—William E. Kuhn. Published 1963, 561 pages, **$15.00.**

First International Conference on Electron and Ion Beam Science and Technology. Edited by R. Bakish. Published 1965, 945 pages, **$24.50.** (Sponsored by the Electrothermics and Metallurgy Division of The Electrochemical Society and the Metallurgy Society of AIME.)

The Electron Microprobe. Edited by T. D. McKinley, K. F. J. Heinrich, and D. B. Wittry. Published 1966, 1035 pages, **$27.50.** A 1964 Fall Symposium.

Chemical Physics of Ionic Solutions. Edited by B. E. Conway and R. G. Barradas. Published 1966, 622 pages. **$25.00.** A 1964 Spring Symposium.

Vapor Deposition. Edited by C. F. Powell, J. H. Oxley, and J. M. Blocher, Jr. Published 1966, 725 pages, **$19.95.**

The Stress Corrosion of Metals by Hugh I. Logan. Published 1966, 306 pages; **$13.95.**

High Temperature Oxidation of Metals by Per Kofstad. Published 1966, 340 pages; **$13.50.**

The Corrosion of Light Metals, by H. P. Godard, W. B. Jepson, M. R. Bothwell, and R. L. Kane. Published 1967, 360 pages; **$13.95.**

High-Temperature Materials and Technology. Edited by I. E. Campbell and E. M. Sherwood. Published 1967, 1022 pages, **$27.50.**

Alkaline Storage Batteries, by S. Uno Falk and Alvin J. Salkind. Published 1969, 672 pages; **$32.50.**

SOCIETY SOFTBOUND SYMPOSIUM SERIES

[a] **Surface Chemistry of Metals and Semiconductors.**
H. C. Gatos, J. W. Faust, Jr., and W. J. La Fleur, Editors.
A 1959 symposium. 526 p. $21.50

[a] **Electrode Processes.** First Conference.
E. Yeager, Editor.
A 1959 symposium. 374 p. $15.50

[a] **Mechanical Properties of Intermetallic Compounds.**
J. H. Westbrook, Editor.
A 1959 symposium. 435 p. $17.50

[a] **Zirconium and Its Alloys.**
J. P. Pemsler, E. C. W. Perryman, and W. W. Smeltzer, Editors.
A 1965 symposium. 205 p. $10.00

[a] **Electrolytic Rectification and Conduction Mechanisms in Anodic Oxide Films.**
P. F. Schmidt and D. M. Smyth, Editors.
A 1967 symposium. 230 p. $7.00

[a] **Vapor Plating.**
C. F. Powell, I. E. Campbell, and B. W. Gonser.
1955. 158 p. $6.50

[a] **Iodide Metals and Metal Iodides.**
R. F. Rolsten.
1961. 441 p. $18.00

[a] **Technology of Columbium (Niobium).**
B. W. Gonser and E. M. Sherwood, Editors.
1958. 120 p. $5.00

[a] **The Structure of Electrolytic Solutions.**
Walter J. Hamer, Editor.
A 1957 symposium. 441 p. $18.00

[a] **Electrets and Related Electrostatic Charge Storage Phenomena.**
L. M. Baxt and M. M. Perlman, Editors.
A 1967 symposium. 150 p. $11.00

[a] **Electron and Ion Beam Science and Technology.** Third Conference.
R. Bakish, Editor.
A 1968 symposium. 725 p. $21.00

[b] **Measurement Techniques for Thin Films.**
B. Schwartz and N. Schwartz, Editors.
1965 and 1966 symposia. 347 p.
$12.00 (softbound) $15.00 (hard bound)

[b] **Electrode Processes.** Second Conference.
E. Yeager, H. Hoffman, and E. Eisenmann, Editors.
A 1966 symposium. 190 p. $5.00

[c] **Vacuum Metallurgy.**
J. M. Blocher, Jr., Editor.
A 1954 symposium. 216 p. $5.00

[c] **Dielectrophoretic and Electrophoretic Deposition.**
E. F. Pickard and H. A. Pohl, Editors.
A 1967 symposium. 138 p. $9.00

[a] **Optical Properties of Dielectric Films.**
N. Axelrod, Editor.
A 1968 symposium. 325 p. $9.00

[a] **Thin Film Dielectrics.**
Fredrick Vratny, Editor.
A 1968 symposium. 680 p. $27.40

[a] **Ohmic Contacts to Semiconductors.**
Bertram Schwartz, Editor.
A 1968 symposium. 356 p. $14.75

[c] **Semiconductor Silicon.**
Rolf R. Haberecht and Edward L. Kern, Editors.
A 1969 symposium. 750 p. $10.00

[c] **Chemical Vapor Deposition.**
Second Conference.
John M. Blocher, Jr. and James C. Withers, Editors.
A 1970 symposium. 872 p. $15.00.

Iron Ore Reduction.
R. R. Rogers, Editor.
A 1960 symposium. 359 p. $12.50
Order from the MacMillan Co., 60 Fifth Ave., New York, N. Y. 10003

Rhenium.
B. W. Gonser, Editor.
A 1960 symposium. 225 p. $12.50
Order from American Elsevier Publishing Co., 52 Vanderbilt Ave., New York, N. Y. 10017

---

[a] Order from University Microfilms, Inc., 300 N. Zeeb St., Ann Arbor, Mich. 48103. Enclose payment with order. Specify an Electrochemical Society volume.

[b] Order from Johnson Reprint Co., 111 Fifth Ave., New York, N. Y. 10003. Specify an Electrochemical Society volume. Prices subject to change without notice.

[c] Orders filled at the list price given, subject to availability, from The Electrochemical Society, Inc., 30 East 42 St., New York, N. Y. 10017. Enclose payment with order.

JOURNAL OF THE ELECTROCHEMICAL SOCIETY

REVIEWS AND NEWS

OCTOBER 1970

Physical and Mechanical Properties of Electrodeposited Copper

III. Deposits from Sulfate, Fluoborate, Pyrophosphate, Cyanide, and Amine Baths[12]

Vernon A. Lamb, Christian E. Johnson, and Donald R. Valentine

National Bureau of Standards, Washington, D. C. 20234

IV. Deposits from Fluoborate Baths

A. General

The compositions of the fluoborate baths are shown in Table III. The concentration of copper metal (molarity) in the low-concentration bath (F-1) was the same as in the Cu-2 sulfate baths. The high-concentration bath (F-2) was similar to a bath described by Diggin (21) and by the commercial suppliers of fluoborate concentrates. Control of the concentration of copper fluoborate was based on chemical analysis. Fluoboric acid control was based on measurement of *p*H with sensitive *p*H paper. Equipment used was the same as for sulfate baths with one exception. To avoid attack of the glass tank by fluoborate, a lining of polyethylene sheet was used. A cotton filter, the same as used in the later sulfate baths, was used for the fluoborate baths. Air agitation was used.

B. Effect of Operating Conditions and Bath Composition on Properties of Deposits

1. Bath temperature.—Data on the effect of bath temperature on tensile strength, elongation, hardness, and internal stress, tabulated in Table XVI, are plotted in Fig. 22. Each of these properties decreases with increase of temperature. Attention is directed to the fact that, as with non-addition agent sulfate baths, ductility decreases with decrease of tensile strength.

Neither density nor electrical resistivity undergoes significant change with change of bath temperature (Table XVI).

2. Current density.—Effect of current density is also shown in Fig. 22. Increase in current density causes tensile strength, elongation, hardness, and internal stress to increase. Again, elongation parallels tensile strength.

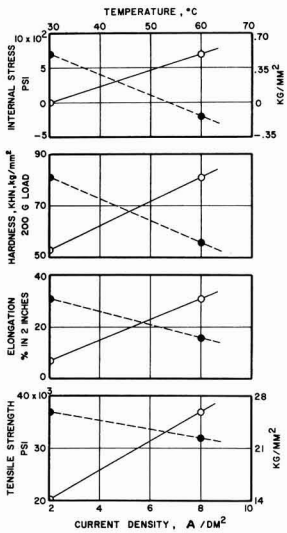

Fig. 22. Relationships of current density and bath temperature to tensile strength, elongation, hardness, and internal stress of copper deposits from a fluoborate bath (F-1). ○—current density, ●—bath temperature.

As with temperature, current density has no significant effect on either density or electrical resistivity.

3. Concentration of copper fluoborate.—The effect of concentration of copper fluoborate on properties may be seen by comparing lines 91 and 93 in Table XVI. The differences due to concentration are insignificant for all of the properties shown except hardness. The small

[12] AES Project 21 Report, part 2. Sections IV-VII published here are the second of three installments of this paper. Part 1 (Sections I-III) appears on pages 291C-318C of the September issue, and part 3 (Sections VIII-X) will appear in the November issue.

Table XVI. Effects of temperature, current density, and concentration of copper fluoborate on properties of deposits from the fluoborate bath

Line No., Table I	Panel No.	Bath symbol	Conc of $Cu(BF_4)_2$, g/l	Bath temp, °C	Current density, A/dm²	Tensile[a] strength, psi	Yield[a,b] strength, psi	Elongation in 2 in. (5 cm), %	Hardness KHN 200g load, kg/mm²	Internal[a,c] stress, psi	Density 25°C, g/cm³	Elec. resistivity 25°C, ohm-cm
90	342	F-1	177	30	2	20×10^3	9×10^3	7	53	Zero	8.925	1.73×10^{-6}
91	343-345				8	37	16	31	81	700	8.926	1.73
92	346			60	8	32	11	16	56	−200	8.925	1.73
93	347	F-2	336	30	8	36	15	31	71	800	8.926	1.74

[a] One pound per square inch (psi) = 0.000704 kilogram per square millimeter (kg/mm²).
[b] 0.05% offset.
[c] Negative values represent compressive stresses.

Table XVII. Comparison of properties of deposits made at high current density from sulfate and fluoborate baths

Line No., Table I	Panel No.	Bath[a] symbol	Conc Cu^{++}, g/l	Bath temp, °C	Current density, A/dm^2	Tensile[c] strength, psi	Yield[b,c] strength, psi	Elongation in 2 in. (5 cm), %	Hardness KHN 200g load, kg/mm^2	Internal[c] stress, psi	Density 25°C, g/cm^3	Elec. resistivity 25°C, ohm-cm
42	297	Cu2-H3	47	60	20	20×10^3	7×10^3	5	58	1400	8.86	1.90×10^{-6}
94	348	F-2	90	50	20	33	12	29	60	1600	8.925	1.75

[a] No addition agent in either bath; identical air agitation.
[b] 0.05% offset.
[c] One pound per square inch (psi) = 0.000704 kilogram per square millimeter (kg/mm^2).

decrease from 81 to 71 KHN with increase of concentration is in the expected direction. It is possible that larger effects exist at lower bath temperatures or at higher current densities.

C. Comparison of Deposits Made with High Current Densities from Fluoborate and Sulfate Baths

A comparison between properties of deposits from fluoborate and sulfate baths, both made at a high current density, 20 A/dm^2, is shown in Table XVII. The general character and properties of the deposit from the fluoborate bath are nearly the same as those of the deposits shown in Table XVI that were made at lower current densities. On the other hand, the deposit from the sulfate bath was weak, brittle, had a very low density and high resistivity, and a high impurity content (see Section VIII-G), properties indicating that the limiting current density was exceeded. These results confirm the reputed high current density capability of the fluoborate bath in comparison with the sulfate bath. The comparison is in one sense unfair, since the concentration of copper ion in the fluoborate bath is nearly twice that in the sulfate bath. However, the solubility of $CuSO_4$ makes it impractical to operate the sulfate bath with a significantly higher concentration than we used, whereas operation of the fluoborate bath with a concentration of copper ion equal to that shown in Table XVII or higher is practicable.

D. Structure

The structure of the deposit represented on line 91, Table XVI, is shown in Fig. 59-2. It has a more fibrous character than the deposit from the corresponding non-addition agent sulfate bath (Fig. 59-1). It is possible, however, that under other conditions fluoborate baths may yield large-grained deposits. Thus, if grain size correlates with strength, one might expect the very weak deposit on line 90, Table XVI, made at a low current density, to have a coarse structure.

V. Deposits from the Pyrophosphate Bath

A. General

Only one bath composition was used for making deposits from the pyrophosphate bath (Table III). The selection of the concentrations of the various constituents was based on recommendations made by several authors (25-27). No addition agents were used. Deposits were bright as plated.

B. Effect of Operating Conditions on Properties of the Deposits

1. Bath temperature.—Comparing lines 98 and 100 in Table XVIII, it is seen that the only property that is affected significantly by a change of temperature of 10°C is internal stress. The change from 1700 psi tensile to 1900 psi compressive with increase of temperature is in the same direction as has been observed for the sulfate and fluoborate baths but is larger.

2. Current density.—The data on lines 95 and 98 of Table XVIII show that increase of internal stress is the only significant change of property due to increase of current density from 2 to 4 A/dm^2.

3. Agitation.—Propeller agitation was tried initially in the pyrophosphate bath. Since the deposits were not uniformly bright over the entire area and tended to be nodular, other means of agitation were tried, as described in Table I, lines 95-100. Air agitation gave the best results, and was used for the deposits for which data are given in Table XVIII. However, several properties of the deposits prepared with other modes of agitation were measured. The results appear in Table I. It is seen that these properties were not affected appreciably by the variations in agitation.

C. Structure

Photomicrographs of the deposit on line 95, Table XVIII, are shown in Fig. 59-3 and 59-4. The structure differs markedly from that of deposits from sulfate or fluoborate baths. There is indication of large columnar crystals with a very fine substructure. Tensile strength and other properties of these deposits vary from those of large-grained sulfate deposits in the direction that one would expect if the grain size were smaller, but the effect is not as large as it is with the finer-grained deposits from addition agent sulfate baths.

Additional data on the structure of these deposits are discussed in Section VIII-F.

VI. Deposits from the Amine Bath

A. General

Several researches have been reported on attempts to develop commercially useful baths based on copper-

Table XVIII. Effects of temperature and current density on properties of deposits from the pyrophosphate and amine baths

Line No., Table I	Panel No.	Bath temp, °C	Current density, A/dm^2	Tensile[a] strength, psi	Yield[a,b] strength, psi	Elongation in 2 in. (5 cm), %	Hardness KHN 200g load, kg/mm^2	Internal[a,c] stress, psi	Density 25°C g/cm^3	Elec. resistivity 25°C, ohm-cm
					A. Pyrophosphate bath					
95	317-320	50	2	38×10^3	20×10^3	39	83	−1600	8.926	1.75×10^{-6}
98	314		4	40	22	33	90	1700	8.926	1.74
100	316	60	4	39	20	39	80	−1900	8.926	1.74
					B. Amine bath					
149	328	55	2	69	41	4	202	−5700	8.891	2.08
151	326-330		4	60	44	4	169	−6000	8.906	2.10

[a] One pound per square inch (psi) = 0.000704 kilogram per square millimeter (kg/mm^2).
[b] 0.05% offset.
[c] Negative values represent compressive stresses.

amine complexes (27-29). Although the baths that have been described have not achieved significant use, it was thought that since the amine bath is a rather different type than the others used in this project it deserved a limited investigation to see whether the deposits had any unusual properties. Several of the baths described in the literature were tried. Most of them did not yield sound thick deposits. Sound deposits were obtained from the bath shown in Table III, which is similar to one described by Greenspan (29). Deposits were fairly smooth at a thickness of 10 mils, but became excessively rough, with a tendency for filamentary growths to start at larger thickness.

B. Effect of Current Density on Properties of Deposits

Because current density is a relatively uncontrollable variable when irregularly shaped objects are plated, it seemed most important in a limited study to include current density as a variable. This was the only variable studied. The results shown in Table XVIII indicate that a change of current density from 2 to 4 A/dm^2 does not significantly change the properties of the deposits.

It is seen that the deposits are fairly strong and very hard. However, their low ductility is adverse. Their high compressive internal stress is noteworthy. Their low density and high electrical resistivity indicate a probable high content of impurity, but this was not investigated.

C. Structure

A photomicrograph of the deposit on line 151, Table XVIII, is shown in Fig. 59-6. The structure is seen to be very fine, with unresolved grains at a magnification of 500X.

VII. Deposits from Cyanide Baths

A. General

Concentrations of the various constituents of the cyanide baths and levels of operating variables were chosen on the basis of a review of the recommendations made in various publications (6, 26, 27). The brightener system identified in Table IV as "Proprietary B" is reported by the vendor to be a selenium type (26).

B. Mechanical Properties

1. The bulge method for measuring tensile strength and ductility.—a. Apparatus.—It is difficult to prepare, handle, and test deposits in the thickness range of 0.001-0.002 in. by the standard tensile pull method. To avoid these difficulties, Read and co-workers have adapted the hydraulic bulge test to the measurement of tensile strength and ductility of thin electroformed deposits (30, 31). Since most of our deposits from cyanide baths were 0.001-0.002 in. thick, the bulge test was the preferred test method. Besides avoiding the technical difficulties referred to above, the method has the advantage that specimens can be made very easily and at low cost by simply cutting out a disk of the material with scissors.

The basic principle of the bulge tester is illustrated in Fig. 23, Part I. The test specimen, in the form of a disk cut from a specimen panel, is clamped between the thick steel base plate and the clamp ring. Oil is pumped through the opening under the copper disk, causing it to expand into the opening in the clamp ring. In our apparatus, the diameter of the disk is 2⅜ in., and of the hole in the clamp ring, 1.5 in. Tensile strength can be calculated from the fluid pressure and bulge height, and degree of elongation or ductility can be determined from the linear stretch of a unit length at the top of the bulge at rupture. We constructed the apparatus that we used. It is the same in principle as the apparatus described by Read and co-workers but differs in details of design. A photograph is shown in Fig. 23, Part II, in which the major components are identified. The gear pump, with a capacity of 1000 psi, was powered by a 1/6 hp integrally coupled motor. Oil was drawn from the reservoir through the filter and pumped through the throttle valve into a parallel

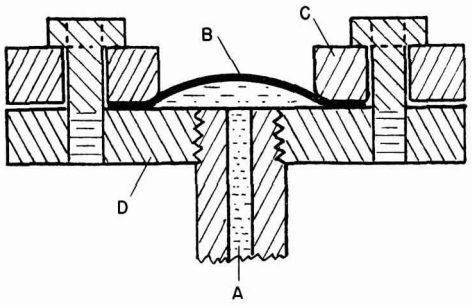

Fig. 23-I. Cross section of head of bulge tester: A—oil inlet, B—bulged disk, C—clamping ring, D—base plate.

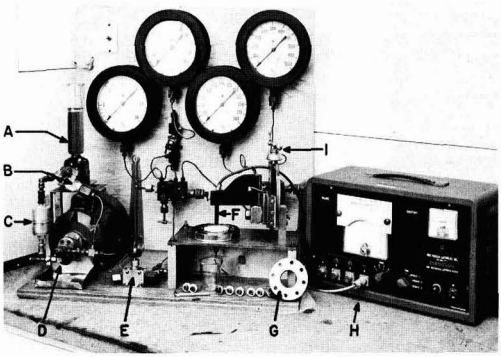

Fig. 23-II. Photograph of complete bulge tester: A—oil reservoir, B—bypass valve, C—oil filter, D—pump, E—throttle valve, F—Dermitron probe, G—clamping ring, H—Dermitron unit, I—vertical micrometer.

array of tubing, one to the bulge and one to each of the four gauges. The line to each gauge was equipped with a cut-off valve. If the pressure limit for the first gauge (30 psi) was exceeded, its valve was closed and pressure read on the second gauge (100 psi), *etc.*, through the third (300 psi) and fourth (1000 psi). Good sensitivity of pressure measurement was thus obtained for any magnitude of pressure encountered. Flow rate and bulge growth were controlled by combined settings of the bypass valve and throttle valve.

An expanded disk is shown in place on the base plate. Oil released on rupture of the disk is caught in the shallow tray surrounding the base plate and flows into the small beaker. The height of the bulge is measured with the Dermitron[13] unit (32) in the following manner. A dummy specimen is laid on the base plate and the probe is lowered with the probe-height control screw until it just touches the specimen, then raised about 0.005 in. The Dermitron controls are then adjusted so that, at this arbitrary distance between the probe face and the specimen, the Dermitron thickness meter reads at the midpoint of the scale and the sensitivity is about 0.001 in. for full-scale needle deflection. Without changing the Dermitron adjustments, the probe is raised sufficiently by the screw to permit placement and clamping of the test specimen. The probe is then returned to its former position, minor readjustments in Dermitron control settings are made if necessary, and the starting height of the probe is read on the micrometer screw. The bulge is then slowly expanded. As it grows, the probe is raised simultaneously with the screw so that the original clearance between the probe face and the specimen is maintained, as indicated by a constant reading at the center point of the Dermitron meter. When the specimen ruptures, growth stops, and, simultaneously, advance of the

[13] An eddy current type of thickness gauge.

screw is stopped. The difference between the reading of the probe-height micrometer screw at this point and at the beginning gives the height of the bulge. The advantages of this height-measuring procedure are (*a*) that the bulge is not mechanically contacted by the measuring device and, hence, not mechanically damaged and (*b*) the procedure is sufficiently simple that one operator can control bulge growth and height measurement simultaneously. We estimate that the measured values of bulge height are accurate to about ±0.001 in. and those of pressure to about ±5% of the observed value. A minimum of six replicate disks from each panel was tested. Variations in pressure among the six were often as much as ±25%. The large variation is judged to result from premature failure of some of the specimens because of the presence of flaws. However, within a given set of specimens, bulge height and pressure were usually closely correlated. The formulas in the next section show that tensile strength is approximately proportional to the ratio of pressure to bulge height and, therefore, even though variations of pressure and height among replicates were rather large, calculated values of tensile strength seldom varied more than ±5%.

b. Bulge test relationships.—(*i*) *Basic relationships.*—The following relationships for obtaining tensile strength and ductility values from bulge measurements are stated without development. For more detail the reader is referred to Read and co-workers (30, 31):

$$\text{Nominal tensile strength} = \frac{PR}{2t} \qquad [1]$$

where P is pressure at fracture, R is the radius of curvature of the bulge at fracture, and t is the initial thickness of the specimen, which was determined from area and mass.

$$\text{True stress} = \sigma = \bar{\sigma} = \frac{PR}{2t_i} \qquad [2]$$

in which true stress, σ, is equal to the load divided by the simultaneously measured cross-sectional area. Use in Eq. [2] of t_i, the simultaneously measured thickness, yields true stress. "Significant stress," $\bar{\sigma}$, is a generalized function which is a measure of the stress under any type of loading. The equality shown in Eq. [2] applies to isotropic material tested either in simple tension or in balanced biaxial tension; the latter is the situation in the bulge test (30).

To obtain values for t_i for substitution in Eq. [2], a grid was printed on the flat specimen before bulging. From the elongation of the grid after bulging, t_i can be calculated on the assumption that the volume of metal underlying an initial grid square remains constant. The radius of curvature, R, is obtained from

$$R = \frac{r^2 + h^2}{2h} \qquad [3]$$

where r is the radius of the hole in the clamp ring and h is the height of the bulge.

Nominal tensile strength (Eq. [1]) is calculated and tabulated in all of the succeeding tables of data obtained by bulge testing. The values are thus approximately comparable to those already discussed which have been determined by tensile pull, which are calculated on the basis of the initial cross section of the test specimen. In one exception, Fig. 25, discussed later in this section, significant stress is used.

Ductility was determined from bulge measurements by measuring the amount of stretch at fracture of a grid printed on the specimens. The grid pattern was transferred with printer's ink from an intaglio engraving in a steel block. Line spacing was 0.05 in. The lengths of four or five grid squares near the peak of the bulge were measured, after bulging, with a microscope. Both axes of grids were measured. The average length of the bulged grid, calculated from these measurements, is designated as L. The initial grid length is designated L_o. "True strain," δ, is defined by the relation

$$\delta = \int_{L_o}^{L} \frac{dL}{L} = \ln \frac{L}{L_o} \qquad [4]$$

The following remarks are intended to show in a brief manner the significance of δ. Consider a uniaxial tensile test, *i.e.* a test of a standard pull specimen. For small values of elongation, *e.g.* up to 10%, $\Delta L/L_o$ is nearly equal to $\ln L/L_o$, where ΔL is the difference between initial and final length of a grid unit. Therefore, for a brittle material that elongates uniformly and does not undergo necking, true strain from Eq. [4], multiplied by 100, is approximately equal to elongation expressed as per cent of a given gauge length such as 2 in. However, for a ductile material with a nominal elongation larger than about 10%, the arithmetic and logarithmic ratios deviate significantly. Also, necking may occur, resulting in a much larger true elongation at the point of rupture than the average over the gauge length. Therefore, while true strain and per cent elongation are both measures of ductility, they are, in general, not numerically comparable.

In tensile pull, strain occurs in only one direction. In bulge testing, strain occurs in all directions radially from the center of the disk. The ability of the metal to elongate in a given radial direction is reduced by its simultaneous elongation in other radial directions. Thus, δ for a bulge specimen will be less than the strain obtained with the same stress applied to a tensile pull specimen. Read shows that a quantity designated as $\bar{\delta}$, significant strain, is identical to true strain in the case of a specimen pulled in simple tension, but that in the case of the biaxial loading of a bulge specimen

$$\bar{\delta} = 2\,\delta \qquad [5]$$

Significant strain from bulge measurements is comparable to true strain from tensile pull, but is not comparable to nominal elongation for the reasons given in the preceding paragraph.

As already indicated above, bulge height and, hence, $\bar{\delta}$ for individual specimens within sets of six sometimes varied as much as ±25%, especially for the relatively brittle deposits. This is comparable to the situation in tensile pull, where, *e.g.*, the difference between 5 and 10% elongation in our measurements (a relative variation of ±50%) is scarcely significant. It is, therefore, not feasible for us to assign a definite evaluation of accuracy to our data on significant strain. However, small differences, *e.g.* ±10%, cannot be considered to be significant.

(ii) Data relating significant stress and significant strain for several types of baths.—It was not practicable to print grids and measure elongation directly for every specimen. Therefore, grids were printed on a substantial sampling of disks from deposits of a given type of bath. Values of $\bar{\delta}$ calculated from the grid data were then plotted as a function of bulge height. The same curves were then used to obtain $\bar{\delta}$ from bulge height for unprinted specimens.

A plot of $\bar{\delta}$ *vs.* bulge height is shown in Fig. 24. The curves for most of the deposits are closely clustered, showing that there is not much difference in what may be termed, by analogy with tensile pull, as their necking characteristics. Curves for two types of deposits do not fit the main pattern. The deposits from a sulfate bath containing 1,5-naphthalenedisulfonic acid addition agent (curve 2, panel No. 114A-E) had significantly higher $\bar{\delta}$ for a given bulge height than the other deposits; *i.e.*, for a given height of bulge, the degree of stretch at the peak of the bulge was abnormally high and, hence, thickness at the peak of the bulge abnormally low. In other words, this deposit showed a pronounced "necking" tendency. Deposit No. 303 (curve

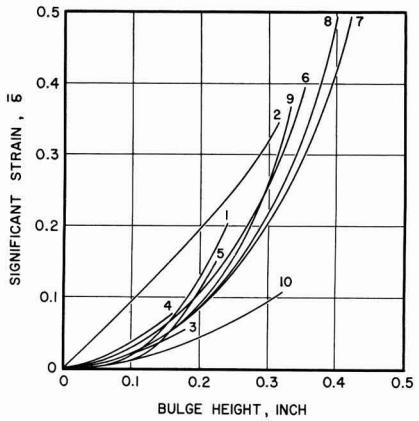

Fig. 24. Relationship between bulge height and significant strain for thin copper deposits from various baths: (1)—Cu2-H3 containing 3.5 g/l triisopropanolamine, 30°C, 2 A/dm^2; (2)—Cu2-H3 containing 1.8 g/l 1,5-naphthalenedisulfonic acid, 30°C, 2 A/dm^2; (3)—CN-2, 60°C, 2 A/dm^2; (4)—CN-5, 80°C, 4 A/dm^2; (5)—CN-4, 80°C, 2 A/dm^2; (6)—CN-6, 60°C, 2 A/dm^2; (7)—CN-7, 60°C, 2 A/dm^2; (8)—CN-8, 80°C, 6 A/dm^2; (9)—CN-8, 80°C, 6 A/dm^2, PR, cycle 15-5 sec; (10)—CN-9, 80°C, 6 A/dm^2.

10), a deposit from the high efficiency cyanide bath containing the proprietary selenium-type addition agent, showed the opposite effect, indicating relatively uniform stretch over most of its area, or lack of necking. One might expect this property to be associated with brittleness, yet specimens from panel No. 303, while of low ductility, were not as brittle as specimens from panels 146 or 195 (Table XXII), which fall in the central group in Fig. 24.

Relationship between significant stress and significant strain for a variety of deposit types is shown in Fig. 25. Most of them show a nearly linear stress-strain relationship up to a fairly definite yield point. Two of them, specimens represented by curves 3 and 4, show brittle failure. A very wide range of ultimate strength is seen, from a low of 28,000 psi for the proprietary high efficiency deposit (curve 10, panel No. 303) to 85,000 psi for a deposit from a standard cyanide bath (curve

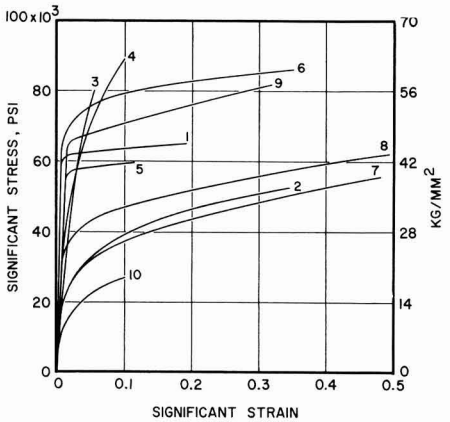

Fig. 25. Relationship between significant strain and significant stress for thin copper deposits from various baths: (1)—Cu2-H3 containing 3.5 g/l triisopropanolamine, 30°C, 2 A/dm^2; (2)—Cu2-H3 containing 1.8 g/l 1,5-naphthalenedisulfonic acid, 30°C, 2 A/dm^2; (3)—CN-2, 60°C, 2 A/dm^2; (4)—CN-5, 80°C, 4 A/dm^2; (5)—CN-4, 80°C, 2 A/dm^2; (6)—CN-6, 60°C, 2 A/dm^2; (7)—CN-7, 60°C, 2 A/dm^2; (8)—CN-8, 80°C, 6 A/dm^2; (9)—CN-8, 80°C, 6 A/dm^2, PR, cycle 15-5 sec; (10)—CN-9, 80°C, 6 A/dm^2.

4, panel No. 195). Only one cyanide-type deposit with a higher strength was encountered in this research (not included in Fig. 25), namely, a deposit made with periodic current reversal from a bath containing thiocyanate (line 143, Table XIV).

c. Comparison of tensile properties obtained by pull and bulge methods.—Table XIX contains comparative values of tensile strength and elongation from pull and bulge measurements. Except for the deposits from cyanide baths on lines 141 and 146, all deposits from both sulfate and cyanide baths were in the range of thickness from 1 to 3 mils.

The first group of data, lines 53-75, is for deposits from sulfate baths. It is seen that, for each deposit, both pull and bulge methods yield the same value for tensile strength, within the normal range of variability of the measurements. On lines 57 and 75 are shown comparisons between our results and those obtained by Read[14] from measurements on specimens from duplicate panels that we supplied to him. Close agreement is seen.

The strength values measured by tensile pull for the deposits from cyanide baths on lines 101 through 125 are seen, with one exception, to be consistently lower than the bulge values. This is probably because premature rupture occurs during tensile pull. As discussed above, tensile pull specimens, when thin and brittle, are more subject to damage in preparation and handling than are bulge disks, and premature failure may be expected. Good agreement is seen in lines 140-146 between tensile pull values of strength for thick cyanide deposits and bulge values for corresponding thin deposits. Good agreement is seen in lines 119 and 121 between our values and those determined by Read.

Turning to comparisons of ductility determined by the two methods (Table XIX), agreement cannot be expected in light of the preceding discussion in Section VII-B-1-b. In both the sulfate and cyanide groups, per cent elongation from tensile pull is significantly less than 100 x $\bar{\delta}$, with one exception in each group. The tensile pull specimens in the sulfate group underwent varying degrees of necking, which would cause differences between the two methods in the direction that is seen. In the cyanide group the differences are probably due mainly to premature rupture of the tensile pull specimens, since the latter were relatively brittle and did not undergo noticeable necking. Good agreement is seen between our values of significant strain and those determined by Read.

2. Effect of thickness on properties of deposits from cyanide baths.—Effects of deposit thickness for several deposits from cyanide baths are shown in Table XX and Fig. 26. Tensile strength and significant strain increase with increase of thickness, while electrical resistivity decreases. The directions of the effects for tensile strength and significant strain are opposite to those for sulfate deposits (Section III-A-3, Table VII, Fig. 2, 3). However, the comparisons are made in a somewhat different range of thickness. The thinnest sulfate deposit was 0.5 mil and most of the thin deposits were 1.0-2.0 mils, whereas the thicknesses of several of the thinnest cyanide deposits are 0.2-0.3 mil. Our explanation of the effects in the case of the cyanide deposits is that these very thin deposits contain pores and defects which cause them to have abnormally low strength and ductility and high resistivity. At a thickness of about 2 mils these effects were diminishing.

3. Effects of operating conditions and bath composition on mechanical properties of deposits from cyanide baths.—a. Bath temperature.—The effect of bath temperature on tensile strength is shown in Table XXI and Fig. 27. Counting sets of three in Table XXI as two pairs, there are 12 pairs. The data for all of these are plotted in Fig. 27. It is seen that for four pairs the effect is minor and for one pair tensile strength decreases with increase of temperature. For the other seven

[14] H. J. Read, Pennsylvania State University, University Park, Pa., Private communication.

Table XIX. Comparisons of tensile strengths and elongations measured by pull and bulge methods

Line No., Table I	Panel No.	Bath symbol	Addition agent		Tensile strength[b,c]		Ductility	
			Name[a]	Conc g/l	Pull	Bulge	Elongation in 2 in. (5 cm) %	By bulge method Significant strain
					psi			
53	162	Cu2-H3	β-NQ	0.1	46	47	9	25
57	114A, C		NDS	1.8	36	35	10	32
	114D[e]		NDS	1.8		33		
65	168		SeO_2	10^{-4} Se	54	62	11	21
67	173		SeO_2	10^{-3} Se	50	56	20	22
75	109A, D		TIPA	3.5	57	57	9	18
	109C[e]		TIPA	3.5		55		19
101	128	CN-1	None		57	66	2	6
105	136	CN-2			43	57	1	10
108	143	CN-2			51	66	2	18
119	205	CN-4			41	50	2	12
	203[e]	CN-4				54		9
121	210, 212	CN-4			58	51	2	22
	210[e]	CN-4				50		16
124	184, 186	CN-5			44	54	7	12
125	187, 188	CN-5			39	63	8	5
140	280	CN-8				61		31
141	281[d]				64		12	
145	300	CN-9	Prop. B			26		9
146	305[d]				28		22	

[a] β-NQ: β-naphthoquinoline; NDS: 1,5-naphthalenedisulfonic acid; TIPA: triisopropanolamine; Prop. B: proprietary brightener for high efficiency cyanide bath, selenium type.
[b] Both pull and bulge values, for comparability, are based on initial thickness of specimens.
[c] Values determined by Dr. H. J. Read, Pennsylvania State University, University Park, Pa.
[d] Specimens 281 and 305 are 18 and 9 mils (450 and 225 μm) thick, respectively. All others are 1-3 mils (25-75 μm) thick.
[e] One pound per square inch (psi) = 0.000704 kilogram per square millimeter (kg/mm²).

Table XX. Effect of thickness on properties of deposits from cyanide baths

Line No., Table I	Panel No.	Bath No.	Bath temp, °C	Current density, A/dm²	Thickness,[a] mil	Tensile[a] strength, psi	Significant strain	Elec. resistivity 25°C, ohm-cm
104	125A	CN-1	40	1	0.25	33×10^3	0.4×10^{-2}	
103	130				0.30			1.87×10^{-6}
102	125				0.35	47	1.1	1.81
101	128				1.4	66	6	1.79
107	133	CN-2	40	2	0.2			1.87
106	138				1.4			1.78
109	140		60	1	0.4			1.80
108	143				1.4			1.76
112	142A			2	0.3	28	0.4	
111	142				0.4	46	1.2	1.80
110	145				2.0	81	2	1.75
114	150	CN-3	60	2	0.4			1.81
113	153				2.0			1.80
140	280	CN-8, PR[b]	80	6	3.0	61	31	1.78
141	281				18	64[c]	12[c]	1.82

[a] Metric conversions: one mil (0.001 in.) = 25 μm; one pound per square inch (psi) = 0.000704 kilogram per square millimeter (kg/mm²).
[b] PR cycle 15 sec cathodic, 5 sec anodic.
[c] Determined by tensile pull. Elongation for specimen No. 281 is per cent in 2 in. All other values in this table were determined by bulge measurements.

Table XXI. Effect of bath temperature on properties of deposits from cyanide baths

Line No., Table I	Panel No.	Bath symbol	Addition agent or other variable	Current density, A/dm²	Bath temp, °C	Tensile[a] strength, psi	Significant strain	Young's[a] modulus of elasticity, psi	Hardness KHN 100g load, kg/mm²	Internal[a] stress, psi	Density 25°C, g/cm³	Elec. resistivity 25°C, ohm-cm
105	136	CN-2	None	1	40	57×10^3	10×10^{-2}	17×10^6	119	8600	8.913	1.74×10^{-6}
108	143				60	66	18	16	135	7400	8.908	1.76
106	138			2	40	53	14		147	6900	8.909	1.78
110	145, 146				60	81	2		159	7800	8.913	1.75
115	197	CN-4	None	2	40	52	10		150	9200	8.916	1.81
117	158				60	53	24	16	129	9200	8.904	1.78
120	208, 209				80	51	25		139	6100	8.917	1.77
116	201, 202			4	40	44	7		144	7500	8.900	1.80
119	205				60	50	12		132	9500	8.908	1.84
121	210, 212				80	51	22		131	6400	8.908	1.79
122	178, 180	CN-5	None	2	40	49	13		143	9300	8.915	1.83
124	184, 186				60	54	12	15	123	9700	8.907	1.78
126	191				80	53	14		139	6200	8.917	1.75
123	182			4	40	48	14		136	7600	8.918	1.83
125	187, 188				60	63	5	16	152	9500	8.900	1.81
127	194, 195				80	78	3		131	6700	8.912	1.79
128	234-236	CN-6	None	2	40	44	19		116	5200	8.913	1.76
130	239, 240				60	64	29		143	5500	8.919	1.88
132	249				80	57	22		158	5800	8.920	1.87

[a] One pound per square inch (psi) = 0.000704 kilogram per square millimeter (kg/mm²).

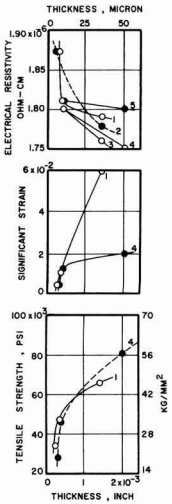

Fig. 26. Relationships between thickness, tensile strength, significant strain, and electrical resistivity of copper deposits from cyanide baths: (1)—CN-1, 40°C, 1 A/dm²; (2)—CN-2, 40°C, 2 A/dm²; (3)—CN-2, 60°C, 1 A/dm²; (4)—CN-2, 60°C, 2 A/dm²; (5)—CN-3, 60°C, 2 A/dm².

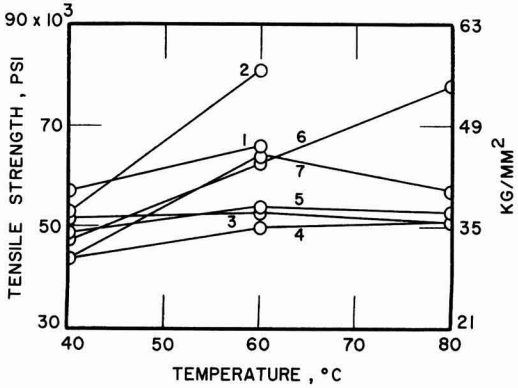

Fig. 27. Relationship between bath temperature and tensile strength of copper deposits from cyanide baths: (1)—CN-2, 1 A/dm²; (2)—CN-2, 2 A/dm²; (3)—CN-4, 2 A/dm²; (4)—CN-4, 4 A/dm²; (5)—CN-5, 2 A/dm²; (6)—CN-5, 4 A/dm²; (7)—CN-6, 2 A/dm².

pairs tensile strength increases with increase of temperature. With one exception, the effect is smaller between 60° and 80°C than between 40° and 60°C. We judge that the predominant effect, increase of deposit strength with increase of bath temperature, which is unexpected, is real. The following hypothesis may explain the effect: In cyanide-type baths current efficiency, and, hence, plating rate, increases markedly with increase in bath temperature. Thus, with other conditions constant, increase in temperature may lead to depletion of copper ions in the cathode film, with consequent decrease of grain size and increase of strength. This effect would be countered by increase in rate of diffusion of complex cyanide ions into the cathode film with increase of temperature, but the latter might be the minor effect because of the large size of the complex ions.

The effect of bath temperature on significant strain is indefinite, as seen in Table XXI. Most of the values vary randomly in the range of 0.1-0.25. The only clues to a relationship are seen in the second and sixth sets of data (lines 106-110 and 123-127, respectively) which show an appreciable decrease of significant strain with increase in temperature.

Variation of modulus with temperature is in the range $(16 \pm 1) \times 10^6$ psi, not a significant variation.

Hardness is not markedly affected by bath temperature. However, there is a small but predominant trend toward increase of hardness with increase of bath temperature. The relationship is, thus, parallel to that between tensile strength and bath temperature, and our explanation is the same.

b. Current density.—Complete data on the effects of current density on mechanical properties are shown in Table XXII. Figure 28, which contains data for those cases where the effects were significant, shows that the predominant tendency is for tensile strength and hardness to increase with increase in current density, and for significant strain to decrease. Several cases

Table XXII. Effect of current density on properties of deposits from cyanide baths

Line No. Table I	Panel No.	Bath symbol	Addition agent or other variable	Bath temp, °C	Current density, A/dm²	Tensile[a] strength, psi	Significant strain	Young's[a] modulus of elasticity, psi	Hardness KHN 100g load, kg/mm²	Internal[a] stress psi	Density 25°C, g/cm³	Elec. resistivity 25°C, ohm-cm
105	136	CN-2	None	40	1	57×10^3	10×10^{-2}	17×10^6	119	8,600	8.913	1.74×10^{-6}
106	138				2	53	14		147	6,900	8.909	1.78
108	143			60	1	66	18	16	135	7,400	8.909	1.76
110	145, 146				2	81	4		159	7,800	8.913	1.75
115	197	CN-4	None	40	2	52	10		150	9,200	8.916	1.81
116	201, 202				4	44	7		144	7,500	8.900	1.80
117	158			60	2	53	24	16	129	9,200	8.904	1.78
119	205				4	50	12	16	132	9,500	8.908	1.84
120	208, 209			80	2	51	25		139	6,100	8.917	1.77
121	210, 212				4	51	22		131	6,400	8.908	1.79
122	178, 180	CN-5	None	40	2	49	13		143	9,300	8.915	1.83
123	182				4	48	14		136	7,600	8.918	1.83
124	184, 186			60	2	54	12	15	123	9,700	8.907	1.78
125	187, 188				4	63	5	16	152	9,500	8.900	1.81
126	191			80	2	53	14		139	6,200	8.917	1.75
127	194, 195				4	78	6		131	6,700	8.912	1.79
129	242-244	CN-6	None	60	1	43	57		141	3,500	8.918	1.88
130	239, 240				2	64	40		143	5,500	8.919	1.88
131	245, 247				4	58	9		135	4,400	8.919	1.86
135	260-263	CN-8	None	80	4	37	22		114	4,500	8.919	1.80
138	268-270				6	40	49		98	4,500	8.925	1.76
139	271-273				8	39	50		129	3,900		1.76
141	281		PR, 15-5 sec cycle, 18 mils	80	6	64[c]	12[c]		147			1.76
142	279		Ditto PR, 3 mils		8	60	23		151			1.76
145-146	300, 305	CN-9	Prop. B[b]	80	4	26	9		74	11,000	8.923	1.80
147	303				6	24	10		76			1.81

[a] One pound per square inch (psi) = 0.000704 kilogram per square millimeter (kg/mm²).
[b] Proprietary brightener, selenium type.
[c] Values measured by tensile pull. Elongation unit is per cent in 2 in. (5 cm).

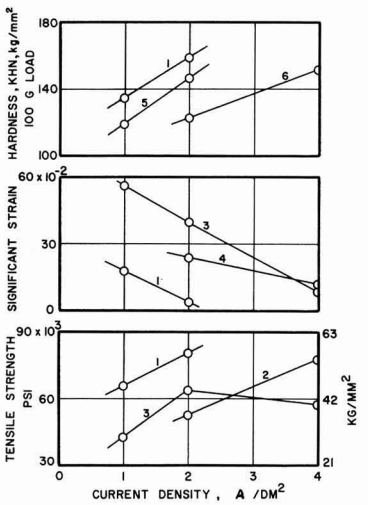

Fig. 28. Relationships between current density, tensile strength, significant strain, and hardness of copper deposits from cyanide baths: (1)—CN-2, 60°C; (2)—CN-5, 80°C; (3)—CN-6, 60°C; (4)—CN-4, 60°C; (5)—CN-2, 40°C; (6)—CN-5, 60°C.

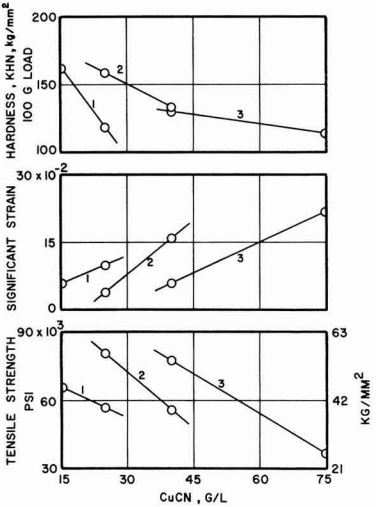

Fig. 29. Relationships between copper cyanide concentration, tensile strength, significant strain, and hardness of deposits from cyanide baths: (1)—CN-1 and CN-2, 40°C, 1 A/dm²; (2)—CN-2 and CN-3, 60°C, 2 A/dm²; (3)—CN-5 and CN-8, 80°C, 4 A/dm².

where there was no appreciable effect are seen in Table XXII.

The range of variation of the modulus is (16 ± 1) x 10^6 psi; *i.e.*, change of current density does not affect the modulus significantly.

c. Concentration of copper cyanide.—The effects of concentration of copper cyanide on mechanical properties are shown in Table XXIII and Fig. 29. There is a consistent decrease of tensile strength and hardness and a trend toward increase of ductility with increase

Table XXIII. Effect of concentration of copper cyanide on properties of deposits from cyanide baths

Line No., Table I	Panel No.	Bath symbol	Bath temp, °C	Current density, A/dm²	Conc CuCN, g/l	Tensile[a] strength, psi	Significant strain	Young's[a] modulus of elasticity, psi	Hardness KHN 100g load, kg/mm²	Internal[a] stress, psi	Density 25°C, g/cm³	Elec. resistivity 25°C, ohm-cm
101	128	CN-1	40	1	15	66 × 10^3	6 × 10^{-2}	17 × 10^6	162	14,000	8.898	1.79 × 10^{-6}
105	136	CN-2			25	57	10	17	119	8,600	8.913	1.74
110	145, 146	CN-2	60	2	25	81	4		159	7,800	8.913	1.75
113	153	CN-3			40	56	16	17	133	9,500	8.907	1.80
127	194, 195	CN-5	80	4	40	78	6		131	6,700	8.912	1.79
135	260-263	CN-8			75	37	22		114	4,500	8.919	1.80
145	300	CN-9			75	26	9		74	11,000	8.923	1.80

[a] One pound per square inch (psi) = 0.000704 kilogram per square millimeter (kg/mm²).

Table XXIV. Effects of concentrations of free sodium cyanide and sodium carbonate on properties of deposits from cyanide baths

A. Effect of free cyanide

Line No., Table I	Panel No.	Bath symbol	Bath temp, °C	Current density, A/dm²	Conc free NaCN, g/l	Tensile[a] strength, psi	Significant strain	Young's[a] modulus of elasticity, psi	Hardness KHN 100g load, kg/mm²	Internal[a] stress, psi	Density 25°C, g/cm³	Elec. resistivity 25°C, ohm-cm
115	197	CN-4	40	2	6	52 × 10^3	10 × 10^{-2}		150	9200	8.916	1.81 × 10^{-6}
122	178, 180	CN-5			10	49	13		143	9300	8.915	1.83
116	201, 202	CN-4		4	6	44	7		144	7500	8.900	1.80
123	182	CN-5			10	48	14		136	7600	8.918	1.83
117	158	CN-4	60	2	6	53	24	16 × 10^6	129	9200	8.904	1.78
124	184, 186	CN-5			10	54	12	15	123	9700	8.907	1.78
119	205	CN-4		4	6	50	12	16	132	9500	8.908	1.84
125	187, 188	CN-5			10	63	5	16	152	9500	8.900	1.81
120	208, 209	CN-4	80	2	6	51	25		139	6100	8.917	1.77
126	191	CN-5			10	53	14		139	6200	8.917	1.75
121	210, 212	CN-4		4	6	51	22		131	6400	8.908	1.79
127	194, 195	CN-5			10	78	6		131	6700	8.912	1.79

B. Effect of sodium carbonate

Line No., Table I	Panel No.	Bath symbol	Bath temp, °C	Current density, A/dm²	Conc Na_2CO_3, g/l	Tensile[a] strength, psi	Significant strain	Young's[a] modulus of elasticity, psi	Hardness KHN 100g load, kg/mm²	Internal[a] stress, psi	Density 25°C, g/cm³	Elec. resistivity 25°C, ohm-cm
113	153	CN-3	60	2	15	56 × 10^3	16 × 10^{-2}	17 × 10^6	133	9500	8.907	1.80 × 10^{-6}
117	158	CN-4			30	53	24	16	129	9200	8.904	1.78

[a] One pound per square inch (psi) = 0.000704 kilogram per square millimeter (kg/mm²).

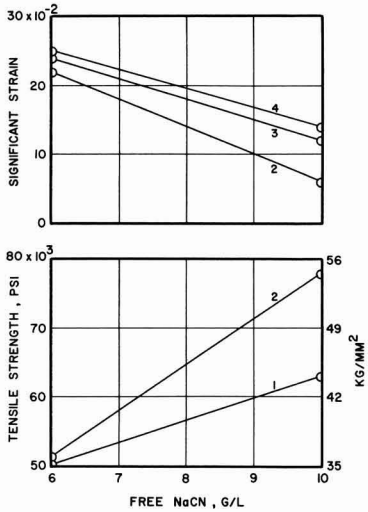

Fig. 30. Relationships between free cyanide concentration, tensile strength, and significant strain of copper deposits from cyanide baths: (1)—CN-4 and CN-5, 60°C, 4 A/dm²; (2)—CN-4 and CN-5, 80°C, 4 A/dm²; (3)—CN-4 and CN-5, 60°C, 2 A/dm²; (4)—CN-4 and CN-5, 80°C, 2 A/dm².

of concentration of copper cyanide. The modulus of elasticity is unaffected.

d. Concentration of free cyanide and sodium carbonate.—Increase in concentration of free cyanide results in increase in tensile strength and decrease in significant strain in most instances. The cases in which a significant effect occurs are shown in Fig. 30. However, examination of Table XXIV shows several cases in which the effect was negligible. Neither modulus of elasticity nor hardness were affected significantly (Table XXIV).

The data in Table XXIV also show that a twofold increase of concentration of sodium carbonate did not produce an appreciable effect on any of the properties except significant strain, which was increased.

e. Concentration of Rochelle salt and effect of potassium ion.—Examination of the data summarized in Table XXV does not give a clear conclusion regarding the effect of Rochelle salt on mechanical properties. Differences are small and tend in both directions. We can only conclude that the effects are minor.

Effect of an all-potassium bath may be seen by comparing lines 130 and 133 in this table. Potassium ion, as compared with sodium, causes significant decreases of strength, ductility, and hardness.

f. pH.—Table IV shows the variation of pH with duration of electrolysis of cyanide baths. Variation of pH is not normally controlled in these baths, which operate at a "natural" pH. It is seen that the initial pH for all except bath No. CN-8 is in the range 11.4-11.8 and increases after working to a stable value in the range 12.6-12.8. This is the direction of shift to be expected due to the low cathode efficiency. Bath No. CN-8 is initially higher in pH due to its high content of KOH, and does not change with working, due to its high cathode efficiency. Under the above circumstances, effect of pH on properties of deposits is of only academic interest. However, a few measurements were made to compare the tensile strength and ductility of panels made at the lower limit of the pH ranges shown in Table IV with those of panels made at the upper limit of the range. No measurable effect was observed.

g. Proprietary brightener.—Baths No. CN-8 and CN-9 are fairly similar in composition, as may be seen in Table IV, except for the presence in CN-9 of the proprietary addition agent of the selenium type. Both are based on potassium salts and have the same copper content. CN-9 is higher in free cyanide and lower in KOH but it is probable that effects of these differences on properties of deposits are less than that of the addition agent.

Comparing lines 135 and 138 with lines 145 and 147 of Table XXII, we see that tensile strength, ductility, and hardness are all significantly smaller for the deposits from the bath containing the selenium-type addition agent. The value of the addition agent lies in its effect on smoothness and brightness rather than in its effect on properties.

h. Periodic current reversal (PR).—The effects of periodic current reversal on properties of deposits from baths CN-8 and CN-9 are summarized in Table XIV. Comparing line 140 with 135-138 we see that PR produces a marked increase in tensile strength. Addition of KCNS (line 143) produces a further significant increase. Deposits from bath No. CN-9 made with PR (line 148) are more than twice as strong as non-PR deposits (lines 145-147). Neither change of current density nor change of PR cycle had significant effects on strength (lines 140 *vs.* 142 and 143 *vs.* 144, respectively). Under none of these conditions used by us was the tensile strength as high as has been claimed by some authors (3).

Effects of PR on ductility are less consistent, but the conclusion in summary is that, for deposits from bath CN-8, the stronger PR deposits are less ductile than the weaker non-PR deposits (*cf.* line 138 with 140-141 and line 135 with 143-144). The strongest deposits (lines 143, 144) have the lowest ductility. On the other hand, the moderately strong PR deposit from bath CN-9 (line 148) has the very high elongation of 45%, which is evidently due to a specific effect of the addition agent.

Hardness is much increased by PR for deposits from baths CN-8 and CN-9 (Table XIV). Whereas variation of the PR cycle had no effect on strength and ductility, the deposit made with the 30-10 sec cycle is significantly harder than that made with the 15-5 sec cycle. The PR deposit from bath CN-9 (line 148) is the hardest encountered in this research, namely, 224 KHN.

Table XXV. Effect of Rochelle salt on properties of deposits from cyanide baths

Line No., Table I	Panel No.	Bath symbol	Bath temp, °C	Current density, A/dm²	Conc Rochelle salt, g/l	Tensile[b] strength, psi	Significant strain	Hardness KHN 100g load, kg/mm²	Internal[b] stress, psi	Density 25°C, g/cm³	Elec. resistivity 25°C, ohm-cm
115	197	CN-4	40	2	0.0	52 × 10³	10 × 10⁻²	150	9200	8.916	1.81 × 10⁻⁶
128	234-236	CN-6			45	44	19	116	5200	8.913	1.76
117	158	CN-4	60	2	0.0	53	24	129	9200	8.904	1.78
130	239, 240	CN-6			45	64	40	143	5500	8.919	1.88
133	252, 253	CN-7[a]			45	38	34	92	8100	8.920	1.74
119	205	CN-4		4	0.0	50	12	132	9500	8.908	1.84
131	245, 247	CN-6			45	58	9	135	4400	8.919	1.86
120	208, 209	CN-4	80	2	0.0	51	25	139	6100	8.917	1.77
132	249	CN-6			45	57	22	158	5800	8.920	1.87

[a] "All-potassium" bath.
[b] One pound per square inch (psi) = 0.000704 kilogram per square millimeter (kg/mm²).

C. Internal Stress in Deposits from Cyanide Baths

1. Effect of thickness.—The uppermost curve in Fig. 8 shows that the cumulative internal stress of a deposit from bath CN-2 (line 105, panel 136, Tables XXI-XXIII) increases nearly linearly with time (*i.e.*, with thickness) to the limit of thickness over which stress was measured (approximately 1.5 mil). With respect to internal stress, this deposit is fairly typical of deposits from cyanide baths. This relationship between stress and thickness is in marked contrast to that for deposits from sulfate baths, such as the deposit from a bath containing naphthalenedisulfonic acid. Internal stress in the latter deposit levels off, with no further increase after reaching a thickness of about ¾ mil (Fig. 8). These contrasting effects correlate with the increase in grain size with increase of thickness for the sulfate deposits (Fig. 20-3), and with the constancy of grain size of the cyanide deposits (Fig. 34).

2. Effect of operating conditions and bath composition on internal stress of deposits from cyanide baths.—*a. Bath temperature.*—Effect of bath temperature on internal stress is shown in Fig. 31 and Table XXI. At first sight the results, shown fully in Fig. 31, appear to form no consistent pattern. However, some relationships may be deduced as follows. Consider first the deposits from baths CN-2, CN-4, and CN-5. The general pattern is that, for these deposits, stress tends to go through a maximum with increase of bath temperature. Of 10 pairs of data involved, only one (curve No. 1) has a contrary trend. Deposits from bath CN-6 (Rochelle type, curve No. 7) have significantly lower stress than the deposits from the other baths and their stress is nearly unaffected by bath temperature.

b. Current density.—There is no consistent relationship between internal stress and current density and in no case is the effect very large (Table XXII). There is indication that the effect of current density on stress tends to be lost at the higher operating temperatures.

c. Concentration of copper cyanide.—The preponderant effect indicated by the data summarized in Table XXIII is decrease of internal stress with increase of concentration of copper cyanide. The effect is definite for lines 101 *vs.* 105 and 127 *vs.* 135. However, there is a borderline reverse effect in lines 110 *vs.* 113.

The high value of stress seen in line 145 is an addition agent effect, discussed in paragraph *f* below.

d. Concentration of free cyanide and sodium carbonate.—There is consistently no significant effect on internal stress due to changes of concentration of either free cyanide or sodium carbonate (Table XXIV).

e. Concentration of Rochelle salt and effect of potassium ion.—The data in Table XXV show that addition of Rochelle salt to a cyanide bath consistently causes a decrease of internal stress.

Comparison of lines 130 and 133 shows that converting a sodium to a potassium Rochelle bath results in a significant increase in internal stress of the deposits. The same change caused decreases of tensile strength, ductility, and hardness, illustrating the lack of correlation of these properties with stress.

f. Proprietary brightener.—Comparison of the values for internal stress on lines 135 and 145 of Table XXII shows that addition of the proprietary selenium-type brightener to a high efficiency bath causes a marked increase in internal stress.

g. Periodic current reversal (PR).—Data relating the effect of PR to internal stress of deposits from cyanide baths are available only for bath No. CN-8 (Table XIV). Comparing lines 140 and 143 with lines 135 and 138, it is seen that stress is only slightly higher in the PR deposits. The large effect observed with sulfate deposits does not occur with cyanide deposits because, as seen in Section VII-C-1 above, stress does not decrease with increase of thickness of the latter.

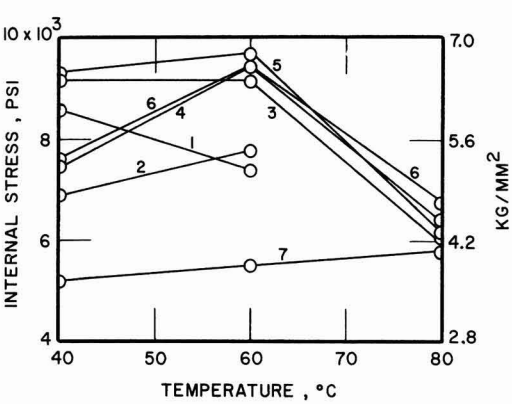

Fig. 31. Relationship between bath temperature and internal stress in copper deposits from cyanide baths: (1)—CN-2, 1 A/dm²; (2)—CN-2, 2 A/dm²; (3)—CN-4, 2 A/dm²; (4)—CN-4, 4 A/dm²; (5)—CN-5, 2 A/dm²; (6)—CN-5, 4 A/dm²; (7)—CN-6, 2 A/dm².

D. Density of Deposits from Cyanide Baths

Excluding the deposits from baths CN-8 and CN-9, which will be referred to subsequently, the average density of all deposits listed in Tables XXI through XXV is 8.911, with extremes of 8.898 and 8.920 g/cm³. For these thin deposits, the accuracy of our measurements (±0.01 g/cm³) was not sufficient to enable us to detect any effect of temperature, current density, and bath composition on density.

It is noted in Table XXII that the densities of the deposits from the high efficiency baths (lines 135, 138, and 146) range from 8.919 to 8.925 g/cm³, significantly higher than the average 8.911 of the low-copper cyanide baths. We believe that these higher values of high-efficiency deposits, in the same range as the densities of deposits from sulfate baths, are real, particularly since some of these high values were obtained from measurements on thick deposits for which accuracy of measurements is judged to be ±0.005 g/cm³ (*e.g.*, line 146, Table I).

E. Electrical Resistivity of Deposits from Cyanide Baths

An analysis similar to that given above for density leads to the following conclusions regarding the effects of various variables on electrical resistivity:

Table No.	Variable	Effect on resistivity
XIV	PR	None
XIV	Added KCNS + PR	Significant increase
XIV	Added proprietary addition agent + PR	Significant increase
XXI	Temperature increase	Variable, minor
XXII	Current density increase	Very small increase
XXII	Added proprietary addition agent (without PR)	None
XXIII	CuCN increase	None
XXIV	Free CN increase	None
XXIV	Na_2CO_3 increase	None
XXV	Rochelle salt addition	Small increase
XXV	Potassium ion (*vs.* sodium)	Significant decrease

F. Relationships between Properties of Deposits from Cyanide Baths

1. Tensile strength and ductility.—Tensile strength as a function of significant strain is plotted in Fig. 32, which contains points representing all deposits from cyanide baths. In general, significant strain decreases with increase in strength. This is the relationship that usually occurs for wrought metals, and was observed for certain addition agent sulfate deposits. It is the opposite of the relation between strength and ductility for nonaddition agent deposits from sulfate and fluoborate baths (Fig. 14 and Fig. 22, respectively). The two deposits that most conspicuously fail to conform to the general pattern are (*a*) the deposit from the proprietary high-efficiency bath made with direct current, which has low ductility for its strength, in comparison with the main pattern; and (*b*) the corresponding PR deposit, which has abnormally high ductility.

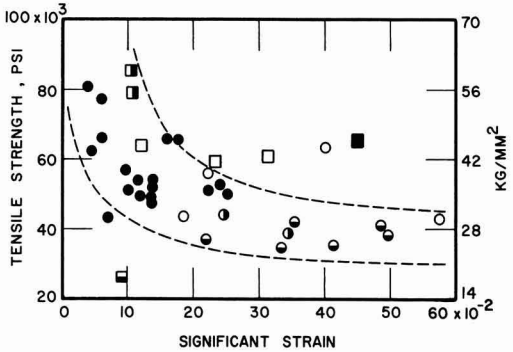

Fig. 32. General relationship between significant strain and tensile strength of copper deposits from various cyanide baths. ●—CN-1 through CN-5, all operating conditions; ○—CN-6, sodium Rochelle salt bath, all operating conditions; ◑—CN-7, potassium Rochelle salt bath, all operating conditions; ◒—CN-8, all operating conditions; □—CN-8 with periodic current reversal (PR), no addition agent; ◧—CN-8 plus 2 g/l KCNS, with PR; ◒—CN-9, proprietary bright bath; ■—CN-9 with PR.

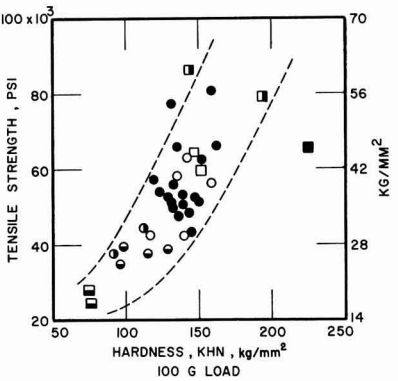

Fig. 33. General relationship between hardness and tensile strength of copper deposits from various cyanide baths. The code defining deposits is the same as for Fig. 32.

2. Tensile strength and hardness.—The general relationship between tensile strength and hardness for all deposits from cyanide baths is shown in Fig. 33, in which there is seen to be a positive correlation between hardness and tensile strength. The relationship is more definite than that for sulfate deposits (Fig. 15).

G. Structure of Deposits from Cyanide Baths

1. Effect of type of bath on structure.—Optical micrographs of several typical deposits from cyanide baths are shown in Fig. 34. Included for comparison are a strike bath deposit, a deposit from a typical low-concentration bath, deposits from both sodium and potassium Rochelle-type baths, a deposit from a standard high-efficiency bath, and a deposit from a high-efficiency bath containing a selenium-type proprietary brightener. The deposits from the low-concentration baths (Fig. 34-1 and 34-2) show a fine columnar structure, which is surprising, because literature references commonly refer to deposits from these baths as being extremely fine grained (33). On the other hand, a cyanide deposit with a structure similar to that of Fig. 34-1 has been reported by R. R. Bair and A. K. Graham [Ref. (26), p. 167]. To verify the structure seen in Fig. 34-1 and to check the possibility that it might be an erroneous work-induced structure, an entirely new section was prepared and examined by both optical and electron micrography. The electron micrographs, shown in Fig. 36, were made from a specimen prepared by a deep electropolish. The same results were obtained, indicating that the observed structure is a true representation of the deposit. The significant features noted in the electron micrographs are:

a. Small micro-twin and columnar grains extending the thickness of the deposit.

b. Surface rippling in the areas below nodules on the upper surface (Fig. 36-2). The electron micrographs were made for us by D. B. Ballard of the NBS Metallurgy Division. Details are given in section X, Appendix.

The addition of Rochelle salt (Fig. 34-3) is seen to cause grain refinement. The deposit from the potassium Rochelle bath (Fig. 34-4) does not contain the nodular structures of the deposit from the sodium salt bath and shows some indication of the presence of fairly large equi-axed grains. The deposit from the high-efficiency bath (Fig. 34-5) is fine grained, whereas that from the proprietary bright bath (Fig. 34-6) shows large columnar grains extending the thickness of the deposit. This structure correlates with its low strength and ductility (Table XXII).

2. Effect of periodic current reversal on structure.—Effect of periodic current reversal on structure is

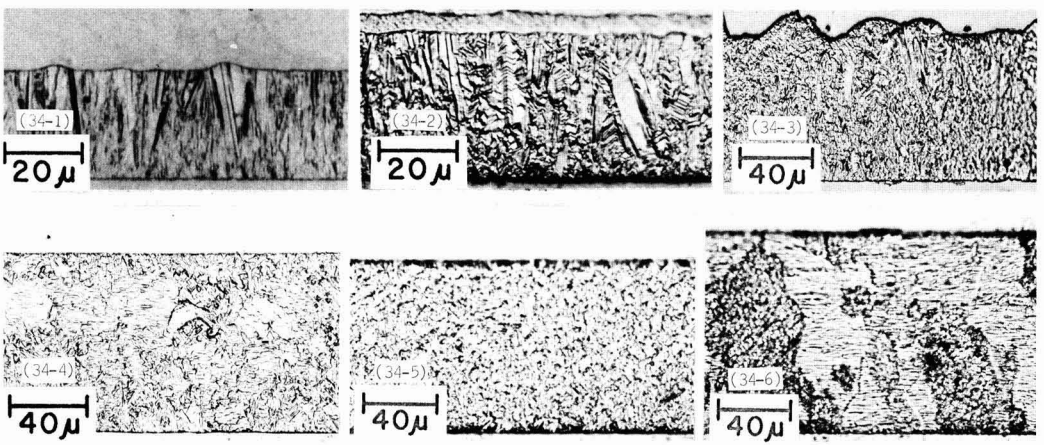

Fig. 34. Effect of type of bath on structure of copper deposits from various cyanide baths: (34-1)—CN-1, 40°C, 1 A/dm²; (34-2)—CN-5, 60°C, 2 A/dm²; (34-3)—CN-6, 60°C, 2 A/dm²; (34-4)—CN-7, 60°C, 2 A/dm²; (34-5)—CN-8, 80°C 6 A/dm²; (34-6)—CN-9, 80°C, 6 A/dm².

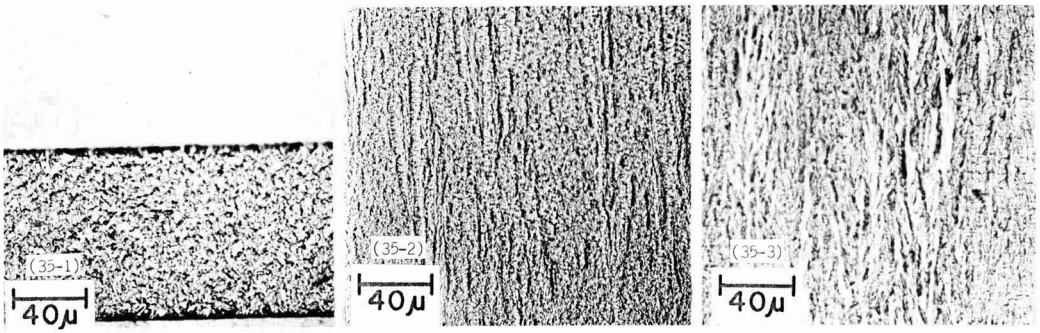

Fig. 35. Effect of periodic current reversal (PR) on structure of copper deposits from a high-efficiency cyanide bath: (35-1)—CN-8, 80°C, 6 A/dm^2, continuous current; (35-2)—CN-8, 80°C, 6 A/dm^2, no addition agent, PR, 15 sec cathodic, 5 sec anodic; (35-3)—CN-8 plus 2 g/l KCNS, 80°C, 6 A/dm^2, PR, 15 sec cathodic, 5 sec anodic.

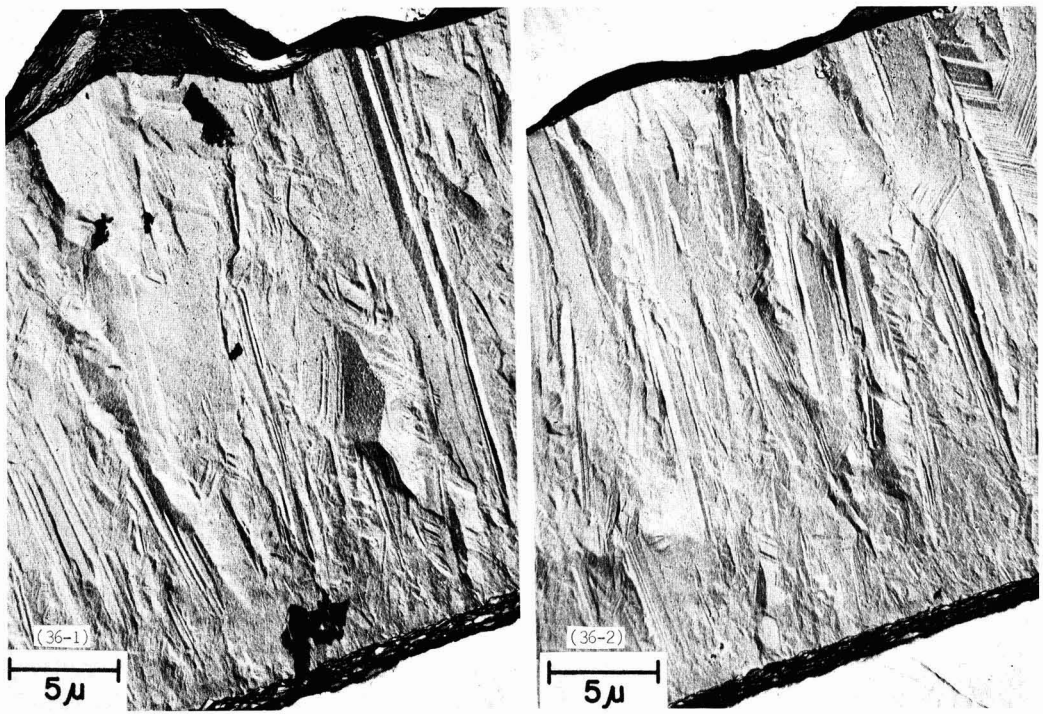

Fig. 36. Electron micrographs of a deposit from cyanide bath CN-1, 40°C, 1 A/dm^2

shown in Fig. 35. Figure 35-1 is a deposit from bath CN-8 made without PR, 35-2 the same with PR, and 35-3 the same as 35-2 except for addition of potassium thiocyanate to the bath. The latter two deposits were both built to a thickness of 18 mils. The addition of the thiocyanate resulted in a brighter final surface and less tendency for nodules to form. Both of the PR structures appear to be finer than the non-PR but with a distinct fibrous character. This shift of structure is consistent with the higher strength and hardness of these deposits (Table XIV). The laminations in Fig. 35-2 and 35-3 due to current interruption are not as distinct as have been shown in other published PR structures (14, 26). This is because the short cycle time that we used (15 sec cathodic, 5 sec anodic) resulted in a thickness per layer of only about 0.04 mil, which is resolvable and faintly visible in the original photographs at 500X but may not show in published prints.

REFERENCES

25. J. W. Dini, H. R. Johnson, and J. R. Helms, *Plating*, **54,** 1337 (1967).
26. F. A. Lowenheim, Editor, "Modern Electroplating," 2nd Ed., John Wiley & Sons, Inc., New York (1963).
27. R. Pinner, "Copper and Copper Alloy Plating," 2nd Ed., Copper Development Association, London, W.I. (1964).
28. A. V. Ryabchenkov, A. A. Gerasimenko, and E. S. Naydena, *Zashchita Metallov.*, **2,** No. 2, 232 (1966).
29. L. Greenspan, *Trans. Electrochem. Soc.*, **78,** 303 (1940).
30. T. A. Prater and H. J. Read, *Plating*, **36,** 1221 (1949); **37,** 830 (1950).
31. H. J. Read and T. J. Whalen, *Proc. Am. Electroplaters' Soc.*, **46,** 318 (1959).
32. F. P. Brodell and A. Brenner, *Plating*, **44,** 591 (1957).
33. H. Fischer, "Elektrolytische Abscheidung und Elektrokristallisation von Metallen," p. 486, Springer-Verlag, Berlin (1954).

Report of the Electrolytic Industries for the Year 1969[1]

Robert G. Milner*

Union Carbide Corporation, Carbon Products Division, Cleveland, Ohio 44101

Thomas C. Jeffery*

PPG Industries, Industrial Chemical Division, Lake Charles, Louisiana 70601

Chlorine-Caustic Soda

I. Production.—The production of chlorine increased in 1969 to a new record of 9,427,000 tons in the United States, according to The Chlorine Institute, Inc. (1). This tonnage represents a gain of approximately 11.2% over the 1968 production of chlorine gas. The 1969 production of chlorine in Canada also reached a new high, 887,000 tons, which is up 14.4% over 1968 figures. During the period 1959-1969, the average annual growth rate has been 8.0% in the U.S. and 11.5% in Canada.

From December 1968 to December 1969, daily capacity increased 12.2% to 28,276 tons in the U.S. and increased 6.4% to 2636 tons in Canada.

Manufacturing in the U.S. operated at 95.6% of capacity, while Canadian producers operated at 93.3% in 1969.

During 1969, the unusual situation of a snug caustic soda market was the rule rather than the exception. Although generally caustic has experienced a slower growth trend than chlorine, lower prices have brought other markets into range (2). Caustic has already taken over most of the alumina processing market, and is making inroads into pulp and paper production at the expense of soda ash. There is some hope that the trend will extend to the glass industry, but most feel business in this area will come slowly.

A 7.5%/yr growth prediction for caustic soda and an 8.0%/yr growth for chlorine would indicate that supplies of caustic will continue to exceed market growth. In addition, theoretical yield of caustic is about 1.1 tons per ton of chlorine. Production figures, however, do not indicate that this yield is achieved in practice.

Some chlorine, approximately 4%, is a by-product of making metallic sodium from salt, with no coproduction of caustic. Production of lithium chloride, soda ash, potassium hydroxide, and in-plant use of caustic account for most of the rest of the discrepancy between the theoretical and the actual output ratio for chlorine and caustic.

Dow Chemical leads U.S. producers of caustic with 30% of the total capacity, followed by PPG with about 9%, Allied and Diamond Shamrock with about 8% each, Olin Mathieson and Hooker with about 6%, Wyandotte 5%, and with FMC, Stauffer, Pennwalt, B. F. Goodrich, Alcoa, and Kaiser rounding out the list of major companies in the industry.

In marked contrast to chlorine, exports of caustic grew at 12%/yr during the period 1960-1967. Most of this production was tied to bauxite processing.

No attempt is made to pinpoint caustic prices due to the many grades, type, and volume of shipments, *etc.*, but it does appear that discounting has been eliminated to a great extent. Most major producers announced $3-$4/ton increases, to the $66/ton range, effective the third quarter of 1969 (3).

II. Expansions.—The best estimates of The Chlorine Institute, Inc., indicate that by the end of 1970 projects now under way will increase combined U.S. and Canadian daily capacity by about 6.5% or to approximately 12 million tons (4, 5).

Company & location	Type of cell	Capacity (tons/day)	Completion date
(A) Shutdown			
Arkla Chemical Corp., Pine Bluff, Ark.	Hooker S-1 Diaphragm	75	Oct. 1969
Stauffer Chemical Co., Huntsville, Ala.	Hooker S-1 Diaphragm	100	Aug. 1969
Stauffer Chemical Co., Dominguez, Calif.	BASF Mercury	150	
(B) Production started			
General Aniline and Film Corp., Linden, N. J.	BASF-Krebs Mercury	250	Nov. 1969
Interprovincial Cooperative Ltd., Saskatoon, Saskatchewan	Kureha HD-4 Mercury	70 Exp.	Jan. 1969
Kaiser Aluminum & Chemical Corp., Gramercy, La.	Hooker S-3B Diaphragm	300 Exp.	May 1969
PPG Industries, Lake Charles, La.	DeNora Mercury	600	Feb. 1969
Reactive Metals, Inc., Ashtabula, Ohio	Downs	50% Exp. metallic sodium-chlorine	Dec. 1969 1st stage
Velsicol Chemical Co., Memphis, Tenn.	Hooker S-4 Diaphragm	Hooker S-1 removed	June 1969
Wyandotte Chemicals Corp., Geismar, La.	Hooker S-4B Diaphragm	350	April 1969
C. Building or planned			
American Magnesium, Snyder, Texas	Magnesium cells	30,000 tons/yr	Bal. 1970
Conso Chemicals Ltd., Abercrombie Point, Nova Scotia	ICI Mercury	$8 million	Early 1970
Dow Chemical Co.,	Dow	24,000 tons/yr	Late 1971
Dallesport, Wash.	Dow	24,000 tons/yr Magnesium (100,000 tons/yr Cl_2)	Late 1973
Dow Chemical Co., Freeport, Texas	Dow Diaphragm	Expansion planned	
Dow Chemical Co., Midland, Mich.	Dow Diaphragm	Modernization planned	1971-1972
Dow Chemical Co., Pittsburg, Calif.	Dow Diaphragm	450	Mid-1970
Dow Chemical Co., Plaquemine, La.	Dow Diaphragm	$2.2 million	2nd Quarter 1970
National Lead Co., Grantsville, Utah	BASF	45,000 tons/yr Magnesium	Late 1971
Oregon Metallurgical Co., Albany, Ore.	Alcan	10,000 tons/yr Magnesium	1st Quarter 1970
PPG Industries Inc., Guayanilla, Puerto Rico	DeNora Mercury	500	Late 1970
Standard Chemical Ltd., Beauharnois, Quebec	Uhde Mercury	220	1970
Stauffer Chemical Co., St. Gabriel, La.	Uhde 30 m^2 Mercury	500	1st Quarter 1970

III. New developments.—A. Pricing.—In the last quarter of 1969, the price of chlorine was raised $2/ton to the $75/ton range, in single unit tankcars, F.O.B. plants, freight equalized. Higher manufacturing and distributing costs were given as the reason for the increase. For that small percentage of total production sold in ton containers, the price was also increased $2 to $97/ton (6, 7).

B. Mercury.—Mercury consumption increased 5% during 1969 with the larger users being the manufacturers of chlorine and caustic soda, catalysts, pulp and paper, and pharmaceutical products.

Mine production was estimated at 29,000 76-lb flasks; secondary production was 50% less than 1968, mainly as a result of a drop in government sales. California and Nevada supplied 63% and 28%, respectively, of the mercury produced in the U.S., with the balance from Alaska, Arizona, Idaho, Oregon, and Texas. The value of primary production was placed at $14,600,000 (8).

Imports of mercury increased approximately 20%. Spain is the largest producer with British Columbia,

[1] This report is sponsored by the Industrial Electrolytic Division of The Electrochemical Society. While it is primarily a summary of production and developments in the chlor-alkali industry, reports of other electrolytic industries are included.
The material presented herein has been gathered from many sources, noted in the References, and does not necessarily represent the opinions of the authors.

* Electrochemical Society Active Member.

Algeria, Turkey, and Yugoslavia also contributing to the world production.

The price of mercury has been as low as $182/flask in August 1963, and as high as $700/flask in June 1965. Lately it has fallen from about $585 to less than $500/flask (9).

Government officials recently said they would like to sell about 73,700 flasks from surplus stockpiles eventually; however, opposition is expected from the domestic industry and through diplomatic channels. The government has been offering stockpiled mercury this year at the rate of 1500 flasks a month.

C. BASF-Wyandotte.—Badische Anilin and Soda-Fabrik AG of Ludwigshafen, West Germany, announced that it is acquiring 98.5% of the outstanding stock of Wyandotte Chemicals Corporation, Wyandotte, Michigan. This represents an investment of about $95 million. In the next three or four years, BASF expects to spend around $105 million on plant expansions and modernization.

In 1968 BASF had sales of $1.4 billion, while Wyandotte's sales were $147 million (10).

Other Alkalies and Electrolytic Processes

Sodium Chlorate.—Production of sodium chlorate in the U.S. was approximately 183,000 tons in 1969, with a projected demand of 244,000 tons by 1973. Of this, 72% goes to the pulp and paper industry, 14% is used in the manufacture of chlorates and perchlorates, and 9% is used for herbicides. The pulp and paper industry employs chlorates for the generation of chlorine dioxide to bleach paper. Cotton defoliation and clearing railroad rights-of-way account for most of the herbicide use.

The domestic producers of sodium chlorate are listed (11):

Producer	Capacity (short tons/yr)
American Potash and Chemical Corp., Hamilton, Miss.	23,500
American Potash and Chemical Corp., Henderson, Nev.	30,000
Brunswick Pulp and Paper Co., Brunswick, Ga.	7,000
Georgia-Pacific Corp., Bellingham, Wash.	5,000
Hooker Chemical Corp., Columbus, Miss.	55,000
Hooker Chemical Corp., Niagara Falls, N. Y.	15,500
Reigel Paper Corp., Butler, Ala.	4,000
Reigel Paper Corp., Reigelwood, N. C.	7,000
Pacific Engineering and Production Co., Henderson, Nev.	6,000
Penn-Olin Chemical Co., Calvert City, Ky.	31,000
Pennwalt Corp., Portland, Ore.	15,000
PPG Industries Inc., Lake Charles, La.	15,000
	214,000 Total

Caustic potash.—Caustic potash facilities currently operable in the U.S. are shown below (12):

Producer	Capacity (short tons/yr)
Allied Chemical Co., Syracuse, N. Y.	30,000*
Diamond Shamrock Corp., Delaware City, Del.	16,000
Diamond Shamrock Corp., Muscle Shoals, Ala.	40,000
Dow Chemical Co., Pittsburg, Calif.	10,000
Hooker Chemical Corp., Niagara Falls, N. Y.	36,000*
International Minerals and Chemical Corp., Niagara Falls, N. Y.	23,000*
Monsanto Co., Sauget, Ill.	45,000
Pennwalt Corp., Calvert City, Ky.	25,000
PPG Industries, Inc., Corpus Christi, Texas	7,000*
PPG Industries, Inc., New Martinsville, W. Va.	8,000
	240,000 Total*

* Includes solid or flake production.

Published price for liquid, in carload or truckload quantities, was $3.80/cwt., F.O.B. producing plant. Flake prices increased during the year from $11.10/cwt. to $11.60/cwt.

Soda ash.—Natural soda ash production reached a total of 2,500,000 tons in 1969; this quantity was valued at $47,800,000 (13). The production rate noted reflects continued price degradation, as the quantity increased 23%, but the value dropped 14% compared to last year. While some production came from the dry lake beds in California, the bulk of U.S. needs was supplied by Green River, Wyoming, as in previous years. Food Machinery Corporation's three shafts in Green River are operating at near capacity of 1,250,000 tons/yr; a fourth shaft is planned, commencing a $5,000,000 expansion program (14). In addition, nearly 2,000,000 tons of sodium carbonate were produced synthetically (15).

Year-end price for both dense and light 58% soda ash climbed 5% from 1968, listing: bagged, $2.20/cwt. and bulk, $1.65/cwt. (16).

Aluminum.—Primary aluminum production in the U.S. increased to 3,800,000 tons in 1969, up from 3,250,000 tons in 1968. Canadian production of aluminum was reported to total approximately 1,063,000 tons in 1969.

Apparent use of aluminum in the U.S., based on shipments of primary metal, net imports, and recovery from scrap, increased to approximately 4,800,000 tons. This year of relatively steady production served to reduce imports of aluminum metal to a level less than 1968, when strikes at plants of two major domestic producers forced consumers to rely on foreign supply (17).

Aluminum ingot capacity under construction or planned for 1969 was as follows (18):

Producer	Capacity (short tons/yr)
Aluminum Co. of America, Rockdale, Texas	50,000
Aluminum Co. of America, Evansville, Ind.	50,000
Gulf Coast Aluminum Corp., Lake Charles, La.	35,000
Kaiser Aluminum & Chemical Corp., Tacoma, Wash.	20,000
Reynolds Metals Co., Longview, Wash.	40,000
National-Southwire Aluminum Co., Hawesville, Ky.	180,000

The price of unalloyed primary aluminum ingot, which had been raised to 27¢/lb early in January 1969, was raised again to 28¢/lb in mid-October.

Domestic production of bauxite rose to 1,800,000 long tons, while imports were 12,000,000 long tons. Approximately 60% of the bauxite imports in 1969 came from Jamaica, 20% from Surinam, and the majority of the balance from the Dominican Republic, Haiti, and Guyana. It is estimated that 67% of the alumina imports were from Australia and about 25% from Surinam (19). Generally speaking, 4 tons of bauxite are required to produce 2 tons of alumina which will yield 1 ton of primary aluminum.

Beryllium.—This year marks the fifth straight year that the use of beryl (a beryllium-aluminum-silicate) has increased, and the U.S. consumption for 1969 exceeded 6000 tons (20). Nearly half of the beryllium metal consumed is used in high-speed aircraft, and the remainder employed in missile components, the nuclear industry, and copper and nickel alloys (to impart fatigue resistance) (21, 22).

Domestic sources for beryllium production are the states of South Dakota, Maine, and Colorado, in that order, for hand-sorted beryl; and Utah for mined bertrandite (another beryllium-aluminum-silicate). General imports of beryl for 1969 should exceed 6400 tons, valued at $2,600,000; interestingly, while the tonnage is nearly a 40% increase over 1968, the foreign value of this material dropped 15%.

The industrial activity evident in 1969 is probably in response to the steadily growing beryllium market. Kawecki Berylco Industries, Inc., and Brush Beryllium Company processed hand-sorted beryl into beryllium metal and alloys; and some concentrates have been shipped from the new (September) Brush Beryllium's Spor Mountain processing plant near Delta, Utah. General Astrometals Corporation has leased the electrofining facilities of Beryllium Metals and Chemicals Corporation. Topaz Beryllium Company (subsidiary of The Anaconda Company) has acquired land in Juab County, Utah, for a proposed beryllium ore concentration plant.

Government inventories at mid-year listed 7387 tons of beryllium-copper master alloy and 229 tons of beryllium metal (exactly the amounts reported for

mid-year 1968); the 11% BeO-bearing beryl figure was 26,559 tons, which is slightly down from a year ago. The General Services Administration sales of beryl in 1969 (including a December 1968 sale) totaled 3475 tons; the price varied from $50.52 to $52.67/short ton unit.

Chromium.—The three leading consumers of chromite increased their usage during the year, as inventories dropped. The metallurgical industry used 739,000 tons in 10 months, an 8.5% increase over 1968, reflecting the high level of stainless steel production. The chemical and refractory industries consumed 175,000 and 253,000 tons, respectively. This was a 5% increase in chromite use by the chemical industry, while the 8% decrease in use for the refractory group continued last year's trend (23).

The metallurgical industry had to turn to surplus chromite from government stockpiles to supplement supply, with the continued economic sanction against Southern Rhodesia imposed in early 1967. The General Services Administration has sold 789,000 tons since January 1967 with 206,000 tons delivered in the first 10 months of 1969.

Negotiations for a plant to produce ferroalloy in Puerto Rico were announced by Air Reduction Company. The plant is to have two furnaces with a combined rating of 40,000 kW; full production is estimated for late 1971 or early 1972. A chromium chemical plant to be built in Wilmington, North Carolina, was announced by Diamond Shamrock Corporation.

Metallurgical-grade chromite prices moved upward for the third successive year. Quoted prices per long ton at Atlantic ports were as follows: Russian, 48% Cr_2O_3, 4-1 ratio $49-$52; Russian 54-56% Cr_2O_3, 4-1 ratio, $55.10-$59.60; and Turkish 48% Cr_2O_3, 3-1 ratio, $47.50-$48.50.

Copper.—In its first full year of operation since 1966, the U.S. Copper Industry posted significantly optimistic gains in 1969.

A record 9% jump in mine production of recoverable copper was recorded, up to 1,560,000 tons over the 1,429,000-ton 1966 previous high (24). Of this amount, more than half (51%) came from Arizona with the states of Utah, New Mexico, Montana, and Nevada contributing another 40% which accounts for the bulk of U.S. production. The U.S. share of free world mine output is now up to about 30% (25).

Based on tonnages of domestic primary material only, smelter production was up almost 32% over 1968, to a projected total for 1969 of 1,520,000 tons. Refinery output of domestic material jumped 35% over last year, and is expected to post 1,450,000 tons for 1969.

Reversing a two-year trend, consumption of refined copper increased (over 2,000,000 tons used in 1969), but fell short of the 2,400,000-ton record year of 1966. Wire and cable alone accounted for 1,300,000 tons (up 9% over 1968); defense programs, primarily for ammunition, took 225,000 tons of copper.

In conjunction with increased U.S. mine production, imports of blister and refined copper dropped this year and are estimated below 1968 receipts by 8% and a plummeting 69%, respectively.

Primary world copper prices have risen 200% in the past ten years, using the London Metal Exchange as a measure; domestic wholesale price indexes show a 60% rise. For the year 1969, the LME average price per pound for copper went from 56¢ to 72¢; U.S. prices mirrored this increase, going from 42¢ to 52¢ in three steps. However, a balance in the copper market is anticipated with the expected elimination of World-U.S. price differentials.

In the recovery field, Powdered Metals Corporation of Phoenix, Arizona, has announced construction plans for the first plant which will employ the new Harlan (George E. Harlan) Process to obtain copper powder from oxide ores (26). The ore is leached with a demineralized water-sulfuric acid solution and the leach liquor is then filtered and electrolyzed. The process is said to reduce the cost of present smelting and electrowinning techniques by 40%. Most of the reduction results from utilization of inexpensive equipment and avoiding costly milling, flotation, and furnacing units. In addition, the components are so simple and light that a portable plant can be trucked to operate on-site at ore deposits once considered too small or remote. Ore-to-powder requires only 4 hr compared to several days using conventional means.

Lithium.—The following companies are involved in processing lithium raw material to lithium primary products: Foote Mineral Company at Sunbright, Virginia, and Silver Peak, Nevada; American Potash and Chemical Corporation, Trona, California; and Lithium Corporation of America, Bessemer City, North Carolina (27). Production data are not available.

Use of lithium in 1969 was at an all-time high. Products employing lithium in their manufacture include: ceramics and glass, greases, welding and brazing fluxes, air conditioning equipment, rubber, and pharmaceuticals. Some newer uses include aluminum reduction cells, and bleaches and sanitizers.

Lithium metal was priced at $7.75/lb in 1000-lb lots; lithium carbonate at $0.46/lb in carload lots; and lithium chloride at $0.85/lb.

The reports on cesium and rubidium, normally included in this section, are omitted this year since the Mineral Industry Survey fails to make any mention of these metals.

Magnesium.—For the year 1969, production of primary magnesium is projected at 89,500 tons, up 2% over 1968; and shipments at 107,000 tons, up 16%. Secondary magnesium recovery is expected to be 15,000 tons. While there was only a minimal rise in exports (4500 tons), imports increased 43% netting about 24,000 tons. The U.S. accounts for over 60% of the world 162,000-ton annual production figure.

The consumption of primary magnesium in 1969 was 100,000 tons, which represents a 3% drop from the 103,000 tons in 1968, as reported by the U.S. Bureau of Mines (28). In contrast, *Business Week* reports 1969 as the sixth consecutive year that magnesium demand has risen, and the third year in a row that demand has exceeded capacity (29). However, all sources agree that magnesium is on the verge of a Cinderella boom; expansions of present capacity are predicted to double by 1971 and reach 300,000 tons/yr in 1972 (30).

The ultimate target of the expanding magnesium industry is an anticipated 400,000-ton potential automotive market within 10-15 years. In the near term, the largest single market for magnesium is in the aluminum-magnesium alloys used in commercial aircraft; machinery is next, and the chemical industry third. The lightweight metal is making a strong bid to replace aluminum; while it still costs more than aluminum, the price differential may shrink with the activity the magnesium producers are exhibiting. New products include rapid transit systems, motors, cameras, power tools for home use, photoengraving, corrosion-resistant paint, and battery casings.

One big name in the industry dropped out in the third quarter of 1969: Alamet Division of Calumet and Hecla Corporation shut down its dolomite (highest grade magnesium, but most expensive process) plant at Selma, Alabama. The major producers now in the field are: Dow Chemical Company, with a 48,000-ton/yr plant to go on stream the last half of 1971 and reach design capacity in 1976 at Dallesport, Washington (31, 32); National Lead Company with a 45,000-ton plant under construction at Salt Lake, due for completion in 1971 (33, 34); American Magnesium Company began operation of its scheduled 30,000-ton plant at Snyder, Texas; and Oregon Metallurgical Corporation at Albany, Oregon, plans to complete its 10,000-ton plant in early 1975 (35). In addition, two large aluminum producers, Alcoa and Kaiser, own property in the magnesium-rich Salt Lake area (36); and two steelmakers, USS and National are taking a close look at producing magnesium themselves (37).

Magnesium compound production increased over 1968 by 14% in volume and 16% in value. Imports of refractory magnesium declined about 20% for the year.

Manganese.—In 1969, approximately 1,800,000 tons of manganese ore containing 35% or more manganese were imported from Brazil, Gabon, Australia, and the Congo. Ferromanganese imports increased to 300,000 tons for the year, primarily from the Republic of South Africa, France, India, and West Germany. Manganese metal imports were down to 1428 tons for the first three quarters, with the majority from the Republic of South Africa.

Domestically, approximately 2,300,000 tons of ore were produced. Montana and New Mexico continued to mine ore containing 35% manganese, but at lower levels than in 1968. International Minerals and Chemical Corporation shut down their blast furnace in Sheridan, Pennsylvania, and stopped producing ferromanganese. High imports and large inventories were given as reasons for this change (38).

December quotations for ore with a content of 46-48% manganese were 49-53¢/long ton. Foote Mineral announced price increases effective January 1, 1970 on all grades of electrolytic manganese, with a typical increase being No. 1 chip to 31.25¢ from 30.25¢/lb (39).

Deepsea Ventures Inc., a subsidiary of Tenneco Inc., was active in carrying on the deep-sea mineral investigations formerly pursued by Newport News Shipbuilding and Dry Dock Company. This work, off the Georgia and Florida coasts, has yielded over 40 tons of manganese nodules that are to be treated in process pilot plants.

Nickel.—International Nickel Company of Canada, Ltd. (Inco) operations in Ontario were closed by a strike of the United Steelworkers of America from July 10 until November 17, 1969. While Inco's Manitoba facilities continued to produce nickel, these account for only 30% of the company's total capacity. In addition, Falconbridge Nickel Mines, Ltd., was out of operation from August 21 until November 22, 1969, because of a strike by the Mine, Mill, and Smelter Workers Union (40). These two stoppages reduced the free world's production of nickel approximately 50%. Upon resumption of work, the increased wage and fringe benefits (worth $1.35/hr) increased Inco's employment costs by approximately 35% (41).

A total of 29 million pounds of nickel has been released from Government stockpiles thus far, compared to the 150 million pounds International Nickel claims to have lost during the four month strike. The stocks must be replaced with the government by July 1972, so it seems certain the shortage will continue (42).

World production of nickel was estimated at 530,000 tons. Imports into the U.S. from all sources were expected to be 125,000 tons with exports at 30,000 tons.

The producer price for cathodes started the year at $1.03/lb F.O.B. shipping point. Following settlement of the 128-day strike, Inco raised the price to $1.28 which was followed by other major producers. Quotations for dealer cathodes according to *Metals Week* were $1.65-$1.75/lb early in the year, but reached $6.65-$7.15 in October. Prices in the $8-$10/lb range were said to have been obtained for small quantities of special forms.

A hydrometallurgical nickel refining process, developed by Sherritt Gordon Mines, Ltd. (Toronto, Canada), has come to the attention of others due to the nickel shortage. Sherritt Gordon has been using this process since 1954 and recently licensed the process to Western Mining Corporation of Australia. A 50-million lb/yr refinery was announced for completion in 1971 or 1972 by The Philippine's Marinduque Mining and Industrial Corporation, using a modified version of the process (43).

International Nickel announced construction of an $80-million refinery marking the first commercial use of the Inco Pressure Carbonyl (IPC) process. This highly automated plant at Copper Cliff, Ontario, is scheduled for completion in 1971. Capacity is stated to be 100 million lb/yr of pellets and 25 million lb/yr of powder (44).

Sodium.—The use of sodium metal was up slightly over 3% in 1969 compared to last year; the 3% figure confirms the growth estimated in this industry for the next 3 years (45). While the sodium business recovered from the 1967-1968 drop, projected quantities based on 8-month figures show the 1969 total at 162,000 tons, which is still under the 1966 165,000-ton high. Of the sodium metal produced, 83% was used to manufacture tetramethyl and tetraethyl lead, 6% was used as a reducing agent in the production of titanium sponge, and the remaining 11% found miscellaneous uses (peroxide production, sodium hydride descaling of metals, chemical and drug intermediaries, and coolant in nuclear power stations) (46).

All major producers increased metallic sodium prices effective on spot in mid-November and on January 1, 1970 for contract business. Brick price (drummed, in 18,000-lb lots) rose 2¢/lb to 24½¢; reactor grades increased to 29¢; and carload lots increased to 18¾¢/lb.

Titanium.—Titanium sponge metal (refined ore) production rose 12% in 1969; sponge consumption leaped 35% over 1968, to about 19,500 tons (47). Foreign sponge imports for the first 9 months indicated a total receipt of 6230 tons. At year's-end, domestic sponge of 99.3% purity held at $1.32/lb, while import (from Japan and the United Kingdom, principally) dropped 0.05 to $1.20/lb (48). Only a small amount of titanium sponge was sold by the General Services Administration in 1969.

Through October, titanium metal (unwrought, waste, and scrap) was imported for consumption in an amount projected to equal 6500 short tons at a value expected to exceed $10,500,000. The bulk of the imports came from Japan (70%), with Russia (15%) and the United Kingdom (10%) making up most of the remainder. Exports, mostly scrap, were up 20%, totaling 3400 tons for 1969.

The price reduction reported last year (49) seems to have produced the desired result as the burgeoning consumption in 1969 indicated. Gains in chemical and construction uses are difficult to measure accurately, but aerospace and the aircraft industry are still prime markets.

No rutile was produced domestically in 1969, and imports increased 15%. To expand domestic rutile production, in June of 1967 the Office of Emergency Preparedness (OEP) reduced the war stockpile of rutile from 200,000 to 100,000 short dry tons. In 1969, import price for 96% TiO_2 rose to a high of $160 per short ton over last year's close at $125.

Ilmenite imports of the mineral concentrate rose 50% over 1968 in the face of a 3% drop in domestic production. Ilmenite is used mostly in making titanium oxide pigment. Quoted prices for 1969 held firm at $30-$35 per short ton for domestic 60% TiO_2-content stocks; and at $20-$21 per long ton for imported 54% TiO_2 material.

Zinc.—Reversing a three-year trend, U.S. mine production of zinc for 1969 rose 4%, to 546,000 tons (50). In conjunction with the expanding lead industry, 33,000 tons of zinc supplied from new mines alone placed Missouri as one of the country's leading zinc producers. While the historically higher zinc producing states increased their output, zinc production in others dropped, which offset the potential gain.

Smelter production of slab zinc zoomed the first half of 1969, but fell off the last half; still, projected output was up from the previous record year of 1966 by 5% and exceeded 1968 by 8%, totaling 1,160,000 tons. To add to this bright picture, shipments led production by a net 9000 tons for the year, considering customer's stores accumulation. Zinc imports of ore and metal approximated those of 1968. The principal suppliers were Canada, Mexico, Australia, and Peru.

Total consumption of zinc for 1969 was 1,800,000 tons with slab accounting for 1,400,000 and the other 400,-

000 tons made up of direct ore use (135,000) and scrap (265,000). In line with the increases noted in production, consumption also equalled the record year 1966. The largest advances in the industry were posted by zinc-base alloys (585,000 tons), zinc oxide (44,000), and in copper-base alloys as a result of full-year operation of brass mills (184,000 tons).

The General Services Administration sales amounted to 25,440 tons from the existing zinc disposal authorization; 22,610 tons remain in inventory.

Prime Western Grade zinc price rose 2¢ during the year, in three steps, to finish 15½¢/lb. The London Metal Exchange price, after fluctuating throughout the year, ended at 14¢/lb.

Electrical Energy

U.S. Generation.—The utility companies and industrial plants in the U.S. combined to produce 1.43 trillion kilowatt hours (kWhr) of electricity this year (51). Reflecting ever-increasing power consumption, this represents an 8.8% gain over 1968, substantially greater than the 5.2% growth in 1968, and the 7.4% average for the 5-year period ending 1967.

Utility production (representing 93% of the nation's total electrical energy capacity) held at the same 9.3% increase over the previous year, to a new record total of 1.33 trillion kWhr. The breakdown by production means shows: 16.7% hydroelectric, 82.7% by steam electric plants, and the balance (0.6%) by internal combustion engines and gas turbines. Each category reached a new high, exceeding 1968 levels by 0.3, 11.2, and 16.9%, respectively.

Steam electric generation using nuclear fuel showed a gain compared to 1968, of from 7.7 to a total of 12.3 billion kWhr; this increase (60%) is still only 0.86% of the country's total energy need. However, it is predicted that, by the year 2000, 50% of the nation's electrical energy requirements will be met by nuclear facilities (52). In 1969, consumption of coal reached 297 million tons, gas nearly 3.15 trillion cubic feet, and oil 188 million barrels. In keeping with the production increases, use of each fuel also rose. Hydroelectric generation also set a record high of 52.8 million kW, topping 1968 by 3.3%. It is estimated that, of the country's total hydroelectric potential (178.5 million kW), only 48.8 million kW, or 27%, has been developed.

There has been some concern regarding the rate at which present resources are being dissipated. Coal, gas, and oil have been carefully studied, and it is estimated that existing supplies will suffice for from 200 to 1000 years (53).

Utility generating capacity posted a record 8.1% increase this year, adding 21,806,000 kW, to a new high of installed capacity totaling 291,058,000 kW. This total capability is ample to supply current U.S. needs. Looking to the future, however, demand for electricity in the U.S. is expected to match the growth rate of the past three decades, which means doubling the generating capacity each ten years (54).

Coupled with the capacity and consumption increases seen in 1968, the industry also experienced delays. Some generating plants and transmission lines were not put into service on schedule, primarily as a result of shortages of skilled labor.

Nuclear Power.—In the U.S. Generation section of this report, it was reported that the total percentage of electrical energy derived from nuclear sources was very small (less than 1%). The past year still succeeded in chalking up a 60% production increase over 1968, even though it was a declining year for orders in the nuclear business. Furthermore, though recent rising construction costs (now about $1.45/kW for conventional *vs.* $2.00/kW for nuclear) have made utility companies hesitate to go the nuclear route, 1972 is predicted as the turning point for the swing to nuclear power (55, 56).

Historically, fossil-fueled steam generating plants have been the major source of electrical energy (57). In 1957, a government-sponsored program to develop and demonstrate the feasibility of nuclear reactors for civilian application was introduced to the electric utility industry. By 1964, $3 billion in study had indicated the cost advantage of a nuclear installation as typically slightly over 5 mills/kWhr, compared to 5-6 mills/kWhr for a fossil-fired plant. In addition, nuclear plants will require considerably less expense for pollution control. Following these findings, a rash of orders were placed for nuclear plants in 1966 and 1967. The explanation for the difference between the fast start and the current restrained status of the nuclear power industry is simply growing pains.

The power plant supply industry was pushed beyond its capacity, as neither facilities nor trained workmen were available to begin; construction costs and inflation have been steadily rising; and delays were experienced in educating a public concerned with thermal and radiation effects. On-stream service has been postponed as much as two years, and the original five years have been stretched to the present 6½-7 years for expansion planning.

The U.S. is well established as the world leader in enriched-uranium light water type nuclear power reactors, but the present generation of nuclear reactors employ less than 2% of uranium's potential energy. For this reason, the government and private industry are actively investigating fast (breeder) reactors for electrical power generation. Breeder reactors will utilize 50% of the latent energy in uranium and will, in fact, produce or "breed" more fissionable material than they consume. The major effect of the fast reactors will be to stabilize the supply and price of uranium; however, commercial exploitation of fast reactors is not expected to begin before the 1980's. Accordingly, power rates will probably fluctuate little in the next ten years, and only begin to drop as a result of breeders in the succeeding ten years.

D-C power.—In evaluating the power transmission figures of the last few years, the recent use of extra-high-voltage (EHV) lines must be taken into account. Power transfer capability increases as the square of the voltage, so comparing only miles of transmission line installed is not comprehensive. The decrease in actual miles from 18,452 in 1968 to 14,555 in 1969 illustrates the point well; in terms of voltage-miles, power transmission installation increased 32% in 1969 (58).

Currently, utility transmission installations are limited to 500-kilovolt (kV) lines, but this year saw the first 765-kV line become operable. Tests are in progress to utilize 1100- and even 1500-kV lines. Also, additional exploration is under way to examine the benefits directly related to direct current EHV transmission systems working in conjunction with alternating current systems.

There was a delay in completing the 853-mile, 750-kV[2] d-c transmission line between the Dalles Substation (on the Columbia River in Oregon) of the Bonneville Power Administration and the Slymar Substation of the Los Angeles Department of Water and Power. Start-up service was rescheduled for Spring of 1970.

Developments of Interest

Petrochemicals by electrolysis.—Electrolysis in organic syntheses has been studied for many years; however, very few processes have reached a commercialized scale. Electrolytic routes to organics may be applicable where product selectivity may be superior to known chemical methods (59).

A good example is the Monsanto process for electrohydrodimerization of acrylonitrile producing adiponitrile in a single, high-selectivity step; it is recognized that existing thermal and catalytic dimerization methods give inferior yields and/or lower conversions. Asahi Chemical of Japan is reported to be planning a 20-million-lb/yr adiponitrile facility. BASF is also said to be working on a similar process.

[2] Erroneously reported as an 825-mile, 800-kV line in the Report for 1968.

When objectional co-products may be avoided, the electrolysis method may have merit. An example would be the electrolytic chlorohydrin process for propylene oxide, eliminating the unwanted production of calcium chloride.

Conversion by chemical means may require reaction conditions so severe in terms of pressure, temperature, residence time, catalyst life, or corrosivity that the cost of the electrolysis system is justified. Direct handling of troublesome reagents may be eliminated, as in 3M's electrolytic fluorination process, and the bromination process developed by Sohio. The use of lower cost raw materials and useful products from both anode and cathode reactions may provide economic advantages.

Continued research in this area is indicated and, when any of the above advantages or a combination of them offset the high power and cell cost, an attractive process will result.

The Kel-Chlor process.—At the April 1969 American Chemical Society meeting in Minneapolis, Dr. Alex G. Oblad, Vice-President of Research and Development for the M. W. Kellogg Company (New York), presented the chemistry involved and the potential market impact of a breakthrough nonelectrolytic process for the manufacture of chlorine (60-62). Essentially, the Kellogg development provides a successful way to oxidize hydrogen chloride to chlorine.

The basic idea is not new. In the same manner, chlorine was first produced in the laboratory by the Swedish chemist Karl Wilhelm Scheele (63), and the concept was refined to commercial use about a century ago by Deacon and Hurter. They employed solid copper chloride as a catalyst; but, by using air as the oxidizing medium, the resultant chlorine was highly diluted with nitrogen, though acceptable for those times. More recent attempts to upgrade the process include increased catalytic activity, which has not proved attractive, or introduction of an organic molecule to react with chlorine and thus drive the reaction equilibrium toward more complete oxidation. The latter are generally termed oxychlorinations, and are useful but limited in application.

With the present-day availability of cheap oxygen, the Kellogg process employs two novel keys to push its descendant of the Deacon reaction to completion: nitrogen oxides as homogeneous (gas phase) catalysts, and sulfuric acid to absorb oxides and steam (64). Briefly, gaseous hydrogen chloride is reacted with hot recycled nitrosyl sulfuric acid to form nitrosyl chloride; in the first oxidation chamber, nitrosyl chloride with oxygen breaks down to chlorine and nitric oxide; conversion is completed in a second oxidizing step, where sulfuric acid absorbs water (steam) and reacts with the nitrogen oxides to yield nitrosyl sulfuric acid, which is recycled. The product chlorine is quite pure and relatively dry and meets the specifications of some applications as is; for more stringent uses, it can be easily upgraded.

In the past, attempts to commercialize hydrogen chloride oxidation processes have stumbled on economically insurmountable corrosion problems. Kellogg reports, however, that in its new process corrosion is not a difficulty and that "available" materials are utilized. Continuous operation of a one-ton/day unit is said to have proven the Kel-Chlor process, and Kellogg is prepared to offer it for license. Operating costs will vary, depending on plant size, from $17 to $10/ton of chlorine produced.

Dr. Oblad points out that, for the first time, the production of chlorine is exceeding that of caustic, dumping more caustic in an already saturated market. In addition, by-product hydrogen chloride from organic chlorinations is also creating an increasing disposal problem. Its developer offers the Kel-Chlor process as the solution to this situation. Neither the electrolysis of aqueous hydrogen chloride nor the electrolysis of magnesium chloride is geared to American market requirements, according to Dr. Oblad.

Two major areas are suitable targets: the production of elemental chlorine itself, and the use of chlorine in chlorination reactions (the largest of which is manufacture of vinyl chloride). As to the hydrogen chloride charge, four processes are listed as adequate sources: 1—steam hydrolyzed magnesium chloride, 2—the by-product from Solvay Process ammonium chloride, 3—the reaction of sulfuric acid with sodium chloride, and 4—the fertilizer industry's conversion of potassium chloride to the more potent potassium phosphate or nitrate.

Manuscript received June 11, 1970. This report was presented at the Industrial Electrolytic Division Luncheon at the Los Angeles Meeting of the Society, May 10-15, 1970.

Any discussion of this report will appear in a Discussion Section to be published in the June 1971 JOURNAL.

REFERENCES

1. Robert F. Schultz, President, Chlorine Institute (Feb. 4, 1970).
2. *Chemical Week*, p. 55, April 19, 1969.
3. *Wall Street Journal*, June 12, 1969.
4. The Chlorine Institute, Inc.
5. *Chem. Eng.*, p. 120, Oct. 20, 1969.
6. *Oil, Paint & Drug Reporter*, Sept. 15, 1969.
7. *Chemical Week*, p. 53, Sept. 13, 1969.
8. Mineral Industry Surveys, U.S. Dept. of the Interior, Annual Preliminary, "Mercury in 1969."
9. *Business Week*, p. 32, Feb. 14, 1970.
10. *Oil, Paint & Drug Reporter*, Nov. 10, 1969.
11. *Ibid.*, Oct. 13, 1969.
12. PPG Industries, Verbal communication.
13. Mineral Industry Surveys, U.S. Dept. of the Interior, Annual Preliminary, "Sodium Compounds in 1969."
14. *Chemical Week*, p. 25, Dec. 24, 1969.
15. Current Industrial Reports, Inorganic Chemicals, U.S. Dept. of Commerce, Oct. 1969.
16. *Oil, Paint & Drug Reporter*, Dec. 29, 1969.
17. Mineral Industry Surveys, U.S. Dept. of the Interior, Annual Preliminary, "Aluminum in 1969."
18. Yearbook of the American Bureau of Metal Statistics, 48th Annual Issue, June 1969.
19. U.S. Industrial Outlook 1970, U.S. Dept. of Commerce (BDSA).
20. Henry C. Meeves, U.S. Dept. of the Interior, Verbal communication.
21. Mineral Industry Surveys, U.S. Dept. of the Interior, Annual Preliminary, "Beryllium in 1969."
22. "Chemical Engineer's Handbook," 2nd Ed., John H. Perry.
23. Mineral Industry Surveys, U.S. Dept. of the Interior, Annual Preliminary, "Chromium in 1969."
24. Mineral Industry Surveys, U.S. Dept. of the Interior, Annual Preliminary, "Copper in 1969."
25. U. S. Industrial Outlook 1970, U.S. Dept. of Commerce (BDSA).
26. *Chem. Eng.*, p. 96, Sept. 8, 1969.
27. Mineral Industry Surveys, U.S. Dept. of the Interior, Annual Preliminary, "Lithium in 1969."
28. Mineral Industry Surveys, U.S. Dept. of the Interior, Annual Preliminary, "Magnesium and Magnesium Compounds for 1969."
29. *Business Week*, p. 52, May 31, 1969.
30. *Chem. Eng.*, p. 60, Aug. 25, 1969.
31. *Oil Paint & Drug Reporter*, June 16, 1969.
32. *Chem. Eng. News*, p. 15, June 9, 1969.
33. *Ibid.*, p. 21, April 21, 1969.
34. *Chem. Eng.*, p. 43, May 5, 1969.
35. *Ibid.*, p. 123, Oct. 20, 1969.
36. *Chemical Week*, p 15, Sept 6, 1969.
37. *Ibid.*, p. 36, May 17, 1969.
38. Mineral Industry Surveys, U.S. Dept. of the Interior, Annual Preliminary, "Manganese in 1969."
39. *Chemical Week*, p. 56, Dec. 17, 1969.
40. Mineral Industry Surveys, U.S. Dept. of the Interior, Annual Preliminary, "Nickel in 1969."
41. *Chem. Eng. News*, p. 16, Nov. 24, 1969.
42. *Ibid.*, p. 15, Dec. 22, 1969.
43. *Chem. Eng.*, p. 108, April 7, 1969.
44. *Ibid.*, p. 106, May 19, 1969.
45. *Oil, Paint & Drug Reporter*, May 19, 1969.
46. *Ibid.*, Nov. 17, 1969.
47. Mineral Industry Surveys, U.S. Dept. of the Interior, Annual Preliminary, "Titanium in 1969."
48. *American Metal Market*. p. 24, Dec. 26, 1969.

49. "Report of the Electrolytic Industries for the Year 1968," *This Journal*, **117**, 9C (1970).
50. Mineral Industry Surveys, U.S. Dept. of the Interior, Annual Preliminary, "Zinc in 1969."
51. Federal Power Commission, Annual Report, 1969.
52. *Chem. Eng. News*, p. 34, Oct. 27, 1969.
53. J. E. Curry, "The Effect of Energy Sources on Electrochemistry," Paper given at Niagara Section Meeting of Electrochem. Soc. Nov. 17, 1969.
54. U.S. Industrial Outlook 1970, U.S. Dept. of Commerce (BDSA).
55. *Chem. Eng. News*, p. 36, Oct. 27, 1969.
56. Federal Power Commission, Annual Report, 1969.
57. U.S. Industrial Outlook 1970, U.S. Dept. of Commerce (BDSA).
58. Federal Power Commission, Annual Report, 1969.
59. *Hydrocarbon Processing*, p. 159, June 1969.
60. *Chem. Eng. News*, p. 14, April 21, 1969.
61. *Chemical Week*, p. 83, April 26, 1969.
62. *Chem. Eng.*, p. 39, May 5, 1969.
63. *Ind. Eng. Chem.*, p. 23, July 1969.
64. *Chem. Eng. News*, p. 14, May 5, 1969.

F. M. Becket Memorial Award

The Electrochemical Society will offer the F. M. Becket Memorial Award to a qualified graduate student for the summer of 1971. This Award commemorates F. M. Becket, a man of great research and administrative ability and a former President of the Society, whose accomplishments in science and industry were outstanding. The stipend valued at $1500 provides a grant-in-aid toward a summer's (at least two months) research and study overseas in the laboratory of a recognized research institute or institution of higher learning, selected from the approved list maintained by the F. M. Becket Memorial Award Committee.

The objectives of this Award are to stimulate and encourage education and participation in the fields of electrochemical science and industry conerned with specialty materials and processes as follows:

a) **Materials** such as refractory metals and compounds, intermetallics, graphite, fused salts, and rare earth metals;

b) **Equipment** for the utilization of electrical energy in materials synthesis;

c) **Processes** using arcs, vacua, plasmas, and electron and ion beams; and

d) **High temperature kinetics and thermodynamics phenomena** such as melting, vaporization, reactions, sintering, diffusion or oxidation occurring at high temperatures, high pressures, or vacua involving high temperature materials.

To be eligible for the Award, the entrant must qualify in one of the two following categories. He must be either (1) a graduating senior of demonstrated ability, regularly enrolled in any recognized college, university, or institute of technology in continental United States or Canada, who intends to seek an advanced degree, or (2) a graduate student, similarly enrolled, who is seeking an advanced degree. No limitations of sex, race, nationality, or religion are to be imposed by the Award Committee in determining the recipient of the Award.

The Award shall be presented on the basis of the following material:

1. A complete transcript of the student's academic record.

2. Two copies of a letter, over the signature of the head of the College or Department in which the student is enrolled, describing briefly his academic work, his campus activities, and presenting an estimate of his abilities.

3. Two copies of a letter, over the student's signature, containing a brief biographical sketch, a detailed description of the nature and extent of his academic work, particularly as it may relate to the field of the Award, and an outline of his plans for the future. The student shall indicate, from the list provided by the Award Committee, his choice of a place of residence under the Award.

Application forms are available from the Executive Secretary, Mr. Ernest G. Enck, The Electrochemical Society, Inc., 30 East 42nd Street, New York, N. Y. 10017. Deadline for receipt of completed applications will be February 1, 1971; and the Award winner will be announced on April 1, 1971.

1971 Spring Meeting

Sheraton Park Hotel, Washington, D.C.

May 9, 10, 11, 12, 13, and 14, 1971

The following Divisions are planning sessions:

Dielectrics and Insulation Division—Symposia on Electronic Applications of Ceramic Materials and Deposited Thin Film Dielectric Materials and Processes.

Dielectrics and Insulation and Electronics Divisions—Symposium on Plastics for Environmental Protection and Encapsulation of Electronic Devices.

Electronics Division—Symposium on Infrared Excited Visible Luminescence, Semiconductor General Sessions, and Luminescence General Sessions.

Electronics and Electrothermics and Metallurgy Divisions—Symposium on New Techniques for Materials Characterization.

Electro-Organic Division—Symposium on New Directions in Organic Electrochemistry and General Sessions.

Electro-Organic and Theoretical Divisions—Symposium on Electrochemistry and Biological Processes.

Electrothermics and Metallurgy Division—Symposia on Chemical Reactions in Gaseous Discharges and Directional Solidification of Eutectics.

Industrial Electrolytic Division—Symposium on Anodes for the Electrolytic Industries.

Theoretical Electrochemistry Division—General Session.

Papers are now being solicited for the meeting to be held in Washington, D. C., May 9-14, 1971. One copy of the usual 75-word abstract is due at The Electrochemical Society, Inc., 30 East 42 St., New York, N.Y. 10017, not later than December 1, 1970, and Extended Abstracts are due not later than January 1, 1971 in order to be included in the Program.

Please indicate on 75-word abstract for which Division's Symposium the paper is to be scheduled. Underline the name of the author who will present the paper. No paper will be placed on the program unless an author will present it in person, or has designated a qualified person to present it. Should clearance of a paper be required by the author's employer, such should be obtained before the paper is submitted.

Notification of acceptance for meeting presentation, along with scheduled time, will be mailed to authors with general instructions no earlier than two months before the meeting. Those authors who require more prompt notification are requested to submit with their abstract a self-addressed post card with full author—title listing on the reverse.

Presentation of a paper at a technical meeting of the Society does not guarantee publication in the Journal.

An author who wishes his paper considered for publication in the Journal should send triplicate copies of the manuscript to the appropriate section, 30 East 42 St., New York, N. Y. 10017.

All papers presented at meetings, become the property of The Electrochemical Society and may not be published elsewhere, either in whole or in part, unless permission for release is requested of and granted by the Society. Papers already published elsewhere, or submitted for publication elsewhere, are not acceptable for oral presentation except on invitation by a divisional program chairman.

The Electrochemist in a Changing World[1]

N. C. Cahoon*

Everyone will agree that we live today in a world that only faintly resembles that of a half century ago. But the changes have occurred gradually and perhaps their significance is not immediately recognized. One therefore should occasionally view these changes in perspective in order to assess their effect on our life and environment. The business of electrochemistry has not been free from changing conditions and I wish to point out some of the interesting aspects of our chosen field during the past decade.

The Growth of Industrial Electrochemistry

It is difficult to measure the growth of a scientific subject such as electrochemistry except in terms of discoveries and major developments. Unfortunately, most of these can best be evaluated several years later. It is much easier, and often more timely, to examine the growth of applied electrochemistry in the industrial field. In this area, both the quantities produced annually and their monetary value offer direct means of comparison with previous years. Because the field of all electrochemically produced materials is a very difficult one to treat in this way, a few examples have been chosen to show representative growth.

The chlor-alkali industry has been evaluated annually by a special committee of the Industrial Electrolytic Division of the Society and these reports (1-10) offer an excellent source of information. Figure 1 shows the annual production of chlorine in the U.S.A. for the last ten years. It is amazing to note that the chlorine industry in this country produced only 10,000 tons in 1902, and the industry has grown until the output today is almost 100 times that of 1902. Moreover, the production has doubled during this decade to around 1 million tons annually. Surprisingly, the points on the log-linear graph deviate little from a straight line for the period 1961-1969. The investment in chlorine-producing facilities in 1969 approximated $1.7-$2 billion. During the past decade, about $1 billion has been invested by the industry to achieve this production level, based on data published in 1964.

Another interesting example is the battery industry. Figure 2 shows the value of annual U.S. shipments of both primary and secondary types during most of the past decade through 1967 (11). The rate of increase of total battery shipments has been similar to that shown in Fig. 1, *i.e.*, an approximate doubling during the decade.

Falk and Salkind (12) in their recent book on "Alkaline Storage Batteries" estimate that the European demand for batteries is slightly smaller than that in this country. Furthermore, the rapid growth of battery-making facilities in many of the emerging nations of the world strongly suggests that the worldwide demand will continue to rise.

Figure 3 shows the growth in the electronic components market (13) during the past decade with separate lines for two important segments, semiconductors and capacitors. All parts of this important industry have doubled in ten years, just as in the chlor-alkali and battery industries.

In the field of metals, the aluminum industry is one in which electrochemistry plays a vital role. Although this industry had an explosive growth in the 1940's and 1950's, it has continued to grow as shown by the annual output data presented in Fig. 4 (1-10). The growth rate shown amounts to more than doubling the output in a decade.

It is difficult to obtain comparable growth data for the other electrochemical industries on which our Society is dependent. Table I shows some estimates of the value of U.S. products of the above four and one additional electrochemical industry for three years, 1967-1969, where the values have beeen available. The growth in the electroplating industry (14) has also been significant. Thus we may conclude that all or most

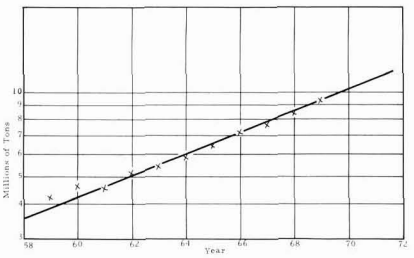

Fig. 1. The annual production of chlorine in the U.S.A.

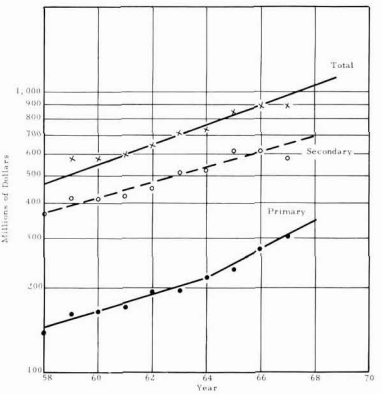

Fig. 2. The value of annual battery shipments in the U.S.A.

* Electrochemical Society Active Member.

[1] The Electrochemical Society Presidential Address, delivered at the Los Angeles Meeting of the Society, May 12, 1970.

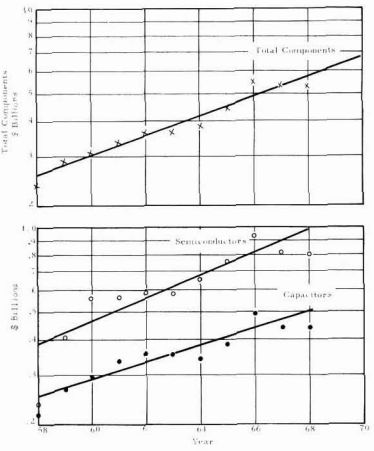

Fig. 3. U.S. factory sales of electronic components

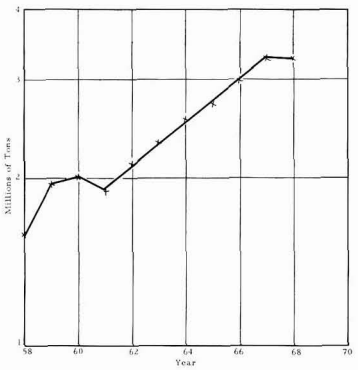

Fig. 4. The annual production of aluminum in the U.S.A.

of the electrochemical industries have experienced significant growth in the past decade. These and other electrochemical industries are the ones which depend on the Society for the leadership in technology that is so necessary to their growth.

In each electrochemical industry, major changes in product or process have helped meet the increased demand. In the chlor-alkali industry, there has been an increasing trend to the use of mercury cells and, in the last few years, a trend toward the use of the metal anode has developed. Pollution charges may speed up these changes if present indications can be believed.[2] The battery industry has profited from the increased consumer acceptance of the alkaline MnO_2-zinc and the sealed nickel-cadmium and silver-zinc rechargeable systems. The alkaline MnO_2-zinc and magnesium primary cells have grown to commercial status. Furthermore, there have been many improvements in existing types which have materially added to the demand. In the electroplating industry, new methods of plating continue to be offered. New processes to be used alone or in combinations have resulted in major improvements in the corrosion resistance of plated products. Processes for plating the exotic metals from fused salt baths have provided economical ways of efficiently utilizing these expensive materials. The developing area of electrochemical machining of metals, which one might hesitate to include in the electroplating group, appears to be well on its way to becoming a sizable industry. Plating onto plastic substrates has reached commercial acceptance and has materially increased the demand for electroplated products. In the electronic industry, the application of solid-state devices, *e.g.*, integrated circuits of many types, has been widely used to provide more portable, more serviceable, more attractive units for industry and consumer alike.

[2] Recent articles (15), appearing in many newspapers, reported that mercury lost from certain chlorine-manufacturing plants had found its way into one or more of the Great Lakes. The mercury content of certain fish had been found high enough to poison humans and fishing had been prohibited.

Table I. Value of U.S. products by industries in millions of dollars

	1967	1968	1969
Chlor-alkali	$1,170	$1,250	$1,400*
Batteries	890	—	—
Electroplating	2,760	3,000	3,300*
Electronic components	5,356	5,294	5,000*
Aluminum	1,972	—	—

* Predicted values.

The important growth in new areas of electrochemistry should not be overlooked. The application of electro-organic synthesis in the preparation of an intermediate for nylon manufacture adiponitrile by the Monsanto organization (16) is an important example. In addition, some new areas of industrial electrochemistry have grown almost explosively. For example, ion-selective electrodes, water detection and determination devices, coulometers, and many instruments devised for the measurement and control of important processes represent perhaps small but rapidly growing industries in the electrochemical area.

In four of the examples discussed above, the growth of production during the past decade has been greater than the approximate 70% increase in the Gross National Product (17). It is of course recognized that the latter includes a large monetary inflation, a fact that must be considered in any direct comparison with the growth of production quantities. Thus the growth in tonnage produced becomes of increased significance. Chlorine is not a consumer product and its growth reflects the increased demand in a wide range of industrial products. Thus it is used in many industrial organic chemicals, such as polyvinyl chloride, and in the paper industry. Batteries and electroplated products are used in a wide range of manufactured goods such as autos, radios, many luxury items, etc. Altogether, the growth of the basic electrochemical industries has made important contributions to the national wealth.

The Electrochemist

The electrochemist has indeed played an important role in the growth of the industry. The strength of the Society resides in the fact that the membership comprises people from academic, governmental, and industrial backgrounds. All groups are important to the continued success of the organization and to continued industrial growth.

In the past decade, the professional man working in electrochemistry has been faced with the problems inherent in an expanding industry. If he worked in industry, he hired and trained more people and probably supervised a larger number of employees than ever before. Since it is very difficult to hire new graduate chemists or engineers with previous training in electrochemistry, the experienced man has been forced to undertake in-plant electrochemical education of his newly acquired help. Many societies, including ECS, and a number of universities have offered short courses on specific branches of technology in an effort to assist in this educational effort in electrochemistry. A part of this training has been directed toward updating the workers already in the field. Along with the workers in other industries, the electrochemist has profited from the rising salaries even though inflation has tended to reduce their real value.

The Electrochemical Society Growth

In view of the fact that the business of electrochemistry has grown tremendously during the past decade,

we may well ask the question, "How has The Electrochemical Society grown during this period?"

The Electrochemical Society is the largest technical society serving the industry and it would be normal to expect that the Society membership would have increased at a rate comparable to that of industrial growth. Figure 5 shows that the actual growth (18) in membership during this period was only approximately 30%. The dashed line shows what it would have been if the growth had kept up with industry, *i.e.*, doubled in the past decade. At the same time, nonmember subscriptions to the Journal increased rapidly but did not quite keep up with the industrial growth rate. It is believed that this curve represents the increased acceptance of our Journal in libraries. The data in Fig. 5 represent world-wide figures and thus may not be directly comparable to the data in Fig. 1, 3, and 4 which represent data on industrial growth in the U.S.A. only.

Undoubtedly, the Society meetings and publications during the past ten years have contributed significantly to the technical knowledge on which industry growth was based. This situation raises a number of important questions that I would like to present a little later in this talk. One of these is the Society membership and a second is the orientation of the meeting programs.

In view of the fact that the electrochemist has apparently been busier than ever before, how has his technical output been affected? The number of papers that this group of workers has presented at various meetings is one measure of the technical output. Since it is virtually impossible to actually count the total number of such papers on a nation-wide scale, let us look at those that have been presented at ECS meetings during the last decade. Figure 6 shows these data and it is clear that there has been a definite and continuous uptrend, but that rate is not as great as in Fig. 1 through 4. Another method of measuring the technical output is the number of technical pages published. Figure 7 shows that the number of pages published by the ECS has not quite doubled in each of the two past decades.

The costs of publication and other Society operations have risen over the past years and it has been necessary to increase the membership dues periodically. Every effort has been made to see that such increases in dues are held to a minimum both in number and amount. The record is shown in Fig. 8. I believe we can claim that the ECS dues have increased less markedly than those of many other Societies. As you will see in later charts, the membership dues have not risen as fast as the Society costs of operation. This fortunate situation has been possible by somewhat larger increases in nonmember subscription rates and by the use of page charges to help defray a part of the cost of publication.

If the data of Fig. 7 and 8 are combined, it is possible to calculate what the Society member paid per page per year for the JOURNAL and ECT when the latter was published. Figure 9 shows this information as the annual cost per page over this period. Surprisingly enough, it has fallen from about 1.6 cents to about 1.2 cents at the present time. When one recognizes that one page in the JOURNAL is about equivalent to three pages in a modern scientific book, this reduces the cost of an equivalent book page to about 0.4 cents. As you know, a page of a modern scientific book costs from 4 to 6 cents—at least ten times the price of the same text space in the JOURNAL.

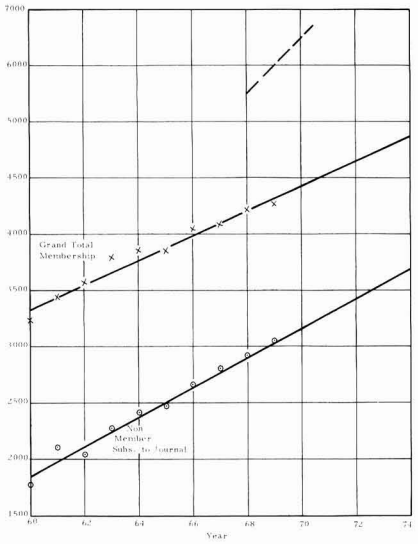

Fig. 5. Growth of The Electrochemical Society

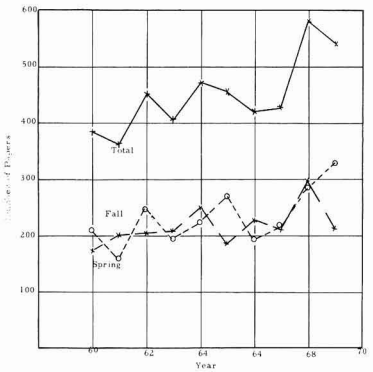

Fig. 6. Number of Technical Papers presented at National Meetings.

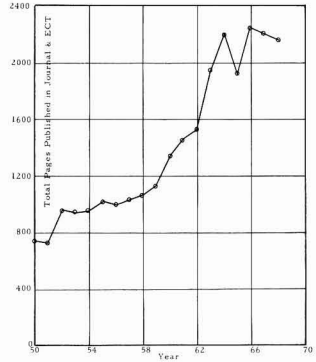

Fig. 7. Electrochemical Society publications

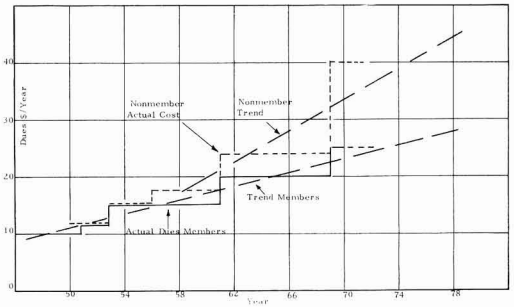

Fig. 8. Electrochemical Society costs to members and nonmembers

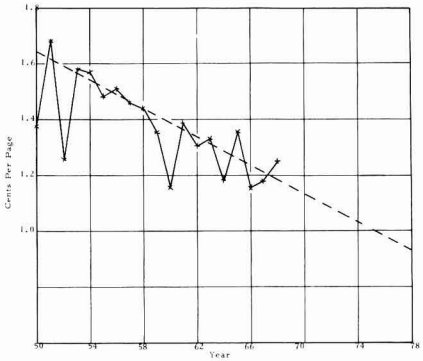

Fig. 9. Page cost of ECS publication to members

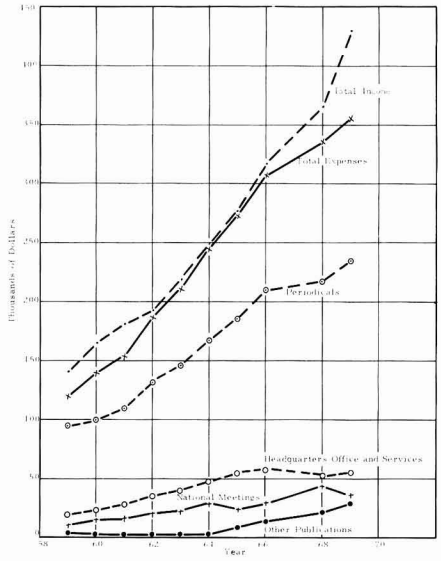

Fig. 10. Annual expenses of The Electrochemical Society

Figure 10 shows a chart giving the annual expenses of the Society over the same period. It is clear that the small surplus is shown by the small area between total income and total expenses. However, we cannot be complacent because we already know that printing costs will rise 5% in 1970. Other costs of operation can be expected to follow upward.

The largest part of the expenditure are the publication costs of the JOURNAL, the abstract booklets, and various softbound monographs. These are the Society communications media and, because they are so popular with members and nonmembers alike, the Society derives important financial support for the activities and the services provided to the members. Some other smaller items are shown on the expense chart, Fig. 10, such as the ECS Headquarters Office costs and National Meeting expenses.

Figure 11 shows the total annual income of the Society over the last ten years and some of the important sources of that income. It is clear that the member's dues are an important item but the amount from this source is not as large as that obtained from nonmember subscriptions. Moreover, the latter are growing more rapidly than the membership. Several small items also help materially to bolster Society income. National Meetings do provide income but they also cost an appreciable amount to operate, so the net surplus is not as large as one might think. However, Royalties on Monographs, income from Extended Abstracts, and

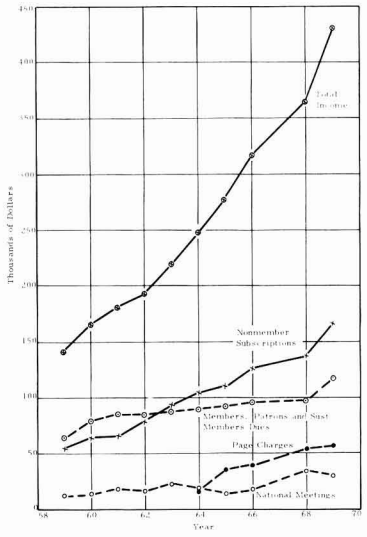

Fig. 11. Annual income of The Electrochemical Society

sales of Society softbound publications amounted to $22,000 in 1968. Not to be overlooked is the income from invested funds. In 1969, this amounted to about $15,000.

In considering these records, it should be recognized that the Society is growing both in size and in its service to the membership. The Headquarters Office has taken on more responsibilities, such as the preparation and sales of Extended Abstracts, once handled entirely by the Divisions. Softbound publications of various symposia are another area where the Headquarters Office has played an increasing role.

These charts emphasize that the Society operations are being managed efficiently. Thus, a small but healthy surplus results. The finances are periodically reviewed by the various committees involved and any surplus is invested in appropriate stocks recommended by the Investment Committee.

The only reason a surplus exists at the end of each year is because a minimum staff is maintained at the Headquarters Office and the Society depends on the time and effort freely contributed by hundreds of its members. In the past, this group of devoted and generous people have built the Society to its present state. The continuation of these contributions is effectively helping the Society to grow today. It should be recognized, however, that as the Society operations become larger and more complex, we must look forward to providing even greater services to the members.

Figure 12 shows the progress made in developing one part of Society finances designated as the Society Reserve fund. About 1959 it was recognized that such a

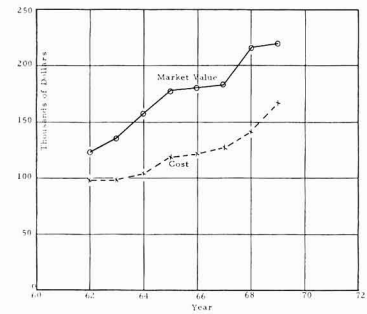

Fig. 12. Society Reserve Fund

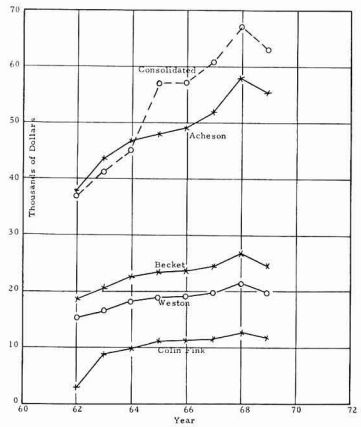

Fig. 13. Market value of principal invested for specific funds

program was vital to the future welfare of the Society. The objective at that time was to build up this portfolio to the point where its value equaled one year's budget. Although the value of this portfolio amounted to over $246,000 at the end of 1969, this objective has not yet been achieved and we recognize we must continue to build this investment as inflation reduces the purchasing power of our money.

Awards

In looking at the finances of the Society, it should be recognized that a number of special funds have been established as memorials to various individuals who have contributed importantly to the Society. These funds are used for various awards given by the Society. Moreover, these funds are not available to the Society for general use in an emergency and must be considered on a separate basis from the Society Reserve Fund. Figure 13 shows how four of these award funds and the Consolidated Fund have grown during the past few years. Table II shows a list of nine awards given by the Society periodically to outstanding scientists and students. In addition to awards made at the Society level, there are a number of awards given by the Divisions and the Local Sections of the Society. These are also listed in Table II. These awards help to encourage interest and excellence in electrochemistry and related fields.

From the list of awards and fellowships given above, it seems quite clear that the Society is fulfilling its objective of recognizing and supporting technical excellence in many fields.

Table II. Electrochemical Society Awards

Award	When granted	Value	Date of origin
Acheson Award	Alternate years	Medal + $1000	1929
Palladium Award	Alternate years	Medal + $100	1951
Edward Weston Fellowship	Annually	$1000	1931
Colin Garfield Fink Fellowship	Annually	$1000	1962
Electrochemical Society Fellowship	Annually	$1000	1960
F. M. Becket Award	Alternate years	$1500	1962
Two Young Author's Prizes	Annually	$150	1929
Joseph Richards Memorial	Occasionally	Lecture funds	1932
Division Awards			
Battery Division			1958
Dielectrics and Insulation			1967
Electronics Division			1969
Local Section Awards			
Cleveland		G. W. Heise Medal	1960
National Capital		Wm. Blum Award	1957
Ontario-Quebec		W. Lash Miller Award	1969
Southern Calif.-Nevada		Graduate Student	1969

Although it may appear that the Society award program is adequate at the present time, it seems clear that these activities should be expanded in the future and definite steps should be taken in this direction. Only by recognizing and rewarding outstanding individuals for their contributions in electrochemistry can the Society maintain its leadership in this important field.

What of the Future?

On the basis of all these considerations, can we make some comments about the future of electrochemistry and of the Society? Probably we should prefix such comments with some hopes and assumptions, thusly:

1. That the general character of the Society remains as it is today.
2. That no major effort to explore or annex new fields of technology is undertaken.
3. That business growth continues in the general direction and at a rate similar to that of the last 20 years.

In view of the encouraging growth of the electrochemical industries in the past decade, it appears safe to predict that their growth will continue. The present trend toward a plentiful supply of low-cost electrical power should encourage new industrial developments in this field. The fact that the electrochemical industries have a broad and diversified base of operations should help materially. Thus we can be optimistic about the future of the electrochemical industries and the opportunities presented to the technical man entering this field.

We have shown that the Society has progressed financially, in several areas of publication, and in awards given to outstanding members. However, when we look at the tardy growth of the membership in Fig. 4, we must agree that the Society has failed to attract many people in the industry. The electrochemical industry grew, they hired more people, trained them as electrochemists, and paid them well. Why, then, have these new electrochemists not joined the Society? In a technically based growing industry, the scientist and engineer are in the forefront of new technology. It is recognized that much of their work and their results may be proprietary. Nevertheless, these people represent an important segment of the technological industry and they can be a very dynamic part of the Society if they can be interested in contributing their time, efforts, and ideas to its growth. How can the Society attract these individuals?

In our present type of meeting, it is difficult for a newcomer from industry to establish a competence and rapport with others in the same field except through the medium of presenting papers. Any individual who seriously follows this discipline will establish a reputation. In doing so, he competes directly with papers offered by the academic segment of the Society. There is often a wide gap between these two groups, even in the same field of electrochemistry, and it is the opportunity of the program-planning officers to bridge this gap if at all possible. For example, it would definitely help the industrial man if symposia subjects were announced well in advance of the meeting so the interested author would have the necessary time to prepare his manuscript and abstracts and obtain clearance before submitting his title to the Society. Actually, it appears to many technical men in industry that their interest in the Society would increase if more industry-oriented papers were presented. Technical men want to talk with their colleagues and counterparts and the Society meetings offer an excellent opportunity. More conferences and less emphasis on formal presentations of papers might help provide the medium for such an exchange.

A Challenge for the Future

Here, then, is the challenge to the Society to redouble its efforts to appeal to a larger number of industrial electrochemists of all disciplines, to encourage them to attend its meetings, and to persuade them to become active members participating in Society af-

fairs. Then, and only then, can our Society feel that it has kept up with the industries it serves. In fact, such growth may be necessary for the survival of the Society as an important factor in the future of applied electrochemistry.

REFERENCES

1. "Report of the Chlor-Alkali Committee of the Industrial Electrolytic Division for the year 1960," J. E. Currey and C. A. Hampel, *This Journal*, **108**, 1001 (1961).
2. "Report of the Chlor-Alkali Committee of the Industrial Electrolytic Division for the year 1961," J. E. Currey and C. A. Hampel, *Electrochem. Technol.*, **1**, 56 (1963).
3. "Report on the Electrolytic Industries for the year 1962; The Chlor-Alkali Report," J. E. Currey and D. E. Swanberg, *ibid.*, **1**, 191 (1963).
4. "Report on the Electrolytic Industries for the year 1963. The Chlor-Alkali Report," D. E. Swanberg and R. H. Geise, *ibid.*, **2**, 170 (1964).
5. "Report on the Electrolytic Industries for the year 1964," R. H. Geise and J. R. Newberry, *ibid.*, **3**, 172 (1965).
6. "Report on the Electrolytic Industries for the year 1965," J. R. Newberry and L. G. Henry, *ibid.*, **4**, 438 (1966).
7. "Report on the Electrolytic Industries for the year 1966," L. G. Henry and J. H. Sullivan, *ibid.*, **5**, 478 (1967).
8. "Report on the Electrolytic Industries for the year 1967," J. H. Sullivan and R. R. Dukes, *ibid.*, **6**, 365 (1968).
9. "Report of the Electrolytic Industries for the year 1968," R. R. Dukes and R. G. Milner, *This Journal*, **117**, 9C (1970).
10. "Report of the Electrolytic Industries for the year 1969," R. G. Milner and T. C. Jeffery, *ibid.*, **117**, 00C (1970).
11. U.S. Dept. of Commerce, 1967 Census of Manufacturers, October 1969. Primary Batteries, *Dry and Wet* Preliminary Report MC 67(P)-36E-2 Secondary Batteries, Preliminary Report MC 67(P)-36E-1.
12. S. U. Falk and A. J. Salkind, "Alkaline Storage Batteries," John Wiley & Sons, Inc., New York (1969).
13. Consumer Electronic Sales Data taken from the Electronic Industries Association Year Book 1969, pp. 55, 56, Electronic Industries Assn., 1721 De-Sales St. N. W., Washington, D. C., Marketing Service Dept.
14. Neil A. Martin, "Scratching the Surface," Barron's pp. 11, 14, 16, Dec. 9, 1968.
15. R. Leger, "Mounting Peril, Mercury Contamination of Fish and Livestock Alarms Health Experts," *Wall St. Journal*, April 28, 1970.
16. Anon., "Electrochemical Process Yields Organics," *Chem. Eng. News*, p. 69, Oct. 14, 1963.
17. U.S. Dept. of Commerce Statistical Abstracts of the United States, 1969.
18. The membership growth publication and financial charts are based on data supplied by the National Headquarters Office of The Electrochemical Society.

SECTION NEWS

Southern California-Nevada Section

The 6th Advances in Battery Technology Symposium, sponsored by the Southern California-Nevada Section, will be held on December 4, 1970 at the Union Oil Auditorium, 461 S. Boyleston Street, Los Angeles, Cal. Some of the invited speakers and topics are:

Elton Cairns, Argonne National Labs —"Electrode Structures for Molten Salt Batteries"

David Feder, Bell Telephone—"Bell System Lead Acid Battery Design"

Galen Frysinger, Electric Storage Battery, Inc.—"Batteries for the 70's"

Jose Giner, Tyco Laboratories, Inc. —"Rechargeable Oxygen Electrode"

George Hoffman, McDonnell Douglas Astronautics Co.—"The All-Electric Bus"

T. Katan, Lockheed Missiles & Space Co.—"Structure and Performance of Oxygen Electrodes"

C. J. Menard, Gould Inc.—"Nickel Plaque Substrates for Cadmium Electrodes."

Attendance is open to all interested persons. The proceedings of the symposium will be published by the Section as in previous years. The registration fee of $10 will entitle attendees to a copy of the proceedings when published.

Further information may be obtained from: E. L. Littauer (Joint Chairman) Manager, Electrochemistry Dept., Lockheed Aircraft Service Company, P. O. Box 33, Ontario, Cal. 91764

NEW MEMBERS

It is a pleasure to announce the following new members of The Electrochemical Society as recommended by the Admissions Committee and approved by the Board of Directors in August 1970.

Active Members

Broyde, Barret, Princeton, N. J.
Dawson, L. R., Summit, N. J.
De Bie, Edouard, Hoboken, Belgium
Fredlein, R. A., Philadelphia, Pa.
Hein, E. R., Doylestown, Pa.
Kumar, Satish, Wappinger Falls, N. Y.
McLintock, G. A., Ottawa, Ont., Canada
Mehlhaff, L. C., Tacoma, Wash.
Nickless, H. C., Haverhill, Mass.
Podbielancik, V. S., Seattle, Wa.
Stroup, E. R., Arlington, Va.
Voegerl, Manfred, Los Angeles, Cal.
Williams, R. L., Blue Bell, Pa.

Student Member

Knights, R. L., Seattle, Wa.

PEOPLE

W. E. Kuhn was recently appointed Research Associate Professor, Materials Science and Metallurgical Engineering Department, University of Cincinnati, Ohio, 45221.

Among his interests will be the development of research programs in fine particle technology and high temperature chemistry. With respect to the former, emphasis will be placed in studies of the fundamentals of powder consolidation and applications to existing and conceptual fabrication processes involving metals, alloys, ceramics and composites. With respect to the latter, processes involving vapor phase reactions utilizing electric arcs and plasmas will be developed. Also, fundamental studies directed ultimately to economic materials production processes will be undertaken.

W. E. Kuhn was formerly Manager of the Materials Division, Spindletop Research, Lexington, Ky. He is a member of The Electrochemical Society and Past Chairman of the Electrothermics and Metallurgy Division. He has edited two Wiley volumes based on symposia sponsored by the Society and is the author of several papers published in the Journal.

NEWS ITEM

ASTM Symposium on Localized Corrosion

Call for Papers

A Symposium on Localized Corrosion is scheduled for the ASTM annual meeting in Atlantic City, N.J., June 27-July 2, 1971. This Symposium is sponsored by ASTM Committee G-1 on Corrosion of Metals, Subcommittee 5 on Laboratory Corrosion Tests.

Papers are invited in the areas of:

1—Recent advances in testing for localized corrosion including intergranular, pitting, crevice, exfoliation and de-alloying corrosion.

2—Recent advances in the understanding of localized corrosion.

Offers of papers with a title and some indication of the content should be sent immediately to: Dr. Michael Henthorne, Carpenter Technology Corp., Reading, Pa. 19603.

A 500-word abstract will be required in December 1970, with the final manuscript due in March 1971.

BOOK REVIEWS

"Advances in Electrochemistry and Electrochemical Engineering", Vol. 7 (Electrochemistry), Ed. P. Delahay. Published by Interscience Publishers (A Division of John Wiley & Sons, New York), 1970. 366 pages; $18.50.

This is the seventh volume in the important series of books edited by Delahay and Tobias, namely "Advances in Electrochemistry and Electrochemical Engineering." This particular volume has been edited by Delahay and deals with some topics in fundamental electrochemistry. It consists of five chapters which are: "The Electrical Double Layer in Nonaqueous Solutions" by Richard Payne; "Reference Electrodes in Aprotic Organic Solvents" by J. N. Butler; "Faradaic and Non-Faradaic Processes" by Roger Parsons; "The Electrochemical Reduction of Organic Compounds" by G. J. Hoytink; "Hydrogen Overvoltage and Adsorption Phenomena Part III. Effect of the Adsorption Energy of Hydrogen on Overvoltage and the Mechanisms of the Cathodic Process," by L. I. Krishtalik.

In his lucid chapter on double layer, Payne has chosen to restrict himself to a discussion of the work on mercury only, probably because the work available on solid electrodes, somewhat

scanty, difficult-to-analyze, and discrepant as it is, does not "contribute much to the basic understanding of the double layer." Payne is quite correct in his conclusion, although some mention of results, even approximate ones, on solid metals would have made his chapter more valuable to the experimental electrochemist working in nonaqueous media. He has presented an excellent critical survey of the experimental work on the subject even though there is virtually no section on the formal theoretical aspects of the various concepts he uses in his discussions. These theoretical matters, of course, have already been discussed in previous reviews and books, etc., on double layer.

Butler's contribution is an extremely useful one since it will undoubtedly be frequently consulted by many electrochemists working in nonaqueous media. He has achieved successfully the difficult task of organizing an enormous amount of work (there are 458 references in this chapter) into a compact and readable chapter. It is unfortunate that he has not included a small section on the theory of reference electrodes (notwithstanding the book by Ives and Janz) in terms of exchange current densities, impurity reactions, mixed potentials, and recovery response subsequent to the polarizing pulse of significant value, etc. This is important because there are a few workers, especially in the field of electro-organic syntheses, who would dip a wire of a nonnoble metal (or even a small mercury pool) in relatively impure solutions and assume that it works satisfactorily as a reference potential. His statement on the criteria for a satisfactory reference electrode (pg. 79) is no doubt quite valuable. It does not, however, deal with the conceptual basis of a satisfactory reference electrode.

Parson's review, on the whole, is an excellent one, which is not at all unexpected. He discusses the now well-recognized idea that in the nonsteady-state measurements, a priori separation of Faradaic and Non-Faradaic processes is not justified for any electrode which is not ideally polarized. This procedure is particularly invalid for electrode reactions having high exchange current densities, e.g. several metal deposition reactions or other electrode processes in which the electrode tends to approach a nonpolarizable situation. Parsons formulates clearly Delahay's recent ideas on the subject as well as previous important contributions of Llopis et al. and some other workers. There are also sections on Barker's equivalent circuit approach to Warburg impedance and on experimental aspects of the subject. Work of several investigators (e.g., Lorenz, Randles, Sluyters, and Reinmuth) on the various aspects of the study of fast reactions also receives some attention. Basically, Parsons has attempted to focus, in a critical way, the impact and importance of Delahay's recent generalized treatment of Faradaic and Non-Faradaic processes against the background of pre-(Delahay-Susbielles) work on the subject. One cannot help noticing the absence of mention of other viewpoints and some criticisms of Delahay's ideas; e.g., the lively commentaries [especially Conway's comparison of Delahay's theory with the converse situation to that which obtains in the Butler (J.A.V.)—Armstrong treatment of the open-circuit decay] of several workers during the discussion of Delahay's paper in the ECS Symposium in 1966. Nor is there any mention of the debate between Delahay and Weir. Parson's assessment of some of these contentions would have definitely added a new dimension to his presentation.

Hoytink's chapter deals with the experimental work on polarographic behavior of aromatic hydrocarbons as well as Hoytink's considerable contributions to the theoretical aspects of the problem in terms of approximate quantum mechanical treatment of the subject. This is a very personal review in the sense that its main theme is to outline the viewpoints and work of Hoytink and co-workers on the subject of aromatic reductions. Hoytink has definitely been a resounding success in achieving his stated goal. From the foregoing comments, it follows that a comprehensive modern review on electroreductions covering the complete spectrum of work done in the last few years (since the article by Popp and Schultz in 1961) has yet to be written.

Krishtalik's chapter is the most provocative article in the book since it deals with the perennial problem of the mechanism of hydrogen evolution reaction (HER) in a somewhat unorthodox manner. As regards presentation, this chapter is not well sectionalized and at points the interlacing of arguments, which do not always seem to follow sequentially, gives the impression of a Joycean exercise in electrochemical writing. In his discussion of HER on mercury, he states that in addition to the ordinary potential region for HER one may define two limiting cases. One region he calls barrierless: in his theory this region is close to the reversible potential and here $\alpha \rightarrow 1$ and the heat of activation is maximum. The other limiting region is activationless: here $\alpha \rightarrow 0$ and heat of activation $\rightarrow 0$. This is in actual fact the region at extremely high potentials where the heat of activation approaches zero since $(\Delta H^* - \alpha \eta F) = 0$. This situation at very high cathodic potentials would then be somewhat similar to the ordinary very fast reactions proceeding with zero or low activation energies.

Krishtalik discusses at some length the theoretical and experimental implications of these rather specialized cases in terms of jargon, not all of which is universally employed.

His review of the material pertaining to the relationship between M-H bond strength and mechanism of HER on various metals leaves a great deal to be desired. He creates some confusion by using interchangeably heat of ad-

sorption and bond energy in scores of sentences where he should have used neither; in fact he means by these terms bond strength (or bond dissociation energy in Pauling's terminology) of an isolated M-H bond. It is incredible that he fails to mention several key papers (Ruetschi and Delahay; Conway and Bockris; recent work of Matthews and Srinivasan with Bockris) and reviews (Kita) on the subject. Nor is there any mention of the all-important discussion of the subject that followed Kita's review paper in the ECS Symposium in 1966. Despite the fact that Krishtalik's review is not quite comprehensive, it contains some of the most controversial, stimulating, and sophisticated arguments to be found in the book. This chapter is not recommended to an investigator interested in HER from the point of view of applied work, e.g. corrosion and protection of metals, etc. However, it is strongly suggested that a graduate student who is in the field of fundamental electronics and is anxious to impress his research director by his electrochemical erudition should achieve a critical mastery (the keyword being critical) of the wealth of arguments presented.

In conclusion, in one respect or another, every one of the chapters contained in this book is a distinguished article. There are some matters of detail, of course, which are contestable. Many of the experimentalists will be grateful to Payne and, especially, Butler for their chapters for years to come. The contributions by Parsons, Hoytink, and Krishtalik, in addition to their being useful to the practicing electrochemist, should also form good subjects for provocative, even electrically charged, graduate seminars.

A final point. It seems that Delahay and Tobias have also succeeded in persuading their publishers to adopt a more electrochemical posture. It is stated on pg (iv) that "The paper used in this book has pH of 6.5 or higher. . . . this will contribute to its longevity." In this connection, it would be interesting to know the pH of the paper used in books published by the Plenum press!

In closing, purchase of this book is strongly recommended to any one pursuing modern electrochemistry.

Ashok K. Vijh
Hydro-Quebec Institute of Research
Varennes, Que., Canada

"Gas-Liquid Reactions," P. V. Danckwerts. Published by McGraw-Hill, New York (1970). 276+XIII pages, $11.50.

"Digital Simulation of Continuous Systems," Y. Chu. Published by McGraw-Hill (1969). 423+XVII pages; $14.50.

"Describing Chemical Engineering Systems," W. E. Ranz. Published by McGraw-Hill (1970). 248+XX pages; $9.95.

"Gas-Liquid Reactions" is a monograph on the chemical absorption of gases into liquids. According to the author, it is written for the process designer, the research worker and as a "working textbook" for the graduate student. It is a useful book—one which no serious worker in mass transfer should be without, if for no other reason than that Professor Danckwerts is a well known authority on the subject, having contributed significantly to its theoretical and experimental understanding.

Some deficiencies are best got out of the way first: The introductory discussion of liquid diffusion and gas-liquid equilibrium, admittedly brief, is so superficial that it could well have been left out altogether. Secondly, although the mass transfer characteristics of industrial absorbers are discussed and diagrams of laboratory apparatus given, there are no flowsheets of industrial processes nor is there much discussion of industrial practice. There are, of course, other sources for this information. But in our opinion, a few such illustrations would have been helpful.

A comparison to the earlier work of Professor Astarita on mass transfer with chemical reaction would not be out of place here. In many aspects of suborganization and content, the two books are similar. Both treat essentially solutions to the one-dimensional diffusion equation for fast and slow reactions of various orders, reversible and irreversible. Both contrast the predictions of the film and penetration models for a variety of absorption systems. Both treat laboratory apparatus, such as the string-of-disks absorber, and industrial equipment, such as the packed tower. But of the two books, "Gas-Liquid Reactions" is the longer. Its philosophical tack is toward practical applications and its overlying organization is by hydrodynamic rather than kinetic regime. Theoretical treatment is illustrated by many examples of worked-out absorption calculations and there is an exhaustive review of the literature. Indeed, of the nearly 300

ADVERTISER'S INDEX

citations about 40 are to the papers of Professor Danckwerts and coworkers.

"Digital Simulation of Continuous Systems" is a well written exposition of MIMIC, FORTRAN and DSL/90. The author, a professor at the Computer Science Center of the University of Maryland, begins with an introduction to digital simulation and the history of the early languages. A description of MIMIC follows, then a chapter each on engineering and mathematical applications. The former are mostly from aerospace engineering and automatic control theory; the latter deal with Fourier series, autocorrelation functions and linear and nonlinear ordinary differential equations. There is a good treatment of FORTRAN and FORTRAN simulation, a discussion of the logic and construction of the SIMIC (a simpler MIMIC language) processor and a final chapter on DSL/90 simulation.

A number of simulation problems and computer programs are presented as examples as well as student exercises at the end of most chapters. Although no examples or applications have been drawn from chemistry or chemical engineering, the book should provide a readable, well organized account of digital simulation to students or to practicing engineers unfamiliar with the field.

"Describing Chemical Engineering Systems" is about mathematical modelling of a variety of chemical engineering systems. And about the thermodynamic and conservation laws that govern such systems. We must admit a bias against programmed instruction manuals with problem sets titled "Things to Do; Things to Think About," and, "More Things to Do and to Think About." Overlooking that, a beginning student armed with a good handbook and a good deal of persistence may well profit from a programmed-learning-via-problems approach to chemical engineering concepts. But in spite of the author's design, a practicing engineer contemplating graduate study would probably do better to choose a specific text in the area he intended to review. Nevertheless, the writing is clear, the notation excellent and there is a wealth of good problems.

Arvo Lannus
Department of Chemical Engineering
The Cooper Union, New York

POSITIONS WANTED

Please address replies to the box number shown, c/o The Electrochemical Society, Inc., 30 East 42 St., New York, N.Y. 10017.

Battery Engineer—12 years' experience in high energy density battery projects ranging through proposal writing, R&D, design, engineering, production, trouble shooting, customer liaison and program management. Personable, competent, gets job done. B.Ch.E. '58 plus graduate credits. Seeks new challenge. Reply Box C-34.

CVD Specialist/Physical-Inorganic Chemist—M.S. in Physical/Analytical Chemistry. 25 years' experience in chemical vapor deposition R&D and consulting. Patents. Publications. Desires position in CVD R&D, or process commercialization in MOS/LSI circuit applications, or high performance materials applications. Age 53. Reply Box C-35.

Physical/Analytical Chemist—M.S. Extensive experience in Solid State Science. Experience includes semiconductor, infrared, analytical and electrochemistry. R & D in semiconductor materials and device fabrication. Silicon, selenium and germanium devices; insulating films; silicon epitaxy; infrared detectors. Also quality control using analytical wet chemistry and instrumental analysis. Reply Box C-37.

Electrochemist—B.A. 1959—graduate studies. Desires challenging position in small to medium size company. Ten years basic and applied research in batteries, corrosion, electrodeposition. Reply Box C-38.

Electrochemist—Ph.D.—Six years' basic and applied research in electrodeposition, high energy density batteries, corrosion, and electroanalytical techniques. Publications. Seeks R & D or teaching position. Reply Box C-39.

Positions Wanted

Society members of any class may, at no cost and for the purposes of professional employment, place not more than three identical insertions per calendar year, not to exceed 8 lines each. Count 43 characters per line, including box number, which the Society will assign.

POSITIONS AVAILABLE

Please address replies to the box number shown, c/o The Electrochemical Society, Inc., 30 East 42 St., New York, N.Y. 10017.

Asst. Director of Research—Electrochemist, Ph.D. minimum 5 years industrial R&D experience. Must be solid man with initiative and drive. Contact in confidence, Electrochimica Corporation, 1140 O'Brien Drive, Menlo Park, Calif. 94025.

Battery Production Manager—man of proven experience wanted to head up production in new operation. Salary plus equity participation. Contact in confidence, Elca Battery Company, 1140 O'Brien Drive, Menlo Park, Calif. 94025.

Battery Design Manager—Man of proven experience wanted to head up new operation. Salary plus equity participation. Contact in confidence Elca Battery Company, 1140 O'Brien Dr., Menlo Park, Calif. 94025.

Sr. Cell Design Engr. & Sr. Process & Tooling Engrs—for battery manufacture. New ground floor opportunities in new battery operation. Contact in confidence Elca Battery Company, 1140 O'Brien Drive, Menlo Park, Calif. 94025.

ELECTROCHEMIST
PHYSICAL CHEMIST
CHEMICAL ENGINEER
ELECTROCHEMICAL ENGINEER
MECHANICAL ENGINEER

Excellent opportunities exist for recognition and advancement in a Research and Development program involving a new product for Pollution Abatement.

Experience is needed in one or more of the following fields:

Electrochemical Manufacturing
Electrodeposition
Fuel Cells
Batteries
Thermodynamics
Hydraulics

A new well-equipped laboratory for this project is situated in the pleasant suburb of Warren, convenient to four major universities, highly recognized elementary and secondary school systems, and within a short distance of Michigan's famous outdoor and recreational activities.

Please send resume and salary requirements to:

Professional Employment Department
The Udylite Corporation
21441 Hoover Road
Warren, Michigan 48089

Equal Employment Opportunity

Udylite representatives will be present at The Electrochemical Society's Meeting in Atlantic City, N.J. Please consult the Society's Bulletin Board at the Registration Board in Chalfonte-Haddon Hall for location.

Call for Papers
139th National Meeting
Washington, D.C., May 9-14, 1971

Divisions which have scheduled sessions are listed on overleaf, along with symposium topics.

1. Symposium Papers.

Authors desiring to contribute papers to a symposium listed on overleaf should check first with the symposium chairman to ascertain appropriateness of the topic.

2. General Session Papers.

Each of the several Society Divisions which meet in Washington, D. C., can plan a general session. If your paper does not fit readily into a planned symposium, you should specify "General Session."

3. To Submit a Meeting Paper.

Each author who submits a paper for presentation at a Society National Meeting must do three things:

A—Submit one original 75-word abstract of paper to be delivered, use the form printed on the overleaf or a facsimile. This abstract is required for consideration for scheduling at the meeting. **Deadline for receipt of 75-word abstract is December 1, 1970.**

B—Submit original and one copy of an Extended Abstract of the paper. **Deadline for receipt of Extended Abstract is January 1, 1971.** See (5) below for details.

C—Determine whether the meeting paper is to be submitted to the Society Journal for publication. See (6) below for details.

Send all material to The Electrochemical Society, Inc., 30 East 42nd Street, New York, N. Y. 10017.

Unless the 75-word and required Extended Abstracts are received by stated deadlines, the papers will not be considered for inclusion in the program.

4. Meeting Paper Acceptance.

Notification of acceptance for meeting presentation, along with scheduled time, will be mailed to authors with general instructions no earlier than two months before the meeting. Those authors who require more prompt notification are requested to submit with their abstracts a self-addressed postal card with full author-title listing on the reverse.

5. Extended Abstract Book Publication.

Division programs will be the subject of an Extended Abstracts volume in a manner prescribed by the Society Board of Directors. The volume is published by photo-offset directly from typewritten copy submitted by the author. Therefore, special care should be given to the following instructions to insure legibility.

A—Abstracts are to be from 500 to 1000 words in length (maximum two pages, single spaced) and are to contain to whatever extent practical all significant experimental data to be presented during oral delivery.

B—Please send original and one copy of the abstract typed single spaced. Use white bond paper, size 8½ x 11 inches, with 1¼ inch margins on all sides. Typing guide forms are available from symposium session chairman and from National Headquarters. Submit all copy in black ink. No handwritten corrections, please.

C—Title of paper should be in capital letters. Author(s) name and affiliation should be typed immediately below. It is not necessary in the heading or body to designate paper as "Extended Abstract" or to quote the divisional symposium involved.

D—If figures, tables, or drawings are used total space for these cannot exceed one page. Submit only the important illustrations and avoid use of halftones. Lettering and symbols should be no smaller than ⅛ inch in size. Type captions no wider than figure dimensions, placing figure caption at bottom of figure and table title at top of table.

E—Mail to The Electrochemical Society, Inc., 30 East 42nd Street, New York, N. Y. 10017, unfolded.

Abstracts exceeding the stipulated length will be returned to author for condensation and retyping.

6. Manuscript Publication in a Society Journal.

All meeting papers upon presentation become the property of The Electrochemical Society, Inc. However, presentation incurs no obligation to publish. If publication in Journal is desired, papers should be submitted as promptly as possible in full manuscript form in order to be considered. If publication elsewhere after presentation is desired, written permission from Society Headquarters is required.

Washington, D. C., Meeting Symposia Plans–Spring 1971
May 9-14, 1971

a.) For receipt no later than December 1, 1970, submit a 75-word abstract of the paper to be delivered, on the form overleaf. b.) For receipt no later than January 1, 1971, submit two copies of an extended abstract, 500-1000 words.

Send all material to The Electrochemical Society, Inc., 30 East 42nd Street, New York, N. Y. 10017.

See details on preceding page.

Dielectrics and Insulation Division Symposia Plans

The Dielectrics and Insulation Division has planned Symposia on Electronic Applications of Ceramic Materials and Deposited Thin Film Dielectric Materials and Processes, as well as a Joint Symposium with the Electronics Division on Plastics for Environmental Protection and Encapsulation of Electronic Devices for the Spring Meeting in Washington, D. C., May 9-14, 1971.

Electronic Applications of Ceramic Materials

This Symposium will cover the general field of electronic ceramic materials. Specific topics to be included will be insulators or substrates for thick and thin film applications and electro-optic materials. A number of invited papers will be presented and contributed papers are also being solicited. For further information contact R. E. Mistler, Western Electric Engineering Research Center, P. O. Box 900, Princeton, N. J. 08540.

Deposited Thin Film Dielectric Materials and Processes

A Symposium on Deposited Thin Film Dielectric Materials and Processes is scheduled for the Spring 1971 Meeting of the Society.

There will be a number of invited papers; contributed papers are also being actively solicited. Subject matter for this symposium includes:

a. Studies on the electrical and mechanical properties of deposited thin film dielectrics.

b. New techniques for the deposition or control of thin film dielectrics.

c. Properties and applications of thin film dielectrics.

Comments and suggestions are welcome and should be directed to the Chairman of the Symposium, F. Vratny, and Co-Chairmen W. R. Sinclair and R. J. Strain, Bell Telephone Laboratories, Inc., Mountain Avenue, Murray Hill, N. J. 07974.

Dielectrics and Insulation and Electronics Divisions Joint Symposium Plans

Plastics for Environmental Protection and Encapsulation of Electronic Devices

The purpose of this Joint Symposium of the Dielectrics and Insulation and the Electronics Divisions is to present and discuss the various means to protect and encapsulate electronic devices and circuits by means of plastics and polymeric materials.

Topics of interest are the packaging requirements and device interactions (electrical mechanical, thermal, and chemical) as well as material types and properties. This includes techniques, equipment, testing, evaluation, repair, and long range reliability.

In particular we encourage papers on the theoretical and explanatory aspects of the behavior of plastics on electronic devices. All types of devices, both passive and active, including discrete semiconductors, integrated circuits, and hybrids will be considered. Suggestions and questions for the Dielectrics and Insulation Division should be directed to the Symposium Co-Chairman, A. Pfahnl, Bell Telephone Laboratories, 555 Union Blvd., Allentown, Pa. 18103. Suggestions and questions for the Electronics Division should be directed to the Symposium Co-Chairman, Ralph Olberg, Fairchild Research and Development Lab, Materials and Processes Department, 4001 Miranda Avenue, Palo Alto, Cal. 94304

Electronics Division Symposium Plans

In addition to the Joint Symposium with the Dielectrics and Insulation Division on Plastics for Environmental Protection and Encapsulation of Electronic Devices and the Joint Symposium with the Electrothermics and Metallurgy Division on New Techniques for Materials Characterization, the Electronics Division has planned a Symposium on Infrared Excited Visible Luminescence. There will also be Semiconductor General Sessions and Luminescence General Sessions.

Infrared Excited Visible Luminescence

The areas of interest for this Symposium will include the preparation, characterization, optical properties, energy transfer and luminescent properties of materials exhibiting luminescence from incoherent multiphoton excitation, as well as discussion of any properties of interest to their use in optoelectronic displays. Papers may range from theoretical investigations to device applications. For further information please contact Symposium Chairman Dr. Ralph Hewes, Lighting Research Laboratory, General Electric Company, Nela Park, Cleveland, Ohio 44112.

Semiconductor General Sessions

Original papers relating to the following areas are being solicited for the Semiconductor General Sessions.

1. Semiconductor Materials Preparation: synthesis, purification, crystal growth, shaping, epitaxy, heteroepitaxy, and thin film deposition.
2. Semiconductor Materials Evaluation: measurements of physical, chemical electrical, and optical properties.
3. Semiconductor Materials Processing for Devices and Integrated Circuits: diffusion, epitaxy, ion implantation, and effects of processing on materials properties.
4. Characterization of Semiconductor Materials for Specific Device and Integrated Circuit Application.
5. Dielectric Films Used on Semiconductor Devices and Integrated Circuits: grown films, deposited films, control of film properties, defects, patterning, MIS effects, breakdown phenomena in dielectric films, thin film capacitors, amorphous film switches, and dielectric isolation.
6. Metal Films Used on Semiconductor Devices and Integrated Circuits: film properties, silicon contact effects, deposition techniques and control, film defects related to substrate topology, electromigration, intermetallic formation, multilayer metallization, and burnout.
7. Resistive Films Used on Semiconductor Devices and Integrated Circuits: deposition techniques, control of film properties, and contact effects.
8. Reliability: physics of failure related to the materials and processes utilized in the fabrication of semiconductor components, and accelerated reliability testing.
9. Radiation Effects Pertinent to the Materials Systems Utilized in Semiconductor Devices and Integrated Circuits.
10. Packaging: materials and technologies important to the encapsulation of semiconductor components, and testing methods and results.

Suggestions and questions should be directed to the Chairman, I. A. Lesk, Motorola Semiconductor Products Division, 5005 East McDowell Road, Phoenix, Ariz. 85008.

Luminescence General Sessions

General sessions on luminescence and laser materials are being organized by the Luminescence Section of the Electronics Division for the Spring 1971 meeting in Washington, D. C. The areas of interest will include such topics as materials and phosphor synthesis, optical and luminescent properties of rare earth and non-rare earth activated phosphors, laser materials and properties, energy transfer, cathodoluminescence and phosphor screen applications.

Papers are being solicited from those workers active in research and development in these areas. The papers may range from theoretical investigations to device applications. While 25 minutes is the usual time allotted for presentation and discussion of scheduled papers, authors desiring more or less time should indicate this when submitting their short abstract. Questions concerning the program should be addressed to the Program Chairman, Frank C. Palilla, General Tele-

phone & Electronics Laboratories, 208-20 Willets Point Blvd., Bayside, N.Y. 11360.

There will also be a Recent News Papers Session. Triplicate copies of the 75-word abstract should be sent to Mr. Palilla at the above address. The submission deadline is April 1, 1971. Authors requiring more or less than the standard 15 minutes should so indicate.

Electronics and Electrothermics and Metallurgy Divisions Joint Symposium Plans

New Techniques for Materials Characterization

The Electronics Division is jointly sponsoring this Symposium with the Electrothermics & Metallurgy Division to be held during the Spring Meeting, Washington, D. C. May 9-14, 1971.

This Symposium will cover new techniques for surface and bulk characterization of materials of interest to The Electrochemical Society. Suitable topics include: scanning electron microscopy, electron microprobe analysis, auger electron analysis, field ion microscopy, and high resolution electron microscopy.

Invited papers will predominate but appropriate contributed papers are also welcome. The Symposium Chairman is Victor A. Phillips, General Electric Research & Development Center, P. O. Box 8, Schenectady, N. Y. 12301.

Electro-Organic Division Symposia Plans

The Electro-Organic Division will sponsor a Symposium on New Directions in Organic Electrochemistry and will hold General Sessions at the Washington, D. C., Meeting, May 9-14, 1971. In addition, this Division is cosponsoring a Symposium on Electrochemistry and Biological Processes with the Theoretical Division.

New Directions in Organic Electrochemistry

This Symposium will be organized by Prof. Ralph N. Adams, Dept. of Chemistry, University of Kansas, Lawrence, Kansas, and Dr. Thomas B. Reddy, Stamford Research Laboratories, American Cyanamid Co., 1937 W. Main St., Stamford, Conn. 06904. The object of the Symposium will be to explore new trends in organic electrochemistry. A round table discussion of important new areas in this field will be conducted. Potential contributors may contact Prof. Adams.

General Sessions

The Electro-Organic Division will also hold General Sessions and papers are needed for inclusion in such sessions. For information please contact Dr. Thomas B. Reddy, American Cyanamid Co., 1937 W. Main St., Stamford, Conn. 06904.

Electro-Organic and Theoretical Divisions Joint Symposium Plans

Electrochemistry and Biological Processes

The Electro-Organic and Theoretical Divisions are scheduling a Joint Symposium on Electrochemistry and Biological Processes for the Spring Meeting to be held in Washington, D. C., May 9-14, 1971. There will be approximately sixteen invited and contributed papers. The topics for discussion will be:

1. Electrochemistry of Biologically Significant Compounds
2. Charge Transfer in Membranes
3. Biological Electrodes

For further information, please contact, Dr. H. P. Silverman, Manager, Biosciences and Electrochemistry Dept., Systems Group of TRW, Inc., One Space Park, R1/2094, Redondo Beach, Cal. 90278.

Electrothermics and Metallurgy Division Symposia Plans

The Electrothermics and Metallurgy Division program for the Spring 1971 Washington, D. C., Meeting will include two Symposia, Chemical Reactions in Gaseous Discharges and Directional Solidification of Eutectics, as well as General Sessions. In addition the Division is cosponsoring a Symposium on New Techniques for Materials Characterization with the Electronics Division.

Directional Solidification of Eutectics

Recent developments in the application of controlled solidification of eutectic systems have identified the possibility of utilizing this technique to produce new materials for high temperature, high strength, as well as optical, electronic and magnetic applications. This Symposium will document the latest developments pertinent to directional solidification of eutectic systems including: theories of controlled eutectic freezing, crystallography and microstructure of eutectic alloys prepared by controlled solidification, as well as, utilization of modern chemical and analytical techniques pertinent to this area. Additional information can be obtained by contacting the Vice Chairman of the Electrothermics and Metallurgy Division, Dr. Joan B. Berkowitz, Arthur D. Little, Inc., 15 Acorn Park, Cambridge, Mass. 02140.

Authors wishing to submit papers for this Symposium should submit the normal 75-word and extended abstract by the appropriate date directly to Society Headquarters.

Chemical Reactions in Gaseous Discharges

The purpose of this Symposium is to discuss homogeneous gas phase reactions occurring in electric discharges and the engineering aspects of reactor design and scale-up. Papers pertinent to economic investigations or systems which possess commercialization feasibility would be particularly welcome. In addition the Symposium will cover research in the area of film deposition from species produced in the gas phase, including sputtering of material from target to a substrate.

Specific topics of greatest interest include:

1. Discussions of the basic mechanisms of discharge reactions and the relationship between the production of atomic and free radical intermediates and the electrical parameters controlling the discharge.
2. Proposals for reactor design and scale-up and evaluation of the economics of applying electric discharge chemistry.
3. Discussions of thin film deposition by the use of discharge devices, exclusive of transport of matter from electrodes.
4. Interpretation of material transfer processes occurring during sputtering glow discharge environments.

Authors wishing to participate in this Symposium should submit the normal 75-word and extended abstract directly to Society Headquarters by the appropriate dates. Additional information pertinent to this Symposium can be obtained by contacting Professor Alexis T. Bell, Department of Chemical Engineering, University of California, Berkeley, Cal. 94720, or Dr. Eric Kay, IBM Research Laboratories, Monterey and Cottle Roads, San Jose, Cal. 95114.

General Sessions

In addition to the Symposia on Chemical Reactions in Gaseous Discharges, Directional Solidification of Eutectics, and the Joint Symposium on New Techniques for Materials Characterization, General Sessions will be scheduled if sufficient papers pertinent to the interest of the Division are submitted. Suggestions and questions should be directed to Dr. Stanley T. Wlodek, Chairman E&M Division, c/o Stellite Division, Cabot Corporation, 1020 West Park Avenue, Kokomo, Ind. 46901.

Industrial Electrolytic Division Symposium Plans

Anodes for the Electrolytic Industries

This Symposium will cover metal, graphite and other nonconsumable anodes for the aqueous electrolytic industries. Papers are solicited covering anode materials, design, preparation, production, economics, mechanisms and operating characteristics in use. Suggestions and inquiries should be directed to the Chairman; Dr. W. C. Gardiner, Crawford and Russell, Inc., Stamford, Conn. 06904; or to the Co-Chairman, Dr. P. A. Danna, Olin Corporation, Research Center, 275 Winchester Avenue, New Haven, Conn. 06504.

Theoretical Electrochemistry Division

General Session

The Theoretical Electrochemistry Division will hold a General Session at the Spring 1971 Meeting to be held in Washington, D. C., May 9-14, 1971. Included in the program will be a panel discussion on the topic "Are Universities Meeting the Current Employment Needs in Electrochemistry"? For further information contact the session chairman, Dr. Christie G. Enke, Dept. of Chemistry, Michigan State University, East Lansing, Mich. 48823.

75-Word Abstract Form
WASHINGTON, D.C. MEETING
MAY 9-14, 1971

ABSTRACT NO. .....
(do not write in this space)

The Electrochemical Society, Inc.,
30 East 42 St., New York, N. Y. 10017

.....
(Title of paper)

.....

.....
(Authors) (Underline name of author presenting paper)

.....
(Business Affiliation)

.....
(Address) (Tel. No.)

.....
ECS Division

.....
and Symposium

Papers presented before a national technical meeting become the property of the Society and may not be published elsewhere without written permission of the Society. Papers presented at national technical meetings must be authored by a member or sponsored by an active member.

.....
Insert name of Society member author or sponsor

(Type abstract in this area—double spaced.)

For Office Use

75-word Abstract sent to: .....

Date Extended Abstract rec'd: .....

Do you require any audiovisual equipment?

☐ 3¼ x 4 in. slide projector

☐ 35 mm (2 x 2 in.) slide projector

☐ other (specify) .....

Is a full length paper on this work to be submitted for Society Journal publication?

☐ Yes ☐ No

THE ELECTROCHEMICAL SOCIETY PATRON MEMBERS

Aluminum Co. of Canada, Ltd., Montreal, Que., Canada

Dow Chemical Co.
Inorganic Chemicals Dept., Midland, Mich.

General Electric Co.
Battery Business Section, Gainesville, Fla.
Chemical Laboratory, Knolls Atomic Power Laboratory, Schenectady, N. Y.
Electronic Capacitor & Battery Dept., Irmo, S. C.
Lamp Div., Cleveland, Ohio
Materials & Process Laboratory, Large Steam Turbine-Generator Dept., Schenectady, N.Y.
Nucleonics Laboratory, Pleasanton, Calif.
Research and Development Center, Physical Chemistry Laboratory, Solid State Physics Laboratory, Schenectady, N.Y.

The International Nickel Co., Inc., New York, N. Y.

Olin Corporation
Chemicals Div., Research Dept., New Haven, Conn.

Union Carbide Corp.
Divisions:
Carbon Products Div., New York, N. Y.
Consumer Products Div., New York, N. Y.

Westinghouse Electric Corp.
Electronic Tube Div., Elmira, N. Y.
Lamp Div., Bloomfield, N. J.
Molecular Electronics Div., Elkridge, Md.
Research Laboratories, Pittsburgh, Pa.
Semiconductor Div., Youngwood, Pa.

THE ELECTROCHEMICAL SOCIETY SUSTAINING MEMBERS

Airco Speer Electrodes and Anodes, St. Marys, Pa.

Allen-Bradley Co., Milwaukee, Wis.

Allied Chemical Corp., Industrial Chemicals Division, Solvay, N. Y.

Aluminum Co. of America, New Kensington, Pa.

American Cyanamid Co., Stamford Research Laboratories, Stamford, Conn.

American Gas & Chemicals, Inc., New York, N. Y.

American Metal Climax, Inc., New York, N. Y.

American Potash & Chemical Corp., Los Angeles, Calif.

American Smelting and Refining Co., South Plainfield, N. J.

American Zinc Co., St. Louis, Mo.

The M. Ames Chemical Works, Inc., Glens Falls, N. Y.

Ampex Corp., Redwood City, Calif.

Applied Electrochemistry Inc. Mountain View, California

Beckman Instruments, Inc., Fullerton, Calif.

Bell Telephone Laboratories, Inc., Murray Hill, N. J. (2 memberships)

Bethlehem Steel Corp., Bethlehem, Pa. (2 memberships)

Boeing Co., Seattle, Wash.

Burndy Corp., Norwalk, Conn.

Canadian Industries Ltd., Montreal, Que., Canada

Carborundum Co., Niagara Falls, N. Y.

Chrysler Corp., Detroit, Mich.

Clevite Corp., Burgess Battery Div., Freeport, Ill. (2 memberships)

Cominco Ltd., Trail, B. C., Canada

Dargo Technical Research Ltd. London N.W.9, England

The Detroit Edison Co., Detroit, Mich.

Diamond Shamrock Corp., Painesville, Ohio

Wilbur B. Driver Co., Newark, N. J.

E. I. du Pont de Nemours & Co., Inc., Wilmington, Del.

Eagle-Picher Industries, Inc., Electronics Div., Joplin, Mo.

Eastman Kodak Co., Rochester, N. Y.

Electrode Corporation Chardon, Ohio

Eltra Corp., Prestolite Div., Toledo, Ohio
C&D Batteries, Conshohocken, Pa.

Engelhard Industries, Inc., Newark, N. J.

The Eppley Laboratory, Inc., Newport, R. I.

ESB Inc., Philadelphia, Pa. (2 memberships)

Esso Research and Engineering Co., Engineering Technology Div., Florham Park, N. J.

Exmet Corp., Bridgeport, Conn.

SUSTAINING MEMBERS (CONTINUED)

Fairchild Semiconductor Corp.,
Palo Alto, Calif.

Falconbridge Nickel Mines Ltd.,
Thornhill, Ont., Canada

FMC Corp.,
Inorganic Chemicals Div.,
Buffalo, N. Y.
Inorganic Chemicals Div.,
South Charleston, W. Va.

Foote Mineral Co.,
Exton, Pa.

Ford Motor Co.,
Dearborn, Mich.

General Motors Corp.,
AC Electronics Div., Milwaukee, Wis.
Allison Div., Indianapolis, Ind.
Delco-Remy Div., Anderson, Ind.
Research Laboratories Div., Warren, Mich.

General Telephone & Electronics Laboratories, Inc., Bayside, N. Y.

Globe-Union, Inc.,
Milwaukee, Wis.

B. F. Goodrich Chemical Co.,
Cleveland, Ohio

Gould-National Batteries, Inc.,
Minneapolis, Minn.

Great Lakes Carbon Corp.,
New York, N. Y.

Harshaw Chemical Co.,
Cleveland, Ohio (2 memberships)

Hill Cross Co., Inc.,
West New York, N. J.

Honam Electric Industrial Co.,
Kwangju City, Korea

Honeywell, Inc.,
Minneapolis, Minn.

Hooker Chemical Corp.,
Niagara Falls, N. Y. (2 memberships)

HP Associates,
Palo Alto, Calif.

Hughes Research Laboratories, Div. of Hughes Aircraft Co., Malibu, Calif.

International Business Machines Corp.,
New York, N. Y.

International Minerals & Chemical Corp.,
Skokie, Ill.

IRC, Division of TRW, Inc.,
Philadelphia, Pa.

Jones & Laughlin Steel Corp.,
Pittsburgh, Pa.

K. W. Battery Co.,
Skokie, Ill.

Kaiser Aluminum & Chemical Corp.,
Div. of Metallurgical Research,
Spokane, Wash.

Kawecki Chemical Co.,
Boyertown, Pa.

Kennecott Copper Corp.,
New York, N. Y.

Leesona Moos Laboratories, Div. of Leesona Corp., Great Neck, N. Y.

Arthur D. Little, Inc.,
Cambridge, Mass.

Lockheed Aircraft Corp.,
Missiles & Space Div.,
Sunnyvale, Calif.

Mobil Oil Corp.,
Dallas, Texas

Molybdenum Corporation of America,
New York, N. Y.

Monsanto Chemical Co.,
St. Louis, Mo.

Motorola Inc.,
Phoenix, Ariz.

M&T Chemicals Inc.,
Detroit, Mich.

Nalco Chemical Co.,
Chicago, Ill.

National Cash Register Co.,
Dayton, Ohio

National Lead Co.,
New York, N. Y.

National Steel Corp.,
Weirton, W. Va.

Nortec Electronics Corp.,
Santa Clara, Calif.

North American Rockwell Corp.,
El Segundo, Calif.

Northern Electric Co.,
Montreal, Que., Canada

Norton Research Corp.,
Cambridge, Mass.

Nova Devices, Inc.
New York, N. Y.

Owens-Illinois Glass Co.,
Toledo, Ohio

Park Electrochemical Corp.,
Great Neck, N. Y.

Pennwalt Corp.,
Philadelphia, Pa.

Phelps Dodge Refining Corp.,
Maspeth, N. Y.

Philips Laboratories, Inc.,
Briarcliff Manor, N. Y.

PPG Industries, Inc.,
Chemical Div.,
Pittsburgh, Pa.

Radio Corp. of America,
Electronic Components and Devices,
Lancaster, Pa.

Republic Foil Inc.,
Danbury, Conn.

Reynolds Metals Co.,
Richmond, Va.

Shawinigan Chemicals Ltd.,
Montreal, Que., Canada

Sonotone Batteries,
Marathon Battery Co.,
Cold Spring, N. Y.

Sprague Electric Co.,
North Adams, Mass.

Stackpole Carbon Co.,
St. Marys, Pa.

The Standard Oil Company of Ohio,
Cleveland, Ohio

Stauffer Chemical Co.,
Dobbs Ferry, N. Y.

Syncro Corp.,
Oxford, Mich.

Teletype Corp.
Skokie, Ill.

Texas Instruments Inc.,
Dallas, Texas

3 M Company
St. Paul, Minn.

Titanium Metals Corp. of America,
Henderson, Nev.

Tyco Laboratories, Inc.,
Waltham, Mass.

Udylite Corp.,
Detroit, Mich. (4 memberships)

United States Steel Corp.,
Pittsburgh, Pa.

Varian Associates,
Palo Alto, Calif.

Western Electric Co., Inc.,
Chicago, Ill.

Wyandotte Chemicals Corp.,
Wyandotte, Mich.

Yardney Electric Corp.,
New York, N. Y.

Zenith Radio Corp.,
Chicago, Ill.